

2. Internationale Konferenz

Euro

Hybrid

Materials and Structures

20.–21. April 2016

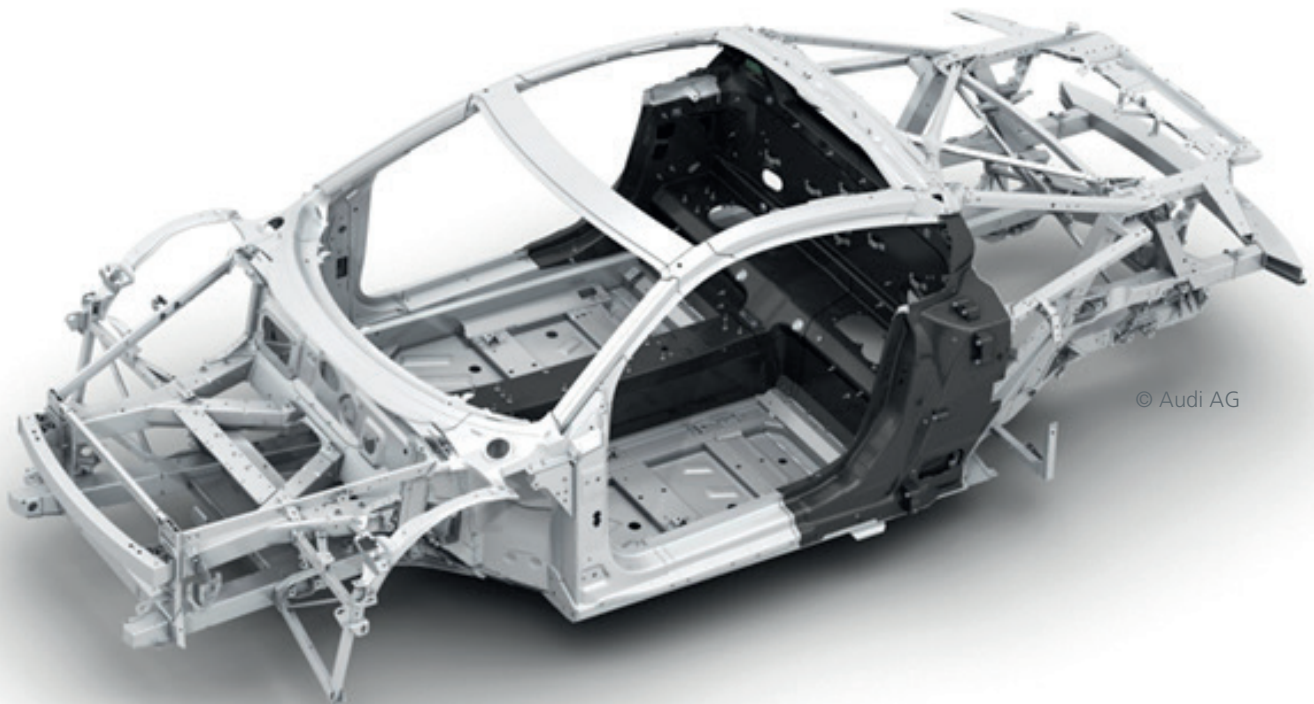
Kaiserslautern,

Institut für Verbundwerkstoffe

Proceedings



Institut für
Verbundwerkstoffe



© Audi AG

www.hybrid.inventum.de

DGM

PREFACE

Euro Hybrid Materials & Structures 2016

It is more and more commonly accepted that energy efficiency and the sparing use of natural resources are playing an even bigger role in the development of modern systems. This applies to vehicles of any type as well as to industrial machinery and buildings. Often, innovative materials act as trailblazers for the implementation of new technologies. To fulfill all requirements, high-performance components can often no longer be designed by using just one single material or material class. In order to use the materials as best as possible, several different materials are usually mixed in one component, especially in the field of lightweight design. If these combinations of materials are joined inherently, they are called multi material design products or hybrid structures. These place special requirements on joining technology, design methods and manufacturing and are challenging in other aspects, too.

This conference and the manuscripts published in this proceedings, covers the full range of hybrid design aspects, from materials to design, manufacturing and application. An effective, resource-conserving use of materials as well as knowledge about how a material or component behaves is absolutely required if you want to implement technologically demanding solutions not just for moving systems.

The goal of the conference is the exchange of information both among the disciplines involved and between the scientific community and industrial users. Kaiserslautern with its Institute of Composite Materials in south-western Germany has been chosen as venue as an important location not only for composite materials but also for materials related chairs at the Technical University and several small and medium enterprises in the field of composite materials. However, the composite community recognizes more and more that best solutions are often realized by intelligent combinations of composite materials with metals. The combination of different materials in hybrid structures and material systems yields to some specific issues. These are addressed in thematic sessions focusing on special topics. Within the proceedings each session is represented by its own chapter.

Chapters with manuscripts of the presentations on recent results from research and development are:

Chapter 1- Interface:

What happens in the interface between the two materials?

Chapter 2 - Corrosion and Residual Stresses:

How about galvanic corrosion and thermal residual stresses in the contact zone of different materials?

Chapter 3 - Characterization:

How to characterize and test hybrid materials?

Chapter 4 - Design:

What is a suitable design and dimensioning method for hybrid structures?

Chapter 5 - Machining and Processing:

How to machine and process hybrid structures and materials?

Chapter 6 - Component Manufacturing:

What is a suitable manufacturing route for hybrid structures?

Chapter 7 - Non-Destructive Testing and Quality Assurance:

How to assure the quality of material and structures?

Chapter 8 - Joining:

How to join components of different materials?

We wish you a lot of new inspirations and solutions for your technical challenges and looking forward to seeing you,

Prof. Dr.-Ing. Joachim M. Hausmann,
Institut für Verbundwerkstoffe GmbH, Kaiserslautern

Prof. Dr.-Ing. Marc Siebert,
PFH – Private Hochschule Göttingen

The Conference Chairs and Editors of the proceeding.

CONTENTS

PREFACE	1
 CHAPTER 1: INTERFACE	
DELAMINATION IN UD-CFRP STEEL HYBRID LAMINATES – PART 1: METHOD IMPLEMENTATION AND INTERFACE VARIATION M. Gall, L. Kregl, G. M. Wallner, C. Eyßell, R. W. Lang, B. Strauß	8
DELAMINATION IN UD-CFRP STEEL HYBRID LAMINATES – PART 2: EFFECT OF DAMP-HEAT AGING L. Kregl, M. Gall, G.M. Wallner, C. Eyßell, R.W. Lang, B. Strauß	12
 CHAPTER 2: CORROSION AND RESIDUAL STRESSES	
INVESTIGATION OF THE ELECTROCHEMICAL CORROSION BEHAVIOUR AND FE-MODELLING OF AN ALUMINUM/STEEL BLIND RIVET JOINT M. Mandel, L. Krüger	17
EXPERIMENTAL INVESTIGATIONS ON RESIDUAL STRESSES DURING THE FABRICATION OF INTRINSIC CFRP-STEEL LAMINATES R. Prussak, D. Stefaniak, C. Hühne, M. Sinapius	22
 CHAPTER 3: CHARACTERIZATION	
INFLUENCE OF MATERIAL PARAMETERS ON THE TENSILE FORCE OF INTEGRAL ALUMINUM CFRP HYBRID STRUCTURES FABRICATED BY CASTING TECHNOLOGY Kunze, Arne I; Clausen, Jan; Van der Auwera, Robin; von Hehl, Axel; Zoch, Hans-Werner; Busse, Matthias	30
LASER-BASED JOINING OF THERMOPLASTICS TO METALS: INFLUENCE OF VARIED AMBIENT CONDITIONS ON JOINT PERFORMANCE AND MICROSTRUCTURE Klaus Schrickler, Martin Stambke, Jean Pierre Bergmann, Kevin Bräutigam	36
CHARACTERIZATION OF INTERFACE PROPERTIES OF FIBERMETAL-LAMINATES (FML) WITH OPTIMIZED SURFACES Matthias Stoll, Kay André Weidenmann.....	38
MULTIFUNCTIONAL METAL-CARBON-FIBER COMPOSITES FOR DAMAGE TOLERANT AND HIGHLY CONDUCTIVE LIGHTWEIGHT STRUCTURES B. Hannemann, S. Backe, S. Schmeer, F. Balle, U. P. Breuer	44
ALGORITHMS FOR THE DETERMINATION OF CURVATURE FROM 3D μ -CT IMAGES – A COMPARISON Pascal Pinter, Benjamin Bertram, Kay André Weidenmann	50
MECHANICAL PROPERTIES OF CONTINUOUSLYDISCONTINUOUSLY FIBER REINFORCED HYBRID SHEET MOLDING COMPOUNDS Anna Trauth, Kay André Weidenmann.....	57

EXPERIMENTAL INVESTIGATION OF AUTOMOTIVE COMPONENTS CONSISTING OF HYBRID FRP-METAL MATERIAL SYSTEMS UNDER CRASH LOADING M. Dlugosch , J. Ihle, D. Lukaszewicz, J. Fritsch, S. Hiermaier.....	63
DEEP- AND STRETCH-FORMING OF STEEL/POLYMER/STEEL LAMINATES Mohamed Harhash, Adele Carrado, Heinz Palkowski.....	69
EXPERIMENTAL TESTING AND ANALYSIS OF THE ENERGY ABSORPTION OF AXIAL-LOADED METAL-CFRP-HYBRID COMPONENTS Corin Reuter, Pascal Bartelt, Manel Ellouz, Thomas Kordisch, Thomas Tröster.....	75
TECHNOLOGICAL AND ECONOMICAL ASPECTS OF NOVEL HYBRID JOINING STRATEGIES BASED ON INTEGRATED FIBRE PENETRATING REINFORCING ELEMENTS Thomas Caspari, Daniel Huelsbusch, Matthias Haack, Andreas Solbach, Claus Emmelmann and Frank Walther	81
RELIABILITY STUDIES ON MOLYBDENUM-COPPERMULTILAYER COMPOSITES Martin Seiss, Tobias Mrotzek, Wolfram Knabl	86
CHAPTER 4: DESIGN	
METHODICAL APPROACH FOR THE DEVELOPMENT OF HYBRID VEHICLE STRUCTURES MADE OF FIBER REINFORCED PLASTICS AND METAL X.F. Fang, M. Grote.....	92
DEVELOPMENT, MANUFACTURING AND TESTING OF A CFRP BELLOWS COUPLING FOR POWERTRAIN APPLICATIONS C. Oblinger, M. Jelinek, H. Lang, A. Baeten, K. Drechsler, G. Reinhart	97
DEVELOPMENT, MANUFACTURING AND TESTING OF A CFRP METAL HYBRID GRIPPER FOR HIGHLY DYNAMIC MANIPULATION PROCESSES M. Jelinek, C. Oblinger, A. Baeten, K. Drechsler, G. Reinhart	105
ADHESION OF POLYIMIDE FOILS IN HYBRID LAMINATES WITH A THERMOPLASTIC MATRIX Maik Trautmann, Daisy Nestler, Guntram Wagner, Camilo Zopp, Lothar Kroll	112
CHAPTER 5: MACHINING AND PROCESSING	
JOINING AND FORMING OF HYBRID ASSEMBLED COMPOSITES WITH SENSORY FUNCTION Alexander Graf, Verena Kräusel, Dirk Landgrebe, Ricardo Decker, Lothar Kroll	118
EFFICIENT AND APPROPRIATE LASERPROCESSING OF HIGHPERFORMANCE MATERIAL Fürst, A., Hipp, D., Klotzbach, A., Hauptmann, J, Wetzig, A., Beyer, E.	125
THERMOPLASTIC AUTOMATED FIBER PLACEMENT FOR MANUFACTURING OF METAL-COMPOSITE HYBRID PARTS S. Ehard, A. Mader, E. Ladstätter, K. Drechsler	129
PRODUCTION, CHARACTERISATION AND PROCESSING OF METAL PLASTIC COMPOSITES WITH MODIFIED CORE MATERIALS M. Wuehrl, M. Klaerner, L. Kroll, M. Riemer, R. Müller, D. Landgrebe, C. A. Geweth, S. Marburg.....	135

HYBRIDRTM - QUALITY CONTROLLED MANUFACTURING OF HYBRID MATERIAL COMPOSITES THROUGH RESIN TRANSFER MOULDING E. Fauster, P. Hergan, R. Schledjewski	142
DEVELOPMENT OF NEW PROCESS CHAINS IN THE OPEN HYBRID LABFACTORY FOR HYBRID INTEGRAL COMPONENTS FOR AUTOMOTIVE MASS PRODUCTION Robin Van der Auwera, Tobias Gebken, Alexander Fürst, Julian Steinberg, Markus Kühn, Franz-Josef Wöstmann, Matthias Busse.....	146
COMPUTATIONAL ANALYSIS OF POLYURETHANE FOAM EXPANSION PROCESS IN FIBER REINFORCED SANDWICH STRUCTURES J. Tröltzsch, I. E. Ireka, D. Niedziela, K. Steiner, K. Schäfer, F. Helbig and L. Kroll	151
MANUFACTURING OF THERMOPLASTIC FIBER-METAL-LAMINATES BASED ON REACTIVELY PROCESSED POLYAMIDE 6 Sebastian Gödde, Cahit Arik, Kay Weidenmann, Frank Henning	157
CHAPTER 6: COMPONENT MANUFACTURING	
OPTIMISED AND COST-EFFICIENT HYBRID SMC STRUCTURES FOR AIRCRAFT COMPONENTS M. Hentschel, M. Fette, J. Wulfsberg, A. Herrmann, N. Stoess.....	164
HYBRID COMPOSITES OF PLASTIC AND ALUMINUM FOAM C. Fiebig, M.E. Steffen, S. Caba, M. Koch	170
POLYMER ALUMINUM HYBRID STRUCTURE JOINT BY INJECTION MOLDING Achim Frick, Steffen Aldinger, Marcel Spadaro	178
INCREASING THE MECHANICAL PROPERTIES OF METALPLASTIC-HYBRIDS BY IMPROVEMENT OF THE INTERFACE – A MICROSCOPIC APPROACH Saskia Müller, Michael Brand, Klaus Dröder, Leif Steuernagel, Dieter Meiners	184
AN INTEGRATIVE APPROACH TOWARDS IMPROVED PROCESSABILITY AND PRODUCT PROPERTIES IN AUTOMATED MANUFACTURING OF HYBRID COMPONENTS K. Dröder, R. Schnurr, J. Beuscher, K. Lippky, A. Müller, M. Kühn, F. Dietrich, S. Kreling, K. Dilger	188
DEVELOPMENT OF A BRACKET ELEMENT WITH A HYBRID METHOD OF CONSTRUCTION (CFRP/TI) Holger Büttemeyer, Andreas Solbach, Claus Emmelmann, Axel S. Herrmann	194
CHAPTER 7: NON-DESTRUCTIVE TESTING AND QUALITY ASSURANCE	
THERMOGRAPHY ASSISTED CHARACTERISATION OF PRODUCTION-INDUCED DEFECTS IN CFRP AND THEIR INFLUENCE ON THE MECHANICAL BEHAVIOUR Jannik Summa, Michael Schwarz, Simon Bernarding, Prof. Hans-Georg Herrmann	201
USING NONDESTRUCTIVE TESTING METHODS TO CHARACTERISE PRODUCTION-INDUCED DEFECTS IN A METAL-CFRP HYBRID STRUCTURE Michael Schwarz, Jannik Summa, Hans-Georg Herrmann	207
ENERGY DISPERSIVE RESIDUAL STRESS DETERMINATION B. Breidenstein, B. Denkena, V. Prasanthan	211
TESTING ULTRASONIC SH WAVES TO ESTIMATE THE QUALITY OF ADHESIVE BONDS IN SMALL HYBRID STRUCTURES Steven Quirin, Selina Neuhaus, Hans-Georg Herrmann	216

CHAPTER 8: JOINING

REACTIVE MULTILAYER SYSTEMS: A NEW TECHNOLOGY FOR JOINING THERMOPLASTICMETAL-HYBRID-STRUCTURES E. Pflug, R. Pautzsch, G. Dietrich, A. Klotzbach, S. Braun, A. Leson	225
INDUCTIVE JOINING OF GLASS FIBER REINFORCED POYPROPYLENE AND METAL Martina Hümbert, Peter Mitschang	230
SINGLE SIDE RESISTANCE SPOT WELDING OF POLYMERMETAL-HYBRID STRUCTURS Martin Bielenin, Konstantin Szallies, Jean Pierre Bergmann, Christian Neudel	236
ANALYSIS OF A MECHANICALLY STRESSED JOINT IN A MULTI-MATERIAL-SYSTEM Arne Busch, Robert Brandt	241
EXPERIMENTAL INVESTIGATION OF DIRECT ADHESION OF CFR-THERMOPLAST ON STEEL Ferhat Yüksel, Roland Hinterhölzl, Klaus Drechsler	247
ENHANCING THE TENSILE STRENGTH IN HYBRID METAL-FRP MATERIALS THROUGH VARIOUS INTERLOCKING STRUCTURE PATTERNS Michael Brand, Markus Kühn, Anke Müller, Klaus Dröder	251
EFFECTS OF MELTING LAYERS ON NANOBONDING USING REACTIVE MULTILAYER NANOFOILS S. Sen, G. Langels, M. Lake, P. Schaaf	257
BONDING BY MICROBRACING: A DIE CONCEPT FOR THE QUANTIFICATION OF INFLUENCING VARIABLES USING MULTI-COMPONENT HIGH PRESSURE DIE CASTING (M-HPDC) P. Messer, A. Bührig-Polaczek, U. Vroomen	262
INDEX OF AUTHORS	268

CHAPTER 1:

INTERFACE

DELAMINATION IN UD-CFRP STEEL HYBRID LAMINATES - PART 1: METHOD IMPLEMENTATION AND INTERFACE VARIATION

M. Gall^{1*}, L. Kregl¹, G. M. Wallner¹, C. Eyßell², R. W. Lang¹, B. Strauß²

¹Johannes Kepler University Linz - Institute of Polymeric Materials and Testing, Austria
²voestalpine Stahl GmbH, Linz, Austria

ABSTRACT: Hybrid laminates composed of carbon fiber reinforced plastic (cfrp) composites and steel sheets are increasingly being investigated and applied for multi-material lightweight automobile structures. Crucial for the in-service performance of hybrid laminates is the interfacial adhesion between cfrp and metal. Hence, part 1 of this paper series describes the implementation of a quantitative adhesion testing methodology and data reduction scheme for cfrp/steel hybrid laminates. Various laminate configurations with different interface treatments and inter-ply were investigated with the proposed method.

Quasi-static mode I testing revealed a clear ranking of the different laminate configurations in terms of interlaminar mode I fracture toughness G_{Ic} . Laminates with no or ineffective inter-ply were shown to have a lower fracture toughness than a pure unidirectional cfrp reference laminate. Fracture toughness values of these laminate types ranged from 0.08 to 0.17 kJ/m², while the cfrp reference achieved $G_{Ic} = 0.28$ kJ/m². Incorporation of a compatible polymeric material serving as a toughening inter-ply between steel substrate and cfrp composite layer allowed for increasing the fracture toughness by one order of magnitude reaching values up to $G_{Ic} = 3.0$ kJ/m².

Conducting cyclic tests with hybrid laminate specimens without effective reinforcement of the cfrp/steel interface was not possible in a reproducible way due to lacking interlaminar toughness and restrictions imposed by the chosen testing machine. However, tougher laminates like the cfrp reference and the hybrid/non-polar series were successfully fatigue tested and reproduced the material ranking observed in quasi-static mode I testing. The hybrids with non-polar polymer inter-ply exhibited the best fatigue performance characterized by the small slope of their Paris fits and their ability to maintain lower crack growth rates than other laminate structures at a given cyclic strain energy release rate range.

KEYWORDS: cfrp steel hybrid laminate, polymeric inter-ply, interlaminar fracture toughness, fatigue delamination, adhesion

1 INTRODUCTION

Hybrid laminates combining carbon fiber reinforced plastic (cfrp) composites with steel sheets offer a high potential for multi-material lightweight structures as currently developed in the automotive engineering sector. Due to the different structural features and the properties of metals and polymers the critical layer is often the interface. A number of methods for improving the interfacial adhesion in hybrid laminates have been proposed in the literature, including mechanical, chemical and electrochemical surface treatments of the metallic laminate component [1]. The utilization of polymeric coupling agents and toughening inter-ply instead of methods focusing on the metal part of the hybrid laminate is also regarded a promising way of in-

creasing interfacial adhesion between cfrp and steel [1, 2]. However, adequate standard testing procedures to characterize the adhesion under service relevant loading conditions (including superimposed environmental and mechanical loading) are currently not available and established. Hence, the main goal of part 1 of this paper series was to develop and apply a quantitative adhesion testing methodology and data reduction scheme for cfrp/steel hybrid laminates. With this fracture mechanics methodology various laminates with different interface treatments and toughening inter-ply were investigated under both mode I quasi-static and mode I cyclic loading conditions. Part 2 of this paper series deals with the effect of damp-heat aging on the interlaminar fracture toughness of cfrp/steel hybrid laminates.

* Corresponding author: Institute of Polymeric Materials and Testing, Johannes Kepler University Linz, Altenberger Straße 69, 4040 Linz, Austria, +43732 2468 6626, markus.gall@jku.at

2 EXPERIMENTAL

2.1 MATERIALS AND SPECIMENS

The hybrid laminates utilized for this study were fabricated from sheets of cold-rolled hot-dip galvanized dual phase steel (DP600) with a nominal thickness of 810 μm supplied by voestalpine Stahl GmbH and unidirectional (UD) carbon fiber reinforced plastic (cfrp) prepregs with a toughened epoxy matrix, a nominal fiber volume content of 60% and a nominal ply-thickness of 220 μm . All cfrp layers of the fabricated hybrid specimens comprised six unidirectional prepreg plies ($[0^\circ]_6$). A surface phosphatization treatment was applied to the steel component of one group of hybrid laminates (see Table 1).

Three different types of polymeric materials were used as toughening inter-ply between the cfrp and steel components of the respective hybrid laminate groups listed in Table 1. The first inter-ply was based on polar polymers and applied onto the steel substrate by a powder coating process. The resulting inter-ply thickness was approx. 200 μm . The remaining two inter-ply were adhesive films based on non-polar polymers with a nominal thickness of 100 μm .

A pure cfrp laminate consisting of 12 UD-ply was fabricated as well and served as a reference for comparison with the hybrid laminates. The crack starter inserts used in all laminate types were taken from a 12 μm thin non-adhesive film made of ethylene-tetrafluoroethylene (ETFE).

Table 1: Laminate configurations

Designation	Laminate configuration
cfrp	cfrp ₆ /crack starter/cfrp ₆
hybrid	cfrp ₆ /steel/crack starter/cfrp ₆
hybrid/phosphate	cfrp ₆ /steel (phosphated)/crack starter/cfrp ₆
hybrid/polar	cfrp ₆ /polar inter-ply/steel/polar inter-ply/crack starter/cfrp ₆
hybrid/non-polar-1	cfrp ₆ /non-polar inter-ply 1/steel/non-polar inter-ply 1/crack starter/cfrp ₆
hybrid/non-polar-2	cfrp ₆ /non-polar inter-ply 2/steel/non-polar inter-ply 2/crack starter/cfrp ₆

All laminates were fabricated in a manual lay-up process and cured in a vacuum bag for 40 min at 160°C. Double cantilever beam (DCB) specimens with a length of 150 mm, a width of 25 mm and a thickness between 3 and 4.5 mm (depending on the laminate stacking configuration) were cut out of laminate panels and milled to shape in consistency with ASTM D 5528 [3]. Load introduction blocks

made of steel were adhesively bonded onto the pre-cracked end of the DCB specimens. The initial delamination length (crack length) a_0 was approx. 48 mm. The lateral specimen face was covered with white correction marker fluid in order to facilitate optical crack tracking. DCB specimens were used for both quasi-static and cyclic test.

2.2 METHODS

Quasi-static and cyclic mode I testing was carried out at ambient temperature using an all-electric dynamic Instron ElectroPuls E3000 testing machine equipped with a 5 kN load cell. Optical crack length measurements were facilitated by a micro-grid calibrated digital camera system.

2.2.1 Quasi-static testing

A constant cross-head speed of 3 mm/min was chosen for all quasi-static mode I tests in consistency with ASTM D 5528 [3]. The image acquisition interval was set between 5 and 10 s.

The interlaminar fracture toughness was calculated in terms of critical strain energy release rate G_{Ic} according to ASTM D 5528 [3] as:

$$G_{Ic} = \frac{n \cdot P_{5\%} \cdot \delta_{5\%}}{2 \cdot b \cdot a_0} \quad (1)$$

In equation (1) the factor n is the compliance calibration parameter defined as the slope of a linear fit in a double-logarithmic plot of specimen compliance C (displacement δ divided by load P) versus crack length a . $P_{5\%}$ and $\delta_{5\%}$ are the load and displacement values in the recorded load-displacement diagram where the initial specimen compliance has increased by 5%. The factor b is the specimen width and a_0 is the initial crack length introduced by the crack starter insert.

2.2.2 Cyclic testing

Mode I fatigue delamination experiments were carried out under load control using a testing frequency of 5 Hz and a load ratio (R-ratio) of 0.5 (see equation (2)) with cyclic peak loads between 40 and 160 N. The R-ratio used for this work is defined as:

$$R = \frac{P_{cyclic,min}}{P_{cyclic,max}} \quad (2)$$

where $P_{cyclic,min}$ and $P_{cyclic,max}$ are the minimum and maximum loads detected during one loading cycle, respectively. For the mode I cyclic strain energy release rate range ΔG_I a linear formulation was chosen as follows:

$$\Delta G_I = G_{I,\max} - G_{I,\min} \quad (3)$$

where $G_{I,\max}$ and $G_{I,\min}$ are the maximum and minimum mode I cyclic strain energy release rate, respectively. The values of $G_{I,\max}$ and $G_{I,\min}$ are calculated using equation (1) and substituting the cyclic maximum and minimum values of load P and displacement δ for $P_{5\%}$ and $\delta_{5\%}$ as well as the current delamination length a_i for a_0 . The image acquisition interval in cyclic testing was chosen between 10 s and 15 min depending on the crack propagation speed.

3 RESULTS & DISCUSSION

3.1 MODE I INTERLAMINAR FRACTURE TOUGHNESS

Quasi-static mode I testing revealed a clear ranking of the different laminate configurations in terms of interlaminar mode I fracture toughness G_{Ic} as depicted in Fig. 1. Laminates with no or ineffective inter-ply exhibited a lower fracture toughness than the cfrp reference laminate. G_{Ic} values of these laminate types were ranging from 0.08 kJ/m² for the hybrid/phosphate configuration to 0.17 kJ/m² for the hybrid/polar laminate. The cfrp reference achieved $G_{Ic} = 0.28$ kJ/m². It is therefore obvious that the polar polymeric inter-ply did not establish a reinforcement of the cfrp/steel interface under the given laminate fabrication parameters. Delamination occurred in a pure adhesive failure manner as observed for the sample groups “hybrid” and “hybrid/phosphate”.

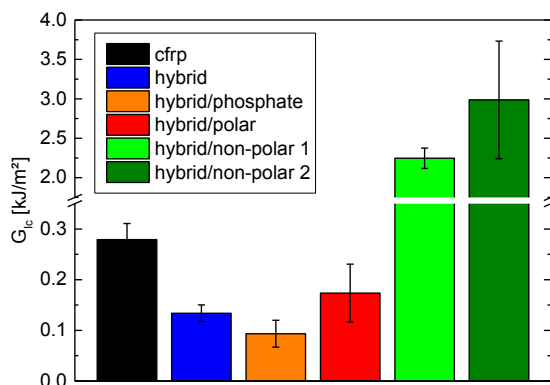


Fig. 1: Interlaminar fracture toughness G_{Ic} of cfrp and hybrid laminates.

However, incorporation of a 100 μ m thin film of a compatible non-polar polymeric material serving as a toughening inter-ply between steel substrate and cfrp layer allowed for increasing the fracture toughness of hybrid laminates by one order of magnitude compared to the reference laminate (note the broken vertical axis in Fig. 1). The two sample groups with non-polar polymeric inter-ply reached G_{Ic} values up to 3.0 kJ/m² which character-

ize the significant improvement of interfacial adhesion. Interlaminar fracture toughness values of this magnitude are comparable to or even higher than reported G_{Ic} values of UD cfrp laminates with toughening polymeric inter-ply [4-6].

3.2 MODE I FATIGUE DELAMINATION RESISTANCE

Hybrid laminate specimens without effective reinforcement of the cfrp/steel interface (hybrid, hybrid/phosphate and hybrid/polar laminate configurations) could not be tested under cyclic mode I loading conditions in a reproducible way with the chosen machine setup. This was due to lacking interlaminar toughness of the fabricated DCB specimens (in case of displacement control) and insufficient sensitivity and precision of the employed testing machine setup with regards to very small force amplitudes (in case of load control). The utilization of a smaller testing machine is recommended for this purpose. However, tougher laminates like the cfrp reference and the hybrid/non-polar series were successfully fatigue tested and reproduced the material ranking observed in quasi-static mode I testing (see Fig. 2). The fatigue diagram in Fig. 2 shows the recorded crack propagation rate in mm/cycle plotted versus the cyclic strain energy release rate range ΔG_I in a double logarithmic representation.

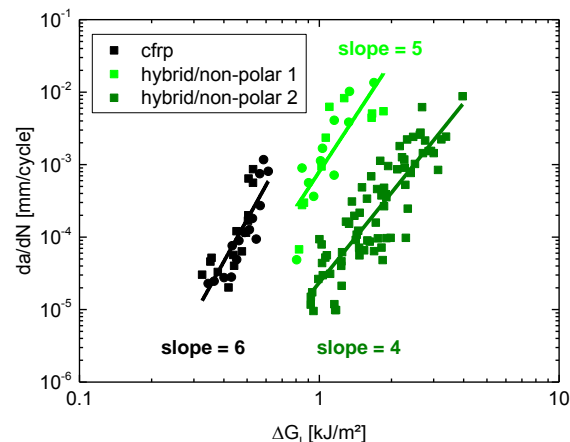


Fig. 2: Fatigue delamination diagram of cfrp reference and hybrid laminates with non-polar polymer inter-ply.

The hybrids with non-polar inter-ply exhibited the best fatigue performance characterized by their ability to maintain lower crack growth rates at a given cyclic load range indicated by the respective data points being located further to the right-hand side in the fatigue diagram in Fig. 2. An additional benefit is the small slopes of their Paris fits which are 5 for the hybrid/non-polar 1 laminate and only 4 for the hybrid/non-polar 2 series compared to 6 for the cfrp reference. This proves the reduced sensitivity against fatigue delamination propagation and underlines the advantages gained by in-

corporation of a suitable polymeric inter-ply into the cfrp/steel interface. Regarding these results, a more thorough investigation into the contributions of each hybrid laminate component to interlaminar crack growth resistance, similar to those undertaken in the case of advanced fiber composites [7-9] seems worthwhile.

4 CONCLUSIONS

In part I of this paper series a fracture mechanics based approach for quantitative adhesion testing of mode I loaded cfrp/steel hybrid laminates was described and successfully applied to various laminate configurations. A clear ranking in terms of interlaminar fracture toughness was established. It was demonstrated that the interlaminar fracture toughness of cfrp/steel hybrid laminates can be increased by one order of magnitude via introducing a compatible non-polar polymeric inter-ply of only 100 μm thickness into the cfrp/steel interface. Additionally, the presence of such a polymeric inter-ply significantly improves the mode I fatigue delamination resistance of a cfrp/steel hybrid laminate.

5 ACKNOWLEDGEMENT

The presented work was performed as part of a collaborative research project of the Institute of Polymeric Materials and Testing (IPMT) of the Johannes Kepler University Linz (JKU) and voestalpine Stahl GmbH. The project was funded by the Austrian Research Promotion Agency (FFG).

REFERENCES

- [1] Sinmazcelik, T., Avcu, E., Bora, M. Ö., Coban, O.: *A review: Fibre metal laminates, background, bonding types and applied test methods*. Materials and Design 32, 3671-3685, 2011.
- [2] Reyes, G., Gupta, S.: *Manufacturing and mechanical properties of thermoplastic hybrid laminates based on DP500 steel*. Composites Part A: Applied Science and Manufacturing 40, 176-183, 2009.
- [3] ASTM: *Standard Test Method for Mode I Interlaminar Fracture Toughness of Unidirectional Fiber-Reinforced Polymer Matrix Composites (D 5528)*, ASTM International, PA, US, 2007.
- [4] Sela, N., Ishai, O. *Interlaminar fracture toughness and toughening of laminated composite materials: a review*. Composites 20, 423-435, 1989.
- [5] Sela, N., Ishai, O., Banks-Sills, L.: *The effect of adhesive thickness on interlaminar fracture toughness of interleaved CFRP specimens*. Composites 20, 257-264. 1989.

- [6] Matsuda, S., Hojo, M., Ochiai, S., Murakami, A., Akimoto, H., Ando, M.: *Effect of ionomer thickness on mode I interlaminar fracture toughness for ionomer toughened CFRP*. Composites Part A: Applied Science and Manufacturing 30, 1311-1319. 1999.
- [7] Lang, R. W., Heym, M., Tesch, H., Stutz, H.: *Influence of constituent properties on interlaminar crack growth in composites*. In: "High Tech – the Way into the Nineties" (Brunsch, K., Gölden, H.-D., Herkert, C.-M., Ed.). 261. 1986.
- [8] Altstädt, V., Lang, R. W.: *Influence of matrix properties on delamination fatigue crack growth in composites*. In: "New Generation Materials and Processes". (Saporiti, F., Merati, W., Peroni, L., Ed.). 385. 1988.
- [9] Cvitkovich, M., Lang, R.W.: *Polymer Matrix Effects on Interlaminar Crack Growth in Advanced Composites under Mixed-Mode Conditions*. In: "ECCM CTS2, Composites Testing and Standardisation", (Hogg, P. J., Schulte, K., Wittich, H., Ed.). 543 - 551, 1994.

DELAMINATION IN UD-CFRP STEEL HYBRID LAMINATES – PART 2: EFFECT OF DAMP-HEAT AGING

L. Kregl^{1*}, M. Gall¹, G.M. Wallner¹, C. Eyßell², R.W. Lang¹, B. Strauß²

¹ Johannes Kepler University Linz - Institute of Polymeric Materials and Testing, Austria
²voestalpine Stahl GmbH, Linz, Austria

ABSTRACT: Steel/composite-hybrids with varying inter-ply were investigated. A unidirectional carbon fiber reinforced prepreg with a toughened epoxy matrix and a nominal fiber content of 60 v% was applied to a cold-rolled steel sheet. As inter-ply both, polar and non-polar polymers were used. Furthermore, the steel surface was modified, e.g. via phosphatization. After damp-heat aging in climate chambers at 60°C and 85% r.h. the laminates were characterized by monotonous tensile testing. Therefore, a novel fracture mechanics testing methodology was implemented, which is described in part 1 of this paper series. As specimen the double cantilever beam geometry was used with fluoropolymer insertion layer as crack-starters. Significant deterioration of interlaminar properties of hybrid, hybrid/phosphated and hybrid/polar inter-ply laminates by damp-heat exposure was found. After 2000 hours the hybrid laminates without inter-ply exhibited premature failure without additional mechanical loading. In contrast, the aging performance of the hybrid with phosphated steel surface was significantly better. The initial critical energy release rate of 0.1 kJ/m² was reduced slightly. The best performance was obtained for the hybrid laminates with non-polar inter-ply, which exhibited a factor of more than 5 higher critical energy release rate.

KEYWORDS: cfrp/steel hybrid, damp-heat aging, adhesion, polymeric inter-ply

1 INTRODUCTION

Multimaterial systems e.g. the combination of carbon fiber reinforced plastics (cfrp) with steel, further called cfrp/steel hybrids, offer a high potential for lightweight structures and are gaining importance in the aircraft and automotive applications, combining beneficial properties of both, fiber reinforced polymers and metals. However, due to their different structural properties the critical layer of these structures is the interface between cfrp and steel, especially when the cfrp is directly applied on the steel surface. To enhance the adhesion performance literature offers approaches like surface treatment of the metal, the usage of adhesion promoters or the application of polymeric adhesives or adhesive films [1–5].

The adhesion performance is significantly affected by super-imposed mechanical and environmental loading. It is well known that humidity at elevated temperatures leads to physical and chemical changes in composite matrix materials and adhesives [6–8]. Hence, the main goal of part 2 of this paper series was to investigate the effect of damp-heat aging on the adhesion properties of

steel/composite-hybrids with and without inter-ply. Furthermore the effect of a non-polar and a polar inter-ply on the adhesion performance after damp heat aging should be examined. Therefore, a novel fracture mechanics testing methodology was used which is described in part 1 of this paper series.

2 EXPERIMENTAL

2.1 MATERIALS

The cfrp/steel hybrid was composed of a unidirectional carbon fiber reinforced plastic prepreg with an epoxy matrix, a nominal fiber content of 60 vol.-% and a layer thickness of 220 µm applied on a cold-rolled dual phase steel (DP600) supplied by voestalpine Stahl GmbH, with a nominal thickness of 810 µm. One test group had additional surface phosphatization prior to specimen preparation.

As toughening inter-ply, between the cfrp and steel component, two different polymeric materials were used. A non-polar thermoplastic polymer with a nominal thickness of 100 µm and a polar polymer with a nominal thickness of 80 µm. Initial cracks were introduced by insertion of a thin fluoro

* Corresponding author: Institute of Polymeric Materials and Testing, Johannes Kepler University Linz, Altenberger Straße 69, 4040 Linz, Austria, +43732 2468 6625, laura.kregl@jku.at

copolymer (ETFE) film during the lamination process.

As described in part 1 of this paper series double cantilever beam specimens (150 x 25 mm², referring to ASTM D5528 [9]) were produced through vacuum bag procedure with 40 minutes at 160°C curing schedule and milled to shape subsequently. Laminate configurations are listed in Table 1. Cfrp layering is identical for all laminates, consisting of 6 UD layers [0°]₆. Prior to testing, steel blocks for load application were adhered to the pre-cracked end of the specimens.

Table 1: Laminate configurations

Designation	Laminate configuration
hybrid	cfrp ₆ /steel/crack initiation layer/cfrp ₆
hybrid/phosphated	cfrp ₆ /steel(phosphated)/crack initiation layer /cfrp ₆
hybrid/non-polar	cfrp ₆ /non-polar inter-ply/steel/non-polar inter-ply/crack initiation layer /cfrp ₆
hybrid/polar	cfrp ₆ /non-polar inter-ply/steel/polar inter-ply/ crack initiation layer /cfrp ₆

2.2 DAMP-HEAT AGING

Damp-heat aging was carried out in a climate chamber at 60°C and a relative humidity of 85% prior to quasi-static mode I testing. Four specimens per configuration were withdrawn after 250, 500, 1000 and 2000 hours.

2.3 METHODS

The quasi-static mode I fracture toughness tests were carried out as explained in part I of this paper series with a constant displacement rate of 3 mm/min according to ASTM D 5528 [9].

Crack propagation was followed by a camera system with a picture recording interval of 5 or 10 s. The time dependent crack length was measured using a reference point marking the generated crack tip by the fluoropolymer film.

Fracture toughness was evaluated using the critical energy release rate G_{IC} following the 5% offset method given in ASTM D 5528 calculated by

$$G_{IC} = \frac{n * P_{5\%} * \delta_{5\%}}{2b * a_0}$$

where n is the compliance calibration parameter, $P_{5\%}$ and $\delta_{5\%}$ are load and displacement derived from the 5% offset method, b is the specimen width and a_0 is the initial delamination length.

3 RESULTS

Results of mode I fracture toughness after damp-heat aging are given in Fig.1 showing the critical energy release rate G_{IC} in dependence of the damp-heat aging time for the investigated laminate configurations.

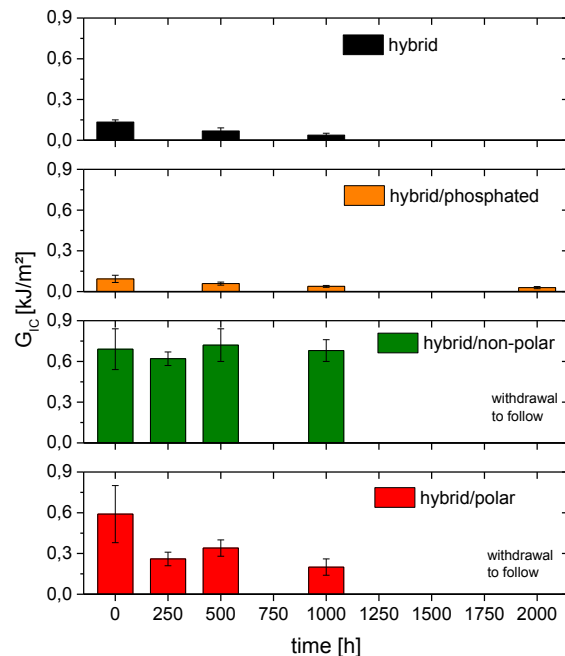


Fig. 1: G_{IC} values after damp-heat aging for the tested laminate configurations.

Prior to damp-heat aging hybrids without inter-ply showed critical energy release rates of 0.13 and 0.09 kJ/m² for the hybrid and hybrid/phosphated specimen, respectively. Due to damp heat aging the G_{IC} values were reduced to 0.04 kJ/m² after 1000 h for both configurations without inter-ply. Testing of the hybrid specimens (without phosphatization or inter-ply) after 2000 h was not possible, since the specimens failed directly after withdrawal from the climate chamber due to internal stresses.

Hybrids with phosphated steel surface revealed lowest critical energy release rates of all tested laminate configurations. However this type of specimen could be tested after 2000 h damp-heat aging, resulting in a G_{IC} value of 0.03 kJ/m². The improved damp heat aging performance might be attributed to the additional corrosion protection of the phosphate [10].

The insertion of an inter-ply resulted in a significantly better fracture toughness performance, increasing the critical energy release rate up to 0.69 and 0.59 kJ/m² for the laminate configurations with non-polar and polar inter-ply, in unaged condition. The fracture toughness was improved by a factor of

5 compared to unaged hybrids without inter-ply. For the specimens with non-polar inter-ply G_{IC} were not affected up to 1000 h of damp-heat exposure still exhibiting a value of 0.68 kJ/m². The 2000 h aging tests are still ongoing for this laminate configuration.

The hybrid with polar inter-ply exhibited a significant dependence on damp-heat aging. After 250 h in hot-wet condition the critical energy release rate had decreased by more than 50% to 0.26 kJ/m². A further slight reduction in G_{IC} was measured after 1000 h. It is supposed that, due to the polar and hydrophilic composition of the polymer, diffusion processes are accelerated weakening the failure interface faster [11]. For this laminate configuration the 2000 h damp heat tests are also ongoing.

Investigation of the fracture surfaces of hybrid/polar specimens revealed different fracture behaviour after 1000 h damp-heat aging compared to the unaged specimen (see Fig. 2). In both cases the crack moved from the crack initiation layer (between cfrp and inter-ply) to the interface between steel and inter-ply at the beginning of the crack propagation. In unaged hybrid/polar specimens the crack moved into the cfrp with further propagation, resulting in extensive areas of polymeric matrix and fibers on the steel-side of the specimen. From this it follows, that the polar inter-ply exhibits good adhesion to steel and cfrp.

After 1000 h the crack moved from the crack initiation layer to the interface between steel and inter-ply for the whole delamination process. Therefore, and due to the lower value of G_{IC} , intense degradation of adhesion between polar inter-ply and steel was concluded.

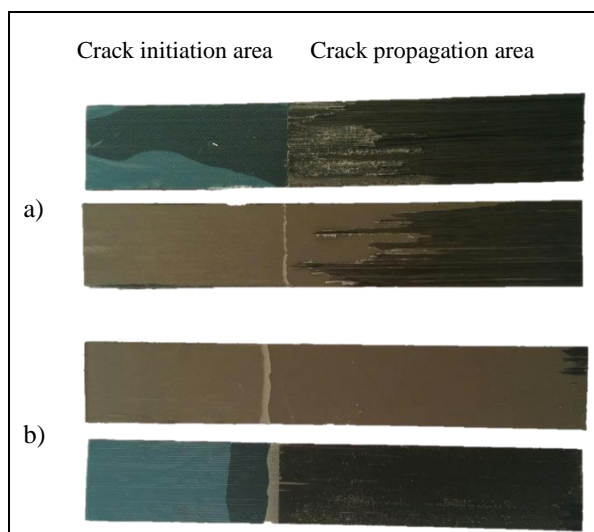


Fig. 2: Fracture surfaces of hybrids with polar inter-ply after a) 0 h and b) 1000 h of damp-heat aging.

4 SUMMARY AND OUTLOOK

It was shown that damp-heat aging significantly influences the adhesion performance of cfrp/steel hybrids. Insertion of the investigated polar or non-polar inter-ply increases the adhesion between cfrp and steel by a factor of about 5.

For applications under hot-wet environmental conditions, however, the polarity of the inter-ply has a negative effect on the adhesion performance. In contrast to the laminate configuration with the non-polar inter-ply the hybrid/polar laminate exhibited a significant decay in G_{IC} (factor of about 3 after 1000 h of damp-heat exposure).

Future research work will deal with the behavior of cfrp steel hybrid laminates under super-imposed mechanical and environmental loading. Therefore, adequate equipment (media containers) for electrodynamic testing machines is under development.

5 ACKNOWLEDGEMENT

The presented work was performed as part of a collaborative research project of the Institute of Polymeric Materials and Testing (IPMT) of the Johannes Kepler University Linz (JKU) and voestalpine Stahl GmbH. The project was funded by the Austrian Research Promotion Agency (FFG).

6 REFERENCES

- [1] Both JC. *Tragfähigkeit von CFK-Metall-Laminaten unter mechanischer und thermischer Belastung*. Dissertation, Technische Universität München; 2013.
- [2] Grujicic M, Sellappan V, Omar MA, Seyr N, Obieglo A, Erdmann M et al. *An overview of the polymer-to-metal direct-adhesion hybrid technologies for load-bearing automotive components*. Journal of Materials Processing Technology 2008;197(1-3):363–73.
- [3] Sinmazçelik T, Avcu E, Bora MÖ, Çoban O. *A review: Fibre metal laminates, background, bonding types and applied test methods*. Materials & Design 2011;32(7):3671–85.
- [4] Venables JD. *Review- Adhesion and durability of metal-polymer bonds*. Journal of Material Science 1984;19:2431–53.
- [5] Lang, R.W., Stutz, H., Heym M, Nissen D. *POLYMERE HOCHLEISTUNGS-FASERVERBUNDWERKSTOFFE*. Die Angewandte Makromolekulare Chemie 1986;145/146:267–321.
- [6] Bowditch MR. *The durability of adhesive joints in the presence of water*. International Journal of Adhesion and Adhesives 1996;16:73–9.

- [7] Ping Z, Nguyen Q, Chen S, Zhou J, Ding Y. *States of water in different hydrophilic polymers — DSC and FTIR studies*. Polymer 2001;42(20):8461–7.
- [8] Brockmann W. *Durability of Adhesion Between Metals and Polymers*. The Journal of Adhesion 1989;29(1-4):53–61.
- [9] ASTM. *Standard Test Method for Mode I Interlaminar Fracture Toughness of Unidirectional Fiber-Reinforced Polymer Matrix Composites*(D 5528-01). PA, US.: ASTM International; 2007.
- [10] Selvaraj M, Palraj S, Jayakrishnan P. *Performance of polymer blends on phosphated steel substrate*. Progress in Organic Coatings 2005;54(1):1–4.
- [11] Marais S, Nguyen Q, Devallencourt C, Metayer M, Nguyen TU, Schaetzel P. *Permeation of Water through Polar and Nonpolar Polymers and Copolymers: Determination of the Concentration-Dependent Diffusion Coefficient*. Journal of Polymer Science Part B: Polymer Physics 2000;38:1998–2008.

CHAPTER 2:

CORROSION AND RESIDUAL STRESSES

INVESTIGATION OF THE ELECTROCHEMICAL CORROSION BEHAVIOUR AND FE-MODELLING OF AN ALUMINUM/STEEL BLIND RIVET JOINT

M. Mandel*, L. Krüger

Technische Universität Bergakademie Freiberg, Institute of Materials Engineering

ABSTRACT: In this study the electrochemical corrosion behavior of an aluminum alloy joint by a blind rivet to a zinc-coated mild steel was investigated. The polarization behavior of each component was analyzed in a 5 wt.% sodium chloride solution. By analysis of the received polarization curves, the expected galvanic corrosion processes during an immersion test of the joint for 6 weeks in the same electrolyte was observed. In addition, the galvanic corrosion at the joint during the immersion test was analyzed by the finite element method using the determined corrosion potentials of the polarization curves. The results of the curve analysis and the finite element simulation are fully in agreement to the corrosion behavior during the immersion test. Furthermore, the long-term corrosion of the joint was investigated by a climate chamber test, according to the VDA 621-415 and an outdoor exposure test, according to the VDA 621-414. Galvanic induced pitting corrosion at the aluminum alloy next to the overlap of the joint is the most intense corrosion mechanism in both tests. Because of this conformity, both tests are comparable. The damage evolution at the aluminum alloy in the outdoor exposure correlates with few cycles of the climate chamber test.

KEYWORDS: Aluminum alloy, Mild steel, Blind rivet joint, Galvanic corrosion, Finite element modeling

1 INTRODUCTION

The requirement to the multi-material design concept is to combine different materials with appropriate properties by adequate joining technologies under high-ambitious ecologic and economic obligations [1]. Due to high degree of automation and low unit cost, riveting is a favored joining technology [2]. Nevertheless, a combination of different electrochemical active materials can accelerate the corrosion processes by galvanic corrosion significantly [3, 4]. For investigation several experimental techniques like polarization experiments, immersion tests or climate chamber and outdoor exposure tests are conducted [5-9]. Beside an experimental investigation a theoretical analysis by the finite element method is also an often practiced method [10, 11]. Nonetheless, different experimental techniques and theoretic approaches do often not harmonize in their results.

In this study the electrochemical corrosion behavior of a blind rivet joint was investigated by several experimental methods and it is shown that a correlation of the test results is possible when the corrosive conditions are similar.

2 EXPERIMENTAL

The rivet joint (Fig. 1) consisted of a sheet of the aluminum alloy EN AW-6060-T6 and a sheet of the hot dipped mild steel S350GD+Z140, which are joint by a galvanic ZnNi coated blind rivet made of mild steel [12, 13].

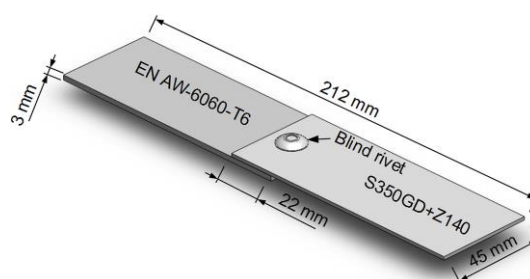


Fig. 1 Schematic illustration of the rivet joint.

2.1 Potentiodynamic polarization

The joint components were potentiodynamically polarized in a 5 wt.% sodium chloride solution using a potentiostat (VSP, BioLogic Science Instruments) by a scan rate of 0.1 mV/s. As the reference electrode a saturated Ag/AgCl and as counter electrode a Pt sheet were used. Before the polariza-

* Corresponding author: Gustav-Zeuner-Straße 5, 09599 Freiberg, +49(0)3731-393176, +49(0)3731-393703, mandel@iw.tu-freiberg.de

tion, the samples were washed with water, ethanol, and finally dried.

2.2 IMMERSION TEST

For investigation of the galvanic corrosion behavior the joint was fully immersed in the 5 wt.% sodium chloride solution for 6 weeks. The electrolyte had an overlap above the joint of 5 mm. To remain a nearly constant electrolyte composition during the test, the electrolyte was replaced by fresh test solution 5 days a week. After the test finish the rivet was drilled out and the joint components were analyzed by optical microscopy (Wild M10, Leica).

2.3 FINITE ELEMENT SIMULATION

For evaluation of the galvanic corrosion behavior the potential distribution along the joint in the fully immersed 5 wt.% sodium chloride solution was determined. As boundary conditions the corrosion potentials extracted from the polarization curves were used. The model was prepared using SolidWorks2009 and the analysis was carried out using ANSYS 11.0 [14]. A schematic drawing of the meshed model is shown in Figure 2.

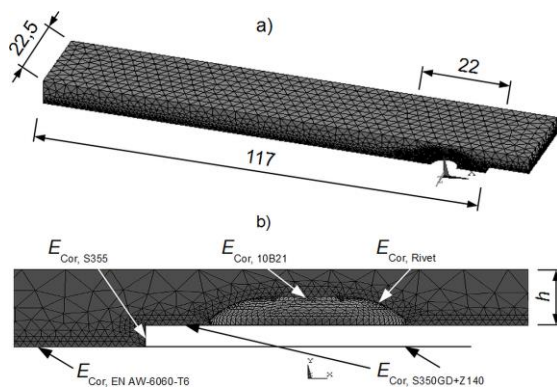


Fig. 2 a) Meshed model of the electrolyte along the joint. b) Detailed view at the joint location. *h* – Overlap of the electrolyte (5 mm).

2.4 CLIMATE CHAMBER AND OUTDOOR EXPOSURE TEST

The joint was exposed in a climate chamber for 13 cycles of the VDA 621-415 [15]. After each cycle 3 samples of the joint was extracted and the pit volume at the end of the overlap was determined by white light interferometry (BMT, Breitmeyer Messtechnik) [16]. Afterwards, the pit volume – VDA 621-415 cycle number relation was analyzed by nonlinear regression using the OriginPro® 8G software [17, 18]. The best fit quality was achieved using the Double-Boltzmann function. In addition, the rivet joint was investigated by an one year outdoor exposure test at the institute for corrosion protection Dresden Ltd, according to the VDA 621-414 [19]. After test finish, the pitting corrosion

attack at the end of the joint overlap was also analyzed by white light interferometry.

3 RESULTS AND DISCUSSION

3.1 POTENTIODYNAMIC POLARIZATION

Figure 3 shows the potentiodynamic polarization curves of each joint component. The extracted corrosion potential for the aluminum alloy is $E_{Cor.} = -0.74$ V vs. Ag/AgCl, $E_{Cor.} = -0.86$ V vs. Ag/AgCl for the ZnNi – coated blind rivet and $E_{Cor.} = -1.02$ V vs. Ag/AgCl for the hot dipped steel. Because of missing zinc coating at the cutting edges of the hot dipped steel, the corrosion potential of the base material (S355) was also determined. The base material is the noblest component in the joint with $E_{Cor.} = -0.6$ V vs. Ag/AgCl.

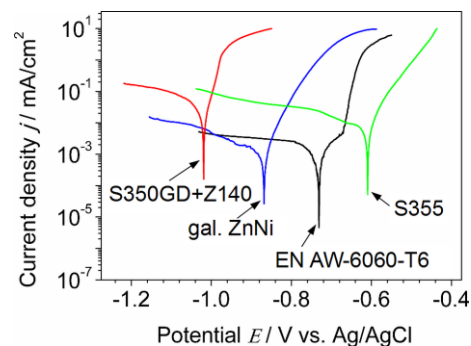


Fig. 3 Polarization curves of the joint components in 5 wt.% NaCl solution.

The sequence of the corrosion potentials clearly marks the hot dipped steel as the most ignoble joint component.

3.2 IMMERSION TEST

Figure 4 presents the photograph of the blind rivet joint after the immersion test.

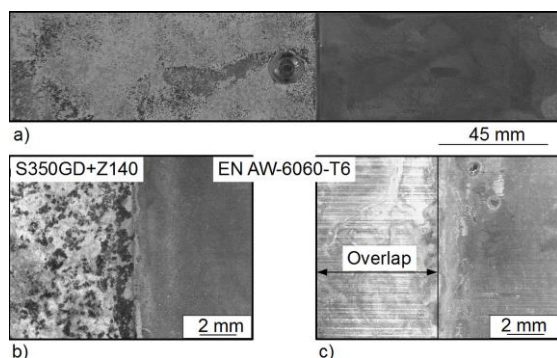


Fig. 4 a) Blind rivet joint after 6 week exposure in 5 wt.% NaCl solution. b), c) Detailed view of the end of the overlap before and after removal of the S350GD+Z140.

The photograph shows a homogeneous corrosion attack at the hot dip of the steel sheet, whereas the

blind rivet and the aluminum alloy reveal no significant corrosion attack. Because of this corrosion behavior it is evident that galvanic corrosion is the main corrosion mechanism and dictates the whole corrosion process. The aluminum alloy and the blind rivet are cathodic protected by the hot dip.

3.3 FINITE ELEMENT SIMULATION

Figure 5 illustrates the calculated potential distribution along the joint during the immersion in the 5 wt.% NaCl solution.

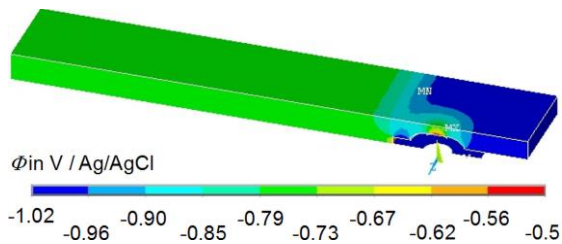


Fig. 5 Determined potential distribution along the blind rivet joint in the 5 wt.% NaCl solution.

As expected, the simulation gives the highest potential gradients at all material transitions. As deduced by the polarization curves (Fig. 3), the highest potential gradient is determined at the overlap region, which consequently leads to the most intense galvanic corrosion attack between the aluminum alloy and the hot dip. The results of the finite element simulation are fully in agreement to the observations after the immersion test (Fig. 4).

3.4 CLIMATE CHAMBER TEST

In Figure 6 some selected states of the joint for different cycles of the VDA 621-415 are presented.

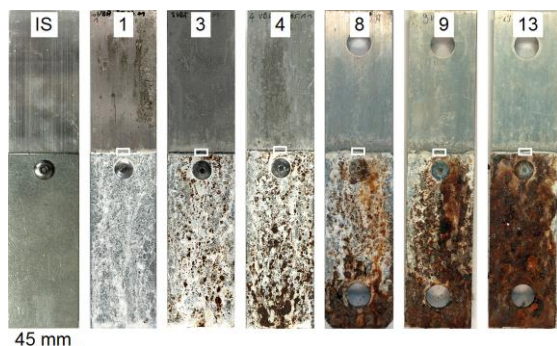


Fig. 6 Photographs of the blind rivet joint at the initial state (IS) and after different cycles of the VDA 621-415. The rectangle marks the regions that were investigated by white light interferometry.

The most intense corrosion attack is observed at the hot dip of the S350GD+Z140, which shows a homogenous attack at the hot dip after the 1st cycle. After 3 cycles red rust at the steel sheet is observed,

which indicates a corrosion attack at the base material. After 13 cycles the hot dip is completely dissolved. A similar behavior is found at the blind rivet, which also shows a continuous dissolution of the ZnNi coating and a red rust formation when the cycle number increases. In contrast to the steel sheet and the blind rivet, the corrosion behavior of the aluminum alloy is more irregular. At the end of the overlap pitting corrosion at the aluminum alloy is observed that passes into a trench formation along the whole joint when the cycle number increases. In higher distance to the overlap, the aluminum alloy behaves passive and shows no significant corrosion attack. The pitting corrosion attack at the end of the overlap was analyzed by white light interferometry in an area of 2×5 mm². The correlation between the calculated pit volume and the VDA 621-415 cycle number is presented in Figure 7. The relationship is best described by the Double-Boltzmann function with V_0 the initial pit volume, V_t – the pit volume after test finish, V_1 and V_2 – the pit volume after a significant rise of the pit volume and $t_{1/2,1}$ and $t_{1/2,2}$ – the inflexion points of the curve. To improve the fit quality, the initial pit volume was defined at $V_0 = 0$ mm³ and parameters $t_{1/2,1}$ and $t_{1/2,2}$ was fixed at 3.5 and 8.5 cycles. The curve fit gives a total pit volume of $V_t = 1.6$ mm³ involving the fractions of $V_1 = 0.49$ mm³ and $V_2 = 1.11$ mm³. The comparison of V_1 and V_2 clearly indicates that the attack by pitting corrosion is higher after the second pit rising at $t_{1/2,2}$.

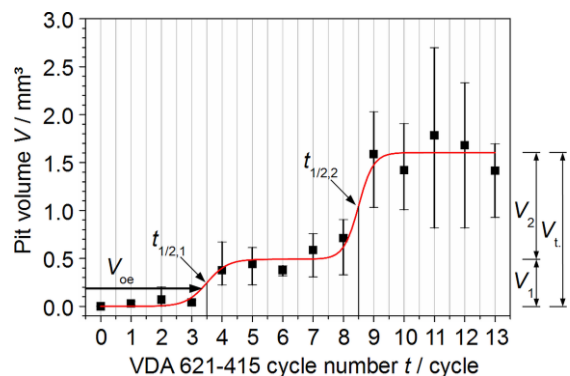


Fig. 7 Correlation between pit volume and VDA 621-415 cycle number and mathematical adjustment by the Double-Boltzmann function. Parameters see text. V_{oe} – pit volume after outdoor exposure.

3.5 OUTDOOR EXPOSURE TEST

In Figure 8 the rivet joint before and after the one year outdoor exposure test is presented. The hot dip of the steel sheet shows a uniform corrosion attack because of homogenous formation of white rust. The ZnNi coated blind rivet reveals no significant signs of disintegration and is completely intact after the test. Similar to the climate chamber test,

the aluminum alloy reveals a distinctive pitting corrosion attack at the end of the overlap region, whereas in higher distance the alloy remains fully passive.

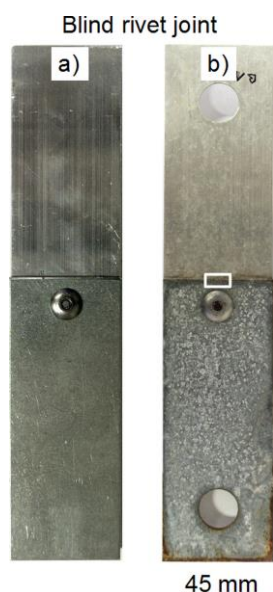


Fig. 8 Blind rivet joint before a) and after b) the one year outdoor exposure test. The rectangle marks the region that was investigated by white light interferometry.

The pitting corrosion attack was also investigated by white light interferometry in an area of 2×5 mm² and the calculated pit volume gave $V_{oc} = 0.19$ mm³. Due to the similarity in corrosion mechanism and the location of the attack at the aluminum alloy the result of the outdoor exposure test is comparable to the climate chamber test. By integration of V_{oc} into Figure 7 it is recognizable that a similar pitting corrosion attack occurs approximately after 3.5 cycles of the climate chamber test. Due to this conformity the same damage evolution at outdoor exposure is observable by the climate chamber test with a reduction in test duration of 93 %.

4 CONCLUSIONS

In this study, the electrochemical corrosion behavior of an aluminum/steel blind rivet joint was investigated. For each joint component the potentiodynamic polarization behavior was recorded. The extracted corrosion potentials were afterwards used as the boundary conditions for a finite element simulation. Furthermore, the analyzed galvanic corrosion properties were evaluated by an immersion test. The results of the simulation are fully in agreement to the observation made after the immersion test.

The long-term corrosion behavior of the joint was investigated for several cycles of a climate chamber test and a one year outdoor exposure test. After each cycle the pit volume was determined at the

end of the overlap region and the correlation was fitted by the Double-Boltzmann function. Finally, due to similar corrosion processes the pit volume after the outdoor exposure was correlated to the results determined by the climate chamber test.

5 ACKNOWLEDGEMENT

The authors gratefully acknowledge the German Research Foundation (DFG) and Allianz Industrie und Forschung (AIF) for their financial support of this work.

REFERENCES

- [1] Lesemann M., Bröckerhoff M., Urban P.: *The prospects of multi-material design for a compact-class front section*. ATZ autotechnology, 8:15-20, 2008.
- [2] Wittel H., Muhs D., Jannasch D., Voßiek J.: *Roloff/Matek Maschinenelemente*. Vieweg+Teubner GWV Fachverlage GmbH, Wiesbaden, 2009.
- [3] Fovet Y., Pourreyron L., Gal J.-Y.: *Corrosion by galvanic coupling between carbon fiber post and different alloys*. Dent. Mater., 16:364-373, 2000.
- [4] Songür M., Çelikkan, Gökmeşe, Şimşek S.A., Altun N. Ş, Aksu M.L.: *Electrochemical corrosion properties of metal alloys used in orthopaedic implants*. J. Appl. Electrochem., 39:1259-1265, 2009.
- [5] Wu Q., Li W., Zhong N.: *Corrosion behavior of TiC particle-reinforced 304 stainless steel*. Corros. Sci., 53:4258-4264, 2011.
- [6] Pardo A., Merino S., Merino M.C., Barroso I., Mohedano M., Arrabal R., Viejo F.: *Corrosion behaviour of silicon-carbide-particle reinforced AZ92 magnesium alloy*. Corros. Sci., 51:841-849, 2009.
- [7] Corvo F., Perez T., Dzib L.R., Martin Y., Castañeda A., Gonzalez E., Perez J.: *Outdoor-indoor corrosion of metals in tropical coastal atmosphere*. Corros. Sci., 50:220-230, 2008.
- [8] Mendoza A.R., Corvo F.: *Outdoor and indoor atmospheric corrosion of non-ferrous metals*. Corros. Sci., 42:1123-1147, 2000.
- [9] Corvo F., Betancourt N., Mendoza A.: *The influence of airborne salinity on the atmospheric corrosion of steel*. Corros. Sci., 37:1889-1901, 1995.
- [10] Montoya R., Galván J.C., Genesca J.: *Using the right side of poisson's equation to save on numerical calculations in FEM simulation of electrochemical systems*. Corros. Sci., 53:1806-1812, 2011.
- [11] Montoya R., Escudero M.L., García-Alonso M.C.: *Effect of impurities and electrolyte thickness on degradation of pure magnesium*.

- A finite element study.* Mater. Sci. Eng., B., 176:1807-1811, 2011.
- [12] DIN EN 573-3: *Aluminum and aluminum alloys – chemical composition and form of wrought products – part 3.* Beuth Verlag Berlin, 2009
- [13] Wegst C., Wegst M.: *Stahlschlüssel*, Verlag Stahlschlüssel Wegst GmbH, Marbach, 2010.
- [14] Mandel M., Krüger L.: *FE-Simulation of galvanic corrosion susceptibility of two rivet joints verified by immersion tests.* Mater. Today: Proceedings, 2S:S197-S204, 2015.
- [15] DIN EN ISO 11997-1: *Paints and varnishes – determination of resistance to cyclic corrosion conditions – part 1.* Beuth Verlag, Berlin, 2006.
- [16] Mandel M., Krüger L.: *Long-term corrosion studies of a CFRP / EN AW-6060-T6 self-piercing rivet joint and a steel / EN AW-6060-T6 blind rivet joint.* Mater. Today: Proceedings, 2S:S131-S140, 2015.
- [17] Ratkowsky D.A.: *Nonlinear Regression Modeling.* Marcel Dekker INC, New York, 1983.
- [18] Seber G.A.F., Wild C.J.: *Nonlinear Regression.* John Wiley & Sons, New York, 1989.
- [19] DIN 55665: *Paints and varnishes – natural weathering of coatings – determination of corrosion protection performance.* Beuth Verlag, Berlin, 2007.

EXPERIMENTAL INVESTIGATIONS ON RESIDUAL STRESSES DURING THE FABRICATION OF INTRINSIC CFRP-STEEL LAMINATES

R. Prussak^{1*}, D. Stefaniak², C. Hühne², M. Sinapius¹

¹TU-Braunschweig, Institute of Adaptive Systems and Functional Integration,
²DLR, Institute of Composite Structures and Adaptive Systems

ABSTRACT: This paper focuses on process-related thermal residual stress in fibre metal laminates, consisting of thin steel foils and CFRP prepreg layers. Different process modifications during fabrication were investigated, modifying temperature, pressure and the vacuum bagging arrangement. The impact of these parameters is measured on the deflection of asymmetrical specimens, enabling the evaluation of the potential of specific configurations. For detailed investigations, a cure monitoring system with fibre bragg grating (FBG) sensors was used to measure the in-plane strains during processing. The investigations show a relationship between cure reaction and processing strains. This allows the characterisation of the co-cure bonding process and the resulting residual stress state in nearly any FML configuration. A new method is presented for quantitative predictions of residual stresses in CFRP-steel laminates. It is characterized by the subsequent removal of the steel layers and in-situ measurements of the resulting strain changes with the help of embedded FBG-sensors.

KEYWORDS: fibre metal laminate, residual stress, co-cure bonding, process monitoring, FBG

1 INTRODUCTION

Intrinsic fibre metal laminates (FML) are hybrid composite materials consisting of metal sheets co-cure bonded to fibre reinforced plastic layers (FRP). No additional joining process is needed as adhesion is realized by the prepreg's resin during its cure [1]. It is used as structural material or as local reinforcement in very different applications [2,3].

The curing temperature during the manufacturing of the hybrid laminates is above the operating temperature. This causes internal stresses between the individual layers or deformations of the laminate as a result of the different thermal expansion coefficients (CTE). These inter-ply stresses may significantly lower the mechanical properties of the hybrid laminate, especially when difference in thermal expansion is high depending in the constituent's fraction and stiffness [4].

Different investigations have been performed to reduce residual stresses in pure composite as well as in fibre metal laminates, utilizing modified curing processes [1, 4], an additional clamping tool to reduce thermal mismatch [5] or post-stretching to reduce residual stress level of an already cured laminate [6].

The interaction between the metallic and composite layer on inter-ply level during the curing process,

particularly during heat up, was generally not taken into account by the majority of these studies. But different investigations performed by Twigg et al. showed that there is even a stress transfer between tool and part [7]. Further investigations showed that the stress is depended on different parameters, as surface roughness, prepreg architecture and specimen geometry [8].

Hence, it can be assumed that the interaction during heat up also influences the residual stresses in fibre metal laminates. The potential of specific process configurations is evaluated in the first part of the paper. A clear understanding of how process-induced strains evolve during the cure cycle is important to optimise manufacturing. Thus in the second part, a simultaneous measurement method is used for the characterisation of the co-cure bonding process and the stress transfer during the creation process. Fibre optic sensors were integrated directly in the laminates and provide information about the strains within the laminate and the residual stress state.

2 RESIDUAL STRESS ALTERATION

The influence of pressure, temperature (described in detail by Stefaniak et al. [4]) and the vacuum bagging arrangement is discussed in preliminary

* Corresponding author: Lilienthalplatz 7, 38108 Braunschweig, +495312952335, Robert.Prussak@dlr.de

investigations. The impact of these parameters is measured on the deflection of asymmetrical specimens.

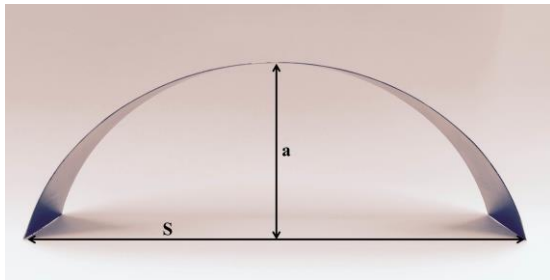


Fig. 1 Measurement of deformed specimen [4]

The deformations of the asymmetrical specimens generated through the internal stresses during fabrication were measured as shown in Fig. 1. The curvature is calculated by the measured geometrical values a and S at room temperature. The assumption of a bimetallic strip allows calculating the stress-free temperature of the radius by Timoshenko [9].

A further possibility is to measure the temperature during reheating of the curved asymmetrical specimens. The geometrical values a and S are recorded (Fig. 1) as a function of the temperature. A Regression analysis of the variable a provides the stress free temperature.

With the help of the measured and calculated temperature the internal residual thermal stress on the metal layers in fibre direction is evaluated based on classic laminate theory [4].

2.1 SPECIMEN CHARACTERISTIC

Two different lay-ups are used, one symmetric and one asymmetric, as shown in Fig. 2.



Fig. 2 Symmetrical and asymmetrical specimens

The asymmetric specimens are manufactured in a double configuration in order to minimize any interaction between tool surface and specimens. It consists of two stainless steel 1.4310 outer sheets with a thickness of 0.12 mm and two HexPly-8552/AS4 centre layers with a thickness of 0.125 mm. The two specimens are separated by an FEP-sheet Nowofol-NowoflonET.

The symmetric specimens consist of one stainless steel 1.4310 centre layer and five HexPly-8552/134/AS4 outer sheets on each side. After the manufacturing process the upper CFRP layers were

mechanical removed, resulting in an asymmetrical specimen with a characteristic deformation.

All specimens are 20 mm in width and they have a length of 200 mm with all fibres orientated in longitudinal direction (0°).

2.2 RESIDUAL STRESS MODIFICATIONS

For the variation of the pressure during fabrication the size of the cover plate is changed. By choosing a larger cover plate, whose bending stiffness is sufficient to prevent unwanted bending between the specimens, the effective pressure on a specimen can be increased [4].

The influence of the temperature profile is investigated by using a ‘smart cure cycle’ with cooling and reheating [4]. The aim of modified cure cycles is to lower the bonding temperature of CFRP – and steel layers. This is based on the exothermic curing reaction which proceeds during the abrupt cooling. As a consequence, the connection between steel and prepreg solidifies at a lower temperature [1]. Furthermore, investigations for different vacuum bagging arrangements as shown in Fig. 3, were carried out on the symmetrical specimens. The goal is to investigate the interaction between tool or operating consumables and the hybrid laminate.

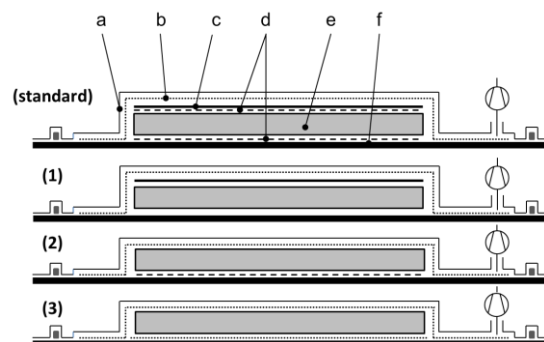


Fig. 3 Vacuum bagging arrangement, (a) Vacuum bag, (b) peel ply, (c) cover plate, (d) FEP-release foil, (e) hybrid laminate, (f) tool

The results of the different process modifications are shown in Fig. 4. The residual stress level is specified as stress free temperature.

The standard process is defined by the manufactured recommend cure cycle (MRCC) with a pressure of 6 bar and the standard vacuum bagging arrangement. MRCC for the HexPly-8552/AS4 prepreg recommends two heat-up ramps and two dwell stages. The autoclave is heated up to 110°C at 1-3 K/min. After the 60 minute dwell it is heated up again at 1-3 K/min to 180°C . After a hold of 120 minutes the autoclave is cooled down at 2-5 K/min.

The results show a significant influence of the various operational parameters. The higher pressure reduces the residual stresses, by increasing the

interaction during the heating process. The experiments with different vacuum arrangements show a significant influence of the peel plies (A(2) and A(3)).

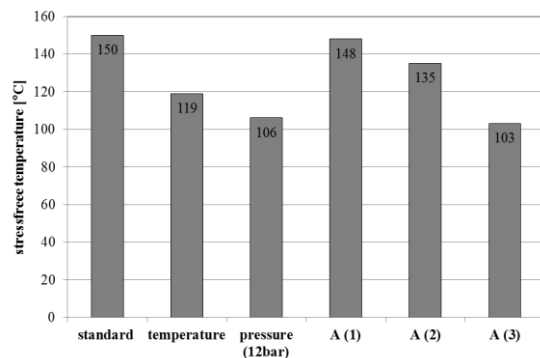


Fig. 4 Residual stress results for different process modifications (curvature measurement)

In the following investigations the measurement of residual stresses using fibre bragg grating sensors is introduced. The simultaneous measurement method enables the determination of the mechanism of the various influencing factors and allows further optimizations. Furthermore, the residual stress state can be determined in nearly any fibre metal laminate configuration.

3 EXPERIMENTAL TESTING (FBG-MEASUREMENT)

3.1 FABRICATION

3.1.1 Specimens characteristic

The lay-up is shown in Fig 5. The hybrid laminate $[0_3|St|0_6]_S$ consist of two stainless steel 1.4310 sheets with a thickness of 0.12 mm and 18 HexPly-8552/AS4 prepreg layers. Six layers were located on the bottom and top of the laminate. The remaining 12 layers are located in the centre of the sample. All fibres are orientated in longitudinal direction (0°). The metal volume fraction (MVF) is 10%, with a total thickness of 2.5 mm. Furthermore a pure unidirectional CFRP laminate $[0_{20}]$ is used.

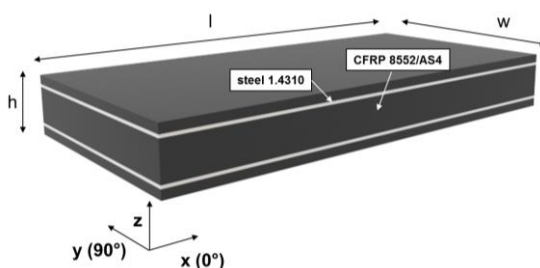


Fig. 5 Specimen geometry and lay up ($l = 200$ mm, $w = 100$ mm, $h = 2.5$ mm)

3.1.2 Co-cure bonding process

All metallic sheet surfaces were treated with an AC-130 sol-gel post-treatment after corundum-blasting with $105 \mu\text{m}$ particles and then added to the laminate stacking within one hour, as described by Stefaniak et al. [2]. All specimens have been manufactured by hand layup. The laminate was thoroughly compacted with a hand roller after each ply. All specimens are manufactured using the standard vacuum bagging arrangement (Fig. 1) with the standard MRCC process, described in (2.2). In contrast, the process is carried out in a furnace. Thereby, no additional pressure is applied.

3.2 SIMULTANEOUS MEASUREMENT OF PROCESSING STRAINS

Fibre bragg grating (FBG) sensors can operate as wavelength-encoded sensors and provide an absolute measurement of the physical perturbation which they experience [10]. In the following investigation the sensors were used for process monitoring during fabrication of CFRP-steel hybrid laminates.

The Bragg grating is a periodical modulation of the refractive index n photo-written in the core of a single mode optical fibre, with a spread of a few millimeters. When the fibre is strained or submitted to a temperature change, a shift of the Bragg wavelength (back reflected wavelength) occurs due to a change of the period of the grating and the refractive index as described in various papers [11].

When a FBG is used to measure strains, the effect of temperature needs to be compensated or removed. Thus the fibre optical measurement method allows the recording of full strain/temperature profiles during the process.

3.2.1 Integration of fibre bragg grating sensors

A polyimide coated silica glass FBG sensor is embedded in the described CFRP- and CFRP-steel hybrid laminates. The gauge length of the bragg grating is 2 mm. The outside diameter, including the polyimide coating, is about $150 \mu\text{m}$.

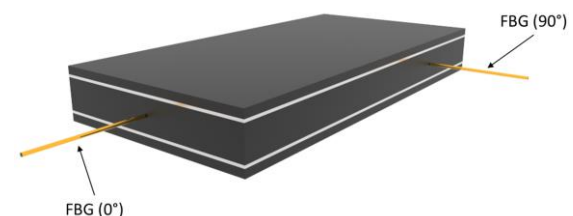


Fig. 6 Location of the embedded FBG-sensors

For the investigations two FBG sensors were embedded in each specimen. The optical fibres are longitudinally (0°) and transversally (90°) placed between the centre layers as shown in Fig. 6. The optical fibres were positioned in a way that the

grating is in the middle of the length or width of the samples.

The cross-section of the CFRP-steel laminate interface including the FBG sensor in longitudinal direction is shown in Fig. 7.

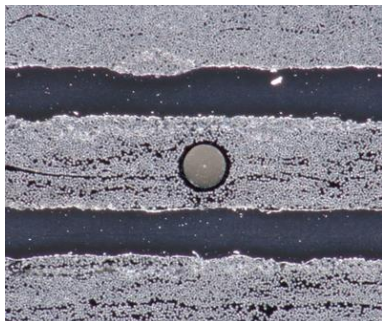


Fig. 7 Micrographics of CFRP-steel laminate with embedded FBG sensor in longitudinal direction (0°)

3.2.2 Experimental setup

The variation of the reflected light wavelength by the FBG during curing in an oven is monitored using an optical sensing interrogator, whose wavelength range is 40 nm. The interrogator operates as light source and spectrometer. The exact wavelength shift can be determined by a peak detection of the reflected wavelength band.

In addition to this, temperature during the curing process is recorded with embedded K-Type thermocouples. Both, temperature and wavelength change were measured with a sampling rate of 1 Hz.

4 RESULTS AND DISCUSSION

4.1 IN-PLANE STRAINS DURING PROCESSING

4.1.1 UD-CFRP Laminate (90°)

Fig. 8 shows the strain for the pure CFRP laminate in transverse (90°) direction and describes the behavior of the resin through its several phases.

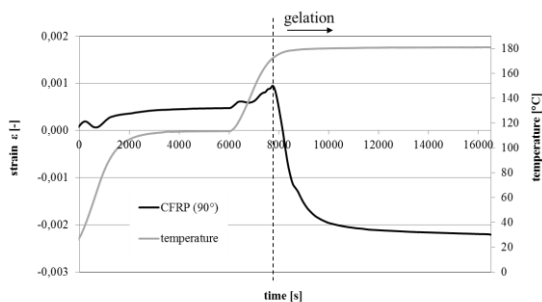


Fig. 8 Measured strains (in 90° direction) during the curing process of a UD-CFRP $[0_{20}]$ laminate

The observed sudden change in slope is a result of the cure shrinkage and reduction of the material thermal expansion coefficient which occurs when the material transforms from a liquid to a rubbery state. The resin gels, as confirmed by the knowledge of the AS4–8552 cure kinetics [12].

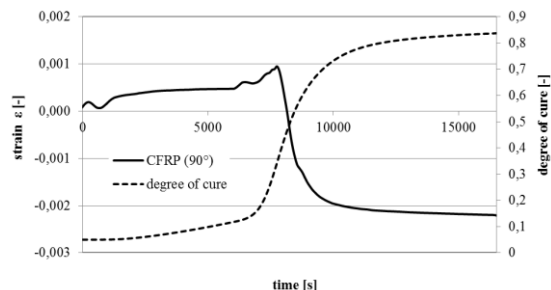


Fig. 9 Measured strains (90° -direction) during the curing process of a UD-CFRP laminate $[0_{20}]$

In order to gain a better understanding of the relationship between the measured strains and the curing reaction, the development of cure during the manufacturing cure cycles is investigated using the model proposed by Johnston [13]. The development of cure for the recommended manufacturing cure cycle is plotted in Fig. 9. This allows the determination of the degree of cure at the point of gelation and takes a value of 0.33. This agrees with previously published data for Hexply-8552/AS4 [12].

For the primary determination of the residual stress state after the curing process all strain plots were set to zero at the point of gelation.

4.1.2 CFRP-steel laminate

The measured strains in transverse and longitudinal direction during the curing process of the CFRP-steel laminate are shown in Fig. 10.

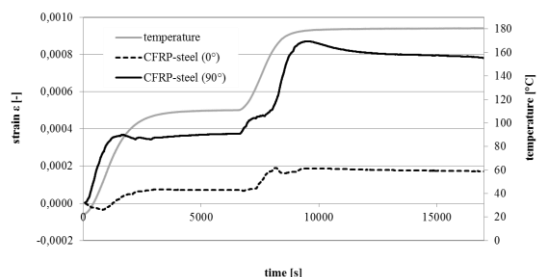


Fig. 10 Measured strains (0° - and 90° -direction) during the curing process of a CFRP-steel laminate $[0_3|St|0_6]_s$

A characteristic peak is seen in longitudinal direction. In contrast to the CFRP in 90° direction, the shrinkage after gelation is restricted through the stress transfer between the matrix, carbon fibres and steel layers. This results in a very small peak

followed by a renewed increase due the thermal expansion.

A characteristic peak cannot be detected in the transverse direction. The shrinkage is overcompensated through the thermal expansion of the steel layers, because of the low stiffness of the UD-CFRP prepreg layers in transverse direction. As a result, the measured strains increase significantly until the constant cure temperature is reached and are then followed by shrinkage induced decrease.

Fig. 11 presents the strain in transverse direction as function of the temperature. It clearly shows the stress transfer between the CFRP- and steel layers during gelation. The slope of the curve sharply increases. The coefficient of thermal expansion (CTE) after gelation of the hybrid laminate reaches nearly the same value as during cooling down. The slight difference could be due to the higher stiffness and the lower CTE of the plastic after vitrification.

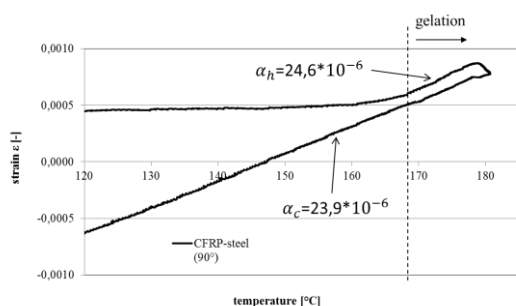


Fig. 11 Measured strain as a function of the temperature during the curing process of a CFRP-steel laminate $[0_3|St|0_6]_s$

4.2 RESIDUAL STRESS MEASUREMENT

The strain level in transverse and longitudinal direction at room temperature after finishing manufacturing is shown in Fig 12. It is also necessary to calculate the strain level in the steel layers in the unbound case to draw conclusion about the residual stresses in the steel layers. The strain data is based on the gel point, where the strain data is set zero as described in (4.1.1).

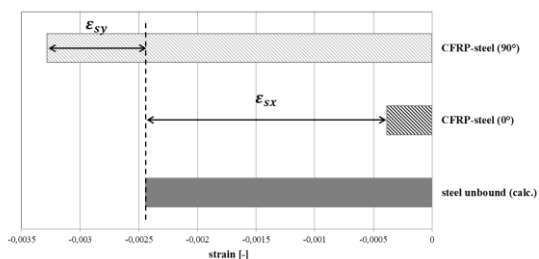


Fig. 12 Measured strains of the cured CFRP-steel laminate at room temperature compared to the calculated strain of unbound steel

The difference between the measured strains in the CFRP-steel laminate and the calculated strain of

steel (unbound) corresponds to the forced strains of the steel layers in the hybrid laminate.

The residual stress state can be determined from these values according to the CLT. The tensile stresses in the steel layers (0°) reach the largest values in the hybrid laminate, because of the low MVF and the high stiffness of CFRP in fibre direction.

The results depend on the definition of the gel point as starting point of the stress transfer. Therefore, an additional method was developed, which provides independent information about the residual stress state in the hybrid laminate. The method bases on the mechanical removing of the outer steel and CFRP layers after manufacturing process, resulting in a UD-CFRP laminate $[0_{12}]$. The strain data during the uncovering of the centre CFRP-Layers is presented in Fig. 13.

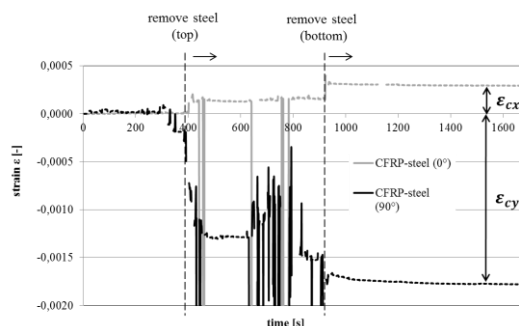


Fig. 13 Measured strains (0° - and 90° -direction) during the uncovering process of a CFRP-steel laminate

It clearly shows the removal of the bottom and top steel layer with a sudden change in strain.

The strain decreases in transverse direction and rises in longitudinal direction. The strain change reflects the elimination of the forced expansion (relaxation). The resulting $[0_{12}]$ UD-CFRP laminate contains no more restricted interlaminar strains.

Thus, the residual stress state can be determined from the strain change through the removal of the steel layers.

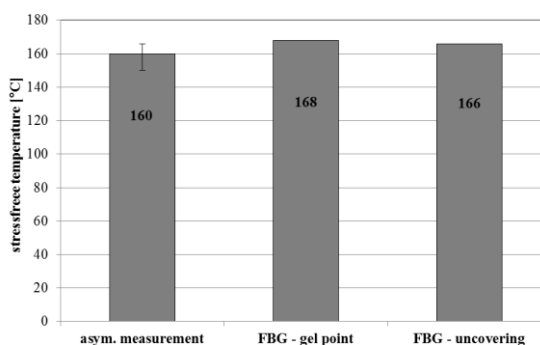


Fig. 14 Residual stress results for standard manufactured CFRP-steel laminates

The results of the residual stress measurement with the different methods for a standard manufactured CFRP-steel laminate are shown in Fig. 14. The stress free temperature is nearly the same for all measurement methods with a temperature between 160°C to 168°C, which is significantly lower than the curing temperature of 180°C.

Furthermore, the small difference between the results of both FBG measurement methods show that there seem to be no significant influence of the interactions before reaching the gel point on the residual stress state, using a standard process with no modifications.

Further investigations will show the impact of the investigated process modifications on this relationship. Thus, quantitative statements of the interaction during the heating process can be made.

5 CONCLUSIONS

In this work the influences of different modifications during fabrication of co-cure bonded UD-CFRP-steel laminates on the residual stresses were presented. The process parameters showed a significant influence and could lower the residual stresses up to 31%, enabling the evaluation of the potential of specific configurations.

In-situ strain monitoring during the manufacturing process of CFRP- and CFRP-steel laminates using fibre bragg grating sensor were performed. The relationship between curing reaction and the measured strains could be clearly detected. The technique captures the thermal expansion and the cure shrinkage during the heating stage and allows the determination of the gel point. In a CFRP-steel laminate, it shows the stress transfer between the CFRP- and steel layers during gelation. The quantitative residual stress value in a CFRP-steel laminate at room temperature could be successfully determined by an uncovering process with in-situ measurement of strain changes.

The measured stress-free temperature of a standard manufactured CFRP-steel laminate is significantly lower than the cure temperature of 180°C. The investigations showed that gelation took place on the second temperature ramp up to the final cure temperature. Thus, the residual stress state is influenced by a small component of thermal strain as well as cure shrinkage of the plastic during heating and the dwell stage until vitrification is reached, which reduces the stress free temperature.

6 ACKNOWLEDGEMENT

This work was supported by the Deutsche Forschungsgemeinschaft (DFG).

REFERENCES

- [1] H.S. Kim, S.W. Park, D.G. Lee: *Smart cure cycle with cooling and reheating for co-cure bonded steel/carbon epoxy composite hybrid structures for reducing thermal residual stress*, Composites Part A: Applied Science and Manufacturing, 37:1708–1721, 2006.
- [2] D. Stefaniak, E. Kappel, B. Kolesnikov, and C. Hühne: *Improving the mechanical performance of unidirectional CFRP by metal-hybridization*, In: ECCM15 - 15th European Conference on Composite Materials, Venice, Italy, 2012.
- [3] T. Sinmazcelik, E. Avcu, M. Özgür Bora, and O. Coban: *A review: Fibre metal laminates, background, bonding types and applied test methods*, Materials and Design, 32(7):3671–3685, 2011.
- [4] D. Stefaniak, E. Kappel, M. Kolotylo, C. Hühne: *Experimental identification of sources and mechanisms inducing residual stresses in multi-layered fiber-metal-laminates*, In: Euro Hybrid Materials and Structures, Stade, 2014.
- [5] J. Xue, W.-X. Wang, Y. Takao, and T. Matsubara: *Reduction of thermal residual stress in carbon fiber aluminum laminates using a thermal expansion clamp*, Composite Part A: Science and Manufacturing, 42: 986–992, 2011.
- [6] S.U. Khan, R.C. Alderliesten, and R. Benedictus: *Post-stretching induced stress redistribution in Fibre Metal Laminates for increased fatigue crack growth resistance*, Composites Science and Technology, 69(3-4):396–405, 2009.
- [7] G. Twigg, A. Poursartip, and G. Fernlund: *An experimental method for quantifying tool-part shear interaction during composite processing*, Composites Science and Technology, 63(13):1985–2002, 2003.
- [8] D. Stefaniak, E. Kappel, T. Spröwitz, and C. Hühne: *Experimental identification of process parameters inducing warpage of autoclave-processed CFRP parts*, Composites Part A: Applied Science and Manufacturing, 43(7):1081 – 1091, 2012.
- [9] G.D. Angel and G. Haritos: *An Immediate Formula for the Radius of Curvature of a Bi-metallic Strip*, International Journal of Engineering Research & Technology (IJERT), 2(12):1312–1319, 2013.
- [10] R. De Oliveira, et al., *Experimental investigation of the effect of the mould thermal expansion on the development of internal stresses during carbon fibre composite processing*, Composite Part A, 39(7): 1083-1090, 2008.
- [11] K.O. Hill, G. Meltz: *Fiber Bragg grating technology fundamentals and overview*, J. Light. Technol, 15(8):1263-1276, 1997.

- [12] T. Garstka a, N. Ersoy , K.D. Potter , M.R. Wisnom: *In situ measurements of through-the-thickness strains during processing of AS4/8552 composite*, Composites: Part A, 38:2517–2526, 2007.
- [13] Johnston AA.: *An integrated model of the development of processinduced deformation in autoclave processing of composite structures*, PhD thesis, University of British Columbia, Department of Metals and Materials Engineering, 1997.

CHAPTER 3:

CHARACTERIZATION

INFLUENCE OF MATERIAL PARAMETERS ON THE TENSILE FORCE OF INTEGRAL ALUMINUM CFRP HYBRID STRUCTURES FABRICATED BY CASTING TECHNOLOGY

Kunze, Arne^{1*}; Clausen, Jan^{2,3}; Van der Auwera, Robin³; von Hehl, Axel¹; Zoch, Hans-Werner^{1,2}; Busse, Matthias^{2,3}

¹ Stiftung Institut für Werkstofftechnik IWT, Bremen

² University of Bremen, Bremen

³ Fraunhofer Institute for Manufacturing and Advanced Materials IFAM

ABSTRACT: The continuously rising demand for advanced lightweight solutions for transportation applications leads to multi-material designs (MMD), which maximize the ratio between energy efficiency during operation and manufacturing costs. Hybrid MMD, using load-path oriented fiber composites and monolithic metal structures, combine different material properties adapted to local requirements. Thus, material oriented joining techniques play a key role to enable the combination of such different material classes and, finally, to meet the envisaged lightweight aim.

The presented research results focus on the mechanical behavior of integral CFRP-aluminum designs utilizing glass-fiber fabrics as the transition structures, which are partially embedded into the aluminum matrix. The particular challenge in fiber-aluminum high pressure die casting is the infiltration and positioning of the glass-fiber fabrics in the casting process. Correlations between different material parameters of fabrics and achievable maximum loads of the final aluminum-CFRP hybrid structure were analyzed. For this, the number of layers and the weight per unit area of the glass-fiber transition structure were varied. The fault tolerance of the manufacturing process was analyzed and reviewed. The impact of manufacturing process on the tensile strength was determined.

KEYWORDS: CFRP, high pressure die casting, aluminum, tensile tests, infiltration

1 INTRODUCTION

In the context of a growing demand for lightweight materials with high stiffness, fiber reinforced plastic - metal hybrid components are increasingly gaining importance. Hybrid materials combine properties of both fiber-reinforced plastics (FRP) and metals and, thus, lead to material properties, which cannot be achieved by the single component itself. On the one hand FRP provide a very high specific strength and stiffness, on the other hand metals show a ductile behavior during crashing. As a result, the materials should not be substituted for each other, but should find the specific material properties for the different requirements in their respective construction systems.

In particular, the automotive industry requires joining technologies for fiber reinforced plastics and metal components in order to optimize the multi-material systems [1]. The conventional bonding methods such as riveting, screwing, gluing or welding have certain disadvantages, such as overlapping areas, thickened material, electrochemical

corrosion, the damage of fibers by drilled holes in fiber-reinforced plastics or the lack of controllability and elaborate surface preparations of adhesive bonds.

The DFG Research Group "Schwarz-Silber" (FOR1224) examines the integral load-path-optimized combination of carbon-fiber-reinforced plastic (CFRP) and aluminum based on transition structures. Within the so called fiber concept fiber materials are used as textile structures for joining CFRP and aluminum [2]. The novel hybrid structure is specially designed for the demand of fiber-fair and corrosion resistance by use of transition structures. The fiber materials in the transition structure serve as load transmission elements and as an insulator to prevent galvanic corrosion. The direct integration of carbon fibers in aluminum would lead to galvanic corrosion of the hybrid structure and carbide reaction products at the fiber-aluminum interface [3] [4] [5].

The textile structures are partially infiltrated with aluminum in the casting process, and connected by suitable layer architectures or loop connections

* Corresponding author: IWT – Stiftung Institut für Werkstofftechnik, Badgasteiner Straße 3, 28359 Bremen, phone: +49 (0)421 218 51352, fax: +49 (0)421 218 51333, akunze@iwt-bremen.de

with carbon fibers and consolidated in injection / infusion processes (see Fig. 1) [6].

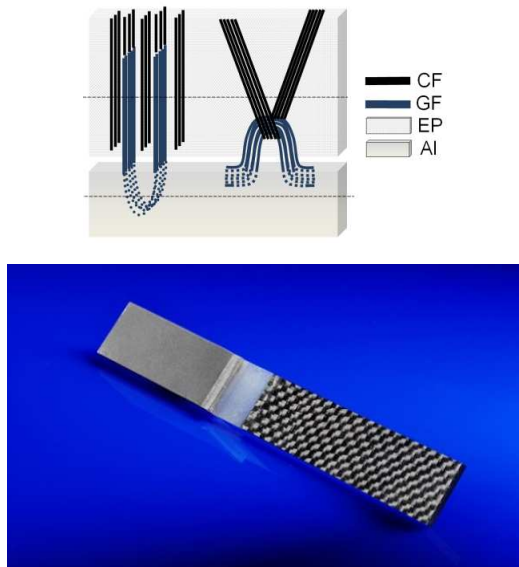


Fig. 1 Schematic illustration of the fiber concept (above), aluminum-CFRP hybrid structure based on the fiber concept (below)

In this article the mechanical properties of CFRP-aluminum hybrid structures are analyzed. The investigation aims for a comparative analysis of different fiber architectures on resulting tensile forces.

Correlations between different material parameters of integrated glass-fiber fabrics with achievable tensile strengths of the total compound of aluminum and CFRP were analyzed. Simultaneously, the fault tolerance of the manufacturing process was reviewed and determined, which manufacturing imperfections show an influence on the failure behavior in tensile tests.

2 FUNDAMENTALS AND PRELIMINARY STUDIES

In previous studies different fiber structures were tested for their infiltration characteristics in the high pressure die casting process. Using metallographic sections the infiltration capacity was determined. It was shown, that glass fiber fabric shows better infiltration characteristics than glass-fiber mats with the same weight per unit area. The infiltration grade of the fiber structures is critically dependent on the textile architecture. For the fiber structures it was verified that both the layer structure (number of layers), and the yarn spacing affect the local permeability and thus the infiltration grade of the structures [7].

3 EXPERIMENTAL

For the preparation of the examined tensile test specimens, the glass-fiber structures have been prestressed with a clamping frame, partially sealed and positioned in the high pressure die casting mold. After the die casting process the so-called partial connections are available for further processing. They consist of an aluminum-glass-fiber composite and a protruding glass-fiber area (see Fig. 2).

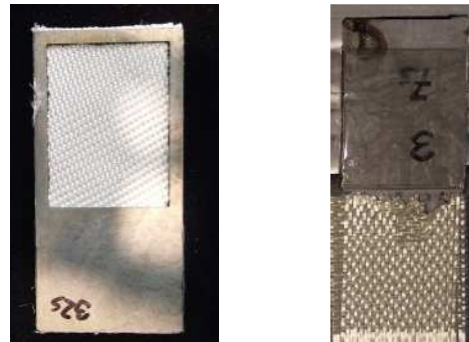


Fig. 2 Glass-fiber insert with clamping frame and sealed area (left), partial connection (right)

In the next production step, a laminate structure with carbon fiber fabric and infiltration with resin is build up. For the examined samples a manual, non-pressurized resin infiltration was carried out with a two-component epoxy resin in a closed mould. Finally, the samples were cut to a width of 20 mm, wherein the clamping frame from the die casting process was cut-out from the sample area.

Several parameters were varied in the DOE, such as the number of layers, type of fabric or weight per unit area of fabric (Table 1).

All specimens were sprayed with a black-white speckle pattern from two sides to prepare them for optical strain measurement (OSM) with a *GOM-Aramis* system. The local strains were measured from two different perspectives during tensile tests (Fig. 3).

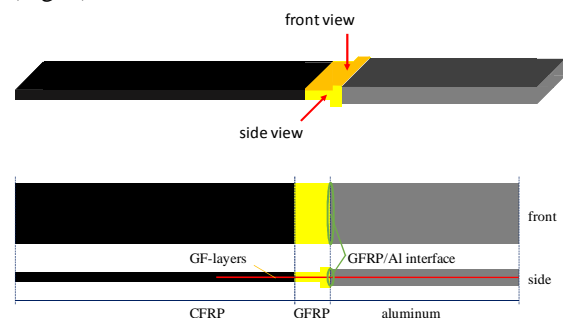


Fig. 3 Perspectives for optical strain measurement with *GOM Aramis*

4 RESULTS AND EVALUATION

Table 1 gives an overview over the relevant specimen parameters on the one hand and the maximum forces during tensile tests on the other hand. There is a tendency, but no direct correlation between specimen parameters and maximum forces. This indicates that the maximum forces are influenced by the specimen parameters as well as by so called structural parameters such as infiltration content or undulation of glass-fibers. In the following chapters it is explained how to detect these structural parameters and how they influence the mechanical behavior of the specimen.

Table 1: Specimen parameters, maximum forces and perspectives for optical strain measurement

Test number	Layers	Fabric	Weight per unit area	Fmax	Perspective (OSM)
VR1-1-1	2	Satin 8	300 g/m ²	1.5 kN	side
VR1-1-2	2	Satin 8	300 g/m ²	1.2 kN	front
VR1-2-1	3	Satin 8	300 g/m ²	1.0 kN	side
VR1-2-2	3	Satin 8	300 g/m ²	1.1 kN	front
VR1-3-1	3	Atlas 1/7	195 g/m ²	1.7 kN	side
VR1-3-2	3	Atlas 1/7	195 g/m ²	1.7 kN	front
VR1-4-1	3	Atlas 1/7	195 g/m ²	3.2 kN	side
VR1-4-2	3	Atlas 1/7	195 g/m ²	2.9 kN	front
VR1-5-1	3	Atlas 1/7	195 g/m ²	1.9 kN	side
VR1-5-2	3	Atlas 1/7	195 g/m ²	2.1 kN	front
VR1-6-1	4	Atlas 1/7	195 g/m ²	2.7 kN	side
VR1-6-2	4	Atlas 1/7	195 g/m ²	2.7 kN	front
VR1-7-1	4	Atlas 1/7	195 g/m ²	2.7 kN	side
VR1-7-2	4	Atlas 1/7	195 g/m ²	2.8 kN	front

4.1 COMPARISON OF INFILTRATION CONTENT IN THE TRANSITION AREA TO THE INFILTRATION CONTENT IN METAL-MATRIX COMPOSITE

In previous studies the infiltration content of fiber structures in the center of the aluminum-glass fiber area was studied (see chapter 2). Because an influence by the sealing may be possible, a metallography is carried close to the transition area and compared with the previous studies on selected samples. Here, no significant difference was found in the local infiltration content (see Fig. 4).

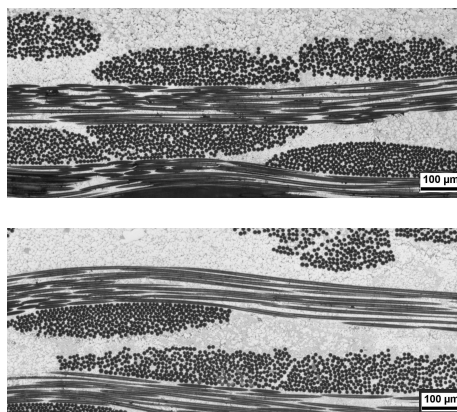


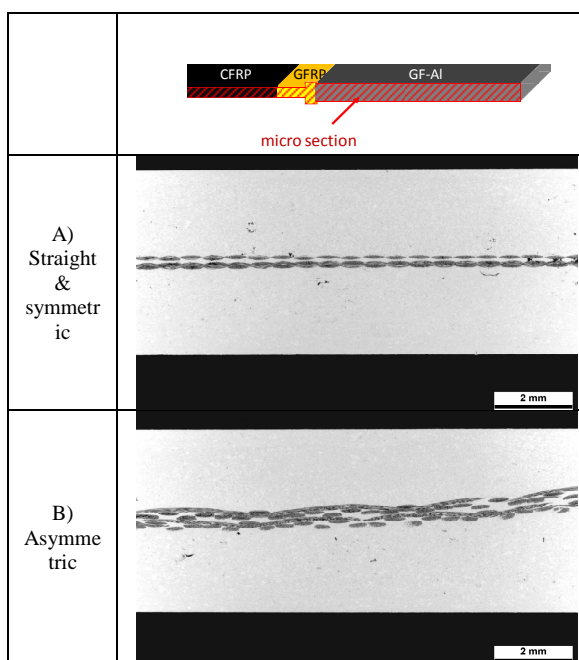
Fig. 4 Metallographic sections of infiltration behavior of GF-Al. Top: middle of aluminum-glass-fiber area; below: close to the transition area between aluminum und GFRP

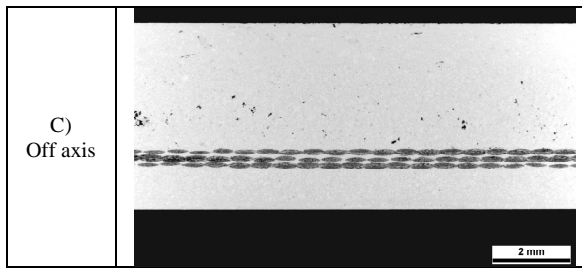
The studies have also shown that a combination of a larger number of glass fiber layers with a high weight per unit area can lead to the fact that the area in the interior of the layers will not be completely infiltrated.

4.2 UNDULATION OF GLASSFIBERS PATHWAY

Investigations have shown that the GF pathway inside the aluminum may be influenced by the casting process (Table 2). The requested pathway is straight and symmetric (A), but macroscopic undulations like asymmetries (B) or off axis (C) may occur as well.

Table 2: GF pathway transverse GFRP/Al interface, recorded before failure





As seen in Table 3, the GF pathway varies not just transverse but also along the GFRP/Al interface. Whereas the GF pathway transverse to the GFRP/Al interface could be recorded with OSM (side view), the GF pathway along the interface is hidden inside the body of specimen and couldn't be investigated by optical strain measurement due to the limitation to surfaces.

Table 3: GF pathway along GFRP/Al interface, recorded after failure

Test number	Diagram	Micrograph
VR1-2-1		
VR1-4-1		
VR1-5-1		

Both the undulation transverse and along the interface may be caused by the casting process using one sprue from one side and may influence the tensile strains and the failure behavior.

4.3 CORRELATION BETWEEN FORCES AND OPTICAL STRAIN MEASUREMENT

Optical measurement of strain and force-displacement can be matched to each other by the test time (Fig. 5). While increasing the force, the mechanical behavior of the specimen is elastic until point (2). At point (3) a first stress concentration can be indicated at the GFRP/Al interface resulting in a crack (4). Before reaching the maximum force, stress concentration can be detected at both sides

along the glass fibers in the GFRP and the glass fiber reinforced aluminum (5-7). After failure (8) the strains decline.

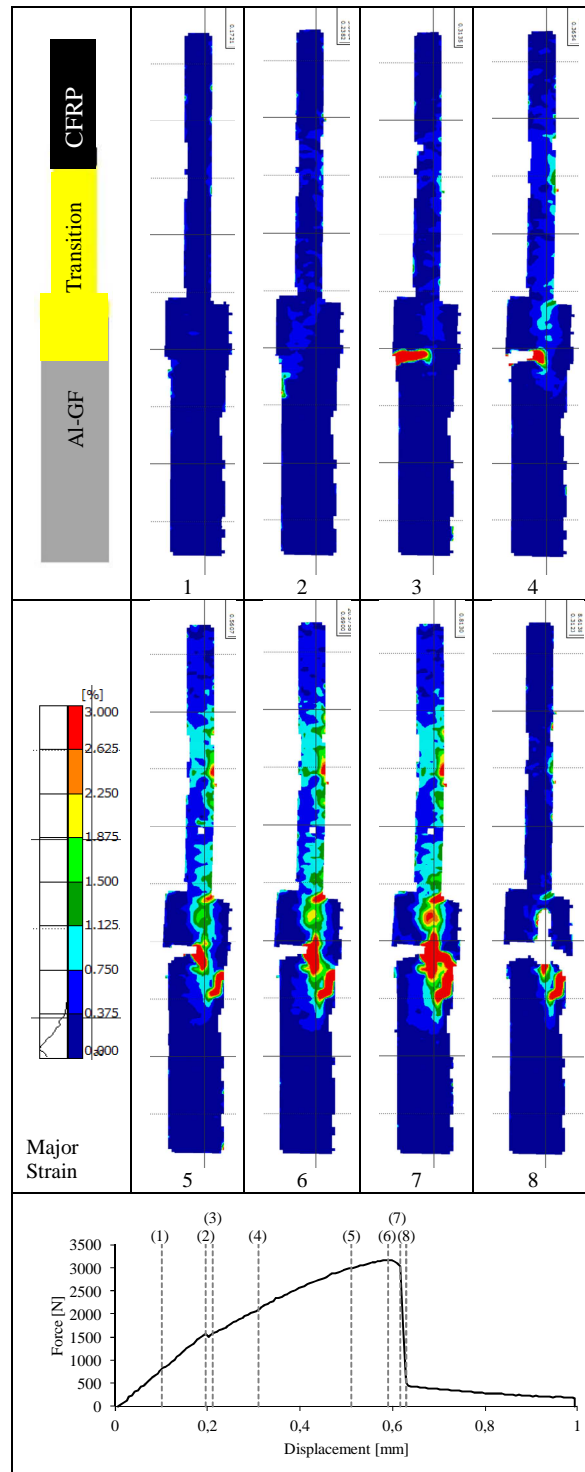


Fig. 5 Correlation between side view optical strain measurement (above and middle) and force-displacement (below) of specimen VR1-4-1

The local strain measurement indicates the strain concentration, the location of initial crack, crack propagation and failure behavior.

The glass fibers of the GFRP are concentrated on or beside the symmetry line, so that there are always unreinforced pure epoxy areas. Due to the weak adhesion forces between epoxy areas and aluminum the first crack occurs in most cases at the interface in this series of test.

After failure of the EP/Al interface the flux of force from the GRFP is concentrated on the glass fibers before transferred by shear to normal forces in the aluminum. This phenomenon is visible as well in the local strains of the test specimens. More explanations are given in chapter 4.4.

4.4 STRAIN CONCENTRATION AND CRACK BEHAVIOUR OF SPECIMEN

Table 4 shows an exemplary specimen where cracking occurs in the GF-Al indicated by red lines at the side view. Obviously the infiltration of the GF with aluminum isn't perfect, so that there is a reduced contact between the glass fibers and the aluminum matrix. Normal forces, rather smooth distributed to all GF layers when entering the aluminum, can be partially transferred via shear to the aluminum matrix from the outer and well embedded layers, resulting in a stress concentration in the middle, less embedded layers. Although the local stiffness of the specimen is unknown, it can be assumed that the stress concentration in the middle less embedded GF layers result in a strain concentration. This phenomenon can be detected in the optical strain measurement (Fig. 5, Table 4 & 6). The Infiltration content is not strictly separated in good outer layer and bad inner layer, but has a gradient and random distribution. This means, the longer the way in the aluminum is, the more forces can be transferred to the matrix even from the middle layers, resulting in a smooth strain concentration (blue area) after a certain distance from the GFRP/Al interface.

Table 4: Cracking of specimen VR1-6-1: above: side view, crack indicated with red lines, middle: microsection, below: OSM

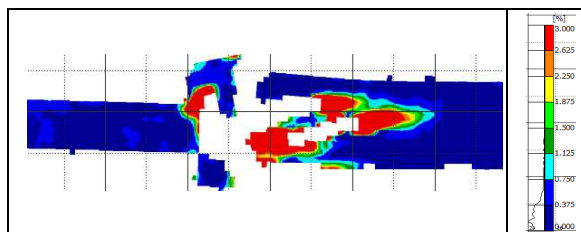
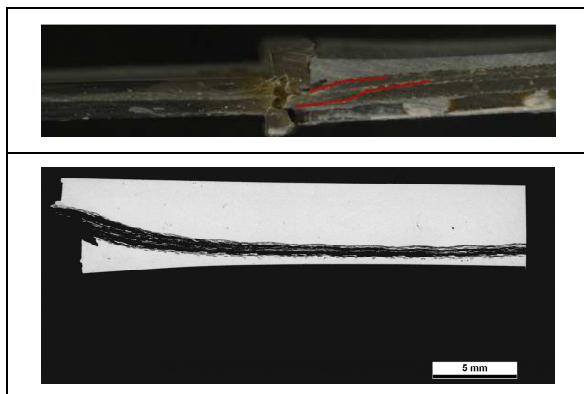


Table 5 shows the summarized influence of specimen properties to strain concentration. It has to be mentioned, that these are tendencies due to difficulties to categorize the effects clearly.

Table 5: Influence of specimen properties to strain concentration: ↑ increasing, ↓ decreasing

Specimen property	Influence to strain concentration
Number of layers ↑	↑
Undulation ↑	↑
Infiltration content ↓	↑

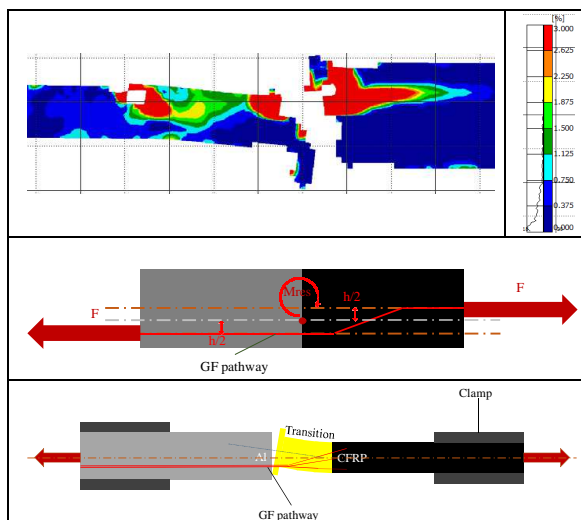
4.5 BENDING OF SPECIMEN

Before testing no distortion could be detected at the specimens. Under tensile loads, a bending of a few specimens could be discovered with unaided eye as well as with OSM (Table 6).

As shown in the micro sections in chapter 4.2 the pathway of the glass fibers is not always straight and symmetric, but can be located on or beside the symmetric line of the specimen. In case of an eccentric pathway, the forces in the transition area are eccentric as well inducing a resulting reverse bending moment.

The eccentricity of glass fibers as well as the bending of the specimen can be detected by local strain measurement.

Table 6: Bending of transition structure due to eccentric glass fibers in VR1-5-1. Above: local strains, middle schematic bending, below: schematic forces



4.6 CORRELATION BETWEEN FIBER PARAMETERS, MANUFACTURING IMPERFECTIONS AND MAXIMUM TENSILE FORCE

The results of the tensile tests were correlated both with the number of integrated fabric layers as well as with so-called structural parameters of the glass-fiber layers. A correlation with results from tensile tests can be determined by correlation of undulation of the glass-fiber fabric in the aluminum sector and infiltration content within glass fiber structures.

A higher number of fabric layers leads to an increase in the length of splitting in the transition area during tensile test. At the same time a higher tensile strength is achieved. A strong fiber undulation leads to an increased tendency for splitting in the transition area while a lower undulation leads to a higher tensile strength. Also, lower infiltration content leads to a larger tendency of splitting in the transition area.

5 SUMMARY AND OUTLOOK

The results of the tensile tests show that besides the material parameters of the used glass fibers, the so-called structural parameters have a major influence on the failure behavior of the investigated hybrid structures.

By recording the tensile tests with the OSM system some conclusions about the behavior of the samples under load such as splitting in the transition area, bending, stress concentrations, crack initiation and crack growth could be made. These results can be transferred inversely on the structural parameters. The use of the OSM system allows, for example, determining the position of the glass fiber layers during the tensile test. So, metallographic micrographs will be partially redundant.

However, some limits must be observed. Strain measurement is possible only at the surface, and no stresses can be measured or calculated without the knowledge of the local stiffness.

The influence of the investigated parameters on the maximum tensile force has been found to be very extensive due to the wide range of influencing factors. Therefore, further studies with statistical validation are required to figure out an explicit correlation of the influencing factors.

6 ACKNOWLEDGEMENT

The authors grateful acknowledge the Deutsche Forschungsgemeinschaft (DFG) for their financial support within the research-group “Schwarz-Silber” (FOR1224) at the University of Bremen.

REFERENCES

- [1] Lehmhus, D., Busse, M., Herrmann, A. S., Kayvantash K.: *Structural Materials and Processes in Transportation – Part I Metals* (von Hehl A.), *Part VI Higher Level Trends* (Lehmhus D.). Wiley-VCH, Weinheim, 2013.
- [2] Clausen, J., et al: *Integration of glass fiber structures in aluminum cast parts for CFRP aluminum transition structures*. *Procedia Materials Science*, Vol. 2, 2013, S. 197–203.
- [3] Wang, W.-X., Takao, Y., Matsubara, T.: *Galvanic corrosion-resistant carbon fiber metal laminates*. 16th international conference on composite materials, Kyoto, Japan, 2007.
- [4] Mehner, A., et al: *Corrosion of Aluminum Alloys in Integral Hybrid Components with Carbon Fiber Reinforced Plastics (CFRP) or Titanium*. Presentation at the Euro LightMAT Conference, Bremen, 2013.
- [5] Yiping Tang, Lei Liu, Weiwei Li, Bin Shen, Wenbin Hu: *Interface characteristics and mechanical properties of short carbon fibers/Al composites with different coatings*. *Applied Surface Science* 255 (2009) 4393–4400.
- [6] Lang, A., Husemann, L., Herrmann, A. S.: *Influence of Textile Process Parameter On Joint Strength For Integral CFRP-Aluminum Transition Structures*. *Procedia Materials Science*, Vol. 2, 2013, S. 212–219.
- [7] Clausen, J., et al: *Integration textiler Strukturen in den Aluminium-Druckguss zur Realisierung integraler CFK-Aluminum-Verbindungen*. Tagungsband zum 7.Landshuter Leichtbau-Colloquium, Landshut, 2015

LASER-BASED JOINING OF THERMOPLASTICS TO METALS: INFLUENCE OF VARIED AMBIENT CONDITIONS ON JOINT PERFORMANCE AND MICROSTRUCTURE

Klaus Schricker^{1*}, Martin Stambke¹, Jean Pierre Bergmann¹, Kevin Bräutigam¹

¹Ilmenau University of Technology, Department of Production Technology

KEYWORDS: laser-based metal plastic joining, ambient conditions, morphology, mechanical properties

EXTENDED ABSTRACT

The application of lightweight potentials in automotive industry, mechanical engineering and aviation industry requires a mass reduction without limiting the loadability, stiffness or fatigue of structural components. The use of new materials and multi-material-design enables functional lightweight constructions. Especially, the joining of thermoplastics to metals has a great potential for the use of the right material at the right place, but shows high requirements on the joining technology. Laser-based thermal joining shows advantages over competitive processes without the need of an addition material (e. g. adhesives) or a connecting element (e. g. screws or rivets) and enables a local and areal bonding with a high load capacity.

In this process, the polymer gets molten by the energy input of the laser beam, thus wets the metal surface and penetrates the surface structures. A solid joint is formed after solidification. The resulting melting layer shows different properties compared to the base material, depending on time-temperature regime, especially in crystallinity and microstructure (figure 1) [1]. An analogue behavior for laser transmission welding of plastics or injection molding of plastics is shown in the literature [2, 3, 4]. According to [1] and [5], these properties can be adjusted by the temperature-time profile and influence the joint performance directly, for example the energy consumption and crosshead travel in tensile shear testing (test speed: $240 \text{ mm}\cdot\text{min}^{-1}$, overlap joint: $50 \times 20 \text{ mm}^2$, laser beam power: 1 kW, laser spot diameter: 5 mm, metal: EN AW 6082 with $t = 1.5 \text{ mm}$, plastic: PA 6.6 with $t = 2 \text{ mm}$):

The energy consumption of the tested joints is increasing from $7.5 \text{ kN}\cdot\text{mm}$ for a joining speed of $3 \text{ mm}\cdot\text{s}^{-1}$ to $25 \text{ kN}\cdot\text{mm}$ for a joining speed of $7 \text{ mm}\cdot\text{s}^{-1}$. The reached maximum force is comparable for both parameters, but the crosshead travel rises from 7.5 mm to 25 mm. In each case, the

fracture of the joint occurs within plastic base material. Thereby, higher joining speeds show a narrow temperature-time profile and a higher cooling rate compared to lower joining speeds [5]. This leads to a higher percentage of amorphous areas in the plastic joining partner, that show a greater movability compared to crystalline areas. Furthermore, the size of the melting layer is increasing.

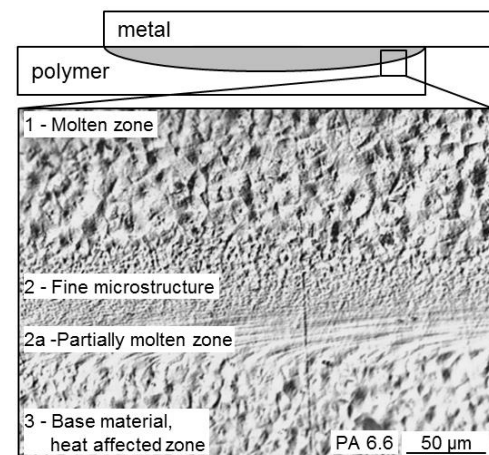


Fig. 1 Microstructure of the melting layer in hybrid joints (PA 6.6 with EN AW 6082) [1]

Based on these results, further investigations for three different melting layers (PA 66), adjusted by the time-temperature regime, were performed. The hybrid joints were aged under outdoor weathering (connected to meteorological data), temperatures above glass transition temperature ($85 \text{ }^\circ\text{C}$, $155 \text{ }^\circ\text{C}$), UV-radiation and salt spray test (according to DIN EN ISO 9227). Thereby, the modification of the microstructure within the melting layer is connected to the mechanical properties for varied ambient conditions.

An extract from the results is presented in Figure 2 and shows the alteration of force-crosshead travel

graphs in outdoor weathering for a reference specimen (weathering: 0 days) and after 28 days for a joining speed of $4 \text{ mm}\cdot\text{s}^{-1}$. A special characteristic due to the proportion of water in PA 6.6 can be proven in comparing the mechanical properties of different joining speeds, because the force-crosshead-travel graphs are harmonizing by increasing aging time. The fracture in tensile shear testing is still within plastic base material.

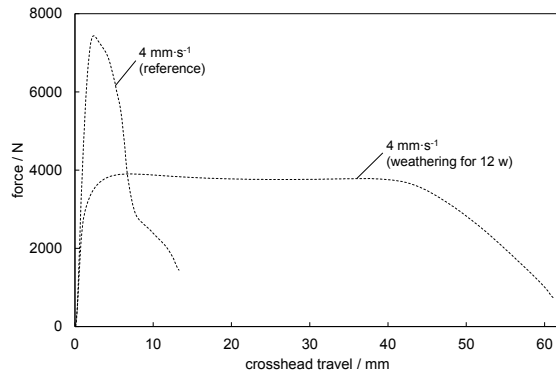


Fig. 2 Force-crosshead travel graphs for outdoor weathering (0 days and 28 days)

In summary, the impact of different joining speeds on temperature-time profile, melting layer and mechanical properties can be shown. Based on three different joining parameters, the influence of varied ambient conditions on joint performance was examined. Thereby, tensile shear tests always showed a failure within plastic base material, even if a change in energy consumption and force-crosshead travel graphs can be proven.

At this point, longer time periods, additional ambient conditions and alternative materials, e. g. polyolefins, have to be investigated. This allows the relation of the shown effects on morphology and mechanical properties to the impact of varied ambient conditions and material characteristics. Furthermore, investigations on the occurring zones within thermoplastic morphology as well as the process influences (e. g. ejection of molten polymer) to mechanical properties will be part of the future work.

REFERENCES

- [1] K. Schricker, M. Stambke, J. P. Bergmann, Experimental investigations and modelling of the melting layer in polymer-metal hybrid structures, *Welding In The World*, DOI 10.1007/s40194-014-0213-0, (2014)
- [2] Ghorbel E. et al., Laser diode transmission welding of polypropylene: Geometrical and microstructure characterisation of weld, *Materials and Design*, 30, 2745-2751 (2009)

- [3] Al-Wohoush M. H. et al., Characterization of Thermoplastic Laser-welded Joints, *Intern. Polymer Processing*, XXVII, 574-583 (2012)
- [4] Nguyen-Chung T. et al., Morphology analysis of injection molded micro-parts, *Journal of Plastics Technology*, 7, 87-102 (2011)
- [5] Schricker, K.; Stambke, M.; Bergmann, J. P.: Adjustment and Impact of the Thermoplastic Microstructure of the Melting Layer in Laser-based Joining of Polymers to Metals. *Lasers in Manufacturing Conference* (2015)

CHARACTERIZATION OF INTERFACE PROPERTIES OF FIBER-METAL-LAMINATES (FML) WITH OPTIMIZED SURFACES

Matthias Stoll*, Kay André Weidenmann¹

Karlsruhe Institute of Technology (KIT), Institute for Applied Materials IAM-WK, Germany

ABSTRACT: Fiber-Metal-Laminates (FML) combine the outstanding specific mechanical properties of carbon fiber reinforced polymers (CFRP) and lightweight metals. Additionally they promise exceptional dynamic properties. However, laminates are prone to fail prematurely due to delamination. The resistance to delamination of a FML can be characterized by determining the interlaminar shear strength and shear energy. The mechanical properties can be increased by optimizing the laminate surfaces to increase adhesion between the composite partners.

The surfaces were optimized by plasma enhanced chemical vapor deposition, by sand blasting and by grinding. Additionally an elastomer interlayer was introduced to increase adhesion and to endure high strains. These surface modifications were compared to a reference FML without modified interfaces. The characterization of the laminates was carried out using the edge shear test to enforce failure due to shear load.

This contribution focuses on the characterization and optimization of the adhesion between composite partners in a laminate. The authors present results of surface optimization in Fiber-Metal-Laminates.

KEYWORDS: Fiber-Metal-Laminate, Interface Characterization, Interlaminar Shear Strength, Materials Testing

1 INTRODUCTION

Lightweight solutions are often based on an extraordinary stiffness to density ratio, but dynamic resistances [1], such as low crack propagation [2] are, depending on the application, even more important. Fiber-Metal-Laminates combine high crack resistance with low density and are already commercially available (c.f. GLARE [3,4]). High specific quasi static properties were prerequisites for the laminates investigated in this study, even though the focus was on interlaminar properties.

The performance of the commercially available composite structures can be optimized by replacing the glass fibers with carbon fibers due to the higher stiffness and strength, yet lower density of the carbon fiber. However the replacement introduces risk of contact corrosion as well as sensitivity to delamination caused by very different coefficients of thermal expansion (CTE-mismatch) [5].

The addition of a surface layer with passivating properties and optimized adhesion can improve the laminate. It may prevent corrosion by electrical

decoupling and counteract delamination by increased adhesion. In this study the metal was coated by plasma enhanced chemical vapor deposition or mechanical treatment was carried out. Additionally the application of an elastomer layer was implemented in the production process. The adhesion of the laminate layers was tested by the edge shear test [6] to characterize the adhesive bond between the carbon fiber reinforced polymer and the metal. The adhesion tested accounts for the resistance to delamination, which is of great interest when testing laminates, as laminates often prematurely fail due to delamination. To inhibit delamination adhesion is to be increased by optimization of the CFRP/metal interface. The maximum shear stress [7] to separate the laminate layers and the energy dissipated will be characteristic values for the adhesion of the laminate.

2 MATERIALS

The Fiber-Metal-Laminates consist of a Carbon Fiber Reinforced Polymer (CFRP) and either an aluminum alloy or a steel layer.

* Corresponding author: Engelbert-Arnold Straße 4, 76131 Karlsruhe, Germany, Telephone: +49 721 608 44163, Fax: +49 721 608 48044, Matthias.Stoll@kit.edu/ Kay.Weidenmann@kit.edu

The FML was manufactured at the Institute for Production Science (wbk) at KIT. A Lauffer type RP 400 OK 920 machine press was used at 150 °C at a pressure of 23 bar for the curing cycle of 5 minutes.

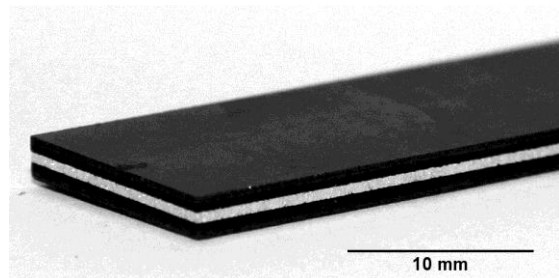


Fig. 1 Fiber-Metal-Laminate with elastomer interlayers

Fig. 1 shows a FML with elastomer interlayers where the layer succession is CFRP – Elastomer – Aluminum – Elastomer – CFRP. This sequence is used for dimensional stability as the CTE-mismatch does not deform the FML. The aluminum can be substituted for a steel layer and the elastomer can be replaced by a CVD coating.

2.1 CARBON FIBER REINFORCED POLYMER

The CFRP used in this study is a Hexcel M77/42%/UD90/CHS with unidirectional high strength carbon fibers and an optimized resin for fast curing cycles to counteract the usually long curing cycles of FML. For the application in the FML a low sheet thickness of 0.1 mm was essential to guarantee a variable layout of the CFRP layer in the Fiber-Metal-Laminate.

The curing temperature of the epoxy matrix was matched to the curing temperature of the elastomer interlayer to ensure the best quality FML with elastomer interlayers.

The CFRP has high specific mechanical properties, because of the high strength fibers and a fiber volume content of 50 %, resulting in a density of 1.5 g/cm³. The unidirectional prepreg sheets were arranged to a biaxial CFRP layer. The recommended curing cycle for this prepreg is 2 minutes at a temperature of 150 °C and a pressure >5 bar.

2.2 METAL

The metal used in the FML was chosen according to high resistance to sheet bending and simultaneously low density. Another restriction was the possibility to roll the metal to a 0.3 mm thin sheet. Therefore the first choice was an aluminum alloy with high strengths.

For high overall mechanical properties disregarding the density restriction of the metal another FML with a steel sheet was fabricated. Steel was

used to vary chemical and mechanical properties on top of the good rollability and availability.

2.2.1 ALUMINUM 2024-T3

Structural applications often use the 2024 alloy in a hardened state. An aluminum 2024-T3 was chosen to ensure comparability as many laminates use this alloy [3,4,7]. The alloy has extraordinary specific strengths and good availability in rolled thin sheets. The minimum thickness of 2024-T3 commercially available is 0.3 mm, being sufficient for the FML.

2.2.2 STEEL TS275

The steel chosen was a carbon steel, as other steels with higher strengths are not commercially available in the desired thickness. The results obtained with this steel can be transferred to other alloys as the surface properties do not differ greatly when the alloy is changed.

3 SURFACE OPTIMIZATION

To counteract premature failure due to delamination between laminate layers the adhesion has to be enhanced by surface optimization.

The optimization may solve the problems caused by the mismatch of thermal expansion coefficients (CTE-mismatch) and corrosion potentials caused by the combination of CFRP and metal sheets.

In this research plasma enhanced chemical vapor deposition, an elastomer interlayer and mechanical treatment will be compared to the reference FML without any interface customization.

3.1 PLASMA ENHANCED CVD

Plasma enhanced chemical vapor (PECVD) deposition was used to deposit a silicone-based coatings on the metal layer. Different kinds of layer compositions were used and are described below.

PECVD was performed by Fraunhofer Institute for Chemical Technology (ICT) in Pfingsttal, Germany. Bulk SiO₂ was used as a surface optimization layer and as a base layer for different PECVD coatings to ensure better adhesion to the metal substrate. The silicone-based layers are desired to inhibit corrosion.

The contact angle of the coating was measured at Fraunhofer ICT and is expected to define the adhesion of the laminate layers. The surface property can be chosen from hydrophobic to super hydrophilic. The hydrophilic layers have a contact angle of 50° on steel and 67° on aluminum. The hydrophobic layer has an angle greater than 90° and the super hydrophilic layer's contact angle is 0°.

Table 1: Properties of PECVD surface optimization

Surface	Properties	Thickness
Bulk SiO ₂	hydrophilic	1.2 μm
SiO ₂ /Si _w C _x H _y O _z	hydrophobic	1.1 μm

nanoporous	Super hydrophilic	100-200 nm
SiO ₂ /nanoporous	Super hydrophilic	1.4 μm

3.2 MECHANICAL TREATMENT

Mechanical treatments for enhanced adhesion of metals to CFRP are based on the principal of form fit. One treatment was grinding the metal layer and the other was sand blasting. Both treatments are predicted to increase adhesion due to the roughened surface.

3.3 ELASTOMER INTERLAYER

The elastomer used in this research was provided by Kraiburg, the registered trade name is Kraibon and it is optimized for applications with CFRP. The mixture chosen, SAA-9579/52, does not only possess enhanced adhesion to CFRP with epoxy matrix but also to aluminum.

The elastomer interlayer promises inhibited corrosion, balancing of CTE-mismatch and increased adhesion. The elastomer layer has a thickness of 0.5 mm and a curing temperature fitted to established CFRP curing temperatures. The curing cycle for the FML is defined by the elastomer, as it is the slower component of the fiber-metal-laminate. The elastomer requires a curing cycle of 5 minutes at >4.8 bar pressure at the given 150°C. Therefore the cycle time is set to 5 minutes at the temperature defined by the CFRP of 150°C.

4 CHARACTERIZATION

The fiber-metal-laminates were characterized using the edge shear test [6] to induce pure shear into the interface. This test was deliberately chosen for these experiments, because the interface can be tested without any interference of the laminate components.

Additionally the specimen had a simple geometry and was small compared to the double notch test [7], allowing a greater number of tests to statistically ensure the results. The 20 x 10 mm² specimens were cut by water jet cutting. The exact dimensions were measured using a micrometer screw. Stresses were calculated using the measured cross section.

The test rig prevents buckling by supporting the specimen during the experiment (c.f. Fig. 2). Also the shear plane can be deliberately put into the interface of the laminate structure to force failure in the desired plane.



Fig. 2 FML with elastomer interlayer in the edge shear test

The experimental set-up induces pure shear stress into the specimen using two edges (c.f. Fig. 2), hence the name edge shear test. The set-up was mounted on a ZwickRoell ZMART.PRO 100kN universal testing machine. The test was carried out with a speed of 1 mm/min to achieve quasi static testing conditions. The tests were performed at room temperature and the interface failed under shear stress. The shear stress is the quotient of the maximum force measured in the experiment and the area of the sample measured before testing. The shear energy is the integral under the stress-strain curve of the edge shear test. All specimens showed comparable stress-strain curves, except the FML with elastomer interlayers. Two representative curves are shown in Fig. 3.

Since the elastomer interlayer alters the interface characteristics drastically the shear strength alone is not significant enough to solely characterize the FML and rank the surface modifications. Therefore the shear energy is considered as well. Fig. 3 shows the two types of stress-strain curves, one being a stiff and brittle and the other being soft and ductile.

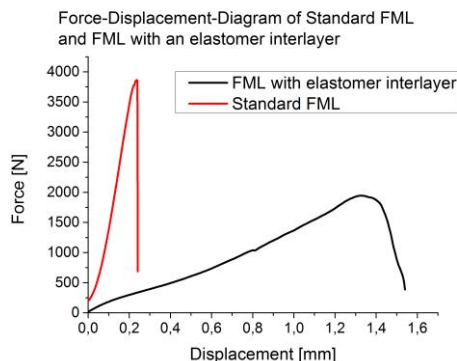


Fig. 3 Force-displacement curves of Standard FML compared to FML with elastomer interlayers

4.1 SHEAR STRENGTH

The shear strength of the laminate shows the maximum shear stress value and characterizes the adhesion strength when loaded with shear stress. FML with modified surfaces are desired to have higher strengths compared to the reference FML. FML with shear soft interfaces such as the elastomer interlayer are expected to have a lower shear strength compared to stiffer layers like the PECVD coatings.

The shear strength for lightweight applications should be divided by the laminate density. To ensure good comparability between all laminates, the absolute values are presented here.

4.2 SHEAR ENERGY

The shear energy is equal to the area under the stress-strain-curve. It is the energy needed to separate the layers of the laminate, which equals the energy dissipated during delamination.

For stiff layers with high strengths and low strains the total energy is expected to be lower compared to the elastomer layers which have lower strengths but much greater strains (c.f. Fig. 2).

The shear energy is a critical value when describing interface properties.

5 RESULTS

All specimens showed failure due to shear stress in the interface between the metal sheet and the CFRP. A total of 16 specimens were tested for every modification of the laminate to generate one value for shear strength and shear energy.

The results of the optimized surfaces tested by the edge shear test will be compared to the reference FML without modified interfaces.

5.1 REFERENCE FML

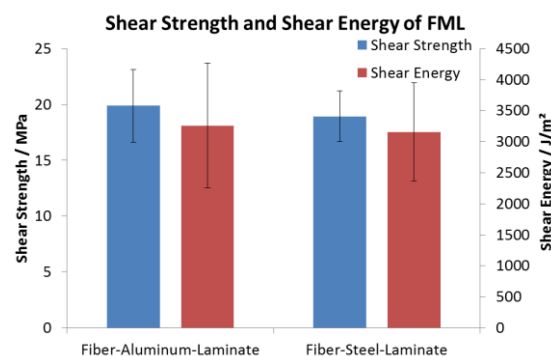


Fig. 4 Interface properties of FML using Aluminum and Steel substrates characterized by the edge shear test

The mechanical interface properties for the reference laminates are shown above (Fig. 4).

The shear strength and energy generally depend on the metal used in the laminate. The metals used for this research, Al 2024-T3 and Steel TS275 and their surface properties with unmodified surfaces do not differ greatly (c.f. Fig.4). The interface properties are marginally lower using steel sheets. The exact values for the interface properties can be found in Table 1 for aluminum and Table 2 for steel.

The surface optimization, however, greatly depends on the metal layer and therefore the results are compared to the laminate with the same metal substrate and unmodified surface. This specimen is called “reference” sample for the respective metal. The densities of the laminates are not accounted for in these results, but it the higher density of steel has to be kept in mind when comparing FML with aluminum and steel layers.

5.2 QUALITATIVE ANALYSIS

The introduction of an adhesive coating does not change the mechanical behavior of the laminate, because all samples had the characteristics of the red curve in Fig. 3.

This statement does not include the elastomer interlayer, which allows large strains and lowers the shear strength. The characteristic curve for this configuration can be found in the black graph in Fig. 3.

This behavior cannot easily be compared to the reference sample. The interface properties of the reference and the elastomer layup are shown in Fig. 5. The aluminum-based FML is shown here, but the steel substrate indicates the same behavior.

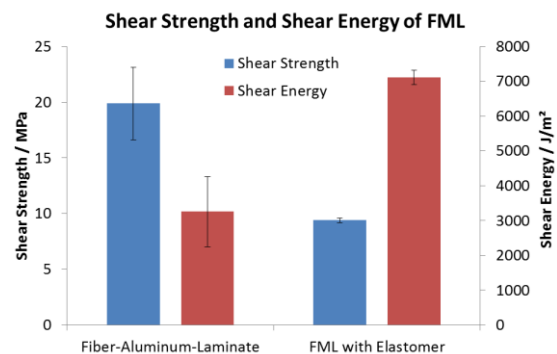


Fig. 5 Interface properties of FML with an elastomer interlayer compared to the reference

As predicted the shear strength of the FML with elastomer is reduced to approximately half of the reference’s strength. The elastomer also causes the shear energy to more than double in value compared to the FML.

Additionally the size of the error indicators shrinks when the elastomer interlayer is applied.

5.3 MECHANICAL CHARACTERIZATION

For each surface optimization 16 samples were tested and the shear strength and shear energy was calculated. The order is according to the succession in Chapter 3. The results are arranged by metal substrate, first the aluminum, followed by the steel substrate.

Table 2: Mechanical characterization of the surface optimization of Fiber-Aluminum-Laminates

Surface	Shear Strength MPa	Shear Energy J/m ²
Reference	19.9 (± 3.3)	3260 (± 1006)
Bulk SiO ₂	20.9 (± 2.7)	3037 (± 559)
SiO ₂ /Si _w C _x H _y O _z	16.2 (± 3.4)	2284 (± 1266)
nanoporous	10.9 (± 3.3)	1590 (± 521)
SiO ₂ /nanoporous	16.5 (± 2.7)	2447 (± 585)
Grinding	17.6 (± 2.7)	2994 (± 691)
Sand blasting	22.6 (± 2.4)	2757 (± 500)
Elastomer	9.4 (± 0.2)	7108 (± 206)

The results shown in Table 2 show the values of shear strength and shear energy of all surface modified FML. Each value is supported by 16 test specimen and is therefore statistically verified.

An increase in shear strength and shear energy would be desirable, but could not be reached by any modification.

A decrease in shear strength can be seen by most surface modifications compared to the reference FML. The only substantial shear strength increase was reached by sand blasting, but is paired with a reduction in shear energy.

The elastomer reduces shear strength and increases shear energy drastically.

Table 3: Mechanical characterization of the surface optimization of Fiber-Steel-Laminates

Surface	Shear Strength MPa	Shear Energy J/m ²
Reference	18.9 (± 2.3)	3158 (± 788)
Bulk SiO ₂	12.0 (± 2.1)	1068 (± 534)
SiO ₂ /Si _w C _x H _y O _z	9.1 (± 1.7)	555 (± 191)
nanoporous	4.1 (± 0.9)	460 (± 53)
SiO ₂ /nanoporous	14.1 (± 2.0)	1287 (± 318)
Grinding	15.4 (± 3.3)	2870 (± 1001)
Sand blasting	29.4 (± 1.2)	9026 (± 1254)
Elastomer	9.4 (± 0.5)	6826 (± 391)

The values for strength and energy in Table 3 show that only sand blasting increased the shear strength and sand blasting and the elastomer interlayer raised the value for shear energy.

The PECVD coatings lowered both values of the interface properties compared to the reference.

5.4 CONTACT ANGLE MEASUREMENT

A contact angle measurement was carried out post mortem to determine, if the adhesion of the coating to the metal failed.

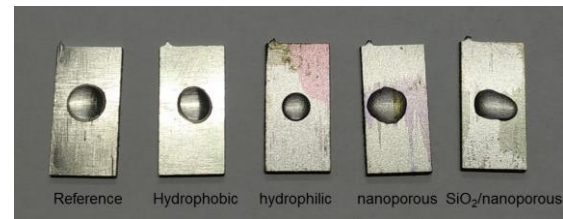


Fig. 6 Contact angle experiments on failed FML specimens

Fig. 6 shows, that the contact angle of all metal layers are similar to the reference. The contact angle of the coating cannot be seen anymore.

6 DISCUSSION

The surface modification by plasma enhanced chemical vapor deposition on aluminum decreased the mechanical properties.

Bulk SiO₂ resulted in an increase in shear strength, but also induced a decrease in shear energy. All other coatings on aluminum could not surpass the mechanical properties of the reference specimen, although the undercuts provided by the nanoporous layer were promising in theory as the layer was ripped off the metal substrate.

The contact angle measurement shown in Fig. 6 indicates that the adhesion of the coating to the metal failed, because the contact angle of all metal layers is close to the reference. Therefore the PECVD was not suitable for FML.

Sand blasting was the only mechanical treatment that showed an increase in strength, but the shear energy was reduced compared to the reference giving this procedure no advantage. The grinding lowered both interface properties. The mechanical treatment is not as extensive as PECVD but presumably does not inhibit corrosion, therefore sand blasting is unsuitable for FML.

The elastomer interlayer reduced shear strength and increased shear energy greatly. Whether the alteration of properties has a benefit has to be decided by the application. Advantages can be found in the high strain tolerance of the elastomer, which would be desirable under strain induced fractures. The layer is desired to inhibit corrosion and balances the CTE-mismatch. It increased the thickness of the FML, but could be suitable for the application in Fiber-Metal-Laminates.

The PECVD coating on steel sheets drastically decreased the mechanical interface properties compared to the reference. Both shear strength and energy were much lower in any configuration of the coating. The contact angle post mortem indi-

cated a failure of the metal/coating adhesion similar to Fig. 6.

Therefore it is concluded that the adhesion of the PECVD-layer to the steel substrate is too low for an application in a laminate. SiO₂ coating may inhibit corrosion, but does not solve the CTE-mismatch.

Mechanical treatment on steel shows promising results, as sand blasting greatly increased shear strength and shear energy. The absolute values of the mechanical properties were the highest, making it an interesting pretreatment. However, the problems caused by contact corrosion and CTE-mismatch cannot likely be solved using mechanical surface treatment. Grinding reduced the interface properties for shear strength and shear energy and therefore is unsuitable.

The elastomer altered the properties on steel similar as on aluminum. It is desired to inhibit corrosion and absorb the CTE-mismatch, making it an interesting choice for the fiber-metal-laminate.

The interface properties of the FML were depicted without focusing on the different densities of aluminum and steel. The values for the steel-based laminates were in the same magnitude as the aluminum-based laminates. Therefore the aluminum-based laminates are more eligible for lightweight applications due to the lower density.

The specimens of all FML modifications failed due to shear stress in the interface between the CFRP and the metal constituent, showing a perfect delamination. No residual CFRP was observed on the metal substrate, proving the desired crack propagation through the interface between laminate partners. Therefore the mechanical properties of the interface between CFRP and metal layer were characterized.

Weidenmann [6] and Hinz [7] forced specimen failure due to shear stress in a different plane namely between the layers of the FRP. The values for shear stress obtained by both were higher than the values in this study.

Hinz [7] monitored fiber/matrix-debonding and matrix cracks in-situ whereas in this study cracks between the laminate partners were observed post mortem. The higher values obtained by Weidenmann [6] and Hinz [7] and the results of this study show that the interlaminar shear strength in the fiber reinforced polymer component is not as critical as the shear strength between the FRP and metal. This conclusion is made based on the crack not propagating through the FRP, but through the interface of the laminate, indicating a higher shear strength in the FRP than in the interface.

7 ACKNOWLEDGEMENT

The research of this paper is kindly supported by the Baden-Württemberg Stiftungs project “Faser-Metall-Gummi-Hybridlaminat (FMGL) – ein neuartiges, nachhaltiges Werkstoffkonzept für den Fahrzeugleichtbau”, support code MAT0012, which is part of the research program “Rohstoff- und Materialeffizienz in der Produktion”.

The authors kindly acknowledge the Gummiwerk Kraiburg as a part of the Kraiburg Holding GmbH & Co. KG for providing the elastomer used in this study, the Fraunhofer ICT in Pfinztal, Germany for carrying out the Plasma Enhanced Chemical Vapor Deposition and the Institute for Production Science (wbk) at Karlsruhe Institute of Technology (KIT) for manufacturing of the Fiber-Metal-Laminates.

REFERENCES

- [1] Ahmadi, H.; Saboiri, H.; Liaghat, G.; Bidkhorji, E.: *Experimental and numerical investigation on the high velocity impact response of GLARE with different thickness ratio*. 11th International Conference on the Mechanical Behavior of Materials, ICM11. Como, Italy, 2011
- [2] T.S.P. Austin, M.M. Singh, P.J. Gregson, P.M. Powell: *Characterisation of fatigue crack growth and related damage mechanisms in FRP-metal hybrid laminates*, Composites Science and Technology 68 [6] 1399–1412, 2008
- [3] Vogelsang, L.B., Vlot, A. *Development of fiber metal laminates for advanced aerospace structures*. Journal of Materials Processing Technology 103 (2000) 1-5
- [4] Vlot, A.: Historical overview, In: Vlot, A. (Hrsg.), Gunnink, J. W. (Hrsg.): *Fibre metal laminates / an introduction*, Verlag Springer Netherlands, 2001, S. 3-21
- [5] Garg, M.; Abdi, F.; Abumeri, G.; Cope, D.: *Characterization of fiber metal laminate subject to various environments*. International SAMPE Technical Conference. Long Beach, CA, United states, 2011
- [6] Weidenmann, K.A., Baumgärtner, L., Haspel, B.: *The Edge Shear Test - An Alternative Testing Method for the Determination of the Interlaminar Shear Strength in Composite Materials*, Material Science Forum 825-826, 806-813 (2015) DOI: 10.4028/www.scientific.net/MSF.825-826.806
- [7] Hinz, St.; Omoori, T.; Hojo, M.; Schulte, K.: *Damage characterisation of fibre metal laminates under interlaminar shear load*, Composites, Part A: Applied Science and Manufacturing 40 [6-7] 925-931(2009)

MULTIFUNCTIONAL METAL-CARBON-FIBER COMPOSITES FOR DAMAGE TOLERANT AND HIGHLY CONDUCTIVE LIGHTWEIGHT STRUCTURES

B. Hannemann^{1*}, S. Backe², S. Schmeer¹, F. Balle², U. P. Breuer¹

¹Institute for Composite Materials (IVW GmbH), Kaiserslautern

²Institute of Materials Science and Engineering (WKK), Kaiserslautern

ABSTRACT: Distinctive attributes of CFRP led to an increasing share of this composite in aviation industry. However, its comparatively poor electrical conductivity and limited damage tolerance require additional systems and elements, compromising today's CFRP lightweight potential. Former research attempts dealing with modified polymer systems could not prove sufficient enhancements. Against this background, a novel hybrid composite material consisting of reinforcing carbon and metal fibers embedded in an epoxy matrix is investigated. Basic idea of this concept is to merge electrical and load-bearing functions by incorporating highly conductive and ductile steel fibers.

Researches on unidirectional reinforced hybrid composites with steel fiber fractions between 10 and 20 vol.% already proved significant enhancements of the electrical and mechanical properties. Compared to conventional CFRP, the electrical conductivity of the hybrid composites is up to five times higher. At the same time, the deformability and damage tolerance of the composite can essentially be risen. The results suggest that an allocation of the steel fibers in core and top layers is advantageous over a homogenous steel fiber distribution. In a next step, this gain of knowledge is transferred to multiaxial laminates with aeronautical stacking sequences. The present paper is focused on the mechanical properties of this hybrid composite.

KEYWORDS: damage tolerance, electrical conductivity, hybrid composite, multifunctionality, steel fibers

1 INTRODUCTION

Due to their superior mechanical properties, carbon fiber reinforced polymers (CFRP) are commonly used in lightweight applications, e.g. aviation or car industry. High structural performance to mass ratio, utilization of anisotropy for tailored strength, stiffness and stability design, excellent fatigue behavior and corrosion resistance are distinguished attributes of CFRP.

However, compared to advanced light metal alloys, such as aluminum-lithium or aluminum-magnesium-scandium, CFRP offers poor electrical conductivity. Additional metal elements are necessary to fulfill all required electrical functions (e.g. copper mesh on the outer skin for lightning strike protection, wires for electrical grounding and bonding, overbraiding of cables to provide sufficient shielding).

In addition, CFRP shows brittle failure behavior, limiting the structure integrity in crash load cases. The damage tolerance against impact events (e.g. hailstone, bird impact, tool drop, tire debris) and

state-of-the-art rivet repair technologies require a minimum wall thickness for substantial areas of the airframe. All these tasks cause additional mass, limiting the lightweight potential that is given by the structural performance of CFRP.

Former research attempts focused on modifying the polymer matrix systems to overcome the main drawbacks. By introduction of conductive particles like carbon nano tubes (CNT), the specific conductance of CFRP could be enhanced [1-2]. However, a sufficient level of conductivity which would guarantee electrical function integration for the modified CFRP similar to that of aluminum alloys or GLARE airframe structures could not be demonstrated.

The impact damage tolerance of thin-walled CFRP structures has gradually been improved by the addition of polymer toughening agents [3-4]. Thermoplastic polymers and rubber particles were introduced in epoxy resin systems in different ways for preregs, enabling substantial improvements of fracture toughness and residual strength. However, even for CFRP airframe structures fabricated with

* Corresponding author: Erwin-Schrödinger-Str., Bldg. 58, 67663 Kaiserslautern, Germany, +49 (0) 631 2017 140, benedikthannemann@ivw.uni-kl.de

the latest generation of toughened prepreg systems, the prescribed minimum wall thickness criteria can still be the limiting design driver.

2 FIBER HYBRID LAMINATES

Different to former research attempts dealing with modified polymer matrix systems, the integration of electrical functions by means of metal fiber incorporation is a promising new approach. Research results in [5-8] show significant improvements in terms of energy absorption, fail safe behavior and structural integrity, when classical composites were reinforced by steel. Metal fibers can either be distributed homogenously in the composite (“homogenized layer concept”) or locally concentrated in individual layers (“separated layer concept”).

Unlike fiber-metal-laminates such as GLARE, the fiber based approach enables stress tailored composite design and multiple shaped structures. Moreover, fully automated manufacturing technologies can be explored by means of processes that are already available and in service for CFRP, e.g. weaving processes for non-crimped fabrics, automated tape laying, fiber placement or resin transfer molding.

However, potential metal fibers have to meet various requirements, in particular superior electrical conductivity, distinctive failure strain, high strength, high stiffness, corrosion resistance, appropriate thermal expansion, availability and low costs.

Copper fibers offer high electrical conductivity and good corrosion resistance, but high density and poor mechanical properties. Fibers made of Aluminum are distinguished by superior weight specific electrical conductivity and reasonable mechanical properties. However, in contact with carbon fibers, aluminum tends to ineligious galvanic corrosion. This is of no relevance for stainless steel fibers. Stainless steel fibers are commercially available with a wide range of

mechanical properties and appearance. Furthermore, the stiffness of standard modulus carbon and stainless steel fibers is comparable. Compared to a standard high tenacity ex-PAN carbon fiber, the electrical conductance of stainless steel fibers is approximately 23 times higher. Due to less alloying, low carbon steel fibers have even better specific mechanical properties. By nickel or copper cladding, the electrical conductivity can be further enhanced. In addition, the cladding enables a sufficient corrosion resistance.

Within the present study twisted bundles of chrome-nickel steel fibers are considered. The bundle consists of seven filaments, each with a diameter of 60 μm . A cross-section polish of the bundles is shown in figure 1. Furthermore, standard modulus/high tenacity carbon fibers of type Toho Tenax HTS40 and epoxy resin of type Cytec CYCOM 977-2 are processed. Selected properties of the fibers are summarized in table 1.

Table 1: Properties of the process fibers [9]

	Carbon fiber ¹⁾	Steel fiber ²⁾
Density / g/cm ³	1.77	7.95 ± 0.01
Tensile modulus / GPa	240 ± 3	176 ± 7
Tensile strength / MPa	4 806 ± 125	897 ± 2
Failure strain / %	1.85 ± 0,04	32.31 ± 2.01
Electr. resistivity / Ωm	1.6×10^{-5}	$(6.97 \pm 0.02) \times 10^{-7}$
Filament diameter / μm	5	60.0 ± 0.4
Roving size	12k	7

¹⁾ Manufacturer information, ²⁾ Own measurements on fiber bundles

3 MATERIAL PREPARATION

Test material is manufactured by a combined process of tape deposition and filament winding technology. Unidirectional layers of preimpregnated carbon fibers are stacked on a flat steel core and wrapped in dry stainless steel fiber bundles. The resin required for steel fiber impregnation originates from the bleed of the prepreg layers and resin films, respectively. In addition, conventional CFRP is prepared as reference materials. All laminates are cured using autoclave technology at a pressure of 6.5 bar with a one hour dwell time at 135°C, followed by a three hour dwell time at 180°C. Subsequently the laminates are released from the winding core. By this procedure, multilayered laminates with different stacking sequences and fiber volume fractions are manufactured. Finally, specimens are retrieved from the cured plates by water jet cutting and prepared for subsequent testing.

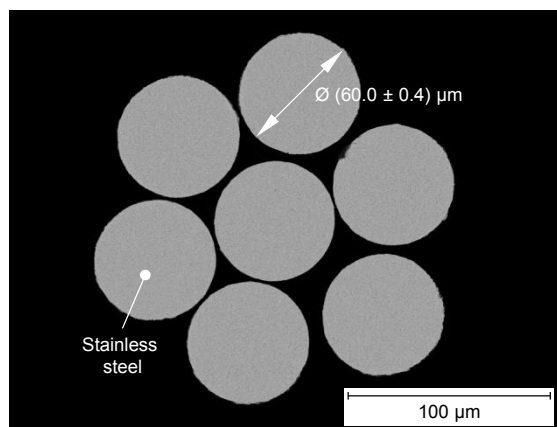
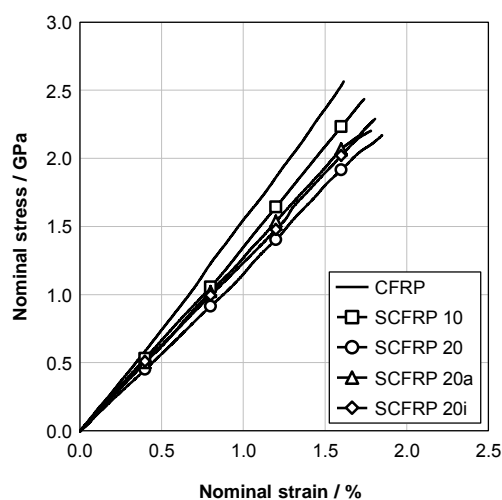


Fig. 1 Micrograph of the processed steel fibers

4 RESEARCHES ON UNIDIRECTIONAL LAMINATES

In a first step, the mechanical properties of unidirectional reinforced laminates are analyzed. Hybrid composites (SCFRP) with a volume share of 10.4 and 18.8% steel fibers are tested and compared with state-of-the-art CFRP [10].

In case of pure tensile load in parallel to the fiber orientation, both CFRP and the hybrid composites show brittle material behavior with similar ultimate strains to failure. Increasing the steel fiber content slightly lowers the tensile strength and stiffness of the composite. Despite the incorporation of highly ductile fibers, a pronounced post failure cannot be observed, figure 2.



Material	E / GPa	σ_{max} / MPa	ϵ_{max} / %
CFRP	146 ± 5	2 491 ± 85	1.61 ± 0.06
SCFRP 10	128 ± 5	2 322 ± 73	1.74 ± 0.04
SCFRP 20	125 ± 7	2 093 ± 72	1.77 ± 0.08
SCFRP 20a	133 ± 3	2 259 ± 78	1.79 ± 0.04
SCFRP 20i	133 ± 4	2 215 ± 31	1.81 ± 0.04

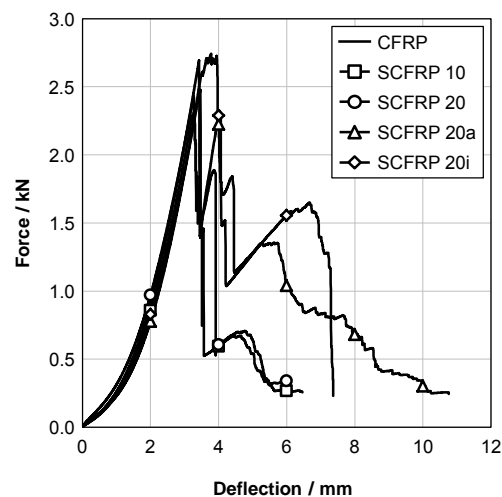
Fig. 2 Properties of unidirectional (hybrid) composites for tensile load in parallel to the fiber orientation

The brittleness of SCFRP is caused by a homogenous stress state. The carbon fibers develop elastic energy in the entire volume of the loaded composite. At the moment of failure, this energy is abruptly released and transferred by the matrix to the ductile steel fibers, causing yielding of the metal. However, the energy transfer occurs very locally at the breakage. The steel fibers plastify only in a narrow area around the fracture, causing merely a slight macroscopic elongation.

Improvements are expected by higher steel fiber fractions (i.e. less elastic energy that must be absorbed by a bigger amount of plastifying steel

fibers), but would cause higher material densities. Furthermore, a reduced fiber-resin-adhesion could enable unhindered deformation of the metal fibers over larger areas, but would certainly impact other important properties, e.g. the transverse tensile strength.

Improvements of the composite failure by incorporation of steel fibers become apparent in case of combined flexural and tensile load, figure 3.



Material	F_{max} / N	s_{max} / mm	AE / J
CFRP	2 715 ± 105	3.58 ± 0.12	3.38 ± 0.09
SCFRP 10	2 396 ± 93	6.11 ± 0.28	4.24 ± 0.21
SCFRP 20	2 406 ± 57	6.33 ± 0.36	5.16 ± 0.34
SCFRP 20a	2 710 ± 115	10.09 ± 0.58	9.41 ± 0.48
SCFRP 20i	2 566 ± 58	7.32 ± 0.29	8.47 ± 0.46

Fig. 3 Properties of unidirectional (hybrid) composites for combined tensile-flexural load

Conventional CFRP shows a brittle material performance. Failure occurs abruptly and singularly. After breakage, the material is not capable of bearing further loads.

By contrast, the hybrid composites exhibit a noticeable post failure behavior. Accompanied by a significant load drop, initial failure occurs at a deflection similar to that of CFRP. Afterwards, the composites can be further loaded at a reduced level of load. In case of the hybrid composite with a homogeneous steel fiber distribution (SCFRP 10 and SCFRP 20), the maximum deflection until final failure is doubled compared to conventional CFRP. An even better material performance can be achieved by localizing the metal fibers exclusively in the top (SCFRP 20a) or core layers (SCFRP 20i) of the laminate. Compared to SCFRP with homogeneously distributed steel fibers, the maximum deflection is further enhanced, while the bearable load remains on an even higher level.

In case of the combined flexural and tensile load,

stress and deformation are inhomogenously distributed in the laminate. Stress peaks occur in the area of maximum bending, while stress states in the remaining regions are significantly lower. Compared to the pure tensile stress state, the carbon fibers consequently store less elastic energy. After failure of the carbon fibers and the corresponding energy release, the steel fibers continue to yield and bear further deflections. By this means, the energy absorption and hence the structure integrity can significantly be enhanced.

5 RESEARCHES ON MULTIAXIAL LAMINATES

The awareness of concentrating the steel fibers in particular plies of the composite to achieve a beneficial material behavior is transferred to multiaxial laminates. As reference material, a 16-layered CFRP laminate with a typical aeronautical stacking sequence is manufactured. The hybrid composite consists of a CFRP core and two additional, pure steel fiber reinforced top layers, figure 4.

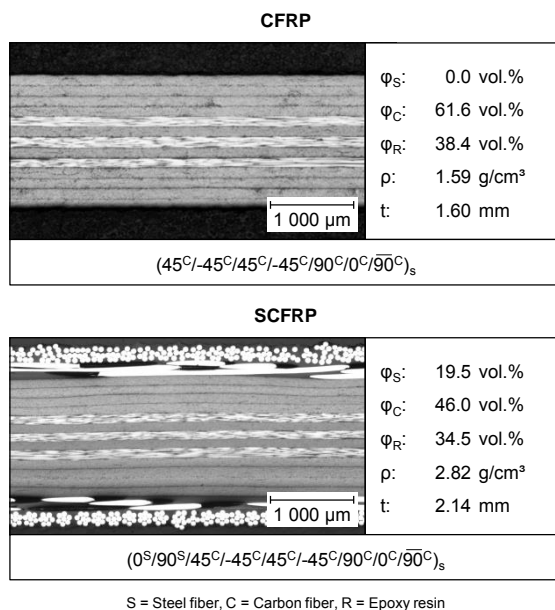


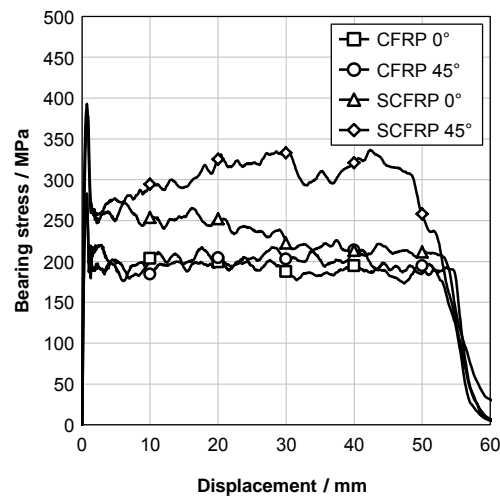
Fig. 4 Microstructure of the analyzed multiaxial (hybrid) laminates

The laminates are tested in regard to their notched properties and their penetration resistance. For this purpose, bearing stress, filled hole tension and penetration tests are conducted.

5.1 DYNAMIC BEARING STRESS TESTS

A metal pin with a diameter of 1/4 in is continuously pulled in in-plane direction through composite plates. The tests are performed with a loading speed of 1 m/s. All laminate configurations show a similar material response: After exceeding an initial trigger load, the bearing stress remains on a

lower, but constant level, figure 5.



Material	σ_{max} / MPa	σ_{mean} / MPa ¹⁾	AE / J
CFRP 0°	292 ± 16	191 ± 8	106 ± 5
CFRP 45°	288 ± 14	200 ± 5	113 ± 2
SCFRP 0°	402 ± 52	233 ± 16	178 ± 13
SCFRP 45°	408 ± 46	302 ± 11	220 ± 6

¹⁾ Determined between 2.000 and 52.825 mm pin displacement

Fig. 5 Results of dynamic bearing stress tests

However, in case of SCFRP more extensive areas lateral to the track of the bolt are degraded, figure 6. In consequence of the spacious plastification of the steel fibers, the mean bearing stress is increased 22% compared to CFRP. Loading the hybrid composite (i.e. the embedded steel fibers) at an angle of 45°, both steel fiber plies equally restrain the movement of the pin. Consequently, further enhancements of the bearable load can be achieved. Compared to CFRP, the mean bearing stress rises 51%.

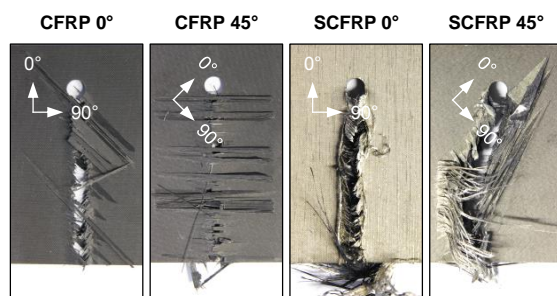
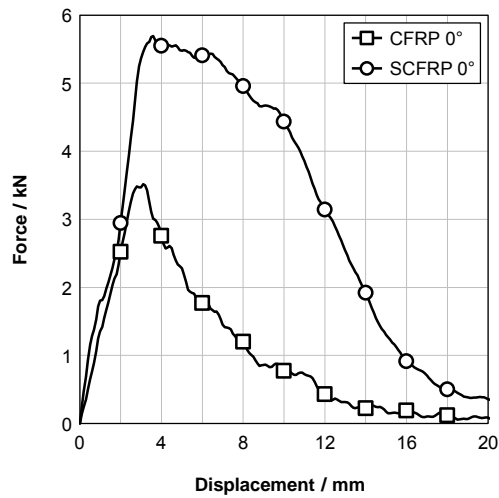


Fig. 6 Failure modes after bearing stress test

5.2 DYNAMIC PENETRATION TEST

Dynamic penetration test are conducted in dependence on DIN EN ISO 6603-2. A metal indenter with a diameter of 20 mm and an impact energy of 193 J is dropped on the flat side of composite plates. The plates are circular clamped

with a free gauge length of 40 mm. Figure 7 summarizes the obtained test results.



Material	F_{max} / N	$l_p / mm^1)$	SEA / J/g
CFRP 0°	3 558 ± 336	5.76 ± 0.57	4.06 ± 0.24
SCFRP 0°	5 737 ± 46	12.54 ± 0.18	7.09 ± 0.09

¹⁾ Displacement, in which the force has fallen to half of the maximum force

Fig. 7 Results of dynamic penetration tests

CFRP exhibits a brittle failure behavior. The failure mode is dominated by delamination and cracking. After exceeding a certain peak load, cracks grow free of energy absorption, mostly at an angle of $\pm 45^\circ$, i.e. in direction of the majority of fibers (cf. figure 8). Only a few carbon fibers break.

By contrast, SCFRP shows a distinctive ductile behavior. The failure mode on the entry side of

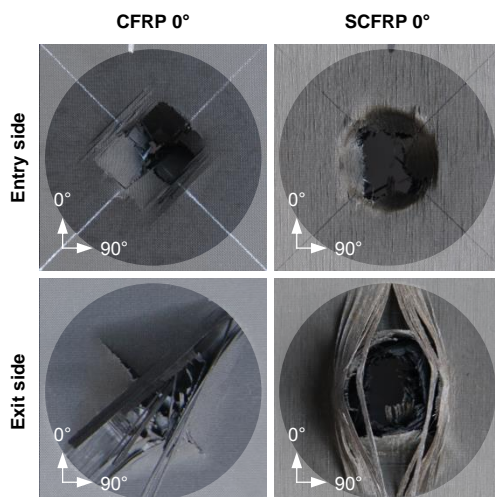


Fig. 8 Typical failure mode after penetration load

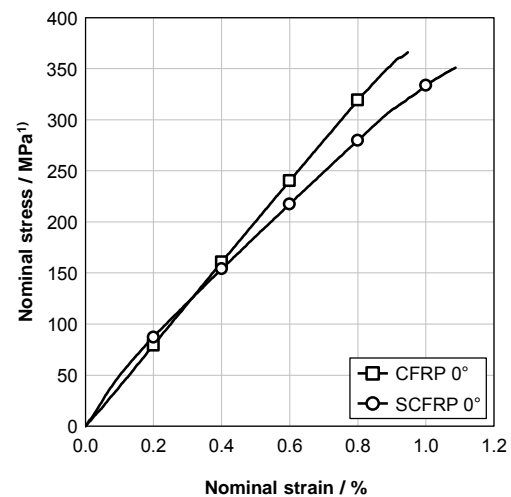
coupons resembles a deep drawing process. On the rear side, bundles of steel fibers of the outer ply detach from the compound and plastify. More spacious deformations are hindered by the grip of

the specimen. Nevertheless, compared to CFRP, the hybrid composite can bear larger deformation, while the load remains on a higher, slightly decreasing level. The displacement, in which the load has fallen to half of the load maximum rises 117%.

5.3 FILLED HOLE TENSION TESTS

Filled hole tension tests are conducted in compliance with AITM 1-0007. Rectangular specimen with a width of 32 mm and a $\frac{1}{4}$ in centered hole (tightening torque: 7.5 Nm) are quasi-statically loaded with a crosshead speed of 2 mm/min. The strain of the specimen is analyzed within a gauge length of 150 mm.

Both CFRP and the hybrid composites show brittle material behavior. Integration of steel fibers into CFRP decreases the tensile strength and the mean stiffness, while the ultimate strain to failure slightly rises, figure 9.



Material	$E / GPa^1)$	$\sigma_{max} / MPa^1)$	$\epsilon_{max} / \%$
CFRP 0°	42 ± 1	366 ± 6	0.95 ± 0.02
SCFRP 0°	34 ± 1	351 ± 8	1.09 ± 0.03

¹⁾ Considering the nominal width of the specimen

Fig. 9 Results of quasi-static filled hole tension tests

6 CONCLUSIONS

Several advantages of CFRP in comparison to aluminum alloys led to an increasing share of this composite in aviation industry. However, its comparatively poor electrical conductivity and limited damage tolerance require additional systems and elements, compromising today's CFRP lightweight potential. For this reason, efforts concentrate on modifying CFRP in order to guarantee the necessary electrical functionality for system installation purposes and to improve its damage tolerance.

Unlike former research attempts dealing with modified polymer matrix systems, this study analyzes the potential of a hybrid composite consisting of reinforcing carbon and stainless steel fibers embedded in an epoxy resin.

Researches on unidirectional reinforced (hybrid) composites prove that in case of combined tensile-flexural load, the structure integrity can significantly be improved. The hybrid composites reveal a distinctive post failure behavior. After initial failure, the composites can sustain further loads. The bearable deflection is increased up to 181%. The test results suggest that an allocation of steel fibers in core or top layers is advantageous over a homogenous steel fiber distribution.

However, in case of pure tensile load, the deformability of the stainless steel fibers could not yet be exploited to obtain a global post failure behavior.

In case of multiaxial laminates, hybrid composites with embedded steel fibers exhibit a higher resistance against bearing failure. After failure initiation, the hybrid material enables better energy absorption capabilities than conventional CFRP.

Furthermore, the penetration resistance of CFRP can be enhanced by incorporating steel fibers. The hybrid composite reveals complex failure modes. Spacious areas of the material can be addressed to absorb impact energy by plastification of the steel fibers.

The bypass failure behavior remains unchanged.

Future work will focus on multiaxial laminates with (electrical and mechanical) optimized lay-up, complemented by further analysis, e.g. compression after impact, fatigue and corrosion resistance. Furthermore, the usability of integrated austenitic steel fibers for in-situ health monitoring (based on phase transition and the change of electrical resistivity) and inductive heating for advanced manufacturing processes will be investigated.

7 ABBREVIATIONS

AE	Absorbed energy	(J)
E	Young's modulus	(GPa)
F_{\max}	Maximum load	(N)
SEA	Specific absorbed energy	(J/g)
s_{\max}	Maximum deformation	(mm)
t	Laminate thickness	(mm)
ϵ_{\max}	Ultimate strain to failure	(%)
ρ	Mass density	(g/cm ³)
σ_{\max}	Maximum stress	(MPa)
σ_{mean}	Average stress	(MPa)
φ	Fiber volume fraction	(vol.%)

8 ACKNOWLEDGEMENT

The financial support of the German Research Foundation (DFG) within the projects BR 4262/2-1

and BA 4073/6-1 is gratefully acknowledged. Prepreg and resin film was kindly supplied by Cytec Engineered Materials GmbH (Östringen, Germany).

REFERENCES

- [1] A. Noll, K. Friedrich, T. Burkhart, U. P. Breuer: *Effective multifunctionality of poly (p-phenylene sulfide) nanocomposites filled with different amounts of carbon nanotubes, graphite and short carbon fibers*. Polymer Composites 34(9):1405-1412, 2013.
- [2] Z. Spitalsky, D. Tasis, K. Papagelis, C. Galiotis: *Carbon nanotube-polymer composites: Chemistry, processing, mechanical and electrical properties*. Progress in Polymer Science, 35(3):357-401, 2010.
- [3] C. Garg, Y.-W. Mai: *Failure mechanisms in toughened epoxy resins - A review*. Composites Science and Technology, 31(3):179-223, 1988.
- [4] R. M. Medina Barron: *Rubber toughened and nanoparticle reinforced epoxy composites*. IVW Schriftenreihe, 84, 2009.
- [5] A. Radtke, V. van Wassenhove, K. van Koert, F. Vöge, D. Moors, O. Geiger, D. Fertig: *Reinforcing with steel cord*. Kunststoffe, 11:67-71, 2012.
- [6] S. Schmeer, M. Steeg, M. Maier, P. Mitschang: *Metal fiber reinforced composite - potentialities and tasks*. Advanced Composites Letters, 18(1):45-52, 2009.
- [7] S. Vandewalle: *Multifunctional steel fibre reinforcement*. Wolfsburg innovations in automotive textiles, Wolfsburg, Germany, October 7th, 2010.
- [8] M. G. Callens, L. Gorbatikh, I. Verpoest: *Carbon nanotube-polymer composites: Chemistry, processing, mechanical and electrical properties*. Composites Part A: Applied Science and Manufacturing, 35(3):357-401, 2014.
- [9] Toho Tenax Europe GmbH: *Product data sheet for Tenax® HTS filament yarn*. 2014.
- [10] B. Hannemann, S. Backe, S. Schmeer, F. Balle, U. P. Breuer: *New Multifunctional Hybrid Polymer Composites reinforced by Carbon and Steel Fibers*. International conference on composite materials, Copenhagen, Denmark, July 19th-24th, 2015.

ALGORITHMS FOR THE DETERMINATION OF CURVATURE FROM 3D μ -CT IMAGES – A COMPARISON

Pascal Pinter^{1*}, Benjamin Bertram¹, Kay André Weidenmann¹

¹Institute for Applied Materials, Karlsruhe Institute of Technology, Kaiserstraße 12,
76131 Karlsruhe

ABSTRACT: The surface curvature of microstructural characteristics (e.g. pores or inclusions) represents a geometric property that influences the mechanical behavior of composite materials significantly. In general, zones of large curvatures at voids or inclusions can be assumed as notches that are favorable sources for crack and hence damage initiation. The determination of local curvature characteristics in non-destructive microstructure evaluation techniques therefore offers the opportunity to investigate stresses and strains close to potential damage initiation sites and allows for an assessment of the crack initiation sensitivity of microstructural features. For the determination of curvature, two methods were investigated and compared: The first method is based on the Hessian Matrix which is applied to the surface voxels of connected regions of the segmented image. The second method computes the local curvature from a patch that is fitted to the local surface of the segmented image. As a benchmark on accuracy, an absolute error was calculated on artificially generated images describing spheres and cylinders with multiple radii where the true curvature is known at each surface point. The results were first used for the optimization of the input parameters of each method and the final comparison. The results show a good agreement between input data and curvature calculated. Recommendations for the adjustment of input parameters for mentioned methods are given.

KEYWORDS: Hessian filter, Gaussian, Mean, Patch, Curvature, Computed Tomography

1 INTRODUCTION

The determination of surface curvatures from micro X-ray computed tomography (μ CT) images is a topic with widely spread applicability. In material science, it offers the ability to describe the shape of pores or inclusions affecting the toughness and elastic properties of materials depending on the orientation and shape of the investigated objects. Therefore, existing methods for the examination of surface curvatures were used and compared with each other. The first one is implemented in the Advanced Normalization Tools (ANTs) [1] and is called patch curvature in the following. It is processed by the observation of a patch of variable size on the surface in each surface point. The curvature is calculated from the approximated Gaussian map in each voxel. Another method is the determination directly from the hessian matrix of the voxel data. This algorithm was implemented with respect to the publication of J.F. Hughes [2], who described the method using the mathematical approaches of Millman and Parker [3] and Dombrowski [4]. Both curvature tools are implemented in *Composight* [5], an open source project pub-

lished by the Institute for Applied Materials (KIT), which offers many tools for microstructure characterization in material science. The corresponding source code can be found on SourceForge [5].

For the validation of the implemented methods, artificial images were used as well as real data from CT-scans. The precision of each algorithm will first be inspected on single spheres of different radius to avoid any influence of neighboring objects. Another test is carried out on multiple touching spheres to get an error that is dependent on the surrounding objects. Nevertheless, in many cases it will be possible to separate inclusions and process them subsequently making the validation on independent spheres more reasonable.

2 MATERIAL AND METHODS

2.1 ARTIFICIAL IMAGES

The artificial images were generated by a self-developed tool, which was programmed in C++ using the ITK library [6]. Input parameters are the radius of the sphere and the edge length of the

* Pascal Pinter, Institute for Applied Materials, Karlsruhe Institute of Technology, Kaiserstraße 12, 76131 Karlsruhe, phone: 0721 – 608 46595, fax: 0721 – 608 48044, pascal.pinter@kit.edu

image in voxels. Fig. 1 shows a sphere that was created by the mentioned algorithm.

2.2 IMAGE ACQUISITION

All specimen images were acquired with an Yxlon-CT precision computed tomography system containing an open X-ray reflection tube with tungsten target and a 2048 x 2048 pixel flat panel detector with a pixel pitch of 200 μm from Perkin Elmer. The scans were carried out on steel balls of ball-bearings (Fig. 2) to get a curvature distribution that can be calculated from the diameter and the surface of the included balls. The resolution of the scan was 0.03mm/voxel.

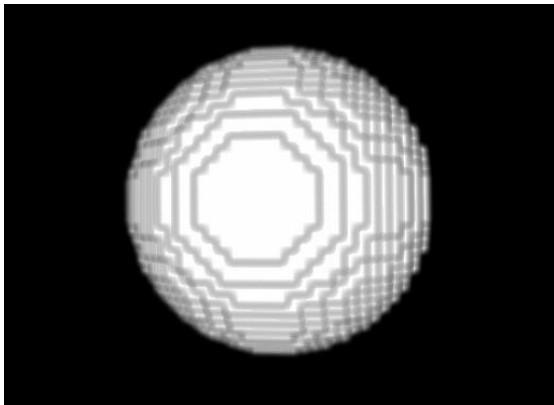


Fig. 1 Artificially generated sphere

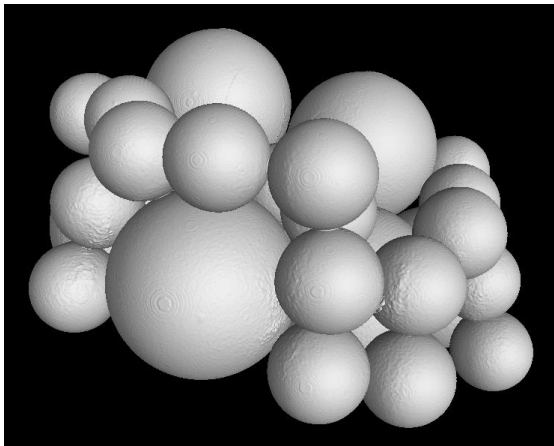


Fig. 2 Balls of ball-bearings

2.3 DETERMINATION OF CURVATURES

The Curvature of objects in a three dimensional space can be described by two principal curvatures κ_1 and κ_2 . These curvatures result from the reciprocal of the local radius of the surface. Furthermore, the mean curvature, which is the mean value of the principal curvatures, can be calculated by

$$H = \frac{1}{2}(\kappa_1 + \kappa_2). \quad (1)$$

Another common description is the Gaussian Curvature:

$$K = \kappa_1 \cdot \kappa_2 \quad (2)$$

In the present work, the mean curvature is considered, because it can be unambiguously visualized in contrast to the Gaussian curvature which can be zero if one of the principals is zero. For that reason, the curvatures on the spheres in the test images should result in $H = \kappa_1 = \kappa_2 = \frac{1}{R}$.

2.3.1 Patch-based

The first approach used is based on the implementation of the Advanced Normalization Tools (ANTs) [1]. It offers many tools for image processing tasks like registration, segmentation and even the extraction of features like curvatures on surfaces. The method respects the surface points and normals on a surface patch which size depends on the radius of a mask ρ that has to be chosen by the user. Another input parameter σ is necessary to smooth the segmented input image before building the first derivative. The smoothing reduces quantification effects resulting from the more or less coarse grid due to the image acquisition. Subsequently, the principal curvatures are calculated from an approximation of the local Gauss map and the eigendecomposition of its derivative [7].

2.3.2 Hessian-based

The second method used is based on the local Hessian matrix that can be calculated directly from the voxel data $G(x, y, z)$.

$$HG(x, y, z) = \begin{bmatrix} \frac{\partial^2 G}{\partial x \partial x} & \frac{\partial^2 G}{\partial x \partial y} & \frac{\partial^2 G}{\partial x \partial z} \\ \frac{\partial^2 G}{\partial y \partial x} & \frac{\partial^2 G}{\partial y \partial y} & \frac{\partial^2 G}{\partial y \partial z} \\ \frac{\partial^2 G}{\partial z \partial x} & \frac{\partial^2 G}{\partial z \partial y} & \frac{\partial^2 G}{\partial z \partial z} \end{bmatrix} \quad (3)$$

J.F. Houghes [2] showed in his publication, that the local principal curvatures can be calculated by solving the eigenvalues of the Weingarten map in matrix form:

3 RESULTS AND DISCUSSION

3.1 TESTS ON ARTIFICIAL IMAGES

$$l = \frac{1}{\|\Delta G(p)\|} \begin{bmatrix} b_1^t HG(p) b_1 & b_1^t HG(p) b_2 \\ b_2^t HG(p) b_1 & b_2^t HG(p) b_2 \end{bmatrix} \quad (4)$$

While $\{b_1, b_2\}$ is any orthonormal basis for the tangent plane on the surface at the point p . Because this problem can be solved on each point of the image, it is important to decide whether a point is a surface point or not. In the present algorithm this is done by a simple edge detection based on the numerical derivative in each direction.

2.4 VALIDATION OF THE ALGORITHMS

The first tests on artificial images were carried out to calculate global errors for the entire images at different radii and characterize the accuracy to find optimal input parameters with respect to the sphere radius. Therefore, the difference of the real curvature and the determined curvature on each surface voxel i was calculated, summed up and divided by the number of surface voxel N to receive a mean error for a certain configuration.

$$\frac{1}{N} \sum_{i=1}^N \left(\kappa_i - \frac{1}{R} \right) \quad (5)$$

For the determination of a percentage error, the mean error can be normalized by the real curvature, which is the reciprocal of R . Therefore, the percentage error is

$$\frac{R}{N} \sum_{i=1}^N \left(\kappa_i - \frac{1}{R} \right) \cdot 100\% \quad (6)$$

On the real images, the influence of neighboring or even touching objects must be examined, because not every microstructure can be separated to multiple objects. The test specimen consists of 21 small spheres with a radius of 2 mm and seven with 4 mm. Thus, the histogram of the output image should show two sharp peaks at the corresponding values in case of a perfect determination. The percentage of both radii in the image can be calculated by the surface fraction of the spheres. Thus, the percentage of the 4 mm radius should be 57.1 %. In the present case, it is also possible to separate the spheres on the touching areas using a watershed filter and save each object to another image. These images can subsequently be calculated without any influence of the neighborhood.

3.1.1 Patch-based method

The Patch-based method was tested on spheres with a radius from two up to twenty pixels. Fig. 3 shows the results of the calculations. The blurring parameter σ has almost no influence on the result as long as it is chosen larger than one pixel ($\rho = 1$). The method shows a large error of up to 45 % at small sphere radii and decreasing errors for larger radii. While the improvement of the results from a mask size of $\rho = 1$ px to $\rho = 2$ px is quite high, the change up to $\rho = 10$ px has a negligible effect. Since the error at small sigma is decreased by around 5 % with the increase of the value, the result at sigma higher than 2 px is almost similar. It has to be noted, that a larger mask size ρ leads to a significant increase in calculation time. Since the error is very high at small radii, this method seems to be less accurate for small pores or inclusions.

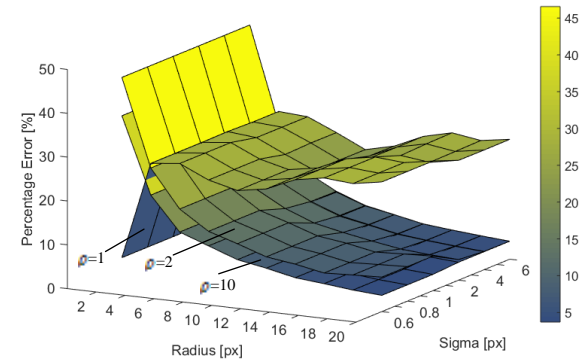


Fig. 3 Error of the Patch-based method with dependence on the sphere radius, the smoothing parameter sigma and the mask size ρ

3.1.2 Hessian-based method

Results from the Hessian-based algorithm show lower errors for all of the tested radii from two up to twenty pixels and smoothing parameters σ (Fig. 4). The calculation time is nearly independent from the chosen parameter, because the derivatives are calculated by a separable recursive filter. There is no identifiable optimum for σ , except the radius of two pixels, the error is below 2 % for all combinations of sphere radius and σ .

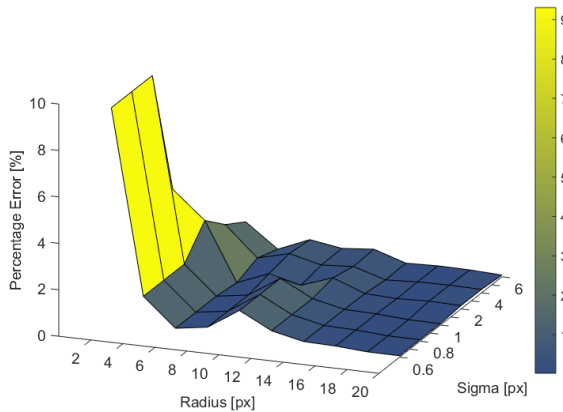


Fig. 4 Error of the Hessian-based method with dependence on the sphere radius and the blurring parameter sigma

3.2 Real test samples

As mentioned in section 2.4, the resulting histogram from the real sample should result in two peaks at 0.0075 1/px and 0.015 1/px, while the percentage of the last one should be 42.9 %. The histogram resulting from the Hessian-based algorithm (Fig. 5) shows peaks at almost exact positions of the curvature. Setting sigma to 3 px leads to a distribution that is spread very broadly caused by the noisy filter response. A sigma of 10 px results in a plausible curve, because the peaks are sharp and symmetric. Setting the blurring parameter to higher values like 20 or 30, leads to an asymmetry in the peaks shifting the maximum to slight lower values. Furthermore, the plateau on the left of the peaks, which equals zero in best case, is shifted to higher values.

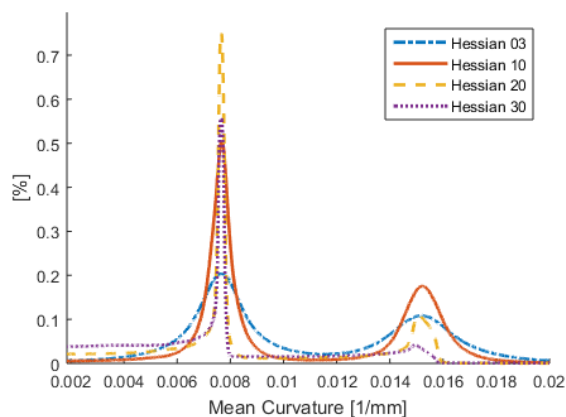


Fig. 5 Curvature histogram of the real sample calculated by the Hessian-based method for different values of σ from 3 up to 30 px

On objects with different curvatures, the parameter selection of the Patch-based method is more complicated. On the artificial images, it looked like there is almost no dependency of the blurring parameter sigma. Tests with larger radii like in the present image show, that it is even possible to

receive plausible results with low σ and high ρ (Fig. 6). Nevertheless, this calculation is very expensive in computation time. A faster approach is the use of higher σ and low values of ρ . But up from a sigma of around 20, the peaks become asymmetric and a plateau appears on the left of the peaks.

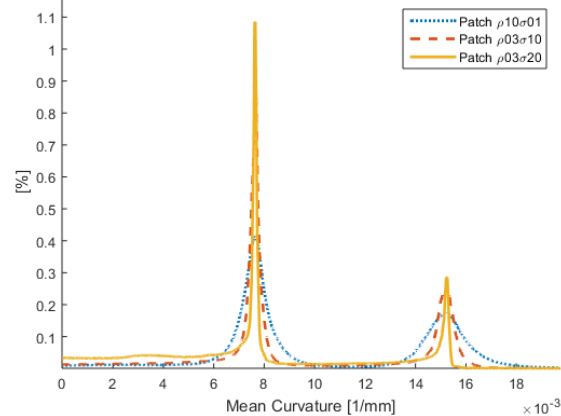


Fig. 6 Curvature histogram of the real sample calculated by the Patch-based method for different values of σ and ρ

As the exact curvature distribution of the spheres is unknown due to the high negative curvatures at the touching points and necks, the spheres were separated by a watershed filter. Subsequently, the curvature was calculated on two images of a small and a large sphere and the histogram of the specimen was built by multiplying the histograms of both images with the number of spheres that were included and summing both of them up to the final histogram in Fig. 7.

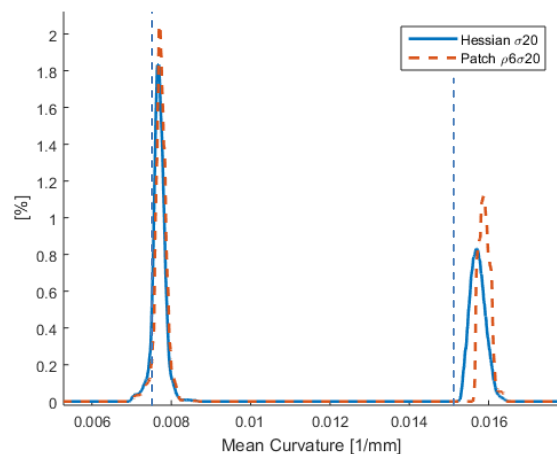


Fig. 7 Curvature histogram of the separated spheres calculated with the Patch- and Hessian-based method

The percentages of the surfaces with a radius of 2 mm resulted in a fraction of 41.7 % for both methods, which is only 1.2 % lower than the theoretical value. The maxima of the peaks are shifted

slightly to higher values, implying that the recognized radii are slightly smaller than expected. Note, that the peaks of the separated images are much sharper than those in the histogram for the entire images (Fig. 5 and Fig. 6). Table 1 shows the maxima of the Peaks for each radius and method.

Table 1: Maxima of the Peaks from Fig. 7

Radius [mm]/[px]	Real Curvature	Patch-based	Hessian-based
4/135.6	0.0075	0.0077	0.00766
2/67.8	0.015	0.0159	0.0157

In the following, the local influence of the input parameters is discussed. Even if the peaks in the histograms seem correct, it may be possible that the curvature in the images is locally wrong. In the following example, a good approach would show a constant positive curvature over the spheres and a very high negative curvature on the connections to neighboring spheres. Fig. 8 shows the results from the patch-based method with a small patch size of 3 and a high smoothing parameter $\sigma = 10$. It can be seen that the curvature on the connections between two spheres changes to negative values even if the distance to the bending is large. This effect is caused by the high smoothing parameter. If σ is set to even higher values (Fig. 10), the influence of the neighborhood is that large that the correct determination of local curvatures is almost impossible. It can be seen, that the gray values change along edges of the same sphere, which should have the same curvature. Furthermore, there are no sharp negative values on the touching points to the neighboring spheres.

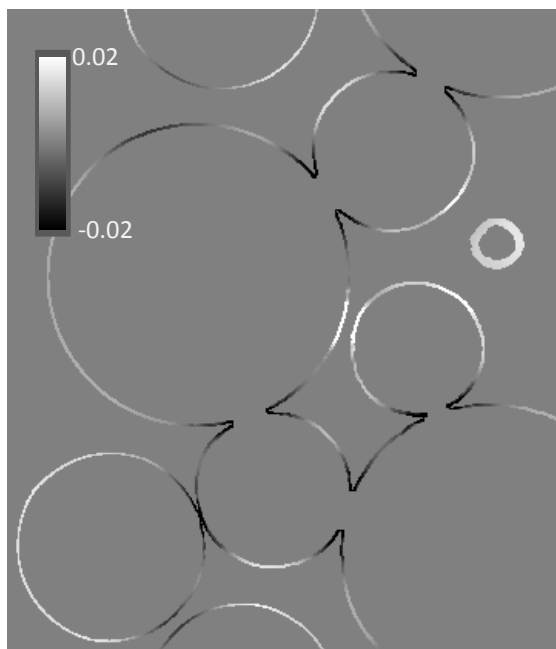


Fig. 8 Patch-based method: $\rho = 3, \sigma = 10$

If the smoothing parameter σ is set to a low and ρ to a high value as depicted in Fig. 11, the local curvature is more accurate, even if the peaks in Fig. 6 are more blurred for this configuration. The processing with a high ρ is computationally very expensive and can cause processing times that are multiple times higher than with small mask sizes ρ . However, this configuration seems to be a good approach to calculate local curvatures on microstructures, if there are sharp changes in curvature

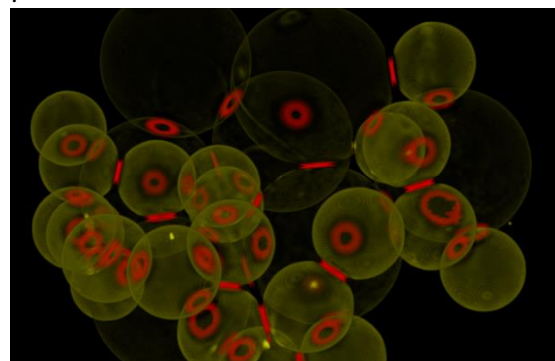


Fig. 9 3D visualization of curvature calculated by the hessian-based method with $\sigma = 10$

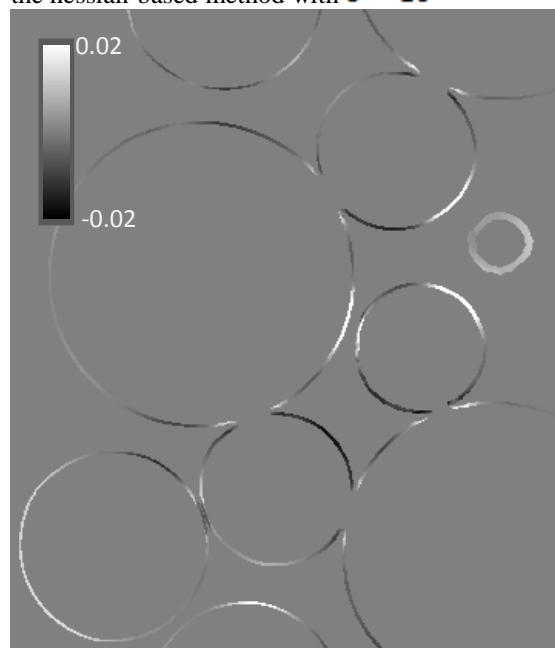


Fig. 10 Patch-based method: $\rho = 3, \sigma = 20$

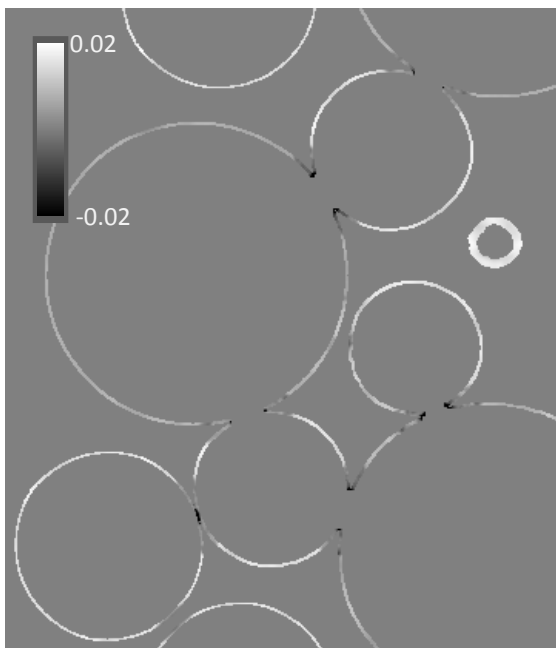


Fig. 11 Patch-based method: $\rho = 10, \sigma = 1$

The Hessian based method had a very low processing time in comparison with the patch-based approach. Fig. 12 shows the result with $\sigma = 3$ px. The curvature on the spheres is very noisy what is even noticeable in the broad peaks in Fig. 5. On the other hand, the negative curvature from the connection to the neighboring objects does not influence the surrounding areas as much as with higher blurring parameters. For the microstructure at hand, $\sigma = 10$ px seems to be a good compromise between localness and noise (Fig. 13 and Fig. 9).

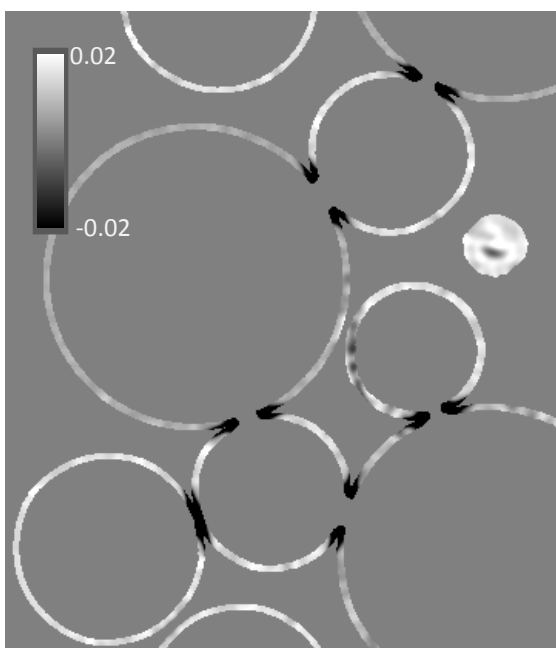


Fig. 12 Hessian-based method: $\sigma = 3$

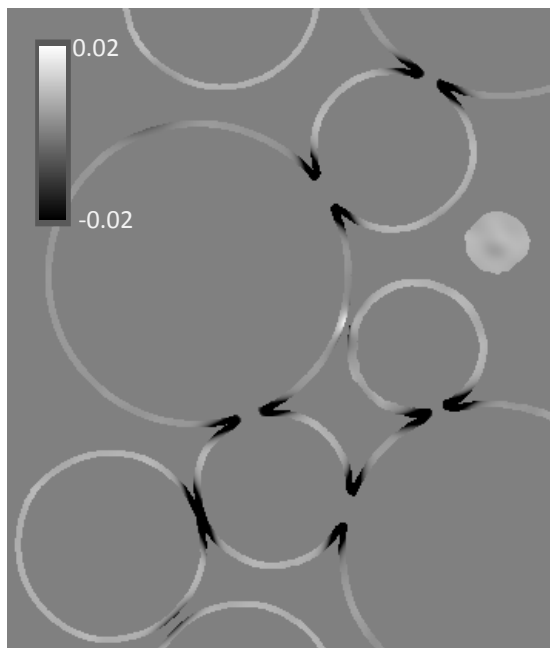


Fig. 13 Hessian-based method: $\sigma = 10$

4 CONCLUSIONS

It can be noted that in general both of the methods work well and offer precise results if the input parameters are set correctly. Nevertheless, it is hard to determine universal parameters for the methods because the optimum is strongly dependent on the investigated microstructure. If the curvatures within an image differ significantly, a compromise has to be found in order for the values to be determined correctly at high curvatures and the result is not too noisy at lower curvatures. For most applications, the Hessian-based method offers good and fast results. For some microstructures with varying curvatures, the Patch-based approach in combination with small σ and higher ρ will offer advantages (cf. Fig. 11) computing local curvatures. For small objects, the Hessian-based algorithm seems to be the better method due to the very small errors resulting from the artificial images.

5 ACKNOWLEDGEMENT

The research documented in this manuscript was initiated by the German-Canadian research group "Integrated engineering of continuous-discontinuous long fiber reinforced polymer structures". The support of the group by the German Research Foundation (DFG) is gratefully acknowledged. The Development of *Composight* was funded by the European Union and the Land Baden-Württemberg during the course of the project EFRE-TC² InnoSMC. Thanks are also due to Dr.-Ing. Stefan Dietrich from IAM-WK for valuable discussions.

6 References

- [1] B.B. Avants, N.J. Tustison, G. Song, P.A. Cook, A. Klein, J.C. Gee: *A reproducible evaluation of ANTs similarity metric performance in brain image registration*, NeuroImage 54 2033–2044 (2011).
- [2] J.F. Hughes: *Differential geometry of implicit surfaces in 3-space-a primer*, Report, Department of Computer Science Brown University Providence, Rhode Island (2003).
- [3] R.S. Millman, G.D. Parker: *Elements of differential geometry*, Prentice-Hall, Englewood Cliffs, N.J., 1977.
- [4] P. Dombrowski: *Krümmungsgrößen gleichungsdefinierter Untermannigfaltigkeiten RIEMANNscher Mannigfaltigkeiten*, Math. Nachr. 38 133–180 (1968).
- [5] B. Bertram, P. Pinter: *Composight. 0.2.0*, Karlsruhe Institute of Technology / IAM-WK, Sourceforge, <http://sourceforge.net/projects/composight/>, 2015.
- [6] Terry S. Yoo, Michael J. Ackerman, William E. Lorensen, Will Schroeder, Vikram Chalanana, Stephen Aylward, Dimitris Metaxas, Ross Whitaker: *Engineering and Algorithm Design for an Image Processing API: A Technical Report on ITK - the Insight Toolkit* 586–592 (2002).
- [7] B. Avants, J. Gee: *The Shape Operator for Differential Analysis of Images*, *Information Processing in Medical Imaging: 18th International Conference, IPMI 2003*, Ambleside, UK, July 20-25, 2003

MECHANICAL PROPERTIES OF CONTINUOUSLY-DISCONTINUOUSLY FIBER REINFORCED HYBRID SHEET MOLDING COMPOUNDS

Anna Trauth^{1*}, Kay André Weidenmann¹

¹Karlsruhe Institute of Technology (KIT), Institute for Applied Materials IAM-WK, Karlsruhe, Germany

ABSTRACT: Chopped glass fiber Sheet Molding Compounds (SMC) offer a high design freedom for complex part geometries featuring high surface quality combined with low material and processing costs. A new approach focuses on the combination of discontinuously reinforced structures based on SMC with unidirectional carbon fiber prepregs. The integration of such prepregs manufactured by an adopted SMC process featuring continuous reinforcements aims to obtain better load-bearing capacities at highly loaded areas. As a first step, continuously-discontinuously (CoDiCo) fiber reinforced laminate sheets have been processed by combining layers of chopped glass fiber and unidirectional carbon fiber prepregs during molding. This work aims to contribute significantly to a fundamental understanding of the structural behavior of different CoDiCo structures by determining macroscopic material properties. Mechanical characterization included quasi-static tension, compression and bending. Impact tests were also performed to assess the dynamic properties.

The results indicate that compared to solely discontinuously reinforced Sheet Molding Compounds, the CoDiCo laminates show increased global strength and stiffness, with the mechanical properties expectedly depending on layer architecture. In general, laminates showed also a higher damage tolerance in comparison to discontinuously reinforced SMC.

KEYWORDS: Sheet Molding Compound, glass fiber, carbon fiber, prepreg, mechanical characterization, material properties

1 INTRODUCTION

The growing demand for fuel efficient and hence light vehicles and aircrafts led to a remarkable development of fiber-reinforced polymeric composite manufacturing methods in the past few years. Sheet Molding Compound (SMC) technology offers the possibility to manufacture structures at a very high productivity combined with good part reproducibility, cost efficiency, surface quality and the possibility to manufacture parts with complex geometries. Sheet Molding Compounds are based on flat semi-finished product of cross-linkable resins with or without filler and additives reinforced by glass or carbon fibers processed to the final geometry using compression molding. Chopped glass fibers are the most common type of reinforcement found in SMC industry. This discontinuous fiber reinforcement offers a high bulk material flow capability, which leads to a high design

freedom. Due to the short fiber length and depending on process parameters, which lead to more or less pronounced anisotropic fiber distribution, discontinuously glass fiber reinforced SMC offer only low stiffness and strength. Better mechanical properties can be obtained in general by using carbon fibers as reinforcement component. Since these fibers are more expensive than glass fibers and causing higher cycle times [1], approaches to combine glass and carbon fiber reinforcements for SMC structures appear more suitable for industrial applications. The first technical application of a hybrid tailored chopped carbon – chopped glass fiber SMC was demonstrated by the 2003 Viper. With this material composition mass reduction and stiffness improvement could be achieved for different structural automotive parts such as the fender support system, windshield surrounding structure and inner door panels [2].

* Corresponding author: Kaiserstraße 12, 76131 Karlsruhe, Germany, Telephone: +49 721 608 46595, Fax: +49 721 608 48044, Anna.Trauth@kit.edu

Cabrera-Rios et al. [3] also studied the relative improvement in physical properties of SMC structures consisting of a combination of chopped glass and chopped carbon fibers in a per ply basis with different ply arrangements. Measurements of tensile and bending properties showed that not only the position of the plies with different fiber types but also the variation of mixture affected the mechanical properties [3].

In contrast to chopped fibers, continuously fiber reinforced structures have a significantly higher load-bearing capacity. With an optimized composition of continuously and discontinuously fiber reinforced structures parts with complex geometries combined with high stiffness and strength could be obtained. This represents a novel material class in the field of fiber reinforced polymers based on the integration of unidirectional continuous carbon fiber placement in the SMC molding process.

First trials to combine chopped glass fiber SMC with unidirectional carbon fibers were done by Gortner et al. [4]. This group placed dry textile preforms together with the SMC semi-finished product in a mold for a standardized SMC process. The chopped glass fiber SMC based on an unsaturated polyester resin. Reinforcement elements were $\pm 45^\circ$ non-crimp fabrics of glass or carbon fibers and a one and two side reinforcement with the two different structures were investigated. Mechanical characterization showed that a local textile reinforcement could improve tensile and bending properties compared to pure glass fiber reinforced SMC.

Wulfsberg et al. [5] combined chopped glass or carbon fiber SMC, also based on unsaturated polyester resins, with prepreg compression molding in a one-shot compression molding and curing process. Mechanical characterization highlighted that different material combinations of chopped and unidirectional fibers lead to an increase of tensile and bending properties.

2 FABRICATION OF CoDiCo SHEET MOLDING COMPOUNDS

In contrast to the approach of Wulfsberg et al. the unidirectional carbon fiber prepreps for this study are themselves manufactured in a modified continuous SMC process with both the matrices of continuous and discontinuous matched each other.

This offers the opportunity to process prepreps in an easier and cheaper way than usual prepreg materials. Additionally, a specific hybrid resin system is used which ensures fiber position and alignment of continuous reinforcement structures while compression molding with (flowable) chopped glass fiber SMC. It offers not only a high viscosity during molding but also increases productivity as there is no more need for maturing. High grammage

carbon fibers can easily be manufactured with this resin system to meet best economical needs of the industry. Realizing combined continuous and discontinuous reinforced structures within one part following this processing route leads to a noticeable improvement of loading path orientated high volume manufacturing.

The International Research Training Group of Integrated Engineering of Continuous-Discontinuous Long Fiber Reinforced Polymer Structures (GRK 2078) aims to contribute significantly to a fundamental understanding of combined discontinuously and continuously SMC structures. This study is a first step to investigate the mechanical properties of laminates based on a combination of sheets out of continuously carbon fiber as well as discontinuously glass fiber (CoDiCo) with different ply arrangement during compression molding.

To manufacture CoDiCo laminates chopped glass fiber SMC and unidirectional carbon fiber SMC were manufactured on two different impregnation lines. Individually manufactured unidirectional carbon fiber SMC sheets were combined with chopped glass fiber SMC during compression molding to create hybrid continuously discontinuously (CoDiCo) laminates.

The discontinuous glass fiber SMC is based on a vinyl ester (type Atlac XP810X by Aliancys). To optimize structural properties no fillers were added. The semi-finished products were manufactured using a flat conveyor plant type HM-LB-800 by Schmidt & Heinzmann and matured for seven days at 30°C . The weight content of the reinforcing glass fiber (type Multistar 272 by Johns Manville) is set to 41 wt.-% which equals 23 vol %).

The unidirectional carbon fiber SMC sheets were manufactured with a labor-scale impregnation line, built at the Fraunhofer Institute for Chemical Technology. In contrast to the described standard SMC manufacturing line, this process based on carbon fiber fabrics (type Panex35 by Zoltek) and a hybrid unsaturated polyester - polyurethane resin system (type Daron 41 by Aliancys). Additionally the labor-scale impregnation line is equipped with a heatable table which allows for heating up of the impregnated fabric to achieve the B-stage pre-curing. To prevent any further chemical reaction and to achieve the full B-stage the semi-finished sheets are subsequently cooled down to room temperature [6].

For this study unidirectional carbon fiber SMC semi-finished sheets with a fiber weight content of 62 wt.-% (50 vol. - %) were manufactured. After maturation the DiCo and Co sheets were cut into plies, stacked and compression molded. To investigate mechanical properties of CoDiCo SMC, two different laminates architectures were realized. These differ in arrangement of the continuous and discontinuous reinforced plies. All laminates con-

sist of three layers. Type A (GCG) has two discontinuously glass fiber reinforced outer layers with an inner layer of unidirectional carbon fiber SMC. The plates had a thickness of 3.3 mm. Type B (CGC) consists of two outer layers reinforced with unidirectional carbon fibers and one discontinuously glass fiber reinforced sheet in the middle (thickness: 3 mm). Besides that purely glass fiber reinforced sheets (G) were manufactured. They had a thickness of 2.3 mm.

For all plates a mold coverage of 100 % was realized so that flow phenomena can be neglected.

After molding for each laminate samples in 0° and 90° with regard to the orientation of the unidirectional carbon fibers were cut by water-jet cutting.

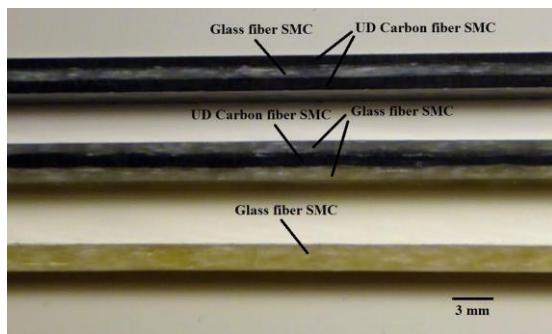


Fig. 1 CoDiCo Laminates: CGC (top), GCG (middle) and G (bottom)

3 CHARACTERIZATION

To understand the effect of continuously reinforced chopped glass fiber SMC and especially to evaluate the influence of ply arrangement on the mechanical properties of CoDiCo fiber reinforced structures tensile, bending, compression and impact tests were performed. Results of the characterization for both laminate types were compared to mechanical properties of purely discontinuously reinforced glass fiber SMC. All tests were carried out at room temperature.

3.1 TENSILE TEST

The quasi-static tensile tests were performed with a ZwickRoell ZMART.PRO universal testing machine equipped with a maximum capacity of 200kN. For laminate type A and B rectangular specimen with length x width x thickness = 230 mm x 25 mm x 3.3 mm for Type A, respectively 3 mm for Type B were used for testing. Additionally, Type B laminates were provided with cap strips. The tensile properties of glass fiber reinforced SMC were determined with dog-bone like specimen with a rectangular measurement section of 60 mm x 20 mm x 2.3 mm (Fig.3). Clamping distance was 150 mm for each sample type and longitudinal strains were measured with an extensometer with a gauge length of 100 mm for the rectangular and 60 mm for the dog-bone like specimen. Testing veloc-

ity was 2 mm/min. For each specimen type 5 samples in 0° and 90° were considered for testing. Elastic modulus was calculated by linear regression between $\epsilon_1=0.05\%$ and $\epsilon_2=0.25\%$.

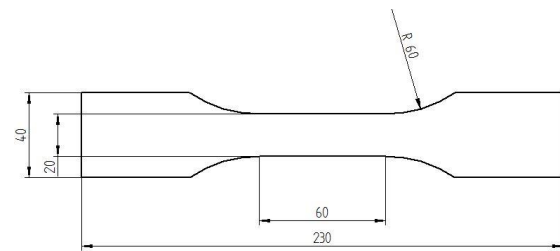


Fig. 2 Dog-bone like specimen used for tensile testing of purely glass fiber reinforced SMC

3.2 BENDING TEST

Three-point bending tests were performed on a ZwickRoell Z2.5 testing machine with a 2.5kN load cell. The rectangular specimen had a width of 15 mm and a thickness to span ratio of 1:32. The testing velocity was calculated according to DIN EN ISO 14125 to guarantee a strain rate of 0.01 1/min for all sample types. Bending stresses and bending strains were also calculated according to DIN EN ISO 14125 and taking into account a corrected formula if measured deformations were $> 0.1 \times$ span length. For each specimen type 5 samples in 0° and 90° were considered for testing. Flexural modulus E_B was calculated via linear regression with stresses measured at $\epsilon_1=0.05\%$ and $\epsilon_2=0.25\%$.

3.3 COMPRESSION TEST

Compression tests were performed on a ZMART.PRO 100kN universal testing machine equipped with a HCCF clamping unit. Measurement length was 12 mm and deformations were detected by two clip-on sensors, one at each side of the specimen to control bending of the specimen. For each specimen type 5 samples in 0° and 90° were considered for testing. Testing velocity was 1mm/min and compression modulus E_C was calculated via linear regression between $\epsilon_1=0.05\%$ and $\epsilon_2=0.25\%$.

3.4 IMPACT TEST

To determine impact properties, dynamic tests were performed with an Instron dynatup 9250HV drop tower. A wedge shape indenter was dropped on rectangular specimen with a constant thickness to span ratio of 1:15. The impact velocity was calculated for the three specimen types to obtain a strain rate of 1×10^3 in each case. For each specimen type at least 3 samples in 0° and 90° were considered for testing. Impact strength was calculated as quotient of maximum energy measured during impact and cross section of the sample.

4 RESULTS

Regarding the elastic properties, the implementation of unidirectional reinforcements in the investigated laminates leads to an increase of modulus for both ply arrangements and for all considered loading cases, if loading direction was parallel to the fibers. For tensile, bending as well as compression the increase of elastic modulus was more distinct for laminate type B with two carbon reinforced outer layers, whereas the biggest increase was reached for bending. For laminate type A flexural modulus is 150% of the elastic modulus of pure glass fiber SMC. With unidirectional carbon fiber reinforced outer layers the modulus was with 70.7 GPa and hence more than ten times (increase of 1090%) the value for glass fiber SMC (6.5 GPa) (Fig. 3).

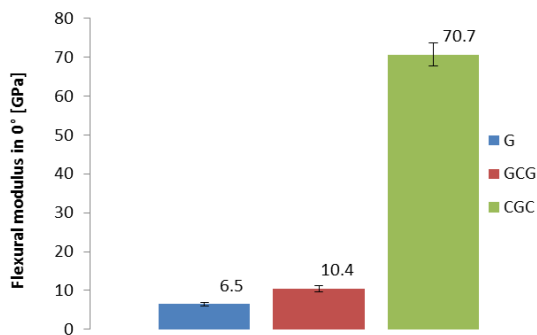


Fig. 3 Flexural modulus for glass fiber SMC (G), laminate type A (GCG) and B (CGC) in 0°

The increase of the elastic modulus for tensile load is also significant for both laminate types. The modulus is 4 times higher for laminate type A and 7.5 times higher for laminate type B compared to the purely glass fiber reinforced SMC (Fig. 4).

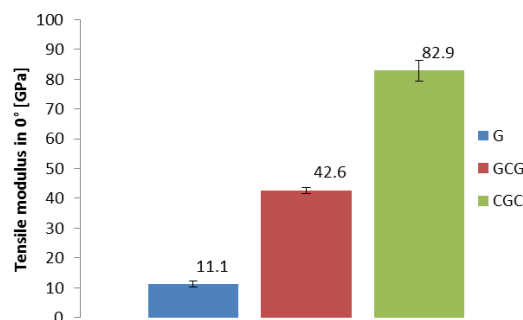


Fig. 4 Tensile modulus for glass fiber SMC (G), laminate type A (GCG) and B (CGC) in 0°

Considering compression load, the modulus increases from 8.6 GPa for pure glass fiber reinforced SMC to 29 GPa (+340%) for laminate type A and 67 GPa (+780%) for type B (Fig. 5).

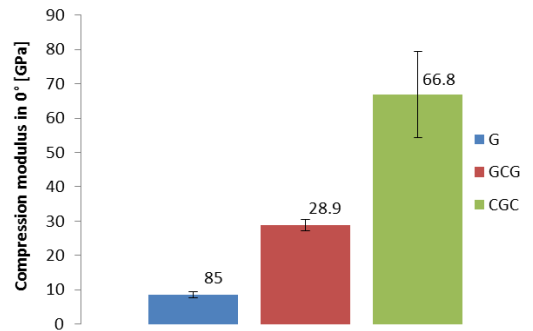


Fig. 5 Compression modulus for glass fiber SMC (G), laminate type A (GCG) and B (CGC) in 0°

If loading direction was perpendicular to the unidirectional fibers, no significant difference between the three considered materials were observed for tensile and compression loadings. For bending loadings, laminate type A showed the highest modulus perpendicular to fiber direction, which was 1.3 times higher than for pure glass fiber SMC. Unidirectional carbon outer layers even weakened mechanical performance by 35 %.

Regarding at compression and bending strength, laminate type B shows the biggest increase compared to purely glass fiber reinforced SMC. There was an increase of 500 % (Fig. 6) considering flexural strength and 280 % for compression loads (Fig. 7) in fiber direction.

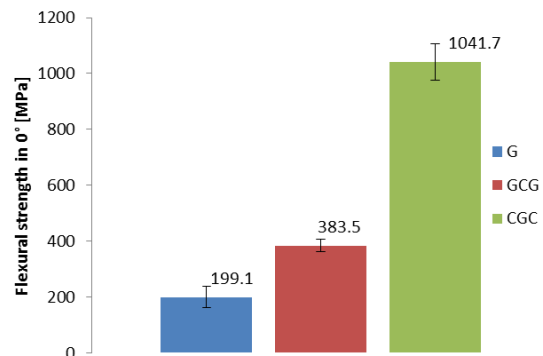


Fig. 6 Flexural strength for glass fiber SMC (G), laminate type A (GCG) and B (CGC) in 0°

For dynamic loads, as for quasi-static loadings, especially the outer layer of the laminate determines mechanical properties. With laminate type A an 80% increase of impact strength in fiber direction was observed. For type B impact strength is even more than twice as high as for purely glass fiber reinforced SMC (Fig. 8).

Considering samples tested perpendicular to fiber direction, for laminate type A as well as for type B impact performance decreases compared to purely glass fiber reinforced SMC from 57 J/m² to 35 J/m² respectively 42 J/m² (Fig. 9).

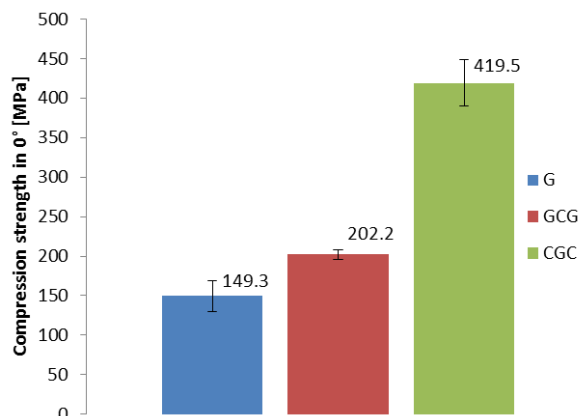


Fig. 7 Compression strength for glass fiber SMC (G), laminate type A (GCG) and B (CGC) in 0°

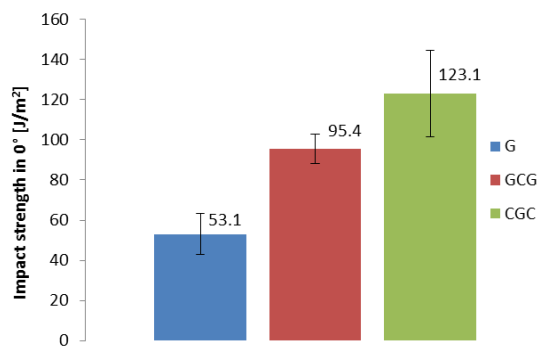


Fig. 8 Impact strength for glass fiber SMC (G), laminate type A (GCG) and B (CGC) in 0°

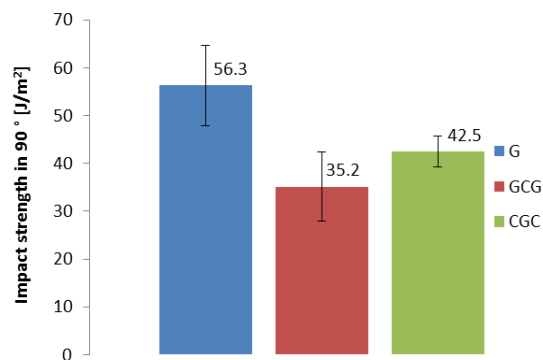


Fig. 9 Impact strength for glass fiber SMC (G), laminate type A (GCG) and B (CGC) in 90°

5 DISCUSSION

This paper proved the possibility to reinforce chopped glass fiber SMC with unidirectional carbon fiber SMC in an one shot- compression molding process. Different laminate architectures were realized which showed an increase in mechanical properties considered quasi-static and dynamic loadings. For all tested loading cases the reinforcement effect was most important for laminates with two unidirectional carbon fiber SMC outer

layers. The biggest increase in modulus and strength was observed for bending. If loads are applied perpendicular to fiber direction, there was no reinforcement observed. In this case, matrix characteristics are decisive for mechanical properties. Especially for compression loadings a high standard deviation was observed evaluating the compression modulus. The inhomogeneity of the laminates caused a slight curvature in the elastic region of the stress-strain curve. This complicated the definition of an evaluation region to determine the compression modulus, which was valid for all tested samples. To evaluate the effect of unidirectional reinforcement and the lightweight potential of obtained laminates a comparison based on resultant laminates' density would be appropriate in general. As the material compositions in this study were adapted to obtain components with the same density, the price was taken into account for an evaluation of the reinforcement effect. For a first theoretical comparison Young's moduli for laminate type B with different ply thicknesses were calculated with the material selection software CES EduPack [7]. Calculation based on measured elastic properties for pure chopped glass fiber and pure unidirectional carbon fiber SMC. As the described manufacturing process was realized on a laboratory scale no manufacturing prices are known for the described material system. Nevertheless, to get an estimation of laminates' prices depending on plies' thicknesses, the prices for thermoset based glass fiber SMC and epoxy based unidirectional carbon fiber laminates were taken into consideration (Fig. 10).

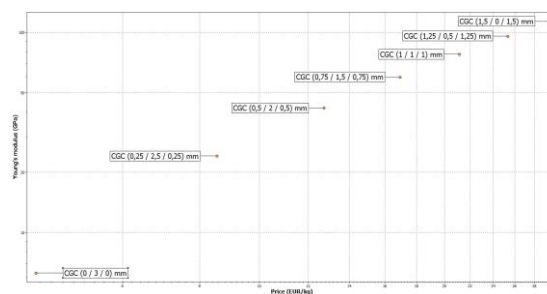


Fig. 10 Price vs. theoretical Young's modulus for different ply thicknesses for laminate type B (CGC) [7]

The theoretical modulus for a laminate architecture with two 1 mm thick carbon fiber reinforced outer layers and a 1 mm glass fiber reinforced SMC sheet in the middle is 79.4 GPa according to the material selection software. With an experimentally measured value of 83 GPa it could be proven that theoretically calculated values can be obtained with the described manufacturing process. Flexural moduli for different ply thicknesses for laminate type A (GCG) and B (CGC) were also calculated based on measured values for pure glass

fiber respectively unidirectional carbon fiber SMC and plotted again versus the prices obtained by the CES EduPack (Fig.11). Theoretical values for laminates with a ply thickness of 1 mm are 8.9 GPa for type A (GCG) and 69.9 GPa for laminate type B. These calculated values fit once again very well with measured moduli (type A: 10.4 GPa and type B: 70.7 GPa). The theoretical estimation underlines the potential of the described approach to combine unidirectional carbon fiber SMC with chopped glass fiber Sheet Molding Compounds in an integrated process.

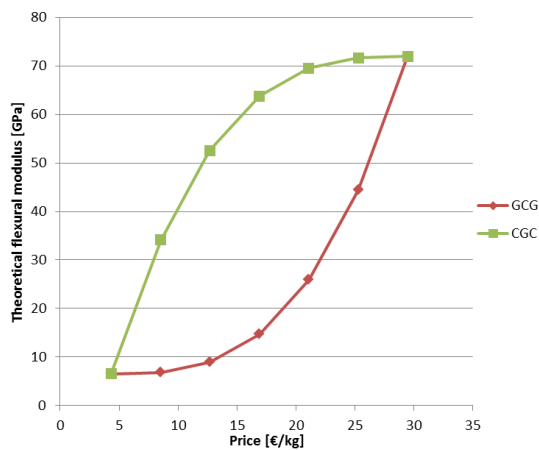


Fig. 11 Price vs. theoretical flexural modulus for different ply thicknesses for laminate type A (GCG) and B (CGC)

The integration of dry carbon fiber $\pm 45^\circ$ non-crimp fabrics, realized by Gortner et al. [4], increased tensile modulus by 220 %. This study proves that a combination of two different SMC semi-finished components with unidirectional carbon fiber reinforcement and based on a one-shot manufacturing process could increase the elastic modulus by 750 %. The difference is also more severe if bending loads are considered. With an increase of approximately 1000 % due to the hybrid compression molding technique this method is once again superior to the integration of dry $\pm 45^\circ$ non-crimp fabrics, with an increase was only 125 % compared to pure glass fiber SMC. The approach presented by Wulfsberg et al. [5] considered unidirectional carbon fiber prepregs as middle ply of a three-layered laminate. This combination tripled tensile modulus and strength. Bending modulus was also doubled whereas there was no difference in bending strength compared to pure glass fiber SMC. The results of this study show, that independent of ply arrangement and also with glass fiber reinforced outer layers the increase of mechanical properties was more important than described by Wulfsberg et al. With the integration of unidirectional carbon fibers in the outer layers the increase

of mechanical properties was even more distinctive.

6 ACKNOWLEDGEMENT

The research documented in this manuscript has been funded by the German Research Foundation (DFG) within the International Research Training Group “Integrated engineering of continuous-discontinuous long fiber reinforced polymer structures“(GRK 2078). The support by the German Research Foundation (DFG) is gratefully acknowledged. The authors also kindly acknowledge the Fraunhofer ICT in Pfinztal, Germany for manufacturing the SMC sheets and laminates with a special thanks to D. Bücheler (Institute of Vehicle System Technology, Karlsruhe Institute of Technology).

REFERENCES

- [1] Boylan S., Castro J.M.: *Effect of reinforcement type and length on physical properties, surface quality and cycle time for sheet molding compound (SMC) compression molded parts*. Journal of applied Polymer Science, 90(9): 2557 – 2571, 2003.
- [2] Bruderick M., Denton D., Shinedling M., Kiesel M.: *Application of carbon fiber SMC for the Dodge Viper*, (n.d.), retrieved from: <http://www.quantumcomposites.com/pdf/papers/Viper-SPE-Paper.pdf>
- [3] Cabrera-Rios M., Castro J.M.: *An economical way of using carbon fibers in sheet molding compound compression molding for automotive applications*. Polymer Composites, 27(6): 718 – 722, 2006.
- [4] Gortner F., Medina L., Mitschang P.: *Advanced SMC-processing in combination with textile reinforcements*. 20th International Conference on Composite Materials, Copenhagen, 2015.
- [5] Wulfsberg J., Hermann A., Ziegmann G., Lonsdorfer G., Stöß N., Fette M.: *Combination of carbon fibre sheet molding compound and prepreg compression molding in aerospace industry*. Procedia Engineering, 81: 1601 – 1607, 2014.
- [6] Karcher M., Gerlitzki M., Thoma B., Henning F.: *Evaluation of a new inlineprepreg process approach to established processes for the manufacturing of structural components out of carbon fibre reinforced plastics*. The 16th annual SPE Automotive Composites Conference & Exhibition, ACCE, Novi (MI), 2014, retrieved from: http://speautomotive.com/SPEA_CD/SPEA2015/pdf/CF/CF2.pdf
- [7] Software „CES EduPack 2015“, Granta Design Cambridge

EXPERIMENTAL INVESTIGATION OF AUTOMOTIVE COMPONENTS CONSISTING OF HYBRID FRP-METAL MATERIAL SYSTEMS UNDER CRASH LOADING

M. Dlugosch^{1*}, J. Ihle¹, D. Lukaszewicz², J. Fritsch¹, S. Hiermaier¹

¹ Material Dynamics, Fraunhofer Ernst-Mach-Institute (EMI)

² Vehicle Safety, BMW Group

ABSTRACT: In the course of a strong trend towards automotive material diversification, hybrid material systems could offer solutions to design lightweight body-in-white structures particularly subject to crash loads in order to meet the demands of both ambitious efficiency goals and increasingly strict vehicle safety requirements. Hybrid material systems consisting of glass- and carbon fiber reinforced plastics and sheet steel are tested under axial impact loading and analyzed regarding their qualitative behavior and relevant crash metrics. The study shows the complex behavior of those material systems and the interaction between the material phases resulting in a complex system of parameter effects and interdependencies. Generally, the hybrid specimens studied indicated their applicability in automotive crash structures by exhibiting comparable results to pure FRP materials while simultaneously being potentially more compatible and cost efficient.

KEYWORDS: FRP-Metal-Hybrid systems, Crash structures, Automotive

1 INTRODUCTION

Motivated by efficiency goals and upcoming strict EU-regulations for CO₂ emissions [1], lightweight design plays an increasingly important role in automotive engineering. Since the load carrying structures in the body-in-white (BiW) comprise ca. 25 % of the entire vehicle weight it is a very promising system for the application of effective lightweight design measures [2].

Novel materials are one way to reduce the weight of the body-in-white while simultaneously meeting the growingly stringent crash safety requirements. Advanced composites like carbon or glass fiber reinforced plastics (CFRP/GFRP) exhibit weight specific crashworthiness characteristics that, though strongly dependent on the composite's constituents and their arrangement, mostly outrival those of metals [3–5]. Metals in turn offer relatively cost efficient solutions with well understood and stable energy absorbing mechanisms. This study explores the possibilities to form synergetic “hybrid” combinations of those different types of materials aiming to exploit their respective benefits in future crash structural applications.

Research on the mechanical behavior of hybrid material systems consisting of advanced composites and metals so far mostly originated from direct applications in complex engineering systems

rather than in the field of fundamental material research. In the 1990s Ford produced a high volume vehicle with a hybrid front end structure composed of a sheet steel framework and injection molded rib reinforcements of glass fiber reinforced polyamide [6]. Next to weight specific increases in strength and stiffness they discovered high integrative potential and good recyclability. Further investigations on hybrid structural automotive components like b-pillars, door sills and roof or floor structures have been conducted by several authors [7–11]. These investigations were often embedded in case and feasibility studies concerning direct applications of hybrid structures with respect to weight savings, production techniques and costs. As a general result, those hybrid structures could be identified as feasible solutions in the respective fields of application with the possibility of moderate to high weight savings, higher integration levels and/or enhanced mechanical properties compared to conventional solutions.

Focusing on the mechanics and the crashworthiness of hybrid structures in automotive crash applications Wang et al. [12] conducted quasi static and dynamic impact tests on steel cylinders circumferentially wrapped with GFRP and found the composite material to be an effective reinforcement to the tubes. According to their results the strengthening

* Corresponding author: Eckerstrasse 4, 79104 Freiburg, Germany, Phone: 0049761/2714-324, Email: Michael.dlugosch@emi.fraunhofer.de

effect grew with an increasing composite to steel ratio, eventually leading to an altered, more effective failure mode. Disadvantageous changes in the failure mode were observed by Bouchet et al. [13] while crushing aluminum cylinders circumferentially wrapped with GFRP. A dependency on the thickness of the tube as well as on the composite reinforcement was found, but no correlation to any sort of surface treatment at the bonding interface. Similar findings were made by Shin et al. [14] wrapping GFRP prepregs around square aluminum tubes. In quasi static crushing tests they discovered a specific reinforcing effect of GFRP depending on the ply orientations and the composite thickness. Kim et al. [15] also studied the crashworthiness of aluminum square tubes reinforced with CFRP subjected to axial low velocity impact. They found that CFRP reinforcements enhanced both the CFE (crush force efficiency) and the *SEA* (weight specific crash energy absorption capability) of the crush tubes by 30 % and 38 % respectively. Related studies were conducted by Bambach et al. [16–22]. The authors analyzed the reinforcing effect of externally applied CFRP on crush tubes of different specifications. The influences of the tube design and material as well as the number and orientation of the CFRP layers on the crash characteristics were investigated. They found substantial improvements in crash performance compared to tubes made of one single material (Mamalis [23]). However, the impact characteristics of composite crush tubes strongly depend on the complex failure mechanisms within the material [24] and thus have a vast range of values for their metrics of crashworthiness such as the *LU* (“load uniformity”) or *SEA* (“specific energy absorption”). Considering other factors such as geometric, bonding or architectural aspects, a direct comparison between the different material systems is difficult. The abovementioned scientific publications indicate significant weight saving potentials inherent in hybrid materials comprised of fiber reinforced plastics and metals. They also indicate their strong dependency on their architectural design and single material constituents. Thus, the conclusions drawn from the test results can only be valid for the respective set of parameters (e.g. specimen geometry) and can hardly be transferred to other settings or even be generalized.

Based on a large experimental study on the characterization of these hybrid material systems on a coupon scale previously conducted by the authors [25], the present study focuses on the dynamic loading of automotive components composed of hybrid material systems under axial compression. The hybrid components studied here follow the concept of composite-intensive hybrids rather than conventional metallic structures reinforced with advanced composites. The aim is to confirm and

complement the findings of the previous studies in terms of the effects of major design parameters and the identification of hybrid mechanisms as well as the full exploitation of the composites’ potentials in crash structural applications.

2 SPECIMENS, TEST SETUP AND EVALUATION

2.1 MATERIALS

In order to represent a type of steel commonly used in BiW designs a dual phase steel named “HCT600X+Z100” [26] – usually applied in energy absorbing structures – is used for the manufacturing of the test specimens. The name is abbreviated as “DPS” (dual phase steel) below.

The composite layups were manufactured using unidirectional glass or carbon fiber mats pre-impregnated with epoxy resin (prepregs). Both the carbon fiber prepreg “PREDO PR-UD CS 300/600 FT 102 38” [27] and the glass fiber prepreg “PREDO PR-UD EST 300/300 FT 102 35” [28] were produced by SGL epo GmbH. To ensure comparability both prepregs contained the same epoxy resin matrix “FT102” [29] and had a fiber areal weight of 300 g/m². The fiber mass fractions were 62 % and 65 % for the carbon and the glass fiber prepreg respectively. The types of reinforcing fibers used in this study were 50k filaments industrial grade carbon fibers and standard E-glass fibers, which are commonly used in engineering applications such as automotive or aircraft systems. Joining of the constituents was achieved through a layer of “BETAMATE 2096” [30], a two-component epoxy structural adhesive widely used in the automotive sector for crash, structural and repair applications. This type of adhesive has proven to be suitable for joining composites and metals in previous test series [31].

2.2 SPECIMEN DESIGNS AND MANUFACTURING

As depicted in Fig. 1 the specimens consisted of a 16-ply FRP base structure externally reinforced with adhesively bonded steel shells. The length of the specimens was 400 mm.

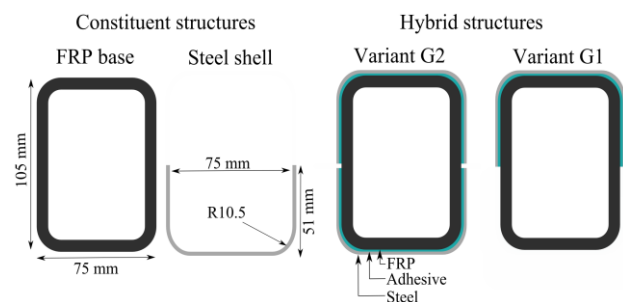


Fig. 1: Cross sectional view of the constituent structures (left) design of the hybrid variants (right)

While the thickness of the adhesive layer was 0.2 mm, the ply thicknesses for *CFRP* and *GFRP* were 0.36 and 0.26 respectively yielding different steel-to-*FRP* cross sectional ratios for the respective fibers. Table 1 shows the entire list of tested variants comprising two designs (G1 and G2), two types of fibers and steel thicknesses and two types of layup.

Table 1: List of tested specimen variants

Designs	Fibers	Steel thickness	Layup
G1 / G2	Carbon	1.5 mm	[0/90 ₂ /0] _{2S}
G1 / G2	Carbon	1.0 mm	[-45/0/45/0] _{2S}
G1 / G2	Carbon	1.0 mm	[0/90 ₂ /0] _{2S}
G1 / G2	E-Glass	1.5 mm	[-45/0/45/0] _{2S}
G1 / G2	E-Glass	1.5 mm	[0/90 ₂ /0] _{2S}
G1 / G2	E-Glass	1.0 mm	[-45/0/45/0] _{2S}
Base	Carbon	-	[0/90 ₂ /0] _{2S}
Base	E-Glass	-	[0/90 ₂ /0] _{2S}
Shell	-	1.0 mm	-
Shell	-	1.5 mm	-

In the manufacturing process the prepregs were manually layered according to the stack of fiber angles in the respective layup and then cured in the autoclave using a specifically designed tool. The bent steel shells were bonded to the cured FRP base structure after applying the adhesive with a spatula. Finally the specimens were bonded to a mounting plate and a 15° arrow trigger was cut to the specimens' top to ensure a stable onset of the progressive damage (Fig. 5, left). The layup selection is based on the findings made by the authors in previous studies (see [25]) and will be abbreviated as "90" for [0/90₂/0]_{2S} and "45" for [-45/0/45/0]_{2S} respectively. The G1-specimen in the first row of Table 1 will thus be referred to as "G1-C-1.5-90".

2.3 EXPERIMENTAL SETUP

All specimens were tested in the Component crash test facility at the Fraunhofer EMI Crash Center schematically pictured in Fig. 2. The dynamic expansion of the air inside a pressure vessel with up to 200 bar propels a push rod and a guided sled of variable mass which then impacts the specimen mounted at the abutment.

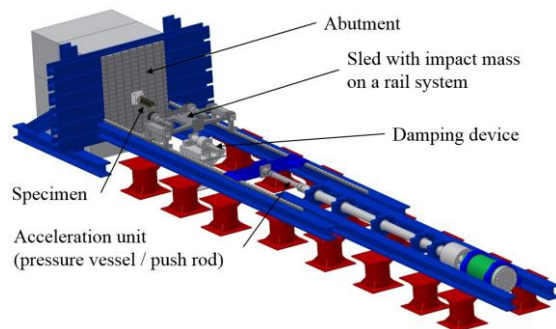


Fig. 2: Component crash test facility at the Fraunhofer EMI

The testing speed was 8.3 m/s (± 0.1) while the kinetic energy was varied according to the anticipated mean crush force of the variant by adjusting the mass of the sled (315 – 795 kg). Each variant was tested twice to check for the reproducibility of the crushing behavior.

The displacement and speed of the sled were measured using a magnetic transient recorder. The force was recorded by a sensor mounted between the bottom plate of the specimen and the abutment. High speed (*HS*) video recordings were made in order to qualitatively assess the damaging process.

2.4 EVALUATION AND METRICS

Next to the qualitative assessment of the different variants' behaviour by interpreting load-displacement plots and analysing failure patterns, several performance metrics have been evaluated, of which not all can be presented in this paper for reasons of scope. Fig. 3 depicts the typical force-displacement plot of an axially loaded hybrid specimen including some crucial parameter definitions.

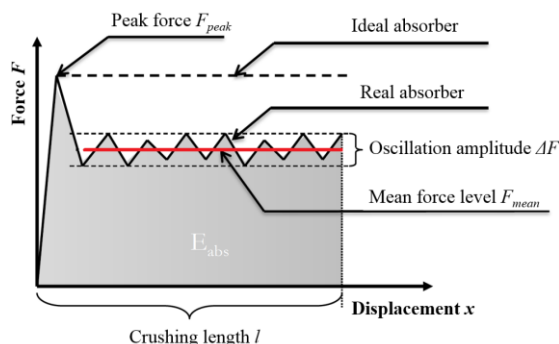


Fig. 3: Schematic force-displacement plot of an axially loaded hybrid specimen (reprod. from [32])

Considering the application background of this study, the (mass-) specific energy absorption *SEA* is the most important performance metric. It is defined as

$$SEA = \frac{1}{m(l)} \cdot \int_l F(x), \quad (1)$$

where $m(l)$ is the mass of the crushed specimen length l and $\int_l F(x)$ equals the energy absorbed by

the specimen, which can be interpreted as the area underneath the force-displacement graph (gray area in Fig. 3).

Another metric to assess the quality of an absorbing structure is the load uniformity *LU*, which is defined as

$$LU = \frac{F_{peak}}{F_{mean}}. \quad (2)$$

Here, F_{peak} is the maximum force usually observed at the onset of the progressive damage and generally highly dependent on the type of trigger [24]. F_{mean} is the arithmetic mean of the force signal excluding the initial peak force. In the design of automotive crash structures an ideal absorber would yield a LU value of 1.

3 RESULTS AND DISCUSSION

In this chapter, an excerpt of the findings is introduced and discussed. First, a qualitative analysis of the testing results is presented, followed by the evaluation of the metrics defined above.

3.1 QUALITATIVE ANALYSIS

The above graph in Fig. 4 shows typical force-displacement plots of one hybrid variant under axial crash loading with the corresponding high-speed video frames (below) at characteristic steps indicated in the graph.

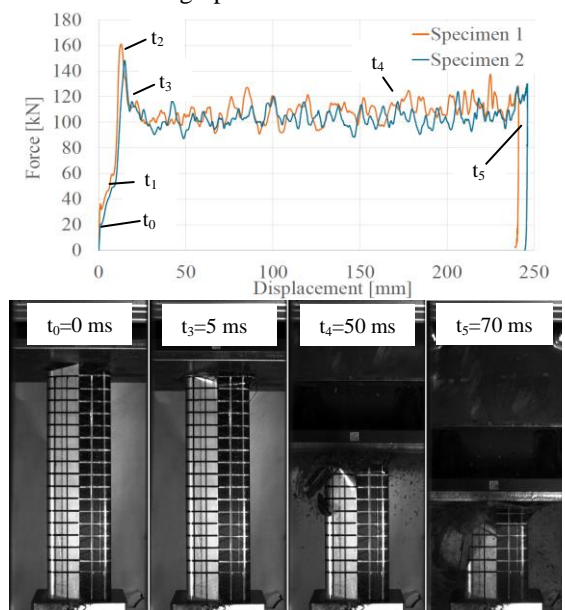


Fig. 4: Force-displacement plots of two specimens of the same hybrid variant with corresponding HS-video frames

At t_0 the impactor sled reaches the tip of the specimen trigger, which is then fully crushed at t_1 . As the plate impacts the entire cross sectional area of the specimen the force increases to its peak value at t_2 . The mean force is evaluated between the starting point of the stable progressive crushing at t_3 , passing t_4 to the rebound of the impactor at t_5 .

Fig. 5 depicts a hybrid specimen before (left) and after (right) testing. It is generally observed, that the steel reinforcement has a significant effect on the failure mechanism of the FRP.

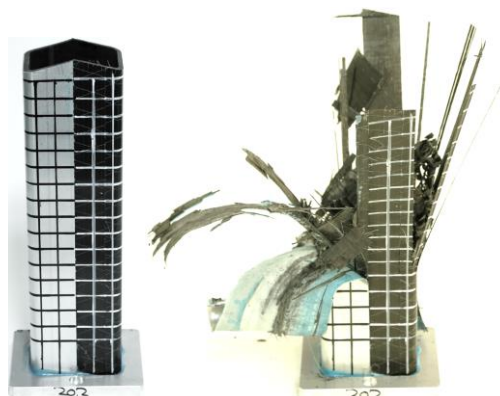


Fig. 5: G1-C-1.0-90 hybrid specimen before (left) and after (right) testing

While areas of unreinforced *FRP* tend to fracture into rather large chunks, the reinforced parts exhibit a brittle and highly disintegrating fracturing pattern. Laminates with a $[0/90_2/0]_{2S}$ -layup and *GFRP*-variants are not as finely crushed as $[-45/0/45/0]_{2S}$ - and *CFRP*-variants respectively. Furthermore, the steel reinforcement urges the *FRP* to fold to the inside cavity of the specimen. The laminates generally exhibit extensive delaminations into single layers. The steel shell shows two different failure patterns – an outside fold with shear wrinkles and an edge-ripping with rolling of the sides - without significant correlations to the parameters of variation or the crushing force (see Fig. 6). Generally, the repeatability proved to be very good in terms of the force-displacement measurements.



Fig. 6: Edge-ripping and rolling (left) and outside folding (right) of the steel shell

3.2 QUANTITATIVE ANALYSIS

The *SEA* of the tested hybrid and pure *FRP* variants is depicted in Fig. 7. The pure steel variants are not part of the diagram, since their partially catastrophic failure mode hinders a valid comparison.

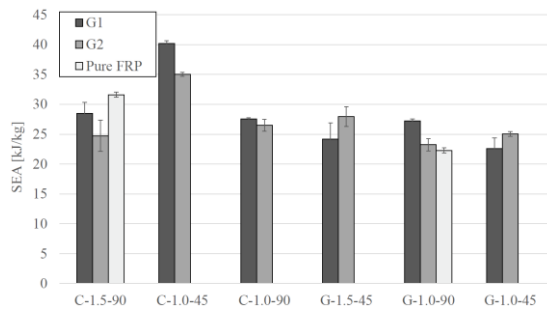


Fig. 7: Specific energy absorption (SEA) of hybrids and pure FRP

Firstly, it is observed that only *GFRP*-hybrids could yield a higher *SEA* than the respective pure *FRP* specimen, where *CFRP* exhibits a 29 % higher value than *GFRP*. While there is no significant dependency for *GFRP*-hybrids, the G1-reinforcement yields a higher *SEA* for *CFRP*-variants. The steel thickness does not affect the *SEA* significantly. The [-45/0/45/0]_{2S}-layup however outperforms the [0/90₂/0]_{2S}-layup, which is particularly seen for *CFRP*. This correlates with a higher level of disintegration described above. The load uniformity of the respective specimens is depicted in Fig. 8.

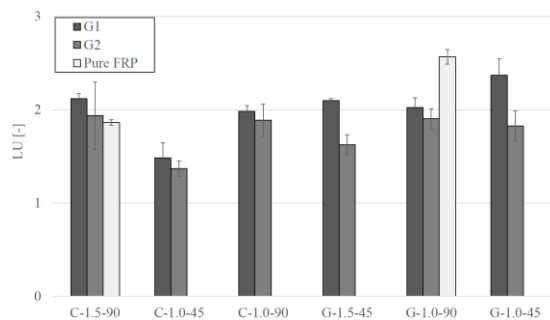


Fig. 8: Load uniformity (LU) of hybrids and FRP

In contrast to *GFRP*, pure *CFRP* yields a lower (better) *LU* than its respective hybrid variant. Generally, G2-reinforcements yield a better *LU* than G1, which indicates advantageous properties of fully hybridized variants. While there is no correlation for *CFRP*, thicker steel yields slightly better *LU*-values for *GFRP*-variants. However, the layup tends to only affect the *LU* of *CFRP* hybrids, where again the C-1.0-45 variants show the best performance. It is noted, that the *LU* is also highly dependent of the trigger type at the specimens' tip. Thus, a geometric optimization of the *LU*-characteristics is generally possible.

4 CONCLUSIONS

The investigation of hybridized *FRP* base structures using steel shells under axial impact loading proved their general applicability in automotive crash structures, because they exhibit a relatively

constant load level as well as *LU*- and *SEA* values at least comparable to those of pure *FRPs*. Considering other aspects, such as compatibility to conventional design and production concepts, scalability or costs [25], hybrids could outperform conventional material systems in those applications. Since there is a highly complex interaction between the two material phases, the effects of - and interdependencies between - the parameters varied in this study are not easily analysed comprehensively and need further investigations. Compared to the other variants, the G1-C-1.0-45 generally exhibited the most advantageous properties.

For reasons of scope only a small set of results could be presented in this paper.

5 ACKNOWLEDGEMENTS

The authors would like to express their gratitude to their colleagues at the department of material dynamics at the Fraunhofer EMI and at BMW for valuable discussions and great support.

REFERENCES

- [1] European Union. 2009. *Regulation (EC) No 443/2009 of the European Parliament and the Council of 23 April 2009.*
- [2] Lehold, J. 2011. *Chancen und Grenzen für eine nachhaltigen FVK-Einsatz im Automobil.* CCEV Automotive Forum 2011, Ingolstadt.
- [3] Thornton, P. H. 1979. Energy Absorption in Composite Structures. *Journal of Composite Materials* 13, 3, 247–262.
- [4] Friedrich, H., Kopp, J., and Stieg, J. 2003. Composites on the Way to Structural Automotive Applications. *MSF* 426-432, 171–178.
- [5] Drechsler, K., Heine, M., Mitschang, P., Baur, W., Gruber, U., Fischer, L., Öttinger, O., Heidenreich, B., Lützenburger, N., and Voggenreiter, H. 2000. Carbon Fiber Reinforced Composites. In *Ullmann's Encyclopedia of Industrial Chemistry.* Wiley-VCH Verlag GmbH & Co. KGaA, Weinheim, Germany.
- [6] Koch, B., Knözinger, G., Pleschke, T., and Wolf, H. J. 1999. Hybrid-Frontend als Strukturbauteil. *Kunststoffe* 89, 3, 82–86.
- [7] Grasser, S. 2009. *Composite-Metall-Hybridstrukturen unter Berücksichtigung großserientauglicher Fertigungsprozesse.* Symposium Material Innovativ, Ansbach.
- [8] Hufenbach, W., Werner, J., and Kiele, J. 2013. Elektromobilität in Ultraleichtbauweise. *ATZ Extra* 18, 2, 42–46.
- [9] Feraboli, P., Deleo, F., Wade, B., Rassaian, M., Higgins, M., Byar, A., Reggiani, M., Bonfatti, A., DeOto, L., and Masini, A. 2010.

- Predictive modeling of an energy-absorbing sandwich structural concept using the building block approach. *Composites Part A: Applied Science and Manufacturing* 41, 6, 774–786.
- [10] Frantz, M., Lauter, C., and Tröster, T. 2011. *Advanced manufacturing technologies for automotive structures in multi-material design consisting of high-strength steels and cfrp*, University of Paderborn.
- [11] Eckstein, L., Ickert, L., Goede, M., and Dölle, N. 2011. Leichtbau-Bodengruppe mit Verstärkungen aus CFK und GFK. *ATZ (ATZ - Automobiltechnische Zeitschrift)* 113, 4, 256–261.
- [12] Wang, X. G., Bloch, J. A., and Cesari, D. 1992. Static and dynamic axial crushing of externally reinforced tubes. *ARCHIVE: Proceedings of the Institution of Mechanical Engineers, Part C: Journal of Mechanical Engineering Science 1989-1996 (vols 203-210)* 206, 53, 355–360.
- [13] Bouchet, J., Jacquelin, E., and Hamelin, P. 2002. Dynamic axial crushing of combined composite aluminum tube: the role of both reinforcement and surface treatments. *Composite Structures* 56, 1, 87–96.
- [14] Shin, K. C., Lee, J. J., Kim, K. H., Song, M. C., and Huh, J. S. 2002. Axial crush and bending collapse of an aluminum/GFRP hybrid square tube and its energy absorption capability. *Composite Structures* 57, 1-4, 279–287.
- [15] Kim, H. C., Shin, D. K., Lee, J. J., and Kwon, J. B. 2014. Crashworthiness of aluminum/CFRP square hollow section beam under axial impact loading for crash box application. *Composite Structures* 112, 1–10.
- [16] Bambach, M. and Elchalakani, M. 2007. Plastic mechanism analysis of steel SHS strengthened with CFRP under large axial deformation. *Thin-Walled Structures* 45, 2, 159–170.
- [17] Bambach, M., Elchalakani, M., and Zhao, X. 2009. Composite steel–CFRP SHS tubes under axial impact. *Composite Structures* 87, 3, 282–292.
- [18] Bambach, M., Jama, H., and Elchalakani, M. 2009. Axial capacity and design of thin-walled steel SHS strengthened with CFRP. *Thin-Walled Structures* 47, 10, 1112–1121.
- [19] Bambach, M., Jama, H., and Elchalakani, M. 2009. Static and dynamic axial crushing of spot-welded thin-walled composite steel–CFRP square tubes. *International Journal of Impact Engineering* 36, 9, 1083–1094.
- [20] Bambach, M. 2010. Axial capacity and crushing of thin-walled metal, fibre–epoxy and composite metal–fibre tubes. *Thin-Walled Structures* 48, 6, 440–452.
- [21] Bambach, M. 2010. Axial capacity and crushing behavior of metal–fiber square tubes – Steel, stainless steel and aluminum with CFRP. *Composites Part B: Engineering* 41, 7, 550–559.
- [22] Bambach, M. R. 2013. Fibre composite strengthening of thin-walled steel vehicle crush tubes for frontal collision energy absorption. *Thin-Walled Structures* 66, 15–22.
- [23] Mamalis, A., Manolakos, D., Ioannidis, M., and Papapostolou, D. 2005. On the response of thin-walled CFRP composite tubular components subjected to static and dynamic axial compressive loading: experimental. *Composite Structures* 69, 4, 407–420.
- [24] Lukaszewicz, D. H.-J. A. 2013. Automotive Composite Structures for Crashworthiness. In *Advanced Composite Materials for Automotive Applications*, A. Elmarakbi, Ed. John Wiley & Sons Ltd, Chichester, UK, 99–127.
- [25] Dlugosch, M., Lukaszewicz, D. H.-J. A., Fritsch J., and Hiermaier, S. 2015. *Gewichtsoptimiertes Design crashrelevanter Fahrzeugstrukturen in Hybridbauweise*. crashMAT 2015, Freiburg [Breisgau].
- [26] Salzgitter Flachstahl. 2009. *HCT600XD (HC340XD*)*. Mehrphasenstähle zum Kaltumformen - Dualphasenstähle, Salzgitter.
- [27] SGL Group. 2014. *PREDO PR-UD CS 300/600 FT102 38*. Technical Data Sheet, Willich.
- [28] SGL Group. 2014. *PREDO PR-UD EST 300/300 FT102 35*. Technical Data Sheet, Willich.
- [29] SGL Group. 2014. *Epoxid-Prepreg FT102*. Produkt Information Epoxid-Prepreg FT102, Willich.
- [30] Dow Automotive AG. 2003. *Betamate 2096*. Technisches Datenblatt.
- [31] Engel, S., Boegle, C., Majamaeki, J., Lukaszewicz, D. H.-J. A., and Moeller, F. 2012. Experimental investigation of composite structures during dynamic impact. In *ECCM15 - 15th European Conference on Composite Materials*.
- [32] Feindler, N. 2012. *Charakterisierungs- und Simulationsmethodik zum Versagensverhalten energieabsorbierender Faserverbundstrukturen*. Dissertation, Technische Universität München.

DEEP- AND STRETCH-FORMING OF STEEL/POLYMER/STEEL LAMINATES

Mohamed Harhash¹, Adele Carrado², Heinz Palkowski^{1*}

¹Institute of Metallurgy (IMET), Metal Forming and Processing, Clausthal University of Technology (TUC), Robert-Koch-Str. 42, 38678 Clausthal-Zellerfeld, Germany

²Institut de Physique et Chimie des Materiaux de Strasbourg, IPCMS, UMR 7504 ULP-CNRS, 23 rue du Loess, BP 43, 67034 Strasbourg cedex 2, France

ABSTRACT: Due to the demands for better environmental impact of the mobile vehicles, developing light-weight sheets become more essential. Steel/polymer/steel (SPS) sandwich laminates can substitute the commercial sheets due to the improved thermal and acoustic damping and specific mechanical properties. In this study, deep drawable steel skin sheets and polypropylene-polyethylene copolymer core layer are the SPS constituents. Symmetrical and asymmetrical SPS are produced via roll bonding using adhesive agent. The mechanical properties of the SPS are firstly evaluated by tensile loading considering the strain development over the SPS surfaces.

The formability is investigated through deep drawing and stretching. The deep drawing working area is determined at varied blank holding forces and drawing ratios. The results revealed, that maximum drawing ratio decreases with thicker core layers and becomes more limited with thinner skin sheets as predicted by the mechanical properties.

The stretching behavior of the SPS laminates is investigated using semi-spherical punch. The stretching behavior of the SPS is negatively affected with increasing the core thickness. Furthermore, the stretching potential depends significantly on the outer skin sheet (not in contact with the punch) for asymmetrical SPS; the dome height increases and accordingly the limiting strains for thicker outer steel skin.

KEYWORDS: Hybrid laminates, forming, deep drawing and stretching, mechanical properties

1 INTRODUCTION

Recently metal/polymer hybrid laminates are applied in several engineering application fields especially in the automotive and aircraft industry. The main advantage of these laminates is their sound damping effect together with improved specific stiffness. Special precautions should be considered during their processing, cutting, forming and joining due to the inhomogeneous thickness structure of the combined layers.

Several examples in use can be found such as GLARE[®], ARALL[®] [1,2], Litecor[®] [3], Bondal[®] [4], Hylite[®] [5–7] and others under development such as metal/carbon or glass fibre reinforced thermoplastic core/metal laminates [8–11]. These sandwich laminates differ in core/skin thickness ratios, core structure and the metallic skin sheet according to their application. The sandwich laminates can be categorized according to the core features as: 1) sound damping laminates (core < 20 % of the total thickness), 2) low density laminates

(core = 40- 60% of the total thickness) and 3) fibre metal laminates, FML, (core: high strength fibre reinforced polymer composite) [12,13].

This paper is concerned with some low density laminates consisting of steel skin sheets and different volume fractions of thermoplastic core ranging from 22 to 67%. These laminates are tailored and produced in the lab facilities which enable optimising and defining the forming limits alike the restricted structure of the commercial products. The effect of varied core thicknesses on the mechanical and forming behaviour of the sandwich in terms of the deep drawability and stretching is studied. Previous contributions of the authors on the formability of sandwich materials can be found in [14–17].

2 EXPERIMENTAL WORK

In this part, the used materials and the SPS production scheme is given. Moreover, the mechanical

* Corresponding author: Prof. Dr.-Ing. Heinz Palkowski; Heinz.Palkowski@tu-clausthal.de; Tel.:+495323722014, Fax: +495323723527

properties and forming behaviour methods are described.

2.1 MATERIALS AND PRODUCTION SCHEME

In this study, a deep-drawable (DD), high corrosion resistance, electrically Sn-coated (tinned) steel (Tinplate®) grade, namely TS 245, was delivered by ThyssenKrupp-Rasselstein GmbH in the two thicknesses 0.49 and 0.24 mm. The core layer used is polypropylene-polyethylene (PP-PE) copolymer foil thicknesses 0.3, 0.6, 1.0 and 2.0 mm. In case of achieving good adhesion strength between the steel and the PP-PE layers, this polyolefin guarantees good forming potential of the SPS laminates due to its superior ductility at room temperature. The metal/polymer adhesion is accomplished by a one-component epoxy resin, Köratac FL201. The SPS are produced following the scheme presented in Fig. 1 in a two-step process. Based on the technical data of the adhesive, the curing process is carried out at 260°C/3 min temperature. The polymer core is preheated at 120°C to improve the adhesion quality.

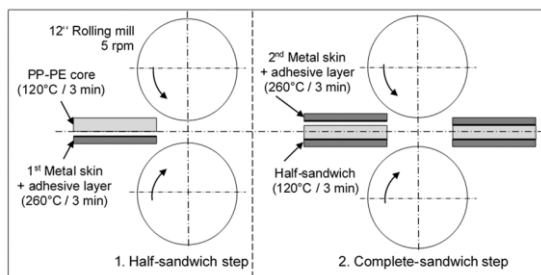


Fig. 1 Lab scale SPS production scheme via roll bonding.

2.2 MECHANICAL PROPERTIES

The general mechanical properties namely the Young's modulus (E), yield strength (YS), tensile strength (TS) and the elongation at failure (ϵ_f) are determined via tensile testing for the different SPS configurations. In addition to that, local strain development over the skin sheets is monitored with a digital image correlation (DIC) system namely GOM-ARAMIS®, by which the normal anisotropy (r-value) is determined, as well. The DIC system is used to obtain the limiting minor (ϵ_2) and major (ϵ_1) strain just before failure. This can be obtained by following the strain path in the failure location from the test start, at which the highest thinning rate takes place as shown in Fig. 2-a). Afterwards, the development of the strains and the thinning rate are plotted in terms of the testing time as shown in Fig. 2-b). The thinning rate curve consists of two regions before failure: a) diffused necking till reaching TS or the so-called uniform strain (ϵ_u) and b) localised necking at which the thinning instabil-

ity starts. The aim is to correlate the thinning rate with the mechanical properties and the impact on the later forming behaviour.

2.3 DEEP DRAWING

The deep drawability of the monolithic steel sheets and their SPS were investigated. The maximum drawing ratio ($\beta_{0,max}$) and the optimum blank holder force (F_{BH}) for different SPS combinations are determined. The drawing ratio β_0 is expressed in equation (1). For this, a Ø33 mm punch with different blank Ø (50 – 80 mm) are used at F_{BH} of 5 – 100 kN at a displacement rate of 0.5 mm/s.

$$\beta_0 = \frac{\text{Blank}\varnothing}{\text{Punch}\varnothing} \quad (1)$$

It is noteworthy that a 0.1 mm thermoplastic foil was used as lubricant between the drawing tools and the blank aiming at minimizing the friction and providing a good surface finish.

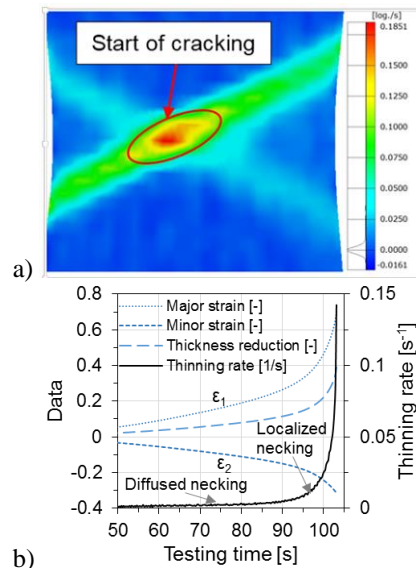


Fig. 2 a) Local thinning rate at the failure position and b) strain and thinning rate development over the testing time.

Moreover, the deep drawability of the different SPS configurations in respect to the forming punch are specified, considering different skin/core thicknesses (Fig. 3). The strain distribution is determined using the DIC system.

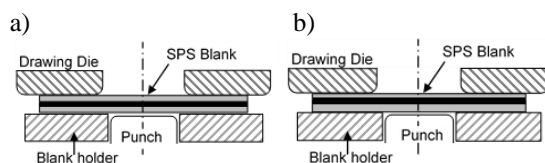


Fig. 3 Illustration of a) symmetrical and b) asymmetrical deep drawing test settings.

2.4 STRETCH DRAWING

Stretch-drawing is performed by forming the SPS and the steel blank with a Ø33 mm semi-spherical punch with a 0.5 mm/s displacement rate, whereby the blank is rigidly clamped at the edges with the blank holder at a given blank holding force (60-100 kN) to avoid sliding/drawing of the blank. The aim is to determine the forming potential under biaxial stretching conditions; the formability is expressed basically in terms of the dome height (the punch stroke till cracking of the outer surface) and the maximum drawing forces. Moreover, the strains (ϵ_2 and ϵ_1) over the outer skin surface are evaluated using the DIC system GOM Aramis® before cracking by applying the time dependent method [18]. For simplicity, the SPS are denoted as follow: 0.49/0.6/0.49 which means symmetrical SPS containing 0.49 mm steel and a 0.6 mm core layer. Asymmetrical SPS is denoted as 0.49/0.6/0.24* where “*” refers to the skin sheet in contact with the forming tool (punch). Table 1: summarizes the tested SPS combinations and the performed evaluation method.

Table 1: An overview of the investigated SPS combinations and the corresponding test.

SPS	Skins	Core	T	$\beta_{0,max}$	SD
0.49/0/0	0.49	-	×	×	×
0.49/0/0.49	0.98	-	×	×	×
0.49/0.3/0.49	0.98	0.3	×	×	×
0.49/0.6/0.49	0.98	0.6	×	×	×
0.49/1.0/0.49	0.98	1.0	×	×	×
0.49/2.0/0.49	0.98	2.0	×	×	×
0.49*/0.3/0.24	0.73	0.6	×	×	×
0.49/0.3/0.24*	0.73	0.6	×	×	×
0.24/0/0	0.24	-	×	×	×
0.24/0.3/0.24	0.48	0.3	×	×	×

where:

T: tensile testing

$\beta_{0,max}$: maximum drawing ratio

SD: stretch-drawing

×: tested condition

3 RESULTS & DISCUSSION

The given SPS show a good adhesion quality. The adhesion results are not the focus of this paper. Some results can be found in [14].

3.1 MECHANICAL PROPERTIES

The mechanical properties in terms of the true stress-strain curves are represented in Fig. 4-a) for the different SPS combinations.

It was found, as expected, that with thicker cores, the SPS exhibited lower strength confirmed the rule of mixture [19]. In addition to that, the r- and n-values which are critical for the forming capacity are negatively affected with increasing core thick-

ness respect to the monolithic steel sheets as shown in Fig. 4-b).

The n-value decreases due to the existing soft polymer core which lessen its strengthening potential.

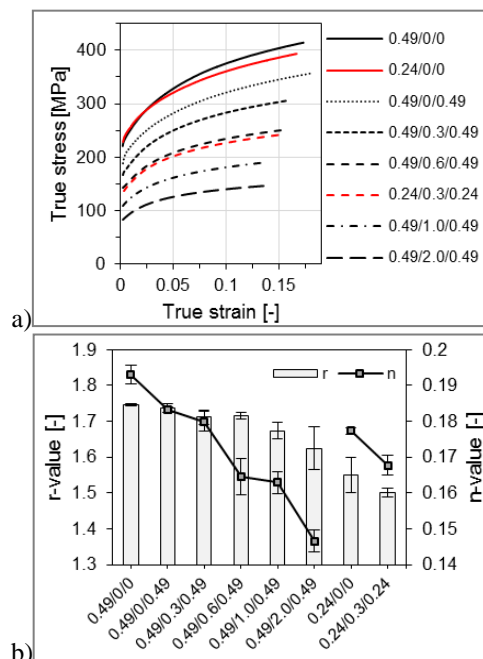


Fig. 4 a) True-stress-strain curves of SPS at different core thicknesses and b) the impact on the n- and r-values.

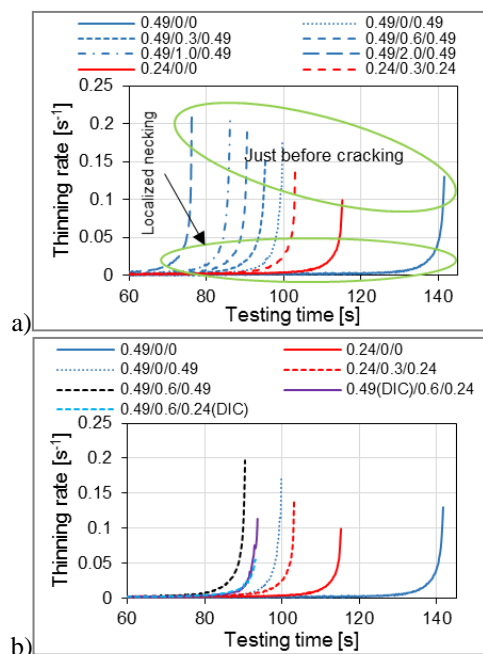


Fig. 5 Thinning rate for a) symmetrical and b) asymmetrical SPS.

The r-value decreases due to the thinning affinity of the SPS especially with thicker soft cores on the expense of the width strain where r is the ratio of

the width to the thickness strain. This result can be emphasized by Fig. 5. Fig. 5-a), which shows the thinning rate of the symmetrical SPS with the testing time. It can be observed that the localized necking starts earlier for the SPS and is further accelerated with increasing the core thickness. However, the limiting strain ($\epsilon_2 - \epsilon_1$) pairs show insignificant differences as shown in Fig. 6.

For the asymmetrical SPS (Fig. 5-b)), two combinations are tested namely 0.49(DIC)/0.6/0.24 and 0.49/0.6/0.24(DIC) where the two different SPS skins are facing the DIC system alternatively, the facing sheet is denoted with (DIC) as shown in Fig. 5-b). The thinning rates of these two SPS are the same till reaching the localised necking, however when the thicker sheet faces the DIC system, higher thinning rate value takes place at failure.

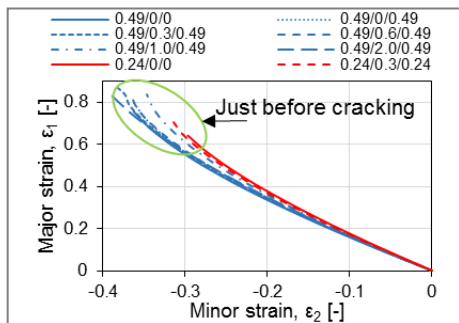


Fig. 6 Thinning rate for a) symmetrical and b) asymmetrical SPS.

3.2 DEEP DRAWING

The deep drawing working area was first determined by defining the different regions with the corresponding defects. As an example, Fig. 7 shows the working area of the SPS 0.24/0.3/0.24. At lower F_{BH} , the blank is completely drawn to cups but with edge wrinkling (EW). Till reaching the $\beta_{0,max}$ value (1.92), no sidewall- or even cup bottom-cracking can be found. After reaching $\beta_{0,max}$, side cracking (C) takes place.

With increasing F_{BH} , completely faultless drawn cups are possible (CD). With further increasing the F_{BH} , flow-out of the polymeric core was found in the region (CD+CF). Moreover, the cup edges were subjected to cracking in addition to the core flow out of the completely drawn cups (CD+CF+EC). These defects accompanied with CD can be simply treated by trimming the cup edges. Therefore, the green shaded area can be considered as the working regions.

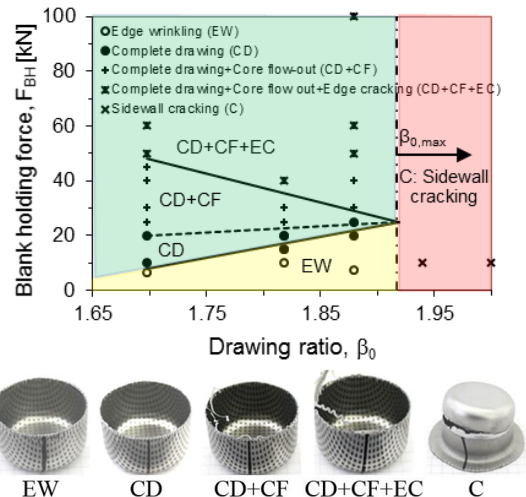


Fig. 7 Deep drawing working area for the 0.24/0.3/0.24 combination and the corresponding cup features/defects.

The working area of some SPS at different skin/core thicknesses is shown in Fig. 8. It is clear that the thicker SPS (0.49/0.6/0.49) exhibited higher $\beta_{0,max}$ compared to 0.24/0.3/0.24 as the thicker skin sheet can withstand higher strains till failure. However, both of the shown SPS exhibit lower $\beta_{0,max}$ compared to the monolithic steel 0.49 mm.

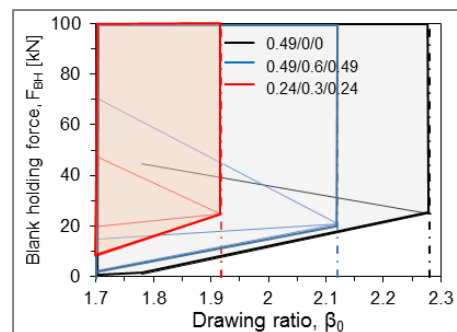


Fig. 8 Comparison of the working area of some SPS considering varied skin/core thickness.

3.3 STRETCH DRAWING

The effect of the core thickness on the stretching behaviour in terms of the dome height till cracking and the drawing force (F_d) is shown in Fig. 9-a). It can be observed that F_d decreases with thicker cores due to the associated lower strength and strengthening exponent. However, no remarkable differences are observed in the dome height of the SPS as well as the monolithic steel where the SPS outer skin sheet are of the same dimension and can break at approximately the same condition.

The thickness reduction at the outer and inner SPS skin sheets is illustrated in Fig. 9-b). The outer skin sheet cracks at lower thickness reduction for thicker cores due to the thinning affinity of thicker cored SPS as described previously in the mechanical

properties. It is observed that the inner layer exhibited lower thickness reduction in respect to the outer layer due to the higher tensile stresses acting on the outer skin sheet.

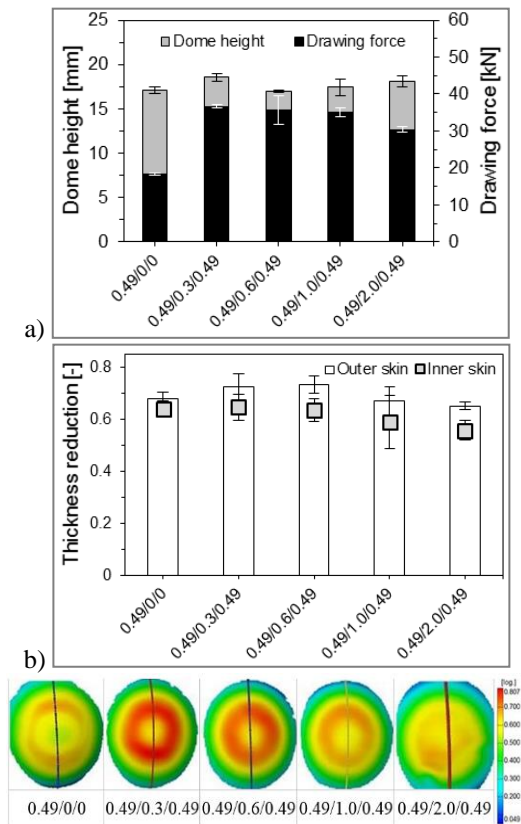


Fig. 9 Effect of the core thickness on the stretch-drawing behaviour in terms of a) the drawing force and dome height and b) thickness reduction at the inner and outer skins at failure.

Furthermore, the effect of the SPS symmetry on the drawing force and dome height is depicted in Fig. 10-a). For the same core thickness, it can be observed that the thicker is the outer skin sheet, relative better stretching behavior occurred; higher F_d and dome height are found. This result is further interpreted in Fig. 10-b), where, if the thinner sheet is not in contact with the punch, lower thickness reduction at cracking is found due to the low forming potential of the thinner sheets. Furthermore, the forming limits expressed in the $(\epsilon_2-\epsilon_1)$ strain points are plotted in Fig. 10-c). It can be stated that the outer skin thickness is the critical determining the SPS cracking limits for symmetrical and asymmetrical SPS.

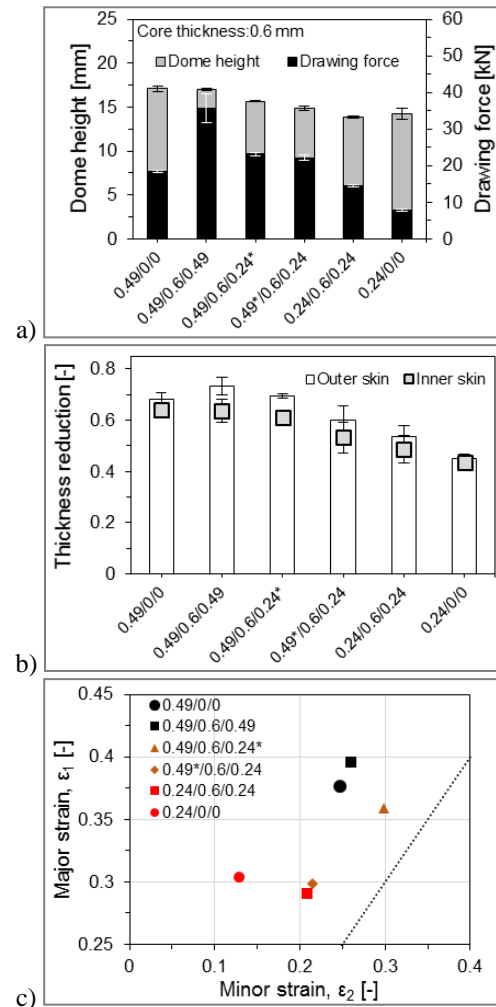


Fig. 10 Effect of the SPS symmetry on the a) drawing force and dome height, b) thickness reduction and c) the $(\epsilon_2-\epsilon_1)$ forming limits just before cracking.

4 CONCLUSIONS

This paper dealt with the effect of the core thickness on the mechanical properties and the local straining especially the thinning rate over the skin sheets. It is found that the thicker core sandwich laminates with the same skin sheet thickness exhibit lower strength as well as limited forming-related properties, such as the n- and r-values. In addition, the thicker SPS are more sensitive to earlier thinning or rather lower uniform strain values. These properties have a direct impact on the forming potential by means of deep- and stretch-drawing. The deep drawability is limited for SPS with thinner skin sheets as well for those that contain thicker cores. The stretch-drawability is significantly affected with the skin/core thickness ratio. It is limited for thinner steel and thicker cores, as well. Moreover, the SPS symmetry offers further weight saving for the SPS and can provide good formability if the thicker skin sheet is not in contact with the forming punch; i.e. the outer sheet.

5 ACKNOWLEDGEMENT

The authors thank DFG (grant: PA 837/23-1) and DAAD (GERLS 2011) for the financial support, additionally ThyssenKrupp Rasselstein GmbH for supplying the steel sheets.

REFERENCES

- [1] Johnson W. S., Li E., Miller J. L.: *High temperature hybrid titanium composite laminates*, Applied Composite Materials, 3(6):379–390, 1996.
- [2] Vermeeren, C. A. J. R., Beumler T., de Kanter, J. L. C. G., et al.: *Glare Design Aspects and Philosophies*, Applied Composite Materials, 10(4/5):257–276, 2003.
- [3] ThyssenKrupp Steel Europe AG: *Leichtbau mit Stahl: LITECOR von ThyssenKrupp Steel Europe geht ins Rennen*, 2014.
- [4] ThyssenKrupp Steel Europe AG: *Bondal®: Steel sandwich material for effective reduction of structure-borne sound*, 2009.
- [5] Jaschinski J.: *Zum Strukturverhalten dünnwandiger Leichtbau-Sandwichbleche* Dresden, Germany, 2012.
- [6] Neugebauer R., Scheffler S.: *Schaffung umformtechnischer Grundlagen bei der Verarbeitung von Metall-Kunststoff-Verbunden*. EFB Hannover, 2006.
- [7] Nutzmann M.: *Umformung von Mehrschichtverbundblechen für Leichtbauteile im Fahrzeugbau*. Shaker Verlag Aachen, Germany, 2008.
- [8] Graf A., Lachmann L.: *Umformeigenschaften von Hybriden Schichtverbunden*. In: 19. Symposium Verbundwerkstoffe und Werkstoffverbunde, Jena, Germany, 511–519, 2013.
- [9] Großmann K., Cherif C., et al.: *3D-Bauteile aus Blech und Textil durch umformende Verbundherstellung*. EFB Hannover, 2013.
- [10] Scholz P., Schieck F., Müller R., et al.: *Umformprozessketten für Bauteile aus Faser-Kunststoff/Metall-Verbunden*. In: EFB T40-Intermezzo der hybriden Werkstofflösungen: Hat Blech eine Zukunft?, Hannover, 151–171, 2015.
- [11] Tekkaya A. E., Hahn M., Hiegemann L., et al.: *Umformen faserverstärkter thermoplastischer Kunststoff-Halbzeuge mit metallischen Deckblechen für den Leichtbau*. In: EFB T40-Intermezzo der hybriden Werkstofflösungen: Hat Blech eine Zukunft?, Hannover, 185–199, 2015.
- [12] Hayashi H., Nakagawa T.: *Recent trends in sheet metals and their formability in manufacturing automotive panels*, Journal of Materials Processing Technology, 46(3-4):455–487, 1994.
- [13] Kim J.-K., Yu T.-X.: *Forming and failure behaviour of coated, laminated and sandwiched sheet metals*, Journal of Materials Processing Technology, 63(1–3):33–42, 1997.
- [14] Harhash M., Carradó A., Palkowski H.: *Forming Potential of Low-Density Laminates*. In: 1. Niedersächsisches Symposium Materialtechnik, Herzogenrath, 53–60, 2015.
- [15] Lange G.: *Beitrag zum Umformverhalten von dreischichtigen austenitischen Sandwichverbunden mit polymerer Kernschicht* Clausthal-Zellerfeld, Germany, 2005.
- [16] Sokolova O., Palkowski H.: *Lokale Verstärkungen in blechförmigen Metall/Polymer/Metall-Sandwichverbunden*. In: EFB T32-Hochfeste und hybride Materialien, Hannover, 111–126, 2011.
- [17] Sokolova O.: *Study of metal/polymer/metal hybrid sandwich composites for the automotive industry* Clausthal-Zellerfeld, Germany, 2012.
- [18] Merklein M., Kuppert A., Geiger M.: *Time dependent determination of forming limit diagrams*, CIRP Annals - Manufacturing Technology, 59(1):295–298, 2010.
- [19] Harhash M., Carrado A., Palkowski H.: *Forming Limit Diagram of Steel/Polymer/Steel Sandwich Systems for the Automotive Industry*. In: Advanced Composites for Aerospace, Marine, and Land Applications, 243–254, 2014.

EXPERIMENTAL TESTING AND ANALYSIS OF THE ENERGY ABSORPTION OF AXIAL-LOADED METAL-CFRP-HYBRID COMPONENTS

Corin Reuter^{1*}, Pascal Bartelt², Manel Ellouz², Thomas Kordisch², Thomas Tröster¹

¹ Chair of Automotive Lightweight Design, University of Paderborn, Pohlweg 47-49, 33098 Paderborn, Germany

²University of Applied Sciences Bielefeld, Faculty of Engineering and Mathematics, Interaktion 1, 33619 Bielefeld, Germany

ABSTRACT: An important measure to reduce fuel consumption for passenger cars is to reduce the vehicle weight. Material lightweight design can be realized by the combination of materials with appropriate specific mechanical properties. Hybrid materials of metal and fiber reinforced plastic (FRP) offer a high potential for lightweight construction. They combine the respective positive material properties, such as the relatively ductile failure behavior of metals, with the high specific stiffness and strength of the FRP. Compared to solitary FRP structures lightweight hybrid structures also provide a cost-effective solution by the local use of expensive FRP. In car-crash management axially loaded energy absorption elements are crucial. Their task is the conversion of kinetic energy and the limitation of forces to ensure occupant protection. While any metallic materials absorb energy by plastic deformation (folding), a continuous failure state (crushing) can be adjusted in hybrid structures with FRP. In the present work, the crash behavior of thin-walled hybrid tubes is tested experimentally. The test specimens are made of uni-directional endless carbon fibers wound on an aluminum cylinder. The specific energy absorption of the solitary and hybrid components are determined in drop tower tests. It was found that the hybrid specimens show significantly higher energy absorptions compared to the metallic structures. However, the specific energy absorption of solitary FRP structures could not be reached. Subsequently, a detailed analysis of the failure mechanisms are performed using X-ray computed tomography. Hereby, different interacting mechanisms are identified indicating a significantly changed stress state.

KEYWORDS: hybrid structures, CFRP, crushing, specific energy absorption, X-ray, computed tomography analysis, energy absorption mechanisms

1 INTRODUCTION

In terms of automotive lightweight design fiber-reinforced plastics (FRP) have proved their appropriateness for several structural applications. One important example is the crash absorber element. Especially in the case of moderate crash velocities, the crash absorber is the most important component limiting effectively the resulting accelerations and absorbing a large amount of the kinetic energy of the vehicle. Fiber-reinforced plastics offer the possibility of high energy absorption in addition to low material density. E.g. in [1] potential weight saving by the use of FRP is specified to 50-60% in comparison to traditional steel construction. The high specific energy absorption is mainly based on

the material's characteristic of a progressive crushing failure mode. The crushing itself is dominated by complex interacting effects. Various research works have described the experimentally observed effects in detail, e.g. [2-4]. As a consequence, this material is suitable for creating a component with a very low weight and at the same time displaying a high force level at failure. However, solitary FRP components show several disadvantages, as a catastrophic failure or high production costs [5]. Hybrid metal-FRP components compensate these disadvantages by the combination of the respective positive material properties, such as the relatively ductile failure behavior of metals with high specific stiffness and strength of the FRP. Though material combination leads to complex mutual effects relat-

* Corresponding author: Corin Reuter, Leichtbau im Automobil (LiA), Fakultät für Maschinenbau, Pohlweg 47-49, 33098 Paderborn, phone: +49(0) 5251 60 5944, fax: +49(0) 5251 60 5333, corin.reuter@upb.de

ed to the failure behavior in crash tests. In [6-7], BAMBACH investigated FRP-steel square tubes and observed increased hybrid energy absorption. In his approach still bonded parts were found after impact which implies a changed state of stress. Nevertheless, there is a need for intensive research activities to evaluate the failure behavior and energy absorption capacity of metal-FRP hybrids.

In the present paper, the energy absorption of four different axial-loaded structures is investigated. Thin-walled circular tubes consisting of two different carbon fiber reinforced plastic (CFRP)-lay-ups, solitary aluminum and CFRP-aluminum are considered. First, the specific energy absorption capacity is determined in a drop tower test. Subsequently, a detailed analysis of the failure mechanisms are performed using X-ray computed tomography. Hereby, different interacting mechanisms are identified. In conclusion, the energy absorption of the hybrid structure is evaluated with regard to the identified mechanisms.

2 EXPERIMENTAL TESTING

2.1 SPECIMEN DEFINITION

In an experimental drop tower, circular tubes made of CFRP (a) and (b), aluminum-CFRP (c) and solitary aluminum (d) are tested. The tubes with an inner diameter of 50mm are built-up with individual layers of uni-directional (UD) pre-impregnated wound carbon fibers. All tubes have a length of 150mm and a top-sided 45° chamfers as trigger. The fiber volume fraction is about 52%.

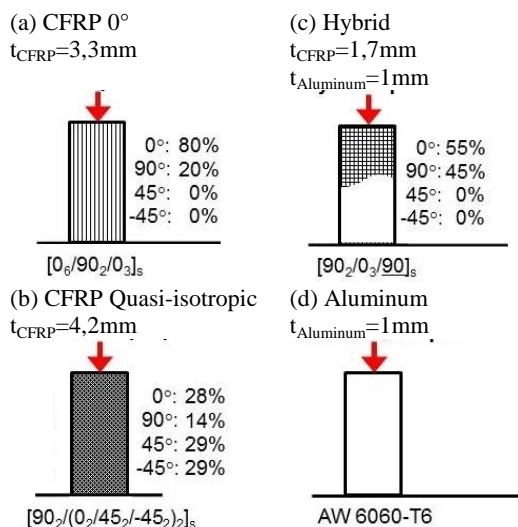


Fig. 1 Specimen definition

Four types of specimens are considered as shown in Fig. 1. In case of the solitary CFRP specimens two different layups are investigated (Fig 1 a-b). Fiber orientation of 0° is parallel to the loading direction and fiber orientation of 90° is tangential to the circular ring cross section of the crash tube.

The hybrid-test specimen is made of a stack of uni-directional endless carbon fibers wound in 0° and 90°-orientation on an aluminum cylinder with a wall thickness (t) of 1mm (Fig. 1 c). The solitary aluminum specimen is AW 6060 T6 with a wall-thickness of 1mm (Fig. 1 d).

2.2 DROP TOWER TESTING

In order to fix (position) the specimens in the drop tower, the tubes described above are centrally glued onto steel plates. The impactor is a massive steel plate which is screwed to the falling drop tower head. The total falling mass amounts to 380kg and the striking velocity is 3.94m/s, thus leading to an introduced energy of 2,950J. For the solitary aluminum specimen the introduced energy is reduced to 1,000J.



Fig. 2 Drop tower set-up

3 EXPERIMENTAL RESULTS

3.1 DROP TOWER RESULTS

Fig. 3 illustrates the deformation and damage behavior of the four different crash tubes after drop tower testing. The 0°-specimen shows cracks in axial direction, while the centre of the specimen is filled with crushed material (Fig 2 a). The cracked outer layers still retain some stiffness, which is confirmed by the re-orientation of the fibers compared to their initial direction. The failure of the quasi-isotropic specimen is more brittle and continuously progressive (Fig. 3 b). The solitary aluminum shows periodical and symmetric folding (Fig 3 d).

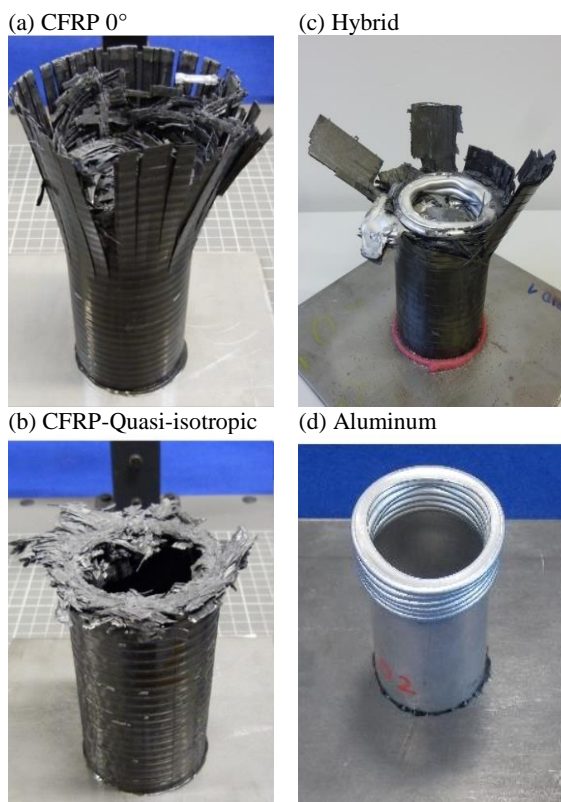


Fig. 3 Specimens after impact

The failure of the hybrid variant can be classified as a combination of the 0° and aluminum variant. The 0°-orientated CFRP-layers are cracked in axial direction. The folding of the metal component is shown to be more irregular due to the CFRP influence. For a detailed analysis of the acting energy absorption mechanisms in the hybrid component, a computed tomography analysis is carried out and described in Chapter 4.

3.2 SPECIFIC ENERGY ABSORPTION (SEA)

For all four crash tubes SEA is calculated by

$$SEA = \frac{1}{m_c} \int F(x) dx \quad (1)$$

where m_c is the mass of the crushed part of the tube, F is the resulting force, and x is the intrusion of the impactor. The resulting specific energy absorption is presented in Fig. 4.

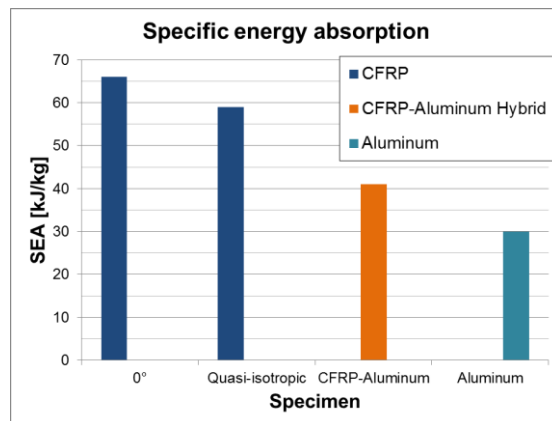


Fig. 4 Specific energy absorption

With an SEA of 66kJ/kg the CFRP-specimen with 0°-orientation indicates the highest specific value. The quasi-isotropic layup shows a SEA of 59kJ/kg and the solitary aluminum a SEA of 30kJ/kg. For the hybrid specimen, a SEA value of 41kJ/kg was measured, which presents an increase an increase by 37% compared to the aluminum specimen, reaching 62% of the maximum SEA measured for the solitary CFRP.

4 DAMAGE ANALYSIS

4.1 ENERGY ABSORPTION MECHANISMS

Different mechanisms resulting in the absorption of the kinetic energy can occur during crash tests of CFRP parts. Fig. 5 outlines characteristic failure mechanisms [8].

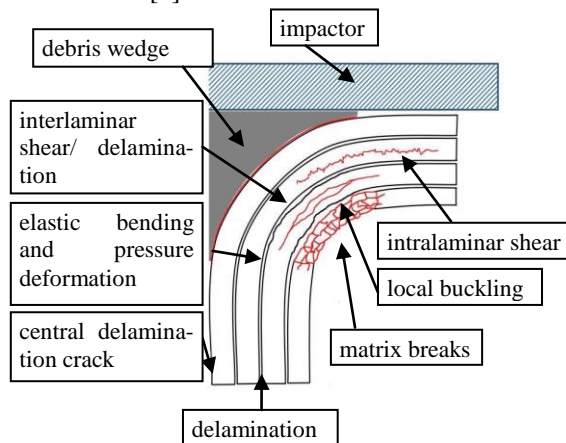


Fig. 5 Energy absorption mechanisms of CFRP

In addition to the depicted mechanisms different types of friction contribute to the totally absorbed energy [3]:

- Friction between CFRP and impactor
- Friction between fragment wedge and CFRP
- Friction between delaminated layers

As described in Chapter 3, in opposite to solitary CFRP structures, the energy absorption in metallic

elements is dominated by plastic deformation. Besides, there are friction effects between impactor and metal and the folds. Axisymmetric and non-axisymmetric progressive failure is also observed [9]. In the current work, a computed tomography analysis is carried out to investigate the energy absorption mechanisms of a hybrid metal-CFRP material combination. The analysis investigates in how far the energy absorption of hybrid material corresponds to the mechanisms of solitary specimens or if specific effects can be identified.

4.2 ANALYSIS AND DISCUSSION OF X-RAY COMPUTED TOMOGRAPHY RESULTS

In order to derive the damage mechanisms of the crashed test parts a X-ray computed tomography (CT) analysis was carried out by a Seifert x|cube 225 facility of GE Measurement & Control Solutions. The following test samples were investigated using the parameters given in Tab. 1. The software for the 3D-tomography analysis was VGStudio Max 2.2 by Volume Graphics.

Table 1: 3D-CT and 2D-X-ray parameters

Specimen	Quasi-isotropic (Fig. 3b)	Hybrid (Fig. 3c)	Aluminum (Fig. 3d)
Investigation type	CT (3D)	CT (3D)	2D-X-ray
Parameters			
Voltage	93 kV	192 kV	135kV
Current	0.7 mA	1.7mA	2.1mA
Focus diameter	0.4 mm	0.4mm	0.4mm
Filter	2mm Cu	2mm Cu	1mm Cu
Exposure time	100ms	100ms	100ms
Gain	1100	1100	1100
Integrated images	16	16	16
CT-rotation steps	1440	1440	-
Flash filter	-	-	+

In Fig. 6 the cross-section of the solitary Aluminum and quasi-isotropic CFRP are compared. The sectional views confirm the description of a continuous progressive failure behavior, which is largely axisymmetric for both materials. The width of the aluminum folds is about 6mm. This leads to a circumferential strain of the crown of the extrados of more than 15%. The cross section of the CFRP variant is analyzed in detail in Fig.7.

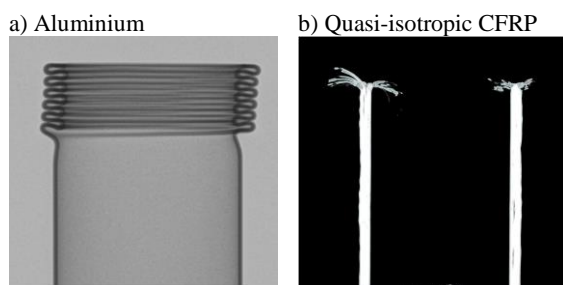


Fig. 6 Cross-sections of the crashed aluminum and quasi-isotropic CFRP specimens

Fig. 7 shows a detailed sectional view of the quasi-isotropic CFRP specimen parallel to the vertical axis of the tube. In this figure exemplarily identified damage mechanisms responsible for the energy absorption of the quasi-isotropic CFRP specimen are highlighted by coloured boxes and indicated by numbers.

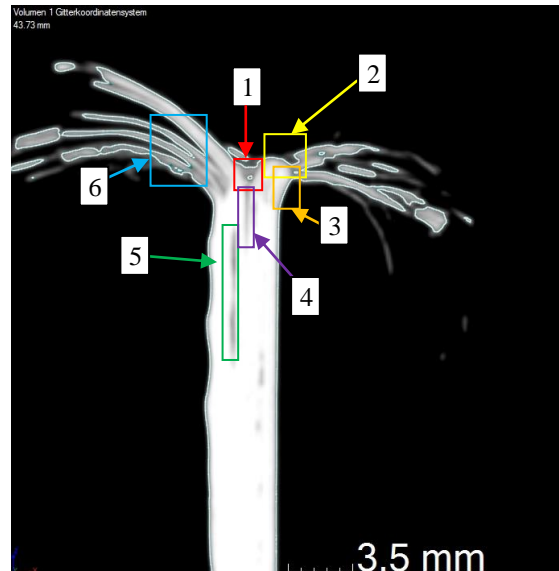


Fig. 7 Cross section of the quasi-isotropic CFRP test specimen after the drop test

The following damage mechanisms were determined:

- 1: debris wedge
- 2: matrix breaks
- 3: elastic bend- and pressure deformation
- 4: central delamination crack
- 5: delamination
- 6: local buckling, interlaminar shear/ delamination and intralaminar shear

The CT-analysis of the hybrid specimen shows numerous specific modifications concerning the energy absorption and failure behaviour. Fig. 8 shows a cross section of the crashed hybrid specimen parallel to the vertical axis of the tube. It can be seen, that neither the aluminum nor the CFRP component acts as it has been found in the solitary structures. However, some basic accordance to the solitary structures can be found. The folding of the aluminum structure appears to be an upending towards the inner part of the tube. Failed aluminum parts that are already deformed are fixed by the surrounding deformed CFRP, resulting in folding. The CFRP structure does not fragment as before and a debris wedge is not formed. The main energy absorption mechanisms of the CFRP-part are identified as local buckling and delamination.

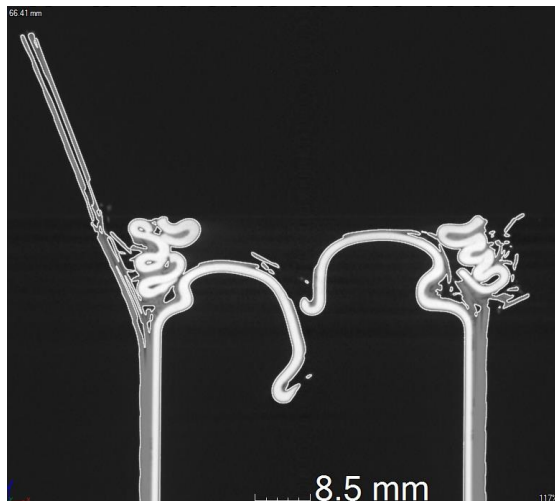


Fig. 8 Cross section of the hybrid test specimen after the drop test (aluminium is white coloured)

However, the analysis of the hybrid specimen shows hybrid specific energy absorption mechanisms. Fig. 9a indicates a CT X-ray view of the hybrid specimen parallel and Fig. 9b perpendicular to vertical axis of the tube. The boxes in Fig. 9a and b present details that are scaled up in the Fig. 9c and d.

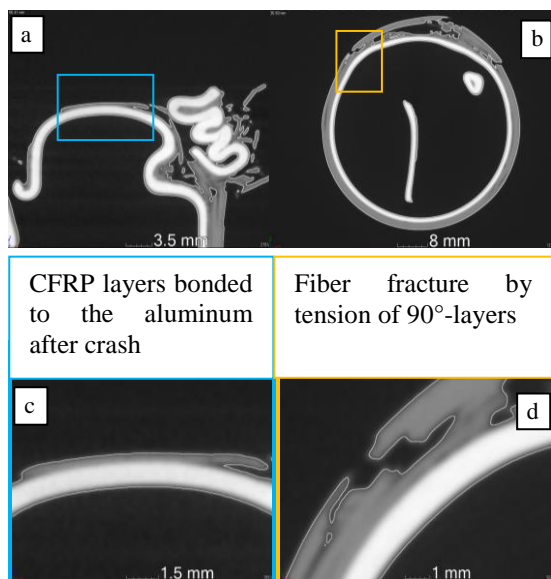


Fig. 9 Detailed X-ray cross section of the hybrid test specimen after the drop test (aluminium is white coloured)

As can be concluded from Fig 9c, the CFRP structure is still bonded to the aluminum structure to a great extent. This bonding in combination with the high plastic strain in the aluminum component and the tension stress applied to the CFRP-layers results in a higher energy absorption compared to a compression stress state because of the higher fracture strength in tension direction.

Fig. 9b and d indicate fiber fracture at the 90° layers. While the circumferential 90°-layers in the solitary CFRP structure mainly function as stabilization elements and crack-stopper, the inner aluminum structure in the hybrid specimen deforms in such a way, that circumferential stress acts on the fibers. Consequently, a more efficient material utilization is shown to be viable.

5 CONCLUSIONS

In conclusion, the presented hybrid structure shows significantly increased specific energy absorption compared to a solitary metal component. However, the SEA does not reach the level of the solitary CFRP specimen. This can be led back to a changed failure behavior. Failure is less periodically and the original beneficial energy absorption mechanisms, as the close folding of the aluminum and the fragmentation of the CFRP, do not come into effect completely. Nevertheless, the presented work could identify additional hybrid specific energy absorption mechanisms, which explains the still high SEA. The analysis results can be considered as a basis for future structural design of hybrid components made of metal-CFRP.

REFERENCES

- [1] Jambor A., Beyer M.: *New cars – new materials*. Materials and Design. Volume 18, Nos. 4, 1997: pp 203-209.
- [2] Hull, D.: *A Unified Approach to Progressive Crushing of Fibre-Reinforced Composite Tubes*, Cambridge, 1990.
- [3] Feindler N.: *Charakterisierungs- und Simulationmethodik zum Versagensverhalten energieabsorbierender Faserverbundstrukturen*. Technische Universität München, München, 2012.
- [4] Feraboli P.: *Development of a Corrugated Test Specimen for Composite Materials Energy Absorption*. Journal of Composite Materials, Vol. 42, No. 3, 2008: pp 229-256.
- [5] Mildner C.: *Numerische und experimentelle Untersuchungen des Crashverhaltens von FVK-verstärkten Metallstrukturbauteilen*. Technische Universität München, München, 2012.
- [6] Bambach M.R.: *Axial capacity and crushing of thin-walled metal, fibre-epoxy and composite metal-fibre tubes*. Thin-Walled Structures, Vol. 48, 2010: pp 440-452.
- [7] Bambach M.R., Jama H.H., Elchalakani M.: *Axial capacity and design of thin-walled steel SHS strengthened with CFRP*. Thin-Walled Structures, Vol. 47, 2009: pp 1112-1121.
- [8] Reich S., *Einfluss der Faserverbund-Sandwichbauweise auf die kollisions sichere Gestaltung von Schienenfahrzeugen*, Technische Universität Berlin, Berlin, 2008.

- [9] Bardi F.C, Yun S., Kyriakides S., *On the axisymmetric progressive crushing of circular tubes under axial compression*, Intern. Journal of Solids and Structures, Vol. 40, 2003: pp 3137-3155.

TECHNOLOGICAL AND ECONOMICAL ASPECTS OF NOVEL HYBRID JOINING STRATEGIES BASED ON INTEGRATED FIBRE PENETRATING REINFORCING ELEMENTS

Thomas Caspari¹, Daniel Huelsbusch¹, Matthias Haack^{1*}, Andreas Solbach²,
Claus Emmelmann^{2,3} and Frank Walther¹

¹Department of Materials Test Engineering, TU Dortmund University
Baroper Straße 303, D-44227 Dortmund, Germany
web page: <http://www.wpt-info.de>
(T. Caspari: email: thomas.caspari@tu-dortmund.de
D. Hülsbusch: email: daniel.huelsbusch@tu-dortmund.de
M. Haack: email: matthias.haack@tu-dortmund.de
F. Walther: email: frank.walther@tu-dortmund.de)

²Institute of Laser and System Technologies, Hamburg University of Technology
Denickestraße 17, D-21073 Hamburg, Germany
web page: <http://www.tuhh.de/ilas>
(A. Solbach: email: andreas.solbach@tuhh.de)

³LZN Laser Zentrum Nord GmbH
Am Schleusengraben 14, D-21029 Hamburg, Germany
web page: <http://www.lzn-hamburg.de>
(C. Emmelmann: email: c.emmelmann@lzn-hamburg.de)

ABSTRACT: The intended substitution of conventional materials by fibre-reinforced polymers (FRP) in manufacturing of hybrid lightweight structures requires innovative joining strategies to combine materials with different physical and chemical properties. In this context, challenges remain with regard to a material-specific application of force to the load-bearing fibre structure of polymer composite parts. To address this matter, a hybrid interface for connecting metallic substrates to a fibre-reinforced polymer by application of integrated form-closure elements (pins) has been proposed and investigated by various groups of researchers. In recent years different manufacturing technologies were employed for adding the fabric-penetrating pin-elements to the subsequent joining surfaces, for example arc welding (CMT) and recently laser additive manufacturing. The latter technology is capable of manufacturing complex shaped parts with equally complex arrangement of pin-structures attached to the surface, but leads to a higher expense. Therefore it is most suitable for high-tech / high-priced applications and materials. In the present study, a laser additively manufactured TiAl6V4-substrate is combined with an in-situ cured carbon-fibre-reinforced polymer (CFRP). Quasi-static tensile (shear) tests and multiple step tests were carried out to assess the mechanical properties of specimens with two differently sized pin-structures as well as a solely adhesively joined reference configuration. By the combined use of 3D deformation measurement and structure-borne noise emission analysis, different structure-related failure mechanisms were detected. Additionally, strategies to transfer this joining technology to more conventional applications are discussed to reduce the material and processing costs.

KEYWORDS: Additive manufacturing, Hybrid structure, CFRP, Damage mechanisms, Fatigue, 3D-Digital Image Correlation

* Corresponding author: Baroper Str. 303| D-44227 Dortmund, phone: +49 231/755-8040, fax: +49 231/755-8029,
matthias.haack@tu-dortmund.de

1 INTRODUCTION

The demand for energy-efficient products constitutes a big challenge for many industries. As a result, great efforts are made to reduce weight or to reduce energy consumption. Therefore, lightweight materials with high specific strength such as fibre-reinforced polymers (FRP) have been an essential point of research over the last decades. Although FRP is becoming increasingly popular, nevertheless metallic components are still needed in many fields of application. Their mechanical properties, especially their isotropic behaviour, are indispensable in many areas. To use the advantages of both materials, it requires hybrid structures.

To join the dissimilar materials, two methods have been established: adhesive bonding and mechanical fastening. The adhesive bonding is used because it enables an easy joining procedure. Unfortunately, it is only connecting the metallic part and the matrix of the FRP. So there is no connection between metal and the actual load-carrying fibres. The strength of the connection exclusively depends on the strength of the adhesive bond. As an alternative joining technique, form closure elements can be utilized. This increases on the one hand the strength of the joint, on the other hand it destroys the fibre structure of FRP partially. One approach is the force fit by fabric-penetrating reinforcing elements (pins). Ucsnik et al. [1] used an arc welding process to create pin structures on a metallic joining partner. Compared to pure adhesively joined specimens the tensile strength could be increased by 11-52%. Unfortunately it is not possible to create a complex pin structure with the arc welding process. To overcome this, Solbach et al. [2] used the laser additive manufacturing (LAM) for preparing the specimens. As an extension of previous research, this paper will evaluate the influence of the pin length on shear strength as well as the accompanying failure-initiating mechanisms.

2 EXPERIMENTAL PROCEDURE

2.1 SPECIMEN PRODUCTION BY ADDITIVE MANUFACTURING PROCESSES

For the characterization of the interface, single shear lap specimens were designed in accordance to DIN EN 1465: 2009-07 (Figure 1). To produce the metallic component, which is made of TiAl6V4, the selective laser melting (SLM) was employed. In order to investigate the influences of penetrative structure, the specimens were manufactured with two different pin

lengths of 0.5 mm and 2.0 mm. Additionally, a specimen without pins was prepared as a reference. The polymer component was manufactured with seven layers of dry twill weave carbon-fibre.

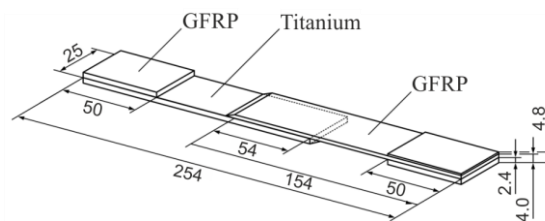


Fig. 1 Structure of Ti-CFRP hybrid specimens

Subsequently, vacuum-assisted resin transfer moulding (VARTM) was used to connect the carbon-fibres with the epoxy resin. Curing took place at room temperature without post-heating.

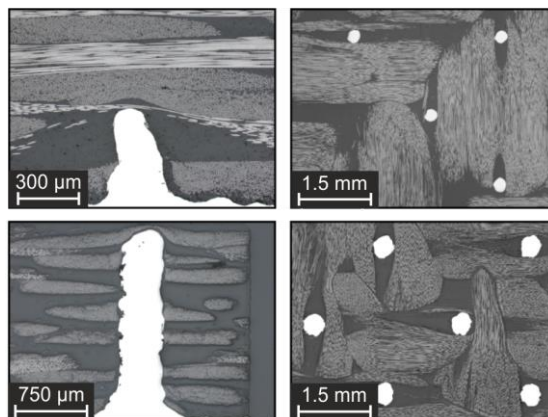


Fig. 2 Compound with 0.5 mm pins (top) and 2.0 mm pins (bottom), cut in axial and orthogonal direction

As shown in the micrographs (Figure 2), the 0.5 mm long pins (top images) only penetrate the first layer of the carbon-fibre-reinforced polymer (CFRP). In comparison the 2.0 mm long pins (bottom images) are connected to nearly every layer. As shown in the right images, both pin lengths pierce the fibre bundles of the twill fabric almost without damage. The fibre bundles widen by piercing the pins and form cavities in which resin can accumulate.

2.2 FATIGUE INVESTIGATIONS

For the comparative assessment of the fatigue behaviour, multiple step tests (MST) [3] were performed on a servo-hydraulic testing system (Schenck/Instron, Type PC63M, $F_{\max} = \pm 50$ kN) with a stress ratio of $R = 0.1$. The excitation

ensued with a sinusoidal load-time function of 5 Hz.

The MST has proven in previous trials as time- and cost-efficient method for material characterization [3]. Figure 3 shows schematically a procedure of MST.

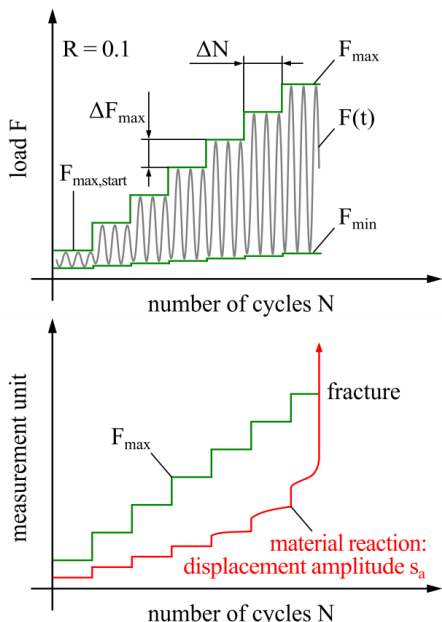


Fig. 3 Experimental procedure of multiple step test (above), typical result of material response in multiple step test (below).

In the conducted trials the starting force was set at $F_{max,start} = 500$ N. Based on this, the maximum force was increased stepwisely by $\Delta F_{max} = 500$ N after a step length (ΔN) of 10^4 cycles until failure. As an index for evaluating the fatigue performance the displacement amplitude s_a was recorded as a material reaction.

2.3 MICROSTRUCTURAL INVESTIGATIONS

Microstructural investigations were carried out to analyse the initial state of the hybrid structures and the fracture surface for determination of damage mechanisms. For the investigations, light microscopy (LM) (Zeiss, Type Axio Imager M1m) and scanning electron microscopy (SEM) (Tescan, Type Mira3 XMU) were utilised.

3 RESULTS

3.1 MULTIPLE STEP TESTS

For evaluating the damage evolution, the displacement amplitude s_a is used. Provided that there are no pre-damages existing, a linear rela-

tionship between displacement amplitude s_a and maximum load F can be assumed. It must also be assumed that s_a is constant in every step. A change in displacement amplitude corresponds to a softening process due to early material fatigue. Based on this hypothesis, for each step a relative change in displacement amplitude $\Delta s_{a,rel}$ was calculated.

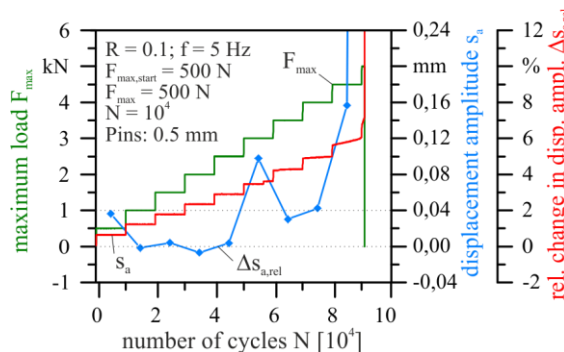


Fig. 4 Multiple step test for a specimen with 0.5 mm pins

In Figure 4, the force-displacement relationship for a specimen with 0.5 mm pins is shown. In this case, an initial material reaction is detected at a maximum load $F_{max} = 3.0$ kN as a sharp increase of displacement amplitude s_a and the dependent variable $\Delta s_{a,rel}$. It is assumed that this is an incipient detachment of the adhesive layer. This effect was observed for all specimens, depending on the dimensioning of the reinforcing elements different damage patterns were occurred.

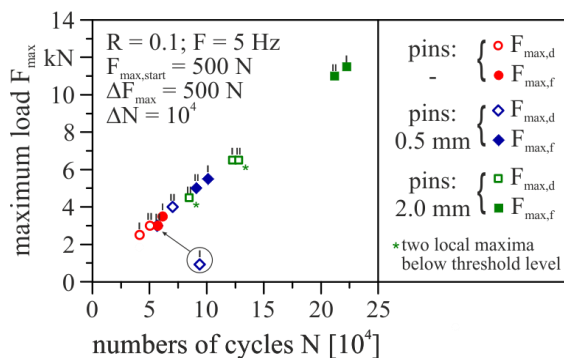


Fig. 5 Evaluation of fatigue tests

The results for the MSTs are displayed in Figure 5. The maximum load at failure (strength $F_{max,f}$) and the maximum load at first damage occurrence (threshold $F_{max,d}$) are visualized for each test.

It is apparent that the 2 mm long pins contribute to a significant enhancement of shear

strength. Compared to the reference sample, the number of cycles to failure increases by 267 % to $N_f = 21.7 \cdot 10^4$ and the maximum strength by 246 % to $F_{max,f} = 11.25$ kN. Furthermore, the point of first damage detection shifts to higher numbers of cycles.

3.2 LOCAL STRAIN ANALYSIS

Due to the flat specimen geometry, it is possible to pursue the inhomogeneous deformation on the surface. For this purpose, digital image correlation (DIC) was used. The DIC system allows visualizing the deformation state with spatial and temporal resolution. In addition to the DIC system, video recordings were taken from the narrow edge of the samples.

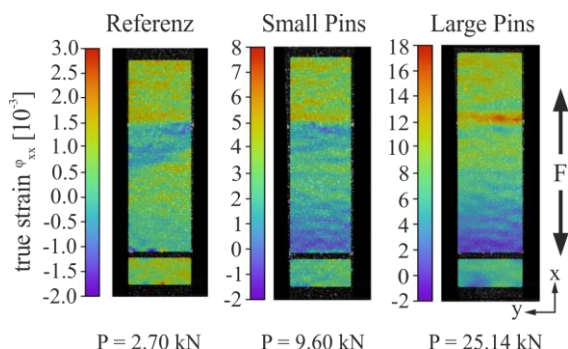


Fig. 6 Strain distribution when reaching the fracture load for each pin length

In Figure 6 the deformation state of the various samples is compared by their local true strain φ_{xx} at their specific fracture load P . It is observed that the length of the pins has a strong influence on the maximum true strain φ_{xx} . Comparing the reference sample with the specimens with 0.5 mm pins, a similar distribution of local strain can be seen on the surface. Only the sample with 2.0 mm pins has local concentrations of φ_{xx} at the joining edge. For all specimens it is necessary to observe the different scales.

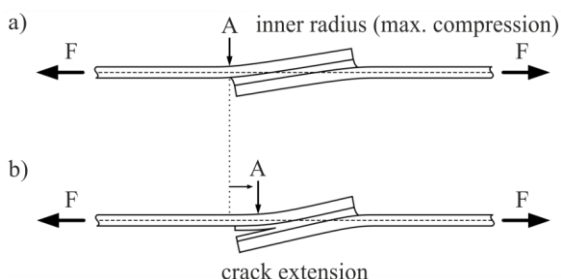


Fig. 7 Deformation behaviour of adhesively bonded single lap joints. Based on [4,5]

Considering the asymmetrical structure of the samples (Figure 7), the local strain distribution on the surface can be explained. Due to the geometry, a bending moment is formed at the joining area of the specimens. By the bending moment, a peel stress is generated at the joining edge, which leads to debonding of the hybrid structure beginning at the joining edge [6].

With this background, the negative local strain (Figure 6) can be explained by a compression of the surface, due to the bending stress.

3.3 MATERIAL DAMAGE

Depending on the pin length different damage behaviours were detected. For the reference samples the fracture developed only in the adhesive area. The same result is also evident in the specimen with the small pin length. SEM-analysis confirmed a combination of adhesive and cohesive failure.

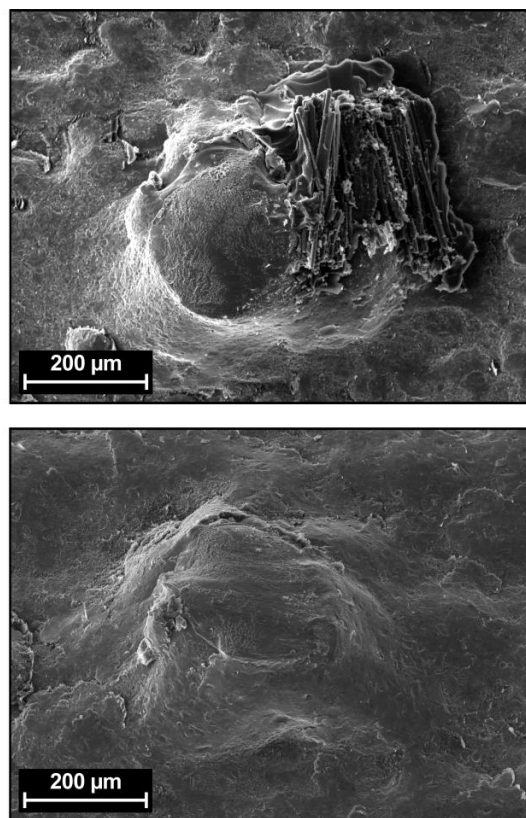


Fig. 8 Analysis the fracture surface of specimens with pin length 0.5 mm

Top image figure 8 shows an intact pin with the length 0.5 mm from the area of the joint edge. In this area, the adhesive dissolves and the pins are pulled out of the CFRP. After the crack induction the pins at the other end of the joining zone are sheared closely above the surface (bottom image Figure 8).

For the longer pins with a length of 2.0 mm there is a completely different fracture classification.

The fracture occurs in the first row of pins, inside the CFRP structure (Figure 9). The detected fracture complies with translamellar crack propagation in plane of axial normal stress σ_{xx} . The pins in the joining area do not show any permanent deformation, while the CFRP fibres are ripped out of the composite. For this reason, the failure can be traced back to a solely cohesive fracture of the CFRP.

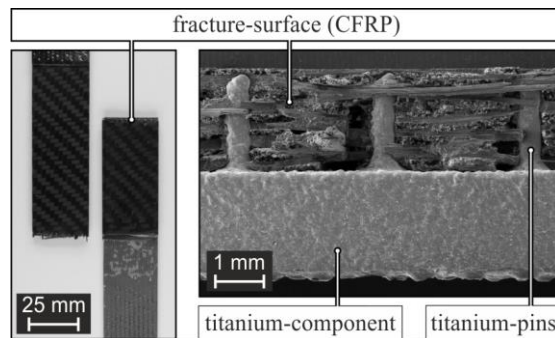


Fig. 9 Analysis the fracture surface of specimens with pin length 2.0 mm.

4 CONCLUSIONS AND OUTLOOK

As part of the test series, a novel interface between CFRP and metals is characterized. The material pairing CFRP and TiAl6V4 demonstrated that the integration of reinforcing elements leads to a significant increase of strength. By the reinforcing elements, the reproducibility of the mechanical properties of the interface is significantly improved. Depending on the type of stress and dimensioning of the reinforcing elements different damage mechanisms increase. The experimental results lead to the conclusion that modified pin arrangement in the joint edge and customized pin geometry will further increase the strength of the interface.

In terms of economic efficiency, alternative ways to manufacture the pins must be pursued. Alternative processes for preparing the pins would be soldering. Also it seems conceivable to penetrate the metal plate with nails. A further point in relation to the economic efficiency is the material that is used for the compound. In this case glass-fibre-reinforced polyamides are a highly promising alternative. The major advantage of glass-fibre-reinforced polymers is that contact corrosion with conventional steel does not exist.

REFERENCES

- [1] S. Ucsnik, M. Scheerer, S. Zarenba and D.H. Pahr, Experimental investigation of a novel hybrid metal-composite joining technology, *Composites: Part A*, 41, 2010, pp. 369-374 (doi: 10.1016/j.compositesa.2009.11.003).
- [2] A. Solbach, D. Huelsbusch, M. Haack, C. Emmelmann and F. Walther, Investigation of fiber reinforced plastic penetration produced by laser additive manufacturing with pin size variation, *Proceedings of the 5th International Workshop on Aircraft System Technologies*, Hamburg, Germany, February 25-25, 2015, pp. 315-323 (ISBN 978-3-84403319-9).
- [3] F. Walther, Microstructure-oriented fatigue assessment of construction materials and joints using short-time load increase procedure, *MP Materials Testing*, 56, 7-8, 2014, pp. 519-527 (doi: 10.3139/120.110592).
- [4] M. Imanaka, K. Haraga and T. Nishikawa, Fatigue Strength of Adhesive/Rivet Combined Lap Joints, *The Journal of Adhesion*, 49, 3-4, 1995, pp. 197-209 (doi: 10.1080/00218469508014356).
- [5] P.N. Parkes, R. Butler and D.P. Almond, Fatigue of metal-composite joints with penetrative reinforcement, *Proceedings of the 54th AIAA/ASME/ASCE/ASC structures, structural dynamics and materials conference*, Boston, USA, April 8-11, 2013, pp. 6400-6409 (doi: 10.2514/6.2013-1879).
- [6] M. Imanaka, K. Haraga and T. Nishikawa, Fatigue Strength of Adhesive/Rivet Combined Lap Joints, *The Journal of Adhesion*, 49, 3-4, 1995, pp. 197-209 (doi: 10.1080/00218469508014356).

RELIABILITY STUDIES ON MOLYBDENUM-COPPER-MULTILAYER COMPOSITES

Martin Seiss^{1*}, Tobias Mrotzek¹, Wolfram Knabl¹

¹Plansee SE, 6600 Reutte, Austria

ABSTRACT: Gallium Nitride chips are getting more and more widespread in radio frequency applications. One reason is the higher power density compared to Gallium Arsenide but there are many other advantages of GaN. However, new thermal management solutions are needed for GaN to match the requirements in thermal expansion and thermal conductivity. A promising solution might be multilayered composites made of alternating layers of molybdenum and copper. The layered structure allows tailored thermo physical properties, such as thermal conductivity and coefficient of thermal expansion, according to the requirements of the application. While these properties are well known for this kind of composite, the reliability is still an open question. For this reason temperature tests according to EN 60068-2-14 were performed. A three layered structure, copper-molybdenum-copper, with 63wt% copper was tested between -40°C and +125°C for 2000 cycles. The copper-molybdenum-interfaces were studied by scanning electron and acoustic microscopy. A degradation of the interface was not observed. Moreover, the thermal conductivity of the samples was not reduced by the thermal cycling.

KEYWORDS: CMC, SCMC, S-CMC, multilayer, thermal conductivity, CTE, coefficient of thermal expansion, delamination, gallium nitride, GaN, thermal management

1 INTRODUCTION

With the increasing success of Gallium Nitride (GaN) based radio-frequency devices, the thermal management of these devices is gaining more and more attention. Thermal management solutions for silicon or Gallium Arsenide (GaAs) are no longer applicable due to the different coefficient of thermal expansion (CTE) and higher thermal conductivity of GaN. Moreover, the smaller footprint and higher operating temperature of GaN devices is resulting in higher heat flux densities compared to silicon and GaAs. Thermal management materials not adapted to the GaN requirements may cause heat damage to chip or induce thermo-mechanical stresses which both lead to failure of the device (Fig. 1).

The CTE of heat spreaders for GaN chips should be slightly higher than the CTE of GaN or other materials used for packaging like Kovar or ceramics so that these materials are under compression. This restricts the possible acceptable CTE of the heat spreader to 6-12 ppm/K. For the reliable dissipation of the generated heat a thermal conductivity of around 300W/m/K is targeted for the heat spreader but also lower thermal conductivities might be acceptable for certain applications.

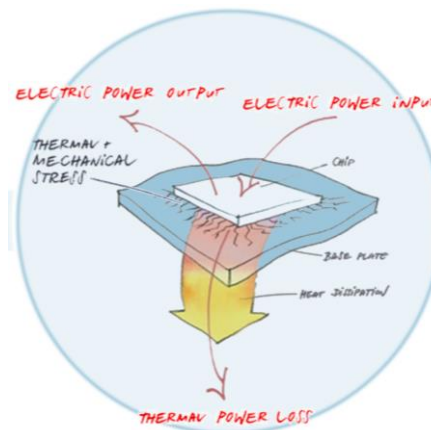


Fig. 1 Heat spreaders with inappropriate thermophysical properties may induce thermal and mechanical stresses into the chip.

As summarized in Tab. 1, pure copper shows a high thermal conductivity but its CTE prohibits the use as heat spreader for GaN chips. Contrary to copper, the CTE of molybdenum is significantly lower but its thermal conductivity is also lower.

* Corresponding author: Plansee SE, 6600 Reutte, Austria, martin.seiss@plansee.com

Both metals can be combined to a composite in order to achieve a low CTE and a high thermal conductivity.

Table 1: Thermal properties of oxygen free copper, molybdenum and the desired properties for GaN heat spreaders [1, 2].

Material	Thermal conductivity at 20°C [W/m/K]	Coefficient of thermal expansion 20°C [ppm/K]
Oxygen free copper	397	16.5
molybdenum	138	4.8
Ideal GaN heat spreader	>300	6 – 12

Multilayered composites with alternating copper and molybdenum layers allow the adjustment of CTE and thermal conductivity by varying the number of layers and their thickness. Typically, those multilayers consist of three or five layers with a symmetric structure. The outer layers are usually copper in order to achieve an appropriate heat spreading. Examples of common structures are shown in Fig. 2.

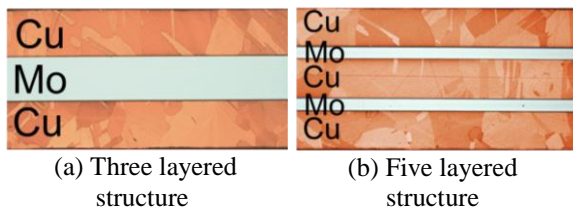


Fig. 2 Example of a three and five layered copper-molybdenum-multilayer composite (polished cross sections).

The thermal conductivity versus the CTE is depicted in Fig. 3. The molybdenum-copper-multilayers cover a wide range of properties allowing tailored solutions for different types of applications [3]. Molybdenum copper 30 (MoCu30) is a composite consisting of molybdenum particles embedded in a copper matrix. The weight fraction of copper is 30%. PMC 141 is a three layered structure with a MoCu30 core cladded with copper. The layer thickness ratio is 1:4:1, i.e. the MoCu30 core is four times thicker than the outer copper layers. Both composites, MoCu30 and PMC 141, are standard materials for the thermal management of silicon based devices.

The molybdenum is lowering the CTE of all these composites. However, the thermal conductivity of the multilayer composites is significantly higher than that of MoCu30 and PMC 141. As a consequence, the layered structure is promising for applications which require high thermal conductivity and low CTE.

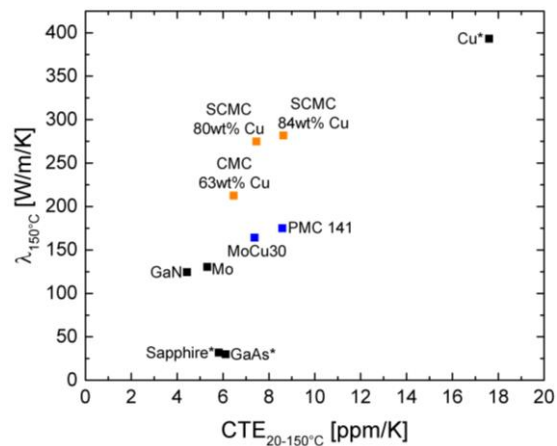


Fig. 3 The thermal conductivity of molybdenum-copper-multilayers (CMC and SCMC) as a function of the CTE. Data points marked with an asterisk are taken from [1, 4].

While the material properties are well understood the reliability of the multilayer composites is still unknown. For this reason, thermal cycling was performed on a three-layered copper-molybdenum-copper structure. These studies were complemented by measurements in a push-rod dilatometer. The main focus of this work was to examine the effect of thermal loading on composite degradation.

2 EXPERIMENTS

In this work samples with a three layered structure of copper-molybdenum-copper were studied. The layer thickness ratio was 1:1:1, i.e. the thickness of all layers was equal to 0.5mm. The sample dimensions were 30mm x 15mm x 1.5mm and the copper fraction was 63wt%.

Thermal cycling was performed according to EN 60068-2-14 in an ESPEC TSD 100 thermal shock tool [5]. The samples were first transferred to a hot chamber at +125°C and kept in this chamber for 30 minutes. Then, the samples were directly moved to a cold chamber at -40°C and also kept at this temperature for 30 minutes. Fig. 4 illustrates the temperature profile of the thermal cycling. Ten samples were taken after 100, 500, 1000 and 2000 cycles.

The samples were analyzed for interface defects by a Winsam Vario III acoustic microscope operating at 150MHz and 50dB. Due to the limited penetration depth both sample surfaces were scanned. Thus the two molybdenum-copper-interfaces could be analyzed for defects.

Polished cross sections were prepared for scanning electron microscopy and studied by a Carl Zeiss Ultra Plus Field Emission SEM. Images were taken in backscattered electron mode.

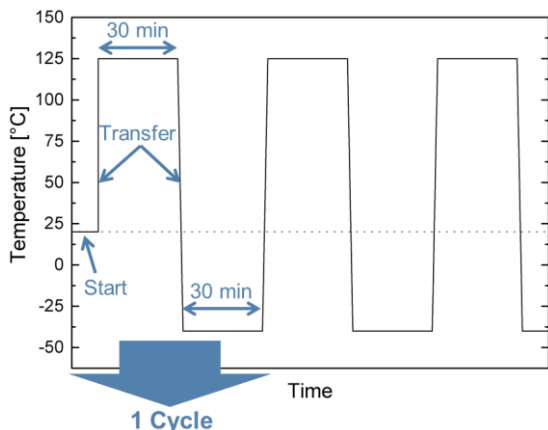


Fig. 4 Test profile of the thermal cycling.

The thermal diffusivity α was measured by a Netzsch LFA 467 HyperFlash. In addition, the specific heat c_p was measured by a Netzsch DSC 204 F1 Phoenix. The density ρ of the samples was determined by hydrostatic weighing. Based on this data, the thermal conductivity of the cycled samples was calculated by the following equation [6]:

$$\lambda = \alpha c_p \rho \quad (1)$$

Moreover, the surface flatness of the cycled samples was measured by a FRT MicroProf 200 (CWL F).

In order to determine the exact length change caused by thermal cycling, another sample with the dimension 15mm x 5mm x 1.5mm was studied using a Bähr DIL 801. This sample was exposed to 5 cycles between -100°C and +200°C. The sample structure and composition was the same as of those used for the thermal shock tests described above.

3 RESULTS

3.1 THERMAL CYCLING ACCORDING TO EN 60068-2-14

The main focus on the cycled samples was to evaluate the effect of thermal load on the molybdenum-copper-interface. It is conceivable that defects, such as pores or delamination, are generated during thermal cycling.

Therefore, acoustic microscopy was performed on all samples and none of them showed any defects at the molybdenum-copper-interfaces (Fig. 5). However, this technique only allows detecting defects larger than approximately 0.3mm. Hence, only the presence of large scale defects can be excluded by acoustic microscopy on the studied samples.

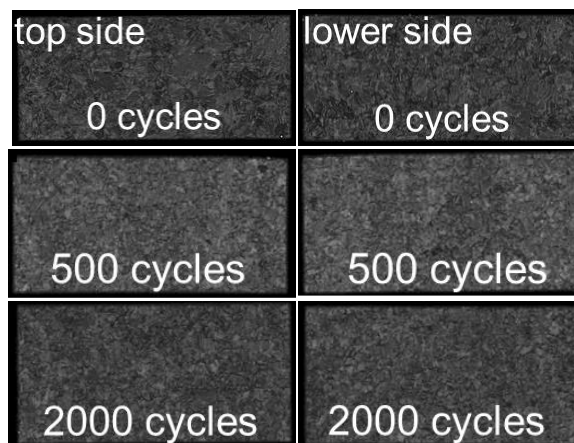


Fig. 5 Top side (left) and lower side (right) images of acoustic microscopy.

SEM imaging was done on the polished cross sections to check for large scale cracks and small pores. The overview images in Fig. 6 do not show any large scale defect at the interfaces. At higher magnifications no degradation of the interfaces was observed.

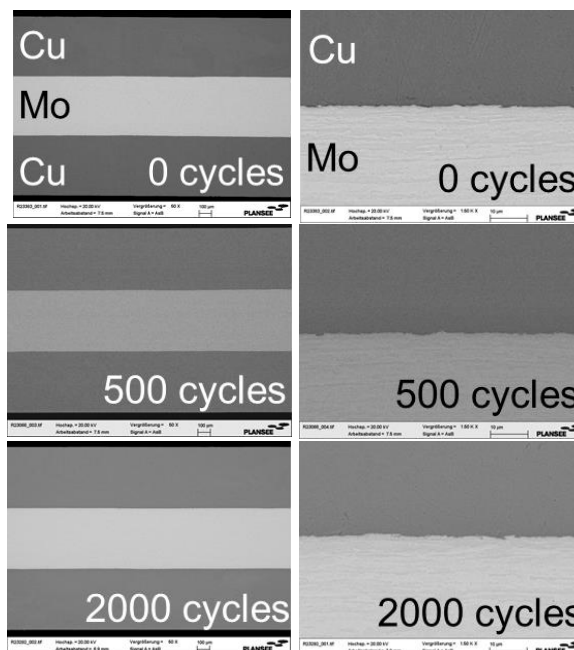


Fig. 6 SEM images at 50x (left) and 1500x (right) magnification.

In addition, the thermal conductivity may indicate if interface defects are present. An increasing number of pores or cracks at the molybdenum-copper-interfaces should result in a lower thermal conductivity. The room temperature thermal conductivity of the cycled samples is plotted in Fig. 7. These results illustrate that the thermal conductivity is not affected by the thermal cycling. Hence, the generation of interface defects can be excluded confirming the previous results.

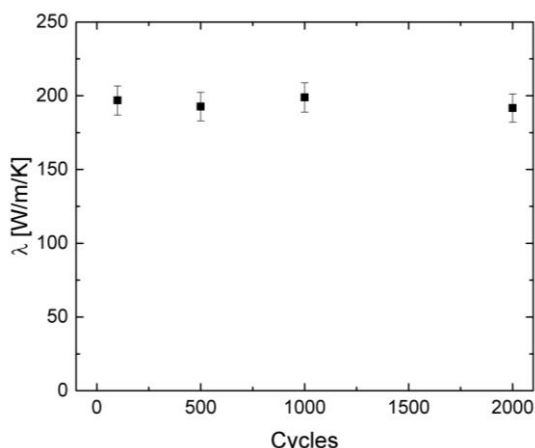


Fig. 7 The thermal conductivity at room temperature of the cycled samples calculated according to Eq. (1).

Besides the generation of defects and delamination at the interfaces, a further concern is regarding the flatness of the multilayer composites. A changing flatness could compress or strain the chip introducing defects into the chip or into the die attach interface which usually causes failure of the device. Our results indicate that the flatness is not affected by thermal cycling, as shown in Fig. 8.

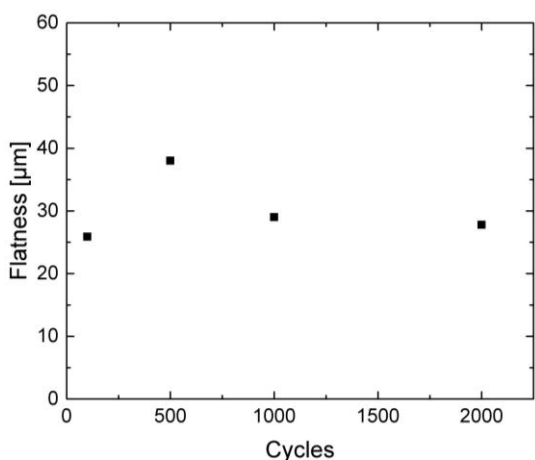


Fig. 8 Flatness of the cycled samples.

3.2 THERMAL CYCLING IN DILATOMETER

A dilatometer allows the exact measurement of the sample length change depending on temperature. The number of temperature cycles is, however, limited by the nitrogen reservoir. Therefore, only five temperature cycles between -100°C and $+200^{\circ}\text{C}$ have been done. Fig. 9 shows the relative length change and temperature profile. After five cycles the length change of the sample was 0.02% which corresponds to absolute length change of 3μm.

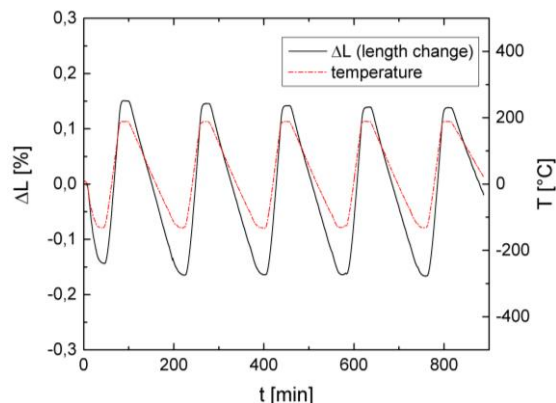


Fig. 9 Measured length change in a dilatometer upon 5 cycles between -100°C and $+200^{\circ}\text{C}$.

4 DISCUSSION

The aim of this work was to test the reliability of the multilayer composites. The main concerns are related to interface stability during operation of the device and degradation of material properties. The thermal cycling according to EN 60068-2-14 did not alter the composite. Large scale defects can be excluded from both acoustic microscopy and the SEM images of the polished sections. However, small scale defects are difficult to observe with these techniques. While the acoustic microscopy resolution is limited to approximately 0.3mm, smaller pores should actually be visible on the SEM images. The combination of the soft copper and hard molybdenum makes a proper cross section preparation difficult. Even if small pores are present, the soft copper is probably smeared over those pores. The etching of the polished samples with a mixture of hydrochloric acid and iron chloride did not shed light on this problem. Due to the higher etching rate of copper a step is generated at the interface which causes a shadowing effect (Fig. 10). This effect makes the observation of small pores difficult.

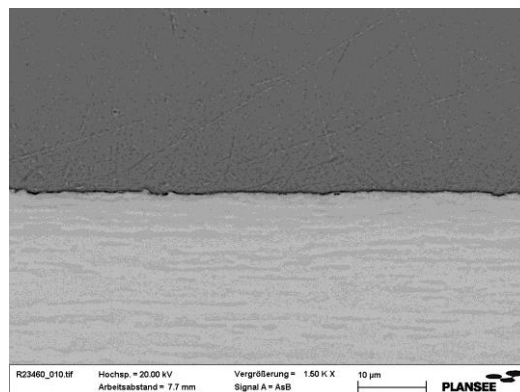


Fig. 10 Etched cross section after 2000 cycles (1500x magnification).

An indirect measure for the defects is the thermal conductivity. The thermal conductivity of molybdenum-copper-multilayer composites can be estimated by the inverse rule of mixture [7]

$$\lambda = 1 / \sum (V_i/\lambda_i + n/h) \quad (2)$$

where n is the number of interfaces, h the interfacial resistance, V_i the volume fraction and λ_i the thermal conductivity of layer i .

If defects were generated by thermal cycling the interfacial resistance should increase and hence the thermal conductivity should decrease. Our results suggest that the thermal conductivity is independent of the number of cycles and hence it can be concluded that the cycling is not introducing defects to the composite.

The push-rod dilatometer measurements indicate a permanent shrinkage of the composite. Although the relative length change is only 0.02% it is worth mentioning. This length change is already noted after the first cycle and it is not significantly increasing after five cycles. Negative effects on the stability of the device are not expected.

5 SUMMARY

Molybdenum-copper-multilayer composites allow a wide variety of structures and hence thermophysical properties which make these composites interesting for the use as heat spreader in GaN based devices. In this work, the reliability of this composite was studied in detail.

It has been demonstrated that after 2000 thermal cycles between -40°C and $+125^\circ\text{C}$ there is no degradation of the composite. Neither pores, cracks nor delamination at the interface were observed. Moreover, the thermal conductivity and flatness of the samples were not altered by thermal cycling. A minor contraction of 0.02% was measured by a dilatometer after five temperature cycles between -100°C and $+200^\circ\text{C}$. This shrinkage is not considered as critical for applications.

Our results provide confidence for the use of molybdenum-copper-multilayer composites as heat spreader.

6 ACKNOWLEDGEMENTS

Part of this work has been conducted within the project AGATE, co-funded by grants from Austria and the ENIAC Joint Undertaking.

REFERENCES

- [1] W. Martienssen, H. Warlimont, *Springer Handbook of Condensed Matter and Materials Data*. Springer, Berlin Heidelberg, 2005.
- [2] A. Lindemann, J. Blumm, *Measurement of Thermophysical Properties of Pure Molybdenum*. 17th Plansee Seminar, vol. 3: AT 14/1 – 14-6, 2009.
- [3] M. Seiss, T. Mrotzek, N. Dreer, W. Knabl, *Thermophysical Properties of Molybdenum Copper Multilayer Composites for Thermal Management Applications*. Material Science Forum, 825-826:297-304, 2015.
- [4] Kyocera, *Single Crystal Sapphire*. Datasheet, Aug. 2015.
- [5] *Environmental Testing – Part 2-14: Tests – Test N: Change of Temperature*. EN 60068-2-14, 1999.
- [6] *Standard Test Method for Thermal Diffusivity by the Flash Method*. ASTM Standard E 1461-07, ASTM International, West Conshohocken, PA, 2008.
- [7] D. P. H. Hasselman, L. F. Johnson, *Effective Thermal Conductivity of Composites with Interfacial Thermal Barrier Resistance*. Journal of Composite Materials 21(6):508-515, 1987.

CHAPTER 4:

DESIGN

METHODICAL APPROACH FOR THE DEVELOPMENT OF HYBRID VEHICLE STRUCTURES MADE OF FIBER REINFORCED PLASTICS AND METAL

X.F. Fang^{1*}, M. Grote¹

¹ Institute of Automotive Lightweight Design, University of Siegen, Siegen, Germany

ABSTRACT: The aim of the presented research project is the development of a front body structure, which consists of glass fiber reinforced plastics (GRP) and metal. The potential of lightweight design should be exploited as high as possible and at the same time in a cost efficient manner. Especially, endless fiber reinforced materials and their mechanical properties are significantly different from classical car body materials like steel. The main aspect is that the final properties are determined during the design process of laminate architecture. Due to the increasing complexity of these materials, new systematic engineering methods are required.

In this paper an approach for a development process is presented. In the first step, the reference structure, a small full electric vehicle, has been analysed to identify the most promising parts, which can be redesigned with FRPs. Then a new hybrid design of the selected parts is developed by the use of commercial optimization software. Finally, these parts are validated in full vehicle crash simulations. This paper ends with a detailed discussion of the project experiences and naming the shortcomings and problems of the presented approach. Based on those, an outlook for the future research regarding the systematic engineering and design of FRPs and hybrid car body are given.

KEYWORDS: Engineering design, Fiber reinforced plastic (FRP), glass fiber, body in white

1 INTRODUCTION

The development of hybrid multi-material car bodies leads to a couple of challenges which cannot be solved completely with the existing engineering methods and development processes. Several requirements, such as aspects of lightweight-design, passive safety, manufacturability and especially cost efficiency are in contradiction. Therefore, the best compromise has to be found. Moreover, these requirements are weighted very differently depending on which kind of vehicle is considered. In this project a full electric vehicle [1] is chosen as reference for the front body structure. Especially for electric vehicles, the demand for lightweight concepts is rather high, because the extra weight for the battery has to be compensated. Moreover, the potential for saving extra weight is higher for full electric vehicles because of secondary weight saving effects in the electric power train [2].

In particular, fiber reinforced plastics and other composite materials increase the quantity of possible design parameters. This is due to their high anisotropy. Therefore, the mechanical properties in

each direction have to be investigated in order to design a load case dependent structural part. Furthermore, the anisotropy gives the possibility to design tailor made parts. For example, if the material preferential direction, i.g. the fiber direction of FRP, which has the best mechanical properties, is in line with the dominating load path of the component, the lightweight potential of composite material can be fully released.

The development process in this project uses the anisotropy as criteria to select highly promising components. These parts are selected for a more detailed investigation and will be redesigned with a hybrid material mix of FRPs and metals.

To fully exploit the lightweight potential, characteristic features of thermoplastics are considered as well, which includes, for example, the possibility of function integration and the feasibility in the injection molding process [3]. Furthermore, a combination of endless fiber reinforced semi-finished products (organic sheets) and injection molding is possible, too [4].

Finally, the digital prototypes of the developed concepts are validated in the crash simulation. The processes are shown in flow-scheme (Fig. 1).

* Corresponding author: Institute of Automotive Lightweight Design, University of Siegen, Germany
Breite Straße 11, 57076 Siegen, phone: +49 271 740-4670, fax: +49 271 740-3786, xiangfan.fang@uni-siegen.de

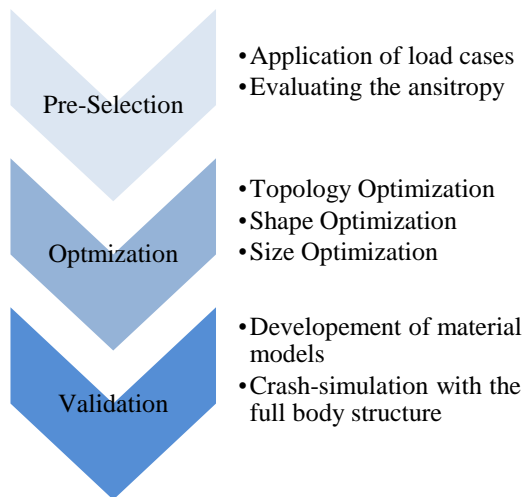


Fig. 1 Flow-Scheme of the development process divided in three sections

The current work is based on earlier publications of the authors [5]. In addition to [5] the process and the development methodology for the systematic engineering and design are described. Basically, [5] describes the redesigned parts and the results of the considered research project. For a better understanding some of these aspects are summarized in this paper as well.

2 PRE-SELECTION OF HYBRID PARTS

In this sub-section, the approach of evaluating and selecting parts and components for FRP will be described. To consider the anisotropy as a selecting criterion, a mathematical approach was defined in [6]. In current investigation additional function was developed and added into a MATLAB tool in order to obtain the output data from a crash simulation. The crash solver which has been used is LS-DYNA. The global quasi static loading conditions, such as torsion and bending, were simulated with ABAQUS and these results can also be processed and analysed by this MATLAB programme.

2.1 THEORY

The mathematical approach, which was developed in [6], uses a dimensionless value that describes the level of anisotropy in every single finite element. The average value of all elements in one part describes the FRP suitability for this part. The closer to 1 this value is, the higher suitability for FRPs and anisotropy this part has. According to that, closing to 0 stands for a very low potential. The element value $K_{element}$, which is called anisotropy value now, consists of three different factors as shown in equation 1. The number of load cases is describes with m .

$$K_{element} = \sum_{i=1}^m (a_i \cdot b_i \cdot g_i) \quad (1)$$

i : element number

These factors are determined for every load case and the element value is corresponding to the summed product of these three values. The first factor a_i is called the anisotropy factor and is described in equation 2.

$$a_i = \left(\frac{\max [|\sigma_{1,i}|, |\sigma_{2,i}|]}{|\sigma_{1,i}| + |\sigma_{2,i}|} - 0,5 \right) \cdot 2 \quad (2)$$

Here the two factors $\sigma_{1,i}$ and $\sigma_{2,i}$ represent the two principle stresses of the element for the load case i . If these stresses differ significantly from each other, a high anisotropy exists in this load case. To reach a correct treatment by overlaying several load cases, the factors b_i and g_i in equation 3 and 4 are also necessary.

$$b_i = \left| \frac{90^\circ - x}{90^\circ} \right| \text{ with } x = |\varphi_{1,i} - \varphi_{ref}| \quad (3)$$

$$g_i = \frac{\sigma_i}{\sum_{i=1}^m \sigma_i} = \frac{|\sigma_{1,i}| + |\sigma_{2,i}|}{\sum_{i=1}^m (|\sigma_{1,i}| + |\sigma_{2,i}|)} \quad (4)$$

The first factor b_i is the so called orientation factor. By the use of this factor, the deviation of mean stress orientation in each load case is considered. Therefore, a reference angle φ_{ref} , which in this case is the arithmetic mean value of all angles $\varphi_{1,i}$, is determined.

Furthermore, it is important to consider the contribution of the first principle stress in each load case for each element. This is done by the weighting factor g_i . Both factors b_i and g_i lead to a high influence of load cases which have a high stress value and are aligned according the reference angle at the same time.

2.2 LOAD CASES

To ensure the part selection is based on realistic data, two static load cases and four crash load cases were examined. The static load cases are the global torsion and bending. The crash loads are: the front impact by Euro NCAP with 40% off set, the front impact according to FMVSS with full coverage, the AZT test for insurance ratings and the frontal pole impact. To consider possible nonlinearities while performing the crash loads, it is necessary to evaluate each load case at different times. To be specific, these moments are at 5 ms (immediately

after the first impact), 10 ms, 20 ms and 30 ms (moment of extremely high deformation).

2.3 RESULTS

The results of the analysis are visualized in Fig. 2. For a better traceability, the figures have been separated between the quasi static loads and the crash loads. The data of the anisotropy values for the crash load cases are in a small range (ca. 0.35-0.55). For the static load cases, the range is larger (ca. 0.20-0.70). This could be caused by the fact that the total of 16 data sets were analysed in the crash analysis. While for the quasi static load case, only two data sets were used. This leads to a balancing effect of rather high and low values.

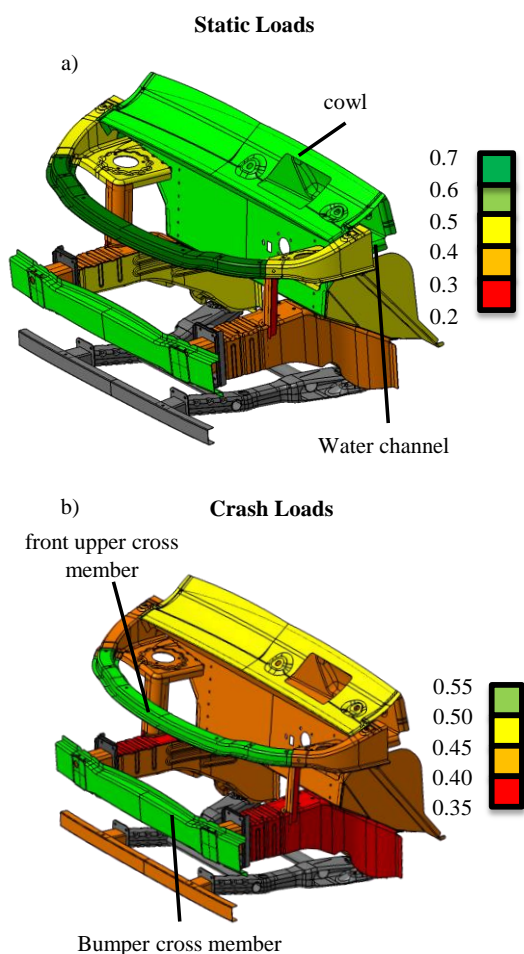


Fig. 2 Visualization of the static (a) and dynamic (b) anisotropy values [5]

In summary, it is obvious that parts bearing bending loads, especially the front upper cross member and the bumper cross member, have rather high anisotropy values. Furthermore, the large parts in the back of the front body, like the cowl and the water channel, show comparatively high anisotropy values as well.

3 OPTIMISED HYBRID PARTS

In this section, the aforementioned pre-selected parts have been redesigned as FRP- or multi-material hybrid parts. One important aspect is the possibility to enable a functional integration for the selected parts.

3.1 SIMULATION

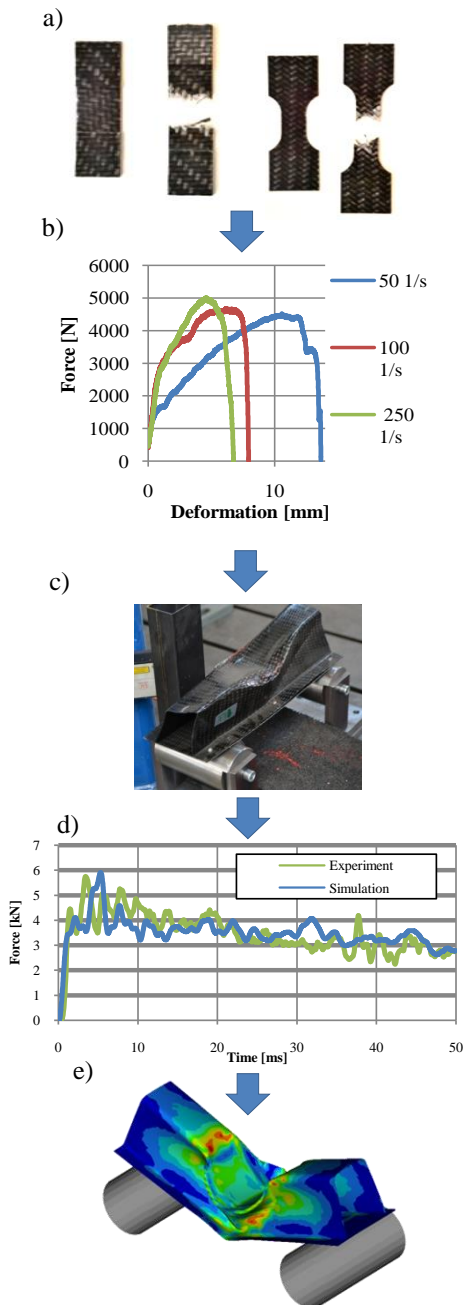


Fig. 3 Development process of the material model: (a) specimen-geometries, (b) evaluation of the mechanical parameter and their strain rate dependencies, (c) specimen of the reference profile in a drop tower test, (d) curve-fitting with the reference load case, (e) contour plot of a crash-simulation with the reference geometry

It is necessary to have appropriate material models to simulate the crash behavior of the FRP parts. The endless fiber reinforced organic sheets are simulated with the LS-DYNA material model No.58: MAT_COMPOSITE_FABRIC_LAMINATE. This formulation can be used for unidirectional layers, fabrics and complete laminates by using shell elements [7, 8]. Furthermore, this model is able to consider strain rate dependent behaviour. The development and calibration of the model is visualised in Figure 3. A detailed description with further information is given in [9].

First of all, coupon tests were performed with strain rates from 0.004 to 250 1/s in order to determine the mechanical properties. Then, 3-point bending tests on a drop tower test bench were performed to generate data with a complex reference load case. Finally, this data is used to calibrate the material model.

For the simulation of the thermoplastic long fiber reinforced material, the material model No. 3: MAT_PASTIC_KINEMATIC was used. In this model, the stress strain curve is approximated by a bi-linear curve. The investigated material is a polyamide (PA) with 40 % glass fiber.

3.2 OPTIMIZATION OF THE COMPONENTS

To systematically redesign the selected components, different optimization methods have been carried out [10].

3.2.1 Cowl and water channel

The water channel and the cowl contribute more than 7 % of the total torsion stiffness of the BIW. For this reason, the torsion stiffness is considered as a key requirement for the redesign. Both parts shall be substituted by organic sheets. The composite layer architecture is optimized by a size-optimization (method). Due to the strict package requirements, it is impossible to change the geometry of the components.

The high anisotropy of both parts leads to a layered set up with a predominant orientation in the vehicles transverse axis (Tab. 1).

Table 1: Layered architecture of the water channel and the cowl [5]

Cowl	Thick-ness	Orien-tation	Water tank	Thick-ness	Orien-tation
Layer 1	0.5 mm	0°	Layer 1	0.5 mm	0°
Layer 2	0.5 mm	0°	Layer 2	0.5 mm	45°
Layer 3	0.5 mm	45°	Layer 3	0.5 mm	-45°
Layer 4	0.5 mm	-45°	Layer 4	0.5 mm	0°
Layer 5	0.5 mm	0°			
Layer 6	0.5 mm	0°			

All in all, this new design of the assembly results in a total mass reduction of more than 2,5 kg.

3.2.2 Upper cross member front

The original design of the upper cross member front consists of two sheet metal parts. The new design has only one. To realize this, the initial upper part is built by thermoformed organic sheet with a major fiber orientation in transverse direction. The initial closing plate below was substituted by reinforcement ribs on the organic sheet part by using injection moulding, which can be combined with the thermo forming of the organic sheet [4].

The optimization is divided into three steps (Fig. 4). In the first step, the organic sheet is designed by shape-optimization. The space inside the part is used for the following topology optimization in the second step. The result is used to interpret the rib structure. Finally, the thicknesses of the ribs and the organic sheets are adjusted by size-optimization again. After all these steps, a total weight reduction of more than 30 % could be reached without sacrificing component performance. All static and dynamic requirements were fulfilled.

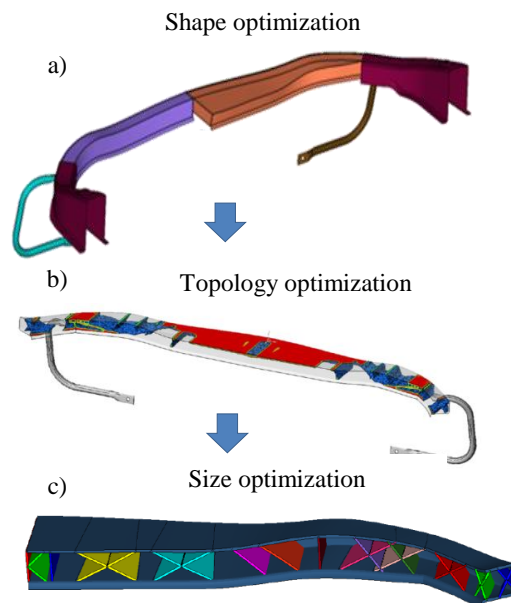


Fig. 4 (a) Shape-optimization of the thermoformed organic sheet, (b) Topology-optimization of the rib structure, (c) Size-optimization of the rib thicknesses

3.2.3 Bumper cross member

The bumper cross member is a part with high crash performance requirements. Nowadays, optimization tools can be used for static load cases or at least quasi-static loads [10]. Several experiments with different quasi-static loads did not lead to a

satisfying result with an acceptable crash performance.

A knowledge based FRP-cross member design, which was designed without using optimization tools, was able to reach the same performance as the steel reference. The weight saving was 26 %, which equals to almost 800 g.

4 CONCLUSION

With the help of described methods, a total weight reduction of more than 5 kg could be achieved by introduction of FRP. The performance regarding to the static and dynamic load cases is as good as or even better than the initial reference of sheet metal design. For example, the passive safety performance is slightly better due to the higher energy absorption capability of the composite material. For all considered parts, only glass fiber reinforced thermoplastics were used to guarantee low material costs. Nevertheless, there are still some challenges which have not been solved yet:

- 1) The crash-simulation of endless fiber reinforced material leads to highly unsatisfying results, when the load cases are different from the reference load case for material calibration.
- 2) The requirement of parts pre selection is only based on the anisotropy. Multi-axial loaded parts cannot be considered.
- 3) The result of the optimization, especially the size optimizations, is strongly dependent on the chosen starting values.

5 OUTLOOK

Several research projects at the institute handle with the shortcomings mentioned above. Therefore, a brief outlook on these projects is given below:

- 1) The first aspect in section 5 has been described in detail in [9]. At the moment, the institute has started to develop themselves improved material models.
- 2) The MATLAB-Tool which has been developed in this project is the fundament for further studies dealing with multi-axial load cases. First results are going to be published soon.
- 3) The results of this extended program can be used for a very first conceptional design of a laminate architecture. This architecture could be the first step for a further and more detailed size optimization.

REFERENCES

- [1] Fang, X.F., Kurtenbach, S., Li, J. (2014) "Cost-effective body structure for an e-vehicle" ATZ- Automobiltechnische Zeitschrift, Springer-Vieweg, (116), pp. 20-27.
- [2] Goebbels, S. et al. (2010) "Analyse der sekundären Gewichtseinsparungen", report of a research project funded by the "Forschungsvereinigung Automobiltechnik e.V."
- [3] Ehrenstein, G. W.: (2006) "Faserverbund-Kunststoffe: Werkstoffe- Verfahren- Eigenschaften" 2. edition, Hanser, München, 2006
- [4] Schuck, M.: (2012) Kombination von Materialleichtbau mit konstruktivem Leichtbau. In: lightweightdesign 5 Nr. 2 S.54-59
- [5] Grote, M.; Fang, X.F.: "Development of a front body concept in a steel-GRP composite construction" . In: ATZ- Automobiltechnische Zeitschrift 117 (2015) Nr. 11 S.62-66
- [6] Durst, K.G.: (2008) Beitrag zur systematischen Bewertung der Eignung anisotroper Faserverbundwerkstoffe im Fahrzeugbau, Dissertation, Institut für Flugzeugbau der Universität Stuttgart,
- [7] LSTC (2014) "LS-DYNA Keyword User`s Manual", Version 971
- [8] Schmeer, S. et al. (2008) "Aktueller Stand und Trends in der CFK-Berechnung im Fahrzeugbau", report of a research project funded by the "Forschungsvereinigung Automobiltechnik e.V."
- [9] Fang, X.F.; Grote, M.: (2015)"Development of a material model for organic sheets for the simulation of FRP-components in full vehicle crash", NAFEMS World Congress, San Diego, 2015
- [10] Schumacher, A.: (2005)"Optimierung mechanischer Strukturen: Grundlagen und industrielle Anwendungen", 1. edition, Springer, Heidelberg, 2005

DEVELOPMENT, MANUFACTURING AND TESTING OF A CFRP BELLOWS COUPLING FOR POWERTRAIN APPLICATIONS

C. Oblinger^{1*}, M. Jelinek², H. Lang³, A. Baeten⁴, K. Drechsler⁵, G. Reinhart²

¹Application Centre for Materials and Environmental Research (AMU),
University of Augsburg, Germany

²Institute for Machine Tools and Industrial Management – Application Centre Augsburg,
Technische Universität München (TUM), Germany

³Fraunhofer ICT, Branch Functional Lightweight Design, Augsburg, Germany

⁴Augsburg University of Applied Sciences, Germany

⁵Institute for Carbon Composites, Technische Universität München (TUM), Germany

ABSTRACT: Fibre reinforced polymers (FRP) are used in a widespread range of aerospace applications due to their excellent quality profile. Furthermore, they play an important role for machine elements in the sectors of automotive, shipbuilding, wind energy as well as in the sports equipment industry. Especially machine elements, which are applied in highly dynamic processes, require a preferable high strength, combined with high stiffness. In addition, a low density and thus a reduced weight of novel FRP components lead to a decreased energy consumption of the entire mechanical system. In this context, a coupling between two drive shafts represents an exemplary machine element for a potential application with FRP.

This paper focuses on the development, manufacturing and testing methods of a bellows coupling made of prepreg-based carbon fibre reinforced polymers (CFRP). Functional requirements lead to a CFRP reinforced interface involving metal bracing elements in order to connect the coupling with its periphery and thus providing a detachable hybrid transition area. A joining concept was developed which enables the compensation and connection functionality of the CFRP bellows coupling. As a production method the prepreg technology is applied. Different lamination procedures have been developed to provide a composite-appropriate drapability. Experimental investigations on tubular test specimens have been carried out in order to check the functionality of the CFRP metal interface. Finally, representative prototypes of the coupling are tested via destructive (static test, dynamic test) and non-destructive evaluation methods (ultrasonic inspection, active thermography). Optimal thermographic testing parameters are applied, which were obtained by the deduction of defined defective test specimens and a proximate, methodological, thermographic parameter study.

KEYWORDS: Bellows coupling, composite, CFRP, metal, hybrid, load transfer, testing, thermography

1 INTRODUCTION

Within the field of lightweight construction, fibre reinforced polymers (FRP) are of increased importance – particularly carbon fibre reinforced polymers (CFRP). In aerospace industry, CFRP structures are broadly applied due to their outstanding characteristic properties [1, 2]. Furthermore, CFRP structures are used in the automotive sector, in shipbuilding as well as in the sports equipment industry [3, 4]. Due to various industrial requirements and specifications, a diversified application of CFRP in aviation on one side and in machine and plant construction on the other side is existent. The aircraft construction is characterised by small piece numbers and a relatively strong impact of

weight saving on fuel consumption. However, in mechanical engineering, high quantities are often achieved and there is a much stronger focus on the production costs compared to the operating costs. A copy-paste substitution of metallic materials by FRP, while maintaining the construction method, does not lead to the desired results in weight-saving and structural improvement. This lies in the fact that metals and FRP possess different material properties as well as different component manufacturing techniques. Each kind of material class provides certain advantages regarding its application. CFRP is often used when other materials reach their limits. Usually this is the case for example with torsion-loaded structures, if the stiffness of

* Corresponding author: Christian Oblinger, Universitätsstraße 1a, D-86159 Augsburg (Germany), phone +49 821 598 3586, fax +49 821 598 3588, christian.oblinger@amu.uni-augsburg.de

metallic shafts is no longer sufficient for high rotational speeds. Nevertheless, components made of pure CFRP are rarely effective in machine and plant construction applications. The CFRP metal hybrid construction is to be applied to make optimum use of the individual advantages of each material class. In mechanical engineering, these advantages lead to a significant increase in efficiency [5, 6, 7]. Particularly, drive shafts comprising a CFRP structure commonly provide weight reductions of up to 50 percent, compared to conventional steel shafts, due to their high specific strength and stiffness [8, 9]. Such lightweight shafts are implemented for the load application and load transfer at the shaft fronts involving metallic (e.g. aluminium, steel or titanium) elements. By an innovative shaft coupling in CFRP metal hybrid construction, an increase in efficiency could also be achieved. This paper presents the development and manufacturing process of a CFRP bellows coupling validated by experimental results with the use of a generic demonstrator device.

2 METHODOLOGICAL CONSTRUCTION APPROACH

The aim of this approach was to develop a CFRP bellows coupling, which is adjustable regarding shaft misalignments and comprising specific geometry features.

2.1 INITIAL SITUATION AND REQUIREMENTS

A shaft coupling realises the torque transmission between two coaxially arranged shaft ends. Figure 1 clarifies schematically the overall structure of the presented shaft coupling configuration and designates the necessary components.

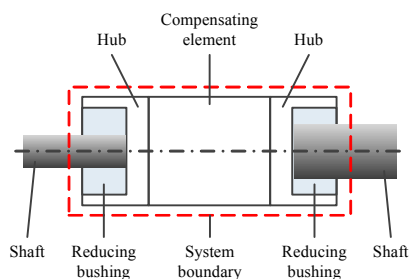


Fig. 1 Schematic of the overall structure of the shaft coupling

The functionalities of a shaft coupling can be fundamentally divided into a transmission, compensating and switching function [10, 11]. The key requirements on the methods demonstrated in the present paper focused on the transmission and compensation functionality. Regarding the compensation functionality, the axial displacement and angular misalignment was considered. These types of shaft misalignment can result from deviations out of production, assembly and load. For this

reason, the entire construction method of the CFRP bellows coupling had to fulfil the compensation and connection functionality. In the next step, characteristic load cases were defined, whereby a generic usage of the results for a generalised application was desired. The most important load cases for the CFRP bellows coupling are summarised in table 1.

Table 1: Characteristic load cases for the CFRP bellows coupling

Nominal torque [Nm]	400
Impact torque [Nm]	600
Maximum speed [rpm]	10000
Maximum twist with nominal torque [°]	≤ 0.45
Restoring force at max. axial displacement of 0.7 mm [N]	≤ 350
Restoring torque at max. angular misalignment of 1° [Nm]	≤ 15

2.2 APPROACH FOR THE FULFILMENT OF THE COMPENSATION FUNCTIONALITY

The compensation functionality of a coupling is achieved by the elastic distortion of the elements intended for the compensation. This work focuses on the development of a CFRP-based compensating element, which combines the advantages of the fibre composite construction and consists of a low number of subcomponents. Regarding the realisation of the compensation functionality, two partly contrary structure-mechanical requirements were to be fulfilled in a single component:

- Transmission of a specific torque without exceeding a threshold on the torsion angle (high torsional stiffness)
- Compensation of axial and angular displacement, whereby the resulting load on the bearings must be within certain limits (low bending stiffness)

In addition to the fulfilment of these requirements, the geometrical dimensions (max. outside diameter of 100 mm) as well as the weight of the CFRP compensating element is to be kept as low as possible. The design of the compensating element was based on a geometrical approach. On the basis of a CFRP shaft, centric bulges of different strengths were analysed regarding the fulfilment of the compensation requirements (see figure 2). The research indicated that a structure with different diameters (bellows-similar geometry) could fulfil these requirements at the best.

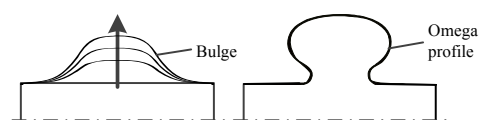


Fig. 2 Sketch of the geometrical approach within the concept phase

The elastic material properties of fibre reinforced materials (elastic modulus as well as shear modulus) represent an additional design parameter, which can considerably be affected by the fibre orientation. In the context of the dimensioning, it could be pointed out that the diameter value of the bellows-shaped hollow body has substantial influence on the structure-mechanical properties of the component. Calculating the torsional and bending stiffness, the diameter influences the respective moments of inertia in third power [12]. Altogether, a compromise between high torsional stiffness and low bending stiffness could be obtained by an appropriate geometrical approach. With regard to the production-orientated realisation of the concept, the bellows geometry was changed in such a way that it is free from undercuts and narrow radii to allow a manufacturing via prepreg lay-up. As a result, the mechanical properties have slightly decreased so that a modification of the construction method with several aligned bellows-shaped elements became necessary (see figure 3).

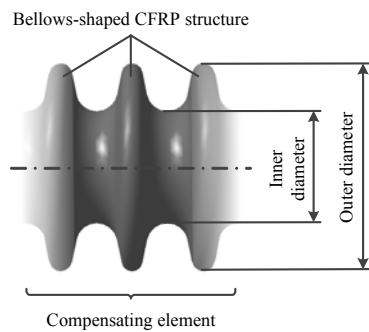


Fig. 3 Schematic of the bellows-shaped structure to fulfil the compensation functionality for the CFRP coupling

2.3 APPROACH FOR THE FULFILMENT OF THE CONNECTION FUNCTIONALITY

This approach focused on the joining techniques not resulting in a deterioration of the macroscopic fibre structure and thus on the load bearing element of the fibre composite. It refers especially to the adhesive joint, the assembly of torsion-loaded components as well as the innovative form-fit joining concepts to be applied. Within the operation range of drive technology, plain shafts (steel solid shafts) of frequently different diameters are to be connected with the hub body detachably and frictionally engaged (see figure 1). After the disassembly of this shaft-hub joint a repeated assembly (two to three times) must be possible. The connected shafts must not be damaged in the operation condition of the shaft coupling (e.g. by substantial fretting corrosion). The applied metallic solid shafts provide the following material-specific characteristics: yield strength is at least 350 MPa, surface is precision-turned or ground with $R_a = 0.8$ mm and tolerance h6 or h7. The developed

connection method provides a detachable interference fit assembly between the CFRP and the metal shaft using a standardised clamping ring (clamping on the inside of the CFRP structure). For this purpose, a cylindrical CFRP interface was provided at the face sides of the outer bellows elements. Figure 4 shows the developed design concept for the fulfilment of connection functionality.

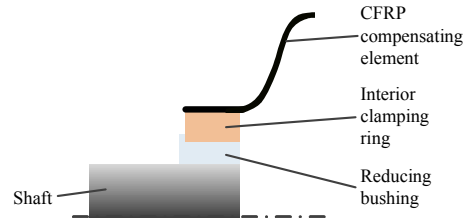


Fig. 4 Schematic of the interference fit assembly (inside clamping connection) at the transition between CFRP and metal for the fulfilment of connection functionality

With this inside clamping joint, the fibre composite is loaded in tensile direction, which leads to more favourable mechanical strength properties. Thereby, an unfavourable pressure load could be avoided, so that the matrix loading is reduced. The variability regarding several connection shaft diameters is provided by different-sized metallic reducing bushings.

2.4 CONCEPTUAL DESIGN OF THE DEMONSTRATOR PART

The generic demonstrator part combines the two construction elements presented above within one unique structure. From the dimensioning, it can be concluded that on the one hand, a larger diameter within the interface leads to an increase of torsional stiffness and to a reduction of effort. On the other hand, additional circumferential layers in the interface are necessary. This results in reduced areas containing interfibre fracture damage. Figure 5 shows the final design concept for the generic CFRP bellows coupling.

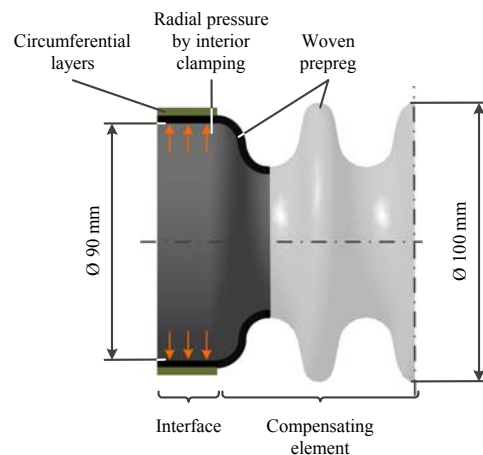


Fig. 5 Schematic of the generic CFRP bellows coupling

3 MANUFACTURING

The hand lay-up prepreg technology has been applied as an appropriate manufacturing method, whereby the main material was the SGL CE 8201-200-45S woven (twill 2/2) epoxy-based prepreg. The nominal thickness of the prepreg is 0.19 mm. For the additional circumferential layers within the interface the SGL CE 1250-230-39 unidirectional epoxy-based prepreg with a nominal thickness in cured state of 0.22 mm per layer was used. Both material systems are chemically compatible. In addition, they require a low curing temperature, which enhances the economical usage of these materials in machine and plant construction.

3.1 TUBULAR TEST SPECIMENS

For the experimental investigation of the connection functionality in accordance with the design concept cylindrical test specimens were manufactured. These provided similar interface geometry (inside diameter of 90 mm), material allocation and lay-up to the actual CFRP bellows coupling. This fact guaranteed the transferability of the experimental results to the present demonstrator part. The basic structure consists of the woven prepreg with $\pm 45^\circ$ layers and an overall thickness of 2.1 mm. The fronts of the test specimens have been reinforced by unidirectional prepreg layers in 90° direction. Through these additional layers, thicknesses of 2.4 mm and 4.8 mm were realised. All test specimens were cured in an autoclave. The temperature program followed the materials supplier's recommendations up to the end of the first dwell at 60°C . The heating began at room temperature up to 60°C at a rate of $2^\circ\text{C}/\text{min}$ and was kept at 60°C for 60 min. Afterwards, the setup was heated from 60°C to 120°C at a rate of $2^\circ\text{C}/\text{min}$ and kept at 120°C for 120 min. Subsequently, the autoclave was cooled down at a rate of $2^\circ\text{C}/\text{min}$. A pressure of 0.5 MPa and a vacuum of 0.005 MPa was applied throughout the cycle.

3.2 DEMONSTRATOR PART CFRP BELLOWS COUPLING

Several approaches have been developed via various tests to ensure the manufacturability of the demonstrator part. These tests contained, for instance, the development of different lay-up strategies (division of the bellows geometry in sections), draping procedures and an identification of cutting geometries for the bellows structure. Significant influencing factors for manufacturability have been identified such as cut sizes, cut geometries as well as wrinkling. Their relevance for the demonstrator part has been assessed. These tests on a prototype tooling have pointed out that draping in x-direction is the most suitable strategy. The complex bellows geometry could be draped in individual layers by segmentation of the woven prepreg in circumferential direction (6 x 60° segments) (see figure 6).

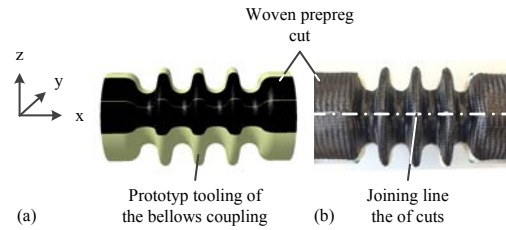


Fig. 6 Lay-up strategy "draping in x-direction" (a) and realised joining of the cuts from edge to edge of the bellows coupling (b)

With the aid of this draping strategy, one woven cut covers the length of the shaft coupling. Thus, six cuts are required per layer with $\pm 45^\circ$ fibre orientation. The angle is measured with respect to the x-axis of the coupling. In the context of this work, a reusable and detachable hybrid core concept was developed. Substantial boundary conditions for this concept study were: form stability with dimensional accuracy of the geometry, simple manufacturing as well as economical feedstocks. In order to ensure the required dimensional accuracy of the entire demonstrator part and thus its functionality, an exact shaping of the hybrid core system was of paramount importance. Close diameter tolerances within the interface could be achieved by using cylindrical metal elements. In view of the divisibility of the core system, a cylindrical metal element can be moved and fixed axially (see figure 7 (a)). For the realisation of the bellows-shaped compensating structure, several core segments of ABS (acrylonitrile butadiene styrene) were applied, which were manufactured with the FDM (fused deposition modelling) procedure. Figure 7 (b) presents one individual core segment for the realisation of the bellows-shaped compensating structure. Nine different segments cover the entire compensating structure distributed over the circumference.

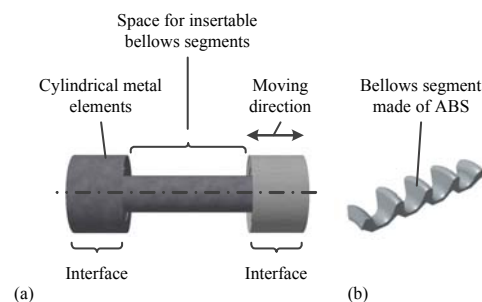


Fig. 7 Schematic of the hybrid core concept for the manufacture of the demonstrator part: cylindrical metal elements (a) and an individual bellows element (b)

The ABS segments can be clamped and removed between the metal elements. The manufacturing of the demonstrator part consisted of several process steps. In the first step, all prepreg cuts were manually tailored and marked to the necessary geometry. In order to recognise related cuts as well as the

lamination sequence easily, the cuts were assembled to kits. After a pre-treatment of the core system, the woven prepreg layers were deposited and compacted at regular intervals. The application of the circumferential layers concluded the manual manufacturing process. Table 2 clarifies the entire design and manufacturing parameters of the CFRP bellows coupling.

Table 2: CFRP-specific design and manufacturing parameters of the bellows coupling

Prepreg	woven fabric	uni-directional
Overall thickness [mm]	2.1	4.8
Covered angles per cutting [°]	60	360
Offset of superimposed layers [°]	30	90 (min.) / 180 (max.)
Number of compacting steps [-]	3	5

In order to protect the ABS structures, the consolidation and curing was performed in an annealing furnace with vacuum bag assembly to prevent any injury of the ABS segments resulting from a conventional autoclave process. In that context, a substitution of the ABS structures with metal segments would lead to an increased stability of these elements. Several prototypes comprising similar manufacturing parameters were produced to examine the complete functionality of the entire manufacturing process with respect to reproducibility.

4 EXPERIMENTAL VALIDATION

In this section, experimental tests are presented, which have been carried out on the manufactured tubular test specimens and the demonstrator parts in order to study the industrial load cases.

4.1 ANALYSIS OF THE TUBULAR TEST SPECIMENS

The experimental examination of the interface was conducted via static torsion tests employing a bracing test bench. The experiments aimed at proving the functional capability of the interface as well as the evaluation of the frictionally engaged transmittable torsional moment. A shaft diameter of 40 mm as well as a reducing bushing socket was attached at one front of the specimen. At the opposite front, a wave diameter of 60 mm was connected. On both connection sides an identical interior clamping ring was used. The test preparation comprised degreasing of the CFRP metal contact areas as well as tightening the interior clamping rings up to their limit. Next, the torque was increased involving the bracing test bench until a slipping through of the detachable connection could be detected. In that context, the first rupture

in the torque-way diagram was rated as the transmittable torque value of the clamping connection. All tubular test specimens fulfilled the industrial requirements (nominal torque ≥ 400 Nm, impact torque ≥ 600 Nm). A comparative determination of the inside diameters (three-point internal measuring gauge) before and after the torsion test revealed no considerable deviation. Via an ultrasonic testing prior and after the torsion test, no damages at the CFRP structure could be detected.

4.2 ANALYSIS OF THE PROTOTYPES

The test phase of the prototypes comprised the application of the above-mentioned, three specific load cases. The necessary preparations were identical to those in section 4.1. Figure 8 demonstrates a section of the test assembly for the determination of the maximum static torsional moment transferable into the CFRP bellows coupling.

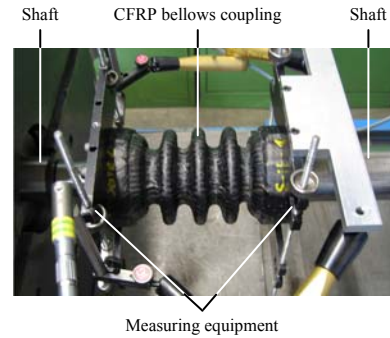


Fig. 8 Experimental setup for the determination of the transferable static torsional moment into the demonstrator part

The dimensional accuracy of the inner diameter at the interface showed a deviation of less than 0.02 mm from the nominal diameter of 90.00 mm within the specified tolerance. By comparison of the experimental results with simulation data, a correlation between simulation and application could be determined, which leads to a validation of the numeric CFRP materials model (see figure 9).

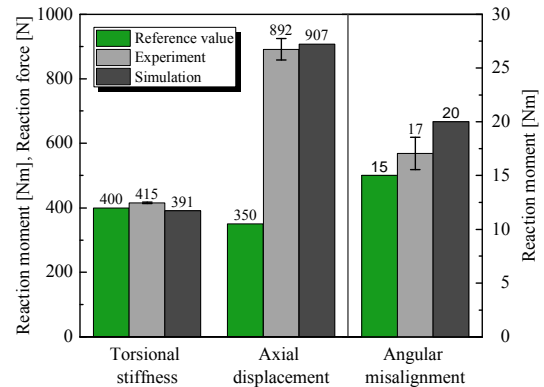


Fig. 9 Comparison of the experimental (mean value and standard deviation) and numeric results with the reference value from the load cases

Solely the demanded maximum axial displacement value could not be fulfilled. Effects on the structure-mechanical simulation adjustment could be pointed out from the manufacturing process. These effects were on the one hand cutting dimensions of woven prepreg plies due to drapery for the avoidance of wrinklings and on the other hand orientation values of the fibres within the cuts. As a third parameter, the thickness changes at the bellows profile due to drapery could be constituted. There existed a material accumulation in the valleys of the bellows geometry and a smaller wall thickness on the bellows. However, this manufacturing-induced effect did not affect the functionality negatively, because the compensation occurs mainly through the springs of the vertical bellows flanks. The maximum stresses resulting from the moment path inside the structure occur at the smallest diameter of the bellows coupling. Thus, a greater wall thickness for the strength of the demonstrator part can be assessed as positive at the smallest diameter. The basic characteristics from the experiments could be verified by means of the finite element method. With one prototype a fatigue test with alternating torque of ± 400 Nm ($f = 5$ Hz) was accomplished. The torsional stiffness of the CFRP bellows coupling was measured regularly during the whole testing sequence (see figure 10).

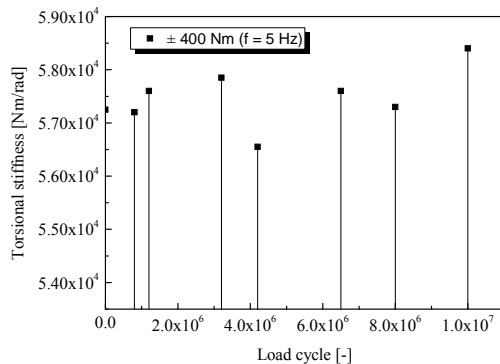


Fig. 10 Progress of torsional stiffness during the fatigue test with alternating torque

The torque change test was finished after 10 million load cycles without visible damages on the structure. A degradation of the torsional stiffness has not been recognised.

5 NON-DESTRUCTIVE TESTING VIA ACTIVE THERMOGRAPHY

The inspection of CFRP metal hybrid components assigning active thermography represents a fast, non-contact, non-destructive evaluation (NDE) technique [13] to identify damages in CFRP structures like delamination (delam.), debonding, porosity, fibre fracture or waviness [14]. It can be employed during [15] and after the manufacturing process as well as concerning in-service testing in particular [14].

5.1 MANUFACTURING OF DEFINED DEFECTIVE ROTATIONAL SYMMETRIC CFRP TEST SPECIMENS

Based on the mechanical load simulation of the CFRP bellows coupling by means of the finite element method, various defective test specimens were methodologically deduced. The simulation results indicated delaminations within a diameter range from 10 to 15 mm located in various structural depths. Apart from the prognosticated defects resulting from utilisation, cavities and porosity were declared as relevant imperfections in the CFRP structure due to potential manufacturing faults. Based upon this knowledge, the hybrid transition area between the CFRP base body of the bellows coupling and an optional metallic bracing element was focused on representatively. With regard to recent studies pointing out relevant parameters of a complete thermographic referencing process [16], three rotationally symmetric, defined defective CFRP test specimens with an inner diameter of 90 mm were manufactured. Table 3 declares the lay-up of the test specimens.

Table 3: Lay-up of methodologically derived test specimens

Layer	Prepreg	Designation	Angle
1-12	woven fabric	SGL CE 8201-200-45S	$\pm 45^\circ$
13-35	uni-directional	SGL CE 1250-230-39	90°

Layers 1 to 12 are consistently laminated by the entire specimen. Layer 13–35 represent reinforcement plies for the coupling's interfaces (load transition areas) (see figure 5 and figure 11). Delaminations with a thickness of 0.13 mm are realised by the integration of polytetrafluoroethylene (PTFE) slides into the CFRP laminate and their removal after the curing process [13]. Air gaps (diameter: 3 mm, 5 mm) were formed by the integration of polystyrene balls into the CFRP laminate. In the course of the curing process, the polystyrene balls dissipate and leave an air bubble in the matrix of the structure [16]. Table 4 describes the defect types and sizes as well their localisations within the CFRP laminate.

Table 4: Defect localisation within the laminate of the test specimens (counted from the inner layer 1)

Defect type	Defect size/ diameter	Localisation under layer
Delam.	10 x 5 mm	2, 4, 6, ..., 34
Delam.	15 x 10 mm	2, 4, 6, ..., 34
Delam.	15 x 15 mm	2, 4, 6, ..., 34
Air gap	5 mm	2, 4, 6, ..., 34
Air gap	3 mm	2, 4, 6, ..., 34

5.2 METHODOLOGICAL DEVELOPMENT OF OPTIMAL THERMOGRAPHIC PARAMETER SETS FOR INSPECTION OF THE LOAD TRANSITION AREA

The examination was performed from the inner and outer surface of the specimens employing the following thermographic equipment:

- Thermographic camera FLIR SC5650 (cooled photo quanta detector, resolution: 640x512 pixel, sensitivity: 20 mK, temperature range: -20 °C to +3000 °C, max. refresh rate: 380 Hz)
- Optical excitation methods via two halogen spots (Hedler, 2 x H25s lamps per spot, 1250 W per lamp and reflector “Hedler MaxiSum”) or flash light (Hensel VH3-6000 Linear head, maximum flash energy: 6000 J)
- Thermography system: edevis® OTVIS and PTVIS, software: DisplayIMG 6

The development of optimal thermographic parameter sets includes a stepwise parameter variation of the excitation (Fourier) frequency applying the method devised in [17]. The developed approach exploits rectangular overlays for the export of phase angle values along failure (F) and reference lines (R) (see figure 11). The defect sizes and depths were pre-referenced via ultrasonic inspection technique.

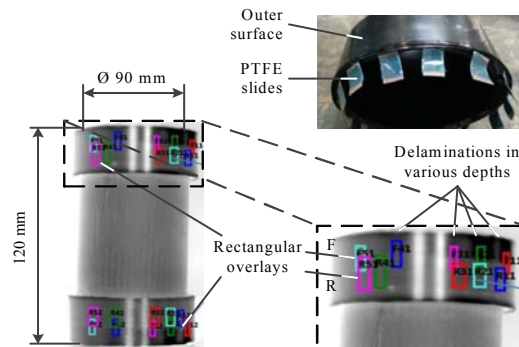


Fig. 11 Thermogram visualising delaminations and rectangular overlays (outer surface)

The investigation induced certain Fourier frequency ranges resulting in a thermographic failure contrast (signal noise ratio, SNR) located above the visibility limit (VL) constituting a value of approximately 1.2 (see table 5).

Table 5: Detectability of defects integrated into the structure of the test specimens (regardless of the thermographic detection focus – inner or outer surface)

Defect type	Defect size/ diameter	Detection depth under layer
Delam.	10 x 5 mm	7 (halogen), 1 (flash)
Delam.	15 x 10 mm	9 (halogen), 3 (flash)
Delam.	15 x 15 mm	9 (halogen), 5 (flash)
Air gap	3 mm	5 (halogen), 1 (flash)
Air gap	5 mm	5 (halogen), 1 (flash)

The analysis of the diagrams reveals the requirement of a proper determination of the Fourier frequency or Fourier frequencies (green marked areas) for a complete examination in relation to delaminations (figure 12) or air gaps (figure 13) up to the maximum thermographic detection depth.

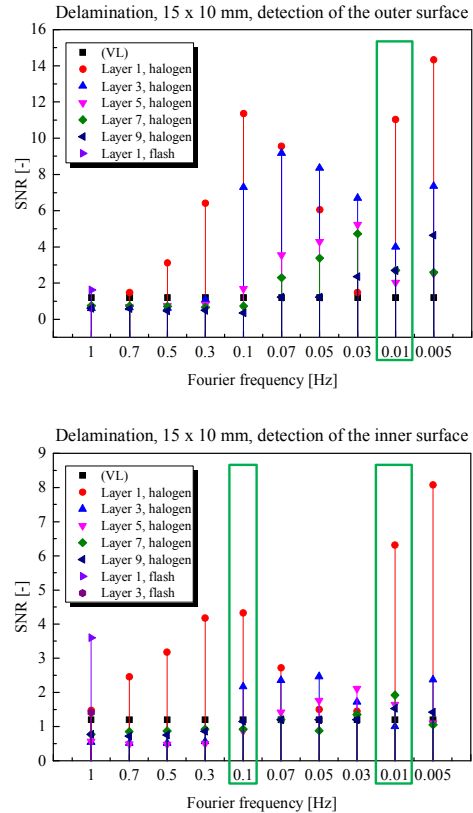


Fig. 12 Exemplary results emerging from stepwise variation of the lock-in frequency in the course of the thermographic detection of delaminations. Visibility limit for failure contrast: VL

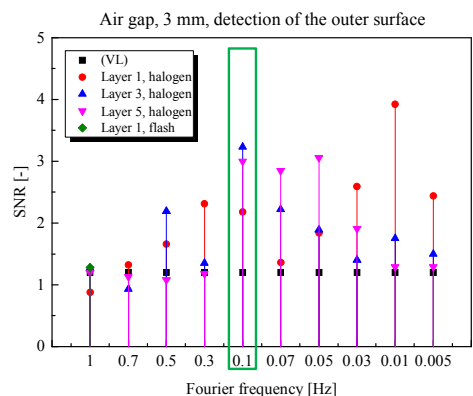


Fig. 13 Exemplary results originating from stepwise variation of the lock-in frequency in the course of the detection of air gaps. Visibility limit for failure contrast: VL

The outcome of the investigation (see figure 12 and figure 13) can be advanced with regard to the ideal

Fourier frequency resulting in an optimal failure contrast in a preferably short measurement time [17]. Further steps conducted in the referencing process enable the completion of the optimal thermographic parameter sets for being implemented into a structured database. The realisation of the knowledge management in the form of a database accelerates the thermographic investigation procedure notably [16, 17].

6 CONCLUSIONS

The presented paper describes a design concept for a CFRP bellows coupling. The concept was based on a novel method to fulfil the requirements of compensation and connection functionality. Drive shafts with different diameters could be detachably connected by a metallic reducing bushing and an internal clamping ring directed to the CFRP interfaces. The compensation functionality was implemented via performing a geometrical approach comprising bellows elements within the CFRP structure between these two interfaces. The CFRP structure permits with three aligned bellows elements a sufficiently rigid torque transmission with simultaneous compensation functionality of axial displacement and angular misalignment. As manufacturing method, the hand lay-up prepreg technology has been applied. The approach revealed the manufacturability of the demonstrator part with the aid of a detachable and reusable hybrid core system. The functional capability of the connection and compensation concept was validated by experimental investigations on tubular CFRP specimens and various prototypes of a CFRP bellows coupling. In the course of NDT assigning active thermography, the determination of adequate excitation frequencies results in the reliable detectability of relevant structural defects up to a maximum thermographic detection depth, within the methodologically deduced test specimens.

7 ACKNOWLEDGEMENT

This work was conducted within the project “FORCiM³A – Forschungsverbund CFK/Metall-Mischbauweisen im Maschinen- und Anlagenbau“, which was funded by the Bayerische Forschungsförderung (BFS).

REFERENCES

- [1] Drechsler K.: *Überblick Leichtbau – Entwicklung, Bedeutung und Disziplinen*. In: Themenheft Forschung: Leichtbau. Universität Stuttgart, 2007.
- [2] Flemming M., Ziegmann G., Roth S.: *Faserverbundbauweisen – Halbzeuge und Bauweisen*. Springer-Verlag, Berlin, 1996.
- [3] Schürmann H.: *Konstruieren mit Faser-Kunststoff-Verbunden*. Springer-Verlag, Berlin, 2007.
- [4] Jäger H., Hauke T.: *Carbonfasern und ihre Verbundwerkstoffe*. Süddeutscher Verlag on-pact, München, 2010.
- [5] Hufenbach W., Lenz F., Renner O.: *Welle-Nabe-Verbindungen für Leichtbauantriebswellen in Faserverbund-Metall-Mischbauweise*. In: VDI-Berichte Nr. 2176, 141-153, 2012.
- [6] Oblinger C., Lang H., Drechsler K.: *CFK/Metall-Mischbauweisen im Maschinen- und Anlagenbau – wichtiger denn je. Nachhaltigkeit und Energieeffizienz durch innovative Leichtbaustrukturen*. In: Umwelt-Technologie und Energie in Bayern, 26-28, 2015.
- [7] Hufenbach W., Lenz F., Birke M., Spitzer S., Münter S.: *Design, Dimensioning and automated Manufacturing of profiled Composite Driveshafts*. Proceedings of ICCM19, Montreal, Canada, 2013.
- [8] Kleschinski M.: *Antriebswellen aus Faser-Kunststoff-Verbunden*. Shaker Verlag, 2007.
- [9] Haldenwanger H.: *Development of plastics parts for the racing and standard versions of the Audi-Quattro*. Warrendale, PA: Society of Automotive Engineers, 1982.
- [10] Muhs D., Wittel H., Jannasch D., Voßiek J.: *Roloff/Matek Maschinenelemente*. Springer Vieweg, Wiesbaden, 2013.
- [11] Niemann G., Neumann B., Winter H.: *Maschinenelemente Band 3*. Springer-Verlag, Berlin, 1986.
- [12] Klein B.: *Leichtbau-Konstruktion*. Springer-Verlag, Berlin, 2012.
- [13] Wu D., Busse G.: *Lock-in thermography for nondestructive evaluation of materials*. Rev. Gén. Therm. (1998) 37, Elsevier, Paris, 1998.
- [14] Zöcke C. M.: *Quantitative analysis of defects in composite material by means of optical lockin thermography*. Dissertation, University of Saarland and Ecole Doctorale MIM of Université Paul-Varlaine / Metz, Saarbrücken and Metz, 2009.
- [15] Ullmann T., Schmidt T., Hofmann S., Jemmalì R.: *In-line Quality Assurance for the Manufacturing of Carbon Fiber Reinforced Aircraft Structures*. In: 2nd International Symposium on NDT in Aerospace 2010, TU.1.A.4, Hamburg, 2010.
- [16] Jelinek M., Seidel C., Reinhart G.: *Thermographic Inspection of CFRP Metal Hybrid Components*. In: CIRPe2015, Elsevier, Cranfield (UK), 2015.
- [17] Jelinek M., Schilp J., Reinhart G.: *Optimised Parameter Sets for Thermographic Inspection of CFRP Metal Hybrid Components*. In: CIRPe2015, Elsevier, Cranfield (UK), 2015.

DEVELOPMENT, MANUFACTURING AND TESTING OF A CFRP METAL HYBRID GRIPPER FOR HIGHLY DYNAMIC MANIPULATION PROCESSES

M. Jelinek^{1*}, C. Oblinger², A. Baeten⁴, K. Drechsler⁵, G. Reinhart³

¹Institute for Machine Tools and Industrial Management – Application Centre Augsburg, Technische Universität München (TUM), Germany

²Application Centre for Materials and Environmental Research (AMU), University of Augsburg, Germany

³Institute for Machine Tools and Industrial Management, Technische Universität München (TUM), Germany

⁴Augsburg University of Applied Sciences, Augsburg, Germany

⁵Institute for Carbon Composites, Technische Universität München (TUM), Germany

ABSTRACT: The current trend in the automotive sector as well as in the aviation industry exhibits an intensified substitution of previously metal structures by fibre reinforced polymers (FRP). This development tendency is gradually extended to the branch of general mechanical and plant engineering. Despite the fact that carbon fibre reinforced polymers (CFRP) involve huge potential concerning a reduction of energy consumption, not all areas of a formerly metal structure can be replaced by pure CFRP. Due to material-specific requirements and industrial demands, some joints or reinforcements remain as metal or plastic elements in the CFRP base body. Particularly, metal elements function as load-bearing connections between the CFRP structure and its periphery.

The present paper focuses on the transformation and testing process of a formerly metal (steel) machine element (gripper arm) which is substituted with a CFRP metal hybrid structure. The final hybrid machine element is employed in a highly dynamic production sequence.

Subsequent to the manufacturing procedure (prepreg lamination), non-destructive testing (NDT) via ultrasonic inspection and active thermography is performed to provide information about possible structural damages beneath the surface of the CFRP metal hybrid component. Specific thermographic parameter sets, in order to obtain an optimal thermographic failure contrast, are already determined in terms of preceding research activities. Now, these parameters are applied to perform the thermographic, non-destructive test of the manufactured gripper arm prototypes prior to the loading test involving predetermined load cases. In order to exert superimposed loads on 3D structures, a novel test stand is developed and utilised.

KEYWORDS: CFRP, metal, hybrid, gripper, development, manufacture, fatigue, NDT, thermography

1 INTRODUCTION

The present development tendency with regard to new industrial applications reveals an increased usage of lightweight components – especially when they are exposed to highly dynamic loads [1]. Fibre reinforced polymers (FRP) are commonly applied to realise stiff and simultaneously lightweight structures, not only in the conventional fields of aerospace and automotive [2], but also in terms of performance improvement in machine and plant construction [1, 3]. Consequently, formerly metal components are substituted with FRP. Thereby, carbon fibre reinforced polymers (CFRP) is a mate-

rial of significance [4]. However, an entire replacement of a previously metal element by CFRP structures is not recommended due to material-specific requirements of the hybrid transition zones [5]. CFRP exhibits low bearing and shear strengths as well as a high notch sensitivity. Furthermore, the joint strength depends – besides the laminate configuration – on the environmental conditions [6]. Advanced coupling techniques such as bonded metallic inserts [7], externally bonded metallic doublers [8] or bolted joints and bushings [9] are developed to fulfil the material-specific requirements of each individual hybrid CFRP-metal transition area.

* Corresponding author: Michael Jelinek, Beim Glaspalast 5, D-86153 Augsburg (Germany), Tel.: +49 (0) 821 56883 56, Fax: +49 (0) 821 56883 50, e-mail: Michael.Jelinek@iwb.tum.de

Nevertheless, the crucial breakthrough of this substitution technique is still awaited. Grimberg and Vordermayer [1] point out the following reasons for the prevailing situation:

- High material and manufacturing costs
- Missing characteristic values for the component design and dynamic testing
- Difficulties in terms of implementing a robust and cost-efficient serial production process
- High effort regarding quality assurance
- Insecurities in the construction of suitable joint concepts and technologies
- Insufficient, secured knowledge about FRP and thus a lack of trust in this material

The substitution of a highly dynamic machine element with a CFRP metal hybrid construction constitutes the scope of the present paper. By this means, the conducted research provides an essential overview of the necessitated processes to be performed in connection with manufacture and quality assurance.

2 METHODOLOGICAL CONSTRUCTION APPROACH

The research approach comprises the methodological development of a CFRP metal gripper arm which is to be integrated into an existing handling system. Thereby, predefined industrial load cases as well as the availability of installation space have to be taken into consideration.

2.1 INITIAL SITUATION AND REQUIREMENTS

Apart from the focus on rotary machine elements (e.g. shafts, rollers and drive couplings), the development and implementation of components referred to as ‘carrier structures’ (e.g. gripper, machine brackets) constitutes one of the major objectives in general machine and plant construction employing CFRP.

The notably high structure-specific strength and stiffness of this material class – particularly when high modulus CFRP prepreg is utilised – indicates the application of CFRP prepreg in highly dynamically stressed components.

The above-mentioned superior material-specific characteristics enable rapid translational and rotatory movements combined with great accelerations. Additionally, high eigenfrequencies of the CFRP components reduce characteristic overshooting in the course of positioning tasks.

The design of the CFRP metal hybrid gripper arm is particularly based on the in Figure 1 presented machine element (non-rotating steel-based component with a non-regular geometry). In that connection, the hybrid structure necessitates high stiffness rather than high strength.

The integration of the gripper arm prototype into the real industrial system requires various hybrid joining techniques in order to connect the basic CFRP structure of the component to its periphery. Two independent interfaces are defined, whereby the lower interface represents the zone of load transmission into the structure. Figure 1 describes the three most important generic load cases of the gripper arm derived from a specific industrial application.

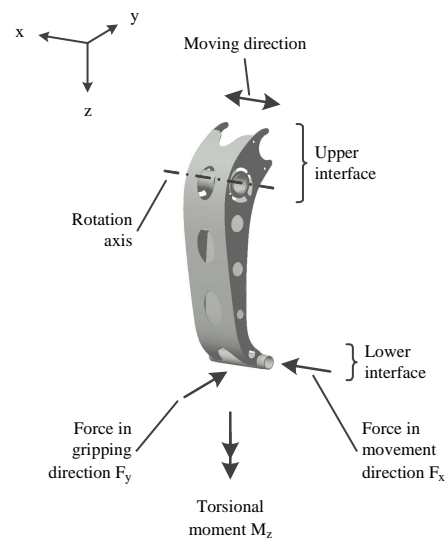


Fig. 1 Prescribed industrial load cases of the metal machine element

The industrial specifications are declared for each load case (Table 1) in particular, divided into horizontal (F_x , F_y) and torsion (M_z) load cases.

Table 1: Overview of the industrial load cases impinged on the lower component interface

Load case	Max. force or momentum	Max. movement
1 F_x	1000 N	3 mm
2 F_y	150 N	3 mm
3 M_z	50 Nm	0.25°

Based on the operating mode of the existing industrial system, cross-section borders for the new hybrid construction concept are identified. Subsequently, an outline including interfering contours of the prospective component dimensions in accordance with the available installation space is derived (Figure 2).

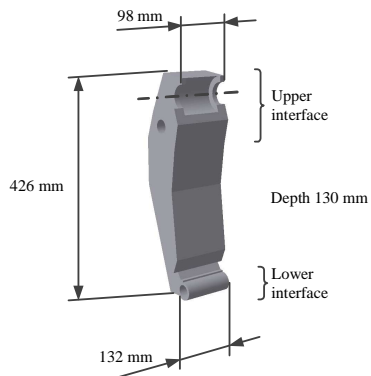


Fig. 2 Cross-section borders with derived outline for the design concept in accordance with the available installation space

In the upper interface of the basic CFRP structure, two load applications for linear guiding are to be provided. The guiding has to enable the rotational movement of the component. The lower interface contains a load application via two bushings in order to realise the attachment of additional mechanical gripper elements (not illustrated). In axial direction (moving direction x), the basic gripper structure is to be designed as slim as possible. In this manner, an extended feasible moving range of the kinematics is reached.

2.2 DESIGN CONCEPT

The construction method of the gripper arm has been developed in consideration of peripheral assemblies as well as fibre composite design guidelines. Due to industrial stiffness requirements, paired with a complex component geometry, prepreg lamination is declared as an appropriate manufacturing technology. The construction of the basic CFRP unit is realised through a closed, two-part shell structure, whereby the separation of the constituents is determined along the longitudinal axis of the component. The joining area is carried out as a circumferential adhesive flange with a single shear connection (Figure 3).

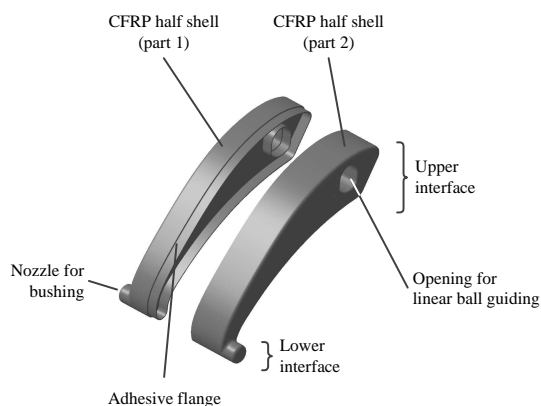


Fig. 3 CAD model of the CFRP half shells

The CFRP base body consists of a thermoset woven fabric prepreg (SGL, CE 8201-200-45S, epoxy-based resin). This material exhibits a low curing temperature range in addition to the high availability which is advantageous for the economical utilisation in machine and plant construction. The basic lay-up of the half shells presented in Figure 3 consists of six layers with a $\{\pm 45, 0/90, \pm 45\}_S$ stacking sequence. In the regions of the load application, eight layers with a $\{\pm 45, 0/90, \pm 45, 0/90\}_S$ stacking sequence are implemented. A two component epoxy paste adhesive is used (Huntsman, Araldite 2015) to bond the CFRP half shells and to integrate the bushings. In the upper interface of the CFRP body, the attachment of the linear ball guiding is realised via two stainless steel plates (1.4301).

Embedding blind rivet nuts (RIVKLE with SKG, size M5) on one side of the upper component interface manifests itself as a feasible connection technique. The opposite side includes blind bolt joints (Cherry Maxibolt CR7620S-06-03). Both joint types create a suitable connection of the basic CFRP structure with the stainless steel plates which are either permanently fixed by blind bolt joints to the structure or attached as removable (blind rivet nuts, screws).

The construction of the stainless steel plates allows a slight compensation of deviation in dimension of the component resulting from the manufacturing process.

In the lower interface, two metallic bushings are integrated into the nozzles via adhesive bond to enable the coupling of additional mechanical gripper elements. Figure 4 illustrates the positions of the selected joint types in the upper and lower interface of the final construction.

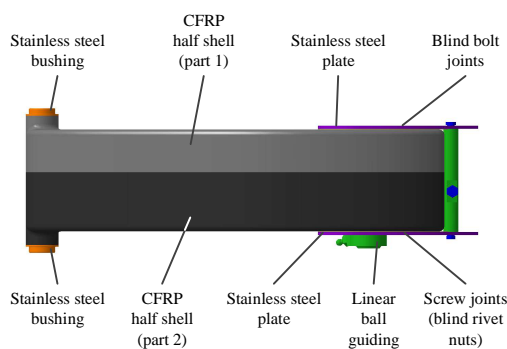


Fig. 4 Design concept for the CFRP metal gripper arm

In order to realise the determined design concept, an assembly device has been developed for the manufacturing procedure. The functionality of the device is based on the actual manufacturing steps of the gripper arm (Figure 5).

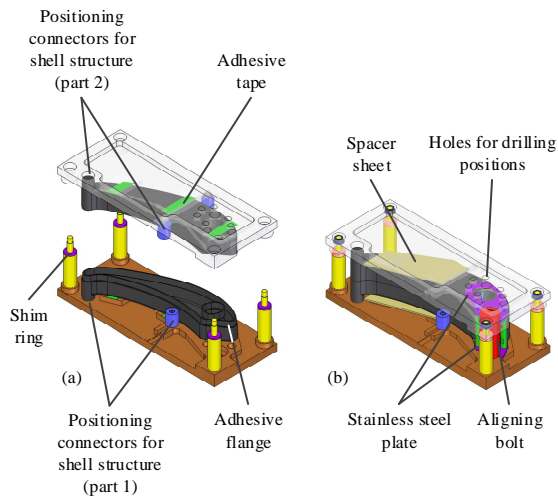


Fig. 5 CAD model of the assembly device for the manufacture of the CFRP metal hybrid gripper arm. Bonding procedure of the CFRP half shells (a), arrangement for drilling (b)

By the assignment of the assembly device, all individual manufacturing steps (alignment and gluing of the CFRP shells, positioning of the stainless steel plates, drilling process) can be accomplished ensuring compliance with the requested tolerances (geometric tolerances, dowel holes).

3 MANUFACTURING

The manufacturing process predominantly utilises the hand lay-up prepreg technology.

In order to obtain a high-quality CFRP surface, the moulds for the CFRP lamination process are produced with a negative shape of the final shell geometry.

A successful approach for the manufacture of the CFRP half shells was devised through various experiments. In the course of the studies, influencing variables of significance (e.g. cutting geometries, cutting sizes and buckle formations) were identified and evaluated regarding their relevance for the structural integrity of the component after the manufacturing process.

Figure 6 demonstrates the two negative moulds with draped prepreg material prior to the creation of the vacuum bag assembly.

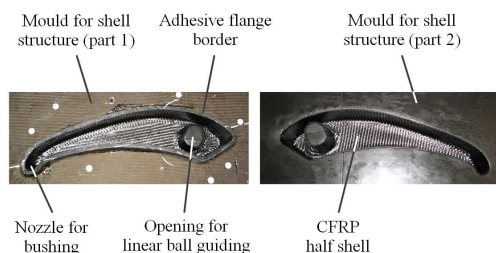


Fig. 6 Moulding tools for the manufacture of the CFRP prepreg half shells

The material utilised within the lamination process is a SGL CE 8201-200-45S woven (twill 2/2) epoxy-based prepreg. The nominal thickness of the prepreg is 0.19 mm.

Ahead of the lamination process, the prepreg feedstock was marked with the required geometry measures and tailored manually. In order to recognise related cuts as well as the lamination sequence easily, the cuts were assembled to kits.

Subsequent to the lamination process, the lay-up was cured in an autoclave.

The temperature program complied with the materials supplier's recommendations till the end of the first dwell time at 60 °C. The heating began at room temperature and was increased up to 60 °C at a rate of 2 °C per minute. The temperature was kept at 60 °C for 45 minutes over the entire dwell time. Afterwards, the set-up was heated from 60 °C to 100 °C at a rate of 2 °C per minute and was held at 100 °C for 100 minutes. Subsequently, the autoclave was cooled down at a rate of 2 °C per minute. A pressure of 0.7 MPa and a vacuum of 0.005 MPa were applied throughout the curing cycle.

Following the curing, demoulding and deburring of the CFRP half shells, the two parts were adhered and merged applying the assembly device.

With the assistance of this device, the tolerated drillings into the basic CFRP structure as well as the positioning of stainless steel plates could be realised successfully. The drilling process was executed on a 5-axis milling machine, which is appropriate for FRP chipping. Subsequently, metallic components (blind bolt joints, blind rivet nuts, screws and bushings) were integrated into the basic CFRP structure. For the implementation of the blind bolt joints and blind rivet nuts, industrial setting tools were utilised.

Figure 7 presents the manufactured CFRP metal hybrid gripper arm.

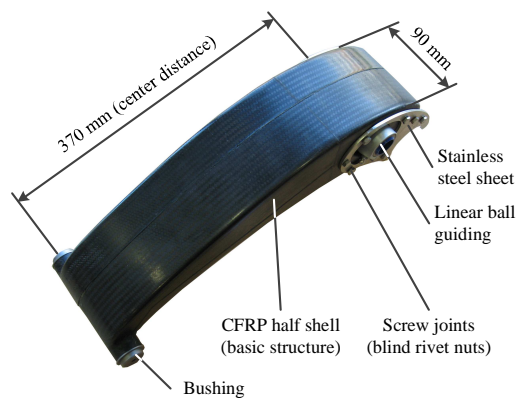


Fig. 7 Assembled CFRP metal hybrid gripper arm

4 NON-DESTRUCTIVE TESTING

Based on recently performed studies regarding optimal thermographic parameter sets resulting in a maximum failure contrast (signal noise ratio, SNR) as well as the optimal SNR in relation to the associated measurement time [10], the provided results are validated analysing three prototypes of the CFRP metal hybrid gripper arm. Thereby, the thermographic equipment listed in [10] is employed.

The application of previously documented parameter sets for the specific testing exercises in relation to the hybrid structural design of the gripper arm [10] led to a high-contrast, depth-dependent thermographic imaging of waviness and delaminations – especially in the area of the adhesive seam of the two CFRP half shells (Figure 8). These imperfections were caused by the manufacturing process and eventually result in a loss of structural stability of the component. The delamination sizes and depths were pre-referenced via ultrasonic inspection.

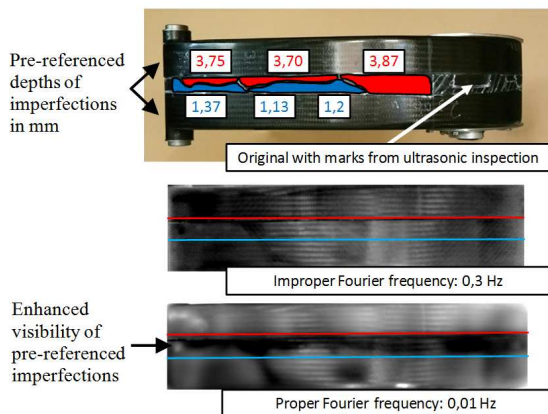


Fig. 8 Pre-referenced prototypes of the gripper arm via ultrasonic technique (above), utilisation of improper (middle) and proper thermographic parameter sets (below) in the course of NDT via optical thermography of the adhesive seam (area between red and blue line)

5 STATIC STRUCTURAL TEST

The industrial requirements regarding strength and stiffness of the recently developed CFRP metal hybrid structure specify three independent load cases of the component (Figure 1). The fulfilment of these industrial demands is explored by static testing of three CFRP metal hybrid gripper prototypes.

The maximum allowed movement of the lower interface (Figure 1) is documented in Table 1. Based on these specifications (predefined load cases), a novel test stand capable of exerting superimposed loads on the entire, three-dimensional structure (Figure 9) was developed.

A slide system coupled with the lower interface of the gripper manipulates test specimens in horizontal direction (x, y). Additionally, a torsion drive provides the functionality of twisting integrated test specimens in particular angles (z).

Each of the three gripper prototypes was prepared with three strain gauges (SG) in fibre direction (Figure 9): upper interface (3), lower interface (2) and adhesive seam (1). Thereby, the following strain gauges were utilised:

- HBM strain gauge (quarter bridge)
- Resistance: $350 \Omega \pm 0.30 \%$
- k-factor (gauge factor): $2.03 \pm 1.0 \%$
- Transverse sensitivity: 0.0 %
- Temperature compensation: Quarz with $\alpha = 0.5 [10^{-6} / K]$

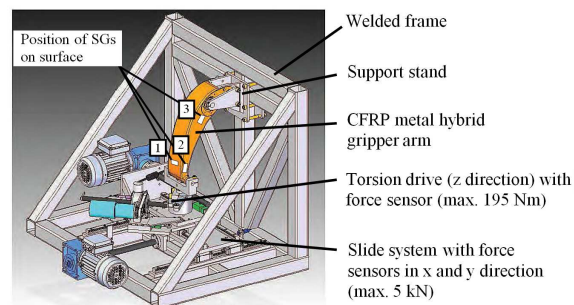


Fig. 9 Test stand construction and preparation of the prototypes with three strain gauges (SG)

The test stand provides the functionality of a flexible clamping mechanism for both, the metal and the CFRP metal hybrid gripper arm.

Figure 10 presents the integrated gripper prototype into the test stand. The connection of the component to the test stand is equivalent to the connection concept in terms of a realistic industrial utilisation.

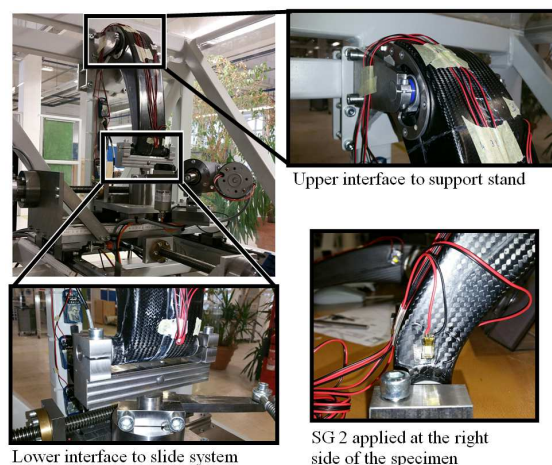


Fig. 10 Integrated prototype into test stand involving three strain gauges (SG)

Figure 11 visualises the exemplary force progression for load case 1 – F_x up to the maximum allowed force of 1000 N and above. At the maximum allowed force or momentum (Table 1), the structural deformation remains negligible.

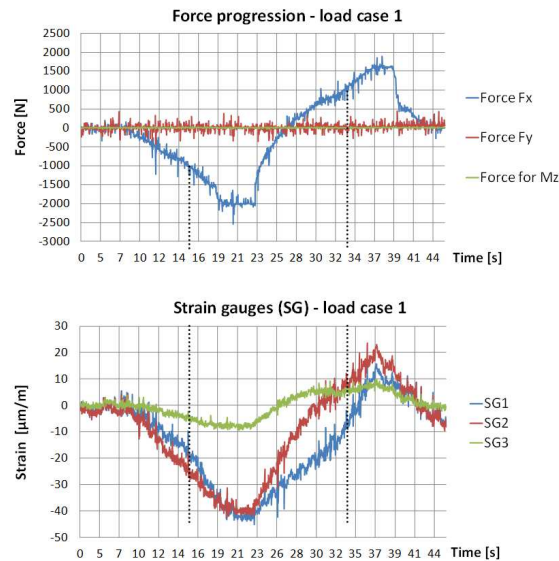


Fig. 11 Force progression diagram (above) and simultaneous strain measurement (below) for load case 1

Table 2 summarises the results of the static test. Evidently, the horizontal movement (load case 1 and 2) of the lower interface is considerably less than expected (range from 0.2 mm to 0.7 mm). Solely the torsion of the structure involving the maximum allowed momentum of 50 Nm (load case 3) results in a notably high rotation of the lower component interface from 0.7° to 1.3°.

The maximum applicable forces (F_x , F_y) from 4 kN to 5 kN and the maximum momentum (M_z) from 55 Nm to 65 Nm resulted in a translational movement of the lower interface from 1.8 mm to 5.8 mm (x, y) and from 2° to 5° (z).

Table 2: Results of the static test regarding the predefined load cases. Movement of the lower component interface

Load case	Movement at max. allowed force or momentum	Max. possible force or momentum	Movement at max. possible force or momentum
1	0.5±0.2 mm	4.5±0.5 kN	5.0±0.8 mm
2	0.3±0.1 mm	4.7±0.3 kN	2.4±0.6 mm
3	1.0°±0.3°	60±5 Nm	3.5±1.5°

The strain gauges characterise structural deformations of the component. These deformations were marginal in the course of introducing the predefined industrial load cases. The structural deformation varies in a range from 1.2 µm/m to 27.8 µm/m for F_x (1000 N) and F_y (150 N).

Torsion at 50 Nm leads to structural deformations from 21 µm/m to 225 µm/m with no signs of structural damage (e.g. cracking noises). Table 3 lists the results of the three strain gauges (SG) adhered on the gripper prototypes (Figure 9).

Table 3: Results of the strain gauges (SG) applied on the surface of the prototypes.

* Strain at maximum possible force or momentum

Load case	SG 1 [µm/m]	SG 2 [µm/m]	SG 3 [µm/m]
1	10.7±6.0	18.8±9.0	4±2.0
	39.3±33.3*	81.0±23.2*	33.2±23.7*
2	3.5±2.0	3.2±2.0	3.5±2.0
	80.1±33.3*	20.0±0.0*	27.5±8.5*
3	26±5	72±11	183±42
	88±36*	311±44*	680±128*

6 CONCLUSION

In consideration of industrial demands, a design concept for a CFRP metal gripper was engineered. A novel CFRP shell structure was manufactured utilising woven fabric prepreg and subsequent autoclave curing. Within the realisation process of the hybrid design concept, three different joining techniques were implemented (blind rivet nuts, blind bolt joints, bushings). Thereby, a specially designed assembly device was employed.

Subsequently, NDT via ultrasonic inspection and optical thermography revealed structural damages resulting from the manufacturing process, and consequently leading to a loss of structural stability of the component. In order to identify these damages, optimal parameter sets for active thermography were utilised.

The final static testing clarified the endurance of the hybrid structure in respect of predefined industrial load cases – except the torsion of the component (rotation from 0.7° to 1.3°, 0.25° allowed).

7 ACKNOWLEDGEMENT

The authors wish to thank the Bavarian Research Fund as well as the partners of the research cluster FORCiM3A (Bavarian research cooperation for CFRP/metal composite design in machine and plant construction) for supporting the investigation comprised in this research project both financially and technically. In addition, the authors would like to thank the GMA-Werkstoffprüfung GmbH Augsburg for the application of strain gauges as well as the referencing of the prototypes via ultrasonic inspection technique.

REFERENCES

- [1] Grimberg G., Vordermayer A.-M.: *Metallbauteile durch CFK-Komponenten substituieren*. Kunststoffe, 89 (1999): 91-94, 1999.
- [2] Eneyew E. D., Ramulu M.: *Experimental study of surface quality and damage when drilling unidirectional CFRP composites*. Department of Mechanical Engineering, University of Washington, Elsevier, Seattle, 2014.
- [3] Lang M., Drechsler K., Baeten A., Körner T.: *Bavarian Research Cooperation for CFRP/metal composite design in machine and plant construction (FORCiM3A)*. Bavarian research & innovation, Augsburg, 2011.
- [4] Jäger H., Hauke T.: *Carbonfasern und ihre Verbundwerkstoffe – Herstellungsprozesse, Anwendungen, Marktentwicklung*. Süddeutscher onpact, Munich, 2010.
- [5] Schumacher J., Bomas H., Zoch H. W.: *Failure behaviour of advanced seam structures for CFRP-aluminium connections*. Procedia Materials Science 2 (2013): 227-233, Elsevier, Bremen, 2013.
- [6] Camanho P. P., Fink A., Obst A., Pimenta S.: *Hybrid titanium-CFRP laminates for high-performance bolted joints*. Composites Part A 40 (2009): 1826-1837, Elsevier, 2009.
- [7] Fink A., Camanho P. P., Andrés J. M., Pfeiffer E., Obst A.: *Hybrid CFRP/titanium bolted joints: Performance assessment and application to a spacecraft payload adaptor*. Composites Science and Technology 70 (2010): 306-317, Elsevier, 2010.
- [8] Hart-Smith L. J.: *Adhesively bonded joints for fibrous composite structures*. McDonnell Duglass paper 7740, Long Beach, CA, 1986.
- [9] Schürmann H.: *Konstruieren mit Faser-Kunststoff-Verbunden*. 2nd edition. Springer, Berlin, 2007. ISBN: 978-3-540-72189-5.
- [10] Jelinek M., Schilp J., Reinhart G.: *Optimised Parameter Sets for Thermographic Inspection of CFRP Metal Hybrid Components*. In: CIRPe2015, Elsevier, Cranfield (UK), 2015.

ADHESION OF POLYIMIDE FOILS IN HYBRID LAMINATES WITH A THERMOPLASTIC MATRIX

Maik Trautmann^{1*}, Daisy Nestler¹, Guntram Wagner¹, Camilo Zopp², Lothar Kroll²

¹Technische Universität Chemnitz, Professorship of Composite Materials

²Technische Universität Chemnitz, Department of Lightweight Structures and Polymer Technology

ABSTRACT: Due to their high temperature resistance and suitability for applications in a vacuum, polyimide foils are an extremely good fit as a substrate material in thin-layer sensors. The three different polyimide foils integrated in hybrid laminates investigated during the course of this research paper are comprised of aluminium alloy (EN AW-6082) and various fibre-reinforced thermoplastics (polyamide 6 and thermoplastic polyurethane). The individual layers are joined by applying high temperatures and a pressure during the hot-pressing process. The adhesion of the infusible polyimide foil and the fused thermoplastics in hybrid laminates is investigated by means of shear-tension tests of lap joints, as well as by 3-point bending tests. The place and type of the malfunction is determined by means of confocal laser scanning microscopy of the fractured surface of the lap joint. The test reveals an excellent adhesion of the polyimide foil in a polyamide 6-based laminate. The thermoplastic polyurethane has poor adhesion to polyimide and tends to form an adhesion-reducing porous structure under unfavourable processing conditions.

KEYWORDS: Adhesion, thermoplastics, polyamide 6, thermoplastic polyurethane, polyimide, hybrid laminates,

1 INTRODUCTION

Hybrid Laminates comprised from metal and fibre-reinforced plastic are perfect materials for lightweight construction. These composite materials are damage-tolerant, extremely rigid and are characterised by an excellent fatigue behaviour [1]. If the composite materials are comprised of a thermoplastic matrix, such as polyamide 6 (PA6), they can be deformed and reshaped with the application of heat [2] and can be processed to form a flat semi-finished product on a large scale [3]. The discontinuous production of the laminates from PA6 is realised at approx. 280 °C in a hot-pressing process [4]. Further investigations have found that thermoplastic polyurethane (TPU) is also a suitable matrix material for the consolidation. It is characterised by improved flow behaviour, which is the reason for a very good impregnation of the reinforcing fibres being obtained. The mechanical properties are similar to the ones of the PA6. However the melting point of TPU is lower (Tab 1). One additional advantage gained from the utilisation of the material is the lower swelling strain, which can cause problems with PA6 [5].

The integration of thin-film sensors [6] for the structural health monitoring within the laminates required a good adhesion between the sensor substrate and the thermoplastic matrix of the fibre-reinforced plastic. Additionally the substrate has to meet various demands. It has to be thin and flexible and needs to enable a coating via the physical vapour deposition. During the production of the laminates, the sensor film is not to fuse. One of the materials fulfilling all these requirements is polyimide (PI). It can withstand high thermal stress and can also be applied in a vacuum [7].

Table 1: Properties of polyamide 6 [8], thermoplastic polyurethane [9] and polyimide [10] thin films

	PA6	TPU	PI
Melting Point / °C	220	190	None
Tensile modulus / GPa	2.5	2.1	2.5
Tensile strength / MPa	80	76	231

2 EXPERIMENTAL

2.1 MATERIALS

The examination was carried out on mechanically blasted, 4 mm thick aluminium sheets EN AW-

* Corresponding author: Technische Universität Chemnitz, Erfenschlager Straße 73, 09125 Chemnitz, +4937153138846, Maik.Trautmann@mb.tu-chemnitz.de

6082 T4. On a lap joint (25 mm x 12.5 mm) between the sheets 50 µm thick films of varying material savings are placed and subsequently thermally bonded (Fig. 1).

The thermoplastic foils utilised are a PA6 from the company mf-folien [8] and a TPU (Dureflex) [9] from Covestro/Epurex Films, which is currently still in development. The carrier material of the sensor, which is placed between the thermoplastic foils, is comprised of three different PI foils. Kapton HN (K_HN), which is provided by Dupont [10] and two different products from the company Dr. Dietrich Müller: Flexiso 16000 (FI16000) and Flexiso 16070 (FI16070). The films are cleaned with ethanol before being thermal pressed.

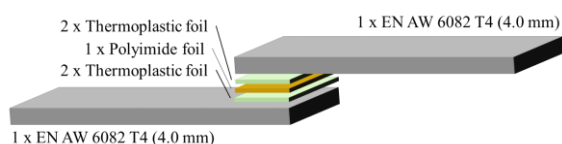


Fig. 1 Utilised material and the structure in a lap joint

In addition to the lap joint, the PI foils are also integrated in hybrid laminates with a fibre-reinforced thermoplastic matrix. The schematic structure of the laminate is showcased in Fig. 2. The aluminium alloy EN AW-6082 T4 is 0.5 mm thick and is mechanically blasted. Beneath the metal sheet two thermoplastic foils void of any reinforcement are placed, under which the PI foil is positioned. The core is comprised of four layers of unidirectionally carbon fibre-reinforced PA6/TPU. Each layer is 0.3 mm thick. These semi-finished products are produced in a pre-consolidated state with a fibre-volume content of approx. 60 % by company Cetex. The production takes place in a continuous production method (Fibre-Foil-Tape Unit).

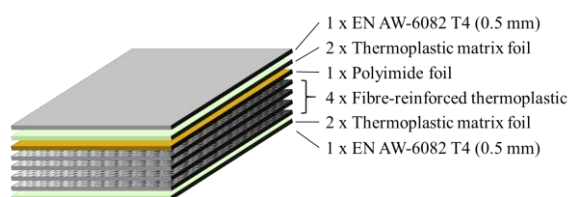


Fig. 2 Utilised material and the structure in hybrid laminate

2.2 PROCESSING

The lap joint is created under a pressure of 1.5 MPa. The downward pacing part of the aluminium is heated to 230 °C until the thermoplastic plastic melts. After two minutes, the cooling is realised by the utilisation of pressurised air. During

the solidification, the pressure is increased to 2.5 MPa.

The consolidation of the hybrid laminates is realised in a pressing tool with shearing edges in a hot press (Dr. Collin GmbH). The top and bottom part of the tool are heated to 275 °C for the PA6 and 230 °C for the TPU. The pressing power is set to 15 MPa.

2.3 METHODS

The samples of the lap joint are tested with a tensile shear test according to DIN EN 1465. The fracture surface of the two partners is examined fractrographically by means of a laser-scanning microscope (LSM). The hybrid laminates are cut into samples with a jet of water, in order to further examine them by means of a 3-point bending test. The flexural strength of these compounds are determined according to DIN EN ISO 14125. Additionally the interlaminar shear strength is determined according to DIN EN ISO 14130.

3 RESULTS

The results of the tensile shear strength (Fig. 3) showcase the fact that the PA6 samples without the PI foils have the highest bonding strength of 26.1 MPa. The integration of the PI foil K_HN results in a reduction of the rigidity of 12.5 % to 23.2 MPa. However the integration of the PI foil FI16000 leads to the further decrease of this value to 14.4 MPa. The compounds with FI16070 showed a medial strength of 21.3 MPa. The results of this foil show a large scattering.

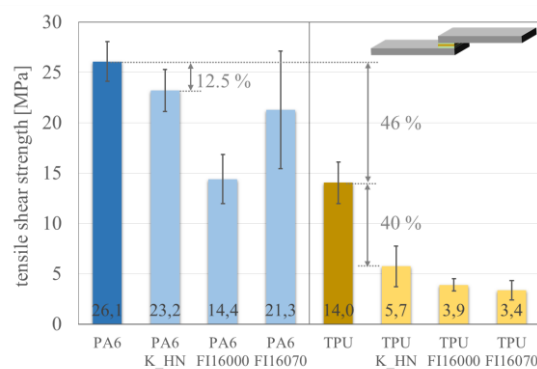


Fig. 3 Tensile shear strength of lap joints (12.5 mm x 25 mm) without (dark bars) and with integrated polyimide foils (bright bars)

The TPU samples are characterised by a tensile shear strength of 14 MPa, which is 46 % lower than the results of the PA6 samples. The additional integration of PI foils reduce this value even further by 40 %. The bonding strength is determined to be less than 6 MPa for all PI samples.

The LSM-examination of the fracture surface of the samples reveals the fact that the PA6 sticks to both sides of the blasted aluminium (Fig. 4a). On the other hand, the surface of the TPU sample showcases a porous structure of the thermoplastic film (Fig. 4b). The pores cover the whole surface and thickness of the foil, which significantly reduce the wetted surface. An image analysis by means of software determined the surface of the TPU layer to be approx. 50 %.

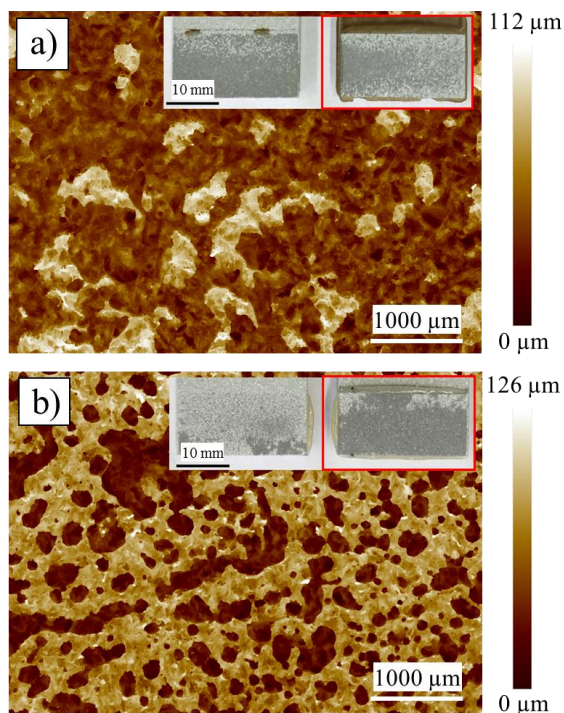


Fig. 4 Macroscopic image (small pictures) and LSM image (large pictures) of the fracture surface of the lap joint: (a) PA6 (bright) adhering residual to aluminium (dark), (b) porous TPU (bright) adhering to aluminium (dark)

The fractographic examination of the PI foil samples is shown exemplary with the type Kapton HN. In combination with PA6 an adhesive malfunction takes place on both sides. Remains of the PA6 can be found on the blasted aluminium (Fig. 5a), as well as on the PI foil (Fig. 5b). The fracture pattern of the TPU samples is characterised by a porous structure with a smooth surface (Fig. 5c). The PI foil side reveals only few TPU remains (Fig. 5d), which indicate a low adhesion.

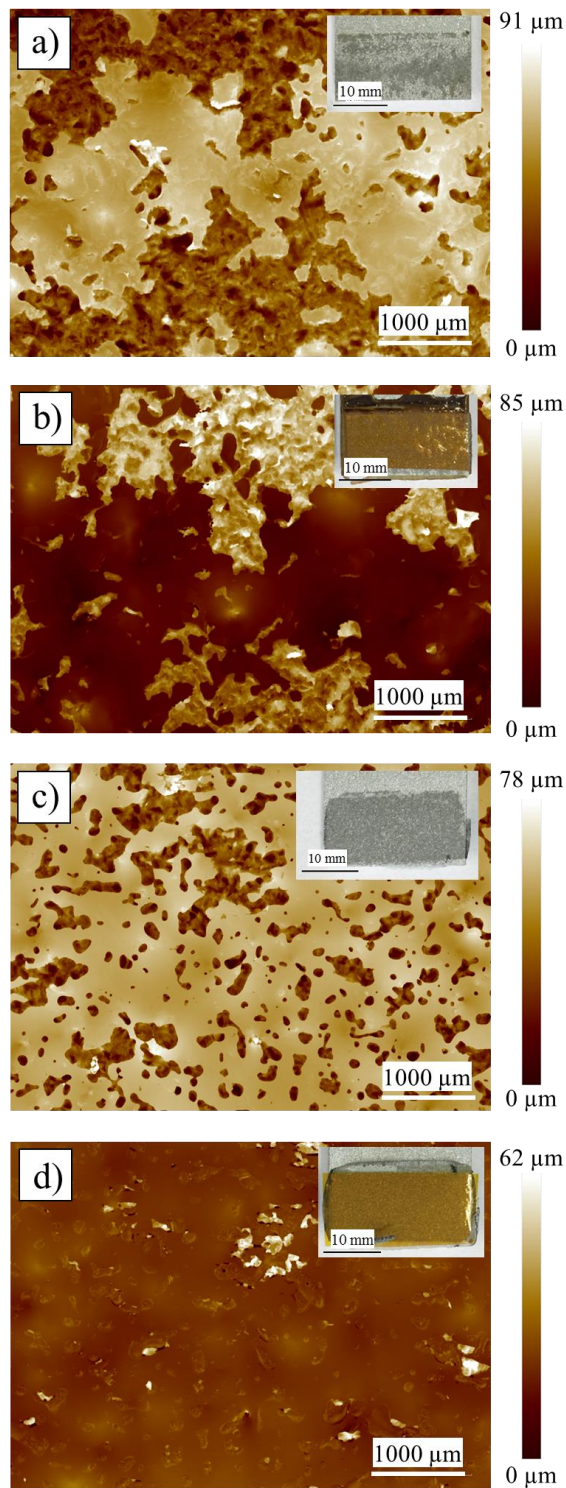


Fig. 5 Macroscopic image (small picture) and LSM image (large picture) of the fracture surfaces of lap joints: (a) PA6 (bright) adhering residual to aluminium (dark), (b) PA6 (bright) adhering residual to PI-foil Kapton HN (dark), (c) porous TPU (bright) adhering to Aluminium (dark) (d) little TPU (bright) adhering to Kapton HN (dark)

The results of the bending tests (Fig. 6) of the hybrid laminates show differences compared to the ones of the lap joints. The highest flexural strength was recorded for laminates with carbon fibre-reinforced TPU without a PI foil. The laminates with integrated PI foils delaminated after the hot pressing. There is no adhesion to be detected between the TPU and the PI foil. However, hybrid laminates from carbon fibre-reinforced PA6 with integrated PI foil show an excellent adhesion. The flexural strength only deviates marginal for samples without a PI foil.

The interlaminar shear strength of laminates with carbon fibre-reinforced PA6 is 44 MPa and is very similar to the one of the samples without a PI foil (43 MPa).

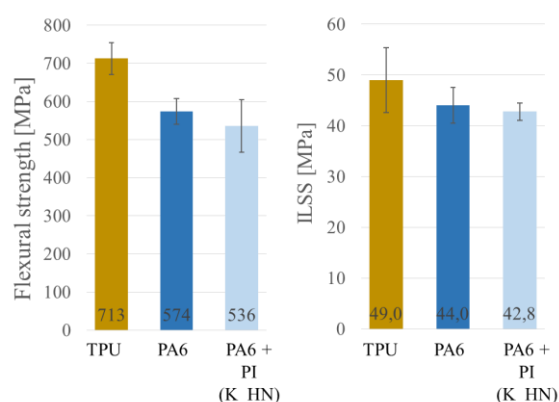


Fig. 6 Flexural strength and interlaminar shear strength (ILSS) of hybrid laminates with and without integrated PI-foil

4 DISCUSSION

The porous structure of the TPU film on the lap joints is most likely a result of the structural framework of the polymer. Thermoplastic polyurethane is comprised of a soft and a hard segment. During the heating process an opening of the binding takes place in the urethane segment, even below the actual melting point [11]. During the test gas was detected for all temperatures over 160 °C. The decomposition products cannot escape through the structure, which results in the development of bubbles. This is promoted further by the low bonding pressure. This formation of pores was not detected for laminates in the TPU. The significantly higher pressure suppresses the development of pores, which results in a homogeneous film.

The mechanical properties of the laminates with TPU are significantly favourable to those comprised of PA6, as described by Zopp et al. Apart from the improved consolidation [5] this could also be attributed to the structural change of the mole-

cules of the TPU. Some parts of the TPU polymer are thermally broken down beneath the actual processing temperature. This also results in a change of the mechanical properties. Due to the fact that the TPU utilised during this investigation being still in development, the actual composition is unknown.

The second interesting point is the adhesion of the thermoplastic regarding the PI. According to the literature, PA6 and TPU have similar surface energies. The lower adhesion of the TPU could be attributed to the significantly lower polar component of the surface energy, or it might be a result of the surface energy changing drastically during the development of the melt. It is a well-known fact that the soft segments have a significantly lower surface energy compared to the hard ones at 175 °C, depending on their type [11, 12].

The adhesion determined between the PA6 and PI is good. The application of PI in fibre-reinforced PA6 is therefore possible. On the other side the TPU is not characterised by a good adhesion regarding the PI film, which means it is not suitable as a bond to the sensor substrate in this state. A possibility to increase this adhesion is the corona treatment of the PI foil. Such an alteration increases the polar component of the surface energy and would promote the adhesion.

5 CONCLUSIONS

For the tensile shear test with different thermoplastic foils and PI foils it can be concluded, that:

- i. The adhesion of PA6 to Al is slightly better than that of PA6 to PI Kapton HN,
- ii. The TPU has porous structure by temperature of 230 °C and low pressing pressure
- iii. The TPU and PI have a poor adhesion

For the bending test of hybrid laminates it can be concluded, that:

- i. The TPU is characterised by an improved performance compared to the PA6 as a matrix material,
- ii. The TPU did have a porous structure under the higher pressure and the temperature of 230 °C during consolidation ,
- iii. There is no adhesion between the TPU and PI
- iv. The PI foils have a low influence on the mechanical properties in PA6

6 ACKNOWLEDGEMENT

This study was performed within the Federal Cluster of Excellence EXC 1075 “MERGE Technologies for Multifunctional Lightweight Structures”.

The authors gratefully acknowledge Mr. Dr. Daniel Wett and the financial support of the German Research Foundation (Deutsche Forschungsgemeinschaft, DFG).

REFERENCES

- [1] Vlot A, Gunnink J. W, editors. *Fibre Metal Laminates - An introduction*. Kluwer Academic Publishers; 2001
- [2] Kräusel. V., Graf, A., Nestler, D., Jung, H., Arnold, S., Wielage, B.: *Forming of new thermoplastic based fibre metal laminates* in The 3rd Global Conference on Materials Science and Engineering - Proceedings of Abstract, Shanghai, 2014, 40–46
- [3] Nestler, D.: *Beitrag zum Thema: Verbundwerkstoffe - Werkstoffverbunde - Status quo und Forschungsansätze*. Habilitation, TU Chemnitz, 2013, Universitätsverlag Chemnitz, 2014, ISBN 978-3-944640-12-9 und <http://nbn-resolving.de/urn:nbn:de:bsz:ch1-qucosa-134459>
- [4] Nestler, D., Jung, H., Arnold, S., Wielage, B., Wagner, G.: *Specific mechanical properties of new hybrid laminates with thermoplastic matrix and a variable metal component*, 20th International Conference on Composite Materials, 19–24 July 2015, Trans Tech Publications, Switzerland, Materials Science Forum Vols 825-826 (2015) 344–352, doi:10.4028/www.scientific.net/MSF.825-826.344.
- [5] Zopp, C., Stenbeck, W., Schultze, D. Kroll, L. Nendel, S., Nestler, D.: *Carbon fibre-reinforced thermoplastic semi-finished products for high-performance applications*. Proceedings of 2nd International MERGE Conference, Chemnitz, IMTC 2015 Lightweight Structures, Proceedings, Verlag wiss. Scripten, (2015)15–23, ISBN 978-3-95735-025-1
- [6] Wett, D., Nestler, D., Wagner, G., Wielage, B., Seider, T., Martin, J., Gessner, T., *Preparation of Ni-C Thin Films for Strain Sensor Applications in New Hybrid Laminates with Thermoplastic Matrix*. 20th International Conference on Composite Materials, 19–24 July 2015, Trans Tech Publications, Switzerland, Materials Science Forum Vols 825-826 (2015) 548-555, doi:10.4028/www.scientific.net/MSF.825-826.548
- [7] McClure, D. J.: *Polyimide film as a vacuum coating substrate*. *Soc. Vac. Coaters* (2010), 30–33.
- [8] Cast Polyamid-Folie PA6, mf-folien GmbH - Technical Datasheet, 2015
- [9] DUREFLEX® X2113 – Aromatic Thermoplastic Polyurethan Film – Development Product, 2015
- [10] DuPontT; Kapton® HN polyimide film technical data sheet, 2016
- [11] Pötschke, P., Pionteck, J., Stutz, H.: *Surface tension, interfacial tension, and morphology in blends of thermoplastic polyurethanes and polyolefins. Part I. Surface tension of melts of TPU model substances and polyolefins*, *Polymer*, 43 (2002) 25, 6965–6972
- [12] Wallheinke, K., Pötschke, P., Macosko, C. W. and Stutz, H.: *Coalescence in blends of thermoplastic polyurethane with polyolefins*. *Polym Eng Sci*, (1999) 39, 1022–1034.

CHAPTER 5:

MACHINING AND PROCESSING

JOINING AND FORMING OF HYBRID ASSEMBLED COMPOSITES WITH SENSORY FUNCTION

Alexander Graf^{1*}, Verena Kräusel¹, Dirk Landgrebe¹,
Ricardo Decker², Lothar Kroll²

¹ Professorship for Forming and Joining, TU Chemnitz

² Department of Lightweight Structures and Polymer Technology, TU Chemnitz

ABSTRACT: The joining of piezo-electric elements in a plastic matrix with a metal sheet enables direct integration of functions into formed sheet metal components. When using monolithic piezo-ceramics the manual steps for joining and contacting are very complex. However, if a thermoplastic material is filled with a high fraction of a piezo-ceramic powder and continuously joined with thin metal sheets, it opens new application fields for this hybrid composite material. In this paper, the research results of the various process steps joining and forming are presented. In a discontinuous joining experiment the attainable bonding strength can be determined in dependence of essential parameters, such as temperature and pressure, and the thermoplastic matrix used. The forming characteristics of the composite materials are determined by V-bending and deep drawing of cups. To avoid failure phenomena, the arrangement of the electrode and the form temperature are varied.

KEYWORDS: Hybrid assembled composite, Forming, Adhesive strength, Piezo-electric polymer compound

1 INTRODUCTION

Plastic/metal-based composites and their production technologies have been under intensive scientific investigation for many years. The development of manufacturing technologies for active and semi-active polymer-based systems with mechatronic and electrical properties is still being researched. Such function-oriented structures have great potential for functionalised lightweight components with energy harvesting, structural health monitoring or vibration and noise damping [1].

A functionalised, piezo-electric plastic compound based on thermoplastic polymers filled with lead zirconate titanate (PZT) will continuously be joined with semi-finished metal sheets by merging the extrusion-moulding technology and the roll-press technology. Thus, these intelligent hybrid assembled composites (HAC) can be manufactured more efficiently, due to the decreased production times and costs in comparison to classic sequential technologies. In addition, the process allows for the first time the in-line large series production of a PZT-based transducer system without the use of energy-intensive sintering processes [2].

The semi-finished HAC is suitable for the integration into hybrid metal/fibre-reinforced plastic (FRP) structures or for further processing in different forming processes to produce functionalised structural parts.

2 INTEGRATION OF PIEZO-ELECTRIC SENSORS IN SHEET METAL PARTS

The number of electrical devices and sensors in automobiles is constantly increasing. To reach the goal of weight reduction the direct integration of functions into components is necessary. One possibility is to print the layer on the sheet metal. Therefore, the forming behaviour of printed strain gages was analysed by tensile tests and determined the forming limited curves [3]. Another alternative is to integrate piezo-elements by micro injection moulding [4]. Therefore, the initial stresses with different combinations were analysed in finite elements calculation. In [5], microcavities were manufactured by forming and the piezo-ceramic fibres were assembled as well as joined with the sheet metal. The forming behaviour was analysed by deep drawing and the signal quality was determined before and after forming.

* Corresponding author: A. Graf, Technische Universität Chemnitz, Reichenhainer Straße 70, D-09126 Chemnitz, Phone: +49 (0)371 531-39938, Fax: +49 (0)371 531-839938, alexander.graf@mb.tu-chemnitz.de

3 PROZESS STEPS OF HAC MANUFACTURING

3.1 DESCRIPTION OF THE PIEZO-COMPOUND

3.1.1 MATERIAL COMPOSITION

The functional component of the HAC consists of a thermoplastic polymer highly filled with a piezo-ceramic powder. The polymer matrix dominates the thermoplastic processability and the ceramic filler generates the piezo-electric effect of the compound. The PZT powder NCE 55 with a particle size between 1 μm and 3 μm (Noliac A/S, Kvistgaard, Denmark) was used as piezo-electric filler.

A high piezo-electric effect requires a large mass fraction of PZT. The maximum filler content is limited by the processability of the compound and is about 70 up to 80 wt% [2, 6] in relation to the polymer matrix used. Due to the large differences in permittivity between the piezo-ceramic particles and the thermoplastic matrix material, an applied electrical field, e. g. for poling, is concentrated in the polymeric matrix [7]. Therefore, a small amount of carbon nano-tubes (CNT) is admixed to the compound to improve its electrical and electro-mechanical properties [8]. Thermoplastic masterbatches of different polymers with CNT contents from 10 wt% up to 20 wt% (Plasticyl, Nanocyl S. A., Sambreville, Belgium) were used as conductive filler. The electrical resistance of the matrix material is clearly lowered even at small amounts of CNT [9]. This leads to higher electrical fields in the PZT particles and a larger permittivity of the compound. However, too large CNT concentrations greatly reduce the electric breakdown strength of the matrix system, and the polarisation voltage, therefore, has to be reduced. The lower voltage leads to poor polarisability and less remanent polarisation which reduces the piezo-electric performance of the compound.

Based on previous experiments [6], for the following investigations filler contents of 70 wt% for PZT and 0.5 wt% for CNT were chosen as a compromise between good processability, high piezo-electric effects and optimised electrical properties. In addition, compounds with 60 wt% PZT and 0.5 wt% CNT were made to determine the adhesive strength between the compound and the aluminium electrodes in dependence of the filler content.

In order to investigate the adhesive strength depending on the matrix system five different thermoplastic polymers were used:

- Polypropylene (PP) Moplen HP 500V (LyondellBasell, Rotterdam, Netherlands)
- Polyamide (PA 6) Ultramid B3L (BASF SE, Ludwigshafen, Germany)
- Polycarbonate (PC) Calibre 603-3 (Trinseo LLC, Berwyn, PA USA)
- Polyethylene terephthalate (PET) Skypet BR8040 (SK Chemicals, Seoul South Korea)
- Polybutylene terephthalate (PBT) Ultradur B4500 (BASF SE)

3.1.2 SAMPLE PREPARATION

The piezo-active compounds were made by blending the fillers with the different matrix polymers in a HAAKE MiniLab II micro compounder (Thermo Fisher Scientific Inc., Waltham, MA USA). The materials were mixed with co-rotating screws for 8 minutes. The processing parameters for the different polymers are listed in Table 1.

Table 1: Processing parameters for compounding

Matrix polymer	Melt temperature [°C]	Screw rotation speed [min ⁻¹]
PP	230	90
PA 6	250	90
PC	300	110
PET	280	100
PBT	260	100

Test samples with a diameter of 28 mm and a thickness of 0.5 mm were made from the different polymers and compounds using a HAAKE MiniJet II micro injection moulding machine (Thermo Fisher Scientific Inc.). The processing parameters of the micro injection moulding are mentioned in Table 2.

Table 2: Processing parameters for micro injection moulding

Matrix polymer	Melt temperature [°C]	Tool temperature [°C]	Injection pressure [bar]
PP	230	60	750
PA 6	260	150	1000
PC	300	170	1150
PET	280	140	800
PBT	260	140	900

3.2 JOINING PROCEDURE

The joining tool for producing the HAC samples (40 mm x 40 mm) is shown in Fig. 1. Before joining, an Al-sheet (EN AW-6082 T4, sheet thickness: 0.5 mm) and a round compound test sample (diameter: 28 mm) were placed in the mould. After the first joining the copper stripes (SE-Cu, thickness: 0.035 mm) were placed on the test samples and joined together in a second process.

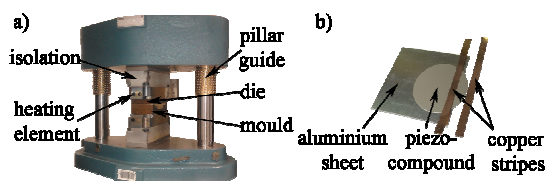


Fig. 1 a) Test-setup and b) Single parts for joining a HAC sample

The single process steps are shown in Fig. 2. At first the tool temperature is increased up to the melting temperature of the polymer. The tool was closed after the test samples were placed in the heated mould. In the heating stage the compound test samples are molten under a constant low pressure of 1.25 bar. In the next stage the joining started with a pressure of 12.5 bar for 180 s. Finally, the tool was cooled down to 80 °C and the joined test sample was removed.

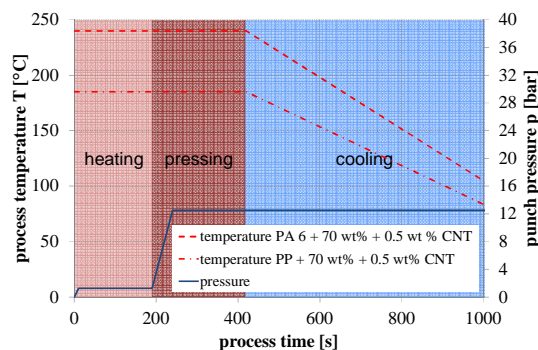


Fig. 2 Process steps of joining piezo-compounds with aluminium sheets [2, modified]

For the determination of the interlaminar shear strength two Al-sheets were joined with a polymer core and cut into samples with a size of 20 mm x 10 mm (Fig. 3). The joining parameters for the different polymers are listed in Table 3. The parameters pressure (12.5 bar) and the holding time (3 min) were constant, only the parameter temperature varied in dependency of the polymer. In contrast, the joining temperature for the filled polymers increased with increasing filling content.

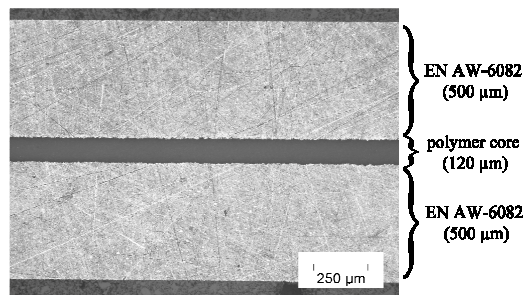


Fig. 3 Microsection of ILSS sample [2]

Table 3: Joining parameters for unfilled and filled polymers

	Polymer/ compound formulation	Joining temperature [°C]
unfilled	PP	165
	PA 6	200
	PC	280
	PET	250
	PBT	250
filled	PP + 60 wt% PZT + 0.5 wt% CNT	175
	PP + 70 wt% PZT + 0.5 wt% CNT	185
	PA 6 + 60 wt% PZT + 0.5 wt% CNT	220
	PA 6 + 70 wt% PZT + 0.5 wt% CNT	240

The test samples for V-bending and deep drawing were also produced with the test setup in Fig. 1. Therefore, the piezo-compound and two copper stripes were joined in the centre of sheet stripes (150 mm x 20 mm) for V-bending and of a circular blank (D = 100 mm) for deep drawing (Fig. 4).

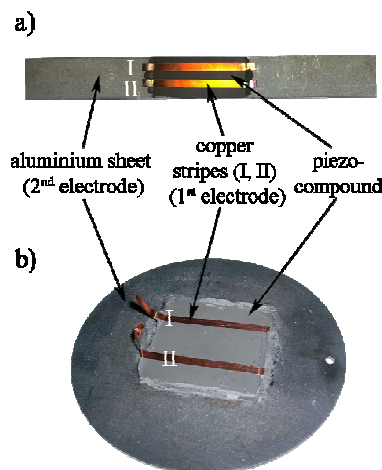


Fig. 4 Joined forming samples for a) V-bending and b) Deep drawing

4 MECHANICAL PROPERTIES OF THE HAC

4.1 INTERLAMINAR SHEAR STRENGTH OF HAC WITH UNFILLED POLYMERS

The interlaminar shear strength (ILSS) of the HAC was determined by the three-point bending test based on DIN EN ISO 14130.

Almost no adhesion between the polymers and the untreated aluminium sheets is apparent. In contrast, the surface treatment of the metal component by means of sandblasting enables positive locking between the metal and the plastic component due to the formation of micro cavities. In the following experiments a grain size of 600 μm was used, whereby a surface roughness of $R_a = 6.96 \mu\text{m}$ is generated. After this treatment, the ILSS is measured from about 7 MPa with PP up to over 33 MPa with PC. The best adhesion shows polycarbonate, where no delamination of the samples occurs. The ILSS of the HAC in dependence of the different thermoplastics used is shown in Fig. 5.

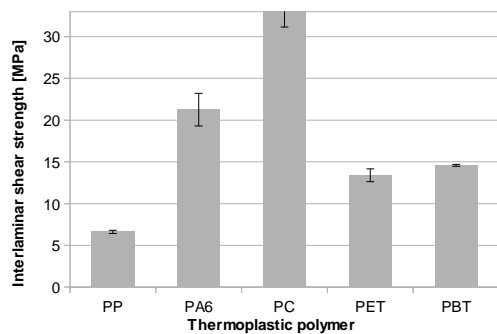


Fig. 5 Interlaminar shear strength of the HAC with unfilled polymers and aluminium sheets

4.2 INTERLAMINAR SHEAR STRENGTH OF HAC WITH PIEZO-ACTIVE COMPOUNDS

The ILSS is not only affected by the surface treatment of the metal component but also by the filler content of the thermoplastic component. In PC, PET and PBT the piezo-ceramic powder leads to strong embrittlement of the compound. As a result, there are only low adhesions to the aluminium sheets. In contrast, the ILSS of the HAC with PP rises clearly with increasing mass fractions of PZT. The increase is up to 115 % at 70 wt% PZT and 0.5 wt% CNT. With the use of PA 6 as matrix material the ILSS decreases by 37 % at 60 wt% PZT and 0.5 wt% CNT. However, the increasing PZT fraction up to 70 wt% leads to an increase of the ILSS by approx. 64 %. These results are shown in Fig. 6.

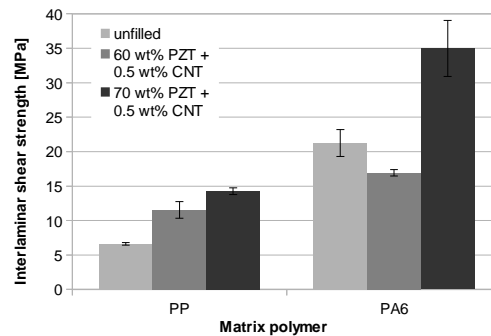


Fig. 6 Interlaminar shear strength of the HAC in dependence of the filler content of the compound

4.3 CONCLUSION

In general polar thermoplastics show higher interlaminar shear strengths than nonpolar thermoplastics. The polar character enables adhesive bonds in addition to positive locking between the metal and the plastic component of the HAC. However, the admixing of PZT powder to PC, PET and PBT leads to worse adhesive strength due to the strong embrittlement of the compound as a result of interactions between the matrix polymer and the ceramic particles. In contrast, the use of the piezo-compounds based on PP and PA 6 with the electrically optimal filler content of 70 wt% PZT and 0.5 wt% CNT results in an increase of the ILSS of the HAC. Furthermore, the drop of the adhesive strength at 60 wt% PZT in PA 6 is also striking. These are probably the results of electrostatic interactions between the electric dipoles in PZT particles and the aluminium sheets as well as additional interactions between the ceramic and the polymer in case of PA 6. The reasons of these interrelations require further investigations.

The low adhesive strength between PC, PET or PBT filled with PZT and CNT and aluminium does not allow the production of active plastic/metal-based composites. For manufacturing the HAC it is only possible to use the piezo-active compounds based on PP or PA 6. Compared to PP, the PA 6 matrix provides a higher ILSS, but it requires more complex processing due to its hygroscopic behaviour and thermal sensitivity.

5 FORMING BEHAVIOUR OF THE HAC

5.1 V-BENDING

The tool set for the V-bending consists of a heated die and a heated V-punch. For the investigation of the forming behaviour of the HAC the piezo-compound was placed on both the punch and the die side. The second investigated parameter was the forming temperature which strongly depends

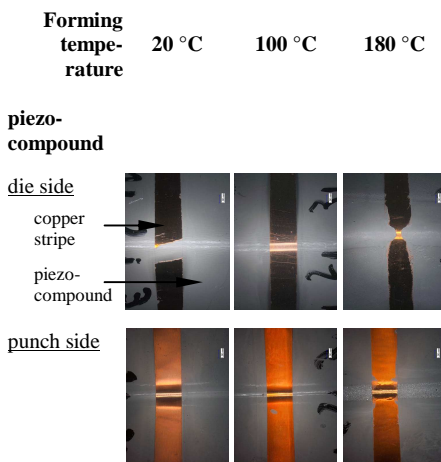
on the polymer matrix of the piezo-compound. This piezo-compound consisted either of PP with 70 wt% + 0.5 wt% CNT or of PA 6 with 70 wt% + 0.5 wt% CNT. The bending radius of 1 mm was constant in all experiments. All parameters are summarised in Table 4.

Table 4: Parameters for V-bending

Compound	Placement compound	Forming temperature	Bending radius
PP + 70 wt% PZT + 0.5 wt% CNT	die and punch side	20 °C; 100 °C; 180 °C	1 mm
PA 6 + 70 wt% PZT + 0.5 wt% CNT	die and punch side	20 °C; 150 °C; 200 °C; 220 °C	1 mm

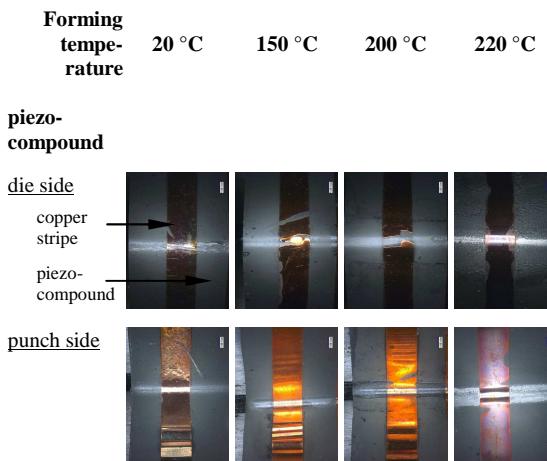
The bended samples were optically investigated for cracks and delamination between the copper and the piezo-compound or between the piezo-compound and the Al-sheet. In Table 5 the results for the V-bending of the samples with PP + 70 wt% PZT + 0.5 wt% CNT are shown. It is visible that the copper stripe cracks at room temperature when the piezo-compound is placed on the die side of the V-bending tool. At 100 °C no cracks are visible in the copper stripe. Hence, the polymer matrix PP is softened and the copper stripes are pushed into the compound. But the high filled piezo-compound is brittle and there are little cracks visible at bending radius. When increasing the temperature up to 180 °C the compound is completely molten and no cracks are visible. Furthermore, the molten compound flows over the copper stripes. On the other hand no cracks are visible in the copper stripe by placing the compound on the punch side. In this constellation the dominating stress is pressure. Therefore, a delamination between the copper and the piezo-compound occurred at room temperature (not visible in Table 5:). With rising forming temperatures the copper stripes are pressed into the softened piezo-compound and no delamination results. It can be seen in the bending radius that the piezo-compound is pressed out at a forming temperature of 180 °C. As a result it can be noted that either the forming temperature was too high or the pressure at the end of the V-bending was too large. Further investigations are planned to obtain the optimal forming parameters.

Table 5: V-bending results for PP + 70 wt% PZT + 0.5 wt% CNT



In Table 6 the results for the V-bending with PA 6 + 70 wt% PZT + 0.5 wt% CNT are shown. By placing the piezo-compound at the die side of the V-bending tool cracks occurred at up to 200 °C. At 220 °C no cracks are visible. By placing the compound on the punch side delamination between the copper and the piezo-compound is the dominating failure phenomenon. At a forming temperature above 220 °C no delamination is visible. To obtain the thickness decrease before and after forming the samples with PA 6 + 70 wt% PZT + 0.5 wt% CNT were measured. The result is shown in Fig. 7. The diagram displays an exponential decrease of the thickness with increasing forming temperature. There are also no differences between placing the piezo-compound on the die side or on the punch side of the bending tool. From the results of forming a HAC with PA 6 + 70 wt% PZT + 0.5 wt% CNT it can be derived that the optimal forming temperature is about 220 °C.

Table 6: V-bending results for PA 6 + 70 wt% PZT + 0.5 wt% CNT



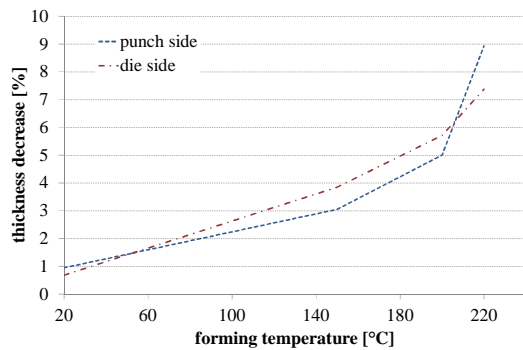


Fig. 7 measured thickness decrease of bended HAC with PA 6 + 70 wt% PZT + 0.5 wt% CNT

5.2 DEEP DRAWING

To form a round cup of the joined HAC samples a tool with a punch diameter of 50 mm and a drawing depth of 30 mm was used. The forming temperature was room temperature (20 °C) and the piezo-compound was placed on both the punch side and on the die side of the blank.

By placing the piezo-compound on the die side the compound delaminates at drawing edge. On the other hand, the samples can be drawn without failure by placing the compound on the punch side of the cup (Fig. 8). With this drawn part the signal quality was measured and the results are mentioned in [2].

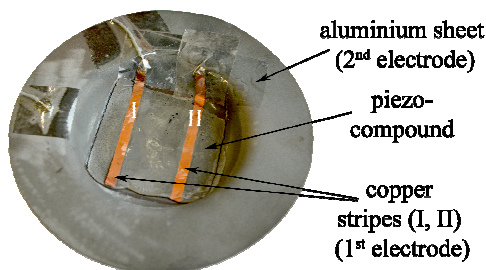


Fig. 8 Formed cup by deep drawing with PA 6 + 70 wt% PZT + 0.5 wt% CNT on the punch side [2]

6 SUMMARY AND OUTLOOK

To join the HAC, it is only possible to use PA 6 or PP as matrix material for the piezo-active compound. The PA 6 matrix provides higher adhesive strength to aluminium than PP, but PP allows simpler processing because of lower thermal sensitivity and no hygroscopic behaviour. At high filler levels (70 wt% PZT and 0.5 wt% CNT), the ILSS of the HAC increases presumably as a result of electrostatic interactions between the ceramic particles and the aluminium sheet. Other thermoplas-

tics like PC, PET or PBT show a strong embrittlement through the admixing of PZT. Thus, the joining with aluminium sheets is impossible.

The investigation of the V-bending of the HAC shows that the formability improves with an increase in forming temperature because the copper stripes are pushed into the compound. But if the temperature is too high, the compound flows over the copper stripes or is pressed out of the samples. The measured thickness of the formed samples shows an exponential decrease of the thickness with rising forming temperature for the HAC with PA 6 + 70 wt% PZT + 0.5 wt% CNT. The optimal forming temperature for a HAC with PA 6 + 70 wt% PZT + 0.5 wt% CNT is about 220 °C. Furthermore, the deep drawing is possible by placing the compound on the punch side. Further investigations are planned for HAC with PA 6 + 70 wt% PZT + 0.5 wt% CNT to find the optimal forming behaviour.

By merging extrusion-moulding technology and rolling technology it is possible to manufacture the HAC more efficiently. In comparison to classic manufacturing with sequential technologies, a combined process decreases the production times and costs. Currently the process parameters in terms of joining and forming are obtained from the investigations with the separate samples and as a vision a continuous process is planned. To enable positive interlocking between aluminium and the piezo-compound, the sheet metal surface is profiled by rolling before heating and joining with the extruded polymer film and the copper electrodes. Afterwards, the HAC is polarized and cut into blanks as semi-finished products for forming functionalised hybrid plastic/metal-based structures with sensory functions.

7 ACKNOWLEDGEMENT

We gratefully acknowledge the cooperation of our project partners and the financial support of the DFG (Deutsche Forschungsgemeinschaft) within the Collaborative Research Center/Transregio 39 “PT-PIESA” and the Federal Cluster of Excellence EXC 1075 “MERGE”.

REFERENCES

- [1] Schulze R., Heinrich M., Nossol P., Forke R., Sborikas M., Tsapkolenko A., Billep D., Wegener M., Kroll L., Gessner T.: *Piezoelectric P(VDF-TrFE) Transducers Assembled with Micro Injection Molded Polymers*. Sensors and Actuators A: Physical, 208:159–165, 2014.

- [2] Kräusel V., Graf A., Heinrich M., Decker R., Caspar M., Kroll L., Hardt W., Göschel A.: *Development of hybrid assembled composites with sensory function*. CIRP Annals - Manufacturing Technology, 64(1): 25–28, 2015.
- [3] Ibis M., Groche P.: *Forming Limit Curves of Electrically Conductive Layers Printed on Sheet Metal Surfaces*. Procedia Engineering, 81: 779–786, 2014.
- [4] Kroll L., Walther M., Nendel W., Heinrich M., Tröltzsch J.: *Initial Stress Behaviour of Micro Injection-Moulded Devices with Integrated Piezo-Fibre Composites*. In: Integrated Systems, Design and Technology 2010. Springer-Verlag Berlin Heidelberg, 2011.
- [5] Müller M., Müller B., Hensel S., Nestler M., Jahn S. F., Wittstock V., Schubert A., Drossel W.-G.: *Structural Integration of PZT Fibers in Deep Drawn Sheet Metal for Material-integrated Sensing and Actuation*. Procedia Technology, 15: 659–668, 2014.
- [6] Decker R., Heinrich M., Tröltzsch J., Rhein S., Gebhardt S., Michaelis A., Kroll L.: *Development and characterization of piezo-active polypropylene compounds filled with PZT and CNT*. In: 5th Scientific Symposium CRC/Transregio 39, 59-64, 2015.
- [7] Goncharenko A. V., Lozovski V. Z., Venger E. F.: *Lichtenecker's equation: applicability and limitations*. Optics Communications, 174:19-32, 2000.
- [8] Ounais Z., Park C., Harrison J., Lillehei P.: *Evidence of Piezoelectricity in SWNT-Polyimide and SWNT-PZT-Polyimide Composites*. Journal of Thermoplastic Composite Materials, 21(5): 393-409, 2008.
- [9] Heinrich M., Decker R., Schaufuß J., Tröltzsch J., Mehner J., Kroll L.: *Electrical contact properties of micro-injection molded Polypropylene/CNT/CB-composites on metallic electrodes*. Advanced Material Research, 1103: 77-83, 2015.

EFFICIENT AND APPROPRIATE LASERPROCESSING OF HIGH-PERFORMANCE MATERIAL

Fürst, A.^{1*}, Hipp, D.¹, Klotzbach, A.², Hauptmann, J.², Wetzig, A.², Beyer, E.^{1,2}

¹Institut für Fertigungstechnik, TU Dresden

²Fraunhofer Institut für Werkstofftechnik, Dresden

ABSTRACT: Near net shape preforms, minimal material consumption as well as tailored processes are required to increase the acceptance of fiber reinforced polymers (FRP) in industry. For this purpose, the application of hybrid yarns facilitate short flow paths of the matrix systems and thus comparatively low impregnation and consolidation pressures. Furthermore future applications combine the advantages of metal structures with FRP. This should be accompanied by appropriate, fast and flexible processes. The remote-laser-ablation expands the area of possible kinds of processing strategies, so that the laser has the potential to be a tool for the future. But the development therefore is accompanied with the understanding of the interaction between tool and material. Laser cutting of FRP is an ambitious process because of the inhomogeneity of both, the reinforcement material and the polymer matrix material. The processing of metal structures leads to increased demands of the laser-system-technology, due to the high reflectivity of the material. This paper shows an experimental set up for combining beam radiation with wavelengths of 1.07 μm and 10.6 μm . Furthermore, the paper will give an outlook on future applications regarding fiber-metal laminates.

KEYWORDS: laser processing, glass- fiber- hybrid yarn, CFRP, fiber-metal laminates

1 INTRODUCTION

Laser processing, as a force and wear free tool can face limitations in milling and drilling [1]. Limitations are governed by the non-homogenous structure and the highly abrasive nature of the reinforcement material. Both drilling and water jet cutting are force inducing cutting processes that can lead to delaminations [2], [3]. Several investigations have shown that remote-laser-ablation is suitable for processing on fiber reinforced polymers with reduced heat affected zones and with feed rates comparable to milling and water jet cutting [4]–[6]. The development of remote-laser-ablation is tied with the knowledge of material properties under the influence of laser beam radiation. In particular, glass and carbon fiber reinforced materials (GFRP, CFRP) are characterized by inhomogeneity in heat conductivity and sublimation temperature for matrix and fiber material. This is a result of high fiber sublimation temperatures (glass fiber $\approx 2300^\circ\text{C}$, carbon fiber $\approx 3600^\circ\text{C}$) on one hand and low decomposition temperatures of the matrix material and the coating of the fibers (300 – 400 $^\circ\text{C}$) on the other. Furthermore, the different absorption behavior of the fiber and the matrix material is an aggravating factor. Prior investigations have shown a drastic difference of absorption behavior between the reinforcement

material and the polymer matrix [7]. Accordingly high intensities are needed to evaporate the reinforcement material. Therefore the ability to focus the beam radiation is a major key for processing. When processing fiber- metal laminates, the metal part is a third part, that has to be considered. Here, also high intensities are needed to melt and evaporate the material [8]. The absorption behavior of the material, as well as the ability to focus the beam are important to consider when there are significant differences in the thermal and optical properties of both materials. Therefore the combination of two laser beams with wavelengths of 1.07 μm and 10.6 μm is a promising approach resulting in a beam combination device that has been developed and implemented into the laboratory scale.

2 LABORATORY SET UP FOR LASER PROCESSING

A laboratory setup for the wavelength combination of a CO₂ – slab laser (3 kW cw) and a Nd:YAG solid-state-laser (SSL) (1,8 kW cw), based on a remote- scanning system has been developed [9]. The wavelengths are combined into a single focused beam, that is deflected by a fast scanning system based on galvanometric driven tilting mirrors.

*corresponding author: Andreas Fürst, Fraunhofer IWS Dresden, Winterbergstraße 28, 01277 Dresden, 0351 833 913544, Fax -3300, andreas.fuerst@iws.fraunhofer.de

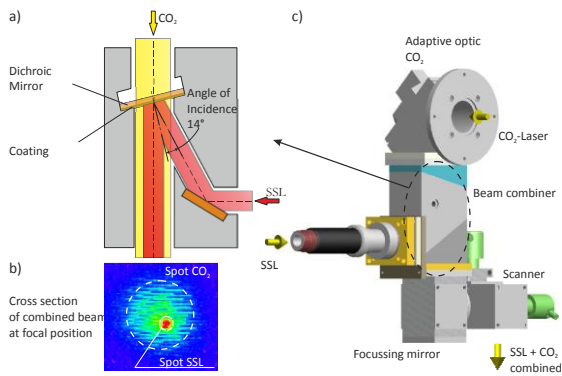


Fig. 1 (a) Cross section of laboratory set up, (b) Cross section of measured intensity distribution, (c) Multiwavelength equipment

This leads to high feed rates and minimized heat affected zones, which is expected due to the shorter interaction time between the laser and the material [10]. To form a complete cutting kerf, the use of remote-laser-ablation with cyclic removal of materials is needed [11]. Fig. 2 shows the increasing cutting depth with increasing number of cycles.

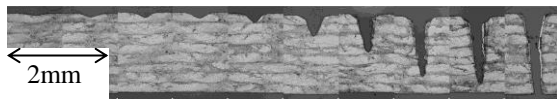


Fig. 2 Cyclic removal of CFRP, from left to right increasing number of repetitions

The beam propagation of each focused beam is measured by a Focus Monitor (Primes GmbH), below beam exit of the scanning module. The difference between the z- position of the beam is compensated by the adaptive mirror. The beam parameters are given in Table 1:

Table 1: Result of beam propagation measurement

Parameter	CO ₂ - Laser	Solid state-Laser (SSL)
Wavelength λ [μm]	10.6	1.09
86% radius of beam waist r_0 [μm]	256	27
Z- Position of focus [mm] (below scanning module)	233	220
Beam parameter product [mm mrad]	3.4	0.6
Rayleighlength z_r [mm]	20.5	1.7

2.1 MATERIAL AND DESCRIPTION OF EXPERIMENTS

To investigate process efficiency, the ablation behavior has to be determined. Therefore a complete thru cut was not necessary. The influence of

ablation depths on the cutting efficiency is taken into consideration due to number of repetitions at a constant beam power P_L and spot velocity v_v . The focal position is set to 1/3 of the material thickness outbound of the top of the material. First results were shown on glass- fiber reinforced thermoplastics and carbon fiber reinforced thermosetting polymer (Table 2:). The material is unidirectional reinforced.

Table 2: Characteristic thermal properties (Quellen)

Material	Heat Capacity [J/(kg*K)]	Evaporation Temperature [°C]	Thermal heat conductivity [W/(m*K)]
Epoxy resin	1400	400- 600	0.21
Carbon fiber	710	3600	78.4
Polypropylene carbon black	1800	460	0,17
Glass fiber	850	2300	1,21

The cuts were performed perpendicular to the fiber orientation. For wavelength synchronous processing the total laser beam power is set constant to 1200 W. The proportion of laser beam power of each beam source is varied from 25%, 50% and 75% of the total laser beam power (Table 3:).

Table 3: Experimental parameters for synchronous laser cutting

Parameter	CO ₂ - Laser	Solid state-Laser (SSL)
Wavelength λ [μm]	10.6	1.09
Power P_L [kW] synchronous 25 % CO ₂ - 75% SSL	0.3	0.9
Power P_L [kW] synchronous 50 % CO ₂ - 50% SSL	0.6	0.6
Power P_L [kW] synchronous 75 % CO ₂ - 25% SSL	0.9	0.3
Spot velocity v_v [m/s]		1
Number of repetitions		5, 10, 20

A process-descriptive parameter is the cutting efficiency R_{eff} [12]. Here R_{eff} is described as the ratio between ablation depth Δt and impacting energy E_{tot} .

$$R_{eff} = \frac{\Delta t}{E_{tot}} \quad (1)$$

The impacting energy E_{tot} is calculated by the mean power of the beam source P_L and the total interaction time between laser beam and material $t_{i,tot}$.

$$E_{tot} = P_L \cdot t_{i,tot} = P_m \cdot n_Z \cdot \frac{l_{SF}}{v_v} \quad (2)$$

Where l_{SF} describes the length of the cutting path and v_V the spot velocity for each repetition and n_Z the number of repetitions.

3 RESULTS AND DISCUSSION

Fig. 3 shows the depth based cutting efficiency for processing of glass- fiber reinforced polymers (GFRP).

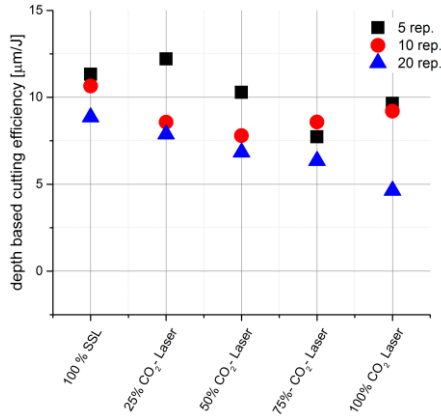


Fig. 3 Depth based efficiency subjected to number of passes for GFRP ($P_L= 1.2$ kW, $v_V= 1$ m/s)

Here the single laser beam with 100% SSL shows the most efficient process. Especially at deep cutting the SSL has to be preferred. Here the high intensities given by the small focal diameter of the SSL- beam is suitable for evaporating the glass-fiber proportion. Additionally the carbon black enhanced polypropylene matrix, leads to a high percentage of absorbed laser power. It must be highlighted, that at low cutting depths, the 25% CO₂ beam is more efficient. Here the comparatively wide focal diameter of the CO₂- laser beam leads to an extended cutting kerf. Thus the removal of the evaporated material is simplified.

Another behaviour arises when processing CFRP (Fig. 4).

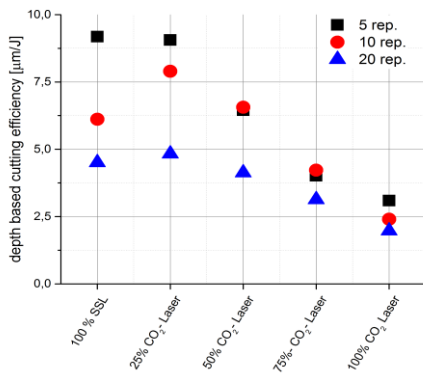


Fig. 4 Depth based efficiency subjected to number of passes for CFRP ($P_L= 1.2$ kW, $v_V= 1$ m/s)

Here the pure CO₂- laser beam does not lead to a high cutting efficiency. Due to the wide focal diameter, only low intensities are achievable. Due to the high heat conductivity of the carbon fiber, high intensity beams with short interaction times are needed for processing. Here the SSL is still suitable. However the 25% of CO₂- laser beam leads to an increased cutting efficiency.

It is assumed, that the wider cutting kerf simplifies the exit of the evaporated residues. Furthermore, the SSL- beam has the opportunity to interact with the notch root instead of the notch edge.

4 OUTLOOK

Remote laser processing has been executed at hybrid materials, consisting of a glass- fiber reinforced plastic and aluminium. The thickness of the GFRP is 2 mm, the thickness of the aluminium is 2.5 mm. Here conventional processes like milling or water jet cutting are limited, due to the different requirements of the tool and the process conditions.

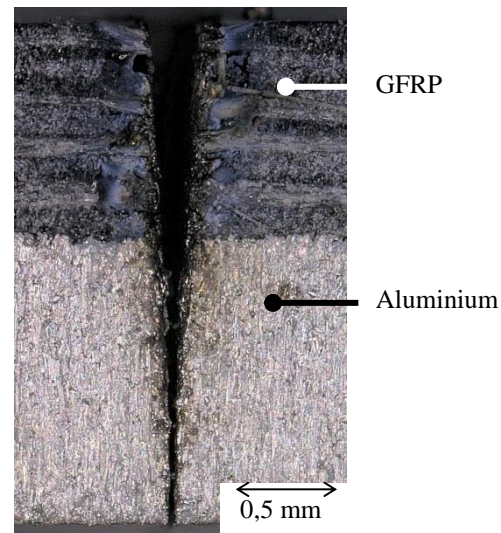


Fig. 5 Cross- section of laser cut hybrid material

Fig. 5 shows a typical cross section of a cut, with the laser beam coming from the GFRP- side. The cutting process was a multicycle- process with an overall cutting velocity of 12 m/min. The GFRP- part is sublimated, whereas the metal part is melted as well as sublimated. The melted proportion of the metal part is removed by sublimation residues. In comparison to metal cutting no burrs or delamination between the metal- and GFRP- structure occurred.

5 CONCLUSIONS

To consider the absorption behavior and the thermal properties of the materials the combination of two laser beams with wavelengths of 1.07 µm and 10.6 µm is a promising approach. Therefore, a

beam combination device was developed and implemented into laboratory scale. The suitability of the developed system has been carried out at GFRP and CFRP. Here the future user is able to choose the proper wavelength of the laser beam or a combination of both. The laser beam radiation complies with the demands of the absorption behaviour and the thermal properties of the matrix- and- reinforcement materials. First trials show the suitability of the remote- technology for processing hybrid materials.

6 ACKNOWLEDGEMENT

Part of this research was funded by the “Deutsche Forschungsgemeinschaft DFG” within the Collaborative Research Centre SFB 639 of TU Dresden, Textile-reinforced composite components for function-integrating multi-material design in complex lightweight applications, project part: D4. Furthermore the samples of the hybrid materials are provided by the Institute of Lightweight Engineering and Polymer Technology (ILK) at Technische Universität Dresden.

REFERENCES

- [1] R. Lässig, “Serienproduktion von hochfesten Faserverbundbauteilen, Perspektiven für den deutschen Maschinen- und Anlagenbau, Studie Roland Berger 2012.” Roland Berger, 2012.
- [2] R. Teti, “Machining of Composite Materials,” *CIRP Ann. - Manuf. Technol.*, vol. 51, no. 2, pp. 611–634, Jan. 2002.
- [3] D. Shanmugam, F. . Chen, E. Siores, and M. Brandt, “Comparative study of jetting machining technologies over laser machining technology for cutting composite materials,” *Compos. Struct.*, vol. 57, no. 1–4, pp. 289–296, Jul. 2002.
- [4] A. N. Fuchs, M. Schoeberl, J. Tremmer, and M. F. Zaeh, “Laser Cutting of Carbon Fiber Fabrics,” *Phys. Procedia*, vol. 41, pp. 372–380, 2013.
- [5] A. Klotzbach, A. Fürst, J. Hauptmann, and E. Beyer, “Investigations on laser Remote cutting of tailored fiber reinforced structures,” *Second Int. Symp. Laser Process. CFRP Compos. Mater.*, 2013.
- [6] J. Stock, M. F. Zaeh, and M. Conrad, “Remote Laser Cutting of CFRP: Improvements in the Cut Surface,” *Phys. Procedia*, vol. 39, pp. 161–170, 2012.
- [7] A. Fürst, A. Klotzbach, S. Hühne, J. Hauptmann, and E. Beyer, “Remote Laser Processing of Composite Materials with Different Opto-Thermic Properties,” *Phys. Procedia*, vol. 41, pp. 389–398, 2013.

- [8] M. Lütke, *Entwicklung des Remote-Laserstrahlschneidens metallischer Werkstoffe*. Stuttgart: Fraunhofer-Verl., 2011.
- [9] A. Fürst, D. Hipp, M. Rose, A. Klotzbach, J. Hauptmann, A. Wetzig, and E. Beyer, “Experimental and Analytical Description of the Multi Wavelength Remote Laser Ablation Process at Fiber Reinforced Polymers,” *Lasers Manuf. Conf. 25- 29 Juni 2015 Münch. Ger.*, Jun. 2015.
- [10] H. Niino, “Laser cutting of carbon fiber reinforced thermo-plastics (CFRTP) by single-mode fiber laser irradiation,” *Laser Appl. Microelectron. Optoelectron. Manuf.*, vol. XIX, p. 89670J, Mar. 2014.
- [11] A. Fürst, M. Rose, A. Klotzbach, J. Hauptmann, T. Heber, and E. Beyer, “Influence of Laser Irradiation on the Failure Behavior of Unidirectional Fibre Reinforced Polymers,” vol. ECCM16–16TH European Conference on Composite Materials, 22.-26.- June 2014, Seville, Spain, Jun. 2014.
- [12] C. Leone, “Investigation of CFRP laser milling using a 30 W Q-switched Yb:YAG fiber laser: Effect of process parameters on removal mechanisms and HAZ formation,” *Compos. Part -Appl. Sci. Manuf.*, vol. 55, pp. 129–142, 2013.

THERMOPLASTIC AUTOMATED FIBER PLACEMENT FOR MANUFACTURING OF METAL-COMPOSITE HYBRID PARTS

S. Ehard, A. Mader, E. Ladstätter*, K. Drechsler

Technische Universität München, Institute for Carbon Composites

ABSTRACT: Automated Fiber Placement (AFP) of continuous fiber reinforced thermoplastic tapes is a promising manufacturing technology for the production of high-performance composite structures. Recent work has shown the possibility to develop the thermoplastic Automated Fiber Placement process (TP-AFP) for joining composite materials and metals. Joining to the metal and laminate consolidation are realized in one automated process, reducing consumables and time intense manual labor. This paper investigates the TP-AFP process for manufacturing hybrid structures by joining CF/PA6 and aluminum. Different surface pre-treatments are analyzed on their impact on the interfacial strength by single-lap shear tests, before and after hot-wet conditioning. Depending on the surface pre-treatment, bonding strength comparable to state-of-the-art joining technologies can be realized. Moreover, it is shown that there are only comparably small process induced deformations due to the local energy input, providing new opportunities for large scale joining of composite and metal structures.

KEYWORDS: Automated Fiber Placement, in situ consolidation, thermoplastic composite, metal, hybrid structure

1 INTRODUCTION

Recent trends in the transport sector are showing an increasing demand of hybrid metal-composite structures to meet the economical, ecological and mechanical requirements for a cost efficient light-weight design. [1]

Mechanical fastening, adhesive bonding or fusion bonding in case of thermoplastic composite materials are the most common manufacturing technologies for generating a hybrid metal-composite structure [2]. Nevertheless, these technologies require many process steps like stacking of the composite layers, consolidation of the laminate and the final joining with the metal.

By the use of thermoplastic Automated Fiber Placement (TP-AFP) technology, composite parts are manufactured according to the mechanical load paths of the structure with a high degree of automation. Expensive manual labor time can be reduced and constant part quality is guaranteed. Moreover, thermoplastic composite materials offer several advantages due to their unlimited shelf life and recyclability. The in situ consolidation of thermoplastic composite materials opens the opportunity for minimizing processing time and costs compared to a thermoset autoclave curing cycle.

Studies at the Institute for Carbon Composites have shown the capability of realizing high quality composite laminates as well as joining CFRP and metal by the laser assisted TP-AFP process. Hybrid struc-

tures are created in a single process step. [3]

Fig. 1 shows a TP-AFP system and the principle of joining CFRP and metal. Endless-fiber reinforced tape material is fed through a fiber placement head to the compaction roller and is positioned on top of the pre-treated metal. By laser radiation, the incoming tape material and the metal substrate are heated to the melting temperature of the composite's matrix. During the compaction by the roller the thermoplastic matrix solidifies and the joint is generated. In order to achieve a sufficient interfacial strength of the joint a surface pretreatment of the metal is essential prior joining.

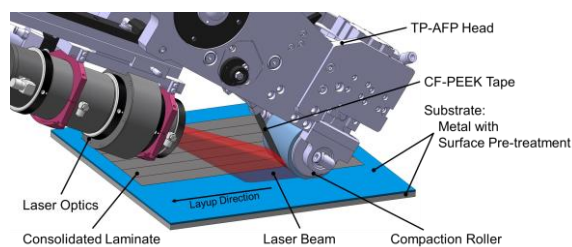


Fig. 1 Schematic illustration of the TP-AFP Process for joining CFRP and metal

This paper investigates the TP-AFP process for manufacturing hybrid structures by joining unidirectional CF/PA6 tapes and EN AW 5754 aluminum substrates. Different surface pre-treatments are analyzed on their impact on the interfacial

* Corresponding author: Institute for Carbon Composites, Boltzmannstr. 15, 85748 Garching, Deutschland
Tel.: +49 (0)89 / 289-15088, Fax: +49 (0)89 / 289-15088, E-Mail: ladstaetter@lcc.mw.tum.de

strength by single-lap shear (SLS) tests before and after hot-wet conditioning. Furthermore, it is shown that process induced deformations can be reduced compared to state-of-the-art joining technologies.

2 EXPERIMENTAL

2.1 USED MATERIALS

Within this study a 2" wide thermoplastic UD-prepreg tape material (Celstran® CFR-TP PA6 CF60-01, Celanese Corporation, Irving, Texas, USA) is used. The chosen matrix is Polyamide 6, the carbon fiber is T700 with a fiber mass content of 60%. EN AW 5754 aluminum was used as metal joining partner. The material properties are listed in Table 1:

Table 1: Properties of chosen materials [4,5]

		EN AW 5754	CFRP CF/PA6
Density	[g/cm ³]	2.67	1.45
Tensile modulus	[GPa]	70	98.1*
Tensile strength	[MPa]	190-240	1938*
Thickness	[mm]	1.5	0.16**
Melting point	[°C]	-	220
CTE	[K ⁻¹ 10 ⁻⁶]	23.9	0*

* Parallel to fiber orientation

** Tape thickness

2.2 SURFACE PRETREATMENT

Recent work has shown that a surface pre-treatment of the metallic surface prior joining is essential for the mechanical performance of the joint [4]. There has been some research in the field of surface pre-treatment of aluminum for fusion bonding with thermoplastic composite materials [2]. Nevertheless, there is no comparable information if these surface pre-treatments are applicable for the manufacturing of hybrids by the TP-AFP process. Therefore, the following selection of mechanical, chemical and physical surface pre-treatments were investigated:

1. Cleaning and degreasing with isopropylalcohol ("IPA")
2. Pre-treatment 1, afterwards sand-blasting with corundum, size F36, at 2 bar pressure ("SB")
3. Pre-treatment 1, then etching in 10 wt% NaOH solution for 60 s at 60 °C, rinsing under distilled water ("NaOH", cf. [7])
4. Pre-treatment 1, afterwards atmospheric pressure plasma treatment by using PB3 plasma generator (relyon plasma GmbH, Regensburg, Germany). Dried compressed air was chosen as process gas. Two different plasma treat-

ments were investigated: With arcing ("PIA") and without arcing ("PlnA"), see Table 2:

Table 2: Plasma treatment parameters

		PIA	PlnA
Frequency	[kHz]	60	60
Working distance	[mm]	12	12
Nozzle velocity	[mm/s]	120	250
Path distance	[mm]	3	5

5. Laser treatment with microscopic structure ("LMS", cf. [8]) and laser treatment with nanoscopic structure ("LNS", cf. [9]), Table 3:

Table 3: Laser treatment parameters

		LMS	LNS
Velocity	[mm/s]	10000	800
Average power	[W]	1000	25
Pulse frequency	[kHz]	-	10
Repetition rate	[-]	3 x 60°	1

6. Coating with VESTAMELT® Hylink hotmelt adhesive promoter ("VMH"), developed by Evonik Industries AG (Essen, Germany)

Preliminary tests showed the need of an additional PA6 polymer coating on top of the pre-treated aluminum surface before joining. This polymer coated material (PCM) has the major advantage that this pre-treatment step can be performed well before the joining step [10]. As mentioned by Todd [11], fusion bonding of thermoplastic surfaces -in this case fusion bonding of polymer coating and CFRP- is not as sensitive as adhesive bonding to surface pre-treatment. Cleaning or soft roughening is sufficient and there is only a limited influence of the surface preparation on the final joint strength. Another advantage is the conservation of the pre-treatment, preventing oxidation of the metal surface. By this, the metal joining partner can be stored for a long period of time before joining. By using a polymer coating the reflective behavior of aluminum at the wavelength of 1040 nm can be reduced. This allows a greater absorption by the substrate and reduces the energy input needed for heating up to the melting temperature of the polymer. Reflections of the laser beam on the aluminum surface may cause local overheating and degradation of the incoming CFRP tape when using high laser power. Furthermore, an insulating layer between carbon fiber and aluminum is generated providing a barrier against contact corrosion. The low stiffness of the coating reduces residual stresses due to the mismatch in thermal expansion as well. Therefore, additionally to pre-treatment 1-5, a coating with 60 µm PA6-film ("PA6", Ultramid®, BASF SE, Ludwigshafen am Rhein, Germany),

respectively 120 μm PA6-film (“2PA6”) was applied via vacuum bagging on a hot stage.

3 MANUFACTURING PROCESS

A modified fiber placement head, derived from tape winding technology from AFPT GmbH (Dörth, Germany) was used within this study to manufacture hybrid structures. In the process, carbon fiber reinforced tapes with thermoplastic matrix are heated by a 4 kW diode laser and in situ bonded to the metal or previously placed tapes (substrate) under application of pressure. By a closed loop control an in situ consolidation of the laminate can be achieved: Laser power and laser angle is adjusted according to the measured temperature in the substrate and incoming tape material, Fig. 2:

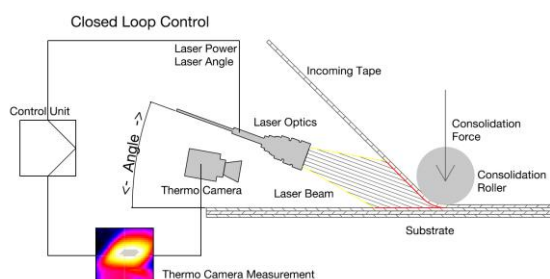


Fig. 2 Principle of TP-AFP process

In order to achieve a sufficient bonding between metal and laminate, different process parameters are needed for the first and the remaining layers. When joining the first CFRP ply and metal, the laser needs to heat up the metallic surface instead of a CFRP substrate. Depending on the optical behaviour of the pre-treated metal surface, the laser spot distribution needs to be headed more towards the substrate, the placement speed is reduced and the temperature setpoint is higher compared to laminate manufacturing. Table 4 shows the process parameters:

Table 4: Process parameters for pre-treatment SB+PA6

		1 st ply	Laminate
Temperature setpoint	[°C]	310	280
Velocity	[m/min]	2	6
Spot size	[mm ²]	46 x 46	46 x 46
Spot distribution	[%]	35/65*	CL**
Consolidation force	[N]	500	500

* Tape / substrate

** Closed loop control

4 SINGLE-LAP SHEAR TESTING

4.1 SAMPLE PREPARATION

SLS specimens according to ASTM D3165 were chosen to characterize the joint strength. A symmetric layup was applied on top of pretreated 200 x 200 x 1.5 mm aluminum sheets. The laminate design is [0/90]_{4s} in order to achieve similar thickness and stiffness compared to the aluminum substrate. These hybrid panels were notched on both sides to get an overlap length of 12.7 mm. Test specimens were milled afterwards to the final size of 25 mm in width and 200 mm in length, Fig. 3.

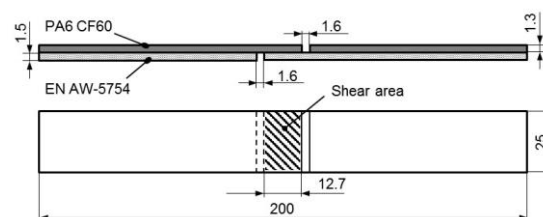


Fig. 3 Dimensions of SLS specimen

4.2 TEST SETUP

After manufacturing a group of specimens of each pre-treatment (except PIA and PInA) were aged under hot-wet (HW) conditions for 14 days at 70 °C and 85% relative humidity (RH). All specimens were tested at room temperature until failure with a crosshead speed of 1 mm/min. Based on the load at failure and the shear area the lap shear strength is calculated. After failure, all specimens were inspected visually for the failure mode. There were basically three types of failure, as shown in Fig. 4.

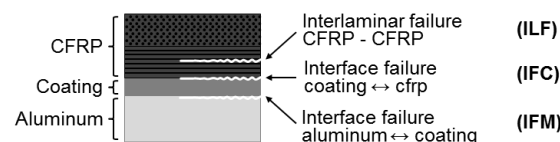


Fig. 4 Failure locations during SLS Testing (cf. [12])

Test specimens with a high test force showed interlaminar failure within the composite (ILF). Besides that, some specimens have an interface failure between coating and tape material (IFC) or a combination of ILF and IFC. Depending on the pre-treatment of the aluminum, interface failure between metal surface and coating (IFM) is observed at specimens with a lack of adhesion between coating and metal.

4.3 RESULTS AND DISCUSSION

The single-lap shear strength depending on the surface pre-treatment and aging history is presented in Fig. 5.

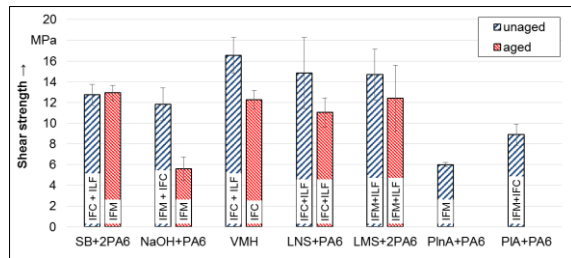


Fig. 5 Mean shear strength depending on surface pre-treatment before and after aging (14d, 70 °C, 85 % RH)

Plasma pre-treatment with and without arcing showed the lowest SLS strength. As shown in Fig. 6, IFM failure mode occurred for PlnA pre-treatment. PIA showed a combination of IFM and IFC, which correlates to the higher lap shear strength. As reported by Habenicht [4] the effect of plasma treatment is time sensitive. Although the specimens were manufactured within 2 hours after pre-treatment, a reduction of the strength cannot be ruled out.

Etching with NaOH showed a SLS-strength of 11.8 MPa but significant drop after hot-wet conditioning to 5.6 MPa. As reported by Brockmann [13], alkaline etching of EN AW 5745 in NaOH results in a nonuniform, thin aluminum oxide layer, providing a good stability against corrosion at least when using epoxy based adhesives. However, aged specimens tested within this study showed a significant loss in strength and a shift of the failure mode towards adhesive failure between the aluminum surface and PA6 film. This is a point for further investigations.

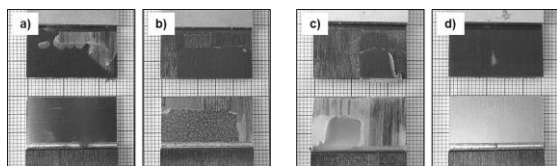


Fig. 6 Fracture surface after SLS Testing: a) PlnA+PA6, b) PIA+PA6, c) NaOH+2PA6, d) NaOH+2PA6 after HW conditioning

With laser pre-treatment, 14.8 MPa (LNS+PA6) and 14.7 MPa (LMS+2PA6) were achieved. After aging both show a reduction in strength of approximately 25%. As shown in Fig. 7, there is no change of the failure mode with respect to the conditioning history.

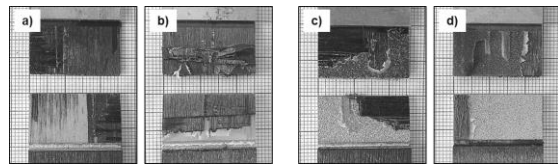


Fig. 7 Fracture surface after SLS Testing: a) LNS+PA6, b) LNS+PA6 after HW conditioning, c) LMS+2PA6, d) LMS+2PA6 after HW conditioning

It can be seen in Fig. 8 that the polymer of the PA6 film penetrates well into the microscopic structure of the aluminum. As reported by Heckert [8], the formation of hot cracks can be observed within the aluminum substrate. Besides this, entrapped air pockets may weaken the joint and lead to a failure between aluminum and PA6 coating. With a nanoscopic structure no abnormalities can be observed at the boundary layer between aluminum and PA6 coating. However, the interface between coating and CFRP is clearly visible, suggesting that there is no sufficient mixing between the PA6 matrix of the tape and the polymer coating. This corresponds to the observed failure mode for the pre-treatment LNS+PA6.

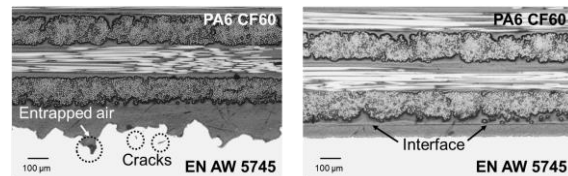


Fig. 8 Cross section of microscopic (LMS+2PA6, left) and nanoscopic surface pre-treatment (LNS+PA6, right)

Pre-treatment SB+2PA6 provides a strength of 12.8 MPa and a failure mode combination of IFC+ILF, respectively IFM after aging (Fig. 9a and Fig. 9b). However, there is no significant influence of hot-wet conditioning on the SLS-strength.

Best results were achieved with the adhesion promoter VESTAMELT® Hylink providing a mean SLS-strength of 16.8 MPa. After aging, a reduction of 27% in strength and a change of the failure mode from IFC+ILF to IFC is observed, as shown in Fig. 9c and Fig. 9d:

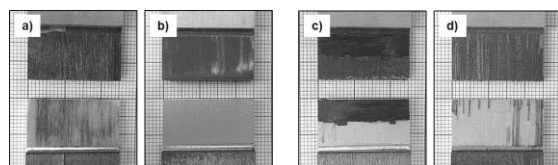


Fig. 9 Fracture surface after SLS Testing: a) SB+2PA6, b) SB+2PA6 after HW conditioning, c) VMH, d) VMH after HW conditioning

Similar to LNS+PA6, there is no visible mixing between CFRP and coating at the combination SB+2PA6 (Fig. 10, left). Despite the high joint strength, VMH shows a lot of voids at the interface between CFRP and coating, respectively within the coating itself. Nevertheless, a diffusion of carbon filaments into the VMH coating can be observed, explaining the high single-lap shear values.

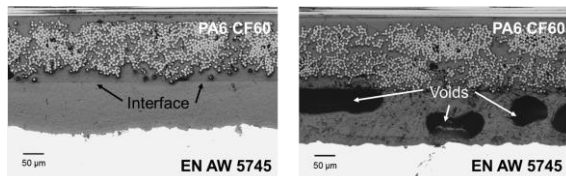


Fig. 10 Cross section of sandblasted (SB+2PA6, left) and VESTAMELT HYLINK surface pre-treatment (VMH, right)

In conclusion, it is possible to create a structural bond between CF/PA6 and aluminum by the use of TP-AFP. The pre-treatment has a major influence on the joint strength and the aging stability. Some of the micrographs show a bond line between CFRP-tape and PA6 coating. Natural PA6, as used in this study as coating material, has a transmissivity of greater 70% at the wavelength of the laser (1040 nm) [14]. Thereby, an influence of the pre-treated aluminum surface on the overall absorption cannot be excluded. A way for reducing this influence of the surface topography on the optical behavior is the use of an pigmented polymer coating. Additives like carbon black increase the absorption of the laser and minimize the influence of the aluminum surface. Depending on the chosen surface pre-treatment, further experiments and a process optimization for joining the first layer may improve the joint strength.

5 OPPORTUNITIES FOR LARGE SCALE JOINING

As shown in Chapter 4, the joint of aluminum and CF/PA6 by TP-AFP provides a bonding strength comparable to established manufacturing methods [15]. In relation to other fusion bonding technologies challenges regarding equipment size, e.g. clamping devices, effectors etc. can be overcome due to the flexibility of the fiber placement head. Furthermore, it turned out that by the use of TP-AFP the process induced deformations on hybrid structures can be minimized compared to other manufacturing methods. Within this study the hybrid sheets manufactured by TP-AFP (see chapter 4) were compared with reference samples manufactured under vacuum on a hot stage, similar to a thermoforming or autoclave process. These “thermoformed” samples showed a tremendous deformation after debagging, while the TP-AFP samples

remained almost flat.

To quantify the difference, a coordinate measuring system (GOM ATOS) was used and samples of both manufacturing processes, TP-AFP and thermoforming, were optically measured and compared. The deformation and maximum displacement is presented in Fig. 11.

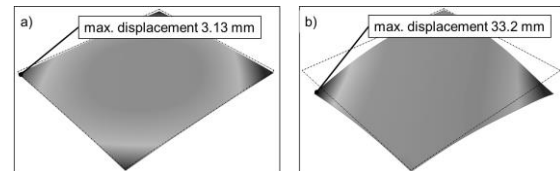


Fig. 11 Displacement of hybrid specimens with pre-treatment SB+2PA6: a) TP-AFP, b) Vacuum + hot stage

There is a maximum displacement of 33.2 mm for the thermoformed and 3.13 mm for the TP-AFP sample. Thermoformed specimens showed pre-cracks between metal and coating due to the resulting shear stress in the interface and were discarded for mechanical testing.

When joining CFRP and metal by this thermoforming process, the whole structure needs to be heated up to the melting temperature of the thermoplastic matrix system. When cooling, the created hybrid structure tends to warping due to the mismatch in thermal expansion between CFRP and metal.

On the other hand, there is only a local heat input, limited to the laser spot size when joining CFRP and metal in the TP-AFP process, as shown in Fig. 2. That way, process induced deformations caused by differences in thermal expansion are limited to the joining area and the global displacement of the structure is minimized after cooling. This possible scalability from coupon level to full scale reduce limitations regarding the structure size of components for fusion bonding.

6 CONCLUSIONS

In the presented work, aluminum sheets were pre-treated by mechanical, chemical and physical processes. Subsequently the laser assisted TP-AFP process was used for joining CFRP to metal. Single-lap shear specimens were manufactured and tested before and after 14 days hot-wet conditioning at 70°C and 85% relative humidity.

It has been shown that by the use of TP-AFP a durable joint of metal and CFRP can be achieved. As reported in other studies, hot-wet conditioning decreases the interfacial strength of the joint and changes the resulting failure mode, depending on the surface pre-treatment of the aluminum.

The highest SLS-strengths up to 16.8 MPa, respectively 12.2 MPa after conditioning were realized by the use of the adhesion promoter VESTAMELT®

HYLINK. As shown in micrographs, further improvements regarding joint strength can be achieved by adjusting first layer process parameters and optimizing the polymer coating towards higher laser absorption.

Due to the local heat input, only small process induced deformation was observed for the TP-AFP specimens. Combined with the in situ consolidation of the CFRP reinforcement, TP-AFP provides an innovative way for large scale joining of CFRP and metal in one automated process.

7 ACKNOWLEDGEMENT

The authors would like to thank Airbus Group Innovations, relyon plasma GmbH, Evonik Industries AG, and Institute for Machine Tools and Industrial Management (TUM) for their kind support and the pre-treatment of the aluminum sheets.

REFERENCES

- [1] Bundesministerium für Wirtschaft und Energie: *Bestandsaufnahme Leichtbau in Deutschland* (2015), URL: <http://www.bmwi.de/BMWi/Redaktion/PDF/Publikationen/Studien/bestandsaufnahme-leichtbau-in-deutschland.pdf> (10.02.2016)
- [2] Ageorges C., Ye L.: *Fusion Bonding of Polymer Composites*. Springer-Verlag Berlin Heidelberg, 2002.
- [3] Radlmaier V. et al.: *Thermoplastic Automated Fibre Placement: Current fields of application and future prospects*. JEC Composites Magazine, 97:39-42, 2015.
- [4] Celanese Corporation: *Celstran® CFR-TP PA6 CF60-01*, Technical Data Sheet, 2014.
- [5] GLEICH Aluminum GmbH: *EN AW-5754*, Technical Data Sheet, 2011.
- [6] Habenicht G.: *Kleben: Grundlagen, Technologien, Anwendungen*. Springer-Verlag Berlin Heidelberg, 2009.
- [7] Lunder O., Olsen B., Nisancioglu K.: *Pre-treatment of AA6060 aluminum alloy for adhesive bonding*. International Journal of Adhesion & Adhesives, 22:143-150, 2002.
- [8] Heckert A., Zaeh M.F.: *Laser Surface Pre-treatment of Aluminum for Hybrid Joints with Glass Fibre Reinforced Thermoplastics*. Physics Procedia, 56:1171-1181, 2014.
- [9] Kurtovic A. et al.: *Laser induced surface nano-structuring of Ti-6Al-4V for adhesive bonding*. International Journal of Adhesion & Adhesives, 45:112-117, 2013.
- [10] Wise R.J., Watson M.N.: *A New Approach for Joining Plastics and Composites to Metals*. Proceedings of the 50th Annual Technical Conference (ANTEC'92), 2113-2116, 1992.
- [11] Todd S.M.: *Joining Thermoplastic Composites*. 22nd International SAMPE Technical Conference, 383-392, 1990.
- [12] Bender B. et al.: *Stoffschlüssiges Fügen von Aluminum und CFK durch die Epoxidharz-Matrix für die Herstellung hybrider Strukturbauteile*. 19. Symposium Verbundwerkstoffe und Werkstoffverbunde, 450-459, 2013.
- [13] Brockmann W. et al.: *Adhesive Bonding: Adhesives, Applications and Processes*. WILEY-VCH Verlag GmbH & Co. KGaA Weinheim, 2005.
- [14] BASF Corporation: *FORWARD TO BETTER UNDERSTANDING OF OPTICAL CHARACTERIZATION AND DEVELOPMENT OF COLORED POLYAMIDES FOR THE INFRARED/LASER WELDING: PART I – EFFICIENCY OF POLYAMIDES FOR INFRARED WELDING* (2003), URL: <http://www2.basf.us/PLASTICSWEB/displayfile?id=0901a5e180004886> (12.02.2006)
- [15] Velthuis R. et. Al.: *Leichtbau aus Metall und Faser-Kunststoff-Verbunden: Verfahrensvergleich*. Kunststoffe, 2007.

PRODUCTION, CHARACTERISATION AND PROCESSING OF METAL PLASTIC COMPOSITES WITH MODIFIED CORE MATERIALS

M. Wuehrl^{1*}, M. Klaerner¹, L. Kroll¹, M. Riemer², R. Müller², D. Landgrebe², C. A. Geweth³, S. Marburg³

¹Technische Universität Chemnitz, Germany

²Fraunhofer Institut für Werkzeugmaschinen und Umformtechnik Chemnitz, Germany

³Technische Universität München, Germany

ABSTRACT: Hybrid metal-plastic composites provide the possibility of combining lightweight design with high material stiffness. Modifications of the polymer core material and thickness influence the properties of the composite in case of damping properties for lower structure borne-sound, stiffness, basis weight and forming properties.

The challenge of simulating a modified metal-plastic composite with different core materials in forming simulations as well as acoustic simulations using standard FE material models is treated in this article. Therefore, a new metal-plastic composite with steel face sheets and a modified Polyamid 6 core was developed. To achieve a variability in core stiffness and adhesion properties the polymer was modified with ground tyre rubber in different fractions which additionally shows an economically way of tire recycling. For the mentioned simulations the raw materials and the produced composites were characterised using different testing methods.

The forming behaviour of the metal-plastic composites was investigated by folding with different radii. For rating the formability of the different composites the springback and the interface integrity were analysed. A significant influence of the core thickness and the core stiffness could be shown. The results of the performed FE simulations predict the experimental punch force displacement curves and the springback behaviour.

The acoustic behaviour of the composite was investigated for different configurations of the core material. A steel plate of the same size was investigated as a reference model. The estimated radiated sound power (ERP) is calculated to characterize the acoustic properties of the samples.

KEYWORDS: Simulation, Metal-Plastic Composites, Elastomer, Forming, Acoustic

1 INTRODUCTION

The treated metal-plastic composite (MPC) materials of this article consist of three layers with metal face sheets and a polymer core material. In general, these hybrid materials offer different advantages mainly based on the properties and thickness of the core material. Thicker and stiffer cores greatly improve the bending stiffness, while thin and softer ones tend to lower the structure-borne sound, especially of large sheet metal structures. Even though, these composites show benefits for different applications, they are mainly used in aerospace and defence industry [1].

The formability of these complex materials has been investigated with different process parameters and materials [1],[2]. Today, forming operations like deep and stretch drawing are simulated in

finite element simulations prior to production. Therefore, the expenses for prototypes and rejects are reduced.

While these methods are highly developed for normal sheet metals, the simulation of metal-plastic composites is still in its early stage.

For this study, metal-plastic composites with different core thicknesses are produced, simulated and experimentally scrutinised. The core material is modified with recycled tyre rubber which satisfies the ecological demand of elastomer recycling and results in a core material with different stiffness and adhesive properties. This wide range of MPC offers the possibility to verify the used simulation models.

* Corresponding author: Technische Universität Chemnitz, Fakultät für Maschinenbau, Institut für Strukturleichtbau, D-09107, +49 371 531-34764, +49 371 531-834764, mario.wuehrl@mb.tu-chemnitz.de

2 INVESTIGATED MATERIALS

2.1 MODIFIED CORE MATERIALS

The use of fine grinded waste tyres, also known as ground tyre rubber (GTR), in polymers is the most inexpensive approach of recycling the infusible and insoluble elastomers. For this study, blends of Polyamide 6 (PA6) and different fractions of GTR were used. By injection moulding test specimens for different static and dynamic tests were produced. The main properties of these compounds shall be shown to present the core characteristics of the researched metal-plastic composite.

The results of the tension test are shown in Fig. 1. The experiment was carried out on a Zwick/Roell Z100 with five specimens of all investigated materials at room temperature. Young's modulus as well as tensile strength decrease with higher fractions of elastomer. While the tensile strength is already decreased significantly with 10 %, there is no influence on the Young's modulus. The elongation at break behaves similarly to Young's modulus but is not significantly reduced by 10 % of elastomer. With higher fractions it reduces from 40.3 % almost linear to 5.9 % elongation.

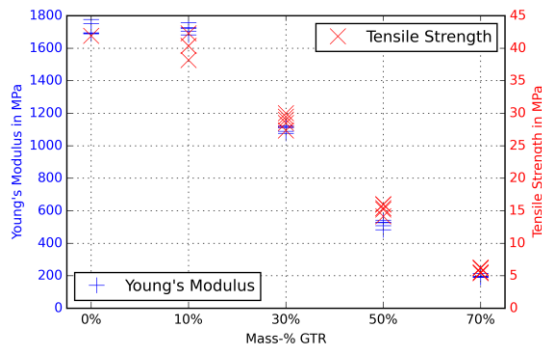


Fig. 1 Results of the tension test

In order to make a prediction for the adhesion properties of the metal-plastic composite, the free surface energy of the developed core materials was investigated (s. Fig. 2). To evaluate the polar and the disperse portions diiodomethane, ethylene glycol and water were used.

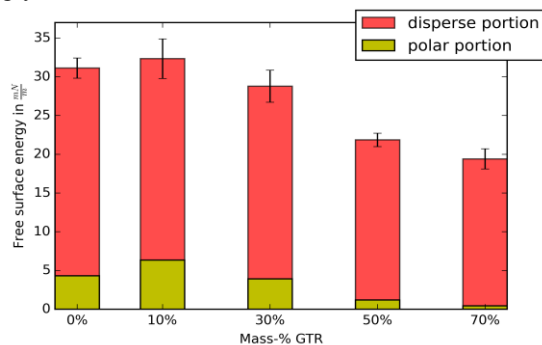


Fig. 2 Free surface energy for the investigated compounds

Both portions decrease with elastomer fractions higher than 10 % leading to the prediction that also the tensile shear strength of the metal-plastic composite will be reduced.

The dynamic properties of the polymer GTR compounds have been determined by tension tests according to ISO 6721-4 (Fig. 3) showing an increased damping for higher GTR fractions.

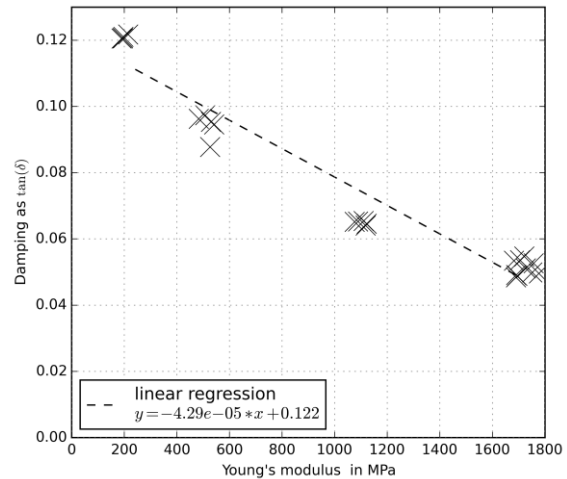


Fig. 3 Relationship of Young's modulus and damping

2.2 DEVELOPED METAL-PLASTIC COMPOSITES

The previously described core materials were further extruded as foil despite for 70 % of elastomer (process failures). These foils were then processed in a variotherm pressing process to the finished metal-plastic composite.

To cover a wide range of properties, two different core thicknesses and different GTR fractions were used (Tab. 1).

Table 1: Produced MPCs

	Mass-% GTR	Core thickness in mm	Face sheet thickness in mm
MgZi_PA6_0,5	0	0.5	0.28
MgZi_10%_0,5	10	0.5	0.28
MgZi_30%_0,5	30	0.5	0.28
MgZi_50%_0,5	50	0.5	0.28
MgZi_PA6_1,1	0	1.1	0.28
MgZi_30%_1,1	30	1.1	0.28

The bending stiffness has been determined in a four-point bending test according DIN 53293. Due to the thin composites, the specimen dimensions of 200 x 15 mm had to deviate from the standard. All tests were executed with a constant speed of 5 mm/min on a Zwick/Roell Z5.0 TN machine at room temperature.

Due to the moment of inertia of composites with thicker cores, the bending stiffness is higher (Fig. 4). The influence of the core stiffness is insignificant according to the measured data.

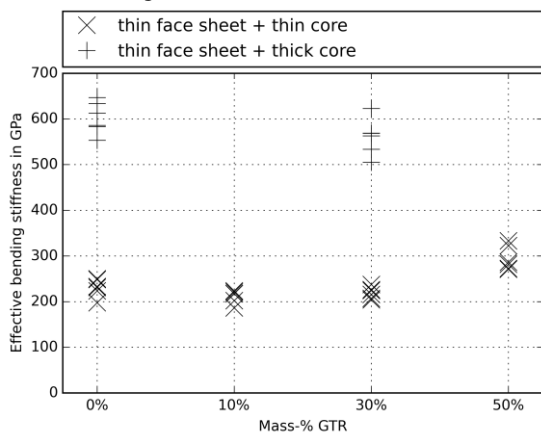


Fig. 4 Results of the bending test for the MPCs

As mentioned in chapter 2.1, higher fractions of GTR increased the damping of the polymer material. This led to the assumption that the damping properties of the MPC might be increased, too. However, it was not able to prove by damping measurements.

From the free surface energy (s. Fig. 2), the adhesion properties of the different MPCs are assumed to decrease with higher fractions of GTR. To evaluate the tensile shear strength, specimens with mutual notches were tested (s. Fig. 5). The distance between the notches was chosen small enough (5 mm) to prevent failure of the face sheets.

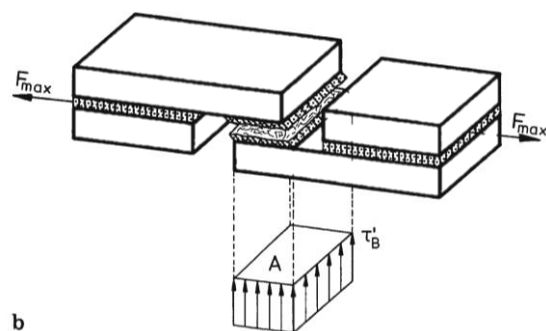


Fig. 5 Specimen geometry for the tensile shear test [3]

The results of the tensile shear test are shown in Fig. 6. As suspected before, the tensile shear strength is reduced for higher GTR fractions. The high variation of the measured data for 10 % GTR indicates a problem in production for the specific blank from which the specimens were cut out. For 50 % GTR the adhesion properties were so low that an alternative adhesive should be taken into account.

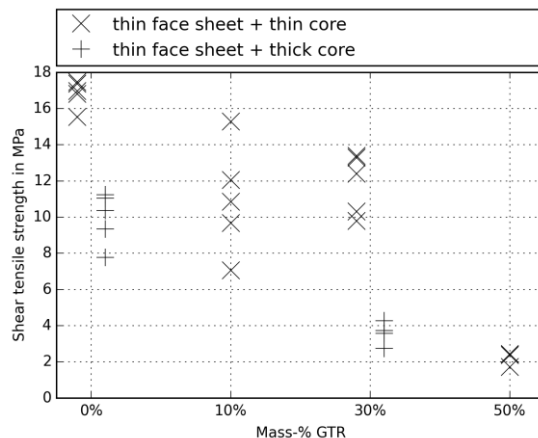


Fig. 6 Shear tensile strength of the investigated MPCs

3 FORMING SIMULATION

3.1 MODELS

The development of the FE-model for the forming of metal-plastic composites involves the modelling of the different materials, the interface and the tools with an appropriate loading and kinematic behaviour. In general, different approaches for the modelling of metal-plastic composites are possible. Each single layer could be modelled by solid or shell elements. Three different basic variants are known (s. Fig. 7) according to the state of the art [4][5]. Concerning face and core sheets there are namely the solid-solid-(1), the solid-shell- (2) and the shell-shell-concept (3).

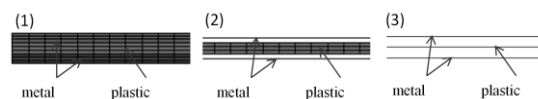


Fig. 7 Modelling variants of metal-plastic composites

To investigate the bending behaviour of the metal-plastic composites numerically, the commercial FE-software, LS-Dyna, is used. The dimensions of the specimen and the tools are considered to the experiments shown in section 3.3. The tools are modelled as rigid bodies and the blank holder is loaded with 200 kN. The plastic core layer of the sandwich material is modelled by three solid elements (ELFORM 1) over the thickness and the metal layer with shell elements (ELFORM 16, NIP 5). Fig. 8 shows the FE-model for the analyses of the bending process. In this study, the connection between the layers is modelled with the LS-Dyna con-tact formulation TIED_SHELL_EDGE TO_SURFACE_BEAM_OFFSET not considering the failure in consequence of delamination.

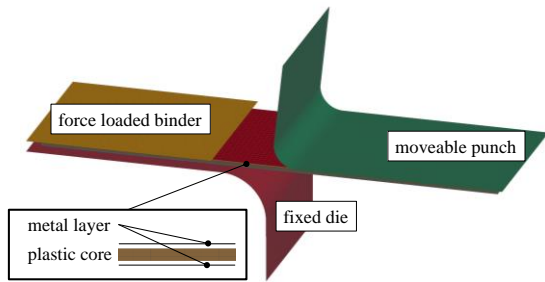


Fig. 8 FE model for the bending process

For the metallic layers the anisotropic material model MAT36 is used. The parameters of the model are determined from tensile tests. The core layer is modelled with the isotropic elastic plastic material model MAT124 including different yield stress/plastic strain curves for tension and compression. The different load curves are determined in tensile and compression tests.

3.2 FORMING EXPERIMENTS

Within the scope of this paper the bending behaviour of the different metal-plastic composites shall be investigated. The folding tests were performed with the tensile test machine ZWICK BZ1-MM14750.ZW01 with a special bending tool (s. Fig. 9). Three bending radii were investigated. The nominal bending angle is 90 degrees. For rating the bending behaviour of the different materials the springback and the interface integrity are analysed. The interface integrity is analysed by metallographic cross sections. Furthermore, force-displacement curves are logged for the comparison between experiment and simulation (see section 3.4).

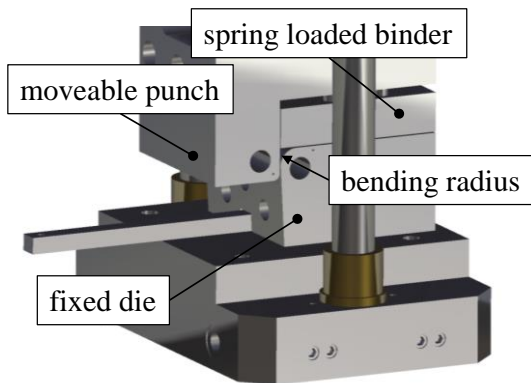


Fig. 9 Bending tool

Table 2: Dimensions of specimen and tool bending radius specimen length specimen width

	Bending radius	Specimen length	Specimen width
Amount [mm]	10; 5; 2	100	30

Fig. 10 shows the measured values of the springback angle for different fractions of GTR and core layer thicknesses by different bending radii. The springback angle was calculated by using the equation (1), where α_{end} is the measured angle after the bending process. The nominal process bending angle is represented by α_0 (here 90°).

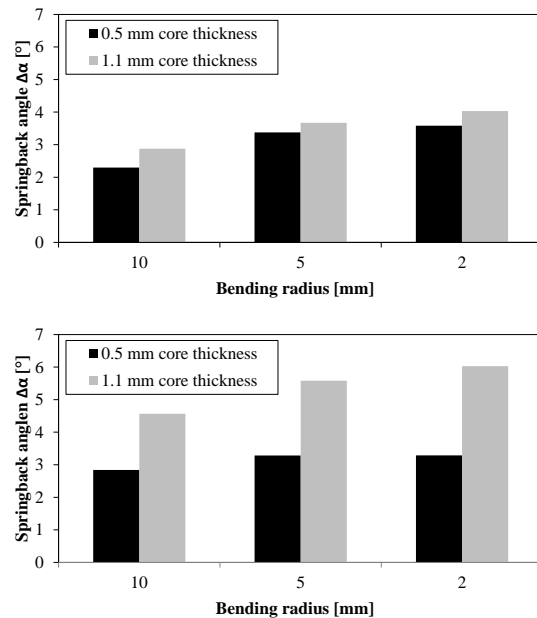


Fig. 10 Springback angle of metal-plastic composites with 0% elastomer recyclate (left) and 30% elastomer recyclate (right)

Within the experiments, the influence of the core layer thickness and core layer stiffness on the bending behaviour is investigated regarding to the material combinations of table 1.

$$\Delta\alpha = \alpha_{end} - \alpha_0 \quad (1)$$

For the specimens with 50% fraction of GTR the springback angle could not be measured due to delaminations. In general, the experiments show an increasing springback angle with an increasing core layer thickness for both GTR contents and all bending radii. Furthermore, the springback angle increases with higher GTR contents. Fig. 11 shows the cross sections of the specimens made with a bending radius of 2 mm. The shear stress increases with decreasing bending radii. Hence, the smallest bending radius induces the highest interface load.

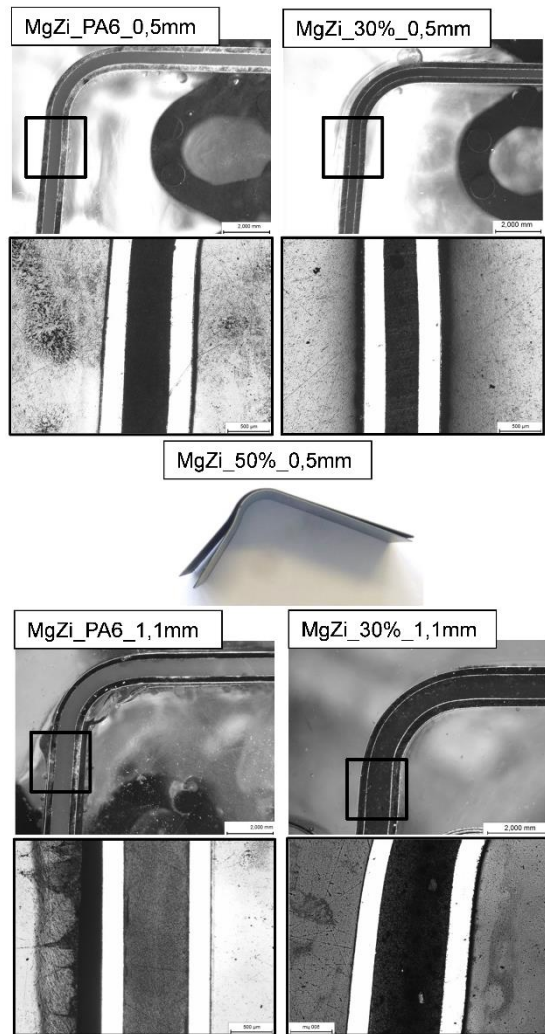


Fig. 11 Cross section of the bending specimens with different volume contents of elastomer recyclate and core layer thicknesses

The analysis of the cross sections for the core thickness of 0.5 mm and GTR fractions of 0% and 30% do not show any delaminations during the bending process. In contrast, wide delaminations are detected for 50% GTR fraction. As a result, the increased core layer thickness of 1.1 mm has no negative influence on the interface integrity after the bending process.

3.3 VERIFICATION OF THE FE-MODEL

The simulation results are verified by the comparison of the force-displacement curves and the springback angles of the previous experimental results. Fig. 12 shows the force-displacement curves from experiment and simulation for three different volume contents of elastomer recyclate and a core layer thickness of 0.5 mm. The results show a good agreement between simulation and experiment for 0% and 30% GTR. For a volume content of 50% elastomer recyclate shows a good agreement until a punch displacement of 15 mm

could be seen. The following deviations are caused by delaminations of the composite. Contrary to this, delamination processes were not modelled in the FE-model. The chosen gap between punch and die, causes a compressive load in the thickness direction of the core layer as well as an increased surface pressure between tool and specimen. This leads to rising friction forces, which result in a disproportionate slope of the punch displacement curve. This effect could be reproduced with the developed FE-model and confirm the validity of the used material and tribological parameter set.

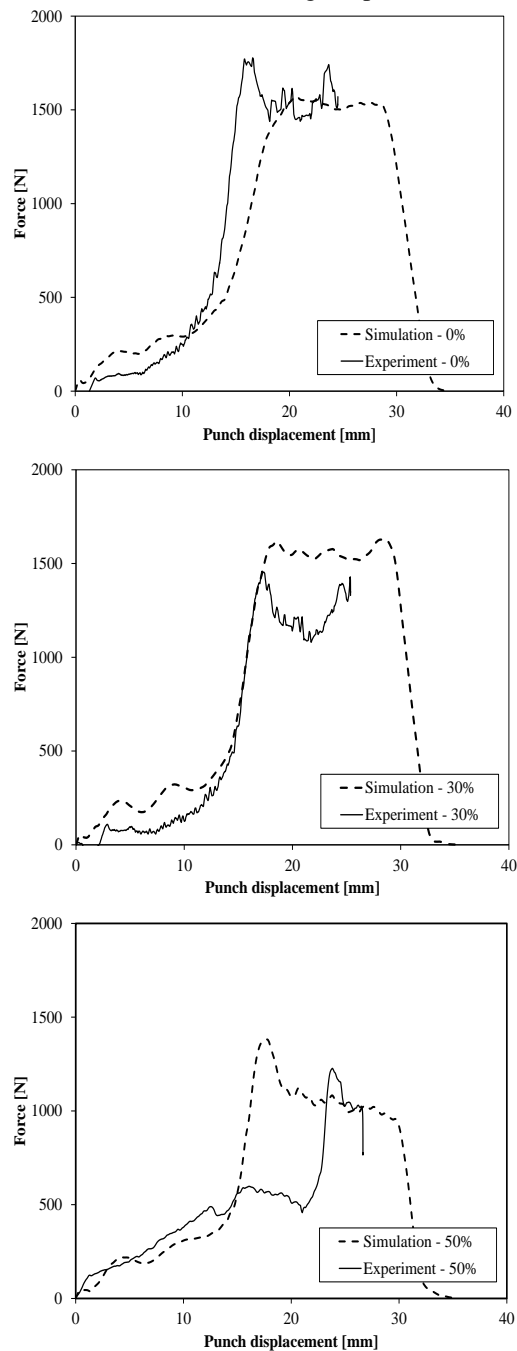


Fig. 12 Comparison of the force displacement curves between simulation and experiment for the bending radius of 10 mm

The analysis of the springback angle determined by the FE-simulation shows a good agreement for 0 % GTR fraction only (s. Fig. 13). For a volume content of 30 % elastomer recycle a significant deviation between experiments and simulation could be caused by the inaccurate determination of the onset of yielding for the polymer filled with elastomer recycle.

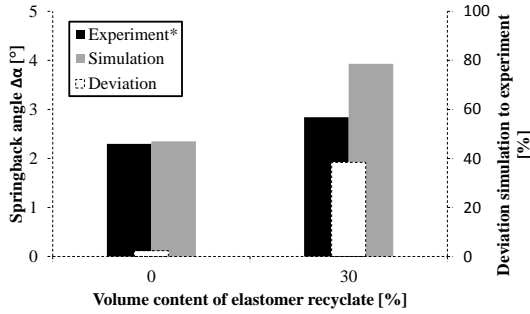


Fig. 13 Comparison of the springback angle between experiment and simulation for the bending radius of 10 mm

In summary, the modelling approach with the shell-solid-shell concept shows good results concerning the prediction of force-displacement curves for the investigated bending process and materials assuming perfect bonding of core- and face sheets, whereas the accuracy of the springback angle can be only proven for materials without GTR fraction.

4 ACOUSTIC SIMULATION

4.1 MODEL

To calculate the radiated sound power, a parametric model of the composite plate is implemented in Ansys® APDL. The dimensions of the clamped plate are 400x200x1 mm. This plate is meshed with quadratic shell-elements of the type shell281 and excited with a harmonic force of $F=1$ N in the frequency range from 0.5 Hz to 2000 Hz. For a fast computation of the structural response, a modified version of the harmonic analysis is implemented [6]. To issue the dynamic behaviour in terms of acoustic radiation, the equivalent radiated sound power (ERP) is applied, which is defined as [7]

$$P_{ERP} = \frac{1}{2} \rho_{Air} c_{Air} \sum_{el=1}^{N_e} A_{El} v_{el} v_{el}^* \quad (2)$$

In this equation A_{el} is the element surface of each element and v_{el} is the velocity of each element in normal direction. The speed of sound is assumed to be $c_{Air} = 343.5 \frac{m}{s}$ and the density of the air is chosen as $\rho_{Air} = 1.204 \frac{kg}{m^3}$. By summing up the sound power according to [8],

$$L_W = 10 \cdot \log_{10} \frac{\sum P_{ERP}}{P_0} \quad (3)$$

a scalar value is obtained for the simulated plate configurations to compare the different configurations of the core material.

The MPCs of this study are compared to a 1 mm thick solid steel plate.

4.2 RESULTS

As shown in Table 1, the solid steel plate emits about 21dB more sound in the investigated frequency range than the composite plates.

Table 3: Emitted sound power level

MPC	L_W [dB]
Steel 1 mm	91.2
MgZi_PA6_0,5	68.3
MgZi_10%_0,5	67.8
MgZi_30%_0,5	68.2
MgZi_50%_0,5	69.8

Interestingly, the emitted sound power level only varies less than 2dB for the different core materials. Two possible reasons for this could be the relatively small increase of the damping ratio and the decrease of the Young's modulus of the plastic core with the increasing GTR portion.

ERP L_W

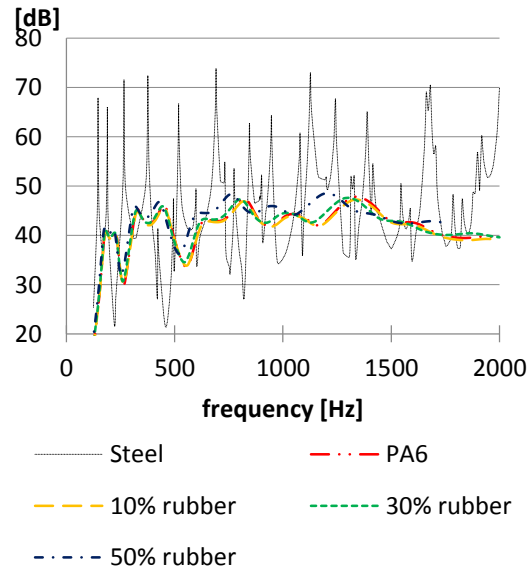


Fig. 14 Sound power level

In Fig. 14 the emitted sound power level of the frequency is displayed. It can be seen, that the peaks shift to different frequencies, due to the different Young's moduli. Therefore, different core configurations could be interesting for different frequency ranges and applications.

5 CONCLUSIONS

In the presented work, different metal-plastic composite materials were successfully produced, characterised and simulated.

Prior to the composite investigations, the core material modification was examined in detail. Stiffness and strength are being reduced almost linearly with increasing GTR fractions whereas the damping behaviour reacts contradictory. The evaluated free surface energy served well for assuming the MPC's adhesive property.

The composite behaviour is dominated by the stiff steel face sheets and follows common sandwich characteristics. Due to negligible shear deformations of the core, the increased damping of the modified polymer material showed no significant influence on the MPC damping nor the sound radiation.

The adhesive properties of the polymer have a strong influence on the forming experiments and the delamination thereby. Delamination again is the most important factor for the differences between the simulated and experimental forming.

However, the forming simulation achieved good results with the shell-solid-shell concept only leaking in the determination of the springback angles for the GTR filled cores.

Further investigations should address the experimental characterisation of the interface shear strength. Common notched tensile specimens show bending of the shear zone whereas tensile specimens in normal directions fail due to insufficient load applications.

Next, including these interface strength in forming simulations is important to achieve more accurate forming simulation results and will help to predict the delamination.

Last, further studies of the core modification and composition of the sheets should generate more shear deformations to be able to benefit from the improved dissipation properties in damping and sound radiation of the MPC.

6 ACKNOWLEDGEMENT

The project is funded as a project of industrial research under grant no AiF 17895 BG of the Research Association EFB e.V. financed and supervised by the German Federation of Industrial Research Associations (AiF) within the framework of the program for the promotion of industrial research and development (IGF) by the Federal Ministry for Economical Affairs and Energy (BMWi).

REFERENCES

- [1] Gresham, J.; Cantwell, W.; Cardew-Hall, M.; Compston, P. & Kalyanasundaram, S.: *Drawing behaviour of metal composite sandwich*

structures, Composite Structures, 75, 305-312, 2006.

- [2] Rajabi, A.; Kadkhodayan, M.; Manoochehri, M. & Farjadfar, R.: *Deep-drawing of thermo-plastic metal-composite structures: Experimental investigations, statistical analyses and finite element modeling*, Journal of Materials Processing Technology, 215, 159-170, 2015.
- [3] Habenicht, G.: *Kleben: Grundlagen, Technologie, Anwendungen*. Springer-Verlag Berlin Heidelberg New York, 2013.
- [4] Keßler, L., Dams, R., Marx, A., Theiss, M.: *Erweiterung der Simulation für die virtuelle Fertigungsprozesskette von Sandwich-Werkstoffen am Beispiel Litecor®*, Intermezzo der hybriden Werkstofflösungen – 35. EFB Kolloquium Blechverarbeitung, Bad Boll, 2015.
- [5] Haufe, A., Schröter, D.: *Car body parts based on sandwich panels: presumption for model building and simulation of the forming process*, ACI Forming in Car Body Engineering, Bad Nauheim, 2015.
- [6] Acton, A. C.: *Clustering results around peaks for full-harmonic analyses in ANSYS*. <http://ansys.net/tips/aacton20080723-clustering.pdf>, 2008.
- [7] Fritze, D., Marburg, S., Hardtke, H.-J.: *Estimation of radiated sound power: A case study on common approximation methods*. Acta Acustica united with Acustica, 95(1), 833-842, 2009.
- [8] Feldmann, J.: *Schallpegelmesstechnik und ihre Anwendung* in Möser M.: Messtechnik der Akustik, 55-113, Springer-Verlag Berlin Heidelberg, 2010.

HYBRIDRTM - QUALITY CONTROLLED MANUFACTURING OF HYBRID MATERIAL COMPOSITES THROUGH RESIN TRANSFER MOULDING

E. Fauster^{1*}, P. Hergan¹, R. Schledjewski¹

¹ Montanuniversität Leoben
Chair in Processing of Composites, 8700 Leoben, Austria

ABSTRACT: HybridRTM terms a publicly funded project, which aims at the development of a processing technique for manufacturing of lightweight structural components from hybrid materials. In particular, components involving metal as well as fibre-reinforced polymer composite materials are manufactured in a single processing step by means of the resin transfer moulding (RTM) technique. Project activities include material development, modelling of material characteristics, process simulation, mould development as well as model-based process control in order to ensure consistently high component quality. This paper outlines the fundamental concept of project HybridRTM and summarizes the most important results gained during the first period of project activities.

KEYWORDS: Metal-FRPC-hybrid structures, RTM processing, model-based process control

1 INTRODUCTION

Lightweight solutions are of increasing importance in various industrial areas, such as automotive, aerospace, mechanical and plant engineering [1]. Typical lightweight materials, such as fibre-reinforced polymer composites (FRPC) and light metals, are incapable to exclusively fulfil the list of requirements requested for these applications. Thus, hybrid material structures are considered as advantageous.

The project HybridRTM aims at the development of a robust single-step RTM processing technique for hybrid material structures composed of a metallic base element and an adhesively bonded FRPC component. Therein, the resin system acts as matrix constituent for the FRPC and as adhesive towards the metal element at the same time. This strategy improves the efficient use of lightweight materials and results in reduced production costs.

1.1 PROJECT OUTLINE

Starting with the definition of a three-dimensional functional model together with the required materials, i.e. metal sheet, reinforcing fabric and resin system, material tests will be conducted in order to determine mechanical, thermal and adhesive material properties. These are subsequently used for FEM simulation runs used to predict the behaviour of hybrid material components, in particular in terms of residual stresses induced by the RTM

process as a result of different thermal expansion coefficients of the constituents [2]. These results will further affect the design of the RTM mould for processing the functional model.

Process development will be supported by identification of relevant process parameters following a design-of-experiments (DoE) approach. Furthermore, a heat-pump concept will be designed for active heat recovery when running the RTM process. Moreover, a novel, model-based concept for process monitoring and management [3,4] will be implemented in order to ensure manufacturing of hybrid structures with consistently high quality. The results and knowledge gained throughout the project will finally be verified by manufacturing parts of the functional model followed by non-destructive and destructive component testing.

1.2 PROJECT CONSORTIUM

The project consortium treating HybridRTM is headed by Montanuniversität Leoben¹, which is involved with two operational units, the Chair in Processing of Composites² and the Chair in Material Science and Testing of Polymers³, and further comprises the company partners Benteler-SGL⁴,

¹ www.unileoben.ac.at

² www.kunststofftechnik.at/composites

³ www.kunststofftechnik.at/materialscience

⁴ www.benteler-sgl.de

* Corresponding author: Ewald Fauster, Montanuniversität Leoben, Chair in Processing of Composites, Otto Glöckel-Str. 2/III, 8700 Leoben, Tel: +43 (0)3842 2708, Fax: +43 (0)3842 2702, ewald.fauster@unileoben.ac.at

bto-epoxy⁵ and Alpex Technologies⁶ as well as the research institutions AIT Austrian Institute of Technology⁷ and LKR Light Metals Technologies Ranshofen⁸.

2 FUNCTIONAL MODEL

In order to demonstrate the know-how elaborated in the project, a functional model was defined at an early stage of the project. The functional model is derived from a mounting carrier of a car rear flap and comprises a carbon-fibre reinforced polymer composite base structure and a stiffening U-shaped metal beam as shown in Fig. 1. Moreover, various concepts for component integration and mounting are considered in terms of additional metal inserts and connection elements. This allows for studying a variety of technical solutions during the project.

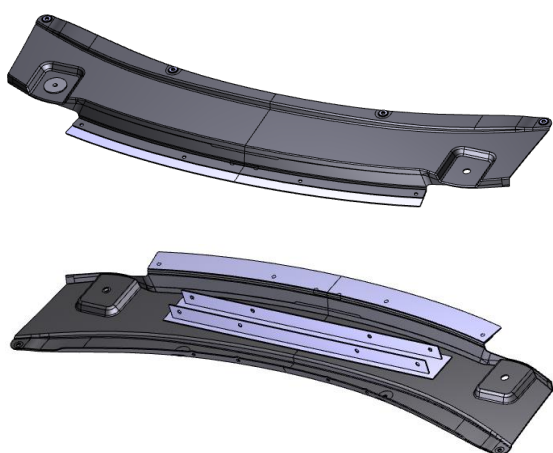


Fig. 1: CAD drawings of the functional model.

2.1 COMPONENT PROCESSING

The hybrid material structure will be manufactured by means of RTM. The metal components will be positioned in the RTM mould prior to inserting the dry preform made from two different types of given carbon-fibre weave fabrics. In order to suppress unwanted galvanic corrosion effects [5,6], blanks of glass-fibre veils will be inserted to separate the metal sheet from the carbon fibre based preform. After closing the mould, the resin system is injected at a certain injection pressure and finally cured by running the required heating cycle.

3 MATERIAL SELECTION

The resin system is of particular interest for the material system as it acts as matrix constituent for the FRPC as well as an adhesive towards the metal elements at the same time. Furthermore, the resin system needs to fulfil specific properties with re-

spect to RTM processing, i.e. low viscosity, long pot life and short curing time.

Thus, a two-component epoxy-based resin system was specifically formulated and optimized for the project purposes. In particular, two different types of epoxy resin (A1 and A2) as well as two types of curing agents (B1 and B2), crosswise combination giving four different resin systems (A1B1, A1B2, A2B1 and A2B2), were investigated in terms of the shear strength evaluated in double-lap shear experiments. The test specimens were manufactured involving three different types of metal sheets (M1, M2 and M3). Fig. 2 shows the shear strength obtained by averaging results from ten specimens tested at each of the twelve material combinations.

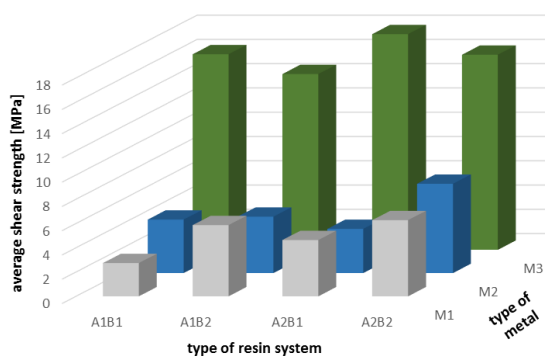


Fig. 2: Average shear strength, evaluated from double-lap shear experiments on hybrid material specimen.

Obviously, the shear strength obtained for experiments with metal sheet type M3 is significantly higher than for the two other metals. The strong deviations are explained by the surface condition of the metals: while M3 showed surface treatment, this was not applied to M1 and M2, respectively. Essentially, merely M3 promises shear strength values required for the component application addressed in this project. Thus, the surface treatment chosen for M3 is considered mandatory for processing the hybrid material structures.

While the experiments conducted on specimen involving resin curing agent B1 show slightly higher shear strength values than those on specimen prepared with B2, the resin type seems to not affect the resulting shear strength significantly. However, processibility is advantageous with resin type A1 due to longer pot life. This finally leads to selecting resin system A1B1 for processing the functional model.

4 THERMALLY INDUCED RESIDUAL STRESSES

After running the heating cycle of the RTM process, the hybrid structure is extracted from the mould and subsequently cools down convectively against ambient air. Due to different thermal expansion coefficients of the metal, fibre and resin constituents, this cooling process is critical as it induces residual stresses which in turn may cause

⁵ www.bto-epoxy.com

⁶ www.alpex-tec.com

⁷ www.ait.ac.at

⁸ www.lkr.at

deformation of the component or even unbonding of the FRPC from the metal part [7,8].

In order to study this effect, flat hybrid material plates were manufactured through RTM with dimensions of 500 x 500 mm² and 2 mm thickness for both, the metal and the FRPC part. As depicted in Fig. 3, the resulting hybrid plates show significant deformations. However, no unbonding effects were observed.



Fig. 3: Hybrid material test plate after RTM processing and subsequent convective cooling against ambient air.

Although the preform layup was chosen symmetrically with four layers of the given carbon-fibre weave fabric, the resulting deformation of the hybrid plate is asymmetric. This is in contrast to predictions from FEM simulations accompanying the process development activities. However, the simulation runs partially involved database material properties, which are likely to deviate from those of the materials used for processing the test plates.

Further activities with respect to material testing, sample preparation as well as simulation model optimization are currently pending. Results of these investigations will be incorporated in the design of the RTM mould for processing the functional model.

5 DESIGN OF EXPERIMENTS

Process development will be supported by identification of relevant process parameters following a design-of-experiments (DoE) approach [9].

While material parameters, most importantly the type of resin system, fabric architecture and fibre volume fraction are given, the processing parameters are to be determined in order to ensure the manufacturing process to run at optimal conditions. At first, a set of processing parameters was identified, that can be adjusted within certain limits:

- (i) mould temperature,
- (ii) resin preheating temperature,
- (iii) resin injection pressure, and
- (iv) rate of resin injection pressure increase with time.

The output variables considered in the DoE analysis are of qualitative as well as quantitative nature:

- (i) mould filling time,
- (ii) resin curing time,
- (iii) degree of porosity, and
- (iv) shear strength.

After specifying a detailed experimental plan, flat plates of hybrid materials will be processed according to the procedure described in Section 2.1 while varying the processing parameters. Measurement of the quantitative parameters together with subsequent test for the quality parameters finally allows for specifying the optimal processing window for the hybrid material combination.

6 SUMMARY

This paper addresses the fundamental approach of project HybridRTM, which aims at the development of a robust single-step RTM process for manufacturing hybrid material structures. The basic strategy of the project is outlined together with a description of the project consortium. Moreover, first results gained in the project, particularly with respect to material selection and process development, are described and an outlook for further activities is given.

7 ACKNOWLEDGEMENT

The authors are particularly thankful for contributions from members of the project consortium, specifically:

- Steffen Stelzer from the Chair in Material Science and Testing of Polymers at Montanuniversität Leoben for providing the data of the double-lap shear experiments,
- Gilbert Cespedes-Gonzales from Benteler-SGL for supporting us with the CAD drawings of the functional model, and
- Stefan Scheibelhofer from LKR Light Metals Technologies Ranshofen for providing the picture of the hybrid material test plate.

Moreover, we kindly acknowledge the financial support provided by the Austrian Ministry for Transport, Innovation and Technology within the frame of the FTI initiative “Produktion der Zukunft”, which is administered by the Austria Research Promotion Agency (FFG).

REFERENCES

- [1] Lässig R, Eisenhut M, Mathias A, Schulte RT, Peters F, Kühmann T et al. Serienproduktion von hochfesten Faserverbundbauteilen: Perspektiven für den deutschen Maschinen- und Anlagenbau. Studie.
- [2] Ding A, Li S, Sun J, Wang J, Zu L. A thermo-viscoelastic model of process-induced residual stresses in composite structures with considering thermal dependence. *Composite Structures* 2016; 136:34–43.
- [3] Fauster E, Schledjewski R. A Model-Based Processing Concept for Thermoplastic Tape

- Placement. In: Proceedings of SAMPE 2012, Baltimore, USA, 2012.
- [4] Konstantopolous S, Fauster E, Schledjewski R. An Adaptive Modular Monitoring & Control System for Composites Manufacturing Processes. In: Proceedings of The 34th International Symposium on Materials Science (ISMS), Risø, Denmark, 2013.
- [5] Peng Z, Nie X. Galvanic corrosion property of contacts between carbon fiber cloth materials and typical metal alloys in an aggressive environment. *Surface and Coatings Technology* 2013; 215:85–89.
- [6] Ireland R, Arronche L, La Saponara V. Electrochemical investigation of galvanic corrosion between aluminum 7075 and glass fiber/epoxy composites modified with carbon nanotubes. *Composites Part B: Engineering* 2012; 43(2):183–194.
- [7] Shin KC, Lee JJ. Effects of thermal residual stresses on failure of co-cured lap joints with steel and carbon fiber-epoxy composite adherends under static and fatigue tensile loads. *Composites Part A: Applied Science and Manufacturing* 2006; 37(3):476–487.
- [8] Shin KC, Lee JJ. Prediction of the tensile load-bearing capacity of a co-cured single lap joint considering residual thermal stresses. *Journal of Adhesion Science and Technology* 2000; 14(13):1691–1704.
- [9] Gou J, Zhang C, Liang Z, Wang B, Simpson J. Resin Transfer Molding Process Optimization Using Numerical Simulation and Design of Experiments Approach. *Polymer Composites* 2003; 24(1):1–12.

DEVELOPMENT OF NEW PROCESS CHAINS IN THE OPEN HYBRID LABFACTORY FOR HYBRID INTEGRAL COMPONENTS FOR AUTOMOTIVE MASS PRODUCTION

Robin Van der Auwera^{1*}, Tobias Gebken², Alexander Fürst², Julian Steinberg²,
Markus Kühn², Franz-Josef Wöstmann¹, Matthias Busse¹

¹Fraunhofer-Institut für Fertigungstechnik und Angewandte Materialforschung IFAM
²Technische Universität Braunschweig

ABSTRACT: The Open Hybrid LabFactory is a new competence and research center for innovative materials, process routes and component solutions in hybrid design for the automotive sector. Along the process chain from injection molding, aluminum casting and hot pressing, different research approaches in hybrid lightweight construction are focused in this project. In cooperation with the Fraunhofer Projektzentrum Wolfsburg and the Technische Universität Braunschweig the publicly funded project EnTraHyb is one of three initial projects funded by the Niedersächsisches Ministerium für Wissenschaft und Kultur. The focus is on load path-design of material transitions for hybrid structures made of aluminum, thermoplastic fiber composites and hybrid injection molding components aiming at economic lightweight. For the research project, a process chain from low-pressure aluminum die-casting, thermoforming and hybrid plastic injection molding was selected with reinforcing fibers as a load path fair transitional structure. In the low-pressure aluminum casting fiber structures are partially integrated to produce a connection of cast aluminum components and fiber reinforced thermoplastics using an injection molded fiber reinforced transition. In an integrated production process, a reshaping of the fiber-reinforced thermoplastic in hybrid injection-compression process is designed beyond to produce highly integrated components with different material classes in a production-ready process chain.

KEYWORDS: hybrid design, aluminum low pressure casting, injection molding, thermoforming, fusion bonding

1 INTRODUCTION

To meet CO₂ requirements of the automotive sector, the mass reduction of body parts plays a significant role [1]. In order to develop material adapted light weight solutions, hybrid structures are necessary [2-4]. In the public-private partnership Open Hybrid LabFactory, economically and environmentally suitable production ready manufacturing technologies for hybrid light weight components made of metals, plastics and textiles are developed. Conventional joining technologies for hybrid structures such as riveting, welding and adhesive joining have several disadvantages including overlapping, through holes for riveting, load path interruption leading to stress concentration that has to be compensated i.e. by increase of wall thicknesses leading to additional weight and contact corrosion [5]. Moreover, adhesive joining of metal castings such as aluminum castings is mostly difficult due to its surface behavior with oxide layers and aging. High cost surface preparations such as laser can be

able to induce robust adhesive bonding but are not always favorable [6]. For this reason, the integrated joining technology becomes more and more important especially for hybrid structures of metals and fiber-reinforced plastics [9-11].

Metal castings have the advantage of free shape molding with undercuts and functionalization leading to complex metal structures for example as rear subframe. On the other hand, fiber-reinforced plastics (FRP) have very high specific strength and stiffness and have a high potential for light weight design. For cost-efficient production of FRP thermoplastic (TP) matrices are favored. With their short production time in isothermal forming processes, TP-FRP can be an alternative to conventional FRP production such as autoclave, resin transfer molding and vacuum infusion. The combination of highly integrated aluminum cast parts, thermoplastics and thermoplastic FRP has very high light weight potential as focused in this project [7-8].

* Corresponding author: Wiener Strasse 12, 28359 Bremen, + 49 421 2246-178, -300, robin.auwera@ifam.fraunhofer.de

2 RESEARCH GOAL

Main goal is a hybrid technology platform, which forms the basis for various research approaches in hybrid lightweight engineering. The research currently focuses on the direct integration of glass fiber structures in the processes of aluminum low-pressure casting, injection molding and thermoforming/hot pressing. Issues of connectivity, interfaces, process design, modelling, simulation and recycling of hybrid components are addressed.

2.1 DEFINITION

The requirement list is divided into demands on geometry, forces, energy, materials, production, use, recycling, inspection, costs and deadlines. Based on this, a component is designed, which is to serve as a technology demonstrator.

The generic structure enables both the presentation of the material transition, as well as a full production ready process chain.

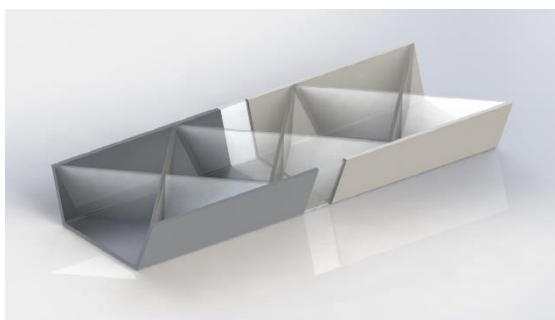


Fig. 1 Hybrid technology platform of low-pressure aluminum die casting and hybrid injection-compression molding, left: aluminum casting, right: thermoplastic FRP, middle: injection molding

2.2 DESIGN, MODELLING AND SIMULATION

The constructive design of the technology platform is done in Design Modeller (ANSYS) based on requirements from work package definition. This also includes manufacturing restrictions from casting, thermoforming/hot pressing and injection molding.

The optimization is based on different command variables from the design including shape, materials thicknesses, material transitions, stiffness, weight, etc. leading to an optimized hybrid structure. Fig. 2 shows the ANSYS model of the aluminum cast glass fiber part with its GF layers.

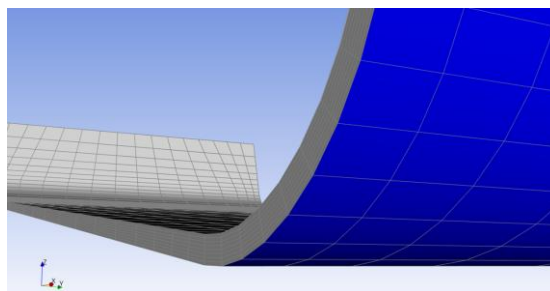


Fig. 2 Design of the technology platform of aluminum glass fiber part in ANSYS ACP

Another main focus is the design suitable for production for different manufacturing processes.

2.3 PROCESS DESIGN

As a next step, the production chain of the hybrid technology platform is defined and the technical feasibility is ensured. For this reason, a set of preliminary tests is performed including low pressure aluminum die casting (LPDC) thermoforming of organo sheets, polyamide 6 (PA6) sheets and glass fibers as well as injection molding with inserted endless glass fibers. The concept derived from this approach is an integral combination of LPDC, PA6 injection molding with continuous filament reinforcement through the different materials ensuring a load path optimized connection into TP-FRP.

The final process chain is made up of aluminum casting, thermoforming and injection molding using the low pressure die casting process and a hybrid injection-compression process. Both processes focus on integration of dry fibers within the molding process and its resulting interfaces.

2.4 TOOLING CONCEPTS

Different tooling concepts for the hybrid technology platform are focused with respect to the manufacturing processes. The tool for the aluminum LPDC process is designed including an integrated fiber fixation and shielding to protect dry fibers from the aluminum melt. The challenge is to put a defined strain on the fibers within the tool to ensure fiber position inside the mold. The low pressure die casting process focusses on a laminar form filling to produce high quality castings with low porosity. This contradicts the requirement of low wall thicknesses and included fibers because of the solidification of the melt along narrow flow paths. To ensure low wall thicknesses, the filling speed has to be enhanced.

The injection molding also includes the fixation of dry fibers to ensure fiber impregnation. Process simulation of the form filling is performed in Moldflow for injection molding and Procast for aluminum casting to design the cavity and gating systems. Furthermore, the thermal characteristics are simulated.

2.5 JOINING TECHNOLOGY

Joining technologies include the approach of load path optimized joining of aluminum and thermoplastics with integrated fibers. Furthermore, the combination of LPDC castings and injection molding parts is examined. Another approach aims for thermoforming of TP-FRP to aluminum castings. In these cases, the cast surface oxide layer prevents components made by injection molding or thermoforming from forming durable interfaces. For this reason, surface modifications are necessary. Laser and plasma based surface treatments are used to modify the aluminum surface for injection molding.

2.6 DEMONSTRATOR IMPLEMENTATION AND CHARACTERIZATION

A set of demonstrator technology platforms is built to validate the manufacturing process of LPDC and hybrid compression injection molding. Furthermore, the demonstrator will be tested in a set of different testing configurations including 3-point-bending tests for validation of the simulation model.

3 EXPERIMENTAL AND SELECTED RESULTS

3.1 LOW PRESSURE DIE CASTING

The Low pressure die casting process is an aluminum casting process for very high quality castings with complex, hollow structures. Because of its process characteristics the cavity is filled against gravity. The melt surface is pressurized to control its flow in the riser tube which leads to low turbulence fill with controlled fill velocity. The potential to produce low wall thicknesses with current series wall thicknesses of 3.5 mm is very high. Research and development work on reduction of wall thicknesses up to 2.5 mm to meet even higher light weight requirements. The overall process and its controlled solidification serve for optimum conditions for mechanical properties with high yield strength (YS) and ultimate tensile strength (UTS). In this process, an AlSi7Mg0.3 alloy is used with general mechanical properties of YS = 240 MPa, UTS = 260 MPa and elongation at break of 7 % at a conventional T6 heat treatment.[12]

The integration of glass fibers into the LPDC process is a challenge due to its low pressure of up to 1 bar pressure difference. The melt temperature is kept constant at 750 °C with mold temperature at 320 °C and the process parameters are chosen to 500 hPa at 2 s. which leads to high melt velocities in order to prevent early solidification at contact with fibers.

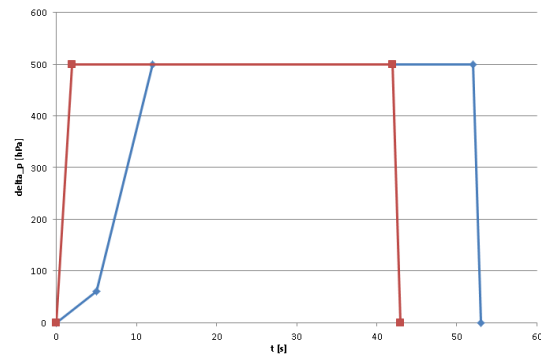


Fig. 3 Casting chart pressure over time, blue: regular filling velocity, red: fast form filling to prevent early solidification

Spontaneous impregnation of fibers does not take place [12] but a macroscopic mechanical interlocking can be achieved that leads to certain interface cohesiveness depending on fabric type and configuration.

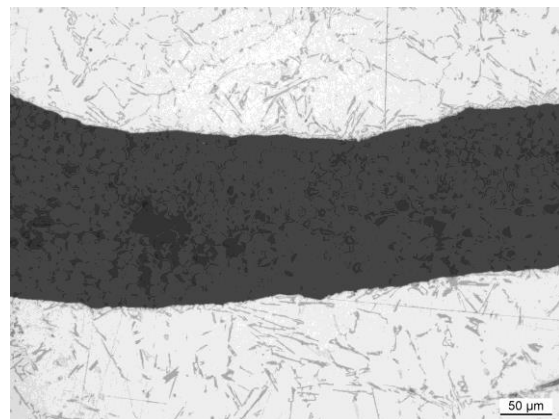


Fig. 4 Metallographic section of AlSi7Mg0.3 with glass fibers

For integral aluminum LPDC and injection molding structures, fibers are shielded partially and then introduced to the thermoforming and injection molding process as depicted in Fig. 6.

3.2 THERMOFORMING AND FUSION BONDING

Within the process of fusion bonding the TP matrix of TP-FRPs is used as a kind of hot-melt adhesive. Because the joint mainly depends on chemical adhesion, a surface pre-treatment of the casted aluminum surface is necessary to enable a structural and especially durable bond. In the case at issue grit blasting as well as a physical surface modification by laser and plasma treatment are used to remove oxide layers and residues of release agents.

As a next step, the aluminum part and the TP-FRP part are placed in a compression die. By heating the press, the aluminum is also heated due to heat conduction and thus the surface of the TP-CFRP is

also heated to the melting temperature of about 240°C. During the pressing process, the pressure is kept constant until the temperature of the TP matrix material drops underneath its melting point.

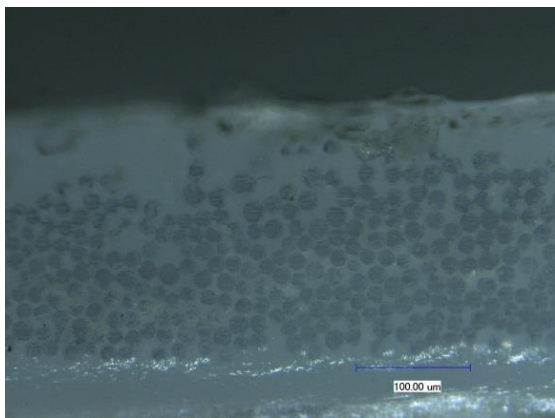


Fig. 5 Impregnated glass fiber strands with PA6 matrix after thermoforming of PA6 foils and glass fibers

Besides fusion bonding, thermoforming is used for the impregnation of the dry fibers which are partly impregnated with aluminum in the LPDC process (Fig. 5). The process steps are similar to those described above for the bonding process. The partly coated fibers and PA 6 TP matrix are placed in a compression die. After achieving the melting temperature of the TP material, the fibers and matrix are held under constant pressure until the fibers are infiltrated by the molten polymer matrix.

The combination of impregnation and fusion bonding completes the joining process via thermoforming.

3.3 INJECTION MOLDING

The injection molding process is a suitable technology for manufacturing parts with complex geometries within short process cycles. During the injection molding process, the insert parts, LPDC aluminum and TP-FRP (with plasma or laser modified surfaces) as well as the implemented glass fibers are impregnated with the injected melt. Hence, the materials are manufactured to a form-fitting hybrid part. In recent investigations, a polyamide 6 and a woven glass fiber textile have been used.

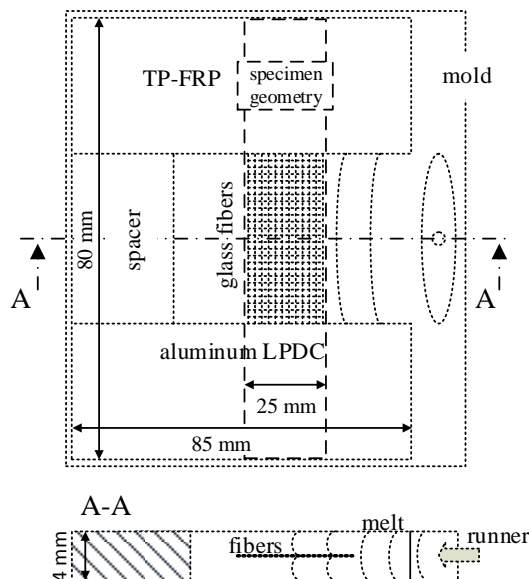


Fig. 6 Tool design of the material components in the mold of the molding injection machine

The mold design considers the fixing of the aluminum LPDC insert as well as the TP-FRP insert. During the process, the endless glass fibers have to be in a plane to avoid moving inside the mold. The positioning of the inserts and the glass fiber textile is improved by using a spacer between the inserts. During the injection process, the melt is split by the fiber textile in two melt fronts, one melt front above the textile and one below (Fig. 6). Therefore, the melt is able to enclose the woven textile and infiltrate it from both sides.

The micrographic preparation (Fig. 7) shows an exemplary infiltrated glass fiber textile with a polyamide 6 matrix manufactured by an injection molding process. The process is conducted with a melt temperature of 260°C, a mold temperature of 70°C and an injection molding speed of 10 cm³/s. Fig. 7 shows a well-infiltrated area (I.) and a poorly-infiltrated area (II.).

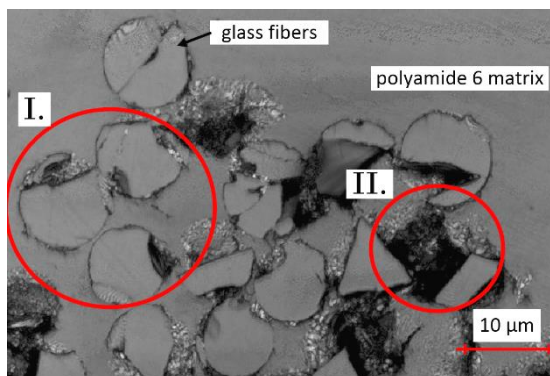


Fig. 7 Impregnation of glass fibers in injection molded polyamide 6 (I. well-infiltrated and II. poorly-infiltrated area)

As a further step, a variation of process parameters like melt and mold temperature, injection speed and pressure will be made in order to influence the degree of fiber textile impregnation.

Subsequent investigations will have to deal with the optimized impregnation of different fiber textiles in the injection molding process.

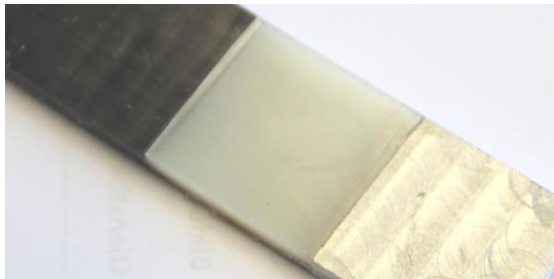


Fig. 8 Hybrid test coupon from aluminum low pressure die casting, TP-FRP thermoforming and PA6 injection molding with endless fibers

4 CONCLUSION AND OUTLOOK

The demonstrator technology platform is designed with respect to requirements and preliminary optimization of the geometry is performed.

In preliminary manufacturing tests, it is shown that integral LPDC parts with endless fibers and thermoplastic matrices can be manufactured for the demonstrator technology platform. This includes aluminum LPDC, thermoforming of the transition zone and also injection molding aiming for the integrated manufacturing process of the hybrid injection-compression process for integral TP-FRP-Aluminum structures with endless fibers.

For further investigations on the integral transition zone, the different interfaces are eventually tested and the respective material data is implemented into the simulation model.

5 ACKNOWLEDGEMENT

The authors gratefully thank the Niedersächsisches Ministerium für Wissenschaft und Kultur MWK for funding the project.

REFERENCES

- [1] Eckstein, L., Hartmann, B., Schmitt, F.: *Leichtbau bei Elektrofahrzeugen*. Automobil-technische Zeitschrift, 11/2010, Springer Verlag, Wiesbaden, 2010.
- [2] VDI Zentrum Ressourceneffizienz GmbH: *Bestandsaufnahme Leichtbau in Deutschland – Kurzstudie*. 2015.
- [3] Gude, M., Lieberwirth, H., Meschut, G., Zäh, M.F.: *FOREL Studie „Chancen und Herausforderungen im ressourceneffizienten Leichtbau für die Elektromobilität*. 2015.
- [4] Lehmhus, D., Busse, M., Herrmann, A.S., Kayvantash, K.: *Structural Materials and Processes in Transportation*. 1. Wiley-VCH, Weinheim, 2013.
- [5] Spähn H., Fäßler K.: *Kontaktkorrosion: Grundlagen - Auswirkung – Verhütung*. Communication from the material testing laboratory of the Badische Anilin und Soda-Fabrik AG, Ludwigshafen (Rhine), Germany, 4, 321 – 331, 1966.
- [6] Roesner, A., et al.: *Laser Assisted Joining of Plastic Metal Hybrids*. Physics Procedia, 12 B: 370-377, 2011.
- [7] Van der Auwera, R.: *Hybride Faserverbund-Aluminiumguss-Strukturen für ein intelligentes Multimaterialdesign*. Vortrag auf der Hybrid Expo, Stuttgart, 2015.
- [8] Lässig, R., Eisenhut, M., Mathias, A., Schulte R.T., Peters, F., Kühmann, T., Waldmann, T., Begemann, W.: *Serienproduktion von hochfesten Faserverbundbauteilen - Perspektiven für den deutschen Maschinen- und Anlagenbau*. Studie Roland Berger Strategy Consultants, VDMA-Forum Composite Technology, 2012.
- [9] Van der Auwera, R., Lang, A., Clausen, J., Specht, U., Schumacher, J., Herrmann, A.S.: *Joining of Aluminium and CFRP Parts using Glass Fibres as Transition Elements*. Vortrag auf der International Conference Euro Hybrid Materials and Structures, 10-11. April 2014, Stade, Germany, 2014.
- [10] Clausen, J., Van der Auwera, R., Wöstmann, F.-J., Schmid, A.: *Integration textiler Strukturen in den Aluminium-Druckguss zur Realisierung integraler CFK-Aluminium-Verbindungen*, Proceedings 7. Landshuter Leichtbaukolloquium, 2015.
- [11] Clausen, J., Specht, U., Busse, M., Lang, A., Sanders, J.: *Integration of glass fibre structures in aluminium cast parts for CFRP aluminium transition structures*. Procedia Materials Science, 2:197–203, 2013.
- [12] Fuchs, H., Egner-Walter, A.: *Casting Processes for Suspension and Chassis Parts Product and Process Options and Potential*. VDI-Berichte Nr. 2274, 2016.
- [13] Mortensen, A., Cornie, J. A.: *On the infiltration of metal matrix composites*. Metallurgical Transactions A, 18A(13): 1160-1163, 1987.

COMPUTATIONAL ANALYSIS OF POLYURETHANE FOAM EXPANSION PROCESS IN FIBER REINFORCED SANDWICH STRUCTURES

J. Tröltzsch^{1*}, I. E. Ireka^{2,3}, D. Niedziela², K. Steiner², K. Schäfer¹, F. Helbig¹ and L. Kroll¹

¹Institute of Lightweight Structures, Technische Universität Chemnitz, Germany

²Fraunhofer Institute for Industrial Mathematics, Kaiserslautern, Germany

³Department of Mathematics, Obafemi Awolowo University, Ile-Ife, Nigeria

ABSTRACT: In this paper, we present numerical simulations of expansion process of polyurethane foam in fiber reinforced sandwich structures. The material and mechanical properties of polyurethane (PUR) foam structures can be enhanced by integration of fiber reinforcement in the mold prior to the injection of the reactant (polyol and isocyanate) polymer blend. In addition, the mathematical modelling and simulation of free rise expansion process of PUR foams in simple geometries suggests that the final morphology of the expanded foam is highly influenced by the interplay between the chemorheological viscosity, temperature, gas volume fraction and degree of polymerization of the foaming mixture. However, in modelling the foam expansion process through warp-knitted spacer fabrics, one must account for the additional effects originating from the porosity and/or permeability of such layers. This additional effect generally introduces another level of difficulty in the mathematical description of such physical setup. The emerging system of nonlinear partial differential equations governing the flow is solved in appropriate geometry and boundary conditions using CoRheoS; an in-house simulation platform based on the finite volume method. With graphical illustrations, we present the flow of the expanding foam in the medium and determine the porosity of the fibrous structure. The results from this ongoing investigation is anticipated to assist foam process and structural engineers in understanding some intricacies that occurs in the porous media flow of expanding polyurethane foams mixtures.

KEYWORDS: Polyurethane foam, spacer fabric, sandwich structure, flow simulation,

1 INTRODUCTION

Recent advancements on improving the mechanical and physical properties, such as tensile strength, durability of structural materials and reduced bulk mass, suggests that sandwich structures made from polyurethane (PUR) foams reinforced with warp-knitted spacer fabrics offers a good substitute [1]. These spacer fabrics possess open diffusion thread architecture with low mass and high dimensional stability making them adequate for fibre reinforced composites. Furthermore, the rigidity effect of these composites are somewhat attributed to the resistance offered by the cured PUR foam matrix, thereby, hindering the spacer threads from rapid bending and buckling under deformation. However, fabricating these special composite structures require that the polyurethane mixture adequately penetrate the spacer fabrics.

During the PUR injection molding process, the reactant polymer blend is injected into a closed mold consisting of some integrated warp-knitted fabrics. The self-expanding nature of the foam mixture enhances impregnation through the porous structure of the spacer fabrics in the mold.

The complexity in the physics of the flow observed in this setup reveals a new level of research inquest. Particularly in porous media flows of expanding PUR foam mixture.

In the mathematical modelling and simulation of such systems, the issue of concern pertains to the porosity of the medium as well as the permeability of the chemorheological materials through such microstructure under non-isothermal conditions. Another intrinsic challenge arises from the spatio-temporal evolution of the foam material properties such as the viscosity. In general, such setups naturally yields fundamental research questions in mathematical modelling of fluid-structure interaction in composite microstructures.

* Corresponding author: Technische Universität Chemnitz, Institut für Strukturleichtbau, Reichenhainer Str. 31-33, 09126 Chemnitz, phone: +49 371 531 35665, fax: +49 371 531 835665, juergen.troeltzsch@mb.tu-chemnitz.de

Obtaining adequate mathematical description for the complex dynamics of expanding foams in reaction injection molding with or without reinforcements is an issue of ongoing research [1-6]. The need for optimally controlled molding processes has resulted to the formulation of various mathematical models capable of describing the mass and heat transfer in reacting PUR system from either mesoscale [3] or macroscale [4-6] view.

In our recent paper [2], an experimentally motivated study on free rise expansion of chemically blown PUR foams revealed that the mixture viscosity plays an important role in the final morphology of the expanded foam matrix. In this case, a coupled system of partial differential equations consisting of the Navier-Stokes equations, degree of polymerization/cure, energy equations and foam fraction were resolved numerically. In addition, we assumed a viscosity model that depends on the degree of cure, temperature and gas volume fraction. In addition, we assumed uniform foam expansion within the domain as well as constant reaction rate parameters. Our simulation results showed a good comparison with experimental data. Furthermore, the injection molding process of polymer melt in integrated fibre reinforcement [7] showed that the Navier-Stokes-Brinkman equations for porous media flow accurately predicts the impregnation and flow profiles in the system. However, the modelling and simulation of the flow of PUR foam through warp-knitted spacer textile structures during reaction injection molding is much more complicated.

This complication arises from the consideration of the resistance to flow by the fibrous textile structures. Therefore, in this study, we explore a combination of the methods and approaches discussed in [2] and [7] to model the flow of expanding foams through such microstructures. More so, a major challenge in the simulation of these processes lies in obtaining appropriate input parameters for our model equations. Hence, the fundamental questions to address are “How good is our choice of viscosity model adopted in [2]?” Secondly, what is the permeability of the microstructure in question? These are very crucial in the successful modelling and simulation of the flow of PUR mixture in porous microstructure. The resulting governing equations are solved numerically for state variables. All our simulations are performed on CoRheoS [8], a finite volume complex rheology simulation platform developed at Fraunhofer Institute for Industrial Mathematics, Kaiserslautern, Germany.

In section (2), we present a brief description of the physical problem considered in this study and in (3) we discuss the experimental setup adopted in estimating the viscosity of the PUR foam mixture via torque measurements. Section (4) present numerical results from the free rise foam expansion

experiment. In addition, we present a validation of our models with the torque measurements from experiments and then present the permeability of the microstructures with pictorial illustrations. Finally, in section (5) we present concluding remarks and future direction for these ongoing investigations.

2 PROBLEM DESCRIPTION

The schematic structure of the fibrous warp-knitted fabric is as shown in Fig. 1. Although in the physical sense, the domain is usually a dense arrangement of fibre network within the structure.

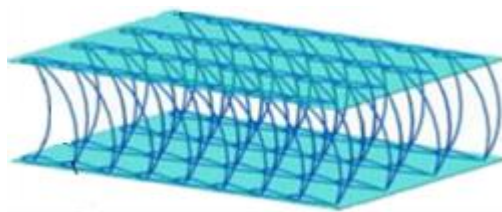


Fig. 1 Structure of the warp-knitted spacer fabrics

In the mold filling experiment, the reacting PUR foam mixture is injected through an inlet into the mold containing the porous fibre network. The foam expands in time with bubble creation and evolution of heat resulting from chemical reactions, thereby, flowing through the porous structure with increasing pressure. Unlike the free rise experiments, here, more quantity of the reactant mixture is required to fill the mold completely [1]. This could be attributed to possible bubble ruptures that would occur when growing bubbles with diameter larger than the allowed gap between neighbouring fibres in the network encounter such obstacles. In the mathematical formulation of the described experimental setup, we adopt the modelling approach developed and discussed in both [2] and [7]. The domain for our numerical simulation is constructed to adequately represent the physical domain of the spacer fibre, see Fig. 2.

One critical part of this problem is obtaining appropriate values for the permeability tensor [7] of the warp-knitted fibre structure. This would serve as input parameter in the Navier-Stokes-Brinkman equation. In this study, we explore a purely numerical approach to estimate the permeability of the network structure (see section (4)). As earlier mention, we also seek to validate the viscosity model adopted in [2] with experimental data from torque measurements during the period of foam expansions. In section the next section, we present a brief description of the experiments on the evolution of material viscosity during foam expansion.

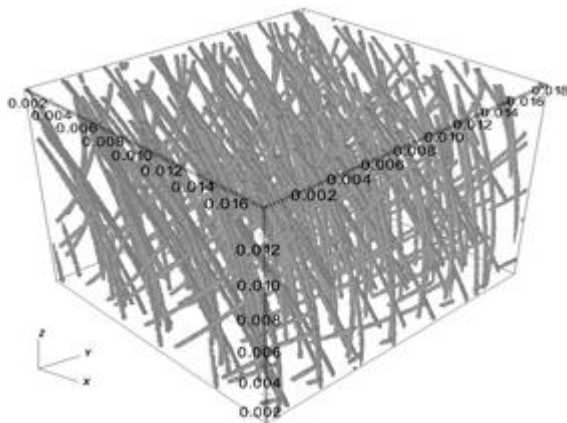


Fig. 2. Geometric description of the computational domain.

3 EVOLUTION OF FOAM VISCOSITY DURING FREE RISE FOAM EXPANSION EXPERIMENTS

The experimental measurement of viscosity of chemically blown PUR foam is often a herculean task. This is due to the volume changes that occur in the measuring fluid resulting from exothermic chemical reaction and evolution of gas within the system. Thus, typical plate rheometer for viscosity measurement used for other reactive fluids such as thermoset resins, are not practicable in this case. The expansion of the foam would normally lead to a discharge of mixture from the measuring gap. Therefore, coaxial oscillating or vibrating rheometers are preferred. This choice naturally allows for changes in volume during viscosity measurement of the mixture. For this purpose, a Searle-type coaxial oscillating rheometer was set up, Fig. 3.

With a polycarbonate rod as the inner cylinder, heat sink to the rod is minimized since the thermal conductivity of polycarbonate is low, while offering good adhesion properties to the polyurethane foam. For the outer cylinder, measuring glasses with scale divisions were used to obtain the time-volume curves (Fig. 3). In addition, we integrated two thermo lines near the walls of the inner and outer cylinder to determine the reaction temperature during the foam expansion. With a video camera, we obtain the volume expansion of the PUR foam in the setup.

A commercial PUR hard foam formula, consisting of a two-component isocyanate to polyol (100:67 mass fractions) system was used for these experiments. The reactants were hand-mixed at room temperature and transferred into the measuring glass, measurement commenced immediately.

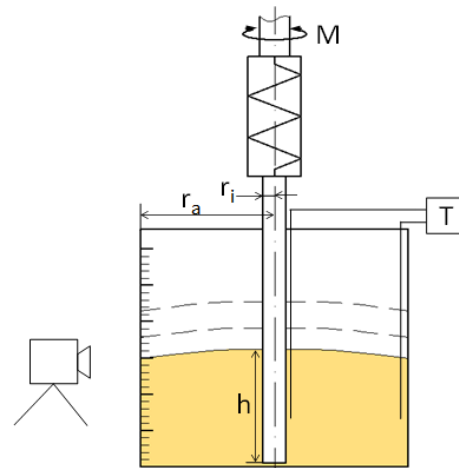


Fig. 3 Setup for coaxial oscillating rheometer

The torque (M) responses of the rheometer were measured over time for the given radius r_i and r_a of the inner, outer cylinder (Fig. 3). With these M values, the shear stresses at the wall of the inner cylinder were computed. The oscillating frequency of the rheometer was set to 6,28 rad/s with a small angular displacement of 0,01 rad. This helps to avoid foam detachment from the oscillating inner cylinder when exceeding the gelling point. At this point, the reacting mixture gradually experiences phase transition resulting to formation of rigid foam matrix. Time dependent immersed depth (h) of the inner cylinder, which increases with foam expansion, was observed with a video camera. The volume of the expanding foam increases in time until a maximum height is reached, and remains constant afterwards, see Fig. 4

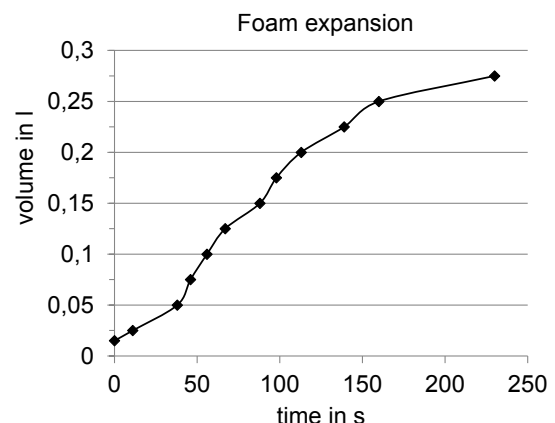


Fig. 4 Temporal changes in volume of expanding foam

The foam expansion strongly influences the measured shear stresses (Fig. 5). This corresponding effect is attributed to the variation in material properties as the exothermic reaction proceeds. The initial drop in Fig. 5 results from changes in temperature, which influences the rate of chemical

reaction as well as the viscosity. Hence, the initial decrease in shear stress and the mixture viscosity leads to accelerated upward flow of the foam front in the material domain. After about 230 seconds, the foam attains distinctive increased volume, which marks the beginning of the hardening phase. In addition, the hardening of the foam material corresponds to the equilibrium of forces between the inner gas pressure resulting from the evolution of CO₂ gas and the flow resistance. At this point, the foam seizes to expand and the viscosity grows infinitely.

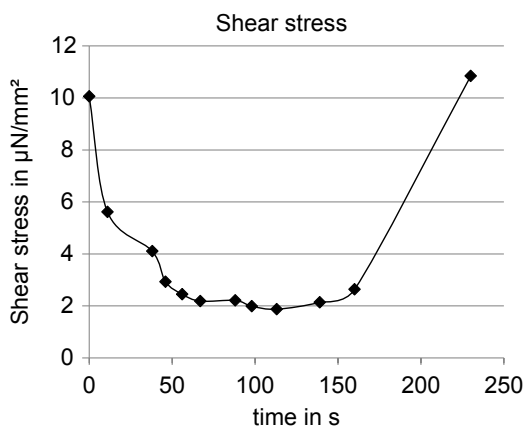


Fig. 5. Plot showing the computed shear stress from torque measurements in the oscillating rheometer.

The measured torque values show a gradual increase in time and as the gelling point is approached, the torque values grow infinitely (Fig 6).

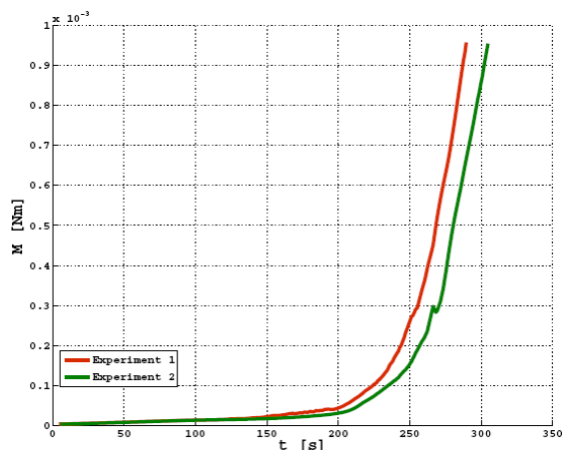


Fig. 6. Plots of the torque measurements from experiments.

The emergence of the curvature of the flow front depends mostly on the evolving fluid viscosity, which strongly depends on the spatial variation of temperatures and the rate of chemical reactions in the mixture. Since the distributions of shear rates between the inner and outer cylinder walls are

unknown, it is therefore not possible to carry out direct calculation of the viscosity in the domain. Rather, the viscosity is estimated using a Newtonian approximation and the information from the varying height of the foam at the inner cylinder wall as well as measured torque values.

4 NUMERICAL SIMULATION VALIDATION WITH EXPERIMENTAL DATA

In our simulation of the free rise PUR foam expansion experiment discussed in [2], our model showed good agreement both for the foam expansion (Fig. 7) and temperature.

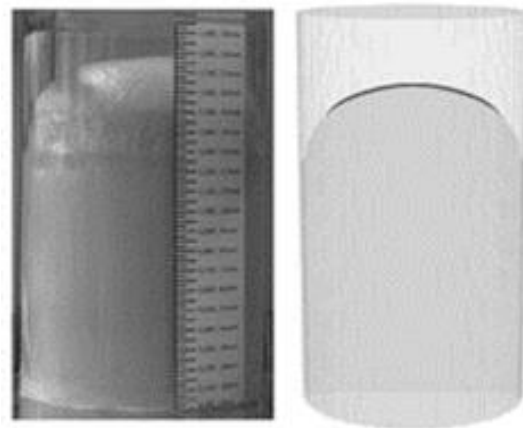


Fig. 7. Comparison of the free rise foam expansion: Left, observation from experiment and right, result from our simulation

However, it would be adequate to obtain relevant parameters for the viscosity model that reflects the behaviour of the measured torque values from experiment as in Fig. 6. In this regard, we adopt the mathematical model in [2] and solve the state equations numerically in appropriate geometry with to obtain the torque values at the wall. Using CoRheoS as our simulation platform, results from our studies show similar behaviour for the torque values at the wall (Fig. 8). The results in Fig. 8 comparing the torque measurement from experiments and that from our simulation show good quantitative agreement between them. Hence, the observation in Fig. 8, proves the validity of our adopted viscosity model, see [2].

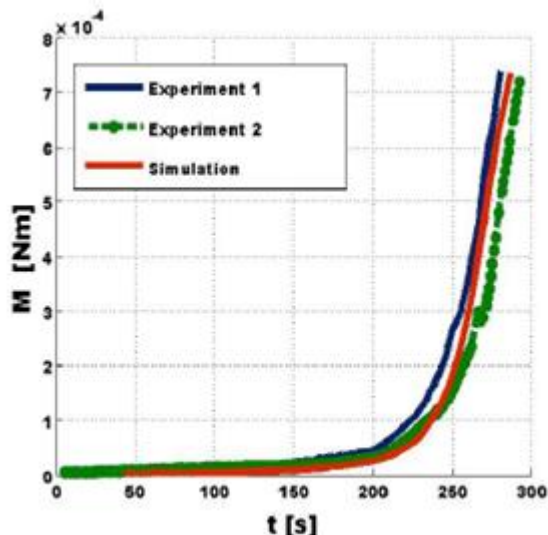


Fig. 8. Comparison between torque measurements from experiments and from our simulation.

As earlier mentioned, the microstructure modelling of porous media flow of PUR foam mixture requires that we obtain appropriate permeability tensor for the warp-knitted spacer fabric through which the mixture is expected to flow. In Fig. 9, we use numerical approach to obtain corresponding values for the permeability tensor. Here, we carry out simulations of the flow of liquid (in blue) through the porous structure presented earlier in Fig. 2. Thus, the effective permeability \mathbf{K} of the fibrous structure obtained in our simulations is

$$\mathbf{K} = 10^{-7} * \begin{bmatrix} 1,68 & 0 & 0 \\ 0 & 1,71 & 0 \\ 0 & 0 & 2,70 \end{bmatrix}$$

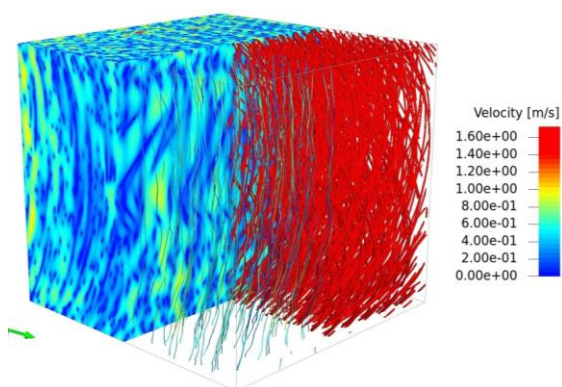


Fig. 9. Simulation of flow of liquid through the warp-knitted spacer fabrics. The green arrow indicates the direction of flow.

5 CONCLUSIONS

In this paper, we presented a framework for the modelling and simulation of flow of PUR foam mixture through porous warp-knitted spacer fabrics in injection moulding. To describe the flow mathematically, we adopted a viscosity model that depends on the degree of polymerization, temperature and the gas volume fraction. This choice of viscosity requires that we obtain relevant input parameters by comparing torque measurements from free rise experiments and those obtained from our simulation under the same physical conditions. Our results when compared with those from experiments showed good qualitative agreement. Furthermore, with numerical simulation of flow of fluid through the given porous structure, we obtain the relevant permeability tensor for the spacer fabrics. Hence, the parameters obtained from these simulations will serve as input parameters to our model for the flow through the prescribed porous media.

To describe the flow through the porous structure mathematically, we explore the Navier-Stokes-Brinkman equations, which have been shown to effectively model flow of non-Newtonian fluids through microstructure [7].

Since this study is ongoing, issues relating to coalescence or rupture of bubbles, non-uniform foam expansion and temperature dependent rate laws for the chemical reactions are yet to be addressed. The future direction of this study is therefore to explore various means of incorporating these relevant physical behaviours into our mathematical models.

6 ACKNOWLEDGEMENT

This work was performed as part of the research project PAFATHERM (grant number 03IPT508X), supported by the German Federal Ministry of Education and Research (BMBF), as well as the Cluster of Excellence MERGE (grant number EXC1075), supported by the German Research Foundation (DFG). Financial support is gratefully acknowledged.

REFERENCES

- [1] Schäfer, K; Tröltzsch, J; Helbig, F; Niedziela, D.; Kroll, L.: *Flexible spacer fabrics for reinforcement of rigid polyurethane foams in sandwich structures*. 20th International Conference on Composite Materials, Copenhagen, 19th -24th July.
- [2] Ireka, I.; Niedziela, D.; Schäfer, K.; Tröltzsch, J.; Steiner, K.; Helbig, F.; Chinyoka, T.; Kroll, L.: *Computational Modelling of the Complex Dynamics of Chemical-*

- ly *Blown Polyurethane Foam*. *Physics of Fluids*. 27, 113102 (2015).
- [3] Bruchon, J; Coupez, T.: *A numerical strategy for the direct 3D simulation of the expansion of bubbles into a molten polymer during a foaming process*. *Int. Journal for Numerical Methods in Fluids* 57 (2008), pp. 977-1003.
- [4] Samkhaniani, N.; Gharehbaghi, A.; Ahmadi, Z.: *Numerical simulation of reaction injection molding with polyurethane foam*. *Journal of Cellular Plastics* 49 (2013), pp. 405-421.
- [5] Bikard, J.; Bruchon, J.; Coupez, T.; Silva, L.: *Numerical Simulation of 3D Polyurethane expansion during manufacturing process*. *Colloids and Surfaces A: Physiochem Eng. Aspect*, 309 (2007), pp. 49-63.
- [6] Seo, D.; Youn, J.R.: *Numerical Analysis on Reaction Injection molding of Polyurethane Foam by Using Finite Volume Method*. *Polymer*, 46 (2005), p. 6482-6493.
- [7] Niedziela, D.; Tröltzsch, J; Latz A.; Kroll, L.: *On the numerical simulation of injection molding process with integrated textile fiber reinforcements*. *Journal of Thermoplastic Composite Material*, 26(1) 74-90.
- [8] Schmidt, S.; Niedziela, D.; Steiner, K.; Zausch, J.: *CoRheoS: Multiphysics solver framework and simulation infrastructure for complex rheologies*. In "NAFEMS World Congress 2013", volume 49, Salzburg (AT), 2013.

MANUFACTURING OF THERMOPLASTIC FIBER-METAL-LAMINATES BASED ON REACTIVELY PROCESSED POLYAMIDE 6

Sebastian Gödde^{1*2}, Cahit Arik³, Kay Weidenmann⁴, Frank Henning²³

^{1*} Karlsruhe Institute of Technology, Institute for Applied Materials,
Karlsruhe, Germany,

² Karlsruhe Institute of Technology, Institute for Vehicle System Technology, Karlsruhe,
Germany

³ Fraunhofer-Institute for Chemical Technology,
Pfinztal, Germany

ABSTRACT: Fiber-Metal-Laminates (FML) are high performance hybrid material systems, composed of thin layers of alternately arranged fiber-reinforced polymer (FRP) and metallic sheets. Combining excellent impact and fatigue behavior with low density, FMLs offer great lightweight potential and are deployed in structural aircraft applications. In conventional manufacture, partially cured thermoset epoxy prepregs, consisting of glass or aramid fibers, and layers of aluminum alloy are piled up, to form semi-finished preimpregnated FMLs, which are further processed to FML-components. With respect to increased recycling regulations, thermoplastic solutions are gaining attractivity. Therefore thermoplastic composite tapes are considered a replacement for thermoset prepregs and are utilized to generate semi-finished preimpregnated FMLs. However, the processing of semi-finished preimpregnated FMLs has major disadvantages in terms of formability and costly preimpregnated materials.

For this reason, an alternative manufacturing process, based on the reactive processing of thermoplastic prepolymers (T-RTM) and semi-finished dry FMLs, has been developed. Semi-finished dry FMLs were generated, using sheets of metal, interspersed with layers of dry glass fiber textiles and placed in a heated mould cavity. Next, exploiting a special sealing concept, low-viscose reactively processed monomer melt, based on caprolactam, was injected in between the metallic sheets and thermoplastic, cast polyamide 6 Fiber-Metal-Laminates (T-FML) manufactured. The sealing system included silicon sealing mats, which prevented the monomer-melt from bypassing the semi-finished dry FMLs.

It became clear that by varying the mould gap, the fiber volume fraction of T-FMLs is precisely adjustable. thermogravimetric (TGA) and microstructural analysis further indicate low void contents and good impregnation qualities for all manufactured T-FMLs, exceeding a certain threshold fiber volume fraction.

KEYWORDS: Fiber-Metal-Laminates, FML, RTM, T-RTM, Cast polyamide 6, Anionic polyamide 6

1 INTRODUCTION

Consisting of thin layers of alternately arranged fiber-reinforced polymer (FRP) and monolithic metallic sheets, Fiber-Metal-Laminates (FML) combine advantages of both material classes, alleviate some of their drawbacks and even feature synergistic behavior. As a result, FML-structures possess high weight specific strength, are more resistant to fatigue, due to their outstanding resistance to crack propagation, and have excellent impact properties [1][2].

Whereas in the aviation industry, advanced hybrid materials like ARALL (Aramid-reinforced aluminum laminate) and GLARE (Glass-fiber-reinforced

aluminum) have been successfully introduced, automotive applications are currently limited to simple-shaped polymer-metal-laminate-components, made from commercially available pre-materials like HYLITE (Tata Steel), USILIGHT (ArcelorMittal) or Litecor (ThyssenKrupp Steel Europe) [1][2][5]. Main obstacles on the way to a mass scale FML-implementation are costly starting materials, like thermoset prepregs, as well as complex manufacturing routes with long processing cycles and poor formability [3][4][5].

The production of FML-components conventionally consists of autoclave-curing of semi-finished preimpregnated FMLs, made from alternately ar-

*Corresponding author: Karlsruhe Institute of Technology, Institute for Applied Materials, Kaiserstraße 12, 76131 Karlsruhe, Germany, phone: 004972160842197, sebastian.guedde@kit.edu

ranging sheets of aluminum alloy and partially cured thermoset epoxy prepregs [1].

To enhance fracture toughness and recyclability, thermoplastic FMLs (T-FMLs) have recently been developed, replacing thermoset prepregs by thermoplastic composite tapes. However, additional adhesive application is usually required to create sufficient metal-tape-interface properties [4][6].

An alternative manufacturing technique for high quality FRP-parts, avoiding costly preimpregnated base materials with potential for large quantity production, is Liquid Composite Moulding (LCM). Common feature of all LCM processes is the impregnation of unwetted reinforcement, placed in a form-giving mould cavity, with liquid, usually thermoset, resin. LCM embraces a large number of different processes that can be categorized, depending on criteria like pressure difference (infusion or injection), tooling (closed- or open-mould), auxiliary materials or process parameters [7][8].

Vacuum Assisted Resin Transfer Moulding (VARTM) utilizes vacuum pressure, an open-mould cavity and a flow distribution media to allow resin material to spread on the fiber textiles surface and to infuse through the parts thickness. It has been proven that VARTM can be adapted to create FML-components also. To enable adequate impregnation however, it is necessary to drill flow paths into the metal sheets [3][9].

Resin Transfer Moulding (RTM) is a closed-mould process, in which resin is pressurized by a dosing-unit, injected in between upper and lower mould and forced to flow through layers of dry fiber textile. Exploiting RTM, FRP-parts with high geometric accuracy as well as surface quality, at short cycle times, can be realized [7][8].

The manufacturing of FML based on thermoset RTM technology has also been investigated and it has been shown that an infiltration of preformed semi-finished dry FMLs is generally possible [10]. A relatively new approach in LCM focuses on the production of thermoplastic FRP-components via RTM and is usually referred to as Thermoplastic Resin Transfer Moulding (T-RTM). Key element are reactively processed, precursors, like ϵ -caprolactam, that polymerize in situ, to form thermoplastic matrices. Combined with an activator and catalyst, ϵ -caprolactam reacts in an anionic ring-opening polymerization to cast polyamide-6 (CPA-6). The low viscous caprolactam monomer melt enables good impregnation qualities and high molecular weight, resulting in superior impact and energy absorption properties. Depending on the FRP-components thickness, cycle times of just three minutes are realizable [7][11][12].

In the scope of this study, the possibility of manufacturing T-FML via T-RTM shall be evaluated. Therefore, T-FML based on reactively processed CPA-6 were manufactured and the Fiber-Volume-

Fraction (FVF) and impregnation quality investigated.

2 EXPERIMENTAL

In this work, semi-finished dry FMLs were generated, combining aluminum alloy sheets with layers of woven glass fiber fabric, and placed in a closed mould cavity, equipped with silicone sealing mats, at varying mould gaps. Next, low viscous monomer melt, consisting of ϵ -caprolactam, catalyst and activator were injected and cured to form CPA-6. The T-FML were then demoulded and further subjected to thermogravimetric (TGA) as well as microstructural examinations.

2.1 MATERIALS

The reinforcement used in this study was E-type glass fiber fabric with twill weave architecture (supplied by Interglas Technologies GmbH., product reference 92125). According to the manufacturer, the textile has an areal density of 280 g/m², a thickness of 0.35 mm and a fiber density of 2.6 g/cm³.

The metal sheets used in this study were 1 mm thick, non-heat-treatable, wrought type 5182 aluminum alloy (supplied by Novelis Inc.). Before processing all sheets were cleaned with acetone.

Semi-finished dry FMLs with sandwich design, composed of four layers of textile reinforcement [layout 0/0/0/0] covered with two sheets of metal, were prepared. Whereas the textile was cut to dimensions of 478 mm x 460 mm, the metal ones were 478 mm x 450 mm. Two edges of the textile and metal were rounded with a radius of 15 mm, to ensure good fitting into the mould.

The components of the in situ polymerized CPA-6 matrix were AP Nylon caprolactam, catalyst Brüggolen C10 and activator Brüggolen C20 (supplied by Brüggemann Chemical). The mixing ratio of caprolactam:catalyst:activator was 94:4:2 by weight.

2.2 MANUFACTURING

The equipment technology utilized in this study consisted of an ATP mixing-, dosing- and injection-unit (type Swissthermo) as well as a Kannegießer mould carrier (type MFT 12.5 x 16.5/10) with a maximum clamping force of 600 kN, equipped with an injection moulding tool.

Central element of the mixing- and dosing-unit are two reservoirs containing the CPA-6 components in liquid state, at a temperature of 110 °C. Whereas Container A was filled with 11.5 kg of caprolactam and 1 kg of catalyst, B contained 12 kg of caprolactam and 0.5 kg of activator. To avoid moisture absorption, both containers were flooded with nitrogen. Prior to injection, all components passed a mixing head and were blended together.

The injection moulding tool has a cavity size of 480 mm x 670 mm and also features closable inlet and outlet valves (Fig. 1).

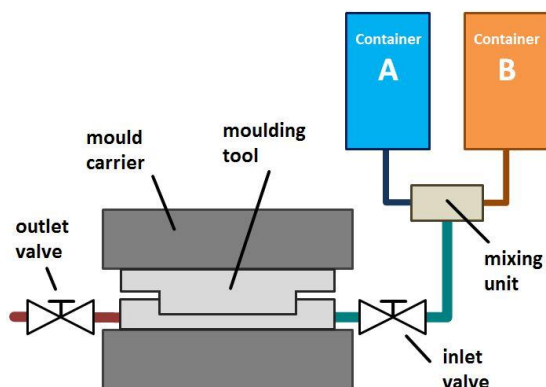


Fig. 1 T-RTM: Schematic structure

A hole (14 mm diameter) was drilled into the lower metal sheet of the semi-finished dry FMLs to enable monomer-melt injection in between the sheets. The semi-finished dry FMLs were then placed inside the lower mould, so that the drilled hole was located above the inlet for resin infusion. To prevent the monomer-melt from bypassing the semi-finished dry FMLs, silicon sealing mats, with a thickness of 2 mm, were placed in between the semi-finished dry FMLs and the lower as well as the upper mould (Fig. 2).

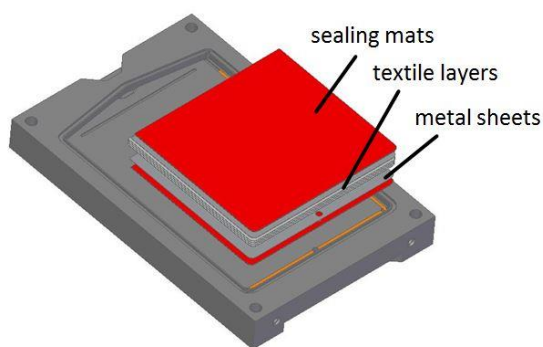


Fig. 2 Lower injection mould, equipped with sealing mats, and semi-finished dry FML

Next, the mould was closed and the maximum carrier load applied. The mould gap was adjusted via sheets placed at the side of the mould. The temperature of the moulding tool was set to 165 °C, resulting in a temperature of 150 °C inside the semi-finished dry FML. The monomer injection was performed in multistage process. At the beginning, air was allowed to evacuate through the outlet valve, while monomer melt was injected through the inlet one. Once the whole mould was filled, the outlet valve was closed, leading to a pressure increase that exceeded the maximum clamp force of the carrier. As a result, the upper

mould started lifting. At a displacement of about 0.5 mm the inlet valve was shut as well. Volume shrinkage of the matrix, due to polymerisation and crystallization effects during curing, were compensated by a back movement of the upper mould. After five minutes of curing time, the mould was opened, the FMLs demoulded and cooled to room temperature. Figure 3 shows a manufactured T-FML inside the lower mould before demoulding.



Fig. 3 Lower injection mould with cured FML

In the scope of this work, eight FMLs have been produced at different mould gaps, ranging from 6.7 mm up to 7.5 mm.

2.3 CHARACTERIZATION

All manufactured FMLs were measured in thickness and weight. Next, the metal sheets were removed and the Fiber-Volume-Fraction (FVF), the density as well as the void content of the FRP-layers examined by means of fluid immersion respectively thermogravimetric analysis. Characterizations were performed on at least three specimens per laminate, having a diameter of 25 mm. The density of the composite ρ_c was determined via fluid immersion method, utilizing a Sartorius Quintix 124-1S lab balance and a Sartorius Density Determination Kit YDY01LP, according to DIN EN-ISO 1183-1 [13]:

$$\rho_c = \frac{W_a \cdot (\rho_{fl} - \rho_a)}{c \cdot (W_a - W_{fl})} + \rho_a \quad (1)$$

where ρ_{fl} is the density of the testing fluid, W_a respectively W_{fl} are the mass of the sample at air and in the testing fluid, ρ_a is the density of air at ambient conditions and c corresponds to a correction factor, relating to the measurement system. The Fiber-Volume-Fraction (FVF) ϕ_c was calculated, after thermal decomposition of the samples in a Nabertherm LV3/11 Ashing Furnace at 600 °C for 4 hours, using the following equation:

$$\varphi_c = \frac{1}{1 + \frac{\rho_f \cdot m_c - \rho_f \cdot m_f}{\rho_m \cdot m_f}} \quad (2)$$

where m_c is the mass of the composite sample before and m_f the mass of the fibers after decomposition. According to the manufacturer the density of the fibers is $\rho_f = 2.6 \text{ g/cm}^3$ and of the matrix is $\rho_m = 1.14 \text{ g/cm}^3$ [14].

The void fraction φ_v results from the difference between measured and theoretical density and can thus be calculated from:

$$\varphi_v = 1 - \frac{\rho_c}{\varphi_c \cdot \rho_f + (1 - \varphi_c) \cdot \rho_m} \quad (3)$$

Samples of the FRP-layers were also investigated using scanning electron microscopy (SEM).

3 RESULTS AND DISCUSSION

The semi-finished dry FMLs have been processed at varying mould gaps. As a result, the manufactured T-FMLs possess different thicknesses and weights and thus differ in their FVFs as well as their impregnation quality.

3.1 FIBER VOLUME FRACTION

The thickness of the manufactured T-FMLs ranged from about 2.7 mm to 3.0 mm, resulting in thicknesses of the FRP-layer of about 0.7 mm to 1 mm. Figure 4 shows the corresponding FVF calculated with equation 1. As can be seen, a wide spectrum of FVF were obtained, covering $\varphi_c = 39.97\%$ up to $\varphi_c = 64.87\%$.

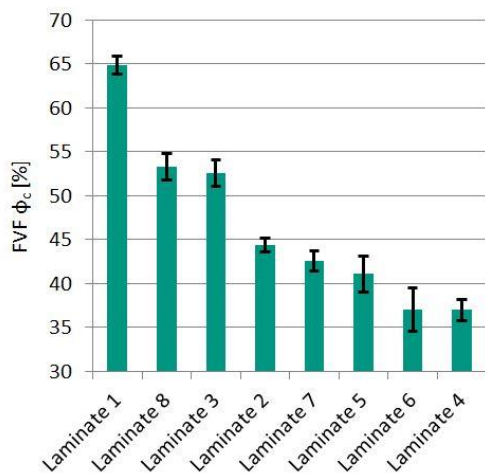


Fig. 4 Fiber-Volume Fraction of FRP-layers

3.2 IMPREGNATION QUALITY

To assess the Impregnation quality, the FRP-layer of each manufactured FML was placed on a 55 W light source, covered with a diffuser and photographed. Next, the void content was measured and Scanning Electron Microscopy images taken.

Figures 5 to 7 show photographs of representative FRP-layers. All layers with $\varphi_c \geq 44.38\%$ (Fig. 2) exhibit a homogeneous lay out, no uncured or non-infiltrated areas and have no significant fiber displacements.

In contrast, all FRP-layers with $\varphi_c \leq 42.61\%$ possess large non-infiltrated areas (Fig. 6). Some of the FRP-layers with $\varphi_c \leq 42.61\%$ also feature extensive, visible fiber displacements (Fig. 7).

The reason for this behavior is missing clamp force on the fiber textile, due to an oversized mould gap, leading to fiber displacements and a monomer melt bypassing certain areas of the reinforcement.

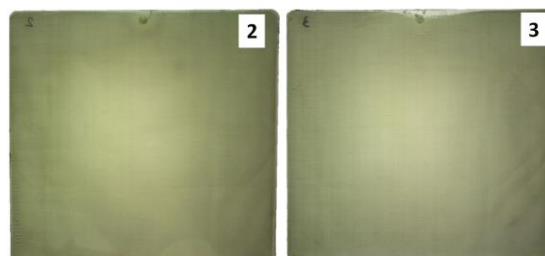


Fig. 5 FRP-layer of Laminate 2 ($\varphi_c = 44.38\%$) and Laminate 3 ($\varphi_c = 52.58\%$): Representative for laminates with $\varphi_c \geq 44.38\%$

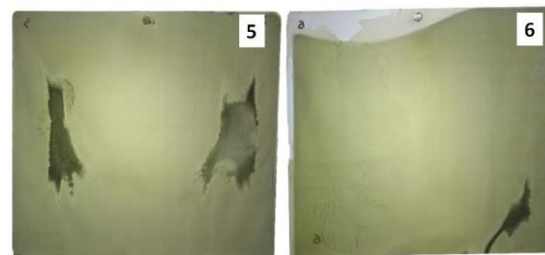


Fig. 6 FRP-layer of Laminate 5 ($\varphi_c = 41.12\%$) and laminate 6 ($\varphi_c = 39.97\%$): Representative for laminates with $\varphi_c \leq 42.61\%$

3.2.1 Void Content

At same positions of each FRP-layer, specimens were taken and fluid immersion analysis conducted. All samples were taken out from areas, appearing fully infiltrated.

Figure 8 displays the void contents determined with equation 3. The measured void fraction of the produced FRP-layers ranges from $\varphi_v = 0.12\%$ to $\varphi_v = 1.23\%$.

Whereas the laminates with $\varphi_c \leq 44.38\%$ show relatively low void contents below $\varphi_v = 0.4\%$, they are slightly higher for the laminates with a FVF of

about $\varphi_c = 53.00\%$ and increase drastically for the laminate with $\varphi_c = 64.87\%$ up to $\varphi_v = 1.23\%$.

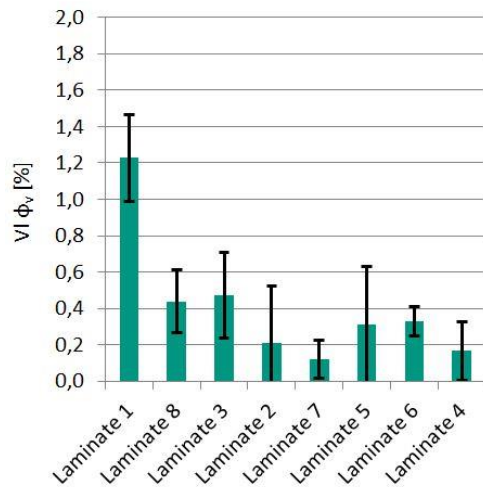


Fig. 7 Void content of FRP-layers

3.2.2 Scanning Electron Microscopy

A representative Scanning Electron Microscopy image of laminate 8 is presented in Figure 9. The images indicate good impregnation of the fiber filaments. Void formation occurs primarily in matrix rich regions in between textile rovings.

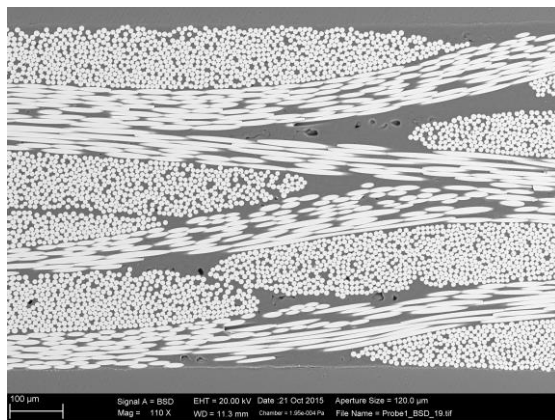


Fig. 8 Scanning Electron Microscopy Image of Laminate 8

4 CONCLUSIONS

Fiber-Metal-Laminates (FML) possess great weight specific strength and fatigue properties. Due to costly starting materials, like thermoset preregs, as well as complex manufacturing routes, their application is currently limited to aviation applications. An alternative manufacturing technique for high quality Fiber-reinforced-polymer (FRP)-parts, avoiding costly preimpregnated base materials with potential for large quantity production, is Liquid Composite Moulding (LCM), in particular Resin Transfer Moulding (RTM).

The Thermoplastic Resin Transfer Moulding (T-RTM) utilizes low viscous caprolactam monomer melt to create thermoplastic FRP from non-impregnated fiber textiles.

In this work, the possibility of producing T-FML from semi-finished, non-impregnated FMLs, via T-RTM, was examined. Therefore semi-finished dry FMLs in sandwich design were processed at varying mould gaps. Next, the T-FML were examined by means of thermogravimetric, fluid immersion and microstructural analysis.

The FVF of the produced FRP-layers, range from $\varphi_c = 39.97\%$ up to $\varphi_c = 64.87\%$. Laminates with $\varphi_c \leq 42.61\%$ show large non-infiltrated areas and extensive fiber displacements. The void contents are in between $\varphi_v = 0.12\%$ to $\varphi_v = 1.23\%$ and increase for higher FVF.

As a result, it can be concluded that the T-RTM process can be utilized to produce T-FML at relevant FVF with sufficient impregnation qualities.

Next steps in enabling a mass scale implementation of FML based on reactively processed polyamide 6 are characterizations of the mechanical properties, optimizations of the polymer – metal interface and investigations regarding the three dimensional in-situ formability during polymer curing.

5 ACKNOWLEDGEMENT

This research is kindly supported by the Deutsche Forschungsgemeinschafts (DFG) project “In situ Hybridization during deep drawing: Thermoplastic Fiber-Metal-Laminate (FML) parts based on reactively processed polyamide 6” (WE4273/13-1; HE6154/4-1).

REFERENCES

- [1] Vlot A., Gunnink J.W. (Eds.): *Fiber Metal Laminates an introduction*. Kluwer Academic Publisher Dordrecht, 2001.
- [2] Krishnakumar S.: *Fiber Metal Laminates – The Synthesis of Metals and Composites*. Materials and Manufacturing Processes, 9(2):295-354, 1994.
- [3] Cano R. J., Loos A. C, Jensen B.J., Britton S.M., Tuncol G., Long K.: *Epoxy/Glass and Polyimide (LaRCTM PETI-8)/Carbon Fiber Metal Laminates Made By The VARTM Process*. SAMPE Journal, 47(2), 2011.
- [4] Langdon G.S., Cantwell W.J., Nurick G.N.: *Localised blast loading of fibre-metal laminates with a polyamide matrix*. Composites Part B: Engineering, 38(7-8):902-913, 2007.
- [5] Nutzmann M.: *Umformung von Mehrschichtverbundblechen für Leichtbauteile im Fahrzeugbau*. Dr.-Ing. Dissertation RWTH-Aachen, 2007.
- [6] Carillo J.G., Cantwell W.J.: *Mechanical properties of a novel fiber-metal laminate*

- based on a polypropylene composite. Mechanics of Materials*, 41(7):828-838, 2009.
- [7] Henning F., Moeller E.: *Handbuch Leichtbau: Methoden, Werkstoffe, Fertigung*. First Edition, Hanser München Wien, 2011.
- [8] Bader M.G.: *Selection of composite materials and manufacturing routes for cost-effective performance*. *Composites Part A: Applied Science and Manufacturing*, 33(7):913-934, 2002.
- [9] De Mendibil O., Aretxabaleta L., Sarrionandia M., Mateos M., Aurrekoetxea J.: *Impact behavior of glass fibre-reinforced epoxy/aluminum fibre metal laminate manufactured by Vacuum Assisted Resin Transfer Moulding*. *Composites Structures*, 150:118-124, 2016.
- [10] Van Tooren M.J.L., Sinke J., Bersee H.E.N.: *Composites: Materials, Structures and Manufacturing Processes*. Dictaat 32, Delft (NL), 1993.
- [11] Van Rijswijk K., Bersee H.E.N.: *Reactive processing of textile fiber-reinforced thermoplastic composites – An overview*. *Composites Part A: Applied Science and Manufacturing* 38(3):666-681, 2007.
- [12] Gittel, D.; Henning, F.: *Thermoplastic composites made of cast polyamide 6 with textile fibre structures: An overview over their synthesis and properties*. Conference handbook, 9th International AVK Conference on Reinforced Plastics and Thermosets, Essen, 2006.
- [13] DIN Deutsches Institut für Normung e.V.: *DIN EN-ISO 1183-1:2012: Plastics - Methods for determining the density of non-cellular plastics - Part 1: Immersion method, liquid pycnometer method and titration method*, 2012.
- [14] Haspel, B.: *Werkstoffanalytische Betrachtung der Eigenschaften von mittels neuartiger RTM-Fertigungsprozesse hergestellten glasfaserverstärkten Polymerverbunden*. Dr.-Ing. Dissertation, Karlsruhe Institute for Technology, Institute for Applied Materials, publication series 48, 2014.

CHAPTER 6:

COMPONENT MANUFACTURING

OPTIMISED AND COST-EFFICIENT HYBRID SMC STRUCTURES FOR AIRCRAFT COMPONENTS

M. Hentschel^{1,2*}, M. Fette^{1,2}, J. Wulfsberg¹, A. Herrmann², N. Stoess³

¹Helmut Schmidt University, Institute of Production Engineering, Hamburg

²CTC GmbH, Stade

³Polynt Composites Germany GmbH, Miehlen

ABSTRACT: Sandwich structures with honeycomb cores and glass fibre reinforced plastics (GFRP) based on phenolic resin as top layers are widely used as material for cabin and cargo applications of aircraft due to their fire, smoke and toxicity (FST) behaviour and their comparatively low weight. The limitation in the geometrical complexity, the long process times for the part production and the manual effort for finishing, assembly and functional integration create a huge demand for optimised and cost-efficient material and process technologies for cabin and cargo applications. Sheet moulding compounds (SMC) can enable geometrically complex, highly integrated parts. In this context the significant reduction of process time and costs is particularly promising. Furthermore the part quality and the reproducibility of manufacturing processes can be increased compared with current components.

This paper deals with the analysis of a direct integration of inserts in SMC structures for aircraft applications. A promising production process of hybrid SMC parts is created. The focus of the present work is the investigation of the anchoring strength between the insert and the SMC structure as well as the explanation of the failure behaviour of the insert-SMC-boundary due to mechanical loads as a function of different SMC materials and inserts.

KEYWORDS: SMC, Inserts, Hybrid, FRP, Aircraft

Nomenclature

CFRP	Carbon fibre reinforced plastics
EP	Epoxy
FRP	Fibre reinforced plastics
FST	Fire, smoke and toxicity
GFRP	Glass fibre reinforced plastics
NDT	Non-destructive testing
SEM	Scanning electron microscope
SMC	Sheet moulding compound
UP	Unsaturated polyester
VE	Vinyl ester

1 INTRODUCTION

For the next 20 years the world's largest aircraft manufacturers, Airbus and Boeing, expect an increase of the passenger volume of 4.9 % p.a. Therefore the number of civil aircraft with at least 100 seats for passengers will rise from currently ca. 21,600 to more than 43,500 in 2034. Due to the additional substitution of mature aircraft through new ones both companies expect a need of more

than 26,000 aircraft cumulated during that period of time just for the single aisle market. [1]

In order to place more fuel saving aircraft on the market in the future, the consequent weight reduction is besides the permanent optimisation of the propulsion unit and the aerodynamics one central focus in the development of future aircraft. Here FRP play an important role. For the production of parts made out of modern composite materials many different manufacturing processes are established. These processes are currently characterised by a low degree of automation, long process cycle times and comparably high production costs.

One promising technology for the reduction of the process times and for the increase of the degree of automation for all new cabin, cargo and also secondary structure components is the SMC technology. Especially for large quantities and a rising demand on civil aircraft this aspect is a huge advantage for using the SMC technology. Furthermore it enables complex shapes, a direct integration of other functional components, e.g. foam sandwich cores or inserts, higher part qualities and an improved reproducibility of the manufacturing process than nowadays. [2]

* Corresponding author: Holstenhofweg 85, 22043 Hamburg ¹, phone: +49(0) 40 / 6541 3580, fax: +49(0) 40 / 6541 2839, email address: martin.hentschel@hsu-hh.de

The combination of among others carbon or glass fibres with various thermosets, such as EP resin, VE resin and UP resin creates specific properties for each application.

Before the SMC technology with its enormous potentials is more established for the production of aircraft applications in the future than currently, many technology developments have to be conducted.

The focus of this work is the investigation of the anchoring strength between the metallic inserts and the SMC structure. For this purpose a promising manufacturing process for SMC aircraft structures including the direct integration of metallic inserts is developed. Additionally, significant test procedures are designed. Furthermore this paper deals with the explanation of the failure behaviour in the contact area between the insert and the SMC. Finally the potentials and the limitations of this kind of hybrid SMC components are analysed.

2 STATE OF THE ART

2.1 SMC TECHNOLOGY

The SMC technology provides various applications in the field of reinforced thermoset composites. SMC components are applied in many industrial sectors, e.g. the electrical and the transportation industry. SMC parts are characterised by several advantages, such as a comparable low density, a good chemical and thermal stability, a high surface quality and an improved functionality. The production of SMC components is very cost-efficient compared with other FRP production processes, especially due to short cycle times, low material costs and an excellent material usage. The SMC technology uses a closed compression moulding process. The usual process temperatures are in a range from 130 °C to 150 °C at a pressure between 80 bar and 120 bar. Under these conditions the curing cycle takes less than five minutes, depending on the matrix system and the part geometry, e.g. its thickness. The semi-finished product, a kind of impregnated sheet, consists of chopped long fibres with a length of typically 25 mm to 50 mm and a thermoset matrix system, such as UP, VE or EP resin. [3, 4, 5]

Some new developments in the field of SMC technology are so called hybrid SMC structures. The hybrid SMC process combines different semi-finished products in order to improve the part's properties. The combination of pre-impregnated continuous fibre reinforcements and SMC for example increases the mechanical properties compared with pure SMC structures. However the material costs and production time are significantly lower compared to standard endless fibre reinforced thermoset composite structures. [2]

2.2 METALLIC INSERTS IN FRP STRUCTURES

In order to enable detachable connections between two parts, inserts are a widespread solution as a part of bolted or pin joints. The insert's basic shape is cylindrical. Typical insert materials, especially for aircraft applications, are stainless steel, brass and titanium. Depending on the application area, e.g. the primary or the secondary structure of an aircraft, the expected loads, the FRP manufacturing process and their environment inserts are specifically designed for each purpose. Hence various inserts exist on the market. Cylindrical, plain outer insert shapes do not achieve an adequate anchoring strength with the surrounding FRP structure in most cases. Therefore a variety of measures can increase the anchoring strength. Undercuts improve the drag against pull-out significantly. Another interlocking based mechanism is the use of knurl patterns which can provide an increase in rotational strength and anchoring strength at the same time. Tapers enable a self-alignment during the conventional, manual installation and can improve the resistance against pull-out. Flanges and fins are another option for a higher anchoring strength. Furthermore the bearing surface is increased which leads to a better load introduction into the FRP structure. The insert material has a large influence on the anchoring and rotational strength primarily due to the adhesive interaction with the resin. An additional increase of the anchoring strength can be achieved through the surface treatment of the inserts. Finally the process of the insert integration in FRP structures has a huge influence on the inserts outer shape. [6, 7]

Currently, inserts are often integrated manually in FRP-honeycomb sandwiches for cabin and cargo applications. The insert connection consists of the insert, the EP based adhesive and the surrounding sandwich structure. The adhesive influences the part weight negatively and its shear strength is the limiting parameter concerning the anchoring strength. [8]

For SMC applications inserts can be integrated during the press step since an accurate positioning of the inserts in the mould is possible. Fig. 1 shows inserts embedded in a SMC dome construction that is state of the art for SMC parts. Due to the insert's undercuts in longitudinal direction the flow of the viscose SMC is modified. So the fibre orientation around the insert is not similar to the direction of forces and the anchoring strength is decreased. [9]

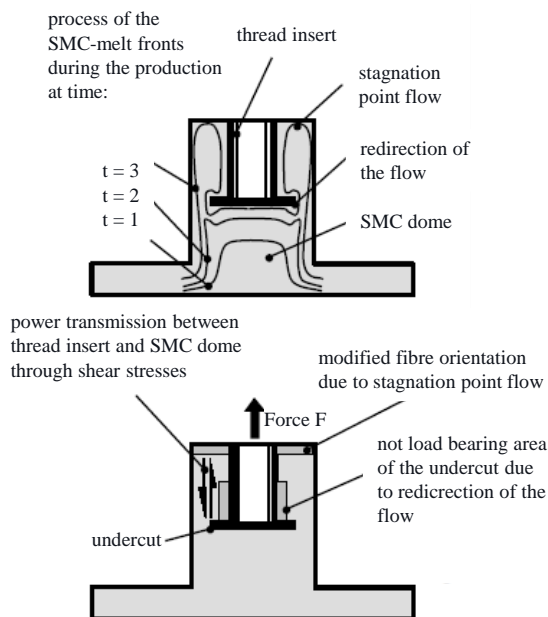


Fig. 1 Flow in a SMC dome construction (top) and consequences for the anchoring-strength (bottom) [9]

3 EXPERIMENTAL ANALYSIS

3.1 REQUIREMENTS ON THE TEST CARRIERS

In order to design, produce and test representative specimens, the requirements on the test carriers have to be defined. Therefore it is important to imply the characteristics of aircraft cabin and cargo components, e.g. their geometry, and the specifications for such parts, e.g. FST requirements, during the design stage. The following requirements were defined:

- Corrosion resistance in the contact area Insert/SMC
- FST behaviour corresponding to Airbus specification
- Low raw material costs
- Load path optimised part geometry
- Good interlocking and firmly bonded connection between insert and SMC
- Thickness analogue current cabin parts
- Possibility of integrating various inserts
- Excellent failure behaviour of the contact area insert / SMC.

The thickness of considered reference structures varies locally, depending on the load paths and for example connection points to other parts. Within the current researches, designed test structures consist of inserts with 5 mm thickness.

Axial pull-out is besides torsion and shear stress in radial direction one of the main stresses of the adhesion between insert and SMC. It is required that the test carriers enable corresponding tests in

order to investigate the failure behaviour of the boundary between insert and SMC on the one hand and to measure the failure forces on the other hand.

3.2 CONCEPT FOR THE INTEGRATION OF INSERTS IN SMC

The mould for the test carriers shall be as modular as possible in order to produce parts consisting of various SMC semi-finished product and insert combinations with a repetitious accuracy. Further the manufacturing process of functional hybrid SMC structures has to enable the processing of a wide range of SMC semi-finished products and inserts. Therefore the following requirements for the manufacturing process were developed:

- Avoidance of joint lines
- Size accuracy of the parts
- High reproducibility
- Near-net-shape cured parts
- Retention of the isotropic fibre allocation
- Possibility of integration in existing manufacturing SMC processes.

Within the methodical design phase of the manufacturing process for the insert integration in the SMC structures four different process concepts were evaluated by the help of a utility analysis.

As a result the manufacturing costs, the adhesion between insert and SMC structure and the retention of the isotropic fibre allocation are defined as most important criteria. The accuracy and the reproducibility of the insert positioning as well as the process cycle time have a high relevance. One-off costs were considered within the utility analysis but are, compared with the other criteria, of small importance. Large quantities of produced parts reduce the influence of the one-off costs on the component costs.

Especially the processing time and the manufacturing costs can be significantly reduced compared with current manufacturing processes by the production of optimised and cost-efficient hybrid SMC structures for aircraft components in the future.

The best evaluated concept is the direct integration of the inserts in the SMC structure during the press and consolidation step. Therefore the mould is hard-faced with the inserts before the SMC stack is positioned in the mould. After this step the production of the test carriers is comparable to the presented SMC process with a pressing force between 40 t (UP and glass fibre based SMC) and 80 t (EP and carbon fibre based SMC), a temperature between 140 °C and 150 °C and a process cycle time of 180 s.

3.3 DEVELOPMENT OF ADEQUATE TEST PROCEDURES

Past the production of the test carriers specimens have to be taken out and tested in order to research the fatigue behaviour of the adhesion between insert and SMC. Moreover it is necessary to measure the maximum forces before the adhesion fails. Currently no international standard describes the pull-out of inserts out of SMC or at least FRP structures.

ASTM D7332/D7332M relates to various test procedures for an axial pull-out of screws out of CFRP structures. In order to keep the experimental set-up as modular as possible for different insert's inner contours a second international standard is taken into account. EN 15337 describes the determination of shear of anaerobic adhesives using pin-and-collar specimens. [10, 11]

Instead of using various screws and bolts for the pull-out of the inserts a set-up similar to the in EN 15337 described enables the use of only one pin for all inserts.

As a result the developed test procedure and experimental set-up, shown in Fig. 2, are a mix of both presented international standards. The tests are designed as compression tests. Therefore the set-up is comparable to EN 15337. The lower bushing (sample holder) fixes the specimen and prevents the introduction of bending loads into the sample. The pressure bolt is connected with the load cell and introduces with a test speed of 1 mm/min the compression loads into the inserts.

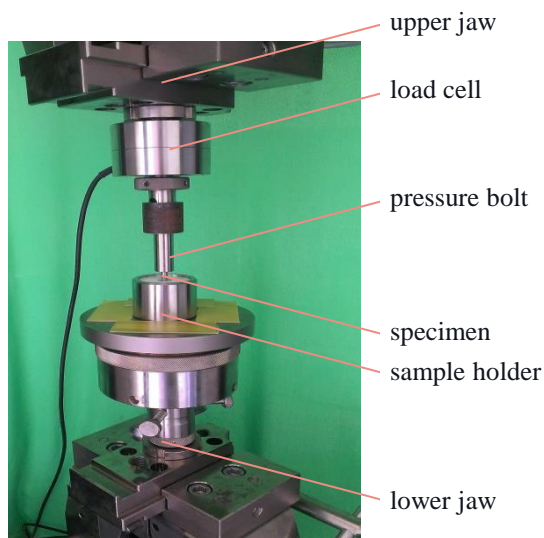


Fig. 2 Experimental set-up

As a result shear stresses in the connection area between the insert and the SMC structure occur. When the test force drops under 50 % of the maximum force the test is finished. It is expected that the courses of curve between ASTM D7332/D7332M and the designed procedure are qualitatively similar.

All samples are circular with a diameter of 40.0 mm and a thickness of circa 5.0 mm, depending on the length of the respective insert. As SMC semi-finished product two different materials are used. HUP 27/25 RN-9010, short HUP 27 GF, consists of a UP resin based matrix and glass fibre reinforcements. This SMC is already qualified for cargo applications. The second tested SMC, EPOPREG 90 CF - 3K, short EPOPREG, consists of an EP resin based matrix with carbon fibre reinforcements in order to increase the mechanical performance and enable new aircraft applications for SMC structures. For this SMC the qualification process is not completed yet. Both SMC are produced by *Polynt Composites Germany GmbH*.

The tested inserts, shown in Fig. 3, are qualified for aerospace applications. They consist of steel or brass alloys and have different outer contours which increase the resistance against axial pull-out.

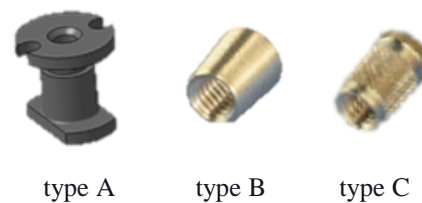


Fig. 3 Tested inserts

For the analysis of the boundary between the inserts and the surrounding SMC structure SEM investigations are performed. NDT is due to resolution limits in the boundary between SMC and the metallic inserts currently not possible in a sufficient way.

4 RESULTS

For each insert/SMC combination five samples were tested. Fig. 4 shows that the observed courses of curve correspond with the in ASTM D7332/D7332M described one. After a first drop in the force-path curve which represents a first crack, the force increases again. After the failure of the adhesion and a large drop, the force can rise up to a higher force than the failure force – the maximum force. Depending on the materials and shape of the bolted connection, failure and maximum force can be the same, like in case of the tested samples. [10]

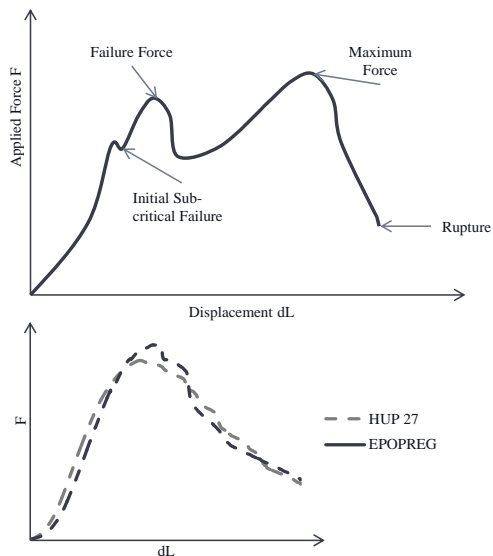


Fig. 4 Courses of curve from ASTM D7332/D7332M [10] (top) and samples with HUP and EPOPREG (bottom)

Depending on the SMC material the courses of curve differ slightly. For the samples with HUP 27 GF no local maximum before reaching the maximum force can be detected when insert types E and F are used. However EPOPREG shows local maxima before the maximum force is reached. Since they are less than 10 N above the surrounding area in the course of curve they represent little failures due to cracks as in ASTM D7332/D7332M mentioned.

The measured maximum or failure forces are, depending on the type of insert, between 15% (type A) and 95% (type B) higher when EPOPREG instead of HUP is used as SMC semi-finished product, shown in Fig. 5.

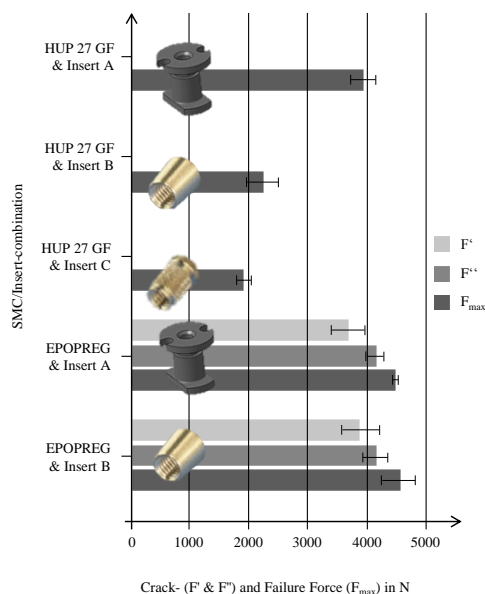


Fig. 5 Results of the tests

5 DISCUSSION

The similarity of the courses of curve between the ASTM D7332/7332M and the conducted tests indicates that the introduction of compression loads into the samples is similar to the introduction of tensile forces described in the mentioned ASTM.

Concerning the insert/SMC adhesion differences between the SMC materials can be detected.

Due to a higher thermal expansion and a higher shrinkage during the cure compared with EPOPREG the crack initiation process between insert and HUP 27 GF already starts before the samples are cooled down from process temperature to room temperature. So the adhesion between insert and SMC is weakened before mechanical loads are introduced. Since first little cracks exist in the contact area, no drops in the course of curve before the maximum force can be detected with HUP 27 GF as SMC semi-finished product.

In contrast to this no cracks after cooling down to room temperature are to be seen in the contact area between insert and SMC with EPOPREG as SMC material. Fig. 6 compares the adhesion between insert and SMC with insert type A depending on the SMC semi-finished product.

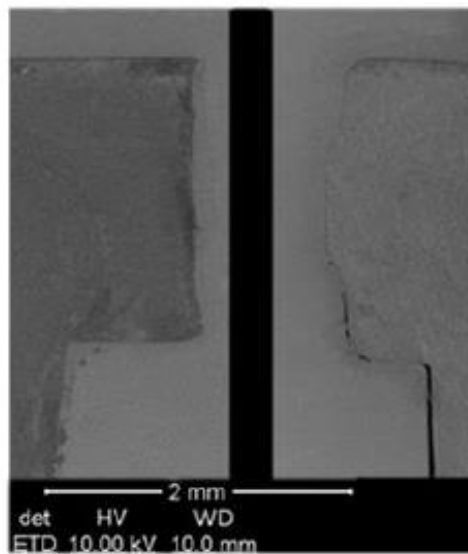


Fig. 6 Comparison of the adhesion between insert and SMC by using EPOPREG (left) and HUP (right)

The differences in the crack initiation process, thermally caused with HUP 27 GF versus mechanically caused with EPOPREG, are one reason for the higher measured maximum forces on the EPOPREG samples.

Another reason is the stronger adhesive connection between the EP resin based EPOPREG and the inserts. The high content of inorganic flame retardants in HUP decrease the, compared with EP, lower adhesive strength of the UP resin additionally.

Since the material and the general geometry of insert types B and C are the same the circa 10 % higher failure force at type B can be explained by larger undercuts due to the male thread compared to the knurling of type C. Insert type A is significantly better embedded in the SMC structure due to its comparably large undercuts. So the glass fibres have to be broken for losing the adhesion between SMC and insert and not only slightly bended like necessary for types B and C. Furthermore the larger outer insert diameter increases the contact surface and consequently the failure force significantly.

Regarding EPOPREG as SMC the failure mechanisms are the same for all tested inserts. Due to the mentioned higher adhesive connection of EP resins the contact area between insert and SMC stays partly intact after reaching the failure force. In this case the SMC structure collapses as a result of too high shear loads. So the failure forces of types A and B are comparably high when EPOPREG is used as SMC.

6 CONCLUSION AND OUTLOOK

The SMC technology is one promising technology for the reduction of process times and for the increase of the degree of automation for manufacturing all new secondary aircraft structures for cabin and cargo components.

Especially the hybrid SMC process obtains further potentials, such as an increased mechanical performance compared to conventional manufactured SMC parts.

Due to the process design it is possible to integrate functional elements, e.g. metallic inserts, directly during the press and curing step. The anchoring strength depends on the SMC semi-finished product, the inserts geometry and material. The within this research gained findings show that an EP resin based SMC achieves a better firmly bonded connection between SMC and insert than an UP resin based SMC.

The inserts influence on the anchoring strength is comparable to the SMCs influence.

The focus of future investigations should be the test of the adhesion between insert and SMC concerning torsion, shear stress in radial direction and dynamic loads. Furthermore the development of NDT is important since e.g. computer tomography and ultrasonic inspection cannot investigate the boundary sufficiently due to the huge differences in density between the metallic inserts and the SMC area.

7 ACKNOWLEDGEMENT

The authors would like to thank the teams of the test laboratories from the *AIRBUS plant Stade* and from the *Institute of Materials Technology* from

the *Helmut Schmidt University*, the *Alcoa Fastening Systems Aichach GmbH*, the *Böllhoff Verbindungstechnik GmbH*, the *SFS intec GmbH* and the *Tucker GmbH* for the excellent cooperation during the concept and the experimental period of this research.

REFERENCES

- [1] FVW Medien GmbH: *Boeing-Prognose: Jet-Nachfrage beschleunigt sich*, 12 June 2015. [Online]. Available: <http://biztravel.fvw.de/boeing-prognose-jet-nachfrage-beschleunigt-sich/393/144402/4070>. [Access on 04 January 2016].
- [2] M. Fette et al.: *Combination of carbon fibre sheet moulding compound and prepreg compression moulding in aerospace industry*. In: *Procedia Engineering*, Volume 81, 1601-1607, 2014.
- [3] H.G. Kia: *Sheet moulding compounds - science and technology*, Hanser / Gardener Publications Inc., Ohio, 1993.
- [4] M. Flemming et al.: *Faserverbundbauweisen - Fertigungsverfahren mit duroplastischer Matrix*, Springer, Berlin, 1999.
- [5] H. Schürmann: *Konstruieren mit Faser-Kunststoff-Verbunden*, 4. Auflage, Springer, Berlin, 2014.
- [6] STANLEY Engineered Fastening: *DODGE® - Fastening Solutions For Plastics*, February 2014. [Online]. Available: http://www.stanleyengineeredfastening.com/sites/www.emhartamericas.com/files/downloads/D4100-rev-E_web.pdf. [Access on 12 August 2015].
- [7] J. Gebhardt et al.: *Experimental investigation and performance enhancement of inserts in composite parts*, Elsevier, Amsterdam, 2014.
- [8] A. Hinkel et al.: *Untersuchung der Festigkeit von Sandwich-Krafteinleitungselementen mit Inserts*, In: *DGLR-Jahrestagung*, Bonn, 2005.
- [9] F. Schievenbusch: *Beitrag zu hochbelasteten Krafteinleitungselementen für Faserverbundbauteile*, Dissertation, Chemnitz, 2003.
- [10] ASTM International: *D7332/D7332M – 09 - Standard Test Method for Measuring the Fastener Pull-Through Resistance of a Fiber-Reinforced Polymer Matrix Composite*, West Conshohocken, 2009.
- [11] Deutsches Institut für Normung e.V.: *EN 15337:2007 - Adhesives Determination of shear strength of anaerobic adhesives using pin-and-collar specimens (ISO 10123:1990 modified)*; German version, Beuth, Berlin, 2007.

HYBRID COMPOSITES OF PLASTIC AND ALUMINUM FOAM

C. Fiebig^{1*}, M.E. Steffen¹, S. Caba¹, M. Koch¹

¹Technische Universität Ilmenau, Fachgebiet Kunststofftechnik, Germany

ABSTRACT: On the background of increasing energy cost and the shortage of resources, lightweight materials become more important in industrial and automotive applications. Nowadays, vehicle designers try to reduce weight by substituting high-density materials with low-density compounds of similar mechanical properties. This work deals with the development of a new hybrid-material combination consisting of aluminum foam (ALF) and thermoplastic (TP) or carbon fiber reinforced plastic (CFRP) covering said foam. As a result of the porous cell structure, aluminum foams show low weight with comparatively high stiffness. In combination with plastic material the distinctive features of both materials can be combined to obtain a new composite material, which unifies their remarkable characteristics. Primary co-processing showed an intrusion of the melt and resin into the foam causing an increased density of the composite. Strategies were developed to avoid this phenomenon. Strength and stiffness characteristics of such structural components were examined.

KEYWORDS: aluminum foam, hybrid composite, injection molding, resin transfer molding, CFRP, thermoplastics

1 INTRODUCTION

Additionally to a pure weight reduction the demand for enhanced mechanical properties, such as stiffness and strength, grows in lightweight design. New hybrid lightweight materials consisting of closed-cell aluminum foam and a TP or CFRP cover layer represent a promising approach, however, its potential being widely unknown. The enclosed gas volume and the associated high porosity of foams are leading to low densities and thus low component weights are achievable. The metallic base material provides high mechanical strength, making metal foams ideal for lightweight applications. Based on previous works, it can be assumed that a foam core surrounding plastic layer may improve mechanical properties. The enclosing plastic layer can also be used to integrate fasteners and provides an enhanced load transmission into the foam. [1, 2, 3]

To successfully produce such hybrid materials in the resin transfer molding (RTM) and injection molding processes, it is necessary to describe and detail the essential process parameters. Mold filling in injection molding processes is theoretically well understood, however, only transferable to reality as the corresponding simplifications for the boundary conditions of an injection mold surface are applicable. The undefined surface conditions of the aluminum foam do not fulfill this requirement.

Unsteady transitions, non-isothermal conditions, asymmetrical temperature profiles and not fully known rheological behavior at the interface between the inhomogeneous foam surface and the plastic melt or the resin lead to additional complexity.

The low pressure resistance of aluminum foam is contrary to the upcoming high pressure during an injection molding process. High pressure causes the outer surface cells of the foam to break resulting into an injection of melt into the foam structure. Preliminary tests have shown that the penetration of the aluminum foam structure by melt pressure-related injury occurs during the injection molding process. One of the explanations for the infiltration of melt is the failure of the cell walls due to the melt pressure. If the pressure-load is higher than the cell wall can withstand, it will break.

The penetration of plastic melt and resin increases the mass of the composite component thus not leveraging the full light weight potential.

2 STATE OF THE ART

2.1 ALUMINUM FOAMS

Metal Foams are solid metal materials, commonly aluminum, with a large volume of gas-filled pores. The properties of the foam depend on its mixture

*Corresponding author: TU Ilmenau, Gustav-Kirchhoff-Straße 4, 98693 Ilmenau, +49 3677 69-3344, christian.fiebig@tu-ilmenau.de

ingredients, its manufacturing route and pores characteristics. The pores are present in an open- or closed-cell structure. Open cell structures are characterized by reticulated structures that have no distinct cell walls. Closed-cell foams in contrast, having vesicular structures with distinct cell walls. The two cell structure types are shown in figure 1. [1, 2]

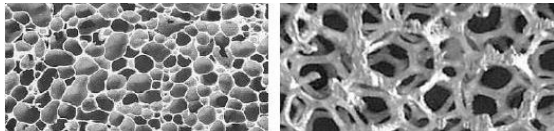


Fig. 1 Closed-cell (left) and opened-cell (right) foam structures [4]

The quantitative description of the structure includes statements about the property-determining characteristics of the aluminum foams. Criterion in describing the properties of metal foams is its density ρ and relative density ρ_f/ρ_s . The relative density describes the ratio of the density of the foam ρ_f to the density of the solid material ρ_s . There are also morphological features such as the pore shape, pore size and pore orientation being of crucial importance. [1]

The pressure behavior of aluminum foam is influenced by several factors. The surface of the foam component also has an influence on the behavior. A closed surface can withstand higher loads than an open surface. These two types are shown in figure 2.



Fig. 2 Comparison of surface properties of different manufacturing processes: (left) powder metallurgical, (right) melt-metallurgical

Compared to compact materials, aluminum foams exhibit a characteristic compression behavior. A typical pressure curve is represented in the figure 3. The curve displays three specific sections representing each a different response to pressure exposure. A quasi elastic deformation starts at onset of compression. In the second section (plateau section) the foam cells are deformed plastically across the entire thickness of the foam. The constant stress occurring in this area is called plateau stress. Further deformation causes a collapse of the cells. The foam reaches the density of the compact matrix material in theory and behaves accordingly. [2, 3, 5]

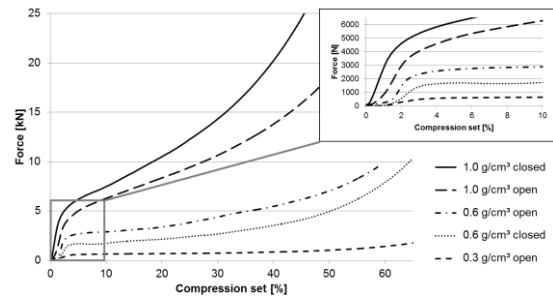


Fig. 3 pressure curves of aluminum foam of different densities

2.2 CALCULATION OF SANDWICH BEAMS

Sandwich composite components are typically made of three layers: two thin cover layers and an intermediate core with low density. The cover and the core layer need to be connected either by bonding or positive locking in order to achieve the desired support effect. [6, 7]

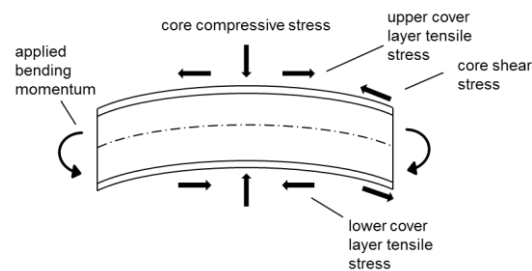


Fig. 4 Sandwich beam with bending load

In a bending case the upper cover layer is strained by tensile stress and the lower by compressive stress (figure 4). These two oppositely directed stresses cause shear and compressive stress in the sandwich core. The requirements for the sandwich materials can be derived from the resulting strains: the core layer and the connecting layer have to be stable against compressive and shear stresses and the cover layers need to provide high tensile and compressive stiffness.

The classical beam theory states that the bending stiffness B_y can be estimated using the elastic bending modulus E_b and the moment of inertia I (eq.(1)). In case of a sandwich this equation has to be applied to the cover and core layers.

$$B_y = E_b \cdot I \quad (1)$$

Figure 5 shows the cross-section of a composite beam. h_{core} is the height of the core, h_{cover} is the height of the cover layer and h_{total} is the distance between the two cover layers.

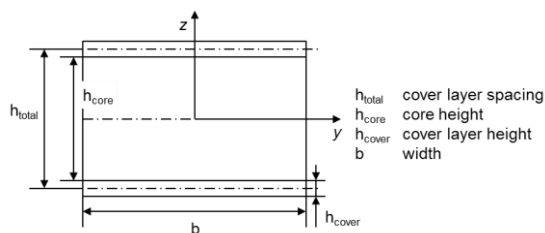


Fig. 5 Geometry of a sandwich beam

The bending stiffness of a sandwich beam is composed of three elements. In particular, these are the bending stiffness of the cover layers, the intrinsic bending stiffness of the core and the Steiner component of the cover layers (eq.(2)).

$$B_y = B_{\text{Steiner,cover}} + 2 \cdot B_{\text{cover}} + B_{\text{core}} \quad (2)$$

The assumptions are resulting from the sandwich theory. The cover layer height is much smaller than the core layer height ($h_{\text{cover}} \ll h_{\text{core}}$). The Young's modulus of the core material is significantly lower than the Young's modulus of the cover material ($E_{b,\text{core}} \ll E_{b,\text{cover}}$). Under these conditions the bending stiffness of the cover layer and the core can be neglected in eq.(3). Regarding the ratio of $h_{\text{cover}}/h_{\text{total}} < 1/4$, they do not have a significant influence. The bending stiffness of the complete sandwich beam can be simplified:

$$B_y = \frac{E_{b,\text{cover}} \cdot b \cdot h_{\text{total}}^2 \cdot h_{\text{cover}}}{2} \quad (3)$$

It is apparent that the bending stiffness of a sandwich composite primarily depends on the modulus of the cover material and the distance h_{total} between the cover layers.

2.3 APPLIED MATERIALS AND PROCESSES

2.3.1 Resin transfer molding

All experiments were performed using HT carbon fiber reinforced plastics. Carbon fibers are suitable for the tests, since they have excellent weight-specific mechanical properties. The modulus of CFRP is mainly determined by the fiber volume content and the elastic modulus of the used carbon fibers. The core material is powder metallurgy aluminum foam with a closed-cell structure. It is characterized by a low density, high weight-specific shear modulus and high weight-specific shear strength. The mechanical properties of the foam are highly density dependent. Aluminum foams offer a good energy absorption capacity. Test components were produced by using the RTM process with an aluminum foam insert. Advantages of this process are a good link of fiber and matrix

and a minimal void generation in the laminate. The desired fiber volume content can be achieved accurately. As a result, components were reproducibly fabricated. The methods' parameters were kept constant to minimize the influence of the fabrication process on the test results.

The laminate of the cover layers consists of six layers of UD-carbon fiber plies in the layer sequence $(0/90/0/90/+45/-45)_{\text{sym}}$. Each single fiber layer has a thickness of 0.5 mm; the aluminum foam insert has a height of 20 mm. The resulting total height of the sandwich composite is 26 mm. The mechanical properties of the CFRP and the aluminum foam are summarized in table 1. The resin used for injection consists of epoxy resin and hardener. Some of the data listed below were measured in the laboratory, others were taken from literature. This data is used for the calculation of the laminate properties by using the classical laminate theory.

Table 1: Properties of the applied fibers and aluminum foam

layer	cover	core
material	carbon fiber UD	aluminum foam
grammage m_{fg} [g/m ²]	600	-
modulus E_{f1} [GPa]	230 [8]	1.8 [9]
modulus E_{f2} [GPa]	28 [8]	-
density [g/cm ³]	1.518 [8]	0.35
fiber volume content φ	50%	-

The specimen are produced in the RTM process. In each case, ten rectangular test components with the dimensions 180x26x20 mm³ are produced. All used sandwich components have the same thickness with little differences resulting from slight height variation of the aluminum foam. The composite density and the flexural modulus E_b in the longitudinal direction were determined for all components. E_b was specified using a 20 kN testing machine following DIN EN ISO 178 [10]. The distance between the jaws was chosen to be $s = 150$ mm and the test velocity is $v = 2$ mm/min (figure. 6).

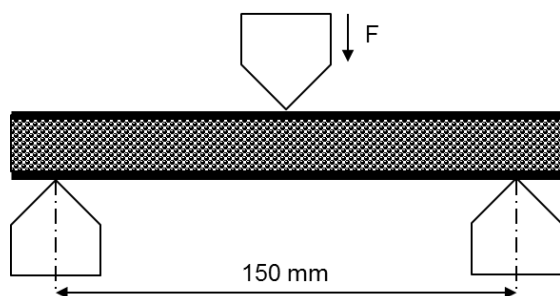


Fig. 6 Beam bending test

2.3.2 Injection molding

The hybrid composite should show a low weight and good specific characteristics. A semi crystalline thermoplastic was chosen as a first matrix for evaluation. Subsequent work will continue to transfer the experiences to high-performance thermoplastics with the objective to further enhance properties.

Polypropylene (PP) was selected, showing low costs, low density and a high melt flow index (MFI). A relatively low viscosity plastic with an MFI of 70 g / 10 min was selected and the rheological parameters were examined to describe the nonlinear flow behavior at different shear rates. Based on this material property, it is possible to calculate the pressure drop in the cavity in a first simplistic approach.

2.4 PURPOSE

The high weight-specific bending stiffness in sandwich structures is mainly achieved through core layers of low density. An ALF completely filled with resin or plastic counteracts this principle. Therefore, the main focus of this work is the avoidance or reduction of resin penetration into the aluminum foam during the fabrication of component samples. The composite density of the sandwich beam is reduced which results in a higher natural frequency of the component. The calculation of the mechanical properties of the sandwich composite is improved. For this purpose, a previously published approach is used to check its applicability to sandwich material. The approach involves the undulation of the fibers in the calculation of the elastic properties of the carbon fiber laminate within the classical laminate theory (CLT).

3 INITIAL DATA AND METHODS

3.1 INJECTION CONCEPT FOR RTM

In order to minimize resin penetration, several methods were tested, e.g. covering the pores with resin or a pre-laminated ply made of fiberglass and resin.

The selected use of flow aids is feasible. Influencing the flow direction and amount of resin will support to achieve this goal. The objective is to impregnate the fiber layers in thickness direction and to stop the injection process right before the undesirable penetration into the aluminum foam would occur.

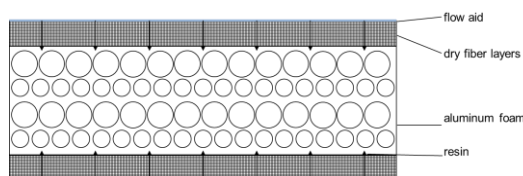


Fig. 7 Principle of injection for RTM process

In this solution, the CFRP/ ALF hybrid composite is complemented by a flow aid above the two cover layers. The structure is shown in figure 7. This aims at the impregnation of the fiber layers in thickness direction of the component. The impregnation of the fibers and the aluminum foam is distributed evenly at each point of the component rather than being part length direction dependent. Thus, it is possible to stop the injection procedure as soon as a sufficient amount of resin is injected. The cover layers are fully impregnated and the surface of the aluminum foam is covered. A lack of flow aids would result in an inhomogeneous distribution of the resin over the length of the component. The desired amount of the injected resin must be determined in order to achieve the best result.

3.2 SURFACE TREATMENT METHODS FOR INJECTION MOULDING

3.2.1 Process selection

Pre-treatment of the surface of the foam core is conducted to reduce melt penetration, which depends on the injection pressure (figure 8). Different methods and objectives are pursued. The closed surface of powder metallurgical foams only has few cracks. On the surface, only few form-locking connections occur. The bond strength can be increased by the surface modification. The main objective of the melt-metallurgical foams with an open surface is to minimize the amount of injected cells.

There are a number of surface treatment methods that can be applied to improve the quality of the connection. At first, the cleaning i.e. the removal of dirt and processing aids by solvent or aqueous systems is applied. Usually the physical and chemical conditions of the surface layer are not changed. After cleaning, the mechanical pre-treatment by grinding, sanding or sand blasting is the most commonly used method.

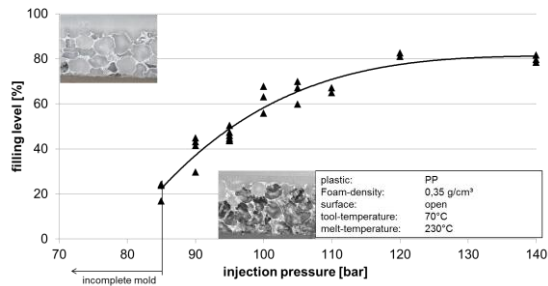


Fig. 8 Correlation between the filling level and injection pressure in the injection molding process

This in particular, removes layers not connected to the metal and changes the surface geometry. These layers consist of oxide and oxide-hydrate layers and negatively affect the adhesive strength. In addition to the cleaning and mechanical change of the surface, also tribological-chemical effects can occur with the use of chemical or thermal pre-treatment. [10]

To minimize infiltration, as well as to improve bond strength a variety of treatment methods are available for aluminum foam surfaces. A wide range of different types of implementation exists for each individual method. So, an organic coating with different materials can be done. In addition, the application and the required additional resources can be different.

The broad combination of different treatment methods complicates a selection. A clear assessment of individual procedures requires a descriptive methodology. A cost-benefit analysis was used to rate the methods. The selection of the evaluation criteria in the specific case is oriented according to the known information about each treatment method. So, the following criteria were selected:

- effectiveness
- interaction with the materials
- process complexity
- material consumption
- availability

In addition to untreated samples, the following surface modifications have been selected and carried out.

3.2.2 Degreasing with solvent

Due to the good availability and degreasing effect acetone with the concentration of 99.5% was used. The solvent was given in a bowl, where the samples were inserted for 2 minutes and dried for 2 hours under certain conditions.

3.2.3 Coating with adhesion promoter Ultramid 1C

Provided by the manufacturer BASF transparent granules of polyamide Ultramid 1C can be

resolved in an alcohol solution. Due to the availability an ethanol solution with a concentration of 60% was used. The granules were mixed in the recommended ratio of 2:8. The samples were sprayed with the solution and dried for 16 hours under normal conditions.

3.2.4 Coating with adhesion promoter Vestamelt X1333

The adhesion promoter Vestamelt X1333-P1 is a powder with a particle size of up to 80 µm suitable for conventional powder coating equipment. The processing was done using a powder spraying device. The processed powders as well as the coated specimen were electrostatically loaded. This enables a steady coating thickness, as well as a coating in undercuts. After applying the powder the samples were thermally conditioned for 10 min at 180 °C.

3.2.5 Blasting with aluminum oxide

The surface treatment of aluminum foam by blasting is possible with different abrasives. Steel grit, glass beads and aluminum oxide were used to determine the effects of the blasting media. Blasting with aluminum is the most preserving technique. With this method the cell walls are destructed but compared with the other blast materials it is far less pronounced. The effects on closed foam surfaces correlate with those on the open surface. For further tests aluminum oxide was chosen as blasting material (figure 9).

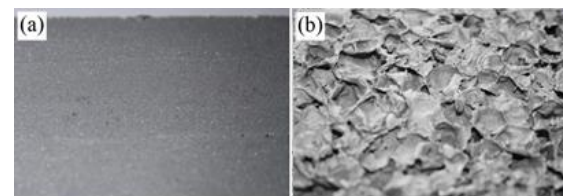


Fig. 9 Effect of different media blasting onto the surface of aluminum foam: aluminum oxide on closed surface (a) and on open surface (b)

The surface treatment was done with particles up to a size of 80 µm at a pressure of 2.5 bars. The average weight gained by the surface treatment is 0.89 g (2.9%) for the samples with an open surface and 0.38 g (0.33%) for samples with a closed surface. The weight gain is to explain through the blasting residue remaining in the foam structure.

3.2.6 Coating with paint-finish

A thermal paint has been used to seal the surface voids (cracks). This meets the requirement for temperature stability and is suitable in environments of up to 500°C (figure 10).

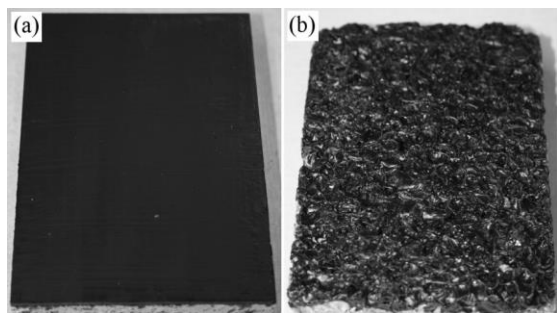


Fig. 10 Coated samples: closed (a) and open surfaces (b)

The low viscosity also simplifies the complete coating of the sample with an open surface. The paint was applied to the aluminum foam core and was fully dried after 16 h and subsequently hardened for 30 min at 240°C. The average weight gain by the surface treatment is 5.38 g (16.08%) for the samples with an open surface and 0.7 g (0.6%) for samples with a closed surface.

3.2.7 Coating by metal spraying

A coating with metal minimizes the effect of imperfections. Additionally, the rigidity of the surface pores can be increased. Molybdenum was used for the coating. The applied metal layer thickness is 0.4 mm. The destruction of the surface is enormous for both open and closed surface (figure 11). The coating with molybdenum causes a significant increase in the weight of the component by 16.78 g (50.3%) for samples with open surfaces and 15.23 g (25.76%) samples with closed surfaces.



Fig. 11 Effects of wire flame treatment on (a) closed surface, (b) open surface, (c) molten pore walls

3.3 FEM BASED SIMULATION

The simulation of the bending test for the CFRP/ALF specimen is performed in parallel to the measurement of the rigidity modulus. A FEM model with the same dimensions as the specimen as well as the experimental setup was created (figure 12). The bending modulus for a bending force of $F_{\text{bend}} = 5 \text{ kN}$ was determined and used for calculating the theoretical specific bending stiffness. The bending stiffness is obtained by using two different Young's moduli. The laminate modulus E_{undu} for the simulation is determined on the basis of published analytical models for fiber undulation [11].

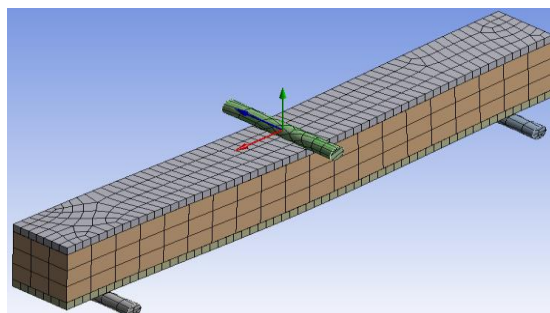


Fig. 12 Simulation model of the CFRP/ALF hybrid composite

The model provides the application of a correction factor depending on the weave used. It is based on the computation of the specific values of the laminate by using the CLT. Initially, the Young's modulus of the test laminate needs to be determined using the CLT.

The material data of the fibers and the matrix as well as the identified fiber volume content form the raw data for the calculation. The next step is a comparison of the measured and calculated values of E_x for the 0°/90° - UD fabric [11]. The second Young's modulus E_{clt} is determined on the basis of literature values as seen in table 1, which form the input parameter for the calculation of the Young's modulus with the CLT.

4 RESULTS

4.1 RESIN TRANSFER MOLDING

The examination of specimen resulted in measured property values shown in figure 14. They indicate that the density of the composite was reduced by the use of the flow aid confirming the assumption on resin penetration into the foamed structure. The components fabricated using the flow aid have completely impregnated layers and a good adhesion of resin to the surface of the aluminum foam (figure 13). The results of the experiments show that a complete impregnation of the cover layers of the hybrid sandwich composite is not achievable without adjustment of the fabrication process resp. the parameters used therefore. When using the flow aid, the total amount of injected resin is reduced compared to a process without a flow aid. The components produced with flow aid only have a limited penetration of the aluminum foam.

The results of the 3-point-bending test show a correlation between density and mechanical properties of the hybrid components. This applies both for the specific flexural modulus as well as for the ratio between measured and theoretical bending stiffness. The varying densities of the components are caused by different core layer densities result-

ing from varying foam density and the amount of resin penetrating the foam.

Measurements indicate that the resin flowing into the core has a positive effect on the bending modulus and the bending stiffness, even though the density increases.

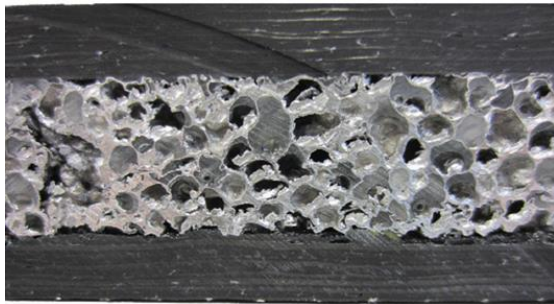


Fig. 13 Section through a sample component

The values of the bending stiffness increases by 218% compared to the concept using the flow aid (figure 14). This leads to the assumption that, contrary to the theoretical perspective, the filled core layer has a measurable effect on the flexural strength of the hybrid component.

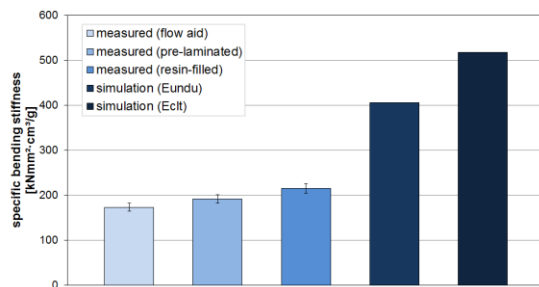


Fig. 14 Specific bending stiffness on measured and simulated test components

The comparison between measured and calculated results shows that the accuracy of the simulation with literature values is insufficient. Using the measured Young's modulus E_{undu} increases the accuracy of the simulation and has the advantage that no reference laminates must be produced. The difference between the measured specific bending stiffness and the simulated bending stiffness is caused by an inadequate model of the ALF. Therefore, further studies are necessary.

4.2 INJECTION MOLDING

The surface-treated aluminum foams were overmolded on one side with the PP. The invading plastic can be measured by weighing the foams before and after the molding process. The total mass of the hybrid bond increases due to the infiltration of the thermoplastic resin. Starting from the case of fully filled foam (level 100%) as well as theoretically unfilled foam (level 0%), a percentile

relationship can be made allowing statements about the injected mass.

A minimization of the injected mass could be achieved by several surface treatments. At the untreated samples a filling level of 46.3% was measured on open surface foams and 7.5% on closed surface foams. The effects of surface treatment on the filling level are shown in figure 15. Blasted and painted treatments lead to a significant reduction of the filling level. In contrast, the wire flame spraying and rolling increase in the filling level. Degreased and coated foams with adhesive promoter show a marginal improvement of the filling level.

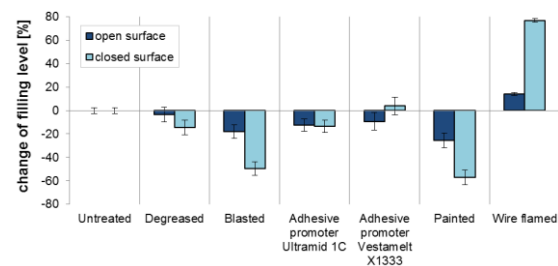


Fig. 15 Effect of surface treatment on the injected mass [7]

Contrary to the expectation, that the abrasive blasting will damage the surface and thus a higher filling rate occurs, the level is reduced. On the one hand, the beam particles can seal the surface cracks, on the other hand an increased flow resistance can occur due to the higher surface roughness. A reduction of the infiltration has been achieved by applying the adhesive promoter. The stiffening of the surface cell wall as well as the overlapping of cracks reduces the mass of the plastic melt up to 13.6%. The best results are achieved by coating the surface with paint. An improvement of the injected mass by 25.7% on open and 57.0% on closed surface were carried out. As shown in the following figure 16 the paint seals the cracks.



Fig. 16 Minimizing the injection mass by a coating

Wire flame spraying caused an increase of the filling level. The effectiveness of the method can be classified as insufficient. Some of the cell walls could be covered by the hard molybdenum but a significant amount of the cell walls were destroyed by the heat input, which rapidly increases the filling level of about 14.1% on open surfaces and 57% on closed surfaces.

5 CONCLUSIONS

This paper shows that the fabrication of a high strength/ stiffness and weight-reduced sandwich composite made of plastics and aluminum foam is feasible. Sample components were fabricated to meet the requirements in an application relative to required strength and stiffness. The design of the hybrid sandwich composite was performed using an internal material model in the ANSYS FEM calculation software which is validated by comparisons with measured results. The RTM fabrication process for CFRP/ ALF hybrid sandwich composites was carried out to a point where the resin penetration can be controlled by means of a flow aid and metering of the required resin for impregnation of all fibers and controlled bonding of the foam surface. In terms of process stability, a fabrication method of fully impregnated fiber layers was demonstrated. Requirements of lightweight component concept and design were demonstrated by this unique and novel material combination once particular processing conditions are applied. The predetermination of mechanical properties leaves room for considerable improvement, in particular with respect to reflecting the bonding and interface characteristics of CFRP and aluminum foam.

The mechanisms of infiltration of the thermoplastic melt in the aluminum foam structure were investigated to produce a hybrid-compound consisting of aluminum foam and thermoplastic. The boundary layer characteristics between the two materials, as well as its adhesion mechanisms have been elaborated.

The minimization of the injected plastic melt has been investigated by applying several treatment methods. The best results were achieved by applying a layer of paint. This treatment method reduces the filling level by 25.7% and 57.0% respectively with open or closed foam surface. An increase of the mechanical properties while keeping the lightweight advantages extends the range of applications for the compound in automotive industry.

REFERENCES

- [1] Hipke T., Lange G., Poss R.: *Taschenbuch für Aluminiumschäume*. Aluminiumverlag, Düsseldorf, 2007.
- [2] Ashby F., Evans A., Fleck A.: *Metal Foams a Design Guide*. Butterworth-Heinemann, Woburn, 2000.
- [3] Gibson L. J., Ashby M. F.: *Cellular solids structure and properties*. Cambridge University Press, Cambridge, 1997.
- [4] Baumeister J., Banhart J., Weber M.: *Werkstoffe im Automobilbau: Hocheffiziente Ener-*

gieabsorber aus Aluminiumschaum. VDI-Verlag, Bremen, 1995.

- [5] Degischer H. P., Kriszt B.: *Handbook of cellular metals*. Wiley, Weinheim, 2002.
- [6] DIN 53290:1982-02: *Begriffe. Prüfung von Kernverbunden*.
- [7] Klein B.: *Leichtbau-Konstruktion, Berechnungsgrundlagen und Gestaltung*. Springer, Berlin, 2011.
- [8] Ehrenstein H.: *Konstruieren mit Faser-Kunststoff-Verbunden*. Springer, Berlin, 2007.
- [9] Schmidt D., Albrecht R., Lange G.: *Analyse von schmelz- und pulvermetallurgisch hergestellten geschlossenenporigen Metallschäumen auf Aluminium-Basis*. In: G. Petzow (Ed.), *Fortschritte in der Metallographie / Metallographie*, DGM INVENTUM GmbH, Frankfurt, 179-184, 2012.
- [10] DIN EN ISO 178:2013-09: *Kunststoffe – Bestimmung der Biegeeigenschaften*.
- [11] Fiebig C., Koch M.: *The influence of fiber undulation on the mechanical properties of FRP-laminates*. In: P. Scharff, C. Weber (Eds.), *Shaping the Future by Engineering*, ilmedia, Ilmenau, 16, 2014.

POLYMER ALUMINUM HYBRID STRUCTURE JOINT BY INJECTION MOLDING

Achim Frick^{1*}, Steffen Aldinger¹, Marcel Spadaro¹

¹Institute of Polymer Science and Processing (iPSP), Aalen University, Aalen, Germany

ABSTRACT: Lightweight engineering by the use of injection molded multi-material hybrid structures is a sustainable solution that promises novel design and providing material, energy and cost efficiency. For instance, hybrid structures combining polymer and aluminum are interesting composites due to their individual material properties that, when fitted together, provide beneficial synergistic effects in joint applications. Screwed joints, which need to be sealed, require time-consuming assembly during manufacturing and their performance deteriorate during service time due to pre-stress loss caused by relaxation effects. In comparison, injection molded and adhesively bonded polymer aluminum joint structures provide an enormous advantage through possible function integration as well as a simple and quick manufacturing process. This paper focuses on the feasibility of manufacturing an adhesively bonded and mechanically strong joint between a TPE-S and aluminum by assembly injection molding without a pre-treatment of the aluminum surface before overmolding. Injection molded double-lap joints were produced and characterized by means of shear test, light and scanning electron microscopy as well as differential scanning calorimetry. The presented results contribute to a better understanding of the effective manufacturing of hybrid structures with excellent service properties.

KEYWORDS: hybrid structure, injection molding, adhesive bonding, leak tightness, TPE-S, aluminum

1 INTRODUCTION

Modern product development targets material, cost and energy efficiency as a major issue of sustainability. As a reason of this, multi material composites and assembly injection molding techniques are increasing in importance. Thus, reducing logistic and assembly effort during the manufacturing process. Light weight hybrid structures with complex shapes are able to bear the occurring load optimally. The manufacturability of sophisticated and innovative functional composites is promised by combining e.g. melt processable and freely shapeable polymeric materials with a load bearing metal frame. Polymers can provide either soft and rubberlike or hard and ductile material properties and can act as electric insulators, whereas e.g. metallic low dense aluminum behaves stiff and provides high electric and thermal conductivity. Normally, polymer aluminum joints are force fitted, e.g. employing a screw fit technique. The major drawback of such technique relates to the relaxation of the polymer during the service time period, which in turn decreases the joint contact pressure with time.

Injection molded and adhesively bonded polymer aluminum hybrid structures enable the combination of complex shaped part geometries and integrated technical functions with rigid load bearing struc-

tural elements, whereby the hybrid joint exhibits a tight and leakage free interface [1].

The overmolding of metals with polymers is already established [2-4] but the manufacturing of an adhesively bonded joint between aluminum and polymer without pre-treatment is not yet intensively studied [5, 6].

The aim of the study is to create a tightly sealed polymer aluminum hybrid structure as well as an adhesively bonded interface by assembly injection molding, without any kind of pre-treatment of the aluminum before overmolding.

2 HYBRID STRUCTURE MANUFACTURING

The investigated material was a commercially available styrene based Thermoplastic Elastomer (TPE-S) with a durometer hardness of 83 Shore A, 11.7 MPa tensile strength and 180% strain at break. The respective measurements were performed on an injection molded dumbbell shaped specimen of type 5A, in accordance to DIN EN ISO 527-2:2012-06. For the metal sheets EN AW 5005 aluminum alloy in accordance to DIN EN 573-3:2013-12 with a degreased surface was used.

Injection molded double-lap joints (Fig. 1) were used to determine the adhesive bond strength between polymer and aluminum.

* Corresponding author: Aalen University, Beethovenstraße 1, 73430 Aalen, Germany, achim.frick@hs-aalen.de

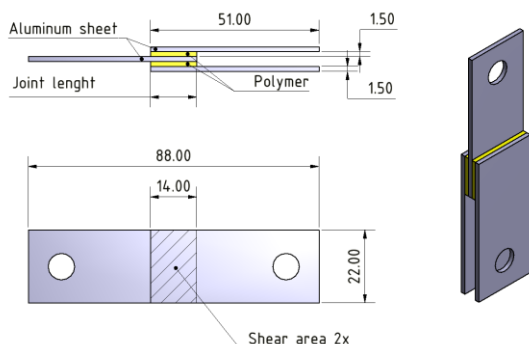


Fig. 1 Polymer-aluminum hybrid structure (geometry of the double-lap joint prior to testing)

The TPE-S aluminum composites were manufactured using an injection molding machine type Arburg Allrounder 220S-150-30 with a screw diameter of 15 mm. The size of the shear area is in total 616 mm² with a polymer layer thickness of 1.5 mm each.

The polymer material was dried before injection molding using dry-air dryer type Bierther DR 202 MT. To feed the dried polymer material to the injection-molding machine, a closed conveying system type Bierther ASM 1 CC was used.

Optimal process settings were obtained by means of Design of Experiment (DOE) analysis to achieve a maximum bond strength.

The investigated specimens were injection molded at a process temperature of 250°C at the nozzle and a volume rate of 35 cm³/s. The mold temperature was kept constant at 70°C.

Fig. 2 shows the 3D rheological simulation of the hybrid structure, employing Autodesk Moldflow 2015 simulation software.

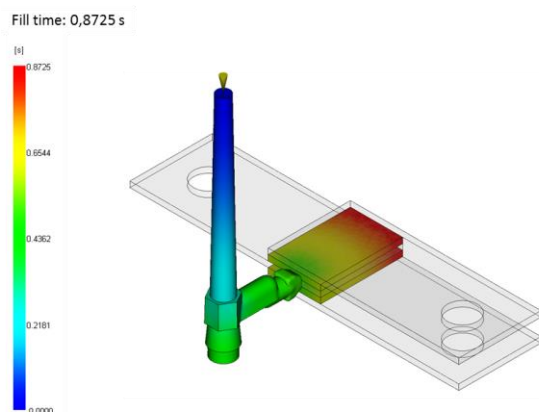


Fig. 2 Filling simulation of the polymer-aluminum double-lap joint (shear test specimen)

The material data used for simulation purpose was selected to be TPE-S from the Moldflow database, which is considered to be similar to the investigated material and provides representative results in filling simulation. The processing parameters were chosen according to the injection molding process.

Fig. 2 illustrates the gating and homogeneous filling of the cavity between the aluminum sheets with polymer. When manufacturing the double-lap joints, the aluminum sheets were pre-heated before being inserted into the mold. Immediately before the overmolding process, the aluminum sheet temperature was measured to be around 80°C. It must be noted that prior to testing, the ready molded hybrid structures were annealed at different temperatures, in order to investigate the possible influence of a thermal treatment after processing on the adhesive bond strength. Fig 3 shows schematically the setup during annealing procedure, where the double-lap joint was kept in a fixed position by an aluminum bracket.

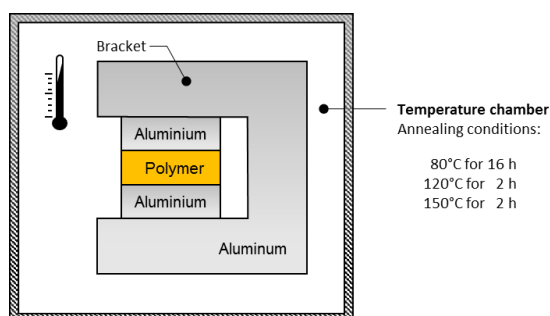


Fig. 3 Setup for annealing the double-lap joint

The different annealing conditions were 80°C for 16 hours, 120°C for 2 hours and 150°C for 2 hours.

3 TESTING METHODS

The following testing methods were employed.

3.1 SURFACE CHARACTERIZATION

The surface roughness of the samples was investigated by employing white light interferometry (WLI) type ZeGage Profiler from ZygoLOT GmbH.

3.2 HYBRID STRUCTURE LEAK TIGHTNESS TEST

In order to qualify the interface performance, the leak tightness of the hybrid structure was tested by employing a leak detector ASM 340, using helium as a test gas at a pressure of 1 bar. The helium sensor side was evacuated and the rate of leakage of helium was measured after 15 min at room temperature (23°C). Injection molded circular shaped double-lap joints, with the same bonding area compared to the shear test specimen, were used to evaluate the leak tightness of an injection molded hybrid structure. The leak test specimens and double-lap joints were manufactured under the same injection molding conditions.

3.3 MECHANICAL TESTING

For the quasi-static tensile tests, a universal testing machine type Zwick Z005 was used at room tem-

perature (23°C) and the adhesive shear strength was measured in accordance to DIN EN 1465:2009-07. The double-lap joints were pre-stressed to 0.5 N with an elongation-rate of 1 mm/min. The actual measurement elongation rate was 10 mm/min and samples were deformed until break. The shear strength was calculated considering a shear area of 616 mm². For each annealing condition 3 measurements were performed and mean and standard deviation were calculated.

3.4 POLYMER MORPHOLOGY STUDY

The influence of the different annealing processes on the morphology of the polymer component of the hybrid structure was studied by employing a differential scanning calorimetry (DSC) type DSC 3+ from Mettler-Toledo GmbH. The investigated temperature range was from -80°C to 250°C with an isotherm of 3 min at the upper and lower temperature limits, whereby the measurement program consists of two heating sections and one cooling section under a nitrogen atmosphere, with a purge gas flux in the cell of 60 ml/min. A heating and cooling rate of 20 K/min was used. The sample mass was 5 ± 0.1 mg and placed in a 40 µl aluminum crucible with perforated lid.

3.5 INTERFACE AND FRACTURE PATTERN CHARACTERIZATION

Light microscopy (LM) and scanning electron microscopy (SEM) were employed for the investigation of the hybrid structure interface and the fracture pattern after mechanical testing of the double-lap joints under shear loading.

A light microscope type Smartzoom 5 from Carl Zeiss AG was used. The SEM images were taken using a type LEO Gemini 1525 from Carl Zeiss AG, which operates using a back scattered secondary electrons sensor. The cross sections of the studied SEM samples were sputter coated using Au/Pd at 20 mA for 40 s while purging the chamber with argon gas.

4 RESULTS AND DISCUSSION

The following results present the feasibility of an injection molded hybrid structure with good adhesive bond strength. The resulting advantage concerning leak tightness is compared to a force fitted joint.

4.1 INTERFACE INSPECTION

Fig. 4 shows the differences between a force fitted joint and an adhesively bonded one. Using a force fit design it requires a constant stress loading, in order to achieve a sufficiently tight joint between the two different materials, whereas the adhesive bond does not require any external force loading. It is obvious from Fig. 4, that the real surface contact in the interface between polymer and aluminum

defines possible leakage paths, which in turn mainly affects the leak tightness of the joint.

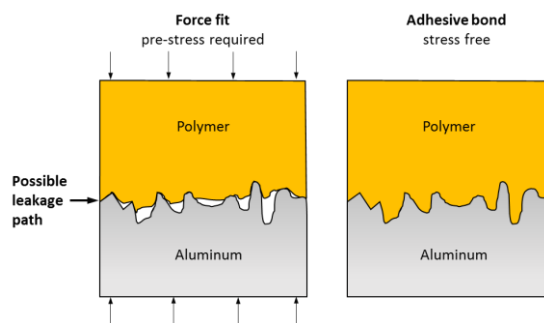


Fig. 4 Fitting possibilities between polymer and aluminum; left: force-fit right: adhesive bond manufactured by injection molding

Joining a conventionally available polymer film and aluminum sheet by a force fit, makes it obvious that there is a tremendous difference in their surface roughness. Fig. 5 shows the measured results using white light interferometry. The different surface topography of the polymer and the aluminum have to be tightly pressed, in order to prevent micro leakage between the contact partners, which is technically almost impossible. Thus, it represents a weak point of any force fitted joint which demands no leakage at the interface. Comparatively, when using the injection molded technique, the joint is benefitted by being covered with a larger real contact area between the polymer and aluminum surfaces directly.

Thus, the real contact area at the interface of both materials increases. If both materials are also compatible, then an adhesively bonded hybrid structure is generated beneficially.

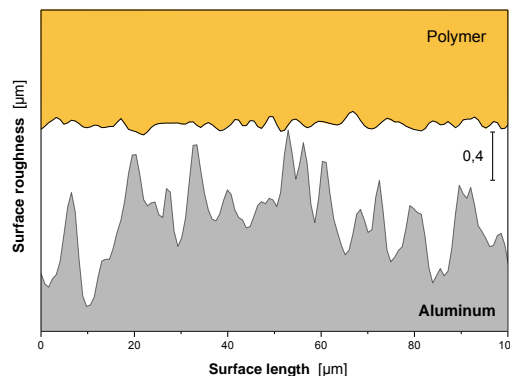


Fig. 5 Initial surface roughness of a polymer film and aluminum sheet before joining by a force fit measured by WLI

4.2 JOINT LEAK TIGHTNESS

The leak tightness measurements, Fig. 6, were performed on circular shaped double-lap joints produced by injection molding, in order to measure the tightness of the contact surfaces and thus qualify the adhesive bond performance. The injection

molded hybrid structure shows an overall reduction in leak rate to about one third when compared to a force fitted joint. For comparison purposes, a circular shaped force fitted joint, which is composed of a high temperature polymeric film and two aluminum rings, was assembled and fitted by screw, Fig. 5. Comparatively, when annealing the injection molded joint, the leak rate is moreover reduced by almost 20 times. This indicates a very effective adhesion between both materials. The almost zero leakage of the injection molded joint is due to a vanishing micro leakage in the interface of the hybrid structure and an excellent adhesively bonded structure.

The results shown in Fig. 6 verify the positive effect of an annealing process regarding reduction of the leak rate of the hybrid joint and thus provides a likely improvement of the achievable bond strength. An annealing procedure seems to be required whereby the optimal thermal post-processing condition ranges between 80°C and 120°C.

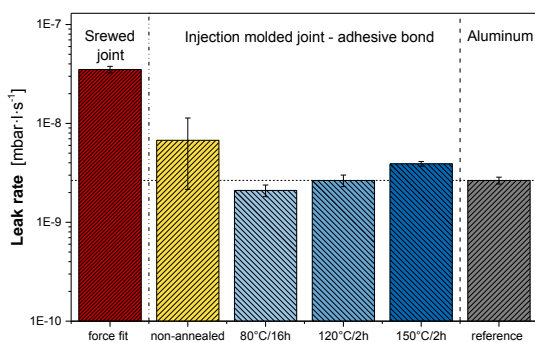


Fig. 6 Leak tightness of injection molded double-lap joints (polymer-aluminum hybrids) compared to a force fitted joint and a massive aluminum sheet

It is interesting to remark that the single helium molecule is much smaller compared to nitrogen and oxygen. Thus, a tightly sealed joint structure which is tested by employing a helium leakage test, provides almost three times better sealing performance regarding air leakage prevention [6].

4.3 JOINT SHEAR STRENGTH

Double-lap joints were used in order to study the mechanical strength properties of the hybrid structure interface. The injection molding processing conditions were the same when compared to the circular shaped double-lap joints, which were tested for their leak tightness (Fig. 6). Fig. 7 illustrates the shear strength of the injection molded double-lap joints. The joints were tested as molded (non-annealed) and after being annealed at different conditions with respect to temperature and time. The annealing contributes to an increase in shear strength. In contrast to the observed leak tightness

results (Fig. 6), it is obvious that the highest shear strength is achieved when annealing the sample at a temperature of 120°C for 2 h. It was also observed that a further increase of the annealing temperature to 150°C for a time span of 2 h shows a drop in shear strength.

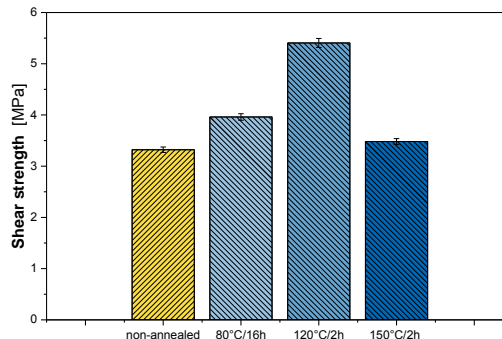


Fig. 7 Shear strength of polymer-aluminum double-lap joints non-annealed and differently annealed

The annealing process has a clear effect on the interfacial strength, where the optimal annealing conditions are shown to be 120°C for 2 h. As a result of the thermal post-treatment, a different strength behavior was observed which is mainly due to changes in the morphology of the polymer and subsequently a change in the interface bonding as well.

4.4 POLYMER MORPHOLOGY

Polymer morphology can be investigated using DSC analysis. Fig. 8 shows the DSC trace for slowly solidified TPE-S pellet from the melt without any melt shearing influence. The other DSC traces illustrate the morphology changes due to injection molding and the post-annealing process. All injection molded samples show a distinct endotherm at about 50°C and differ in the shape of their endothermal peak at about 98°C.

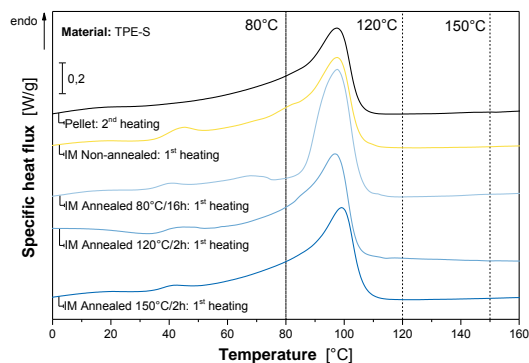


Fig. 8 DSC traces of TPE-S pellet and injection molded samples (IM)

The annealing temperatures were chosen to be 80°C, 120°C and 150°C. The 80°C annealing con-

dition is located slightly below the TPE-S endotherm while the other two conditions are located about 20°C to 50°C above as indicated in Fig. 8. The recommended melt processing temperature range of the TPE-S ranges from 200°C to 250°C and is considerably above the chosen annealing temperatures. As a result of this, the injection molded joints maintain their dimensional stability during the three different annealing procedures, even if the temperature exceeds the material endotherm at 98°C.

It is considered that the TPE-S morphological changes detected by DSC, can be related to the interfacial strength improvement. The thermally induced changes in the morphology seem to benefit the interaction between polymer and aluminum.

4.5 JOINT INTERFACE

In order to gather information about the interfacial bonding between polymer and aluminum, a light micrograph was taken from the cross section of the double-lap joint. The hybrid structure was therefore embedded in a cold curing resin, sectioned and the sectional surface polished and investigated using both LM and SEM techniques.

Fig. 9 shows the light micrograph of the interface of a non-annealed double-lap joint. The polymer covers the aluminum surface smoothly. There is a boundary layer visible in the polymer, which attaches to the metal surface. It is clearly seen that the polymer interface differs from the polymer bulk morphology, which was analyzed by DSC.

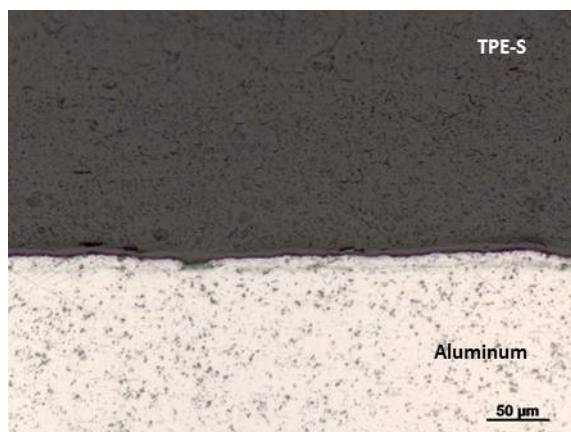


Fig. 9 LM micrograph of the interface between polymer and aluminum

Fig. 10 shows SEM images of the same sample, taken after different annealing conditions. The interfacial bonding between TPE-S and aluminum is observed. It is found that the images provide different polymer morphologies depending on the thermal treatment conditions. Nevertheless, it is yet unclear if SEM sample preparation generates also certain artifacts, as the sample was sputter coated multiple times (1, 2 and 3 times) prior to SEM

imaging. The polymer surface shows thermal induced deformation after annealing.

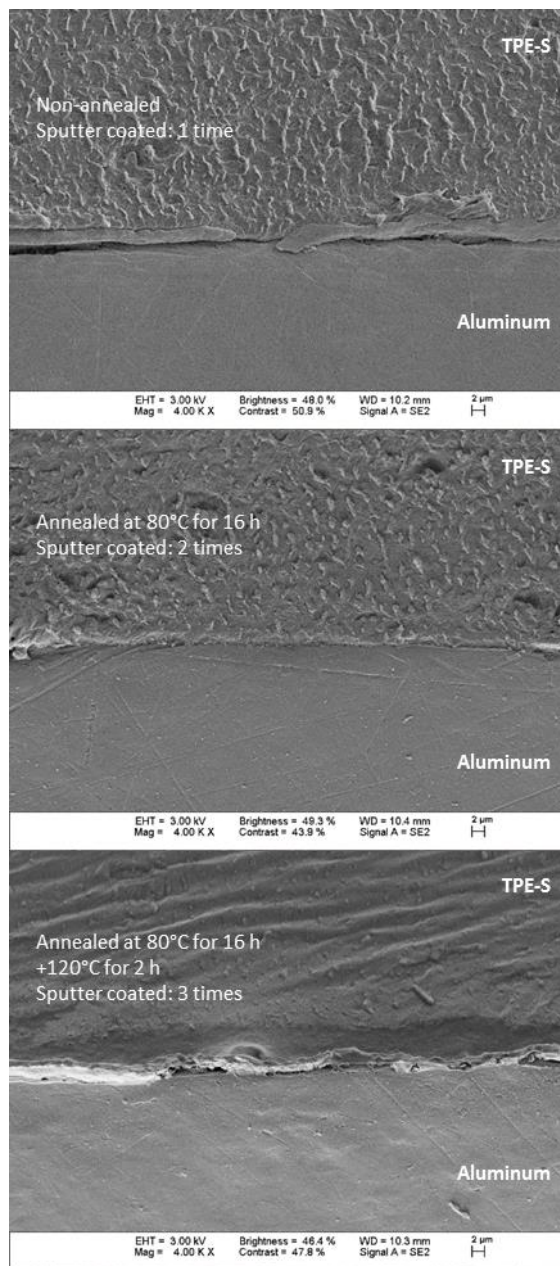


Fig. 10 SEM micrographs of the interface between polymer and aluminum after different annealing conditions

4.6 JOINT FRACTURE PATTERN

Fig. 11 shows the fracture pattern of the differently annealed double-lap joints tested under shear. The non-annealed sample shows no residual polymer on the interface and ruptures by adhesion failure. Similar behavior was observed after annealing at 80°C. When annealing the sample at a temperature of 120°C or above, a partial cohesion fracture occurs during shear tests. The partial cohesion fracture indicates an improved adhesive bonding between polymer and aluminum and therefore the bonded structure is able to withstand a higher me-

chanical load which confirms the measured shear stress results (Fig. 7) and correlates with the morphological changes studied.

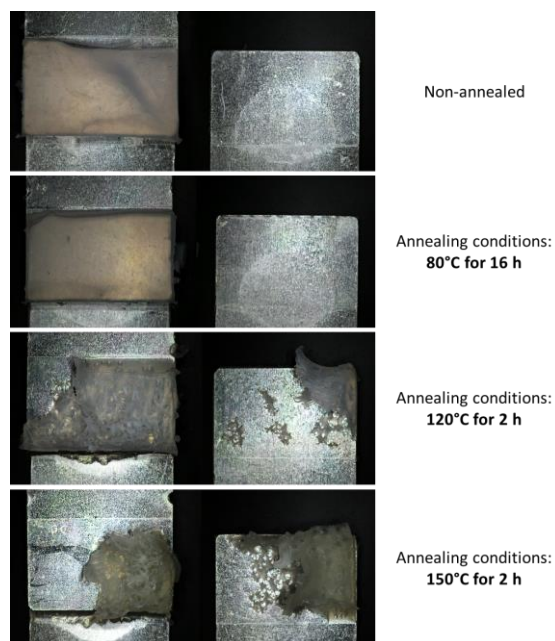


Fig. 11 Shear test fracture pattern of differently annealed double-lap joints

Fig. 12 shows a highly magnified fracture pattern micrograph of a shear tested double-lap joint annealed at 120°C for 2 h. It is found the polymer remains cohesively fractured on the aluminum due to excellent bonding to the metallic interface.

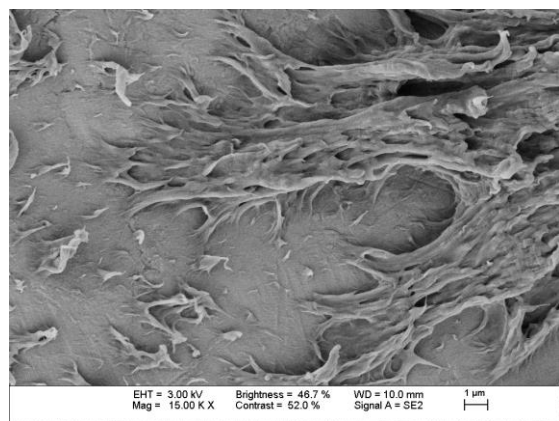


Fig. 12 SEM fracture pattern micrograph of a double-lap joint annealed at 120°C for 2 h

5 CONCLUSIONS

The results of this study prove the feasibility of injection molded soft polymer aluminum hybrid structures adhesively bonded at the interface without any kind of pre-treatment of the metallic surface before overmolding. The investigated polymeric component was a TPE-S with a durometer hardness of 83 Shore A. A manufactured double-lap joint composed of TPE-S and aluminum pro-

vides a good shear strength of about 3.5 MPa, which can still be enormously increased by thermal annealing. After such treatment the strength raises around 160% up to about 5.5 MPa. The increase in mechanical strength correlates with the improvement of the leak tightness of the injection molded joint at its interface. It also correlates with the change from adhesion to cohesion failure mode during shear test. Obvious morphological changes occur within the polymer and at the interface due to thermal post-treatment at a temperature above the material endotherm, which is supposed to be related to the soft segment of the segmented TPE-S polymer.

The results of the study promise a possible substitution of sealed assembly by injection molded hybrid structure.

6 ACKNOWLEDGEMENT

We would like to express our gratitude to German Federal Ministry for Economic Affairs and Energy for supporting this research within the BMWi grant code 03ET6048C.

REFERENCES

- [1] Heinle C., Vetter M., Brocka-Krzeminska Z., Ehrenstein G.W., Drummer D.: *Tight Material Bonds within Mechatronic Systems by Assembly Moulding*. J. Plast. Technol., 5(6):427-450, 2009.
- [2] Gruzicic M.: *Injection over molding of polymer-metal hybrid structures*. American Journal of Science and Technology, 1(4):168-181, 2014.
- [3] Ramani K., Moriarty B.: *Thermoplastic Bonding to Metals via Injection Molding for Macro-Composite Manufacture*. Polym. Eng. Sci., 38(5):870-877, 1998.
- [4] Amancio-Filho S. T., Dos Santos J. F.: *Joining of Polymers and Polymer-Metal Hybrid Structures: Recent Developments and Trends*. Polym. Eng. Sci., 49(8):1461-1476, 2009.
- [5] Fabrin P.A., Hoikkanen M.E., Vuorinen J.E.: *Adhesion of Thermoplastic Elastomer on Surface Treated Aluminum by Injection Molding*. Polym. Eng. Sci. 47(8):1187-1191, 2007.
- [6] Klein R., Burlon K., Meyer C., Gallei M., Appold M., Rehahn M.: *Novel Coupling Agents as Adhesion Promoters between Thermoplastics and Metal*. In: Euro Hybrid Materials and Structures 2014, 8-12, 2014
- [7] Jitschin W., Sharipov F., Lachenmann, R.: *Wutz Handbuch Vakuumtechnik*. Jousten K. (Ed.). Springer-Verlag, 2009.

INCREASING THE MECHANICAL PROPERTIES OF METAL-PLASTIC-HYBRIDS BY IMPROVEMENT OF THE INTERFACE – A MICROSCOPIC APPROACH

Saskia Müller^{1*}, Michael Brand², Klaus Dröder², Leif Steuernagel¹, Dieter Meiners¹

¹Institute of Polymer Materials and Plastics Engineering, TU Clausthal, Germany

²Institute of Institute of Machine Tools and Production Technology, TU Braunschweig, Germany

ABSTRACT: Nowadays, the role of lightweight construction grows significant to minimize resource consumption and emissions. Classic metallic material design often gets to its limits related to weight saving. Therefore, fiber-reinforced plastics (FRP), which have a high potential for lightweight construction due to their anisotropic material properties, are increasingly being used. A further increase through lightweight material can be achieved by the combination of metal and FRP materials to hybrids, which merge the benefits of each component. However, the production of these hybrid components reveals new questions especially on the boundary between metal and FRP, which exists currently in adhesive mechanisms (glue). Prior investigations described the new mechanical patterning method, which supports the adhesion between the interfaces of plane samples by an additional interlocking effect (roughening of the metallic component) to yield a significant increase in the structural integrity of hybrid components and the resulting mechanical properties.

To characterize the influence of the surface treatment related to the fibers an optic analysis of the interfaces between metal and FRP was performed with polished micrograph sections of the hybrid samples. These results were important for the production process of hybrid components.

KEYWORDS: Metal- Plastic- Hybrids, Interfaces, CFRP, Interlocking Effect

1 INTRODUCTION

Due to the increasingly restrictive CO₂ legislation, the demands in terms of weight reduction and functional integration of component concepts are increasing. So, integral combinations of different materials and functional elements move towards hybrid components in the focus of research and development. A major trend in the range of plastic-metal composites consists in the development of innovative products [1, 2, 3, 4]. Experts estimate that nowadays more than 60 % of all metal parts are connected to plastic [5].

The implementation of modern lightweight technologies in high performance applications requires structural and material investigations. One possibility is combining different materials like metal and plastic in hybrid technology.

As lightweight design is an important factor in the development of automobile chassis [6], it is crucial to maintain or even improve the material and struc-

tural properties. Hybrid parts based on the combination of metal and plastics possess those properties. However, the performance potential of hybrid materials mainly depends on the bonding strength between both materials.

In order to use the full potential of hybrid materials, new joining technologies within the hybrid parts were evolved. Therefore the surface of the metallic part is structured to establish a mechanical interlocking joint and to increase the transferable forces within the joint zone.

To qualify the interlocking effect it is important to know how the interfaces between the metal and plastic part looks like after joining. Therefore a microscopic study of the interfaces was performed on polished micrograph sections of the hybrid samples and correlated to the mechanical properties.

* Corresponding author: Agricolastr. 6, 38678 Clausthal-Zellerfeld, 05323-72-4849, saskia.mueller@tu-clausthal.de

2 STATE OF THE ART

At present, hybrid structures- of metal and plastics or fiber-reinforced plastics (FRP) - can be manufactured by various methods. A disadvantage of most commonly used methods is the large number of manufacturing steps and therefore the limitations in terms of productivity [7]. So far, different materials have been joined by e.g. adhesive bonding [8], bolts [9], rivet shanks [10] and screws [11]. Mechanical joining techniques can transmit high forces on the final assembly. Such are, for example, detachable connections like clamp and screw connections or non-detachable connections like riveting [12]. However, a disadvantage of these mechanical joining techniques is fiber damaging which results from drilling holes for the joint elements. Adhesive bonding has been established as a joining technology [13] and is becoming more important. However, the transmitted loads are limited by the adhesion. Thus, complex preparations are required for the components surface. To improve the bonding properties, structuring methods have been developed that allow an additional interlocking effect. One of them is the IGEL technology [13]. It is based on implementing pin structures using cold metal transfer welding (CMT) on a metal surface. In component manufacturing, the pins penetrate the fiber material and thus create an interlocking connection. Another approach is the creation of a micro clamping effect on micron level. In this structuring process, a laser beam is used to ablate the metal in combination with melting the metal [14]. Another known method which follows the same principle is the Surfi-Sculpt™ technology which uses electron beams without ablating material [15]. All of these research approaches have to generate an undercut surface to increase the structural integrity between metal and FRP for each specific application.

In this investigation a new method by using undercuts is used. Within the scope of this paper, the influence of the undercuts on the fibers is tested according to the damage of the fibers and the transmitted force.

3 STRUCTURE GENERATION

To generate structures, a test stand is set up (see Fig.1). It consists of a modified machining center with a special tool and workpiece holder. The tool and the tool holder are rigidly connected to the working axis of the machine. As a result, the tool can be moved path-controlled in all dimensions. The impact angle between the tool and the workpiece surface can be varied continuously via the workpiece holder.

The test stand enables the generation of single structures with previously defined parameters and comparison with the simulation.

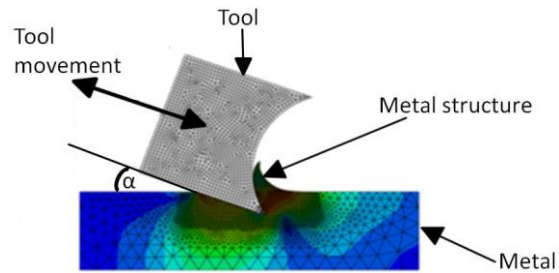


Fig. 1 Test stand for generating structures

Different structuring forces of e.g. 400 N, 1000 N and 1800 N as well as impact angles α of e.g. 15° or 30° can be set to create the structures. Other investigations have shown that the geometry of the structure strongly depends on the impact force and impact angle [16]. In this investigation the structures were generated with $\alpha = 30^\circ$ and 1000 N to create an interlocking effect between the metal and the plastic component.

4 EXPERIMENTS

The samples were produced with aluminum 2017 connected with a unidirectional non crimp fabric in 0/90 layers (with an epoxy resin matrix) in dependence on the DIN 1465 for pull out tests. Dimensions and geometry are shown in Fig. 2.

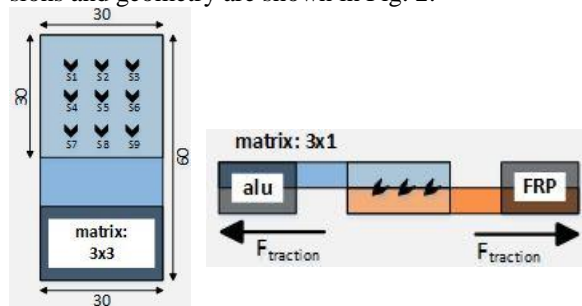


Fig. 2 Left: sample of structured aluminum; right: sample of FRP (2 mm thickness) and aluminum (2 mm thickness) for pull out tests

To estimate the influence of the undercuts, which are metal structures with cutting edges, to the fibers the following series were performed for pull out tests on the one hand and generating microscopic pictures on the other hand. The pull out tests should show the mechanical properties, and according to this the pictures should verify if there is a connection with degraded fibers, which leads to lower mechanical properties of the hybrid sample. The goal of the experiments is to optimize the preparation process and to increase the mechanical properties of the hybrid samples.

Table 1 lists the produced samples. Each series contains six samples of the microscopic study and six samples of pull out tests (as shown in Fig. 2, right).

Table 1 Produced samples

Series	Material1	Material2	Preparation
1	Aluminum 2017	CFRP	Aluminum sandblasted
2	Aluminum 2017	CFRP	First layer: natural fiber (flax)
3	Aluminum 2017	CFRP	-

First and third series were developed to investigate the influence of the produced structures in comparison to those with a bigger surface by an additional sandblasting. But it is assumed, that the carbon fibers were cut by the sharp structures. Because of the elastic properties the natural fibers (flax) were used as the first layer in series 2 with respect to the expectation, that these fibers have a better behaviour to surround the structures so that higher forces can be transmitted.

4.1 SAMPLE PREPARATION FOR MICROSCOPIC STUDY

The structured hybrid area of 30 x 30 mm² of selected samples was sawed for further preparation for the microscope pictures. These 4 mm thick pieces were embedded in a 2 components epoxy resin. After curing, the samples were abraded to a defined level and pictures of the polished surface were taken by a digital microscope (Keyence).

4.2 PULL OUT TESTS

To test the influence of the preparation of aluminum the other samples, which were not sawed, pull out tests were performed with the universal testing machine (Zwick/Roell).

The results are shown in Fig. 2. Here the mean value of a series with its standard deviation in elongation as well as in force is depicted.

By using the additional natural fiber, the tensile strength of series 3 could be nearly doubled. As expected, the highest tensile strength reached the sandblasted series 1.

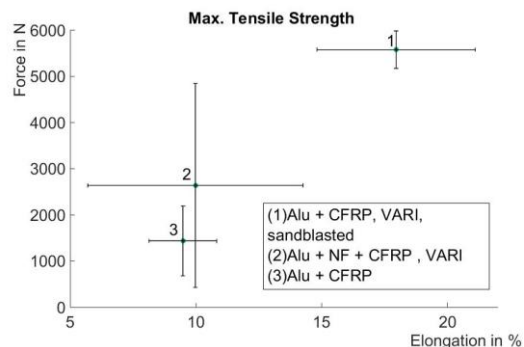


Fig. 2 Resulting maximum tensile strength of pull out tests

5 MICROSCOPIC STUDY

In the following pictures the micrograph pictures of the three series are shown. In these pictures the fiber orientation around the structures is depicted. In Fig. 5, the first layer of carbon fibers is cut by the sharp structures. In comparison to that, Fig. 3 shows, that the structures, which are sandblasted, do not cut the carbon fiber. The fibers are contouring the structures. Fig. 4 shows the sample with natural fiber as first layer. Here, the natural fiber is cut as well, but is adapted to the structure and fills out the gap. In series 1 and 3 there is only matrix in this gap. In series 2 the force can be transferred by the natural fibers as well.

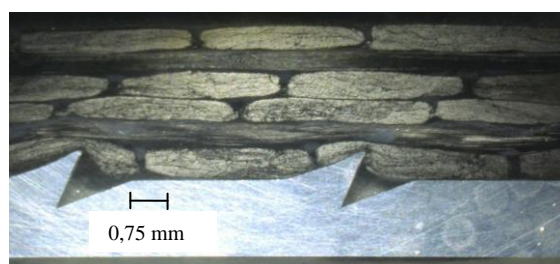


Fig. 3 polished micrograph sections series 1

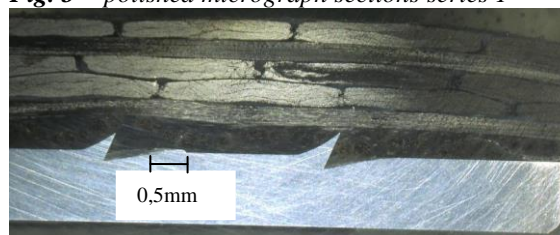


Fig. 4 polished micrograph sections series 2

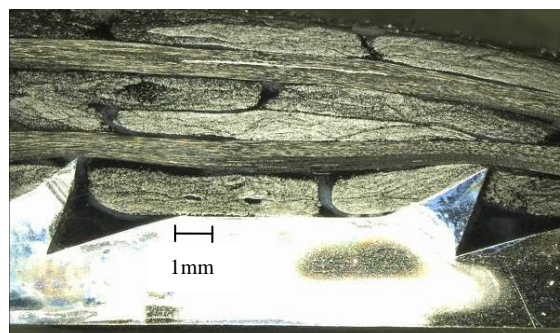


Fig. 5 polished micrograph sections series 3

6 CONCLUSIONS

This investigation shows not only how to increase the mechanical properties of the hybrid samples, but also how to protect fibers of degradation by the cutting edges of the metal structures. To increase the mechanical properties two optimization processes could be analysed. On the one hand the cutting edges were sandblasted to smooth them, on the other hand natural fibers were used to fill the gap at the undercuts between metal and FRP. In a

next step the combination of the sandblasted metal structures with using natural fibers should be analysed.

7 ACKNOWLEDGEMENT

The authors would like to thank the Federal Ministry of Economics and Technology (BMWi) for the financial funding via the Europäische Forschungsgesellschaft für Blechverarbeitung (EFB) and the Arbeitsgemeinschaft industrieller Forschungsvereinigungen (AiF), Project No. 18112N.

REFERENCES

- [1] Bonten, C. *Produktentwicklung - Technologie-Management für Kunststoffprodukte*, Carl Hanser Verlag, München, 2002
- [2] Ehrenstein, G. W. *Handbuch Kunststoff-Verbindungstechnik*, Carl Hanser Verlag, München, 2004
- [3] Erhard, G. *Konstruieren mit Kunststoffen*, 4. Auflage, Carl Hanser Verlag, München, 2008
- [4] Kircher, W. *Neue Märkte erschließen mit Hybridbauteilen und Oberflächenveredelung*, Kunststoffe, Carl Hanser Verlag, München, Nr. 4, 2007
- [5] Spinnarke, S. *Hybridtechnik auf dem Vormarsch*, Produktion, Verlag moderne Industrie GmbH, Landsberg/Lech, Nr. 29-30, 2010
- [6] Brendecke, T., Götz, O., Groß, M., Schneider, F., *Lightweight construction of chassis components*, ATZ worldwide, 10 (2008) 32-36
- [7] Amancio-Filho, S.T., dos Santos, J.F., *Joining of Polymers and Polymer-Metal, Hybrid Structures: Recent Developments and Trends*, J. Polym. Eng. Sci., 49 (2009) 1461–1476, DOI: 10.1002/pen.21424
- [8] Wibbeke, T., Horstmann, M., Timmermann, R., *Optimierte Blindnietverklebungen in Leichtbauanwendungen, Adhäsion Kleben & Dichten*, 49 (2005) 42-44
- [9] Draht T., *Einseitig Verbinden ohne Vorlöcher*, Lightweight Design, 1 (2008) 20-23
- [10] Goushegir, S.M., dos Santos, J.F., Amancio-Filho, S.T., *Friction Spot Joining of aluminum AA2024/carbon-fiber reinforced poly(phenylene sulfide) composite single lap joints: Microstructure and mechanical performance*, J. Mat. & Des. 54 (2014) 196-206, DOI: 10.1016/j.matdes.2013.08.034
- [11] Szlosarek, R., Karall, T., Enzinger, N., Hahne, C., Meyer, N., *Mechanical Testing of Flow Drill Screw Joints Between Fiber-Reinforced Plastics and Metals*. J Mat. Test, 55 (2013) 737-742. DOI: 10.3139/120.110495
- [12] Endemann, U., Glaser, S., Völker, M.: *Kunststoff und Metall im festen Verbund*. In *Kunststoffe*. Carl Hanser Verlag, München, 2002
- [13] Chimani, C.M.: *Leichtmetallentwicklungen für hybride Leichtbaulösungen*. AIT Austrian Institut of Technologie. LKR Leichtmetallkompetenzzentrum Ranshofen GmbH. Fill-Academy, Gurten, 2012
- [14] Hopmann, C., Böttcher, A., Fischer, K., *Investigations of bonding approaches and initial bond strength for the intrinsic manufacturing of laminary bonded hybrids made of thermoplastic composite and metal*. J. Plast. Tech. 9 (2013) 253-274
- [15] Thomas, G., Vincent, R., Matthews, G., Dance, B., Grant, P. S.: *Interface topography and residual stress distributions in W coatings for fusion armour applications*. J. Mat. Sci. Eng. 477 (2008) 35-42
- [16] Dröder, K., Brand, M., Gerdes, A., Große, T., Dilger, K., Fischer, F., Lippky, K., Grefe, H.: *An innovative approach for joining of hybrid CFRP-Metal parts by mechanical undercuts*, EURO HYBRID - Materials and Structures 2014, Stade, Deutschland, 2014, ISBN 978-3-88355-402-0,

AN INTEGRATIVE APPROACH TOWARDS IMPROVED PROCESSABILITY AND PRODUCT PROPERTIES IN AUTOMATED MANUFACTURING OF HYBRID COMPONENTS

K. Dröder¹, R. Schnurr^{1*}, J. Beuscher¹, K. Lippky²,
A. Müller¹, M. Kühn¹, F. Dietrich¹, S. Kreling², K. Dilger²

¹ Institute of Machine Tools and Production Technology,
Technische Universität Braunschweig, Germany

² Institute of Joining and Welding,
Technische Universität Braunschweig, Germany

ABSTRACT:

In order to increase the economic potential of fibre-reinforced plastic (FRP) lightweight design, the manufacturing of hybrid components in multi-material design is aspired. The objective of a multi-material design is that the combination of different materials makes use of their particular advantages. On the one hand, the hybrid approach enables functional specific lightweight design. On the other hand, it enables cost advantages in contrast to pure FRP design due to adjusted material usage. A key requirement to force the way of hybrid lightweight constructions and design into automotive large-scale production is a continuous and automated process chain. Besides the single processes, the automated linking between them is of high importance. At this, the properties of the processed materials represent a lot of automation challenges, e.g. the reliable handling of limp and tacky heated thermoplastic FRP. This paper introduces a proposal for an integrative approach in automated manufacturing of hybrid components by benefitting of the combination of different materials.

KEYWORDS: Hybrid lightweight components, Automation, Pre-assembly, Manufacturing

1 INTRODUCTION

The application of conventional lightweight strategies to open up further weight saving potential and high volume markets in automotive sector reaches its economic limits. Furthermore, fibre reinforced plastics (FRP) do not provide an alternative for volume markets because of their high manufacturing costs yet.

In order to increase the economic potential of FRP-based lightweight constructions, the manufacturing of hybrid components in multi-material design is aspired. The approach of multi-material design aims at the combination of several material classes, e.g. fibres, plastics and metals, with different properties into one component. The objective is that the combination makes use of the particular advantages of the materials. On the one hand, this component integrated hybrid approach enriches the opportunity of functional specific lightweight design. On the other hand, it enables cost advantages to pure FRP design due to adjusted material usage.

There are two manufacturing routes to produce hybrid components [Fig. 1]. The first one is to manufacture several parts of different materials with material-specific production technologies separately. Afterwards the parts are joint by adhesives or mechanical joining techniques in a downstream assembling process to get a hybrid component. In the second route different materials are combined in an earlier stage of the manufacturing process and are processed jointly. Additional joining operations in a downstream assembly are not necessary.

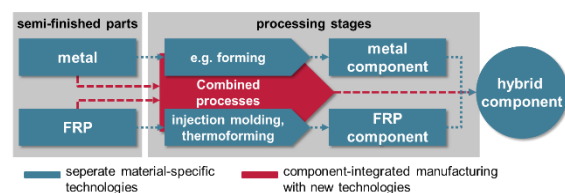


Fig. 1 Two manufacturing routes of combining metallic and FRP in one component

* Corresponding author: Institute of Machine Tools and Production Technology, Technische Universität Braunschweig Langer Kamp 19b, 38106 Braunschweig, Germany, phone +49 531 7697, fax +49 531 5842, e-mail r.schnurr@tu-braunschweig.de

Due to the mostly conventional material-specific orientated plant concepts, an economical manufacturing of integrated hybrid components in high quantity is not feasible.

Therefore, the approach of component integrated hybrid lightweight design is accompanied by the requirement of developing production technologies that expand conventional plant concepts, allow manufacturing of appropriate component complexities and ensure a high degree of automation in a continuous process chain [1-4].

Within the scope of this paper, the automation challenges with focus on handling operations in processing FRP in combination with other materials are discussed. Furthermore, an integrative approach in automated manufacturing of hybrid components is introduced. This approach expands current approaches and benefits from the combination of different material properties, not only in the finished component, but also during the manufacturing process.

2 PROMISING TECHNOLOGY

A current technology of producing FRP components in high quantity is the manufacturing of thermoplastic-based components [5]. In contrast to resin based technologies, here, tailored, pre-impregnated and consolidated fabrics with thermoplastic matrices (TP-FRP) are heated and then processed in a combined thermoforming and injection moulding process. The result is a shaped FRP component with injected functional elements [6,7]. The processing is inspired by sheet metal forming and plastic injection moulding, which already allow large scale production in their particular material class.

Current developments of TP-FRP processing provide first automation solutions to produce pure FRP components in a continuous process chain. Semi-finished parts are automatically placed in an oven, removed and inserted in the mould [8]. However, processing several semi-finished parts of different material classes, which is required to enable component integrated hybrid lightweight manufacturing, are not considered yet.

3 AUTOMATION CHALLENGES

Despite of intensive research, implementation of FRP stays out of high-volume production. Besides the high material costs, especially missing automation solutions for required reliable handling operations during or in between single process steps are the reason for this.

3.1 MATERIAL PROPERTIES

Difficulties in development of automated and continuous processes mainly result of the properties of the used materials during manufacturing process.

Unlike conventional used materials in automotive sector like metal sheets, which are mostly easy to handle, fabric-based materials have specific properties, which lead to automation challenges.



Fig. 2 Dry (left) and pre-impregnated fabrics (right) with their difficult handling properties

The properties of two fabric materials, dry fibres and impregnated fibres with thermoplastic matrix, serve as example to illustrate these challenges (Fig. 2). Dry Fabrics made of carbon or glass fibres are sensitive semi-finished parts. They have a low bending stiffness, which results in a limp behaviour. This is advantageous for shaping, but there is a danger of damaging several fibres or losing their orientation during handling operations. Furthermore, the dry woven fibres are air-permeable until they are infiltrated by matrix material. [2]

The handling of fabrics with thermoplastic matrix is uncritical as long as their temperature is under their melting point. To enable shaping, they have to be heated during processing to heat the matrix material. In this condition, the semi-finished part changes its bending stiffness from high to low. Moreover, the surface becomes tacky because of the melted thermoplastic. This condition lasts only for a short time window after stopping heat supply due to the low heat capacity of the used materials.

3.2 HANDLING REQUIREMENTS

These properties lead to the following requirements in handling operations:

- (1) The limp (and air-permeable properties of dry fabrics) behaviour requires a careful gripping concept, which ensures an adequate support of the material. The complexity of gripping structures increases with increasing size and geometry.
- (2) Contact surfaces of the handling tools can damage the material and cause wear of grippers because of adhesion. Contact points between part and gripper have to behave non-adhesive.
- (3) Furthermore, the low heat capacity of the thermoplastic leads to a fast heat dissipation by conduction at the gripping points and convection due to handling movements. The handling equipment has to ensure that the heated part does not cool down under melting temperature during transport operations.

3.3 EQUIPMENT APPROACH

In order to meet the described requirements, there are several research approaches in developing material and process adjusted handling tools as extension to available standard grippers. Examples for meeting the requirements (1) and (3) are functional integrated handling tools, which allow sensitive handling of limp dry fabrics by low-pressure gripping. They are described at [9] and [10]. Besides the ability of performing form-flexible handling operations, integrated heating equipment is considered.

Handling of heated fibre-reinforced thermoplastics is mostly performed by three different kinds of grippers: A typical gripping principle for limp textiles is a needle gripper. Application in handling of limp and tacky fabrics is described in [11]. The disadvantage is puncturing of the fabric, which could cause damage of the fibres.

Another handling principle is a tenter frame. The cut-out is fixed by clamps or hooks at the outer contour and tensioned by springs in the frame [12]. The lateral fixing causes blend.

The third gripping method is a high temperature proof vacuum gripper (e.g. from J. Schmalz GmbH or Gimatic Srl). A flat and supporting suction bag prevents local deformation and damage of the TP-FRP, a polytetrafluoroethylene (PTFE) coating prevents adhesion between gripper and part.

The described handling techniques mostly find application in handling of single flat semi-finished parts. For implementing these techniques in manufacturing processes of hybrid components with several cut-outs and complex geometries (even three-dimensional preforms [8]), elaborate handling structures have to be developed.

4 A PROPOSAL FOR AN INTEGRATIVE APPROACH

The described automation challenges in handling fiber reinforced plastics during manufacturing process mainly come to the fore, if this kind of material is processed separately.

4.1 PRE-ASSEMBLING OF HYBRID PREFORMS

In pure FRP processes like resin transfer molding (RTM) [9] or in the thermoplastic-based process Ultralitec [13], several cut-outs are combined and fixed to a near-net-shape preform. After this pre-process, the fixed cut-outs are transferred into subsequent shaping and consolidation processes.

In case of a preforming process for hybrid components, the authors designed a process chain, where several cuttings of TP-FRP and metallic sheet are pre-assembled in cold and solid state and pre-formed by folding or bending with local heating. Afterwards the whole preform is heated above melting temperature of the thermoplastic matrix

and then transferred into the consolidation tool, where the component reaches its final contour and strength due to shaping and injection molding (Fig. 3). [14]

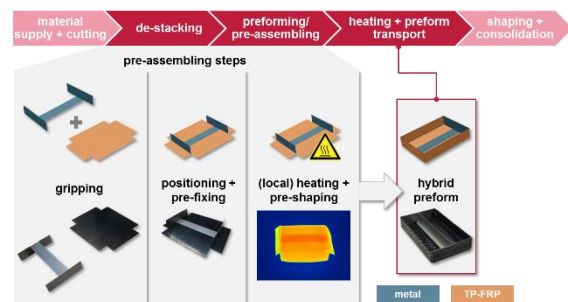


Fig. 3 Pre-assembling process of TP-FRP preform with metallic structure

4.2 BENEFIT FROM COMBINATION OF MATERIAL PROPERTIES

The combination of different materials during the pre-assembling process leads to a combination of different properties and their mutual influence. Due to partially contrary properties (bending stiffness, adhesion, heat capacity) of the used materials (Table 1), there is the potential of benefitting from a material combination by influencing the properties of the preform selectively. Therefore, it is hypothesized that this consideration may be used for adjusting not only the mechanical properties in the final component, but also for processing properties.

Table 1: Benefit from combination of different contrary material properties

property	TP-FRP	metal
bending stiffness	↓	↑
adhesion	↑	↓
heat capacity	↓	↑

Based on the partial contrary properties of the used materials, three main categories can be influenced during the manufacturing process:

1. Shape accuracy
2. Handling properties
3. Local heat management

(1) As described before, TP-FRP are only processible if the thermoplastic matrix is melted. In this condition the TP-FRP is shapeable, but it does not remain in a shaped state without any support. Depending on the geometrical complexity of the final component, it could be necessary to perform a pre-shaping before final shaping and consolidation. An integration of a metallic support structure into the component may influence the local bending stiff-

ness and thus the shape accuracy of the preform at critical positions.

(2) Closely linked to this are the properties, which influence the handling of the heated TP-FRP. In order to avoid difficulties in gripping limp and tacky parts, metallic support structures and gripping points can be provided. This may reduce the complexity of the gripping structure, the danger of material damage and wear and may enable a larger selection of gripping principles than described in 3.3.

(3) The low heat capacity of TP-FRP can be influenced by metallic inserts. Due to their higher heat capacity, temperature dissipation may be decreased locally to enable larger time windows for processing.

Due to an intelligent product design, which considers the required properties in the final component and the processing properties, automated manufacturing processes may be enabled.

5 FEASIBILITY STUDIES

For the purpose of confirming the hypothesized and described approach above, first feasibility tests to evaluate the influence of shaping accuracy, handling properties and heat management were performed. As testing geometry of a hybrid preform, a folded box, made of a single cut-out was defined (210x150x40 mm). The used material was a 1.0 mm thick pre-impregnated TP-FRP containing 66% of woven continuous glass filament. Inside the box metallic support structures (DC01, 0.5 mm) with different geometries were inserted. The boxes were manufactured as shown in Fig. 3 in a manual process.

5.1 INFLUENCING SHAPE ACCURACY

In order to evaluate the influence of metallic support structures to the shape accuracy of a reheated preform, deformation results of different support geometries were investigated. Therefore, solid pre-shaped boxes with and without metallic support structures were reheated in a convection oven up to 270°C. The boxes were placed upside down during the heating process, to benefit from gravity. After 15 minutes, the boxes were taken out of the oven and were cooled down under melting temperature to become solid again.

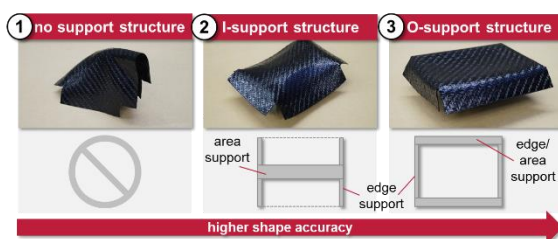


Fig. 4 Deformation results of reheated TP-FRP preforms with different support structures

Fig. 4 shows a selection of investigated support geometries and the deformation results. The box without a support structure (1) collapses during the heating process. The result is an undefined geometry. The originally box geometry no longer exists.

Geometry 2 offers a sufficient support at the short edges and in the middle of the base area. The missing support at the long edges leads to deflection. Moreover, the folded edges have lifted up.

Geometry 3 picks up the deflection at the long edges. The area support is divided and moved to the outer side. The deformation result shows, that this adjustment provides both a sufficient edge and area support. The deflection in the area is low. Compared to geometry 2 the edges lifted up less, but the shape accuracy is worthy of improvement. It has to be taken in account, that for this feasibility test, no joining between the TP-FRP and the metallic part was investigated. Overall, a significant improvement of shaping accuracy of the reheated preform can be determined.

5.2 INFLUENCING HANDLING PROPERTIES



Fig. 5 Handling shaped TP-FRP preform by a simple magnetic gripping tool

Furthermore, the influence of metallic support structures to handling properties in heated condition was investigated. Therefore, feasible gripping principles were identified and tested, which ensure save handling operations of the heated hybrid preform. Whereas pure heated TP-FRP parts can only be handled by grippers described in chapter 3.3, the hybrid preform enables the application of further gripping principles because of the metallic insert, which provide solid, non-tacky contact areas. Thus, clamping grippers can handle the preform, if they grip at metallic flanges. The magnetic properties of the DC01 insert also allow the application of magnetic grippers.

In order to ensure a form-stable handling of a heated FRP box without support structure (Fig. 4, left), a corresponding gripping structure with several geometry-adjusted gripping point has to support the preform. Due to the support structure in the

preform, the amount of gripping point from the handling tool can be decreased. This also decreases the complexity of the whole handling structure. Fig. 5 shows handling of the tested geometry by only one magnetic gripping point attached at the robot hand.

5.3 INFLUENCING HEAT MANAGEMENT

The need for reconsolidation of TP-FRP parts and the subsequent processing in injection moulding processes leads to a demanding process heat management. On the one hand warming up the TP-FRP above the melting temperature causes a lofting effect of the material thickness. This deconsolidation effect has to be undo by applying pressure at high temperature and cooling down. On the other hand, local melting of TP-FRP parts during the directly plastics injection in the subsequent process is required. Directly plastics injection is for example used to create fins at the part surface. To reach the aim of an integrated process chain one approach is to combine both sub-processes and keep the temperature of the TP-FRP until the hybrid component is cooled down during the injection moulding process.

The difficulty of this approach is to meet the time slot of processability because of cooling due to convection. Using the testing geometry 2 the impact of the metal support structure on the heat management was investigated.

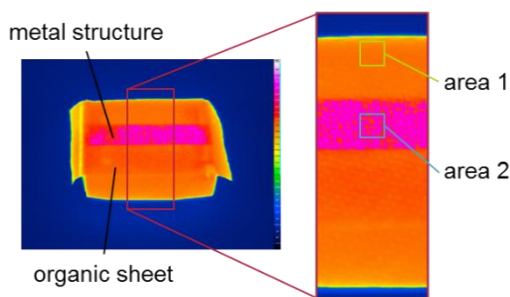


Fig. 6 Influencing the surface temperature of the TP-FRP through usage of a metallic structure

Therefore, a hybrid preassembled specimen was heated in a convection oven up to 270 °C and the cooling behaviour was analysed with a thermographic camera. Fig. 6 shows the temperature distribution after 15 seconds cooling time. In area 1 is just 0.5 mm TP-FRP located, in area 2 is TP-FRP support with a 0.5 mm metal structure. The diagram shows a clear contrast in temperature for those areas.

The temperature profiles of both areas and the temperature difference are shown in Fig. 7. Compared to area 1 the high heat capacity of the metal structure causes a considerable difference of the temperature in area 2.

As a result, depending on the material thickness the supporting structure enables larger processing time slots for local areas for subsequent processing steps and improves furthermore their processability, e.g. by improving flow paths for injection molding.

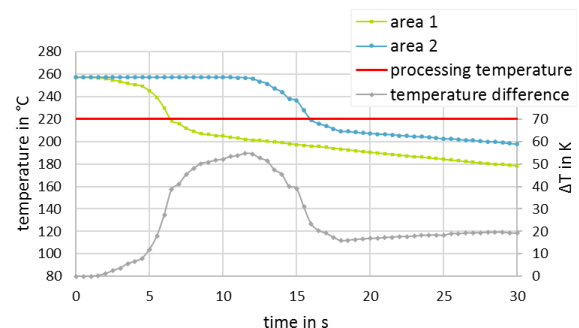


Fig. 7 Comparison of heat dissipation

6 CONCLUSIONS AND OUTLOOK

Because of the demand for new manufacturing chains in hybrid lightweight production, this article described the automation challenges and requirements in handling of fibre-reinforced (thermo-) plastic materials. Beside available conventional equipment solutions, which meet the requirements of careful handling and decreasing heat dissipation more or less, an integrative approach of benefitting from multi-material lightweight design was presented. It was hypothesized, that a component integrated material combination may not only lead to influencing the properties of the final component, but also the properties during automated manufacturing processes. First feasibility tests showed, that an intelligent combination of material properties influences shape accuracy, handling properties and local heat management.

Future work will have to develop a methodology for specific design of preforming processes. Moreover, different joining principles of hybrid preforms and their implementation are to be investigated. Eventually, the mechanical behaviour of hybrid structures will have to be investigated.

7 ACKNOWLEDGEMENT

This research and development project is funded by the German Federal Ministry of Education and Research (BMBF) within the Forschungscampus "Open Hybrid LabFactory" and managed by the Project Management Agency Karlsruhe (PTKA) under research funding scheme 02PQ5100. The authors are responsible for the contents of this publication.

REFERENCES

- [1] K. Dröder, C. Herrmann, A. Raatz, T. Große, M. Schönemann, C. Löchte: Symbiosis of

- plastics and metals: integrated manufacturing of functional lightweight structures in high-volume production, in: *Kunststoffe im Automobilbau*. VDI-Verlag, Düsseldorf, Germany 2014
- [2] C. Cherif: *Textile Materials for Lightweight Constructions: Technologies - Methods - Materials – Properties*, Springer, Heidelberg/Berlin, Germany, 2015
- [3] L. Ickert, D. Thomas, L. Eckstein, T. Tröster: *Beitrag zum Fortschritt im Automobilleichtbau durch belastungsgerechte Gestaltung und innovative Lösungen für lokale Verstärkungen von Fahrzeugstrukturen in Mischbauweise*, Berlin, Germany 2012
- [4] E. Staiger, O. Diestel, C. Cherif, S. Bräunling, A. Hardtmann, K. Großmann: *CFK-sheet metal hybrid composites*, in: *7th International Textile Conference*, Aachen/Dresden, Germany, 2013
- [5] M. Schuck: *New processes for large scale automotive production of composite application*, *SAMPE Journal*, vol. 48, no. 1, 2012
- [6] H.-P. Heim: *Injection Molding of Multimaterial Systems*, in: *Specialized Injection Molding Techniques*, William Andrew, 2016
- [7] N. Reynolds, A. B. Ramamohan: *High-volume thermoplastic composite technology for automotive structures*, in: *Advanced Composite Materials for Automotive Applications*, Wiley, 2014
- [8] S. Seidel: *Anforderungsgerechte, thermoplastische Preforms für den Hochleistungsleichtbau*, TuTech Verlag, Hamburg, Germany 2015
- [9] C. Ehinger, G. Reinhard: *Robot-based automation system for the flexible preforming of single-layer cut-outs in composite industry*, *Prod. Eng. Res. Devel*, vol. 8, no.5, 2014
- [10] H. Kunz, C. Löchte, F. Dietrich, A. Raatz, F. Fischer, K. Dröder, K. Dilger: *Novel form-flexible handling and joining tool for automated preforming*, in: *Science and Engineering of Composite Materials*, vol. 22, no. 2, deGruyter, 2015
- [11] J. Mitzler, J. Renkl, M. Würtele: *Hoch beanspruchte Strukturbauteile in Serie*, in: *Kunststoffe*, vol. 3, 2011
- [12] M. Bochsinger, K. Edelmann, T. Lange, T. Menken, S. Sperling, E. Tschakrow, T. Wirtz: *Apparatus for producing a component and methods*, patent no.: DE 102008020347 B4, 2012
- [13] V. Altstädt, A. Spörrer, M. Mühlbacher, P. Michel, S. Seidel: *Großserientauglicher Hochleistungsleichtbau mit DU-Tapes*, in: *Lightweight Design*, vol 5, no. 2, 2012
- [14] R. Schnurr, C. Lippky, C. Löchte, F. Dietrich, Franz; K. Dröder, S. Kreling, K. Dilger: *Introduction of a production technology for the pre-assembly of multi-material-preforms aiming at a large scale production*, in: *20th International Conference on Composite Materials*, Copenhagen, Denmark, 2015

DEVELOPMENT OF A BRACKET ELEMENT WITH A HYBRID METHOD OF CONSTRUCTION (CFRP/TI)

Holger Büttemeyer^{1*}, Andreas Solbach², Claus Emmelmann^{2,3}, Axel S. Herrmann^{1,4}

¹Faserinstitut Bremen e.V., Bremen

²Institut für Laser- und Anlagensystemtechnik, TU Hamburg-Harburg, Hamburg

³Laser Zentrum Nord GmbH, Hamburg

⁴Universität Bremen, Fakultät 4: Produktionstechnik, Bremen

ABSTRACT: This publication presents the first test results of a multi-material, lightweight bracket. Hereby the bracket consists out of metal as well as Carbon Fiber Reinforced Plastics (CFRP). Two metallic elements have been generated using Hot Working and Laser Additive Manufacturing to enable a classical and safe force initiation area. Between those parts a carbon fiber preform has been integrated which was done by Tailored Fiber Placement. Using a Resin Transfer Molding process the CFRP/metal Bracket was finished. Afterwards the bracket has been tested using Non Destructive Testing and Destructive Testing. It was shown that the bracket was capable to carry an average load of 33.1 kN in direction of gravitation and 9.2 kN along the pitch axle.

KEYWORDS: multi-material combination; CFRP; titanium alloy; TFP; RTM; hot working; 3D-Printing

1 INTRODUCTION

In aviation industry fuel consumption and the magnitude of payloads are a matter of interest. Therefore, the demand of designing lightweight structures for aircraft systems is mandatory. Today, most parts are made out of metallic material and manufactured using conventional milling and casting processes. The low specific strength of metallic material results in relatively heavy parts. Reducing the amount of metal used by replacing it with a multi-material combination like carbon fiber reinforced plastic (CFRP), is one opportunity to save weight. However, the challenge of integrating CFRP based parts into existing plane concepts is the local load transmission into the part. Because of performance reasons the part should look different for CFRP than for metallic parts. Whereas metal parts will be combined using conventional joining technologies like riveting and screw connections CFRPs show their best performance when parts are connected along big surfaces without damaging the fibers. One solution for this challenge is the integration of loop connections, which provides metallic joining areas enlaced by CFRP.

In the following publication this joining concept was examined keeping the force initiation points from a standard aircraft bracket made from aluminum (figure 1).

Additional to the mentioned advantage regarding weight saving, new production methods can be implemented to avoid waste of material caused due to high milling rates of close to 90 %. Additionally, using different other materials than aluminum has the advantage that the bracket could be connected to a CFRP without coatings which protect the interface from contact erosion.

2 MULTI-MATERIAL CONCEPT

To replace the aluminum in the bracket it is important to understand the function of each different area of this part. The part consists out of two force initiation areas. One is located at the upper area and contains a flange where the bracket is fixed to the aircraft structure. The other area is located at the bottom hole where other parts can be connected using a compression connection. Furthermore, this area of the part will be called hull area. Between those force initiation areas, the load paths can be determined and replaced by CFRP. Therefore, the gained multi-material design approach consists out of two metallic load transmission parts and a complex CFRP structure which is connecting those (figure 2).

* Corresponding author: Am Biologischen Garten 2, 28359 Bremen, phone +49 (0)421 218-59650, fax +49 (0)421 218-58710, buettemeyer@faserinstitut.de



Fig. 1 Conventional aluminum bracket

Simultaneously to the design development the material selection was performed for the metallic components as well as for the CFRP. Additionally, different coatings have been integrated into the bracket for insulation and electrical conduction.

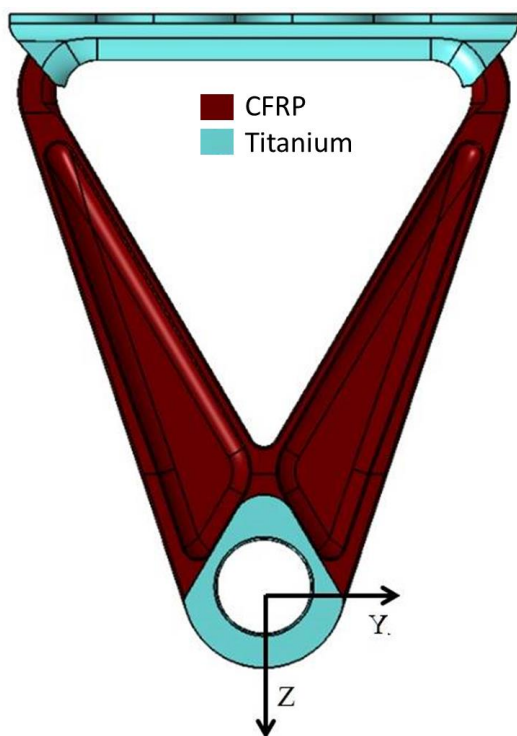


Fig. 2 New design of a multi-material bracket

2.1 LOAD TRANSMISSION AREAS

The load transmission areas have been made from Ti-6Al-4V which is a titanium alloy that is a standardized material for aircraft systems. This isotropic material has the advantage of a much easier processing regarding critical strength in riveting and screwing. [1] Further advantages in connection with CFRP are a low electrochemical potential, a low thermal expansion coefficient, high stiffness and a high specific strength compared to other metallic materials. [2, 3] For each metallic part a different manufacturing method has been chosen. Both manufacturing processes have been processed under Argon atmosphere to protect the metal from oxygen- and hydrogen embrittlement. [4] Finally the parts have been post-processed using a thermal heat-treatment above the solidus temperature to eliminate residual stresses. The cooling process has been done using argon atmosphere.

2.1.1 Hull Area

The metallic interpretation of the first load initiating element is shown in figure 3. It consists out of two main functionalities. On the inner hole the part offers an interface to a compression connection, on the outer side of the hull it enables a guidance for the CFRP which includes further lateral support structures. These lateral supports are beveled with a minimal wall thickness of 0.4 mm.

Because of the complexity and the need for accuracy during the following manufacturing processes this part has been generated using Additive Layer Manufacturing (ALM) which allows a high design freedom as well as a near net shape design. As ALM technology a laser based process has been chosen in which the 3D-Part is digitally separated into 2D-layers. These layers have been iteratively melted into a powder bed using the heat of the laser beam. The whole process took place using an EOS eosint M270 xt, with a laser spot diameter of about 80 μm .



Fig. 3 Isometric view of the 3D-Printed hull with inner insulation coating

2.1.2 Flange Area

The flange area, as it is shown in figure 4, was manufactured out of a sheet metal using hot working. Hot working has the advantage that the deformation takes place above the recrystallization temperature. Hence cracks which would appear using cold hardening can be avoided. The influence of the flange radius has been investigated in a previous study [5].

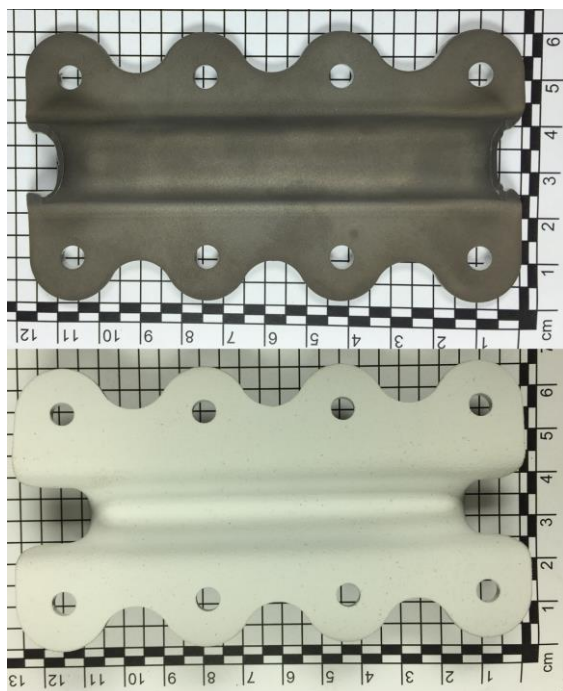


Fig. 4 Hot worked titanium flange: upper picture: top view; lower figure: insulated bottom view

2.2 LOAD TRANSFER AREA

For the area between the load transmission areas, CFRP was chosen because of the high magnitude of the specific strength in the direction of the fibers.

To create this reinforced plastic system several manufacturing processes had to be performed. First, textile preforms have been manufactured using the Tailored Fiber Placement technology (TFP) in which fiber roving's are laid down and fixed using a defined path. A benefit of this technology is that this process can be fully automated. Like mentioned before, a loop design was chosen to offer good mechanical behavior. This loop connection revolves a metallic hull in the vertex area and a metallic flange on the opposite area. The preforms have been generated using crossed loops because of the advantageous behavior regarding transverse loads. [6] A 12.000 filament carbon fiber roving of the supplier Toho Tenax with the identification HTS45 E23 was chosen. This fiber roving is put down and fixed by a fixing fiber on a stitching ground which are two biaxial non-crimp

fabrics with fiber orientations of $-45;+45;-45;+45$. This non-crimp fabric is supplied by Saertex with the identification number S37CX000 and consists of a basis weight of 218 g/m². After the load path of the fiber roving had been determined, a simulation was done to check the required loads. Then, a stitching data was established for preparing the tailored fiber placement process. A digital mockup of the preform is shown in figure 5. Two preforms were required for one hybrid bracket.

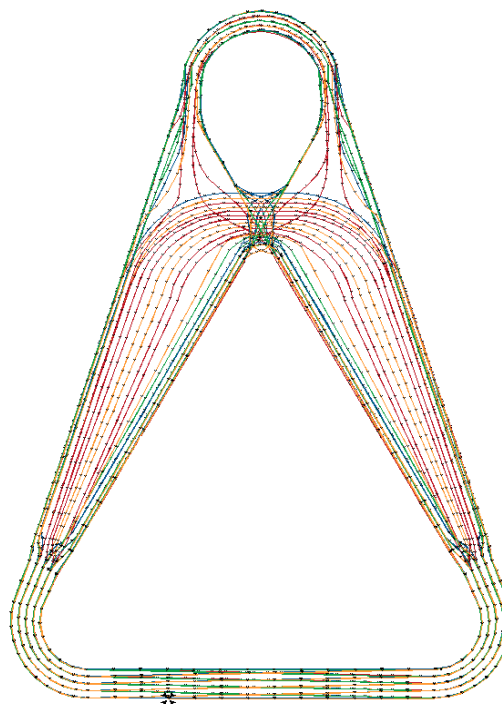


Fig. 5 Stitching data with load paths

2.3 COATINGS

The parts of the bracket have been covered by two different coatings. One coating provides insulation between the CFRP and the titanium. It is made out of aluminum oxide to avoid long term corrosion on the CFRP/titanium interface. Former tests have shown that the thickness of this layer has to be bigger than 0.2 mm to guarantee electrical insulation. Additionally to the material interfaces a path on the surface of the CFRP was coated between the two metallic parts. On top of this insulation path an electro conductive coating made out of copper was placed to transport creepage from the hull to the flange.

3 RTM PROCESS

The multi-material Bracket has been completed with Resin Transfer Molding (RTM). Textile preforms had been prepared and the substrate fabric had been cut out (Figure 6). Afterwards the metal-

lic hull and flange had been inserted into the textile preform.



Fig. 6 Textile preforms made by tailored fiber placement

The combination of fibers and metallic elements has been placed in a mold which includes three biscuits (Figure 7). The first biscuit is used in the middle as an inflow for the resin. The other two were used as an outflow for the resin. They have been integrated at the end of the hull and in the middle of the flange. RTM6 supplied by Hexcel was used as an aircraft certificated epoxy system [7]. RTM6 was injected at 120°C mold temperature while the resin itself has a temperature of 80°C. The curing temperature is 180°C for 90 min. The injection pressure was 0.2 MPa. The post pressure increased up to 0.5 MPa. The graph in figure 8 shows the whole curing process concerning time and temperature. After curing the brackets, they were demolded.



Fig. 7 Integrated fiber preform with metallic parts in the RTM-mold

4 QUALITY ASSURANCE

Different methods have been used to control the parameters of the Parts and RTM Process before and during the infusion of the epoxy system. Before placing the preform in the mold all metallic parts had to be measured because of the low magnitude of their tolerances. If the metallic parts would be bigger than the nominal dimension they

would not fit into the mold. If they would be much smaller, resin build ups will be created during the RTM-process.

The geometry of the preform manufactured by TFP has also been measured, cut and weighed. During the curing process, the temperature of the mold was permanently controlled and recorded.

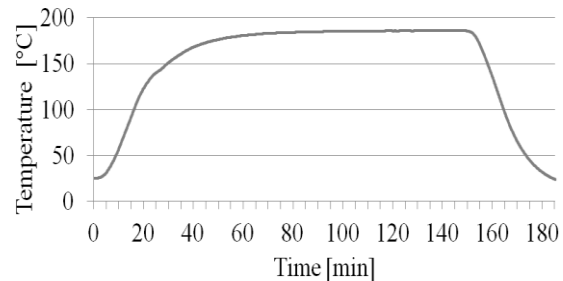


Fig. 8 Curing cycle concerning temperature and time

5 TESTING

After the RTM Process the bracket has been analyzed by Non Destructive Testing (NDT) and Destructive Testing (DT). The NDT took place using a computer tomography (CT) scanner. Hereby, voids of the epoxy system, local fiber orientation and delamination could have been examined. Figure 9 shows a cross section of the bracket with the focus of the orientation of the fiber rovings.

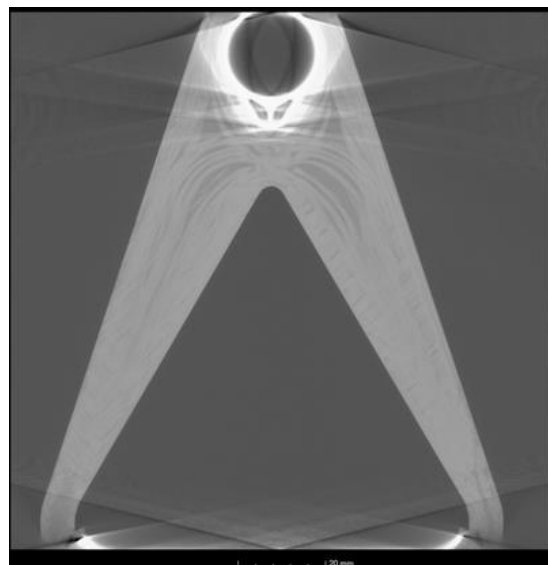


Fig. 9 CT picture of bracket with focus on the CFRP section

The DT was done using a Z250 supplied by Zwick Roell. The test speed was set at 2 mm/min. Six Brackets were tested; Three in z-direction and three in Y-direction (Figure 2). All specimens were tested until total failure. For testing a special test rig had been developed and can be seen in figure 10. On top of the bracket a kind of fork structure is

holding a bolt. This bolt initiates the force into the hull of the bracket. The bracket itself is fastened by the flange with rivets connected to a solid structure. This solid structure allows the placement of the bracket in two different orientations.

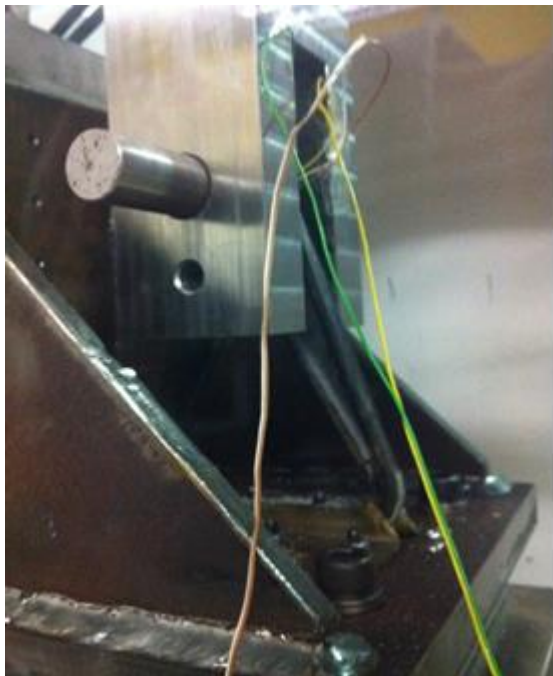


Fig. 10 Test equipment for Hybrid Brackets

6 RESULTS

The average load in z-direction achieved a magnitude of 33.14 kN with a standard deviation of 10.64% (Figure 11). First acoustic failures have been noticed at 10 kN. No damage can be seen at the hull area. The flange had a slight plastic deformation in the transition zone. The curves shown in figure 11 seem to be mostly linear with increased prolongation towards high forces. In the end the specimens failed in a brittle way with a displacement of more than 4 mm.

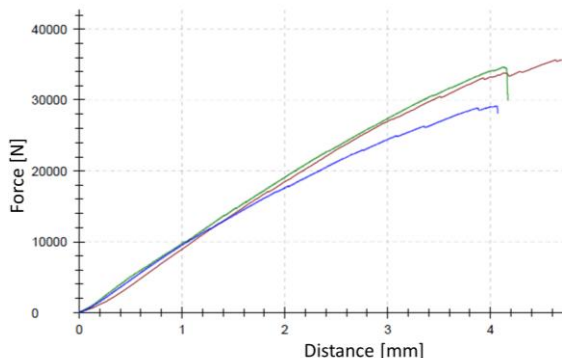


Fig. 11 Load-displacement-diagram in Z-direction

The tests in Y-direction have shown a different failure behavior than the ones tested in Z-direction.

The load-displacement-diagram is shown in figure 12. All curves started equivalent to each other. When the load reached 3 kN the brackets started to deform plastically. This plastic distortion was about 5mm with an increased load of 2 kN. Then the stiffness of the bracket increased again until an ultimate load average of 9.19 kN with a standard deviation of 13.83 % was reached. The total load displacement has been measured between 18 mm and 20 mm and failed at the tensile zone of CFRP. One specimen achieved 27 mm displacement with many load drops before failing. This effect was due to a failure in the compression zone of the CFRP.

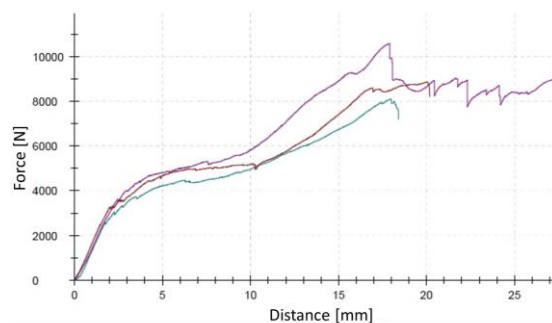


Fig. 12 Load-displacement-diagram in Y-direction

The failure mode in both load directions were fiber failures which were located in the border of the transition zone between the CFRP the metallic flange (Figure 13). Fiber failures in specimens which were tested in Y-direction were located at the tensile-load area of the CFRP at the transition zone.



Fig. 13 Typical failure mode for test in Z-direction

7 CONCLUSIONS

The load-displacement-diagram of the test in z-direction shows a typical failure mode of CFRP. The curve increased constantly and failed abruptly. During the increase, little load drops were noticed. These load drops have been interpreted as inter-fiber failure. Before the total failure took place fiber failures have been located at the border of the transition area between supported CFRP and the unsupported CFRP in the region of the metallic flange. Those fiber failures weakened the CFRP

bar. It is generally assumed that the fiber failures are caused by the flange corner which leads to additional notch stresses in this area.

The second load case with a load in y-direction is not anymore symmetrical to the axis of the bracket. Therefore, the CFRP bars get loaded each in a different way. The bar in the direction of the force is under pressure, the bar which is not in the direction of the load is under tension. All in all the DT in y-direction shows a good-natured failure of the bracket. When the load reached 4kN plastic deformation in the bracket was determined. During further displacement, little load reductions were detected, caused by failures in the fiber-matrix interface. Furthermore, the compression bar has been deformed. Due to this deformation the CFRP bar was separated from the flange element till the curved interface has ended and the straight interface between flange and CFRP starts. It can be assumed that failure of the bracket starts either at the compression zone caused by the high deformation of the CFRP bar or at the tensile zone through a strong notch effect.

In the compression bar as well as the tensile bar of the CFRP fiber failures have been determined as the reason for total failure. These fiber failures were located at the transition area of the CFRP and titanium flange for the z- and y-load case. Therefore, this spot is weakening the whole bracket and should be changed to increase the mechanical performance. One option to increase the mechanical performance is supposed to be an increased support area of the CFRP which should decrease the magnitude of the notch stresses. Another option would be to integrate titanium foils into the preform parts to decrease the notch stresses.

In further investigations the failure behavior will be analyzed depending on the magnitude of force. So an interrupted process will be implemented with a certain displacement.

All in all, the development of a hybrid bracket achieved better mechanical performance when comparing it with the conventional aluminum bracket. The advantage of the hybrid bracket is the weight reduction up to 30 % of the original weight. Another similar multi-material design which will be tested soon shows a weight reduction up to 50 %.

8 ACKNOWLEDGEMENT

The authors are grateful for financial support from the German Federal Ministry of Economics and Technology (BMWi) within the project “Hybrid Bracket – Development of a functional and weight optimized hybrid brackets for aircraft structures”.

Additionally, we are also very grateful to our project partners which are: 3D CONTECH GmbH & Co. KG, DE-21147 Hamburg; FormTech GmbH, DE-28844 Weyhe-Dreye; Nordwig Werkzeugbau

GmbH, DE-21147 Hamburg; Titan Praecis Metallurgie GmbH, DE-24558 Henstedt-Ulzburg.

REFERENCES

- [1] Wilmes H., Herrmann A.S., Kolesnikov B., Kröber I.: *Festigkeitsanalysen von Bolzenverbindungen für CFK-Bauteile mit dem Ziel der Erstellung von Dimensionierungsrichtlinien*, DGLR-Jahrestagung 1999.
- [2] Schürmann H., *Konstruieren mit Faser-Kunststoff-Verbunden*, Springer-Verlag Heidelberg, 2. Auflage, 2007.
- [3] Donachie M., *Titanium: A Technical Guide*, 2nd Edition, ASM International, America, 2000.
- [4] Woei-Shyan L., Chi-Feng L.: *Plastic deformation and fracture behaviour of Ti-6Al-4V alloy loaded with high strain rate under various temperatures*, Materials Science and Engineering: A, Volume 241, Taiwan, ROC, 1996.
- [5] Büttemeyer H., Schiebel P., Solbach A., Emmelmann C., Herrmann A.S.: *Performance of various designs of hybrid loop-loaded CFRP-titanium straps*, *Proceedings of 20th International Conference on Composite Materials (ICCM), Copenhagen, Denmark, July 19 -24, 2015*.
- [6] Bleser W.: *Beitrag zur Analyse und Gestaltung der Krafteinleitung von Faser-Kunststoff-Verbinden*, Shaker Verlag Aachen, 2014.
- [7] Hexcel Cooperation, *HexFlow RTM6 Product Data*, 2014.

CHAPTER 7:

**NON-DESTRUCTIVE TESTING AND
QUALITY ASSURANCE**

THERMOGRAPHY ASSISTED CHARACTERISATION OF PRODUCTION-INDUCED DEFECTS IN CFRP AND THEIR INFLUENCE ON THE MECHANICAL BEHAVIOUR

Jannik Summa^{1*}, Michael Schwarz¹, Simon Bernarding¹, Prof. Hans-Georg Herrmann^{1,2}

¹Chair for Lightweightsystems (LLB), Saarland University, Saarbruecken, Germany

²Fraunhofer Institute for non-destructive Testing (Izfp), Saarbruecken, Germany

ABSTRACT: A novel hybrid-joint, suitable to series production, is currently developed. It overcomes the gap in stiffness by inserting a thermoplastic element between metal and carbon fiber reinforced polymer (CFRP). The main goal in terms of quality assessment is to characterise the defect-caused damage propagation (effects of defects) by means of destructive and non-destructive testing (ndt) of artificially implemented defects.

Assuming that flaws are most-likely to occur within the CFRP, close to the transition zone, first investigations are carried out on the effects of defects in pure CFRP component. Thus artificially implemented defects, i.e. missing roving, gapping, 10° misalignment, pleat and delamination, are characterised by active thermography in terms of type, size and location. A subsequent correlation of the mechanical properties under quasi-static tensile tests and fatigue experiments of a defect-free reference and the imperfect samples is carried out. In order to evaluate the damage propagation, the mechanical experiments are complemented by *in situ* passive thermography.

KEYWORDS: Effects of Defects, passive Thermography, mechanical testing

1 INTRODUCTION

To exploit the full potential of lightweight design, the application of metal to CFRP hybrid-joints increases. The main challenge that arises with these Material-compounds is located at the joining zone between the two components, as the discontinuity in mechanical properties causes structural attenuations [1] and the appearance of production induced defects may be promoted in this region.

As explained more precisely in chapter 2, a thermoplastic polymer is introduced between the metal and the CFRP component to counteract the gap in stiffness and to improve the fatigue properties.

The main objective of applying quality assessment is to detect existing flaws with subsequent evaluation of their severity, which is mainly based on the knowledge of the damage propagation processes. Although mass of investigations had been carried out on the damage mechanisms of each of the involved materials [2-4] in the past decades, less is known on the damage mechanisms of metal to CFRP hybrid-joints. This is even more the case, if one considers production induced flaws and their influence on the response of the hybrid-joint to mechanical loading.

Therefore it is necessary to investigate internal material degradation, which can be measured as mechanical property degradation as well as local temperature changes due to irreversible deformations. For the last parameter, *in situ* passive thermography has excellent capabilities investigating temperature changes with high lateral resolution [5].

Assuming, that defects occur within the CFRP adjacent to the joining zone, first investigations focus on the effects of defects in pure CFRP component by means of passive thermography damage monitoring. This is carried out under quasi-static and fatigue tensile loading on CFRP samples with different defects, which were artificially implemented within the RTM process.

2 CONCEPT OF THERMOPLASTIC INSERT

Instead of bolting or applying adhesives, the two-dimensional conjunction between the metal component and the CFRP-laminate is achieved by geometrical optimization which results in a tight fit. Thereby the metal, which is EN AW-6082 aluminum (AlSi1MgMn), is encased with Polypropylen (PP) by direct injection over-moulding. In

* Corresponding author: Campus E3.1, 66123 Saarbruecken, Germany, jannik.summa@izfp-extern.fraunhofer.de

the subsequent step this insert is embedded into the CFRP laminate within a Resin-transfer-moulding (RTM) –process.

The CFRP-laminate contains of four layers $[0^\circ/90^\circ, \pm 45^\circ]_s$ of 3K plain weave with 30 vol% carbon fibre (Torayca FT300B) embedded in the epoxy matrix (Biresin CR170/CH150-3). The overall laminate thickness is 1 mm.

The benefits are a fast and cheap process chain with improved metal to PP adherence due to microscale mechanical interlocking [6] and improved corrosion resistance [7]. Moreover the thermoplastic polymer is capable of function integration, i. e. better drapery, surface structuring, and reduces the gap in stiffness, which counteracts the discontinuity in mechanical properties.

Moreover the geometrical optimization intends a homogeneous stress distribution in the whole joining zone, which contributes to structural integrity and fatigue resistance.

However by adding this thermoplastic component two interfaces are created. It is assumed that production induced defects, of which gapping, pleat, missing roving, 10° misalignment and delamination were investigated, are most-likely to occur within the CFRP adjacent to the thermoplastic polymer (PP). Thus the interface between those is of particular interest.

3 EXPERIMENTAL SETUP

In order to differentiate the effects arising from the interfaces of the hybrid-joint and the effects of defects, first investigations were carried out on the pure CFRP component containing different defects (i. e. missing roving, gapping, 10° misalignment, pleat, delamination).

The same laminate was used as for the hybrid-joint. According to [8] sample type 2, the geometrical parameters were chosen to be 120 mm length, 20 mm width and 1 mm thickness. The clamping length was chosen 25 mm on each side.

In the first step, active thermography was applied characterising size and position of the defects, which were artificially implemented into the laminate.

For this purpose a dualband infrared camera QWIP 384 by Thermo Sensorik[®] was used, which attains 384×288 pixels with a spectral range between $4.4\text{--}5.2\mu\text{m}$ (MWIR) and $7.8\text{--}8.8\mu\text{m}$ (LWIR).

After active thermography the samples were mounted on wedge grips on an Instron 8500 with a 100 kN load cell. Longitudinal strains were measured using an axial clip on extensometer. Tensile tests were carried out displacement controlled with 2 mm/min cross-head speed, whereas fatigue tests were driven displacement controlled with 5 Hz frequency and a displacement ratio $R = 0.1$.

The maximum relative displacements ranged from 40 % to 70 % of the displacement of fracture of the

defect-free reference, which was found to be 1,16 mm.

The mechanical testing was complemented with an InfraTec VarioCAM[®] HD head bolometer camera with a resolution of 1024×768 pixels. The camera's interval of spectral sensitivity ranges from $7,5$ to $14\mu\text{m}$ and its temperature resolution lies beneath $0,05\text{ K}$ (at $T = 303,15\text{ K}$).

4 DEFECT CHARACTERISATION BY ACTIVE THERMOGRAPHY

Application of active thermography is based on an external excitation technique, like ultrasonic, eddy current or flash light. An infrared camera is recording the heat flow by means of the time dependent surface temperature of an excited sample. In this process defects act like heat barriers, which are depicted as bright areas in the thermography picture. In this work flash light is used as excitation source.

In Fig. 1 (left) a defect-free CFRP-sample is shown at 75 ms after excitation. It belongs to the undisturbed, upper laminate-ply. Moreover the orientation of the carbon-fibers can be extracted. Fig. 1 (middle) depicts a CFRP-sample before mechanical testing containing an artificially implemented delamination between the first and the second layer. In the middle of the sample, a bright area is evident, which can be identified as the delamination. In Fig. 1 (right) the same CFRP-sample is displayed but after mechanical testing. In contrast to the image before mechanical testing, the bright area in the middle of the sample appears brighter and broader. This indicates that the delamination became bigger and worse due to mechanical loading. However, the biggest difference is the crack on the left side in the middle of the sample. It occurs at the weakest point of the sample and lead to failure.

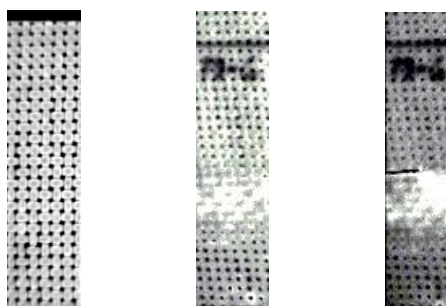


Fig. 1 Left: $[0/90^\circ]$ -Ply of a defect-free CFRP-sample, middle: sample with delamination before - and right: after mechanical testing

5 PASSIVE THERMOGRAPHY

Besides the possibility of external excitation, thermography can also be applied as a passive damage monitoring technique, as friction and deformation

processes act as internal excitation of the sample. As Reported by Rösner and Netzelmann [9], the measured temperature change can be expressed as a superposition of the thermoelastic temperature variation ΔT_{el} , and the contributions to temperature change due to heat dissipation ΔT_{diss} and heat exchange with the environment ΔT_{loss} .

$$\Delta T(t) = T(t) - T_0 = \Delta T_{el}(t) + \Delta T_{diss}(t) + \Delta T_{loss}(t) \quad (1)$$

Where ΔT is the total temperature change and T_0 the absolute reference temperature at time $t = 0$. The elaborate review of Pitattesi [10] accounts for the classical theory of thermoelastic stress analysis under adiabatic conditions for a homogeneous orthotropic material.

The MIDA (mechanical induced dissipated heat analysis) technique is perfectly applicable to fatigue experiments, as it accounts for the incremental temperature increase per cycle. A good correlation between heat build-up measurements and accumulated residual strains and scalar damage factor, respectively, is reported by Arif [11].

The work of Roche [5] showed the successful characterisation of subcritical damages based on the analysis of the lateral temperature distribution.

6 TENSILE FAILURE

Mechanical testing was carried out on defect-free specimens, which were taken as reference, as well as specimens containing missing roving, gapping, 10° misalignment, pleat and delamination. All such defects were located in the upper [0/90°] layer. The results of the tensile tests are given in Figures 2-5. To consider scattering, five samples were tested for each of the values.

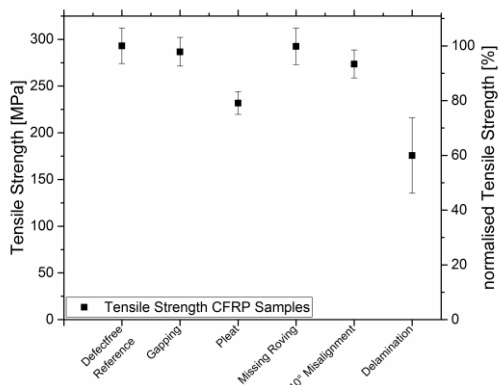


Fig. 2 Tensile Strength of tested CFRP Samples, right scale: tensile strength normalised to the defect-free reference

Fig. 2 reveals that gapping and missing roving have almost no effect on the tensile strength, since the deviation referring to the reference is less than

the scattering. In contrast to that, the pleat and the 10° misalignment caused a drop of 20 % and 5 %, respectively. The most crucial attenuation can be found for the delamination, whose tensile strength reaches only 60 % of the reference strength. It can be further noted, that higher scattering resulted for samples containing delamination.

The similar tendency can be found for the displacement of fracture, which is shown in Fig. 3. Deviation caused by gapping and missing roving lie within the scatter of the reference. A slight decrease can be observed for 10° misalignment whereas pleat and delamination cause a drop of approximately 25 %.

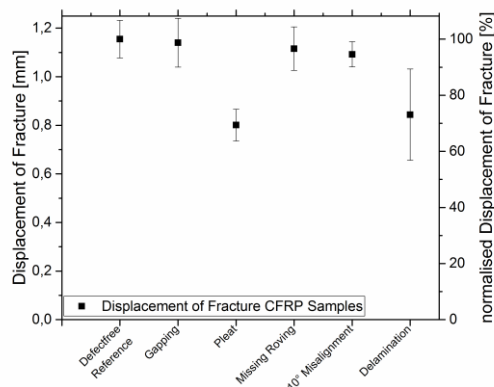


Fig. 3 Displacement of fracture of tested CFRP, right scale: displacement of fracture normalised to the defect-free reference

Figures 4 and 5 show the results for the breaking elongation and E-moduli, respectively. As observed for the tensile strength and the displacement of fracture, the missing roving remains effectless. In the case of gapping and 10° misalignment the breaking elongation is even higher than the reference value, which can be attributed to an equivalent drop in E-modulus.

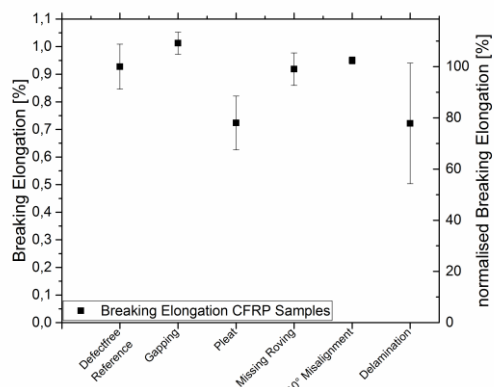


Fig. 4 Breaking elongation of tested CFRP Samples, right scale: breaking elongation normalised to the defect-free reference

Contrary effect is evident in the case of pleat, for which the E-modulus was found to be 113 % of the

reference value, corresponding to a 20 % drop in breaking elongation. It has to be noted, that the E-modulus of the sample with pleat is only valid preliminary to the first occurrence of damage, where the pleat opens and nonlinear behaviour follows.

Serious weakening of the material by delamination is indicated by means of serious drops in both, stiffness and breaking elongation of 40 % and 21 %, respectively.

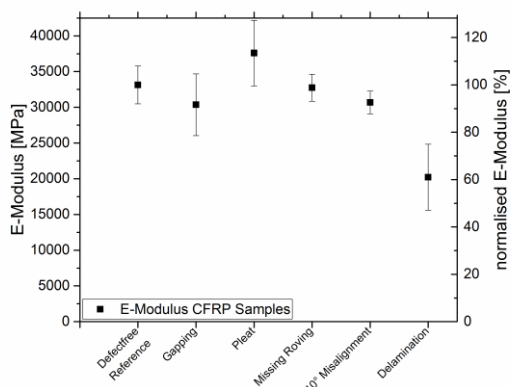


Fig. 5 E-Modulus of tested CFRP Samples, right scale: gives the E-Moduli normalised to the defect-free reference

As mentioned above, highest scattering comes along with artificially delaminated specimen. Assuming that the delamination sizes are not perfectly identical, this observation is a strong indicator for the mechanical properties being highly sensitive to the delamination size.

The investigations are complemented by passive thermography, which allows characterising the spontaneous heating of the fracture surface.

A representative example for a specimen with gapping is shown in Fig. 6.

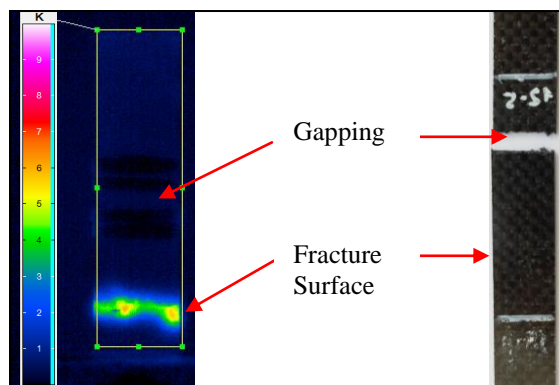


Fig. 6 Left: differential Temperature-image, heating due to tensile fracture, right: Picture of broken sample

It points out, that the fracture plane does not coincide with locus of the gapping. Thus, mechanical and thermographical results indicate, that the gap-

ping has no crucial influence on the structural integrity under quasi-static tensile loading.

The thermographic images for pleat and delamination, which caused the biggest attenuations in mechanical properties, are given in Fig. 7.

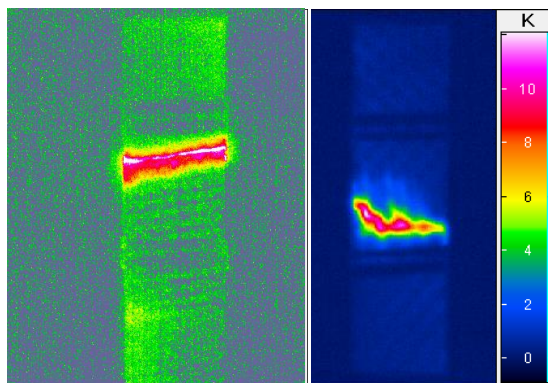


Fig. 7 Differential Temperature-image, heating due to tensile fracture, left: fracture plane coincides with pleat, right: CFRP sample with delamination

In Fig. 7 (left) it the tensile fracture of a sample with pleat can be seen. The contrast in differential temperature image results from the spontaneous heating due to the fracture. In contrast to randomly emerging breakage in Fig. 6, the fracture strictly coincides with the pleat. Since the fracture locus represents the weakest spot, it is clear, that the pleat is a critical defect, which causes significant attenuations of the mechanical properties of the CFRP. Fig. 7 (right) shows a broad, zigzagging rupture zone. It can be seen from the corresponding active thermography analysis in Fig. 1 that the rupture emerges within the delaminated region. Hence the delamination represents the weakpoint and causes severe material property degradations, which was seen from the results of mechanical testing. Ultimately delamination has to be treated as a crucial defect.

7 EFFECTS OF DEFECTS IN FATIGUE

The results of fatigue experiments are summarized in Table 1. Since missing roving showed almost no effect in tensile tests, it is not further considered in fatigue experiments. Note that the relative displacement of 70 % is greater than the static displacement of fracture for samples containing pleat or delamination.

Table 1: Cycles to Failure for different defects and displacements

	Relative Displacement	Cycles to failure	Standard deviation
Defect-free	70 %	729680	388833
Gapping	70 %	1,17e6	-
10° misalignment	70 %	53856	37818
Pleat	50 %	1075	1424
	40 %	30344	20906
Delamination	50 %	51067	34337

Additionally, the representative development of the E-moduli is shown in Fig. 8.

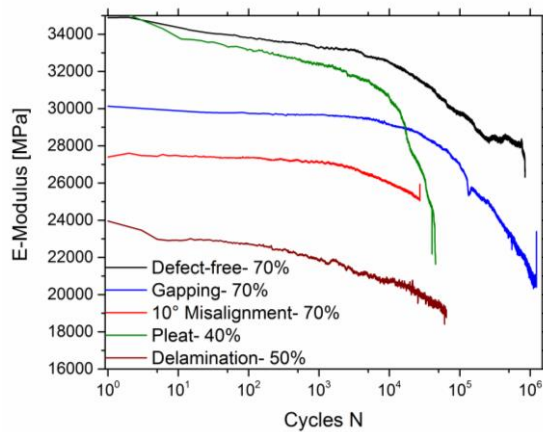


Fig. 8 Development of E-moduli during fatigue testing, legend gives different relative displacements

Along the defect-free samples most resisted the loading for more than 10^6 cycles, whereas some broke earlier. Therefore higher scatter could be found. The samples with gapping survived almost the same amount of cycles but with lower scatter. Though higher degradation of the E-modulus, which corresponds to the scalar damage factor [12], is evident in Fig. 8 for cycles higher than 10^4 . For specimens with 10° misalignment, subjected to a relative displacement of 70 %, the average lifetime being 54000 cycles, lowest degradation previous to fracture could be observed.

The lifetime under fatigue conditions was more sensitive to pleat and delamination, as the average lifetime showed a significant drop for those defects (see table 1). This is confirmed by Fig. 8, as the delaminated specimens suffered significant degradation within the first cycles. Moreover the highest degradation rate appeared at the gapping. A possible reason could be a change in the damage mechanisms which results in accelerated damage propagation.

However, the degree of damage at which the specimens fail seems arbitrary. Therefore passive thermography investigations are added to improve the characterisation of the damage development. Figures 9 - 11 show the differential temperature developments for a defect-free specimen, one with pleat and one with delamination, respectively.

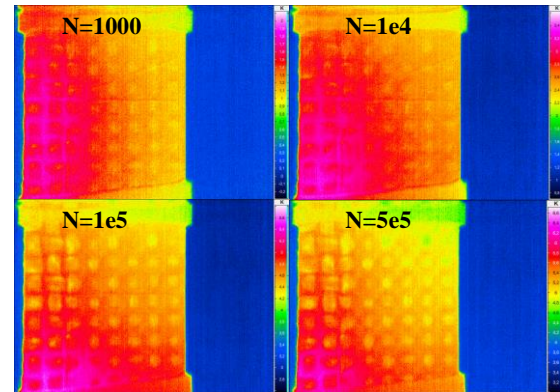


Fig. 9 Differential temperature image of defect-free sample during fatigue, corresponding to Fig. 8 at $N=10^3, 10^4, 10^5, 5 \cdot 10^5$

In case of the defect-free sample, the temperature increases delocalised until approximately $1 \cdot 10^4$ cycles, which coincides with the regime of linear degradation in Fig. 8. For times greater than 10^4 cycles the evolution of a hot spot at the lower left corner is obvious. This can be assigned to the accelerated decrease of mechanical properties, which is in good agreement to Harris [13]. He proposed that matrix micro-cracking is the dominant damage mechanism in the initial stage until a characteristic damage state is attained. Interlaminar damage propagation follows, by means of delamination, until final failure occurs.

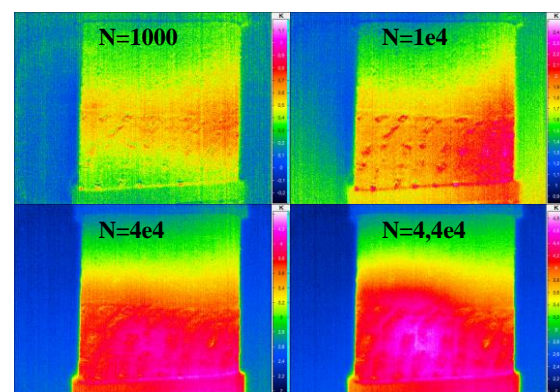


Fig. 10 Differential temperature image of delaminated samples, corresponding to Fig. 8 at $N=10^3, 10^4, 4 \cdot 10^4, 4.4 \cdot 10^4$

It can be seen in Fig. 10 that the pleat causes primary temperature increase surrounding the pleat at low cycles. Therefore significant deformation can be assumed in the disturbed region, which results

in the formation of a hot spot at medium cycles ($<10^4$). Subsequently the evolution of a dominant hot spot, ending in final failure, is observed, which fits well to the predominant rapid stiffness degradation in Fig. 8, starting at approximately 2000 cycles.

In case of the delaminated specimen (Fig. 11) a hot spot has already developed at 1000 cycles and coincides with the region, where the delamination was identified by active thermography (Fig. 1). This indicates that interlaminar damage propagation was directly activated due to the presence of the delamination. If matrix micro-cracking and intralaminar damages propagate, they have minor significance in case of the delaminated sample.

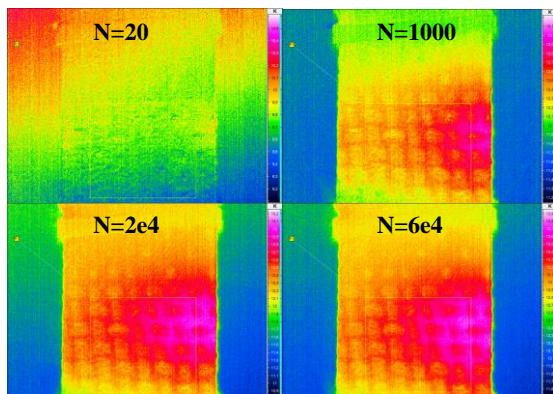


Fig. 11 Differential temperature image of delaminated sample, corresponding to Fig. 8 at $N=20, 10^3, 2 \cdot 10^4$ and $6 \cdot 10^4$

8 CONCLUSIONS

Active thermography is presented as a highly sophisticated method characterising the size and location of defects in the range of approximately 500 μm . It enabled the characterisation of damage development, introduced by mechanical loading.

Passive thermography damage monitoring during quasi-static tensile tests allowed assessing the severity of different defects.

Negligible deviations of mechanical behaviour were observed due to the defects missing roving and gapping, 10° misalignment caused slightly stronger deviations. Additional thermographic investigations depicted that the fracture plane didn't coincide with the gapping. Therefore missing roving and gapping can be treated as non-crucial disturbances of the CFRP-laminate under quasi-static tensile tests. Samples with 10° misalignment represent the borderline, since they showed no significant, but visible, effect. Massive attenuations of the tensile mechanical properties could be observed for samples containing pleat or delamination. Thermographic images of the tensile fracture confirmed the severity of both defects, as the fracture locus could be related to the region affected by the defects.

Experimental results on the degradation behaviour under fatigue condition were shown as well. Defect-free samples showed significant scattering. In the presence of gapping the samples survived as long as defect-free samples. Though, higher degradation rate was observed, which can be attributed to a slight promotion of degradation due to gapping.

Contrary was found for samples with 10° misalignment, pleat or delamination. They are seriously weakening the laminate, which resulted in crucial attenuation of the fatigue resistance and consequently in much earlier rupture.

Comparative study on the damage developments of defect-free specimens and such with pleat and delamination was supported by passive thermography. It revealed that in the presence of both, pleat and delamination, the formation of a dominant hot spot, which indicates interlaminar damage, was heavily accelerated.

9 ACKNOWLEDGEMENT

The authors kindly thank German Research community for the funding of this project and our colleagues from wbk KIT, LKT Dortmund and Fraunhofer IZFP Saarbruecken.

REFERENCES

- [1] Casas-Rodriguez J.P., Ashcroft I.A., Silberschmidt V.V.: Composites Science and Technology, 68, 2401-2409, 2008
- [2] Cantwell W.J., Morton J.: Journal of Strain Analysis, 27 (1), 29-42, 1992
- [3] Senthil K., et al.: Composite Structures, 106, 139-149, 2013
- [4] Greenhalgh E.S., Hiley M.J.: Fractography of Polymer Composites: Current Status and Future Issues, London Imperial college, 2015
- [5] Roche J.M., et. Al.: Proceedings of the QNDE, 2012, Denver
- [6] Grujicic M., et. Al.: Journal of Materials Processing Technology, 197, 363-373, 2008
- [7] Amancio-Filho S.T., dos Santos J.F., Polymer Engineering and Science, 1461-1476, 2009
- [8] DIN EN ISO 527-4: 1997
- [9] Rösner H., Netzelmann U., Hoffmann J., Karpen W., Krumb V., Meyendorf N.: Thermographic Materials Characterization, 246-285, 2004
- [10] Pitarresi G., Patterson E.A., Journal of Strain Analysis, 38 (5), 405-417, 2003
- [11] Arif M.F., et. Al. : Composites : Part B, 61, 55-65, 2014
- [12] Ladeveze P., Le Dantec E. : Composites Science and Technology, 43, 257-267, 1992
- [13] Harris B. : Fatigue in Composites, Woodhead Publishing Ltd, 2003

USING NONDESTRUCTIVE TESTING METHODS TO CHARACTERISE PRODUCTION-INDUCED DEFECTS IN A METAL-CFRP HYBRID STRUCTURE

Michael Schwarz^{1(*)}, Jannik Summa¹, Hans-Georg Herrmann^{1,2}

¹Chair for Lightweight Systems, University of Saarland, Saarbrücken, Germany

²IZFP Fraunhofer Institute for Nondestructive Testing, Saarbrücken, Germany

ABSTRACT: In this work different nondestructive testing methods, such as active and passive thermography as well as ultrasonic with special probes, so-called EMAT's (ElectroMagnetic Acoustic Transducer) will be applied for the characterisation of a metal-CFRP (Carbon Fibre Reinforced Polymer) hybrid structure. To validate these testing methods, different kinds of artificial defects are inserted into the hybrid structure. It is shown that active thermography is very suitable to detect the artificial inserted defects not only in the hybrid structure but also in the CFRP structure itself. Furthermore the bonding between metal and the polymer is characterised very well. Likewise CFRP samples are investigated by passive thermography while being mechanically loaded through tensile or fatigue tests to give a predication about the influence of the defects on the mechanical properties (effects of defects). Finally an outlook on an optimised geometry of the hybrid structure as well as on further excitation methods for active thermography is given.

KEYWORDS: Nondestructive testing, thermography, EMAT

1 INTRODUCTION

Through the worldwide regulations concerning CO₂ the topic lightweight design is becoming more and more important. To achieve a significant decrease in weight, lighter materials as aluminium, magnesium and CFRP have to be used increasingly. However a complete substitution of existing materials by expensive CFRP cannot be economically used for series production. Thus, an intelligent hybrid structure consisting of an aluminium and a CFRP component turns out to be an alternative solution. To overcome the gap in stiffness between aluminium and CFRP a polymer is inserted. But through this polymer two interfaces are created where defects occur most likely [1].

By using nondestructive testing methods possible process-induced defects should be detected at these interfaces and in the CFRP itself. In order to validate the used testing methods, artificial defects (e.g. delamination, missing rovings, pleat, misorientation of the fibres and gapping) are implemented in the hybrid structure and the CFRP. The used nondestructive testing methods are thermography and ultrasonic. To detect defects at the interface CFRP-polymer and in the CFRP itself thermography is used. For the investigation of the interface aluminium-polymer an ultrasonic testing method with special transducers is used, the so-called EMAT which is characterised by couplant-

free testing. This method has been used only for metals and bondings so far, so the utilisation for hybrid structures gives new interesting areas for an application.

2 THERMOGRAPHY

There are two general methods of measurement in thermography: passive and active thermography. To achieve a thermal contrast active thermography needs an external excitation. Excitation sources can be therefore halogen lamps, ultrasonic, eddy current, laser or flash generators. The excitation method in this case is a flash generator. An infrared camera with Stirling cooler is capturing the thermal radiation after the sample is excited (see Fig. 1). Since defects act like thermal barriers they are depicted as bright areas in the infrared image.

No external excitation is needed for passive thermography. The detected temperature-contrast is generated by internal heating due to deformation and friction processes, for example within destructive testing like tensile or fatigue tests.

Commonly applied methods are MIDA (mechanical induced dissipated heat analysis) or TSA (thermal stress analysis), which enable the identification of weak spots or defects by local temperature hot spots [2].

By choosing thermography as nondestructive testing method there is the possibility to detect defects

* Corresponding author: University of Saarland, Saarbrücken, Germany, Michael.Schwarz@izfp-extern.fraunhofer.de

at the interface of the hybrid at the end of production process. However, it is not only possible to execute the measurements before and after destructive testing (by active thermography), but also to perform insitu tests (by passive thermography). Finally, there is the strong possibility to compare the different thermography methods to achieve the best characterisation of defects.

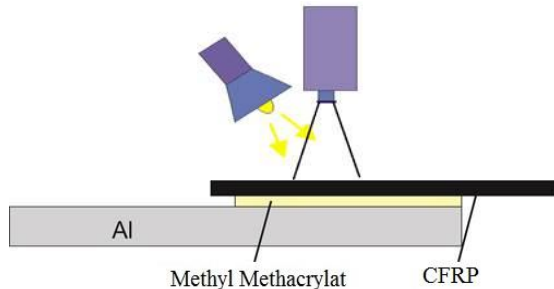


Fig. 1 Measurement configuration of thermography testing

3 EMAT

The ultrasonic testing method with EMAT gives the advantage of couplant-free testing. Therefore more advantages are created like fast and cheap testing. However, the sample either has to be conductive or ferromagnetic. Because of that fact the suitability of CFRP is limited.

The ultrasonic testing with electromagnetic acoustic transducers is excited either by the Lorentz force or by magnetostriction. To achieve the effect of magnetostriction, the analysed material has to be ferromagnetic. While applying an external magnetic field, the ferromagnetic material creates a mechanical deformation, similar to the piezoelectric effect. This deformation occurs parallel to the external magnetic field. Despite the occurring eddy current in the material, dynamic magnetic fields are also induced, which create dynamic forces. These forces are parallel to the external magnetic flux.

To get the effect of the Lorentz force, the used material has to be conductive. In this case special induction coils are used. These induction coils are passed by a current impulse and generate eddy currents in the windings by induction. By overlapping these generated eddy currents with a magnetic field perpendicular to the surface, periodic alternately Lorentz forces will occur. These Lorentz forces induce particle deflection acting as sources of ultrasonic waves in the material [3] (see Fig. 2). By using surface acoustic waves with this kind of ultrasonic testing the interface between the metal and the polymer can be investigated. Especially the quality of the connection between the two components and also defects can be characterised.

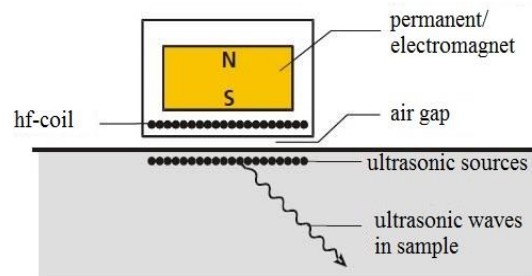


Fig. 2 Principle of an EMAT-probe [Quelle: F. Niese, Dissertation, 2010]

4 MECHANICAL TESTING

Mechanical testing was carried out on $[0^\circ/90^\circ, \pm 45^\circ]_s$ CFRP samples containing 30 vol% of a 3K plain weave (Torayca FT300B) embedded in the epoxy matrix (Biresin CR170/CH150-3).

According to [DIN EN ISO 527-4:1997] sample type 2, the geometrical parameters were chosen to be 120 mm length, 20 mm width and 1 mm thickness. The clamping length was chosen 25 mm on each side.

The specimens were mounted with wedge grips on an Instron 8500 with a 100 kN load cell. An Axial clip-on extensometer was used measuring longitudinal strains.

The tests were carried out displacement controlled. Tensile tests with 2 mm/min cross-head speed and fatigue tests with 5 Hz frequency and a displacement ratio $R = 0.1$. Different maximum relative displacements were chosen ranging from 40 % to 70 % of the fracture displacement of the defect-free reference, which is 1.16247 mm.

Mechanical experiments were complemented with an InfraTec VarioCAM[®] HD head bolometer camera with a resolution of 1024 x 768 pixels. The cameras interval of spectral sensitivity ranges from 7.5 to 14 μm and its temperature resolution lies beneath 0.05 K (at $T = 303.15$ K).

5 RESULTS

In Fig. 3 the front and rear side of a sample with an artificial implemented gapping defect is shown. Both figures are recorded after mechanical testing. In the left picture the front side of the sample is shown and the gapping defect can be seen in the middle of the sample. Around this gapping, there can be detected bright areas, which are an indication for delamination that occurred during the mechanical testing. In the right picture the rear side of the sample is shown. Similar to the picture of the front side you can see many bright areas which are also an indication for delamination.

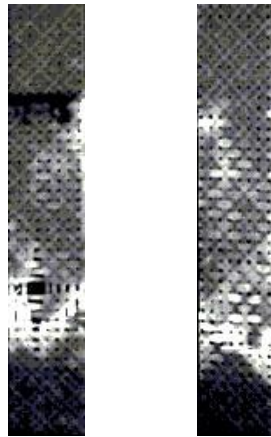


Fig. 3 Front and rear side of a sample with delamination and gapping defect after mechanical testing

In Fig. 4 the front and rear side of a sample with a missing roving defect which has been removed artificially is shown. In the left picture on the right side you can see where the vertically roving has been removed, also you can see some bright areas in the middle of the sample. These bright areas are, like in Fig. 3, a hint for delamination that occurred due to mechanical testing.

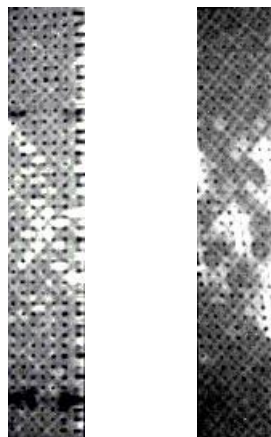


Fig. 4 Front and rear side of a sample with delamination and missing roving defect after mechanical testing

In Fig. 5 two thermographic pictures of aluminium-CFRP bonding are shown. The aluminium and CFRP components are linked through a methyl methacrylate adhesive. In one case there is a perfect bonding between the aluminium and CFRP component and in the other case there is an artificial delamination between the two components. In the left picture there is a specimen with almost perfect bonding and in the right picture there is a specimen with a delamination in the middle of the bonding area. The bright areas at the edge of the picture represent the CFRP component, the dark area in the middle stands for the used adhesive. In the right picture there is also a bright area in the

middle of the adhesive area, which is a sign for the artificial delamination in the bonding.

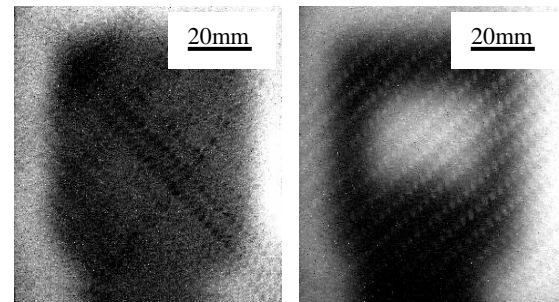


Fig. 5 Bonding of aluminium-CFRP components without and with delamination

In Fig. 6 an aluminium sample with and without bonding has been characterised by ultrasonic testing methods with special probes, the so-called EMAT`s. In the picture the ultrasonic signal is depicted. The signal for the sample without bonding is coloured red and the signal for the sample with bonding is coloured black. The three signals are the same for the two samples. Thereby the leftmost amplitude is the excitation signal and the next two signals are the direct signal transmitter-receiver and the signal with reflection at the "short" end, number 1 and 2, respectively, concerning Fig. 7. The signals 3 for the reflection at the "long" end, 4 for a complete circulation and 5 for a complete circulation plus direct signal transmitter-receiver are only present for the sample without bonding (red). For the sample with bonding (black) the signals 3, 4 and 5 are completely damped.

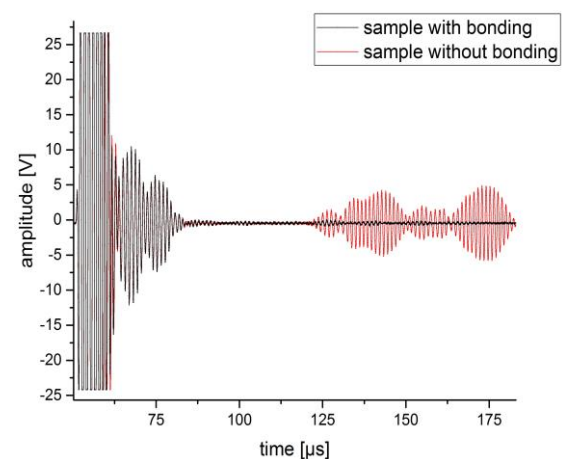


Fig. 6 EMAT-measurement of sample with and without bonding

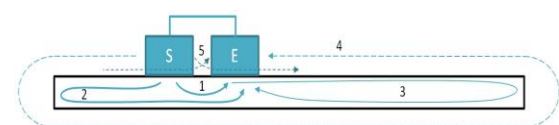


Fig. 7 Signals for EMAT-measurement

In Fig. 8 and Fig. 9 the sample with a gapping defect is shown with passive thermography during a tensile test. Fig. 8 shows the sample at a number of cycles of 10^3 and Fig. 9 at a number of cycles of 10^6 . After 10^3 cycles the temperature is evenly distributed over the whole sample. After 10^6 cycles the temperature is concentrating on the area where the artificial gapping defect is. Concerning to this aspect it can be said that the weakest point of the sample is where the artificial defect is implemented.

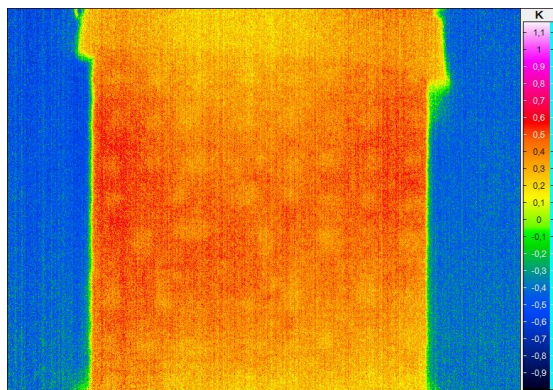


Fig. 8 Passive thermography picture of sample with gapping after 10^3 cycles

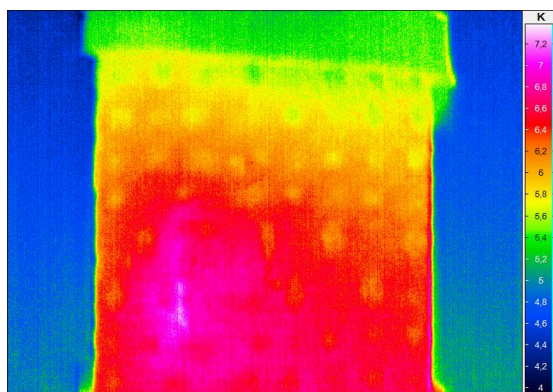


Fig. 9 Passive thermography picture of sample with gapping after 10^6 cycles

6 CONCLUSIONS

As described in this paper the nondestructive testing methods thermography and ultrasonic are suitable to detect and characterise different defects. Thermography has been used to detect different defects like gapping, missing roving and delamination, in the CFRP samples and the bonding samples. With the ultrasonic testing method the difference of the signal between an aluminium sample with and without bonding has been demonstrated. By combining them more information about the condition of the sample can be generated. Especially the bonding can be characterised.

Furthermore the combination of active and passive thermography gives insights into the behaviour of the sample during mechanical testing and the effect on the structure. It has been shown that the weakest point is around the area of defects. Therefore it is very important to detect possibly all flaws in the used hybrid structure.

In further works an optimisation of the aluminium-CFRP sample will be performed. Additionally other excitation methods for active thermography will be validated and compared to the already used ones for a better characterisation.

7 ACKNOWLEDGEMENT

The authors gratefully acknowledge the funding by Deutsche Forschungsgemeinschaft and also thank their colleagues from Fraunhofer IZFP Saarbrücken and their research partners from wbk at Karlsruhe Institute of Technology and LKT at TU Dortmund.

REFERENCES

- [1] Casas-Rodriguez J.P., Ashcroft I.A., Silberschmidt V.V.: *Delamination in adhesively bonded CFRP joints: Standard fatigue, impact-fatigue and intermittent impact*, Composites Science and Technology 68: 2401–2409, 2008
- [2] Rösner H., Netzelmann U., Hoffmann J., Karpen W., Kramb V., Meyendorf N.: *Thermographic Materials Characterization*. In Nondestructive Materials Characterization 67, Springer, Berlin-Heidelberg, pp. 246-285, 2004
- [3] Salzburger H.-J., Niese F., Dobmann G.: *Emat Pipe inspection with guided Waves*, Welding in The World 56: 35-43, 2012

ENERGY DISPERSIVE RESIDUAL STRESS DETERMINATION

B. Breidenstein¹, B. Denkena¹, V. Prasanthan^{1*}

¹Institute for Production Engineering and Machine Tools – IFW
Leibniz Universität Hannover

ABSTRACT: In the manufacturing of massive high performance components demands such as light-weight and increasing functional integration become more important. Through the use of different material, for example high-strength steel or aluminum, hybrid massive components, whose properties are specially adapted to the respective application can be manufactured. One of the challenges is to measure induced residual stress gradients in the joining zone, which directly influence the cohesion of the material compound. The residual stresses are specifically influenced by machining, for example turning, milling or grinding [1]. To investigate the residual stresses before and after machining and analyze the influence of these residual stress gradients on the service life of the composite, a non-destructive method of measuring depth-resolved residual stress is necessary. But the current standard $\sin^2\psi$ -method with angular dispersive residual stress measurement does not allow a non-destructive depth-resolved residual stress measurement. Therefore the $\sin^2\psi$ -method is used with an innovative energy dispersive measurement technique in the collaborative research center 1153 (CRC 1153). Energy dispersive residual stress measurements allow the non-destructive and depth-resolved measurement of residual stresses in the hybrid transition zone with lesser workload and, consequently, lower costs compared to angle dispersive measurement technique. However, this measurement method has not yet been explored in terms of ensuring high quality and reproducible results. Therefore, the accuracy and reproducibility of energy dispersive measurement method is examined by comparing with qualified measuring methodologies such as angle dispersive residual stress measurement methodology.

KEYWORDS: energy dispersive, X-ray diffraction, angle dispersive, residual stress

1 INTRODUCTION

One of the main objectives in aerospace and automotive industry is the reduction of fuel consumption, and therefore the reduction of the total vehicle weight. On the other hand, the aim is to increase quality characteristics and security which often requires the installation of additional components and therefore leads to an increase of the total weight. The requirement regarding a lower fuel consumption is justified ecologically and economically, but cannot be achieved solely by the development of the drive technology.

The lightweight construction can be realized by the use of alternative materials. Light alloys such as aluminum and magnesium are promising materials, but because of their relatively low strength and low melting temperatures they cannot be used for every component. In addition, materials are preferably used in specific areas, which are characterized by a special physical property, such as wear resistance

at cylinder liners or corrosion resistance in aircraft tanks. Both, the thermomechanical stresses and the necessary physical properties of the materials often set a limit to the conventional lightweight construction of sole substitution of materials [2,3].

For this reason, in recent years, increasingly more attention is paid to a load-oriented material use. During the design phase, the component is analyzed with respect to the thermal, mechanical and chemical load, and is divided into different areas. The choice of materials depends on the required physical properties (absorption, thermal conductivity, etc.) and the expected strain during operation. In terms of lightweight construction, materials are selected with the lowest possible density for the remaining areas of the element. This design strategy results in the formation of components in composite construction, also known as combinations of materials, material composites, hybrids or compounds [2-4].

* Corresponding author: Institute for Production Engineering and Machine Tools – IFW, Leibniz Universität Hannover, An der Universität 2, D-30823 Garbsen, Phone: 0511/762-19091, email: prasanthan@ifw.uni-hannover.de

The aim of the CRC 1153 is to realise a new process chain to produce load-adjusted hybrid solid components by using joined semi-finished workpieces. The joining of the materials is carried out by a friction welding process. This results in a transition zone in which the alloying ingredients connect and mix partially.

Due to different expansion coefficients of the materials, residual stresses are caused during cooling, which are influenced by subsequent machining of the component. The currently used angle dispersive method has the disadvantage that an electrolytic material removal is necessary for a depth resolved residual stress measurement. This method is unsuitable for the measurement with high local resolution, necessary in the joining zone, and moreover the removed material distorts the stress equilibrium. Therefore in order to characterize the residual stresses before and after processing as well as to analyze their influence on the operational behavior without any distortions, a non-destructive depth-resolved measurement method is of utmost importance [5, 6]. The new method of energy dispersive residual stress measurements allows for the non-destructive and depth-resolved measurement of residual stresses in the hybrid transition zone [8]. The energy dispersive diffraction method yields reasonable results even under “simple” low-flux laboratory conditions. Thus, mainly for the reason of restricted availability of beamtime at the (very few) synchrotron beamlines being operated in the energy dispersive mode, the laboratory method is a viable alternative for residual stress analysis on polycrystalline materials [12]. But this measurement method has not yet been explored in terms of ensuring high quality and reproducible results, though. Therefore, the precision and reproducibility of this measurement method need to be investigated in comparison with qualified measurement methodologies such as the angle dispersive residual stress measurement methodology.

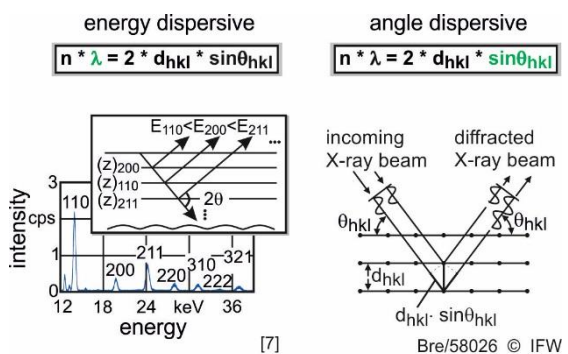
Challenges to be overcome in non-destructive determination of residual stresses are presented below. In the study presented here, the residual stress measurement is first studied in mono materials (steel and aluminum samples) in order to qualify the energy dispersive method. After the investigation of mono materials, the energy dispersive residual stress measurement will be examined in hybrids.

Depth gradients using the angular dispersion and the energy dispersive method are created for ground and milled samples. By comparing the residual stress depth profiles of both methodologies, the measurement parameters of the energy dispersive measurement are adapted and qualified. This advanced energy-measurement method will be used in the future as an instrument to measure reproducible residual stress depth profiles in aluminum and steel, as well as their mixed phases in

order to analyze the influence of residual stresses on the lifespan of hybrid components.

2 MEASUREMENT METHODS

In general, the X-ray determination of residual stresses is based on the physical phenomenon of the X-ray diffraction of a crystal lattice. Based on the Bragg reflection phenomenon (Fig. 1), the lattice spacings can be determined within a crystal lattice, and residual stresses can be calculated [9, 10].



λ : wavelength, d_{hkl} : lattice plane distance, θ_{hkl} : diffraction angle

Fig. 1 Residual stress determination methodologies

In the energy dispersive measurement, the sample is irradiated with polychromatic (white) X-radiation. The diffracted radiation is hereby no longer detected angular but energy dispersive at a fixed angle 2θ , which remains constant throughout the measurement (Fig. 1, left). Thus, all interference lines are determined simultaneously in the direction of measurement in one diffraction spectrum. The detected intensity peaks are a function of wavelength λ or photon energy E_{ph} . Since the various interference lines are distinguished by different energy levels in the spectrum, they can be attributed to different depth information. In angle dispersive-measurements, the wavelength λ is constant and the diffraction angle is varied (Fig. 1, right). To calculate the related lattice spacings from the interference lines of the energy dispersive method, the Bragg equation of the angle dispersive method is used (Fig. 1, right) with the following relation between wavelength λ and photon energy E_{ph} :

$$E_{ph} = h \cdot \frac{c}{\lambda} \quad (Eq. 1)$$

With Planck's constant $h = 4.135 \cdot 10^{-15}$ eVs and the speed of light $c = 299792458$ m / s [10]. Hence the Bragg equation in its energy dispersive form follows as:

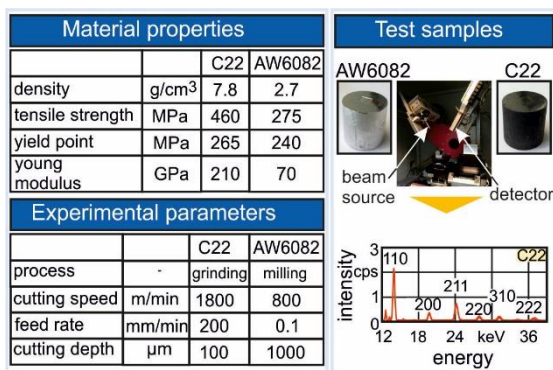
$$d^{hkl} = \frac{h \cdot c}{2 \cdot E_{ph}^{hkl} \cdot \sin \theta} \quad (Eq. 2)$$

From the measured lattice spacings, the strain can be measured according to standard DIN EN 15305 [13]. The tension can be calculated through the determined strain [9]. Furthermore, the energy dispersive and angle dispersive methods differ in the depth resolution of the measurement. The main disadvantage of angle dispersive measurements is the determination of residual stresses only in surface near areas without depth resolution. In order to investigate deeper areas, material must be removed electrolytically. Consequently, the component will be destroyed. By varying degrees of penetration of radiation of different energy photons, which are diffracted at different lattice planes, only energy dispersive methods offer the possibility determining non-destructively depth-resolved residual stresses. The IFW is one of the few research centers which already use this energy dispersive method to determine residual stresses.

3 EXPERIMENTAL SETUP AND INVESTIGATION

The aim of this investigation is to analyze the quality and the reliability of the energy dispersive method. Therefore, residual stress measurements were carried out on machined mono materials by both angle and energy dispersive methods.

The workpieces used in this examination are extruded steel C22 and extruded aluminium AW6082. The design and material properties are displayed in Fig. 2. C22 was machined on a grinding machine. Aluminium is more difficult to machine with a grinding process. Therefore, for this specimen the surface preparation has been carried out on a 4-axis machining center DMG Mori DMU 125P through a milling process. The cutting tool is a face mill with six indexable inserts made of cemented carbide HW-K15. The specimens were machined without cooling.



Pra/81130 ©IFW

Fig. 2 Material characterization and experimental procedure

Based on the classic angular dispersive $\sin^2\psi$ process, the energy dispersive $\sin^2\psi$ method is veri-

fied. On ground and milled samples residual stress depth profiles are created on one hand by the $\sin^2\psi$ -method with electrolytic material removal and on the other hand by the non-destructive energy dispersive method. By comparing the depth profiles of both methods, the energy-measurement is qualified. In this study, a number of machining tests on the aluminum alloy AW6082 and on quenched and tempered steel C22 were performed. Because of the clarity and the similar course or validity of the obtained results, only some selected significant results of C22 and AW6082 are presented (Fig. 2).

The angle dispersive X-ray stress investigations were carried out with Cr $K\alpha$ radiation on a Seifert XRD 3003 ETA diffractometer. The $\sin^2\psi$ -method was applied with a variable Bragg angle. Measurements were carried out with a 2 mm point collimator. Peak position was analyzed by the center of gravity method. X-ray constants were taken from Eigenmann et al. [11].

Energy dispersive X-ray stress investigations were performed with W-anode tube on the same diffractometer as the angle dispersive measurements. The $\sin^2\psi$ method was applied in a tilting angle between -80° and $+80^\circ$ degrees with a step size of 5° . The Bragg angle applied for the energy dispersive measurement is $\theta = 12.5^\circ$. For the residual stress determination, the intensity of the secondary radiation is measured as a function of photon energy. A correct peak identification with respect to the peak position, as well as the correct assignment of the hkl level, are important for an accurate determination of the residual stress. To this end, the measurement data is first smoothed by a Savitzky-Golay filter. Furthermore, a background correction is made in order to reduce noise elements. Then the parabolic fit is performed using the pseudo-Voigt function. The peak positions obtained are not directly given as a photon energy, but in the form of channel numbers that have to be converted into photon energy in the next steps. The following is a complex analysis, in which different variables as the photon energy, lattice plane, strains, residual stresses and depth of penetration of X-radiation are calculated. The determination of the residual stress based on the fact to apply the strain ϵ hkl over the \sin^2 of specimen tilt angle ψ . The pitch of the regression line gives the internal stress σ . The pitch is determined by the method of least squares.

4 RESULTS

From the measurements according to the classical angular dispersive $\sin^2\psi$ process, residual stress depth profiles have been determined as a reference for each material group in two measurement directions. The C22 sample shows compressive residual stresses about $\sigma = -300$ MPa at the surface, which

tends towards zero with increasing depth into the material (Fig. 3).

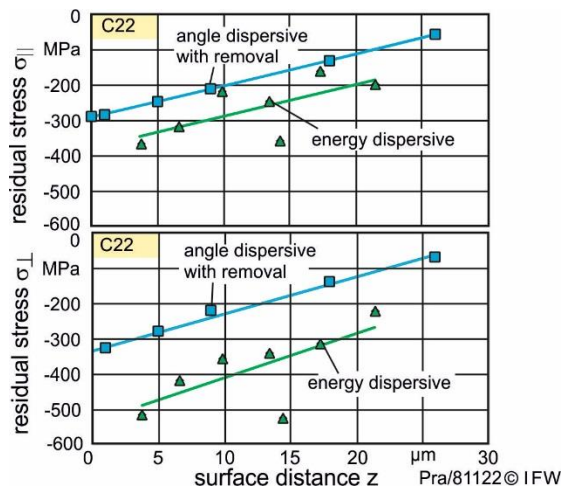


Fig. 3 Comparison of residual stress depth profile of C22 (top: parallel to the feed direction, bottom: perpendicular to the feed direction)

Judging by the qualitative curve shape, residual stresses measured through the energy dispersive method show an acceptable approximation to the angle dispersive measured course, but with a constant offset. The deviation is higher in the vertical direction than in the parallel direction. The number of measurement points corresponds to the number of detected hkl-planes. The angular dispersive curve has lower compressive residual stresses than the energy dispersive course. The reason for this lies in the fact that in the angle dispersive measuring method a depth profile is only possible through electrolytic removal. Consequently, the residual stress state is altered by the destruction of the surface, which establishes the different positions of the two curves. Considering the residual stress depth profile on the AW6082-sample in Fig. 4, a strong scattering of the measurement points could be noted.

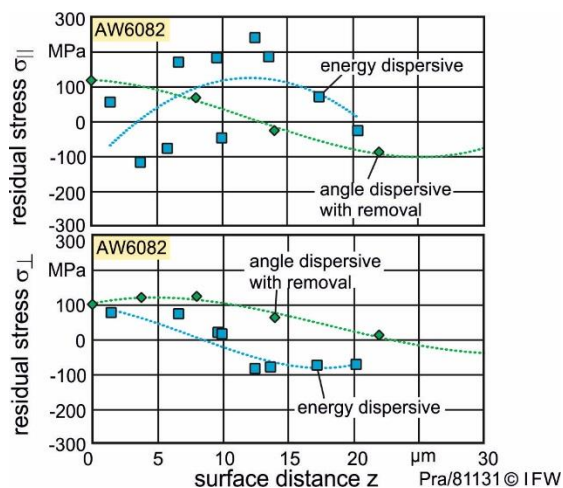


Fig. 4 Comparison of residual stress depth profile of AW6082 (top: parallel to the feed direction, bottom: perpendicular to the feed direction)

Both, aluminum and steel samples were extruded in the manufacturing process. Therefore, a texturing of the material is suspected. To verify this assumption, texture investigations are performed on two groups of materials.

The pole figures provide information on the texturing of the material. Texturing has an influence on the strain distribution over the \sin^2 of the sample tilt angle ψ . With sufficiently strong texturing a deviation from the strictly linear distribution is to be expected.

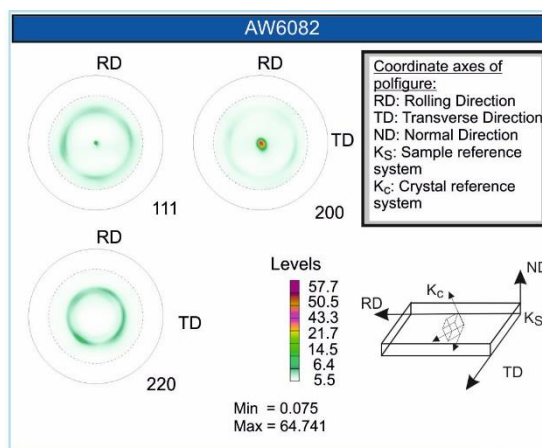


Fig. 5 Pole figures of AW6082

Fig. 5 shows the pole figures of AW6082. Since it has a cubic crystal system, three pole figures for a reliable analysis are sufficient. The circular intensity profile with areas without any intensities and a broadband intensity scale from 5.5 to 57.7 indicates a highly textured sample.

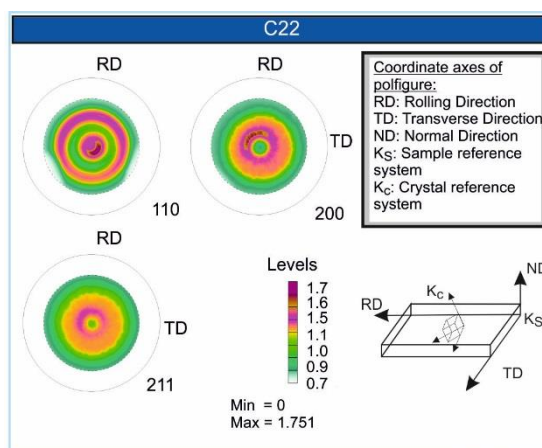


Fig. 6 Pole figures of C22

However, Fig. 6 shows the pole figures of the C22 sample, which also has a cubic crystal system. Furthermore, in this case, a minor fiber texturing

can be observed. But compared to AW6082, it is less critical because no intensity-free regions occur. Due to the strong texturing at AW6082, the determined residual stress depth profiles are therefore not reliable. In contrast, the results of residual stress measurement C22 can be considered to be reliable due to the slight texturing and less dispersion.

5 CONCLUSIONS

In the classical angular dispersive method, an electrolytic erosion of the material is required for the determination of a residual stress gradient and thus, the component is destroyed. By varying degree of penetration of radiation, energy dispersive methods offer the possibility of determining in a non-destructive way depth-resolved residual stresses with a significantly reduced work load.

On two different prepared samples of material (C22, AW6082) energy and angle dispersive measurements are carried out. The results are compared with each other. The results show an acceptable approximation of the energy dispersive method to the classic method in the C22 samples, but with a certain offset. Due to the strong texturing of the AW6082 samples, these results are less reliable. While in the angle dispersive diffraction method the depth resolution is unlimited through destructive material removal, the limits of the energy dispersive diffraction method lies in the non-destructive measurable depth. But through using more peaks with lower intensity the depth resolution can be extended.

In conclusion, the described procedure can produce reliable results for residual stress gradients. To evaluate this method with respect to composite materials, further studies are carried out, as measured at the target in the transition area of the materials, and these findings are then compared with the classical method. Upon successful completion of this project, an innovative non-destructive measurement method becomes available, with which the internal stresses within a hybrid component can be measured non-destructively.

6 ACKNOWLEDGEMENT

The authors would like to thank the Deutsche Forschungsgemeinschaft (DFG) for their support carrying out the investigation as part of the collaborative research center 1153: Function adapted process planning for the machining of hybrid components.

REFERENCES

- [1] Breidenstein, B.: *Oberflächen und Randzonen hoch belasteter Bauteile*, Habilitation, Fakultät für Maschinenbau, Leibniz Universität

Hannover, Institut für Fertigungstechnik (IFW), 2011.

- [2] Dauensteiner A.: *Karosseriewerkstoffe auf dem Weg zum Ein-Liter-Auto. Der Weg zum Ein-Liter-Auto*, Springer Verlag Berlin Heidelberg New York, S.65-112, 2002.
- [3] Neukirchner H., Findeisen B., Kromer B.: *Leichtmetall-Zylinderkurbelgehäuse mit Stützstrukturen*, MTZ Motortechnische Zeitschrift 61(12):862-870, 2000.
- [4] Noaker P.M.: *New waves in manufacturing – Material matters*, Manufacturing Engineering, 116:45-54, 1996.
- [5] Brinksmeier E., Cammet J. T., König, W., Leskovar P., Peters J., Tönshoff H.-K.: *Residual stresses – measurement and causes in machining processes*, CIRP Annals-Manufacturing Technology, Vol. 31: 491-510, 1982.
- [6] Tönshoff H.-K.: *Eigenspannungen und plastische Verformungen im Werkstück d. spanende Bearbeitung*, Dissertation, TH Hannover, 1965.
- [7] Klaus M.: *Röntgendiffraktometrische Ermittlung tiefenabhängiger Eigenspannungsverteilungen in Dünnschichtsystemen mit komplexen Aufbau*, Dissertation, Technische Universität Berlin, 2009.
- [8] Buras B., Staun Olsen J.: *X-ray Energy-Dispersive Diffractometry Using Synchrotron Radiation*, ZJ. Appl. Cryst. 10: 431-438, 1977.
- [9] Macherauch E., Müller P.: *Das $\sin^2\psi$ -Verfahren der röntgenographischen Spannungsmessung*. Z. angew. Physik, 13:305-312, 1961.
- [10] Meschede D.: *Gerthsen Physik*, Springer Heidelberg Dordrecht London New York, 2010.
- [11] Eigenmann B., Macherauch E.: *Röntgenographische Untersuchung von Spannungszuständen in Werkstoffen*, Mat.-wiss. und Werkstofftech. 27, 1996.
- [12] Genzel Ch., Kraemer S., Klaus M., Denks I.A.: *Energy-dispersive diffraction stress analysis under laboratory and synchrotron conditions: a comparative study*, Journal of Applied Crystallography 44: 1-12, 2011
- [13] DIN EN 15305: *Non-destructive testing – Test method for residual stress analysis by X-ray diffraction*, German version EN 15305:2008/ AC:2009

TESTING ULTRASONIC SH WAVES TO ESTIMATE THE QUALITY OF ADHESIVE BONDS IN SMALL HYBRID STRUCTURES

Steven Quirin^{1,2*}, Selina Neuhaus², Hans-Georg Herrmann^{1,2}

¹ Chair for Lightweight Systems, Saarland University, Saarbrücken, Germany
² Fraunhofer Institute for Nondestructive Testing IZFP, Saarbrücken, Germany

ABSTRACT: Shear Horizontal Guided Waves (SH-waves), a special type of ultrasonic waves, were used to investigate the applicability for an assembly of aluminium sheet or tube with a polymer structure. For any kind of joining technology, the polymer-metal phase boundary can be considered as a weak point and prone to failure. In order to get information about the structural integrity of the joining, Nondestructive Testing (NDT)-methods are essential. Concerning adhesive joints, some important aspects are not yet accessible by any ready-to-use method: the strength of adhesive bonding, as well as defects like weak boundary layer and “kissing bonds”. Surface waves excited in one of the bonded parts exactly interact with this desired region. SH-waves proved beneficial waveform but because of insufficient testing equipment, it has not been possible up to now to examine small structures and samples, e.g. lap joints complying with EN 1465. With state-of-the-art technology, Electromagnetic Acoustic Transducers (EMAT) have been developed to excite the highly pure and short-pulsed waves needed. The study evaluates relevant factors beside a variation in adhesion that can affect the ultrasonic signal in polymer-metal hybrid components in general and lap joints for future tests in particular.

KEYWORDS: Non-destructive testing, ultrasonic wave, adhesive bond, metal-polymer hybrid

1 INTRODUCTION

Lightweight design and functional integration is becoming more and more important for new and advanced products in different industrial areas. Hybrid components play an important role combining different materials and their particular properties to a high-performance system. The study focuses on an assembly of aluminum sheet or tube and a polymer structure. The connection can be established by (a) gluing or (b) direct joining by welding [1, 2] or by injection overmolding processes resulting in direct-adhesion of the polymer and metal phase optionally supported by a primer [3]. Injection overmolding can be considered highly suitable for automotive industry series-production due to low cycle time for complex shaped parts [3, 4]. In order to get information about the integrity of the joining in the real structure, Nondestructive Testing (NDT)-methods are essential. But beyond laboratory setups, only few can fit industrial requirements for in-process measurements. Additionally, there is so far no NDT technique available to ensure the strength of the adhesive bond in multi-material systems [5], allowing only an incomplete assessment of joint quality

[6]. In the study presented, a special form of ultrasonic waves has been used to point out its advantages and applicability for laboratory and industrial tasks.

2 NON-DESTRUCTIVE TESTING OF ADHESIVE BONDING

For any kind of joining technology, the polymer-metal phase boundary can be considered as a weak point and prone to failure. Two types of defects can occur: (1) localized defects, e.g. lack of adhesive, void, disbond, kissing bond (zero-volume disbond), etc. and (2) deviation of mechanical properties such as poor curing, porosity and weak adhesion. Lack of adhesive can be commonly detected by active thermography, well-established in automotive and aerospace industry [6]. Various testing techniques are adequate to find defects like pores or debonding [5]. They can be detected because of the phase contrast due to the vacuum or gas phase enclosed. Thus they are also visible with electromagnetic wave based methods, e.g. X-rays. By using the Fokker Bond Tester, disbonds and voids as well as the cohesive properties and strengths can be tested by the analysis of through-thickness vi-

* Corresponding author: Campus E3.1, 66123 Saarbrücken, steven.quirin@izfp-extern.fraunhofer.de

bration changes since decades [7]. But the quality and strength of adhesive bonding, i.e. the connection between two materials by chemical bonds and intermolecular forces, is not yet accessible by any ready-to-use method [5], just as weak boundary layer and kissing bonds, characterized by edge-to-edge surfaces but with interfacial weakness. Contamination of the adherend's surface is a common source for these defects. They must not be underestimated for fatigue prediction. In addition, diffusion of fluids along these zones is thermodynamically facilitated, degrading adhesion further and weakening the polymer by swelling.

The high potential of adhesive bonding technology is reduced by the inevitable demand for accurate processing conditions and need of extensive process control. This is one reason limiting its application especially in small and medium-sized enterprises. A NDT-method for quality assurance is much asked for.

3 ULTRASONIC SH-WAVES

Shear Horizontal Guided Waves (SH-waves) are a special form of ultrasonic waves propagating in plates. They are characterized by an oscillation of the lattice atoms in the plane parallel to the surface and perpendicular to the direction of propagation. The oscillation happens throughout the whole thickness of the plate, if it is in the dimension of or less the ultrasonic wavelength. This vibration propagates along the plate's length and is reflected at sharp edges, i.e. at the end of the plate.

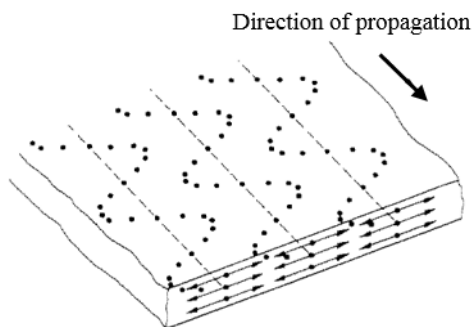


Fig. 1 Horizontally polarized shear waves (SH-waves) guided through a plate (adapted from [8])

3.1 PHYSICAL PROPERTIES AND QUALITIES

3.1.1 For evaluation of interfacial adhesion

SH-waves have several advantages [5, 9, 10] and also proved to be promising for application on adhesive bonded samples consisting of two metallic plates [11-16] as well as polymer/composit parts [14, 17]. Because ultrasound is a mechanical wave propagating by displacement of atoms, it is directly linked to the mechanical bondings. Surface waves

excited in the bonded parts exactly take effect in the desired region at the adhesive-adherend interface and accumulate information while propagating along the bond. Because of their long-range propagation capability (Fig. 2), waves can be excited apart of the joint which can be covered and at inaccessible position. The surface waves at the top and bottom site of a thin sheet are coupled simplifying the excitation throughout the plate and the joint.

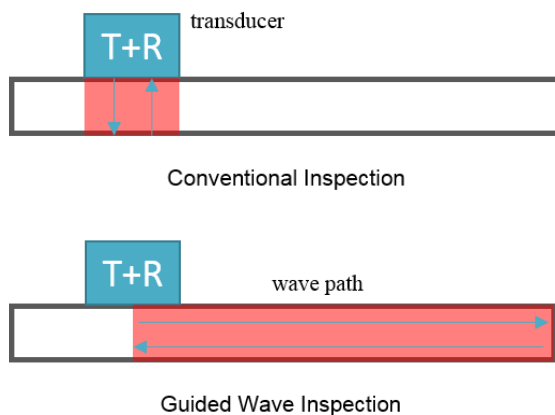


Fig. 2 Comparison between conventional ultrasonic testing technique and Guided Waves

The property that particularly emphasizes shear waves, is that adhesive bonded joints are mainly designed for and submitted to shear loads, so shear resistance of the interface is a critical parameter [16]. It has been shown that kissing bonds, when subjected to compressive stress, remain invisible [18]. So Guided Lamb waves, characterized mainly by out of plane oscillation ("Shear Vertical Guided Waves"), in most cases fail to detect these imperfections [18]. In-plane oscillation parallel to the surface, characteristic for SH-waves, is the wave form of choice not only because kissing bonds can be detected theoretically. They are also non-sensitive to liquids on the surface because only adhering solid matter is able to transmit shear forces. A disbond filled with liquid should be detected as well. How SH-waves can be used for the evaluation of interfacial adhesion is part of actual research [14-16, 19].

The study utilizes that the energy loss of the incident wave is highly concentrated in a small area around the interphase between polymer and metal acting sensitive to mechanical boundary conditions. The hypothesis that different extent of adhesion is measurable with the method can be suggested. It was assumed at early times [11, 13] and then confirmed by simulations based on several models [14-17]. But scientific evidence is not yet satisfied as separation of effects is difficult and not yet complete. Comparison with tensile testing and different non-destructive testing methods should be carried out. In a preliminary study presented in

chapter 4, ultrasonic testing results had been compared with X-ray tomography what could give an appropriate hint but was also affected by other variables. This study focuses on the variables that occurred and that affect the measured signal on the same way as the quality of the bond.

3.1.2 For robust measurement

The coupling and propagation of guided waves throughout the plate allows variable positions for the transducers. The whole width of the join is interrogated without scanning or even moving of the transducers (Fig. 2).

SH-waves have some physical advantages compared to the nature of Lamb-waves oscillating out of plane: One major problem is, that Lamb-waves are dispersive and that more than one mode exists at any given frequency. Mode conversion can occur at boundaries [20].

The SH_0 wave mode is dispersion free, i.e. the propagation velocity is constant and not influenced by frequency or wall thickness deviations. No mode conversion occurs at the end of the plates. So the shape of the wave packet remains unchanged as it propagates along the structure. The higher wave modes are dispersive but they are not propagable under a threshold value of the product of frequency and wall thickness. For this reason, a mode selection is possible with excitation frequency. To do so, the resulting US wavelength has to be more than twice the wall thickness. This results in signals that are clearly linked to one location of reflection and that contain all information about every energy loss on its way.

3.2 EXCITATION AND MEASUREMENT

The ultrasonic wave form of SH-waves has special requirements for testing equipment. Lamb-waves were popular earlier than SH-waves because excitation was easier and they are till today used more often because of existing testing equipment. They have some disadvantages concerning testing of adhesive bonds mentioned above. However, excitation of SH-waves apart of laboratory setting [12, 14, 17] is difficult with piezoelectric transducers. A piezo element hammering onto the surface cannot move the lattice atoms in a plate directly that way that is needed for in-plane oscillation parallel to the surface. That is the reason why practical SH-wave research advances since the development of Electromagnetic Acoustic Transducers (EMAT). They are suitable for generation and detection of ultrasonic shear waves in metallic and/or ferromagnetic materials. Therefore excitation is only possible in the aluminium plate considering the hybrid samples to be examined. Sound is generated directly in the plate by Lorentz Forces using the combination of small permanent magnets and electric coils driven with a high frequency alternating current. The transducers have been designed as a comple-

mentary pair of sender and receiver based on an intensive research and expertise in this area at Fraunhofer Institute for Nondestructive Testing IZFP. We assume insufficient testing equipment available why small structures and samples, e.g. lap joints complying with standards DIN EN 1465 (Determination of tensile lap-shear strength of bonded assemblies) or EN ISO 9664 (Test methods for fatigue properties of structural adhesives in tensile shear), are not examined in actual research. The difficulty with small samples is, that the width of a pulse is high comparing with the amount of time it needs to travel around. The wave propagates in both directions sent off the transmitter along the plate's length. It is then reflected at sharp edges, i.e. at the end of the plate if it has no defects (Fig. 3). Because the acoustic attenuation of the metal is low, the ultrasonic pulses pace around several times. They are reflected again and again at the end of the plate (Fig. 4).

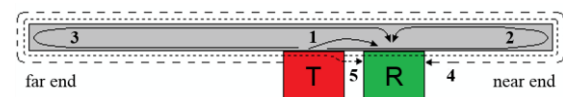


Fig. 3 Schematic illustration of the propagation of ultrasonic pulses resulting in different signals in time domain

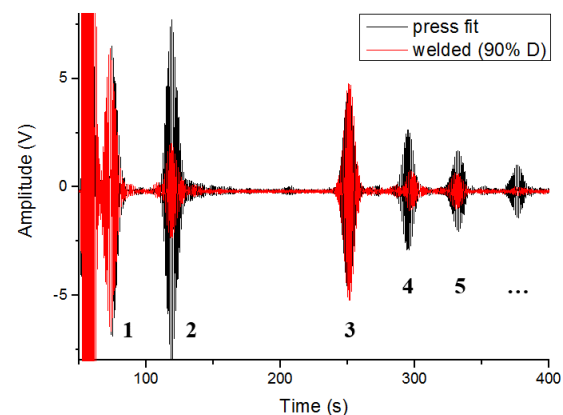


Fig. 4 Oscillograms of two different joints described in chapter 4: a press fit and a welded joint. Signals according to previous figure. The joint is located at the near end. The better joint causes a drastic attenuation of signals passing it.

It is necessary to keep the signals separated to allocate them. Because of the fixed sound velocity, the pulses have to be as small as possible and the distances as large that the first three signals (1) the direct signal from sender to receiver, (2) the one reflected at the near end and (3) the one reflected at the far end of the plate, do not overlap to avoid interference. Then the attenuation of the waves that passed the join can be measured. Narrow ultrasonic pulses need high frequency transmitter driven by

an alternating current of the same frequency. They can only be built with the appropriate knowledge of high frequency technology. Transmitters from 200 to 600 kHz are diffused and commercially available. An early work [13] obviously used transducers, which origin cannot be retraced today, with the upper working frequency of 1 MHz in an experimental setup comparable to the favoured. The plates were both steel plates, so beside the Lorentz Forces the magnetostriction could be used for excitation of guided waves. In the experimental configuration, the amplitude was measured through the adhesive joints with transmitter and receiver placed on different plates. In polymer-metal hybrid components, space is much more limited because only one metal part is available to place both transducers upon. It does not seem to be possible up to now to test lap joints of aluminium plates complying with DIN EN 1465 or EN ISO 9664 or small hybrid components. With state-of-the-art technology, equipment to excite the highly pure and short-pulsed waves needed for the samples dimension has been built (results are shown in Fig. 5). A positive side effect of EMATs has not been mentioned yet: excitation is contact-less and couplant-free, facilitating industrial use.

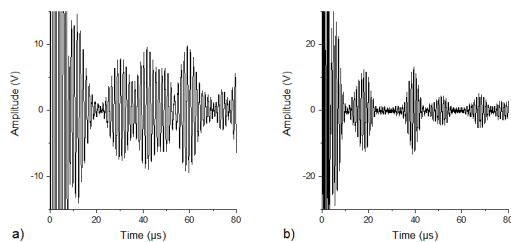


Fig. 5 Comparison between a) 800 kHz Transducer: signals overlapping and interfering on an aluminium structure of 110 mm length, b) 1 MHz Transducer: clearly separated signals even on a structure of 100 mm length

4 PRELIMINARY EXPERIMENTS

A preliminary study has been conducted with aluminium tubes of diameter about 10 mm, wall-thickness about 0.5 mm and length about 400 mm. The aluminium tubes have been joined with a polymeric connector (diameter and length 15 mm) at several ways:

- applying force obtaining a press fit
- solvent welding with acetone
- add an adhesive layer on the tube
- welding (radial force applied to get different shrinkage of the polymer onto the tube)

The polymer part was made by rapid prototyping. Another tube was embedded in a two component reactive polyurethane system prevented from flow-

ing into the tube. The results are summarized here. Fig. 4 shows the oscillogram of two different joints. Only the amplitude of the first three signals will be plotted for further comparison (Fig. 6). You can see that the direct signal transmitter to receiver (1) and the echo from the far end of the tube (3) are similar from top to bottom. The signal (2) from the end where the joint is located, shows a peak size that drastically decreases. The signal to noise ratio even in case of the lower signals is very high. Looking at the very different kind of joints, the order is logically comprehensible and the results correspond to X-ray tomography carried out for 6 of the samples. The signals are certainly caused by the different joint qualities of the samples but it could not be reduced to adhesion because dimension of the joint area could not kept constant, e.g. in case of welding, and the nature of the interface shows a huge difference (Fig. 7). The signals were highly influenced by tilt of the transducer on the curved surface of the tube which has been tried to suppress here and by the reflecting end of the tube. The latter is visible especially in signal (3) where the tube has been slightly deformed during joining process. This can affect results at the joint as well, looking at Fig. 7a.

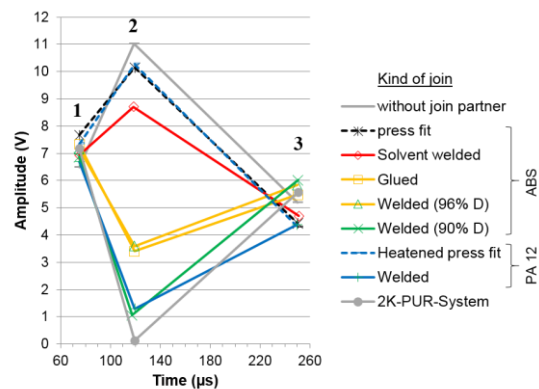


Fig. 6 The first three Guided wave signals measured on samples with different kinds of join

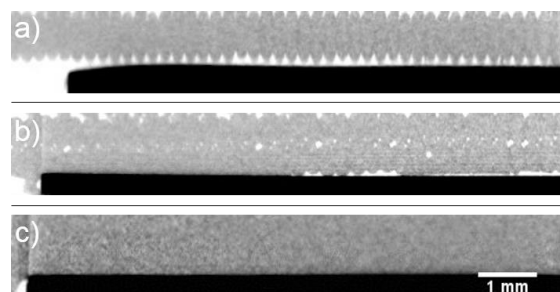


Fig. 7 X-ray tomography of the aluminium-polymer interface of a) press fit, b) solvent welding and c) welding. The polymer part shown was made by Fused Deposition Modelling.

5 EXPERIMENTAL SETUP

The experiments were carried out on aluminum sheets of 25 mm width and 150 mm length produced by waterjet cutting. Plate thickness was 1 mm and 1.5 mm. Commercial two component epoxy casting resin was used for embedding one end of the sheets. Immersion depth ranged from 1.5 to 14.5 mm. The polymer part was also varied in size and weight by changing the filling level keeping the immersion depth equal. The shape of the polymer part was given by the mixing cup and almost cylindrical.



Fig. 8 Aluminum sheet embedded in epoxy resin at one end

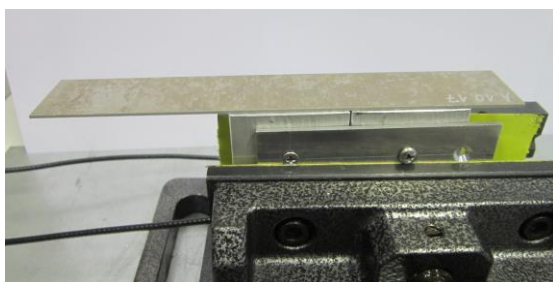


Fig. 9 Measurement setup of a sheet without a join partner, 800 kHz transducers

Size of aluminum sheets was based on international standard DIN EN 1465 and EN ISO 9664. Length has been chosen 150 mm to conduct testing with two different EMAT transducers and compare results. Existing EMAT transducers of 4 mm track wavelength (800 kHz) and newly built up ones of 3 mm track wavelength (1 MHz) were used. Only 1 MHz transducers proved appropriate for the length of 100 mm complying with the standard (Fig. 5). Samples can be placed onto the transducers because of their proportions. Sheets were pressed onto the transmitter and receiver which are designed as a pair with fixed spacing. The distance to the free end of the sheet was kept constant.

6 RESULTS

Results are expressed as amplitude of the signal contemplated divided by the amplitude of the direct signal transmitter to receiver. It is denoted as normalized amplitude and a degree of attenuation on the wave path and damping of the join.

6.1 INFLUENCE OF SAMPLE AND MEASUREMENT

Repeatability of measurements is very good (Fig. 10 et seq.). Three plates have been machined at the face side to evaluate the influence of face surface. Waterjet cutting left the surface rough cut. It was then grinded at three different grades. The measurements did not show a relationship. For 1 MHz transducers all results laid in the standard deviation for repeatability of measurements. For 800 kHz transducers the results were scattered in a window up to three times the standard deviation. An influence of the contact force between sheet and transducers couldn't be found either. Contact force was varied with weights from 0.8 kg to 3.0 kg applied onto the same area. However, holding the samples with fingers, applied pressure has a distinct influence probably because of increasing damping area in contact. This can be eliminated by having a metallic connector between fingers and sample, which is anyway needed to avoid influence of electric capacity of human skin.

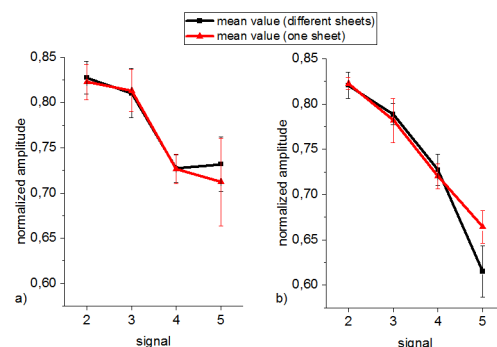


Fig. 10 800 kHz transducers: Mean value and standard deviation for measurements of five different sheets (black) and the same sheet measured five times (red) a) 1 mm sheets b) 1.5 mm sheets

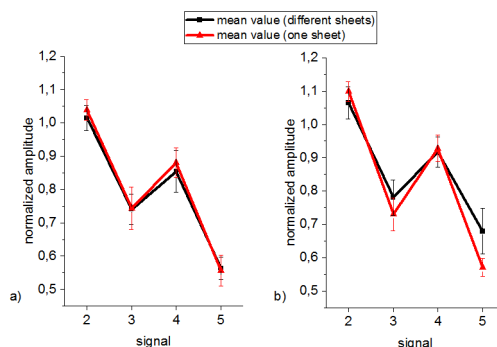


Fig. 11 1 MHz transducers: Mean value and standard deviation for measurements of five different sheets (black) and the same sheet measured five times (red) a) 1 mm sheets b) 1.5 mm sheets

6.2 INFLUENCE OF JOIN DIMENSIONS

Join dimensions were varied in size of the epoxy part and immersion depth of the aluminum sheet. Line (1) indicates the maximum immersion depth that can be realised with an amount of epoxy determined by the size of the mixing cup. Looking at this line, one could already state there is a clear empirical correlation between the size of the joint area and the damping of the ultrasonic signal. But taking into account that the weight of the joint changes in the same way, another explanation is also possible. The study clearly illustrates that the mass of the polymer part adhered has a big influence onto measured signal in this experimental setup. Realising samples with equal weight and different immersion depth leads to an apparently linear relationship between joint area and ultrasonic signal. Error bars resemble the respective standard deviation taken out of Fig. 10 or Fig. 11. The confidence interval of the 800 kHz transducers is much better than the one of the newly built 1 MHz transducers but the results are reproduced nevertheless (Fig. 13, Fig. 15).

1 mm sheets:

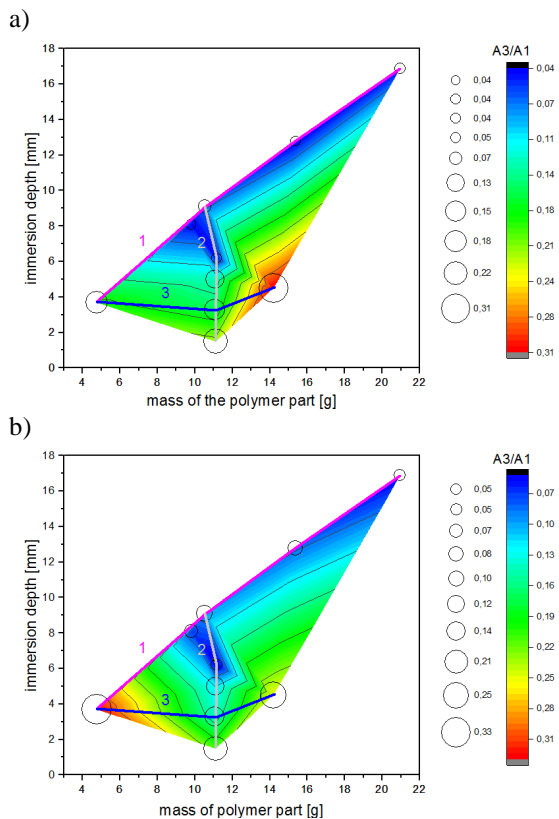


Fig. 12 Signal received from the joint: Normalized amplitudes (A3/A1) of 1 mm sheets measured with a) 800 kHz, b) 1 MHz transducers

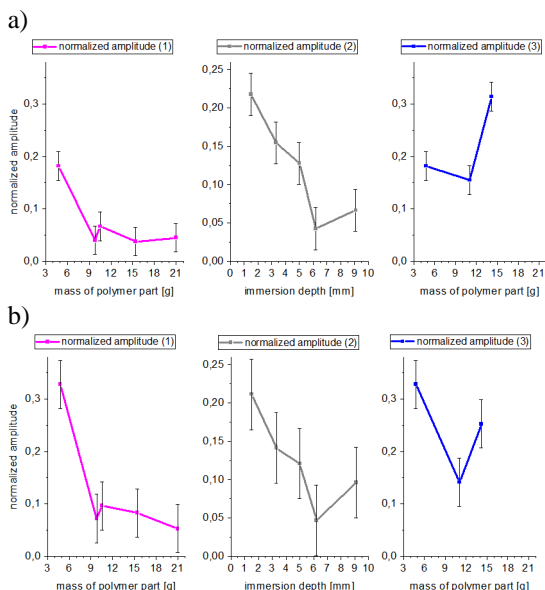


Fig. 13 Illustration of measurements along indicated lines a) 800 kHz, b) 1 MHz transducers.

1.5 mm sheets:

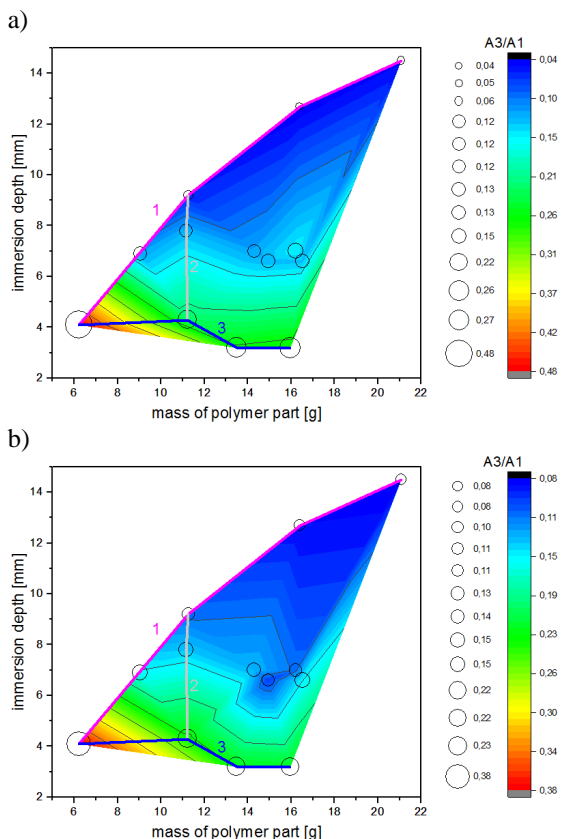


Fig. 14 Signal received from the joint: Normalized amplitudes (A3/A1) of 1.5 mm sheets measured with a) 800 kHz, b) 1 MHz transducers

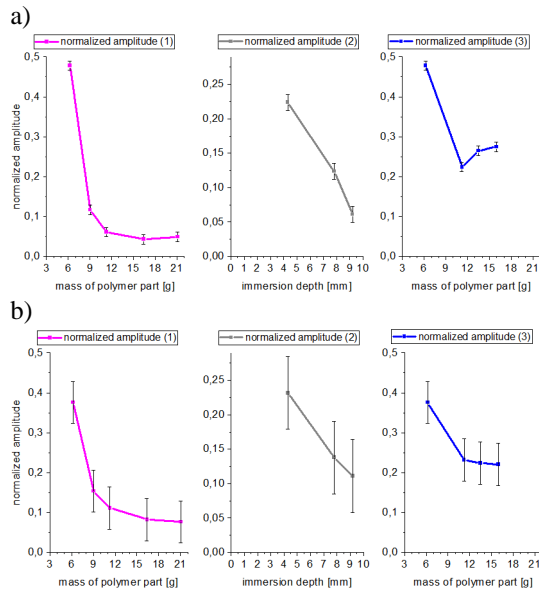


Fig. 15 Illustration of measurements along indicated lines a) 800 kHz, b) 1 MHz transducers

7 CONCLUSION

The study evaluated relevant factors beside a variation in adhesion that can affect the ultrasonic signal detected from adhesive joints. Samples of aluminum sheets immersed in epoxy resin at one end were used. Different relationships between joint area and ultrasonic signal could be found. They all correspond to reports in the literature that the quality of an adhesive bond can be determined by the attenuation of guided wave signal as the ultrasound-based method mechanically interrogates the bond. A comparable measurement of a joint made of one metallic sheet and a polymer has not been published before. Results confirm that the extent of the adhesive-adherend interface can be measured. Realising samples with equal weight and different immersion depth leads to an apparently linear relationship between joint area and ultrasonic signal. A high potential to detect disbonds and lack of adhesive can be concluded. The study illustrates that the mass of the polymer part adhered has also a big influence onto measured signal in this experimental setup, where sample size is comparatively small. An explanation could be given by a) the oscillating mass induced by the vibrations of the metal sheet and affecting ultrasonic attenuation or b) emerging of leaky waves propagating in the polymer. The measurements did not show a relationship between face surface roughness and reflected ultrasonic signal. Nevertheless, an influence of the reflecting edge was distinct in a preliminary study. Conclusion can be given that not the roughness but the shape of the edge is crucial. The influence of surface roughness of the bonding area has not been

investigated yet. Surface treatment and roughness plays an important role considering adhesion of polymer and metal [3]. The results have to be taken into account if a study of lap joints between a metal sheet and a polymer or composite part should be realised.

For the study, a combination of physically pure wave excitation and smallest transducers known was used. SH-waves, the guided waveform used, proved beneficial for adhesive bond inspection and also have several advantages for industrial use: The application is easy and the measurement time is very low compared to other testing procedures. Even at this point of research, an in process IO/NIO classification is worth to be examined.

REFERENCES

- [1] Velthuis R., et al.: *Leichtbau aus Metall und Faser-Kunststoff-Verbunden (light weight design using metals and fiber reinforced plastics)*. Kunststoffe, 11(11), 52-56, 2007.
- [2] Balle F., Wagner G., Eifler D.: *Ultrasonic metal welding of aluminium sheets to carbon fibre reinforced thermoplastic composites*. Advanced Engineering Materials, 11(1-2), 35-39, 2009.
- [3] Grujicic M., et al.: *An overview of the polymer-to-metal direct-adhesion hybrid technologies for load-bearing automotive components*. Journal of Materials Processing Technology, 197(1), 363-373, 2008.
- [4] Lanza G., Herrmann H. G., Stommel M.: *Großserientaugliche Verbindungselemente für den hybriden Leichtbau*. Lightweight Design, 8(2), 48-53, 2015.
- [5] Ehrhart B., Valeske B., Müller C. E., Bockenheimer C.: *Methods for the quality assessment of adhesive bonded CFRP structures-a resume*. In Proceedings of Int. Symposium on NDT in Aerospace, Hamburg, Germany (pp. 22-24), 2010.
- [6] Fery J. H., Herrmann H. G., Valeske B., Boller C.: *Zerstörungsfreie Prüfung und Charakterisierung von Leichtbausystemen*. Lightweight Design, 5(3), 14-19, 2012.
- [7] Guyott C. H., Cawley P., Adams R. D.: *The non-destructive testing of adhesively bonded structure: a review*. The Journal of Adhesion, 20(2), 129-159, 1986.
- [8] Krautkrämer J., Krautkrämer H.: *Werkstoffprüfung mit Ultraschall*. Springer-Verlag Berlin Heidelberg New York, 1986.
- [9] Salzburger H.-J., Hübschen G.: *Fehlerprüfung und Schabungskontrolle von Stumpfschweißnähten an Feinblechen und dünnwandigen Rohren – Erprobte Ultraschalltechniken mittels SH-Plattenwellen und EMUS-Prüfköpfen*. Deutsche Gesellschaft für Zerstö-

- rungsfreie Prüfung e.V. (DGZfP): DGZfP-Jahrestagung 2003.
- [10] Salzburger H.-J., Niese F., Dobmann G.: *EMAT pipe inspection with guided waves*. *Welding in the world*, 56(5-6), 35-43, 2012.
 - [11] Yew C. H.: *Using ultrasonic SH waves to estimate the quality of adhesive bonds: a preliminary study*. *The Journal of the Acoustical Society of America*, 76(2), 525-531, 1984.
 - [12] Yew C. H., Weng X. W.: *Using ultrasonic SH waves to estimate the quality of adhesive bonds in plate structures*. *The Journal of the Acoustical Society of America*, 77(5), 1813-1823, 1985.
 - [13] He F., Rokhlin S. I., Adler L.: *Application of SH and Lamb wave EMAT's for evaluation of adhesive joint in thin plate*. *Review of Progress in Quantitative Nondestructive Evaluation* (pp. 911-918). Springer US, 1988.
 - [14] Pérès P., Barnoncel D., Balasubramaniam K., Castaings M.: *New Experimental Investigations Of Adhesive Bonds With Ultrasonic SH Guided Waves*. 18th International Conference on Composite Materials, 2011.
 - [15] Arun K., et al.: *An EMAT-based shear horizontal (SH) wave technique for adhesive bond inspection*. In *AIP Conference Proceedings-American Institute of Physics* (Vol. 1430, No. 1, p. 1268), 2012.
 - [16] Castaings M.: *SH ultrasonic guided waves for the evaluation of interfacial adhesion*. *Ultrasonics*, 54(7), 1760-1775, 2014.
 - [17] Le Crom B., Castaings M.: *Shear horizontal guided wave modes to infer the shear stiffness of adhesive bond layers*. *The Journal of the Acoustical Society of America*, 127(4), 2220-2230, 2010.
 - [18] Kundu T., Maji A., Ghosh T., Maslov K.: *Detection of kissing bonds by Lamb waves*. *Ultrasonics*, 35(8), 573-580, 1998.
 - [19] Castaings M., et al.: *Ultrasonic characterization of cohesive and adhesive properties of adhesive bonds*. *The Journal of the Acoustical Society of America*, 138(3), 1766-1766, 2015.
 - [20] Cawley P., Alleyne D.: *The use of Lamb waves for the long range inspection of large structures*. *Ultrasonics*, 34(2), 287-290, 1996.

CHAPTER 8:

JOINING

REACTIVE MULTILAYER SYSTEMS: A NEW TECHNOLOGY FOR JOINING THERMOPLASTICMETAL-HYBRID-STRUCTURES

E. Pflug*, R. Pautzsch, G. Dietrich, A. Klotzbach, S. Braun, A. Leson

Fraunhofer Institute for Material and Beam Technology IWS, Dresden, Germany

ABSTRACT: The industrial usage of functional joining techniques for hybrid structures of metals and thermoplastics becomes increasingly important especially when considering lightweight constructions. There are specific challenges that occur when dealing with joining connections of polymers and metals originating from their different chemical and thermal material properties. The main task is to create reliable joints without influencing favorable materials properties of the involved components. In addition to that, a short process time with great reliability in combination with an acceptable long-term stability is required. Existing industrial bonding techniques are reaching their limits in many applications and new technologies are needed. In that context so called Reactive Multilayer Systems (RMS) are a new and innovative way for joining polymers and metals. RMS consists of several few hundreds of single layers of two materials being deposited alternately on top of each other. The film thicknesses of these layers are in the nanometer range. By applying an external activation energy these multilayers are reacting exothermic. The thermal energy during that reaction is released within milliseconds and can be technically used as a heat source for fast thermal direct bonding. The overall amount of heat energy can be precisely controlled by adjusting the layer design of the RMS. With tailored conditions the right amount of thermoplastic material can be melted and bonded to the metallic counterpart without burning it.

KEYWORDS: Reactive Multilayer Systems, Hybrid-Joins, lightweight constructions, polymers, heat source

1 INTRODUCTION

Many branches in industry have set their focus on lightweight constructions during the past years to achieve weight and cost reduction. This is also the reason for a steadily increasing effort to use polymers in different industry branches like the automotive or electric industry [1]. Established bonding techniques like welding, gluing or diverse mechanical methods produce firmly bonded surfaces but reach their limits in some applications: One example are welding processes being applied on polymer materials with integrated highly sensitive electronic components which are used in microelectromechanical systems. The significant heat load during the welding process can negatively influence the functionality of the electric devices. Furthermore it is hard to control the formation of intermetallic phases which influence the mechanical and electrical properties of the component. In addition to that there is potential for reduced process times and costs compared to currently used technologies without compromising quality aspects. Looking at gluing, long-term stability can be a problem which can cause unwanted failures during

application. There is also a huge potential for new technologies which enable to join material combinations which have not been considered yet or which have been rated as being very hard to be used in a joining process. The combination of polymers and metals is just one example where totally different material properties make it really hard to create a mechanical stable joint with conventional techniques. Considering this example it is the goal to create a reliable and long-term stable joint without influencing favorable materials properties of the involved components. Established joining technologies are in many cases pushed to their limits. For this reason the need for new, innovative processes and joining methods is substantial [2].

By developing and practically applying this new joining technology using Reactive Multilayer Systems (RMS) for the combination of polymers and metals two main goals are being pursued: one is to get a fundamental understanding of the physical and chemical processes during joining, the other one is to examine the structural and mechanical changes that occur in the material during that process. Besides the needed research work, it is also

necessary to set standards of this new joining process to allow this innovative technology to be used for industrially relevant products.

2 REACTIVE MULTILAYER SYSTEMS (RMS)

RMS are multilayered thin foils which are made of at least two different metallic materials. By applying a certain amount of energy to the foil, e.g. by an electric spark or laser pulse, its internal multilayer stack reacts exothermally with a self-sustaining reaction. This leads to the release of heat which can be used to melt a solder or the base material itself. The thickness of the single layers is in the nanometer range. The thickness of the whole RMS can be varied between a few micrometers up to few tens of micrometers.

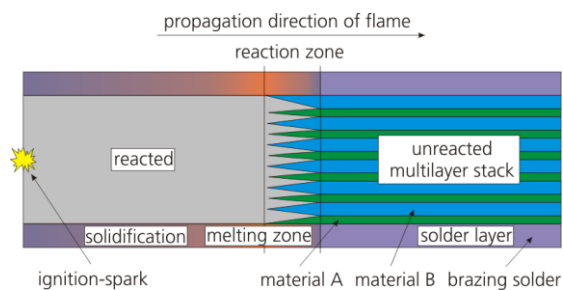


Fig. 1 Schematic picture showing design and functionality of RMS

RMS have the advantage to be tunable to their application. RMS properties like energy content, reaction velocity and maximum temperature can be regulated by the choice of the materials system itself as well as by the design of the multilayer structure. The materials are classified into different groups: low-energy RMS like Ti/Al, medium-energy RMS like Ni/Al and high-energy systems like Zr/Si. See Tab. 1 **Fehler! Verweisquelle konnte nicht gefunden werden.**

Table 1: RMS-properties depending on the chosen material system

RMS-material system	released formation energy [kJ/mol]	adiabatic reaction temperature [°C]
Ti/Al	-36	1227
Ni/Al	-59	1639
Zr/Si	-72	2250

In addition to that the amount of heat released and the reaction velocity can be influenced by the stoichiometric ratio of the single film thicknesses. Because of that it is possible to create a defined heat source which quickly releases its energy without causing thermal induced distortion of the materials or mechanical stress. This enables to join

thermo-sensitive components as well as materials with different coefficients of thermal expansions. Fig. 2 illustrates such a joining process schematically. In detail the RMS is placed between to components while pressure is being applied to the system from both sides. By initiating the exothermal reaction of the RMS foil during that process, the two components are joined together within a few milliseconds. Since an intermetallic phase is formed during the reaction, the joining zone possesses a high thermal and electric conductivity [3].

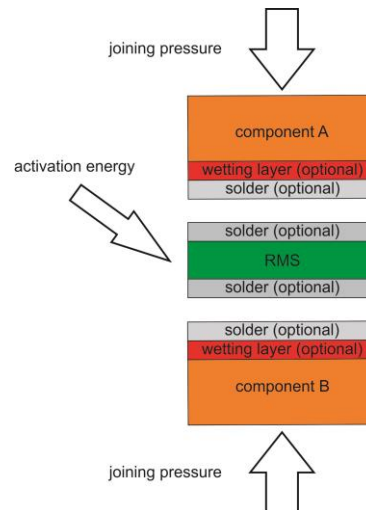


Fig. 2 Principle of the joining technique using RMS

3 POLYMER JOINING CONNECTIONS WITH RMS

3.1 Simulation of heat propagation

As basis for further investigations on the RMS, computer aided simulations were conducted to get information about the heat flow during the ignition of the foil. The aim of this investigation was to get first information on the required design of the multilayer structure of the RMS when using them on polymers and to reach maximum stability of the join without damaging the material. Equivalent parameters which can be changed to regulate the RMS properties like energy content, reaction temperature and velocity, are the stoichiometric ratio, the design of the multilayer and the choice of the used material system. With the help of the simulations this parameters were defined. Furthermore it was possible to gain information about the behavior of the liquid phase of the polymers during the joining process. The simulation deals with the evaluation of a suitable RMS. Through multiple iteration processes a specific Ni/Al-system was designed to be used as RMS for polymer joins. The most promising results led to a Ni/Al-RMS with a total thickness of 40 μm with a stoichiometric ratio (Ni:Al) of 20:80 and 30:70 considering atomic percentage. Using this type of RMS the reaction

temperatures are lower compared to RMS which are used to join steel components. In Fig. 3 and 4 the layout of the simulated system as well as the temperature time relation during joining of PA6 polyamide are shown. Data points were collected as a function of different depths of the material.

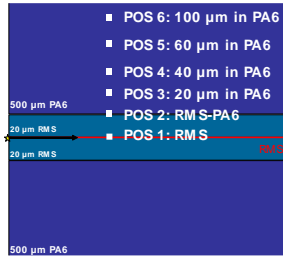


Fig. 3 Layout of the model design for joining PA6 with PA6 by RMS

First of all the results show how fast the RMS joining process really is: it lasts approximately 70 ms until the temperature drops below 100 °C. Another important information is that the thickness of the liquid phase reaches about 40 μm from the surface into the PA6 material. The solidification of this liquefied material forms at the end of the process an interlocking join between the compounds.

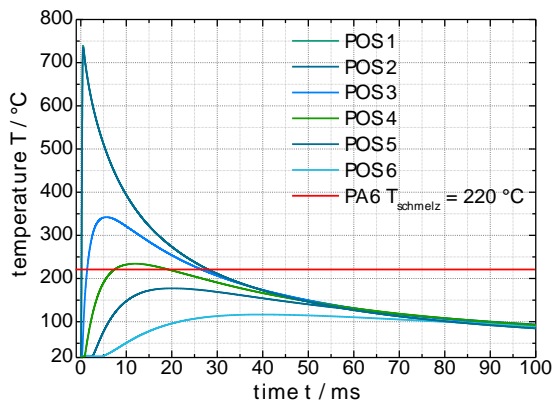


Fig. 4 Temperature–Time relation of PA6–PA6 RMS join

3.2 RMS JOINING OF THERMOPLASTICS WITHOUT FIBER REINFORCEMENT

The simulation results were used to joining processes dealing with thermoplastics that are not fiber reinforced. Research on possible improvements caused by pre- or post-treatments as well as experiments concerning surface activation have been conducted. Evaluation did not show the necessity of any of these treatments to achieve better results. In conclusion mechanical stable thermoplastic joins have been created without damaging or weakening the materials. This leads to the assumption that the heat input into the material itself is limited to a minimum. In combination with an external pressure on the components, the creation of small thin zone of liquefied polymer-phase leads to a practical

method for effectively join thermoplastics. The reaction products of the RMS are embedded into the solidified phase. An example for a thermoplastic join is given in Fig. 5.

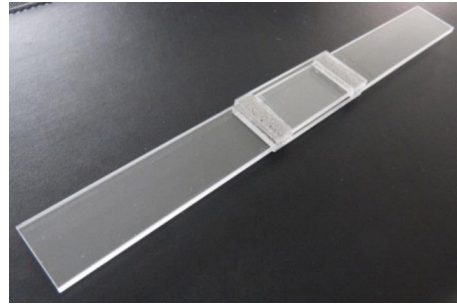


Fig. 5 RMS join of components made of thermoplastics without fiber reinforcement

With supersonic microscopy, a non-destructive analyzing method, the influence of the joining pressure was closer examined. Fig. 6 shows the corresponding samples. There is an optimum pressure at which the area of the bonded contact surface between the two components is maximized (light grey area). Tensile testing on such well-joined samples showed material failure within the material, not in the joining zone. This means that the overall tensile strength of the joined samples is no longer limited by the mechanical stability of the joining zone but by the materials itself. Dark grey colored areas indicate gas inclusions. However, these are only rarely formed at higher joining pressures.

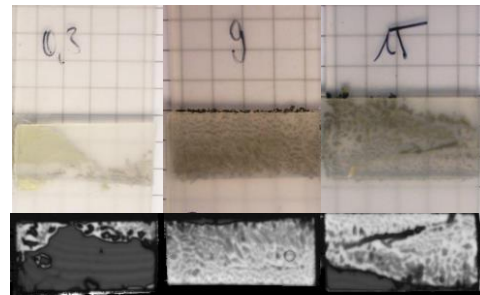


Fig. 6 Supersonic microscopy of thermoplastics joined by RMS technology; left: low joining pressure, right: raised joining pressure (source: Fraunhofer IKTS Dresden)

Materials failures during tensile testing start with necking of the sample outside of the joining zone. If further mechanical loads are applied the sample eventually rips at this local zone of plastic deformation, Fig.8 [4].



Fig. 7 Tested tensile specimen made of thermoplastics joined by RMS technology

3.3 RMS JOINING OF FIBER REINFORCED THERMOPLASTICS

Based on the promising results for RMS joining of thermoplastics without fiber reinforcement, further steps to use this technology for the application with reinforced thermoplastics have been performed. Research included glass- as well as carbon-reinforced thermoplastics. Previous simulation results on the structure of the used RMS were adopted. Experimental implementation showed that the overall results concerning strength of the joining zone are promising when applying slightly more pressure during the joining process and using RMS with higher energy content. This holds for both, glass- and carbon-reinforced thermoplastics. Fig. 8 shows a corresponding sample. Due to the enormous tensile strength of the fibers, materials failure for now occurs within the joining zone. It has been found out that content and density of the fibers play an important role when looking at the bonding properties of the components.

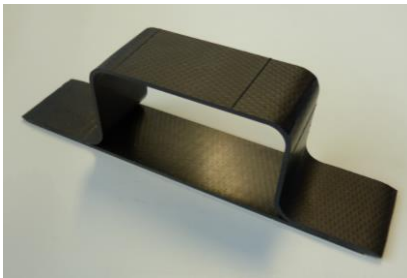


Fig. 8 RMS join of fiber-reinforced thermoplastic

4 THERMOPLASTIC METAL-HYBRIDS JOINED WITH RMS TECHNOLOGY

In the first attempts of joining thermoplastics and metals with RMS the general applicability of the RMS technology for the fabrication of hybrid-connections could be proved, figure 10. It was necessary to carry out an adaptation of the RMS properties, especially the amount of energy released during the process needed to be raised. The low energetic Ni/Al-RMS, which are used for

thermoplastic connections, achieved no satisfactory results because the energy amount was insufficient. Too much heat dissipated within the metal, resulting in a lack of energy for joining the hybrid samples. Therefore, the energy amount of the Ni/Al-RMS had to be increased so that hybrid connections are finally possible. Furthermore a pretreatment or activation of the thermoplastic was omitted. In addition to that different pre-treatment methods of the metal component were studied with the goal to increase the overall strength and stiffness of the joined hybrid samples. Used technologies for realizing this treatments were for example laser structuring, adhesion layers and the combination of both. Laser structuring introduces pits into the metal surface, i.e. increases the surface roughness. This leads to mechanical clamping in the joining area and a better adhesion between the components in general. Mechanical properties like the firmness of the join are tried to be increased by this method. The same aim is pursued with the approach of the adhesive layer, in which case more cohesive connections are created. If both pretreatment methods are combined, there is further potential to increase the strength. However, current results of tensile tests on hybrid connections were not satisfactory, so that further studies are definitely needed. The failure due to mechanical stress occurred predominantly in the joining area and not in the material [5].

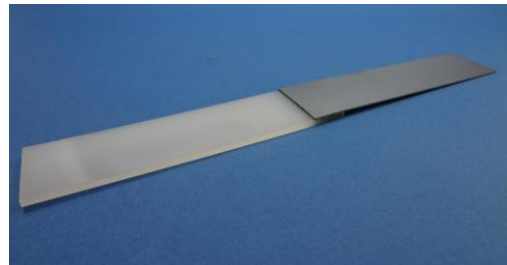


Fig. 9 RMS join of a thermoplastic-metal-hybrid

5 CONCLUSIONS

With the possibility of being able to adapt the properties of RMS according to the used materials and the application, thermoplastic- as well as thermoplastic-metal-hybrid-connections were fabricated and studied successfully. Particularly the energy amount of the RMS has carefully been studied to avoid damage of the thermoplastics and simultaneously fabricate stable connections. Research showed that different RMS are necessary for thermoplastic- and thermoplastic-metal-hybrid-connections, because heat dissipation effects play an important role. In addition to that parameters like the optimal joining pressure were studied and optimized to guarantee satisfying results concerning the joining quality. Looking at thermoplastic joins material failure during tensile tests occurs

within the material, whereas failure at hybrid connections occurs locally in the joining area. To summarize the results it can be concluded that the successful application of RMS technology has been experimentally proven in both cases. This indicates the overall great potential of RMS joining technology for a broad range of applications.

6 ACKNOWLEDGEMENT

This work was partly funded by European Union and the Free State of Saxony within the project ECEMP (100112077) and within the IGF-project 19035 BR/1 of the German Welding Society (DVS).

REFERENCES

- [1] DVS-Berichte Band 294: *Forschungsbedarf zum Fügen von Kunststoffen im Leichtbau und im Bereich der erneuerbaren Energien*, DVS Media GmbH, Düsseldorf, 2012.
- [2] Fachzeitschrift im Fokus: *Fügen von Kunststoffen im DVS*, DVS Media GmbH, Düsseldorf.
- [3] G. Dietrich, M. Rühl, S. Braun, A. Leson, Fraunhofer IWS Dresden: *Hochpräzise Fügungen mittels reaktiven Nanometermultischichten*, *Vakuum in Forschung und Praxis* (Februar 2012) Vol. 24 Nr. 1, 9-15.
- [4] A. Leifert, G. Mondin, S. Dörfler, S. Hampel, S. Kaskel, E. Hofmann, J. Zschetzsche, E. Pflug, G. Dietrich, S. Braun, S. Schädlich: *Fabrication of Nanoparticle-Coating Films and Nano Layers for Alloying and Joining*, *Advanced Engineering Materials*, 2014.
- [5] Diplomarbeit Robert Pautzsch, *Technische Universität Dresden: Fügen von Metall und Thermoplast mittels reaktiver Multischichten*, 2015.

INDUCTIVE JOINING OF GLASS FIBER REINFORCED POLYPROPYLENE AND METAL

Martina Hümbert^{1*}, Peter Mitschang¹

¹Institut für Verbundwerkstoffe GmbH, Kaiserslautern

ABSTRACT: Semi-finished products based on glass fiber reinforced polypropylene are becoming increasingly popular in the automotive and commercial vehicle industry. They combine low material costs with good mechanical and chemical properties. In addition, they can be processed efficiently in series production using extrusions or forming processes. To use these components in vehicles whose structural components still mainly consist of metals, new joining processes aside from riveting and adhesive bonding are necessary, which also meet the needs of fiber reinforced thermoplastics. Thermal joining methods, such as induction joining, use the matrix polymer itself as adhesive. Moreover, they offer the great advantage that a positive connection between the metal surface and the thermoplastic material can be established when the metal is pretreated by means of a laser. This study shows the development of an inductive joining process in combination with laser treatment of the metal surface using the example of the underbody assembly of a bus. Initial findings show that a positive connection can be generated, which shows similar performance for the demonstrator parts similar performance compared to riveting and an increase in single lap shear strength of up to 105% on coupon level compared to a sand blasted reference.

KEYWORDS: Hybrid components, positive connection, laser treatment, induction joining

1 INTRODUCTION

Semi-finished products based on glass fiber reinforced polypropylene are becoming increasingly popular in the automotive and commercial vehicle industry. They combine low material costs with good mechanical and chemical properties. In addition, they can be processed efficiently in series production using extrusions or forming processes. The resulting components are then used in vehicles whose structural components still mainly consist of metals. Thus, a joining problem arises at the interface which is so far often solved by screwed and riveted joints. Still, the required holes destroy the reinforcing structure and preloading of screws leads to creeping of the thermoplastic polymer. Moreover, adhesive joints are difficult to realize due to the low surface energy of polypropylene.

However, about 60% of the automobile manufacturers plan to engage in hybrid material systems, including composites [1]. A weight saving potential of more than 35% is expected by using “the right material in the right place!” [1]. The possible applications are various: components for underbodies, cross beams, longitudinal supports, seat shells, back seat structures, crash elements, and door panels [2, 3].

While hybrid material design offers a high potential, it is accompanied by the challenge of manufacturing, material and weight.

E.g. a single car of the 2010 model of Audi’s A8 has 1847 punch rivets, 632 flow drill screws, 104 clinch points, 66 m welding lines, 202 welding points and 44 m adhesively bonded lines [4].

This massive material input can be reduced by thermal joining methods which use the matrix polymer itself as adhesive. Moreover, they offer the great advantage that a positive connection between the metal surface and the thermoplastic material can be established. For this purpose, the metal is treated, e. g. by a laser, so that a pattern of small, homogeneously distributed undercuts is produced on the surface.

This approach has already shown great potential in joining processes, such as laser joining [5]. In addition, Schulze et. al. [6] found that laser treating leads to the highest initial bonding strength and the highest humidity resistance when joining carbon fiber reinforced polyether ether ketone and titanium.

A very promising thermal joining technology is induction joining because it offers fast and efficient heating. It is based on the ability of an electromagnetic field to transfer energy without physical con-

* Corresponding author: Erwin-Schrödinger-Straße, Geb. 58, 67663 Kaiserslautern, Germany, 0049 631/2017-340, martina.huembert@ivw.uni-kl.de

tact. When an electrical conductor is placed in an alternating electromagnetic field (generated by an induction coil), eddy currents are induced. According to Joules first law, a current flowing through a conductor causes the conductor to heat up. This effect can be used to heat an electrically conductive part, for example made of steel or aluminum, which is placed near an induction coil [7, 8]. A further factor responsible for induction heating is magnetic hysteresis, which is only possible if the conductor is made of a magnetic material (e.g. steel or nickel). The alternating electromagnetic field causes the elementary magnets to oscillate and the resulting friction is transformed to thermal energy [7, 8].

When inductive heating is combined with pressure application, the adjacent polymer is melted by heat conduction. In case of a rough metal surface, the polymer flows into the undercuts [9]. Thus, a form closure between polymer and metal surface is generated (see Fig. 1).

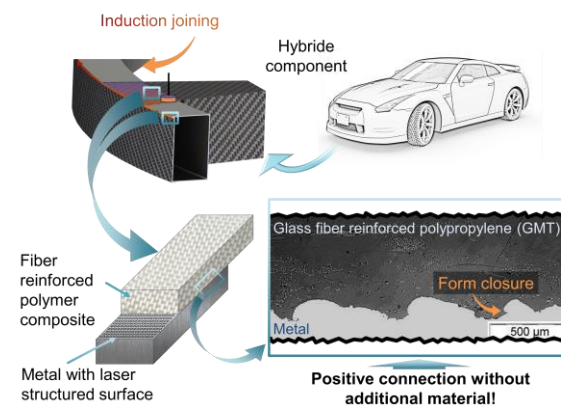


Fig. 1 Generating a positive connection via induction joining

Within this study, the development of an inductive joining process in combination with laser treatment of the metal surface is demonstrated using the example of the underbody assembly of a bus.

2 MATERIALS AND PRETREATMENT

Up to now, steel mounting brackets are riveted to the under body shield in order to connect it to the bodywork. The underbody shield consists of GMT (Glass mat thermoplastics) and SymaLITE (Low weight reinforced thermoplastics), which both have polypropylene (PP) as matrix polymer (see Table 1).

Table 1: Material properties of the underbody shield

Property	GMT[10]	SymaLITE [11]
Initial laminate thickness	4.8 mm	5.9 mm
Area weight	4,992 g/m ²	2,523 g/m ²
Density	1.04 g/ m ³	0.424 g/m ³
Fiber content	23 wt%	30 wt%
Melting temperature	160°C	160°C

In the new approach, the steel brackets are replaced by aluminum brackets. Still, in preliminary trials steel (DC01) was used. Both steel and aluminum were pretreated by means of a laser. Two different surface topologies, a coarse and a fine structure, were generated on each material (for roughness values refer to Fig. 2). The properties of the structure are a result of both material and process properties. Therefore, the same structuring process leads to different topologies when the material is changed. The pretreatment is carried out with an ultra-short pulse laser. It melts the surface of the metal and generates vapor, which ejects the molten metal. As a result, a pattern of melt accumulations along grooves is generated. In this case, “fine” and “coarse” mainly refers to how close these grooves are next to each other. A scan of a coarse and a fine structure on steel and aluminum is shown in Fig. 2.

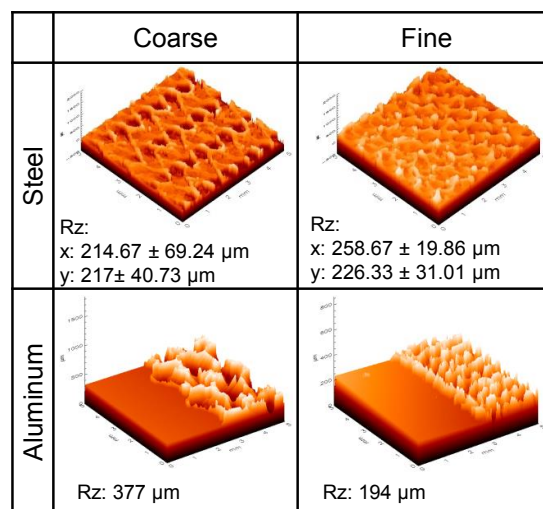


Fig. 2 Surface topology and roughness of laser structured steel and aluminum surfaces

3 PRELIMINARY TRIALS

In preliminary trials, the influence of the laser structure on the single lap shear strength was analyzed. To that, steel plates with a size of 100 mm x 25 mm and a thickness of 2 mm were

either sand blasted or treated with a coarse or fine laser structure. Moreover, the specimens were cleaned in an ultrasonic bath filled with acetone for 15 min before sandblasting (if applicable) and again before joining.

The steel specimens were then joined to GMT specimens of the same dimensions but with a thickness of 4.8 mm in a discontinuous induction joining process. The overlap was adjusted to 12.5 mm according to DIN EN 1465.

The joining process consists of three phases: heating, transfer, and cooling under pressure, as displayed in Fig. 3.

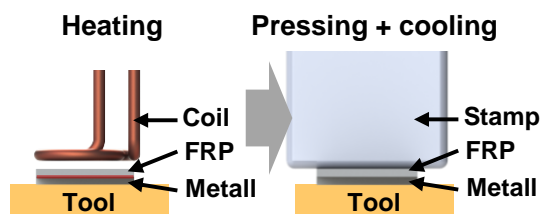


Fig. 3 Schematic depiction of the discontinuous joining process

During the heating phase, the steel specimen, which is placed below the GMT, is heated by the induction coil and the heat is conducted into the GMT specimen. In the cooling and pressing phase, pressure is applied with an aluminum stamp. The molten GMT then flows into the undercuts of the steel surface until the polymer solidifies and a bond is generated.

For the joining process, a self-designed test rig with a Ceia Power Cube inverter was used. The inverter feeds a pancake coil with an alternating current at a frequency around 400 kHz and has a maximum output power of 2.8 kW. The process parameters are listed in Table 2.

Table 2: Process parameters used for the preliminary trials

Generator power [%]	50
Heating time [s]	5
Consolidation force [N]	500
Consolidation time[s]	50
Coupling distance [mm]	6
Overlap (according to DIN EN 1465) [mm]	12.5

The resulting lap shear specimens were then tested in a Zwick tensile testing machine with the following parameters:

- 250 kN load cell and hydraulic clamps
- Free length: 112.5 mm
- Testing speed: 1 mm/s

The results are displayed in Fig. 4.

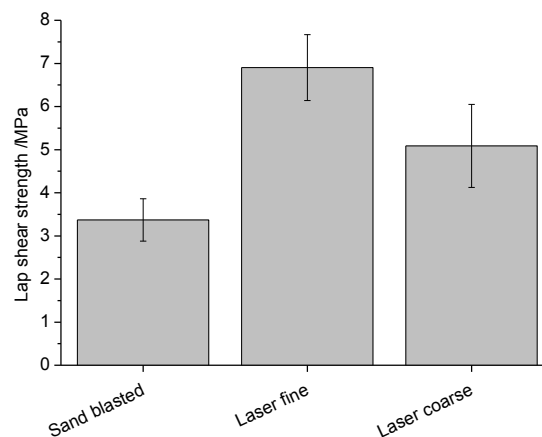


Fig. 4 Interdependency of surface structure and lap shear strength for steel and GMT

It can be observed, that the fine laser structure more than doubles the lap shear strength compared to sand blasting. This is a result of the positive connection between polymer and laser structured steel surface, which can be observed in Fig. 5.

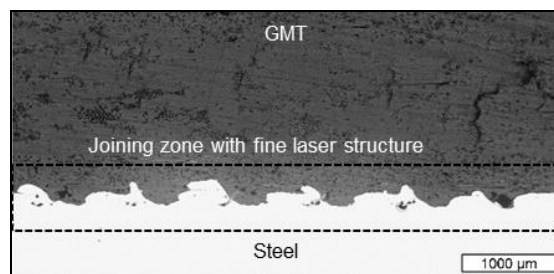


Fig. 5 Micrograph of the joining zone of GMT and steel (fine laser structure)

4 DEMONSTRATOR JOINING

The demonstrators consist of an aluminum bracket and a SymaLITE® section of the underbody shield with a GMT patch in the joining zone. The two components are shown in Fig. 6. The surface of the aluminum bracket was pretreated by means of a laser, again with either a coarse or a fine structure.

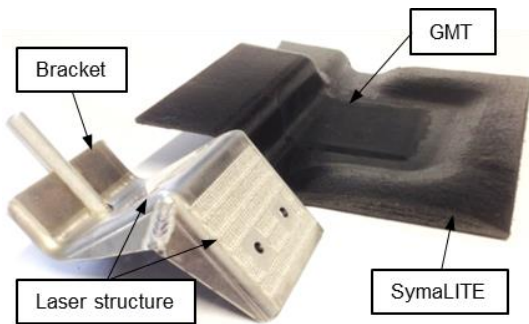


Fig. 6 Components of the demonstrator part

Due to its complexity, the demonstrator must be joined on a different, self-designed, test-rig with a Hüttinger TrueHeat 5010 inverter. It features a frequency range of 50 kHz to 800 kHz, which allows the use of a variety of coil geometries. Moreover, it provides a maximum power output of 11.2 kW and a maximum output current of 280 A. The demonstrator rests on a tool, which is slightly tilted so that pressure is applied to the bottom of the bracket and to its rear side. Therefore, a custom made coil as well as an adjusted stamp are necessary. The current output of the generator is controlled by a pyrometer, which supervises the surface temperature on the aluminum bracket. Moreover, an infrared camera monitors the surface temperature. Fig. 7 shows the joining setup during the pressing phase.

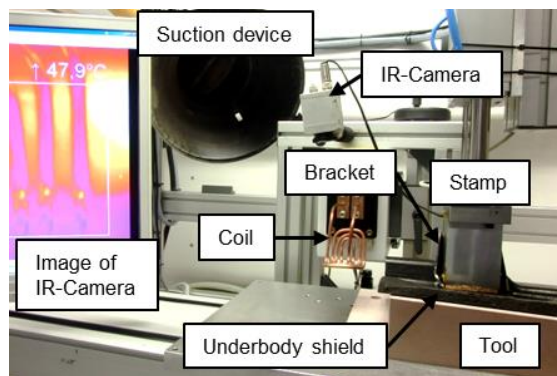


Fig. 7 Test rig for demonstrator joining during the pressing phase

For the first trials, a simple sequence of heating and pressing was used. It was found that 260 °C surface temperature, which leads to approx. 220 °C in the joining zone, is optimum for joining. But it became obvious, that the heat conduction from the bracket to the GMT is insufficient and not enough polymer is melted. That leads to an incomplete filling of the undercuts in the bracket's surface and, as consequence, many voids in the joining zone. Thus, a second heating and pressing sequence with a 20 s plateau at welding temperature was added, as shown in Fig. 8.

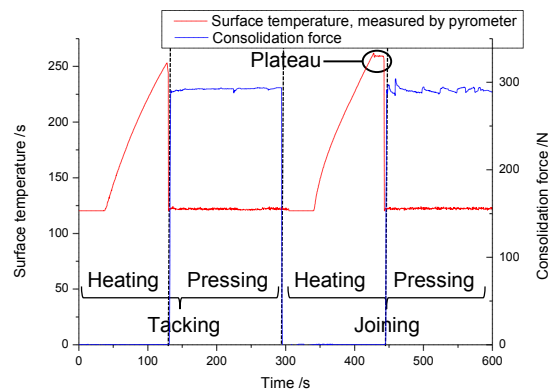


Fig. 8 Surface temperature and consolidation force over process time during the final sequence of heating and pressing phases

The “tacking”-step generates a preliminary wetting in the joining zone, which leads to an increased heat conduction during the heating phase of the “joining”-step. As a result, more polymer is melted and all undercuts in the aluminum surface can be filled (see Fig. 9).

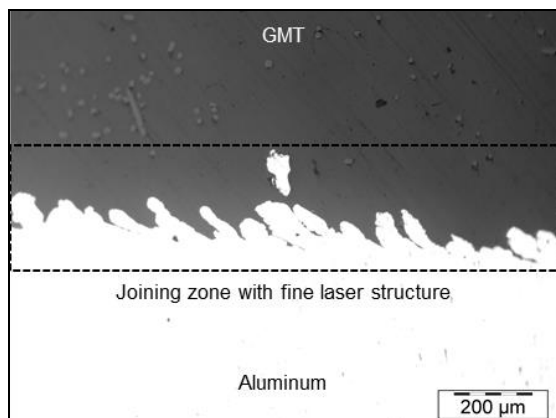


Fig. 9 Micrograph of the joining zone of GMT and the aluminum bracket (fine laser structure)

To slow down the cooling process and to maximize melt-flow, as it can be observed in Fig. 10, a layer of cork was attached to the bottom of the stamp. This cork also leads to a more even pressure distribution in the joining zone.

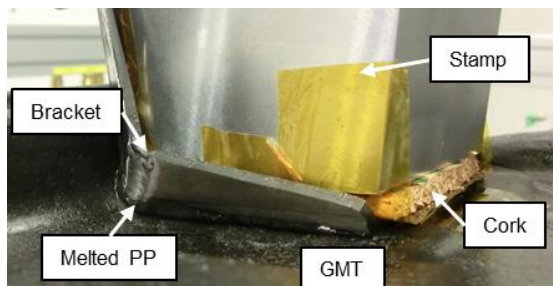


Fig. 10 Flow of melted PP during the second pressing phase

5 TESTING OF THE DEMONSTRATOR PART

The performance of the demonstrator part was tested via a pull-off test in a Zwick tensile testing machine using a custom made clamping unit, which is shown in Fig. 11.

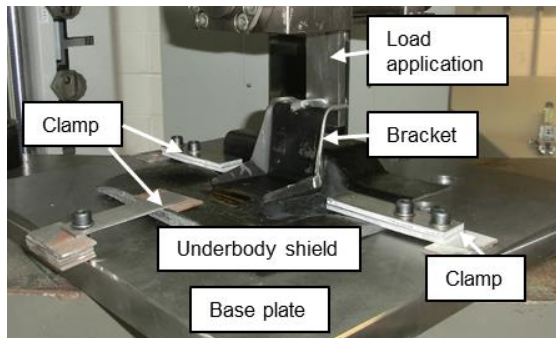


Fig. 11 Setup of the pull-off test

The bracket was pulled up by the load application and the force is recorded by a load cell until failure occurred.

All demonstrators failed outside the joining area in the same way at approximately 2.7 kN, as the one shown in Fig. 12.

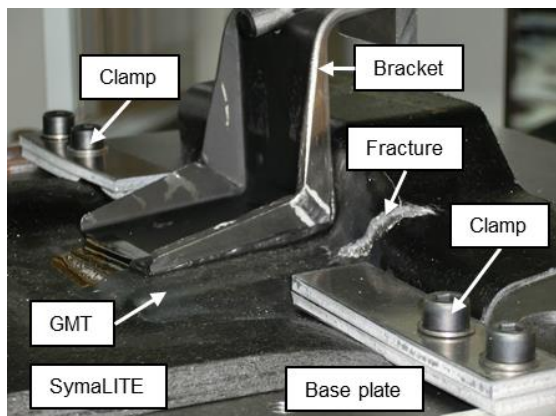


Fig. 12 Failure of an induction joined demonstrator

In addition, riveted demonstrators were manufactured and tested with the same setup. They showed exactly the same behavior as the induction joined parts regarding failure, see Fig. 13, as well as regarding deformation during the test, see Fig. 14.

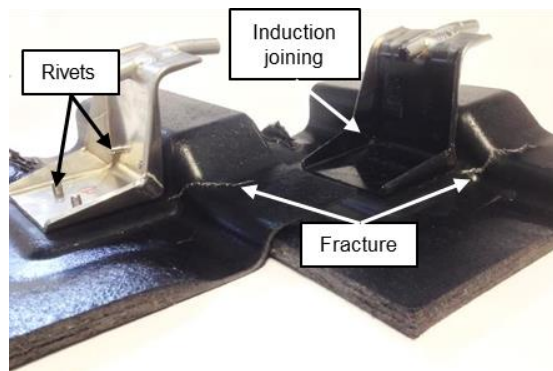


Fig. 13 Comparison of the failure of a riveted (left) and an induction joined (right) demonstrator

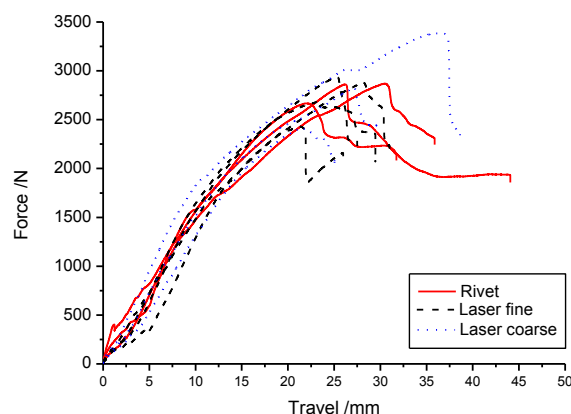


Fig. 14 Comparison of the deformation of riveted and induction joined demonstrators during testing

The results of the pull-off test are summarized in Fig. 15.

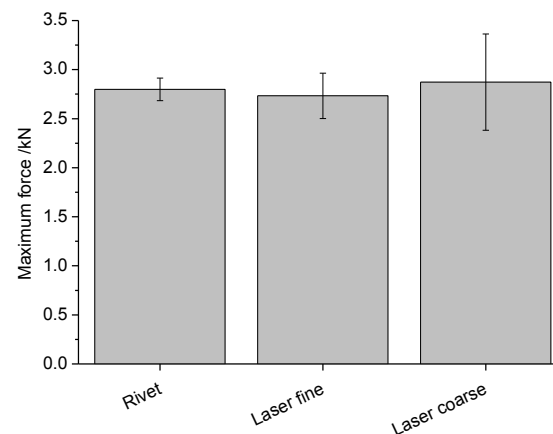


Fig. 15 Interdependency of joining method and the maximum force at which the demonstrator part fails

As mentioned before, it becomes obvious that the induction joined demonstrators show the same performance as the riveted parts, because failure always occurs in the SymaLITE section of the

underbody shield itself. That means that induction joining is suitable to replace the riveting.

6 CONCLUSIONS

This study shows that induction joining is a very promising method for the manufacturing of hybrid components. Especially in combination with a laser structured metal surface, a high joint strength can be achieved due to a positive connection generated between polymer and metal. This approach is even more beneficial, if the polymer itself has a low surface energy (as for example PP) and is therefore difficult to bond by adhesion.

In case of the underbody shield, which is presented in this study, a riveting process for the installation of a mounting bracket was replaced by induction joining. During component testing, all parts failed within the part itself and not in the joining zone. Thus, induction joining is suitable to replace the riveting process and the weight of the rivets and the drilling of holes are made redundant. Moreover a re-design of the joining section reveals the chance to reduce the mass of the bracket element dramatically and make use of the better bonding performance of the induction joining process.

7 ACKNOWLEDGEMENT

We want to thank our partners from the European research projects

- Ybridio (This project has received funding from the European Union's Seventh Framework Programme for research, technological development and demonstration under grant agreement no 309560)
- FlexHyJoin (This project is receiving funding from the European Union's Horizon 2020 research and innovation programme under grant agreement No 677625)

and especially HBW Gubesch GmbH.

REFERENCES

- [1] Singh, H: *Mass Reduction for Light-Duty Vehicles for Model - Years 2017-2025*. (Report No. DOT HS 811 666). Program Reference: DOT, Contract DTNH22-11-C-00193. Contract Prime: Electricore, Inc., 2012.
- [2] www.automotiveit.eu: *Verbundwerkstoffe als Schlüsseltechnologie für den Leichtbau*. URL: <http://www.automotiveit.eu/verbundwerkstoffe-als-schlu%CC%88sseltechnologie-fu%CC%88r-den-leichtbau/siemens-subnet/id-0048071>, recalled at 07.02.2016.
- [3] VDI Zentrum Ressourceneffizienz: *Kohlenstofffaserverstärkte Kunststoffe im Fahrzeugbau – Ressourceneffizienz und Technologien*. March 2013.

- [4] www.volkswagenag.com: *Audi A8 gewinnt „Euro Car Body Award“*. URL: http://www.volkswagenag.com/content/vwcorp/info_center/de/themes/2010/11/Audi_A8_wins_the_Euro_Car_Body_Award.html, recalled at 07.02.2016.
- [5] Roesner, A.; Scheik, S.; Olowinsky, A.; Gillner, A.; Reisgen, U.; Schleser, M.: *Laser Assisted Joining of Plastic Metal Hybrids*. Physics Procedia, 12, Part B: 370–377, 2011.
- [6] Schulze, K.; Hausmann, J.; Wielage, B.: *The Stability of Different Titanium-PEEK Interfaces against Water*. Procedia Materials Science, 2: pp. 92–102, 2013.
- [7] Rudnev, V., Loveless, D., Cook, R. and Black, M. : *Handbook of Induction Heating*, Dekker, New York and Basel, 2003.
- [8] Mitschang, P.; Velthuis, R.; Emrich, S.; Kopnarski, M.: *Induction Heated Joining of Aluminum and Carbon Fiber Reinforced Nylon 66*, Journal of Thermoplastic Composite Materials, 22 (6): pp. 767–801, 2009.
- [9] Didi, M.; Emrich, S.; Mitschang, P.; Kopnarski, M.: *Characterization of Long-Term Durability of Induction Welded Aluminum/Carbon Fiber Reinforced Polymer-Joints*, Advanced Engineering Materials, 15 (9): pp. 821–829, 2013.
- [10] Quadrant AG: *Product data sheet: D100F23-F1*. 2007.
- [11] Quadrant AG: *Product data sheet: SymaLITE ULtra A SL110G55L2558S7 NG*.

SINGLE SIDE RESISTANCE SPOT WELDING OF POLYMER-METAL-HYBRID STRUCTURES

Martin Bielenin^{1*}, Konstantin Szallies¹, Jean Pierre Bergmann¹, Christian Neudel²

¹Technische Universität Ilmenau, Department of Production Technology, Gustav-Kirchhoff-Platz 2, 98693 Ilmenau, Germany

²AUDI AG, 85045 Ingolstadt, Germany

ABSTRACT: This paper shows an alternative approach for thermal joining of thermoplastic-metal hybrid joints by means of a single side resistance spot welding technology. The advantages of single side resistance spot welding are short cycle times, high joint strengths, elimination of additional elements (screw, rivet, adhesive) and thereby avoiding of damages by penetrating to the joining partners. In this work hybrid joints between metals (EN AW-6016-T4 and DX56D+Z100MB) with technical thermoplastic (PA6.6 and PA6 GF47) were examined. Within this work conventional weldability lobes were determined showing high welding current ranges. Additionally, the influence of pretreatment of the metal joining partner by sandblasting and laser structuring on the joint connection were investigated.

KEYWORDS: multi-material design, polymer-metal hybrid joint, thermal direct joining, resistance welding,

1 INTRODUCTION AND STATE OF THE ART

Nowadays lightweight design contains an increasing number of multi material structures in order to adapt specific properties to local requirements. Lightweight structures are applied in automotive engineering, aviation and aerospace engineering as well as in machinery and plant engineering to realize weight reduction. For each component the optimum material can be selected. The combination of plastics and metals has a high potential for lightweight structures. To combine these very different materials in recent years joining technologies has become more and more important for industrial applications.

Conventional joining techniques for plastic metal hybrid structures exhibit disadvantages as they require extensive surface preparation and curing times (adhesive bonding) or include additional elements and manufacturing steps (mechanical fastening by drills and screws).

A new technology is the thermal direct joining enabling an areal joint with high load capacity without using any additional material.

In this process the metal partner is heated up to the temperatures above the melting temperature of the thermoplastic. When a specific joining temperature

is reached, the heated metal is pressed under defined force to the thermoplastic. The thermoplastic matrix penetrates the surface structure. After solidification a joint between the polymer and the metal is formed [1].

Regarding thermal joining, extensive research has been performed on applying a surface treatment by mechanical [1, 2], chemical [3] or physical processes [4] to the metal joining partner to increase the joint strength.

The heat required to transfer the thermoplastic matrix material into a molten state can be achieved by conductive heating [5], electromagnetic radiation [1, 6], induction fields [7] and ultrasonic signals [8] as well as resistance heating by electric current [9].

The conventional resistance welding process offers a number of advantages including little surface preparation, the simplicity and low cost of equipment, simple process control as well as automation and since the electrodes are clamped, small gaps between the sheets can be bridged [10].

Resistance spot welding has been the main process in steel dominated sheet processing industries, especially in automotive body production [10]. Investigations regarding resistance spot welding of polymer metal hybrid with conventional equipment without the need of an additional heating element do not exist.

This paper presents an alternative approach for thermal joining of polymers to metals by resistance spot welding. Compared to conventional resistance spot welding techniques both electrodes are placed on the surface of the metal applying a slight amount of pressure. Due to the current flow and the induced resistance heating of the metal, the polymeric material will be plastified at the metallic interface by heat conduction, as shown in figure 1.

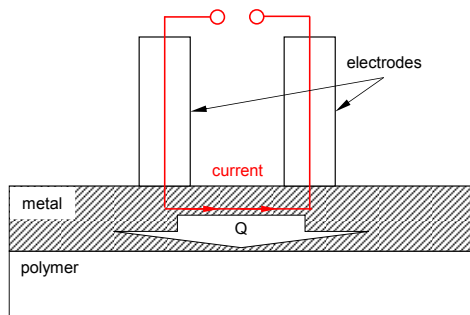


Fig. 1 Principle of single side resistance spot welding of polymer-metal hybrid joints.

2 Experimental Setup

Welding trials were conducted on an alternating current 416 kVA pedestal-type DALEX PMS 11-4 welding machine equipped with a control system MPS 100. The investigations were carried out by electrode caps type F with 5.5 mm face diameter and 50 mm radius. The distance between the electrodes was set by 25 mm as shown in figure 3.

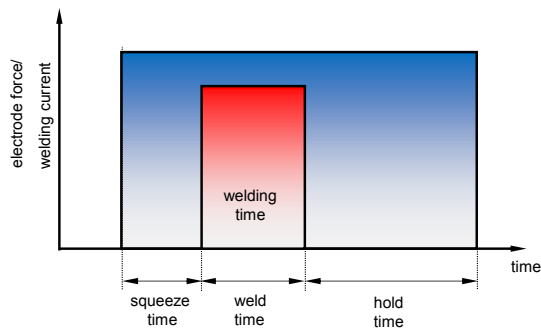


Fig. 2 Weld cycle definitions

Figure 2 schematically represents the welding cycle used in this study. After iterative welding trials the following welding parameters were chosen for spot welding:

- electrode force: 950 N/electrode
- squeeze time: 200 ms
- welding time: 200 ms – 1800 ms
- welding current: 2.5 kA – 16 kA
- hold time: 1000 ms

Both samples were positioned with 20 mm overlap. The sample geometry is shown in figure 3.

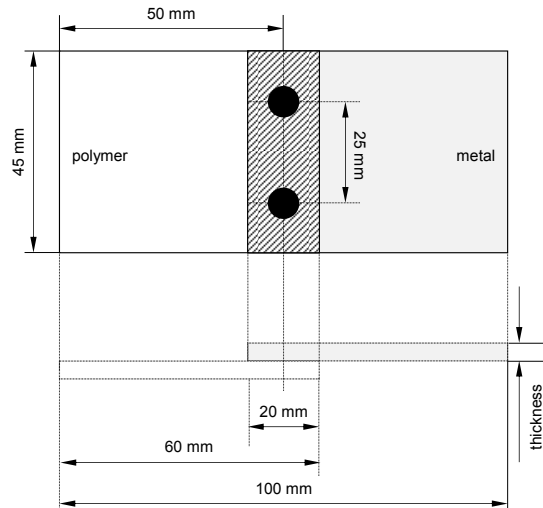


Fig. 3 Dimensions of specimens and electrode arrangement

EN AW-6016-T4 ($t = 1.15$ mm, $t = 1.5$ mm and $t = 2.0$ mm) and hot dip galvanized steel DX56D+Z100MB ($t = 1.0$ mm) were used as metal joining partner. As plastic joining partner glass fibre reinforced polyamide 6 with a fibre volume content 47 %, a fibre orientation of $0^\circ/90^\circ$ ($t = 2.0$ mm) and polyamide 6.6 ($t = 2.0$ mm) were used.

In order to improve the load capacity of the joints within the overlap the metal surfaces were pretreated by laser structuring with a Nd:YAG-Laser (ns-pulsed, $\lambda = 1064$ nm, $P_{\max} = 20$ W, $d_{\text{fok}} 30$ μm) and sandblasting with medium sized glass beads (corundum F 60) as abrasive media with a pressure of 6 bar. Before welding the metal sheets were cleaned with isopropanol to remove residues.

The mechanical properties were examined in a standardized tensile test with testing speed of 10 mm/min. For adequate statistical validation all experiments were repeated 4 times.

3 Results and Discussion

3.1 Joint formation

Figure 3 shows overlap macrographs to visualize the single side resistance spot welding process on DX56D+Z100MB and PA6.6 using high and low welding current.

The size of the molten area depends mainly on welding current and welding time. This indicates that the process conditions influence the joint zone formation. As seen in figure 4a two separated fusion zones left under the electrodes can be identified by using 6.1 kA welding current. With the application of higher welding currents one continuous fusion zone can be observed due to a higher resistance heating process in the metal (figure 4b).

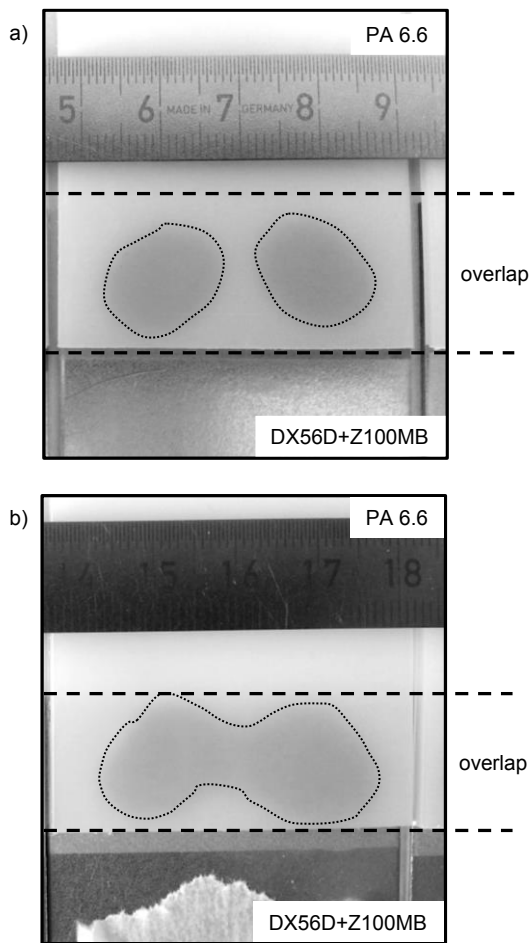


Fig. 4 Joint zone formation by $t=600$ ms at different welding currents, a) 6.1 kA, b) 8.3 kA

3.2 Weldability lobes

In order to show the reliability of resistance spot welding process thermoplastic-metal hybrid joints, the corresponding weldability lobe diagrams were produced. For a specific material combination, electrodes, process conditions and electrode force the weldability lobe shows a region of acceptable

welding parameters. In this study the welding times were varied in steps of 400 ms from 200 ms up to 1800 ms. The electrode force was kept constant at 950 N/electrode, determined in preliminary investigations.

A typical example of a weldability lobe for the material combination DX56D+Z100MB and PA6.6 is shown in figure 5. The vertical axis represents the welding time and the horizontal axis the welding current. The points displayed represent the parameters used for the experiments. The diagram can be divided into 3 sections. The black dots represent the area of good weldability. Samples welded with processing conditions in this region always have good mechanical and optical characteristics. Both borders separate the weldability range from the other sections where acceptable welds cannot be achieved. On the left side of the processing window, the welding current is too low and the energy input is insufficient for a complete weld to be achieved. These parameter combinations produce joints with less than 500 N load capacity in tensile testing. On the right side of the parameter range, high welding currents result in excessive melt ejection of the polymer.

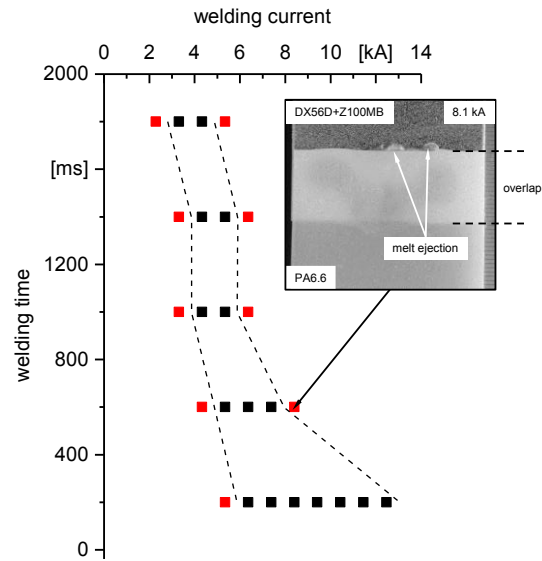


Fig. 5 Weldability lobe for DX56D+Z100MB ($t=1.0$ mm) and PA6 GF47 ($t=2.0$ mm)

As an example for EN AW 6016-T4 weldability lobes for different sheet thicknesses are shown in figure 6. Compared to DX56D+Z100MB, EN-AW 6016-T4 exhibits a significantly higher thermal and electrical conductivity causing higher welding currents generating adequate joints.

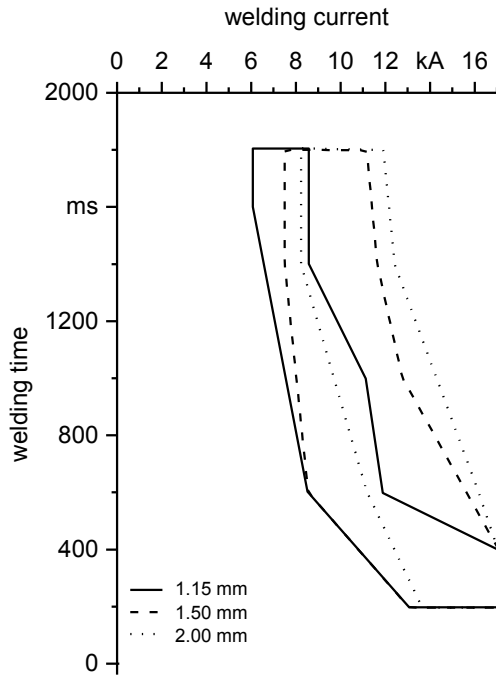


Fig. 6 Weldability lobe for EN AW-6016-T4 ($t=1.0$ mm) and PA6 GF47 ($t=2.0$ mm)

It should be also noted that because of its dependency on many parameters, the weldability lobe is unique for each welding set up and combination of materials.

3.3 Influence of surface pretreatment

In order to achieve a higher load capacity of the joint two different surface structures were examined. Abrasive sandblasting and laser structuring have been applied on EN AW-6016-T4 in order to increase their potential for joining with PA6 GF47. Regarding the laser structuring, an optimized parameter determined in preliminary investigations were used. Table 1 shows the manufacturing parameters for surface pretreatment by laser structuring.

Table 1: Parameters for laser structuring EN AW 6016-T4

	Unit	Value
Laser power	W	20
Scan velocity	$\text{mm}\cdot\text{s}^{-1}$	100
Pulse repetition rate	kHz	25

To evaluate the structures, micrographs are prepared based on cross sections as shown in Figure 7. Surface pretreatment by sandblasting generates a smooth, slightly rippled surface as shown in figure 7a. In contrast exactly defined structures with high depths and aspect ratios can be produced by laser structuring (figure 7b). Furthermore, undercuts and notches can be achieved.

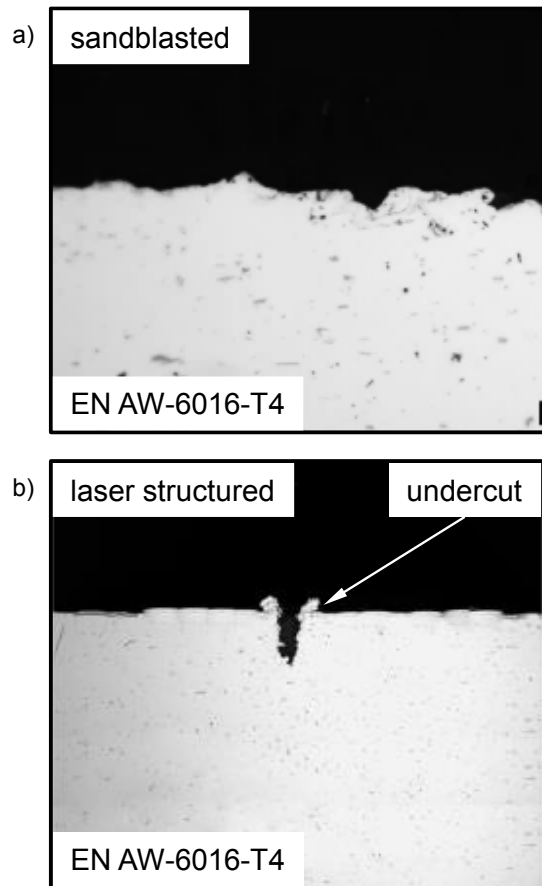


Fig. 7 Cross sections of different surface pretreatments of EN AW-6016-T4 a) sandblasting, b) laser structuring

After pretreating the metal surface, single side resistance spot welds were performed and the mechanical strength was evaluated by lap shear test. The tests were performed with a load velocity of 10 mm/min using a tensile testing machine, the measured load-displacement curves are shown in figure 8.

The sandblasted specimen failed abruptly, achieving a maximum load of 3.0 kN at a displacement of 0.4 mm. The failure surface shows mostly adhesion failure with remains of PA6 matrix as shown in figure 9a.

The laser structured specimen beared up to 6.0 kN an increase about 100 % compared to the sandblasted samples. The higher load capacity during the test and the larger displacement resulted in a higher amount of absorbed energy caused by the mechanical interlocking structures. In this case residues of PA6 matrix and ripped glass fibers can be identify on the failure surface.

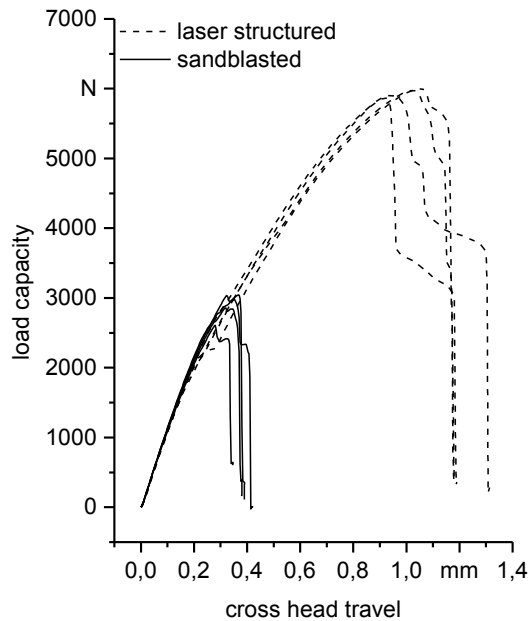


Fig. 8 Measured load-displacement curves of pre-treated EN AW 6016-T4 ($t=1.15$ mm) and PA6 GF47 ($t=2.0$ mm)

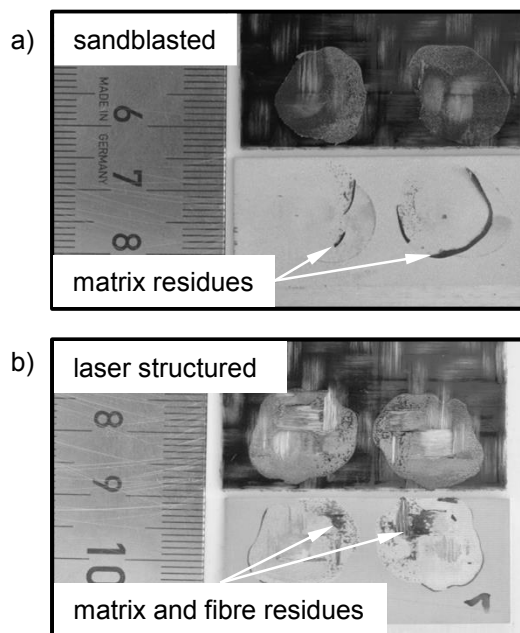


Fig. 9 Fracture behavior of EN AW 6016-T4 and PA6 GF47 joints, $I=9.9$ kA, $t=600$ ms

4 CONCLUSIONS

Single side resistance spot welding of polymer-metal hybrid structures is a joining technique which allows a reproducible joining at low cycle times and low costs compared to conventional methods. For given welding parameter combinations, weldability lobes with high current ranges for polymer-metal hybrid joints were developed.

It could be determined that an optimized surface pretreatment improves the shear strength in tensile testing up to 100 %.

Further investigations will concentrate on construction methods for an optimized accessibility to the joint zone and the joint behavior under application conditions such as dynamic or thermal cycling. Furthermore, disturbance variables such as gap bridging and sheet inclines will be examined.

REFERENCES

- [1] Bergmann, J. P.; Stambke, M.: *Potential of laser-manufactured polymer-metal hybrid joints*, Physics Procedia 39, S. 84-91, 2012
- [2] Schricker, K.; Stambke, M.; Bergmann, J. P.; Bräutigam, K.; Henckell, P.: *Macroscopic Surface Structures for Polymer-Metal Hybrid Joint manufactured by Laser Based Thermal Joining*, Physics Procedia 56, 782-790, 2014
- [3] Ramarathnam, G.; Libertucci, M.; Sadowski, M. M.; North, T. H.: *Joining of Polymers to Metal*, Welding Research Supplement, Dezember, S. 483-490, 1993
- [4] Amend, P.; Pfindel, S.; Schmidt, M.: *Thermal joining of thermoplastic metal hybrids by means of mono- and polychromatic radiation*, Physics Procedia 41, S. 98-105, 2013
- [5] Flock, D.: *Wärmeleitungsfügen hybrider Kunststoff-Metall-Verbindungen*, Rheinisch-Westfälische Technische Hochschule Aachen, Diss., 2011
- [6] Schricker, K.; Stambke, M.; Bergmann, J. P.: *Experimental Investigations and Modelling of the Melting Layer in Polymer-Metal Hybrid Structures*, Welding in the World, 2014, DOI 10.1007/s40194-014-0213-0, 1-6, 2014
- [7] Bobzin, K.; Theiß, S.; Poprawe, R.; Roesner, A.; Haberstroh, E.; Flock, D.; Reisgen, U.; Wagner, N.: *Der Exzellenzcluster "Integrative Produktionstechnik für Hochlohnländer" der RWTH Aachen University - Herstellung hybrider Metall-Kunststoffbauteile durch moderne Fügeverfahren*, Joining Plastics, Jhg. 2008, Nr. 3, S. 210-216, 2008
- [8] Balle, F.; Wagner, G.; Eifler, D.: *Ultrasonic spot welding of aluminum sheet/carbon fiber reinforced polymer-joints*, Materialwissenschaft und Werkstofftechnik, Jhg. 2007, Bd. 38, Nr. 11, S. 934-938, 2007
- [9] Reisgen, U.; Schiebahn, A.; Schönberger, J.: *Innovative Fügeverfahren für hybride Verbunde aus Metall und Kunststoff*, Lightweight Design, Jhg. 2014, Bd. 7, Nr. 3, S. 12-17, 2014
- [10] Neudel, C.: *Mikrostrukturelle und mechanisch-technologische Eigenschaften widerstandspunktgeschweißter Aluminium- Stahl-Verbindungen für den Fahrzeugbau*. Erlangen: Meisenbach GmbH Verlag. Diss., 2013

ANALYSIS OF A MECHANICALLY STRESSED JOINT IN A MULTI-MATERIAL-SYSTEM

Arne Busch^{1*}, Robert Brandt¹

¹ University of Siegen, Siegen, GERMANY

ABSTRACT: In this article a cyclic loaded joint in a simple multi-material-system will be discussed. The multi-material-system consists of a high strength steel, a glass fibre reinforced plastic (GFRP) and a frictional connection, i.e. single and double lap bolted joints, respectively. The tests are either controlled by displacement or load. The displacement controlled test is statically performed whereas the load controlled test is statically and cyclically loaded as well. Our target is to define a failure criterion which can be applied for to set dimensioning of a bolted joint via a frictional connection between steel and GFRP. For the interpretation of the load-displacement-curves a simple model regard to the specific material properties, steel as isotropic and GFRP as anisotropic material, and the frictional connection of the bolted joint. For analysing the friction behaviour in the bolted joint the preload is determined, too. On the basis of materialographical analysis of the static and cyclic loaded specimens the expected results of the model will be verified.

KEYWORDS: multi-material, GFRP, bolted joint, frictional connection, slip

1 INTRODUCTION

There are different ways of connecting construction materials. Generally these connections are distinguished by its ability to transmit loads in frictional, form-fit and adhesive bonded connections.

To realize a frictional connection a preload must be established. A preload can be applied by spring-elements or bolted joints. Bolted joints are well established in engineering. Generally two ways of load transmitting are distinguished. On the one hand the preload of the bolt in combination with the friction between the two structures results in a frictional connection. On the other hand the form-fit connection between bolt and hole leads to bearing stress. The bearing stress usually defines the strength of a connection between FRP and metals by a bolted joint [1]. The impact of a preload is rated in some studies, e.g. CREWS [2] and XIAO [3], but only with respect to the failure mode bearing of holes. A reason for dimensioning such a connection by due by merely considering bearing stress is the rather complex behavior of a frictional connection. One problem is the relaxation of the FRP perpendicular to the fiber direction resulting in a decrease of the preload [4]. Furthermore, it might be difficult to differentiate between static and kinetic friction, respectively. Because of these

intricacies SCHUERMAN [5] describes a heuristic approach for a failure criterion based on the changes of stiffness of a specimen containing a joint.

Here a multi-material-system, consisting of a glass fiber reinforced plastic (GFRP) and shot peened high strength steel, connected by a bolted joint will be analyzed. The specimens are statically and cyclically loaded by means of a tensile shear test. We are targeting at a definition of a failure criterion for a cyclically loaded connection which differentiates between static and kinetic friction in order to avoid the risk of bearing of hole.

2 EXPERIMENTAL SETUP

2.1 SPECIMENS DESIGN AND MATERIALS CHARACTERIZATION

On the one hand a high strength bainitic steel, 51CrV4, which has been shot peened, is used. The tensile strength is about $R_m = 1600$ MPa and the Young's modulus $E = 210$ GPa. The shot peened surface has a roughness of $R_z = 12.53$ μm . On the other hand unidirectional GFRP sheets, manufactured by means of a prepreg process, consist of an epoxy matrix and e-glass fibres. This GFRP is characterized by the tensile strength parallel to the fibre direction $R_{||}^+ = 1300$ MPa, the compressive strength perpendicular to the fibre direction

* Corresponding author: University of Siegen, Am Eichenhang 50, 57076 Siegen, +49 271 740 3641, arne.busch@uni-siegen.de

$R_{\perp} = 140 \text{ MPa}$ [6] and its Young's modulus parallel to the fibre direction $E_{\parallel} = 42 \text{ GPa}$.

A multi-material tensile shear test specimen, denoted as specimen #1, consists of two steel sheets separated by one unidirectional GFRP sheet (s. Fig. 1). The unidirectional GFRP sheets are aligned such that the fibres are oriented parallel to the load axis. For this double lap bolted joint a bolt of size M10 is used. Additionally a set of full steel specimens, denoted as specimen #2, is manufactured as well, where the GFRP sheet is substituted by one steel sheet with similar dimensions.

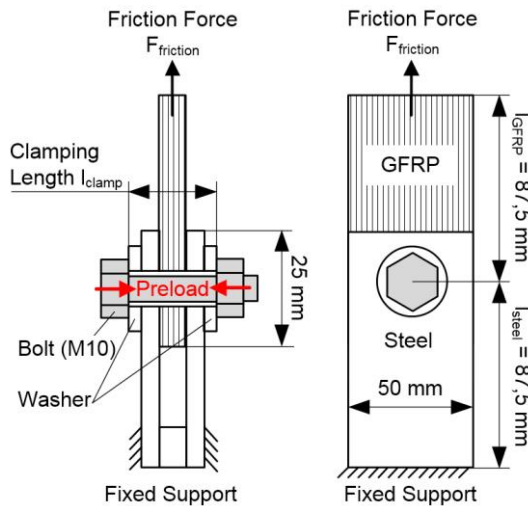


Fig. 1 Double lap specimen with a bolted joint

For transmitting the maximum friction force $F_{friction}$ it is beneficial to make use of the entire compression cone of the bolt. Therefore the diameter of the compression cone is estimated to be $d_{cone} = 21.5 \text{ mm}$, determined by the clamping length, $l_{clamp} = 15 \text{ mm}$ (s. Fig. 1), the outside diameter of the plane head bearing surface of a bolt d_w and the substitutional outside diameter of the basic solid at the interface D_A [7]. Thus the minimum edge distance of the centre of the bolted joint is set to be at least $e_2 = 12.5 \text{ mm}$ (s. Fig. 2). A clearance

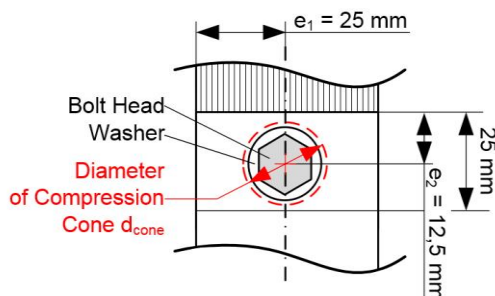


Fig. 2 Detailed view of the bolted joint

of about 1 mm between bolt and the hole edge (s. Fig. 3) is provided, so that a maximum perma-

nent slip of 1 mm between steel and the GFRP sheet may occur and can be measured.

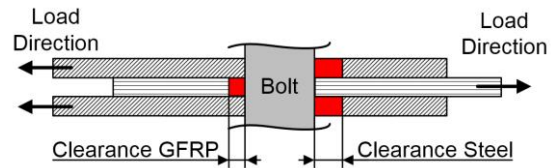


Fig. 3 Clearance of the bolted joint

Controlling the friction force $F_{friction}$ means that a preload F_{pre} has to be established. According to Coulomb's friction law (1) the friction force $F_{friction}$ is given by

$$F_{friction} = \mu \cdot F_{pre} \quad (1)$$

where μ is the coefficient of friction. In order to control F_{pre} , the bolt is prepared by fixing a small strain gauge into an axially drilled hole in the centre of the bolt (s. Fig. 4). This strain gauge is located at the center of the clamping length.

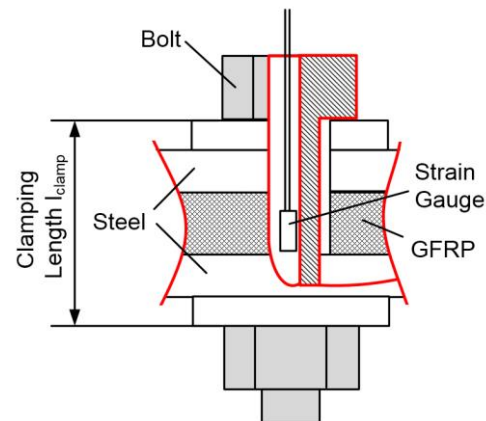


Fig. 4 Strain gauge preparation for evaluating preload

Furthermore it is beneficial to be able to estimate the preload and to control the surface pressure in the circumference of the bolt. Since the anisotropic GFRP has only a small range of tolerable stress perpendicular to the direction of the fibres, the maximum stress applied may not exceed the tolerable value given by the compressive strength perpendicular to the fibre direction $R_{\perp} = 140 \text{ MPa}$ for static loads [6]. Due to this, the preload is set to become $F_{pre} = 10 \text{ kN}$ which corresponds to 50 % of the maximum preload of a M10 bolt with strength grade 8.8 [8], leading to a surface pressure of $p = 46 \text{ MPa}$ [8], so that no damage shall occur.

2.2 TESTING METHOD

For characterizing the behaviour of a fictional connection by a bolted joint, three different tests are performed. The test setup is shown in Fig. 5.

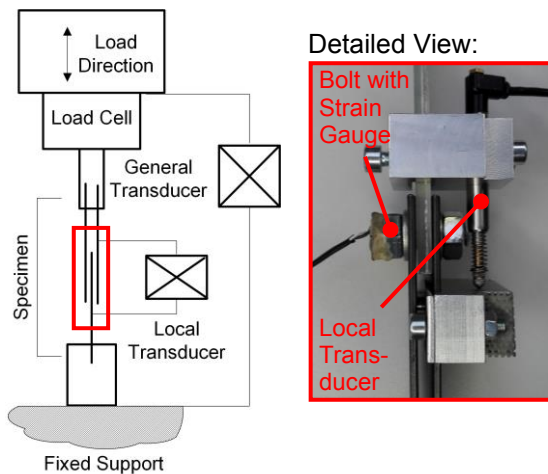


Fig. 5 Test setup with additional displacement transducer for the local displacement

- Test #A denotes a strain controlled pull-out test similar to a tensile test. The displacement Δl is controlled by a general transducer while the load is recorded by the load cell. The test is performed until bearing between bolt and sheet takes place.
- Test #B denotes a load controlled pull out-test. The specimens are progressively loaded and controlled by the load cell. A local displacement transducer is fitted to the joining zone for the measurement of the displacements between the components of the tensile shear test specimens. The load-time history is shown in Fig. 6. The load is progressively raised after each relief of load until kinetic friction takes place.

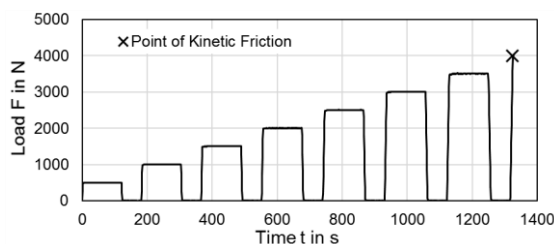


Fig. 6 Load-time history of test #B

- Test #C denotes cyclic load controlled tests. The specimens are cyclically loaded with two different load spectrums. The loads are controlled by the load cell while the cyclic displacement is detected by the local transducer, similar to test #B. Test #C₁ is executed with a load amplitude of $F_{a1} = 750$ N and a mean load of $F_{m1} = 750$ N. Test #C₂ is executed with a load amplitude of $F_{a2} = 1500$ N and a mean load of $F_{m2} = 1500$ N. The frequency for the 10 first cycles is set to be $f = 1$ Hz, the other load cycles are performed with a frequency of $f = 6$ Hz.

The permanent slip s , measured by using the output of the local transducer, is here defined as the irreversible displacement Δl_{irr} between the sheets of the specimen after the relief of loading (s. Fig. 7), near to the frictional connection.

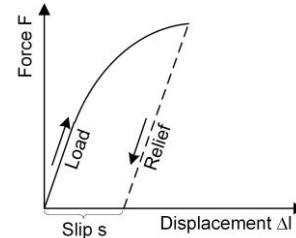


Fig. 7 Definition of permanent slip

3 RESULTS

3.1 TEST RESULTS

Two load-displacement curves of test #A for one specimens #1 are shown in Fig. 8. The first test is

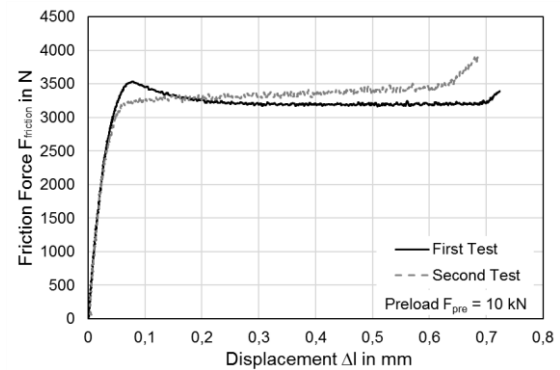


Fig. 8 Curve of a pull-out tests of specimen #1

performed with the undamaged specimen #1 as manufactured. A second test is performed with the same specimen #1, however, after the first degrading pull-out test has been executed and after disassembling and reassembling the specimen. Thus the influence of a damaged surface of the GFRP after the first test can be measured. The curve of the first test shows a local maximum (Fig. 8) which tags the border between static and kinetic friction. During the second test no local maximum occurs anymore, which means that there is a continuous transition between static and kinetic friction. This behaviour, however, is only observed by using specimens #1. By testing Specimen #2 a stick slip effect appears. After reaching a critical load an abrupt transition to kinetic friction happens which is repeated several times (s. Fig. 9). This characteristic performance remains almost unchanged for the same specimen in the second test.

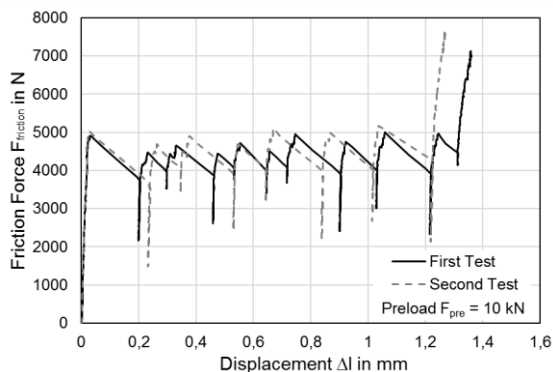


Fig. 9 Curve of a pull-out test of specimen #2

Complementary to the load-displacement curve of test #A the static permanent slip s_{per} is analysed in test #B. Fig. 10 shows the static permanent slip of specimens #1 and #2, respectively. For specimen #1 only a small permanent slip of $s = 5.7 \mu\text{m}$

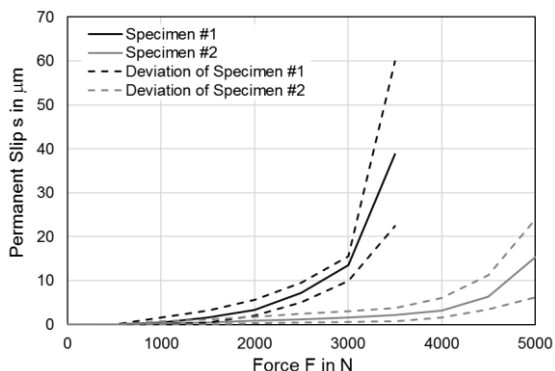


Fig. 10 Static slip behaviour of test #B

occurs up to a force of $F = 2000 \text{ N}$, followed by a fast increase up to a maximum slip of $s = 60 \mu\text{m}$ at $F = 3500 \text{ N}$. The behaviour of specimen #2 is similar, but the area of the small static permanent slip is much larger and the following increase less compared to specimen #1.

The cyclic permanent slip of specimen #1 is measured during the tests #C₁ and #C₂ respectively. Fig. 11 shows that only a slight increase of permanent slip occurs for the first 1000 cycles and the increase is further slowed down afterwards.

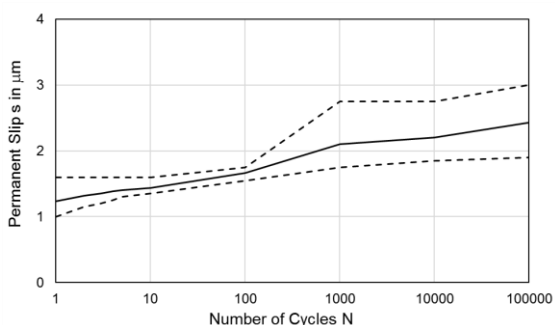


Fig. 11 Cyclic slip behaviour of test #C₁

The average cyclic permanent slip at the end of test #C₁ is $s_{per} = 2.43 \mu\text{m}$. Compared to the static permanent slip $s_{per} = 1.55 \mu\text{m}$ at the same load of test #B means an increase of 57%. Test #C₂ of specimen #1 shows a different behaviour (Fig. 12), which can be split into 3 phases. During the first cycles only a slight increase of permanent slip occurs. Between 10 and 100 cycles permanent slip grows significantly and by reaching 100 cycles a saturation of permanent slip can be observed. The

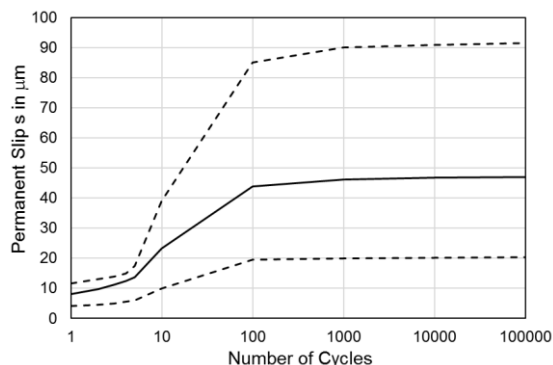


Fig. 12 Cyclic slip behaviour of test #C₂

average cyclic permanent slip at the end of test #C₂ is $s = 47 \mu\text{m}$. Compared to the static permanent slip $s = 13.55 \mu\text{m}$ of test #B means an increase of 247%.

3.2 MATERIALOGRAPHIC ANALYSIS

In Fig. 13 the GFRP surface of specimen #1 is shown after applying the preload. The here shown section is located next to the drill hole. After mounting and disassembly some indentations of the shot peened plate are visible in the GFRP surface, so that a certain micro form-fit connection occurs as well. With increasing distance to the drill

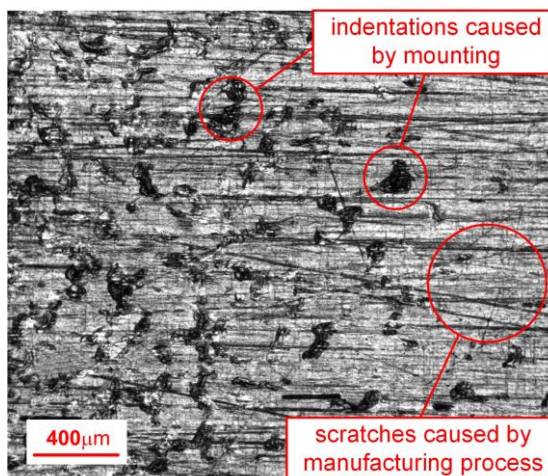


Fig. 13 Surface of the GFRP after applying the preload

hole the concentration of indentations drops. Fig. 14 shows the GFRP surface of a disassembled specimen after a first pull-out test. The surface is

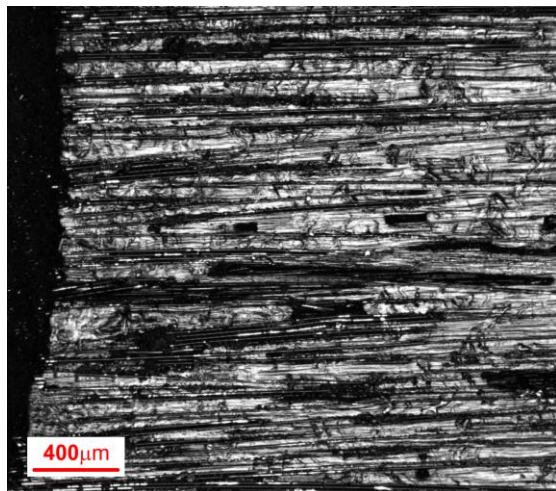


Fig. 14 Surface of the GFRP after the first pull-out test

shattered which is here indicated by many striations parallel to the fibre direction.

4 CONCLUSION

4.1 DISCUSSION OF RESULTS

The discussion of results is based on three assumptions:

- I. The specimen subjected to a load is deformed and exhibits a reversible (elastic) displacement Δl_{rev} .
- II. An irreversible displacement Δl_{irr} merely takes place in the frictional connection.
- III. The GFRP is deformed and damaged by shattering the resin matrix by the indentations of the shoot peened steel.

According to assumption #I and #II the total displacement of specimen #1 Δl in test #A is made up of Δl_{rev} and Δl_{irr} . According to assumption #II the irreversible displacement Δl_{irr} is equal to the permanent slip s which is measured by the local transducer in test #B. Therefore, as a conclusion from assumptions #I and #II, the total displacement Δl is made up by Δl_{rev} and s , i.e.:

$$\Delta l = \Delta l_{rev} + s \quad (2)$$

The reversible displacement Δl_{rev} of the specimen #1 can be extrapolated using the initial part at minor loads of the pull-out curve of test #A where no slip occurs. Fig. 15 shows the composed curve (red line) made up by the reversible displacement Δl_{rev} (dotted line) and the slip s (blue line) and the pull-out curve (black line) of test #A as well.

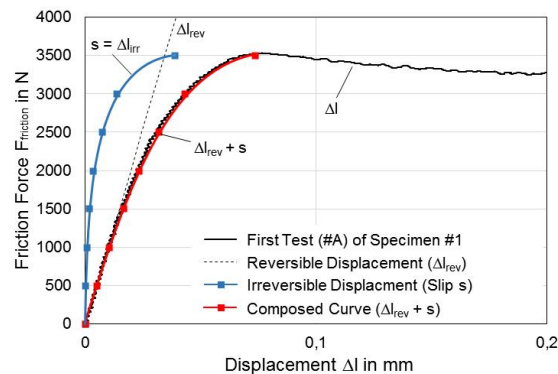


Fig. 15 Combination of reversible and irreversible displacement

The results of the composed curve, representing the right side of equation (2), are well corresponding to the first pull-out curve of test #A, representing the left side of equation (2). Therefore our conclusion based on the first and second assumption is verified. The reversible displacements Δl_{rev} occur in the specimen and slip s merely occurs in the frictional connection.

Our third assumption stems from the materialographic analysis. In Fig. 13 the plastic deformation of the indentations can be seen. After the first test #A the surface of the GFRP, which is built up by resin of the matrix, is shattered (s. Fig. 14). The failure mechanism is discussed in a micro mechanical model.

4.2 FAILURE CRITERION FOR A FRICTIONAL CONNECTION

Specimen #1 has to a certain extend a form-fit connection which is provided by the shot peened steel sheets causing indentations into the resin of the GFRP sheets (s. Fig 13). A simple illustration (Fig. 16) shows the micro form-fit connection.

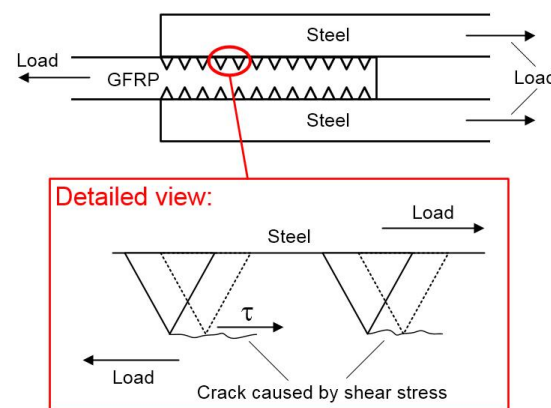


Fig. 16 Model of the micro form-fit connection

As soon as a pull-out load is applied, a shear stress τ and an elastic shear deformation occur at the bottom of the indentations. With increasing shear stress τ small plastic deformations will appear and

macroscopic permanent slip s occurs. This slip increases up to a critical shear stress τ_{crit} when static friction changes to kinetic friction. The regime of kinetic friction is linked to the occurrence of a shattered GFRP surface. It is assumed here, that the critical shear stress τ_{crit} corresponds to the local maximum between static and kinetic friction which is mainly generated by the micro form-fit connections. This assumption can be made plausible by the second pull-out test #A of specimen #1, where no local maximum between static and kinetic friction occurs. The surface of the GFRP is already damaged, so that almost no form-fit connection appears.

Failure of a frictional connection is defined here as the transition from friction to bearing of hole. For a reliable design of a frictional connection two kinds of loadings have to be considered. On the one hand there are operating loads, as tested and described in the chapters before, and on the other hand there are overloads by special incidents or misuse which are not treated here. According to the above definition failure occurs if no clearance between hole and bolt remains. Considering fatigue strength for finite life a maximum friction force well below $F_{\text{max}} = 3000 \text{ N}$ is reasonable. For a frictional connection which is fitted for the first time a load of $F_{\text{max}} = 3000 \text{ N}$ is in the upper area of the static friction with a safety margin of $\Delta F = 500 \text{ N}$ to the transition from static to kinetic friction. Furthermore, test #C₂ discloses a saturation for the amount of slip s under a cyclic load. The total maximum slip for specimen #1 under the cyclic load in test #C₂ is $s = 0.091 \text{ mm}$ which is clearly less than the clearance of 1 mm of the bolted joint.

A failure criterion for a frictional connection in a multi-material-system has been derived and quantified. It considers the active principle and the performance of the connection. By this way a maximum tolerable force F_{max} for fatigue strength for finite life has been established. However, overloads by special incidents or misuse are not included. This has to be treated elsewhere.

5 ACKNOWLEDGEMENT

The authors gratefully acknowledge the cooperation partner Muhr und Bender KG, Attendorf for the assistance of generating specimens and the support for the material tests.

REFERENCES

- [1] Thoppul, S. D.; Finegan, J.; Gibson, R. F.: *Mechanics of mechanically fastened joints in polymer-matrix composite structures – A review*. Composites Science and Technology 69 (2009) 3-4, pp. 301–329.
- [2] Crews, J. H. [JR.]: *Bearing Fatigue of a Graphite/Epoxy Laminate*. In: Kedward, K. D.: *Joining of Composite Materials ASTM STP*. 1981, p. 749.
- [3] Xiao, Y.; Ishikawa, T.: *Bearing strength and failure behavior of bolted composite joints (part I: Experimental investigation)*. Composites Science and Technology 65 (2005) 7-8, pp. 1022–1031.
- [4] Schürmann, H.: *Konstruieren mit Faser-Kunststoff-Verbunden*. Berlin, Heidelberg, New York, NY: Springer, 2007.
- [5] Schürmann, H.; Elter, A.: *Beitrag zur Gestaltung von Schraubenverbindungen bei Laminaten aus Faser-Kunststoff-Verbunden*. Konstruktion 1/2-2013 (2013), pp. 62-66.
- [6] AVK-Industrievereinigung Verstärkte Kunststoffe e.V.: *Handbuch Faserverbundkunststoffe/Composites*. Fourth ed. Wiesbaden: Springer Vieweg, 2014.
- [7] Kloos, K.-H. u. Thomala, W.: *Schraubenverbindungen: Grundlagen, Berechnung, Eigenschaften, Handhabung*. Fifth ed. Berlin, Heidelberg, New York: Springer, 2007.
- [8] VDI-Richtlinie 2230. *Systematische Berechnung hochbeanspruchter Schraubenverbindungen Zylindrische Einschraubverbindungen*. Berlin: Beuth, 2003.

EXPERIMENTAL INVESTIGATION OF DIRECT ADHESION OF CFR-THERMOPLAST ON STEEL

Ferhat Yüksel^{1*}, Roland Hinterhölzl², Klaus Drechsler¹

¹ Fraunhofer Institute of Chemical Technology branch Functional Lightweight Design,
Augsburg, Germany

² Institute for carbon composites, Technical University of Munich, Germany

ABSTRACT:

In this work a novel joining technology for carbon fiber-reinforced thermoplastic (CFRTP) and metal is investigated. Here, the meltability of the thermoplastic is used for direct adhesion on the steel surface without an additional adhesive.

Based on CFRTP tapes with polyamide 6 matrix (PA6) an unidirectional layup is manufactured with the facility FiberForge RELAY®. In this process the layup is stacked by ultrasonic welding points and is so far not consolidated to a laminate. Two preforms are positioned into a tooling with a steel sheet in between to manufacture double lap joint (DLJ) test specimens. The tooling is heated up over the melting temperature of PA6. Afterwards the tooling is taken into the heat press while the press plates have a constant temperature of 80°C. The heat press applies pressure and cool down the tooling at the same time. Meanwhile the consolidation of the preforms to laminates and simultaneously the direct adhesion on the steel surface are carried out. Two surface treatments on the steel sheet are compared by tensile tests. The test results show high joint strength up to 22 kN / 19,3 MPa.

KEYWORDS: direct adhesion, thermoplast, hybrid, joint

1 INTRODUCTION

Joining technology plays an important role in hybrid structures made of fiber-reinforced plastics and metal. Especially composites with thermoplastic matrix systems have a limited suitability in adhesive bonding. Otherwise mechanical bonding methods like screwing or riveting lead to stress concentration around the holes and additional weight [1].

One possible joining technology for thermoplastics with metal is the direct adhesion by using the meltability of thermoplastics. In [2] the direct adhesion is investigated with unreinforced and short fiber reinforced thermoplastics and metal. Here, the metal is heated up over the melting temperature of the thermoplastic part. Afterwards the thermoplastic is pressed under a defined force on the heated metal. By cooling down the joint is realized.

In this work the direct adhesion is experimentally investigated with endless carbon fiber-reinforced thermoplastic (CFRTP) and steel. Before adhesion the CFRTP is in a preform condition out of several tape layers and not consolidated to a laminate. The

consolidation of the preform is performed simultaneously with the joining. For this reason only one process is needed to manufacture the CFRTP and to join with the metal part.

2 MATERIALS, PREFORMING AND SURFACE TREATMENT

The double lap joint (DLJ) test specimens consist of two thermoplastic unidirectional laminates bonded to a steel sheet. To increase the joining strength two surface treatments are carried out on the steel surface.

2.1 MATERIALS

For the manufacturing of the test specimen a unidirectional CFRTP tape with polyamide 6 (PA6) matrix is used. The carbon fiber content of the CFRTP tape is 60% by weight.

The metal component is a high strength steel for automotive structures called HSLA340.

* Corresponding author: Am Technologiezentrum 2, 86159 Augsburg, phone: 0821 90678220, fax: 0821 9067840220, ferhat.yueksel@ict.fraunhofer.de

2.2 PREFORMING

The FiberForge RELAY® is an automated tape laying (ATL) facility that can produce flat preforms for consolidation out of unidirectional fiber-reinforced thermoplastic tapes. The layup is stacked by ultrasonic welding points to fix the tapes to each other and keep the layup for further handling.

With this ATL facility preforms were manufactured with 14 layers and unidirectional layup for the joining process.

2.2.1 SURFACE TREATMENT

Two surface treatments are investigated on the steel sheet. One is sandblasting (SB) with special fused alumina. The second surface treatment is coating of the blank steel sheet with the adhesion promoter Vestamelt® Hylink (VH) of Evonik Industries.

Previous tests with sandblasted specimen showed without any additional matrix in the adhesion area no joint is possible or the joint strength is very low. The reason for this is obviously the missing matrix material that in this case should work like an adhesive.

To investigate the influence of additional PA6, a PA6 foil with a thickness of 0,2 mm or 0,4 mm is melted on the surface treated steel sheet within a vacuum bag and a temperature of 250°C. In Table 1 the investigated configurations of surface treatments are shown.

Additionally, all surfaces are cleaned with Acetone before joining to ensure that they are free from contaminations.

Table 1: Configurations of surface treatment and additional PA6 foil

Sample name	Surface treatment	PA6 foil thickness [mm]
SB1	SB	0,2
SB2	SB	0,4
VH0	VH	-
VH1	VH	0,2
VH2	VH	0,4

3 JOINING PROCESS

First, the CFRTP preforms and the metal sheets are positioned in the tooling for heating and consolidation. The tool is designed such that two configurations can be manufactured at the same time. The surface treated steel sheets are on the right and the left side of the tool. In the middle is a blank steel sheet that is not intended to join with the CFRTP but to ensure a uniform heating and cooling in the stacking during the joining process. In Fig. 1 a sketch shows the right half of the tooling with the stacking in it.

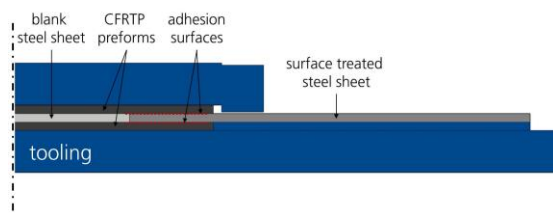


Fig. 1 Detail of the symmetric cross section of the tooling with the stacking

The tooling is heated up and the temperature of the upper and the lower CFRTP preform is measured with thermocouples. The heating is ongoing until the preforms reach a temperature of 270°C.

The tooling is now transported into the heat press. The heat press builds up a pressure of 15 bar on the stacking. The heat press plates have a constant temperature of 80°C, hence the tooling with the stacking cools down. Now, the consolidation of the preforms to laminates is ongoing and at the same time the joining is realized. By reaching 100°C in the CFRTP laminates the press process is ended and the tooling can be opened.

4 TESTING

Six test specimens per configuration are cutted out of the manufactured plates. The laminates and the steel sheet have each a thickness of 2 mm, so the DLJ has an overall thickness of 6 mm. The adhesion area is 25x25 mm². The DLJ geometry with dimensions can be seen in Fig. 2.

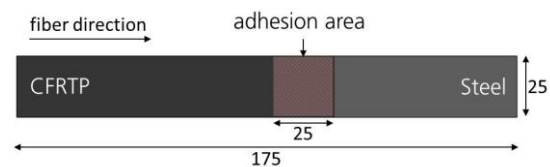


Fig. 2 DLJ test specimen with dimensions in mm

All test specimens were conditioned before testing according to the standard DIN EN ISO 1110 to ensure the laminates reach the moisture content that would be obtained in standard atmosphere.

The tests were performed based on the standard DIN EN 1465.

5 RESULTS

5.1 SANDBLASTING

The two sandblasted specimens show nearly the same joint strength. SB1 has a mean joint strength of 17,5 MPa and SB2 18,1 MPa. The main difference is in the maximum displacement. SB2 behaves overall softer than SB1 because of the thicker PA6 foil insertion and thus SB2 reaches more displacement till maximum strength.

Fig. 3 shows a diagram with typical stress-displacement curves of both configurations. The curves show plastic behaviour by almost constant force after the first stress peak. The DLJ keeps shearing until ultimate damage even reaching a higher maximum strength in comparison to the first stress peak.

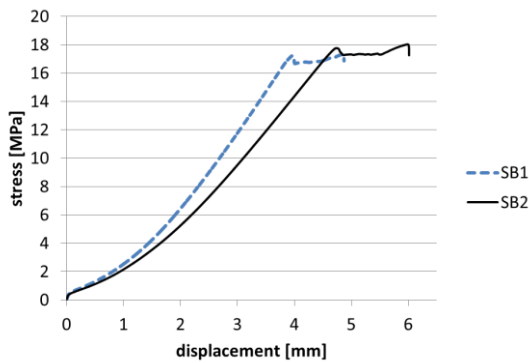


Fig. 3 Typical stress-displacement curves for the configurations SB1 and SB2

The failure behavior of the sandblasted specimens is a mixture of adhesive and cohesive failure. Fig. 4 displays the interface between CFRTP and sandblasted steel surface. It can be seen, that partially CFRTP is still bonded on the steel surface after damage.



Fig. 4 A mixture of cohesive and adhesive failure in the interface between CFRTP and sandblasted steel

5.2 VESTAMELT® HYLINK

For the surface treatment with the adhesive promoter the results show a similar behaviour like for the SB specimen in case of displacement. The displacement at maximum strength increases with the insertion of PA6 foil.

Furthermore, in contrast to the SB specimen, the joint strength increases significantly by PA6 foil insertion. The VH treatment with no additional PA6 foil reaches a mean joint strength of 15,4 MPa. Here, the curve shows no plastic behaviour after the stress peak and the joint fails suddenly. With insertion of PA6 foil the joint strength increases for VH1 to 16,8 MPa and plastic behaviour occurs before ultimate fail. Also, the joint strength increases with doubling the inserted PA6 foil thickness reaching 19,3 MPa of mean joint

strength for the configuration VH2. The typical stress-displacement curves are shown in Fig. 5.

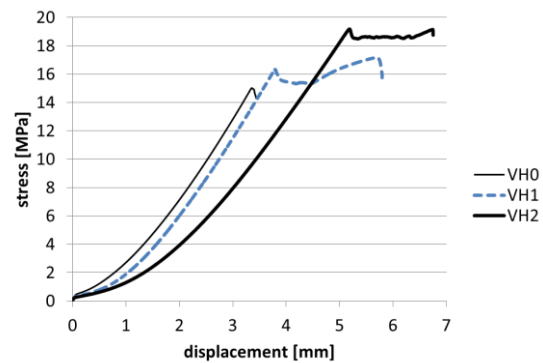


Fig. 5 Typical stress-displacement curves for the VH configurations with no and additional PA6 foil with different thicknesses

The VH configurations show mainly an adhesive failure in the joint. The adhesive promoter is still bonded on the steel surface. In Fig. 6 the failed interface of a VH treated specimen is illustrated.



Fig. 6 VH treated specimens fail mainly in an adhesive way in the interface between the CFRTP and the adhesive promoter

5.3 COMPARISON OF SURFACE TREATMENTS

In Fig. 7 the stress-displacement curves of SB1 and VH1 are compared, where it can be seen that these are very similar to each other. Only VH1 is reaching more displacement after the first peak till ultimate fail.

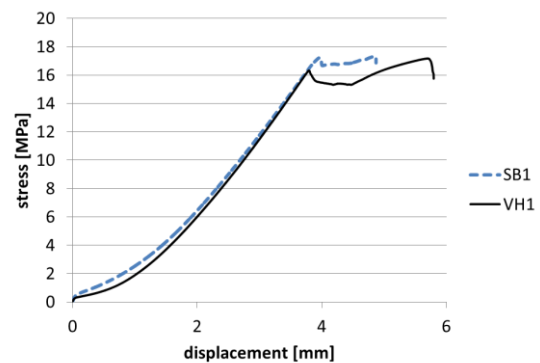


Fig. 7 Comparison of surface treatments with insertion of 0,2mm thick PA6 foil

The comparison of the configurations with 0,4 mm PA6 foil insertion is in Fig. 8. Here, again the displacement and the joint strength are in the same range.

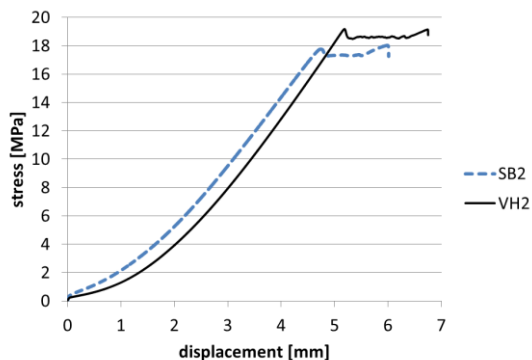


Fig. 8 Comparison of surface treatments with insertion of 0,4mm thick PA6 foil

Overall the VH treatment is slightly better by taking higher displacement and joint strength in contrast to SB.

In Fig. 9 the determined joint strength with standard deviation and the equivalent maximum force is summed up for all configurations.

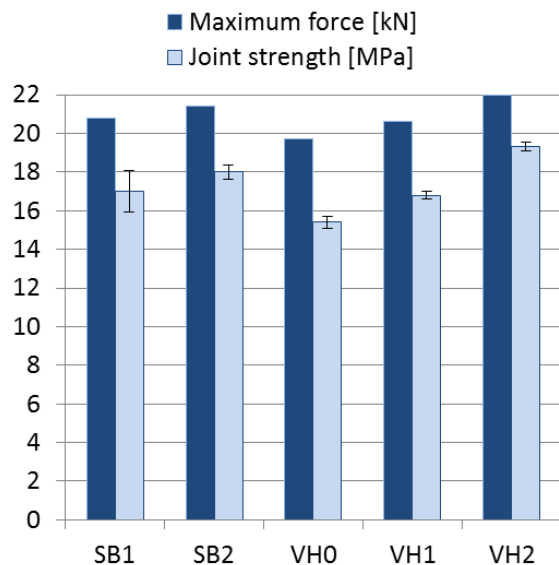


Fig. 9 Maximum force and joint strength with standard deviation of all configurations

6 CONCLUSIONS

The direct adhesion of CFRTP with metal is a joining technology that offers an automatable and reproducible process. Especially the consolidation and the joining process are realized in one step, thus subsequent processes like in adhesive bonding are not needed. Furthermore, in this work it's shown that high joint strength are achievable.

In the investigations CFRTP preforms made with the FiberForge RELAY® are combined with surface treated steel to consolidate the preforms and at the same time joined with the steel sheet to DLJ specimens. Surface treatments were sandblasting and coating with the adhesive promoter Vestamelt® Hylink.

The positive effect on the joint strength and the maximum displacement by the insertion of additional PA6 foil in the adhesion area could be determined. Up to 25% higher joint strength is achieved for the VH treated specimen with the insertion of PA6 foil.

Further investigations are planned to characterize the interface between steel and CFRTP for modeling and design of components. Subsequently the goal is to use this joining technology in component level.

7 ACKNOWLEDGEMENT

The authors thank “Bayerische Forschungsförderung” (Bavarian Research Fund) for promoting this work and Evonik Industries AG for providing the adhesive promoter.

REFERENCES

- [1] Schürmann, H.: *Konstruieren mit Faser-Kunststoff-Verbunden*. Springer-Verlag Berlin Heidelberg New York, 2007.
- [2] Flock, D.: *Wärmeleitungsgefügen hybrider Kunststoff-Metall-Verbindungen*. Doctoral thesis, RWTH Aachen, 2011.

ENHANCING THE TENSILE STRENGTH IN HYBRID METAL-FRP MATERIALS THROUGH VARIOUS INTERLOCKING STRUCTURE PATTERNS

Michael Brand^{1*}, Markus Kühn¹, Anke Müller¹, Klaus Dröder¹

¹Technische Universität Braunschweig, Institute of Machine Tools and
Production Technology

ABSTRACT: This paper aims at investigating the mechanical interlocking effect between metal and fiber-reinforced plastics (FRP) under tensile load. The effect is achieved by a structuring process which generates mechanical undercuts on the metal surface. A series of experimental tests was performed to determine the effectiveness of the interlocking effect. EN AN 2017A and PA6GF30 were used as material combination and hybrid specimens were manufactured by injection molding. The results show a linear correlation between the size of a single structure and the respective tensile strength. Significantly more than 600 N could be transmitted per single structure. Furthermore, the correlation between the number of structures and transmitted loads is linear until failure. With the same structure size, a cycle layout was found to provide a higher tensile strength than a U shape pattern. To assess the influence of different layouts, a numerical FEM analysis in ABAQUS (simulation) and optical measurements were employed. The results show an unequal stress distribution within the overlap zone. It can be concluded that the cycle layout does provide a higher tensile strength, however, plastic deformation of the overlap zone occurs much earlier compared to U shape patterns.

KEYWORDS: Interlocking Effect, Structural Integrity, Hybrid Parts, Lightweight Design, FRP + Metal

1 INTRODUCTION

The reduction of CO₂ emissions and saving fossil fuels are a central challenge in aerospace and automotive industries. The combination of metal and fiber-reinforced plastic (FRP) parts can be used to decrease the overall mass and to combine the advantages of both materials. As a result, light and stiff parts can be produced. The key to make the benefits available as well as the limited performance factor are joining technologies.

Nowadays, hybrid structures, a material combination of FRP and metal, are manufactured in a large number of production steps. Adhesive Bonding is the most frequently used technology to join dissimilar materials [1]. However, the disadvantage of this joining technology lies in the necessity for complex surface preparation in the joining zone. Furthermore, adhesives are potentially critical in terms of aging, application and inline quality control. Therefore, additional mechanical joining elements such as rivets, bolts or screws are used [2-5]. These joining technologies can transmit high loads

on the final assembly, however, the load-bearing fibers are often locally destroyed, whereby the strength of the component can be reduced. Another approach to enhance the tensile strength of hybrid metal-FRP structures is creating an additional interlocking effect through metal structuring. One of these approaches is the IGEL technology which creates a pin structure on a metal surface by means of cold metal transfer welding (CMT). In component manufacturing, the pins penetrate the fiber material and thus create an interlocking connection [6]. However, applying new material to the metal surface is less favorable than removing material. Thus, some approaches create interlocking surface structures from the basic metal itself. These methods are using a laser beam to generate a micro or rather a macro clamping effect. The process used is a combination of ablating and melting the metal [7,8]. Another known method which can be used by flat metal sheets is grid metal. In this structuring process, a slotting tool generates thin mechanical undercuts on the metal surface [9]. A further structuring method is the creation of individual macro-

* Corresponding author: Langer Kamp 19 38106 Braunschweig, +49 531 391 7142, m.brand@tu-braunschweig.de

scopic undercut geometries on metal surfaces [10, 11]. It can be constituted that mechanical interlocking is a suitable and reliable method to increase structural integrity in hybrid structures. This paper presents investigations regarding the correlations of size, density and patterns of the interlocking structures in relation to the structural integrity of the joining partners.

2 INTERLOCKING EFFECT

The interlocking effect is based on mechanical undercuts which result in a form fit within the hybrid part. Therefore, the structures can be used in several manufacturing processes like injection molding, hot pressing, resin transfer molding (RTM) or vacuum assisted resin infusion (VARI).

2.1 STRUCTURING PROCESS

The structures were produced in a stamping forming process on the metal surface. Therefore, special tool geometries were developed which allow manufacturing of different forms of the clamping structures by variation of the process parameters. The structuring process is schematically illustrated in figure 1.

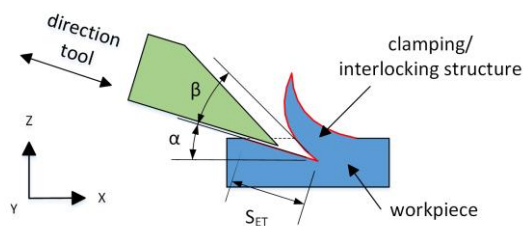


Fig. 1 Schema of the structuring process

During the analysis of the structuring process, several tool geometries were tested. The best results were achieved with a tool which creates a semi-circular cut with a circumferential cutting edge. The most important parameters are the impact angle (α), the wedge angle (β) and the impact depth (S_{ET}). As process parameters, an impact angle of 20° and a wedge angle of 90° were found to provide the highest strength during preliminary investigations, regardless of the material to be structured. The impact depth of the tool, however, was dependent on the material thickness of the materials of both sides (metal and FRP).

2.2 MECHANICAL INTERLOCKING

During manufacturing of a hybrid component, a form closure between the structures and the plastic was generated (Figure 2, middle). By using continuous fiber-reinforced materials, an additional load

application through direct interlocking between metal and fibers could be realized (figure 2, right).

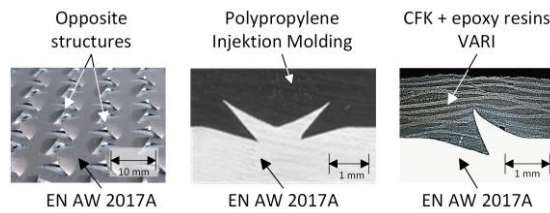


Fig. 2 Mechanical interlocking effect

Variation of structure orientation allows surface clamping and adaption to specific load paths in the component (figure 2, left).

3 EXPERIMENTAL INVESTIGATIONS ON STRUCTURE SIZE

The size of the structures can be influenced by the adjustment of the impact depth of the structuring tool. To determine the influence of the structure size, an experimental single lap shear test was carried out. Therefore, specimens were prepared which were provided with one single structure. Before the hybrid specimens were manufactured by injection molding (PA6GF30), the structures had been measured to determine the projected area (A_{PX}) by means of a microscope. The projected area as depicted in figure 3 contributes to the overall strength of the hybrid joint.

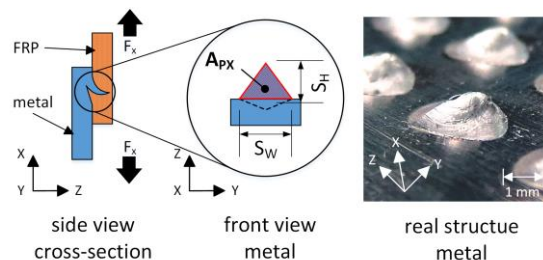


Fig. 3 Definition of the projected area

For the tests, structured specimens were prepared with a A_{PX} range from $0,74 \text{ mm}^2$ to $2,87 \text{ mm}^2$. Evaluation of the tests showed a directly linear correlation between the projected area A_{PX} and the associated transmittable load (see figure 4). Specimen failure primarily occurred due to FRP breakage, whereby the metal structures were observed to fail on occasion (figure 5).

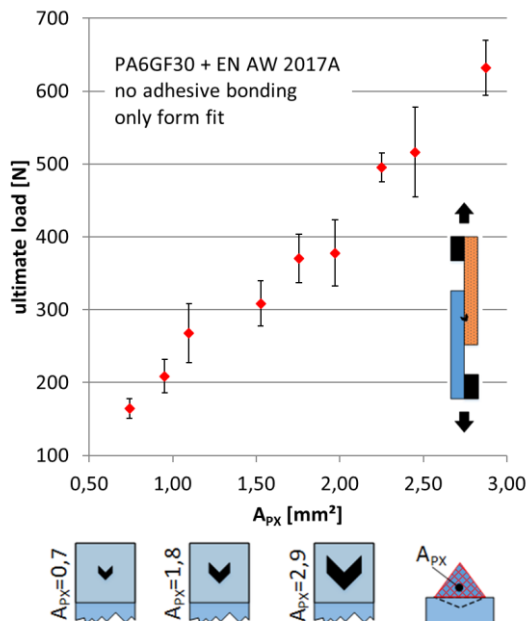


Fig. 4 Correlation of projected area and ultimate tensile strength

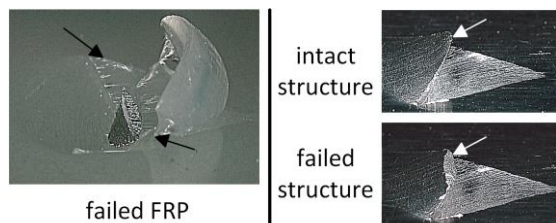


Fig. 5 failed reinforced plastic, failed metal structure [10]

4 INVESTIGATIONS ON STRUCTURE DENSITY

Another approach to increase transmittable loads in hybrid joints is increasing the number of structures in a predefined overlap area, hence the structure density. For the investigation, specific structures were manufactured for the purpose of creating a projected area A_{px} of 2.87 mm², whereby only the number of structures was varied. The overlap area was set to 30 x 30 mm. The material thickness of plastic and the metal was 2 mm. The results of the tensile testing depicted in figure 6 show an approximated linear correlation between transmitted loads and the number of structures.

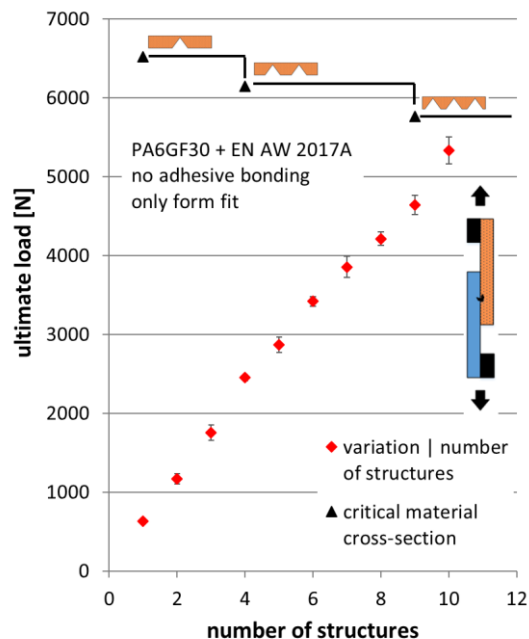


Fig. 6 Dependence of transmittable load on number of structures

In the experiments, the maximum ultimate load amounted to 5332 N. This value was achieved using 10 structures. A further increase of the number of structures did not result in further enhancement of ultimate tensile loads due to the limited ultimate strength of the FRP. The ultimate load of PA6GF30 correlated with the number of structures as shown in figure 6 as the critical cross-section was diminished by an increasing amount of structures. The respective cross-section arose from the number of structures that were set in a row (figure 7). In a pattern with 4 to 8 structures, 2 structures were in a row, from 9 structures, 3 structures were in a row.

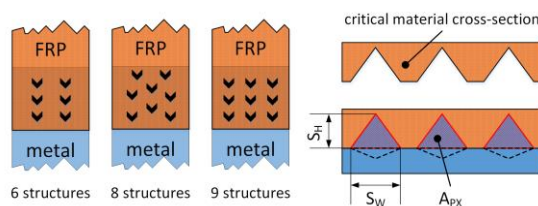


Fig. 7 Structural arrangement and critical material cross section

These results indicate, that the structure pattern on metal surfaces constitutes a key factor for hybrid joint strength enhancement and shall be subject to further investigation.

5 INVESTIGATIONS ON STRUCTURE PATTERNS

The respective structures can be created individually on a metal surface and their layout pattern can easily be varied. To investigate the influence of different structure patterns, studies were carried out by simulation and were validated experimentally. In order to understand the mechanisms and to validate the simulation model, photogrammetric deformation measurements were conducted during the tensile tests using a GOM ARAMIS system. Therefore, samples were prepared with 9 structures and a constant average projected area A_{PX} of 2.9 mm². From preliminary investigations, 5 patterns were selected that were to be investigated with regard to ultimate tensile load. The patterns investigated were a matrix shape, a circular shape, a zig-zag shape, a pyramid shape and a U shape pattern (figure 8).

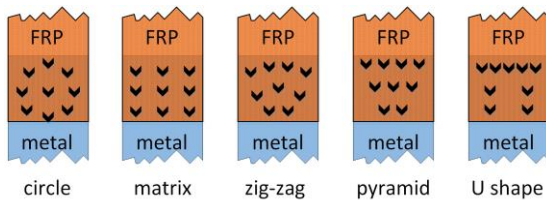


Fig. 8 Investigated structure patterns

5.1 SIMULATION OF STRUCTURE PATTERNS UNDER TENSILE LOAD

To identify the structure pattern with the highest ultimate tensile load in a hybrid joint, a numerical analysis was performed in ABAQUS using the finite element method (FEM). For the simulation, the geometry of the interlocking structures was simplified to save simulation time, proportions of the structures were considered. The JOHNSON-COOK material law was used to model the hybrid specimens. This visco-plastic model defines the yield stress as a function of strain rate and temperature. The parameters for the aluminum material were taken from literature [12]. The parameters for the polymer were determined by separate tensile tests and adapted to the model. In the FEM model, the tensile test was simulated. Figure 9 shows the FEM model for a 3x3 matrix structure pattern.

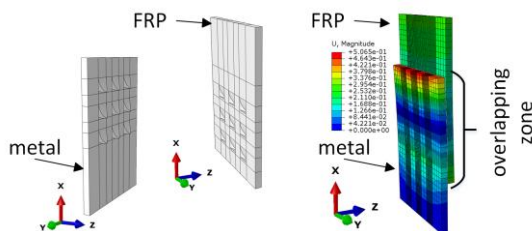


Fig. 9 FEM-Model

The mesh in the area of the structures was refined with tetrahedral elements. As boundary condition, the metal workpiece was fixed in Z direction as well as the rotation around the Z-axis. The load was applied into the upper part of the FRP component and pulled in X direction until the specimen failed. These results are depicted in figure 10.

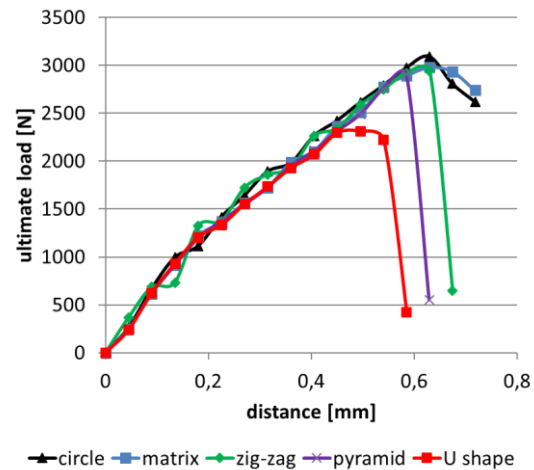


Fig. 10 Result of the lap shear test in ABAQUS

The slope to failure of the specimen are identical for all pattern. The breaking forces are almost identical, but an exception is the U pattern. This specimen fails significantly earlier. Here the critical cross-section of the FRP part was significantly smaller in all other pattern. This is due to the reduced cross section of the FRP material which is a result from the structure pattern.

5.2 ANALYSIS OF THE MATERIAL STRESSES

For the analysis of the stress conditions in the overlap zone and for the validation of the simulation model, experimental investigations were conducted using a GOM ARAMIS system with stereo camera. For these tests, the metal specimens were prepared with the same patterns (Figure 8) and manufactured by injection molding to a hybrid composite.

In figure 11, results from simulation and experiments are comparatively assessed. Both analysis methods show the same failure behavior of the specimen in the first row of five structures. This behavior results from the minimized polymer cross-section in this area. The optical measurements show a distinct stress peak within the first row structures which eventually results in joint failure.

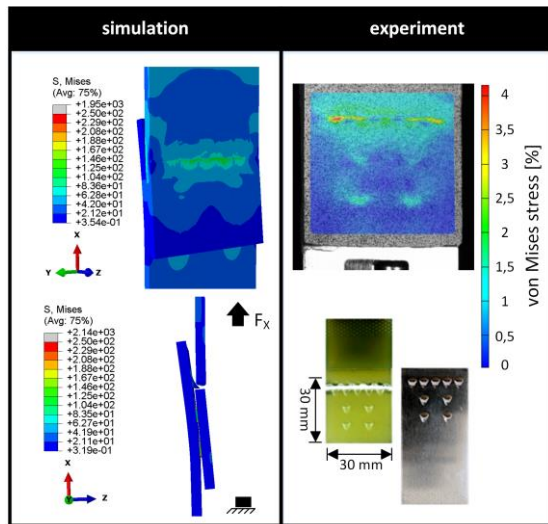


Fig. 11 U shape pattern

The same comparison was also carried out for the circle pattern. Also in this pattern, the increased stress values in the upper region of the overlapping zone could be observed. The stress distribution here focuses primarily only on the top structure (figure 12). This creates a stress peak and the FRP prematurely fails locally in this area, before the entire specimen fails.

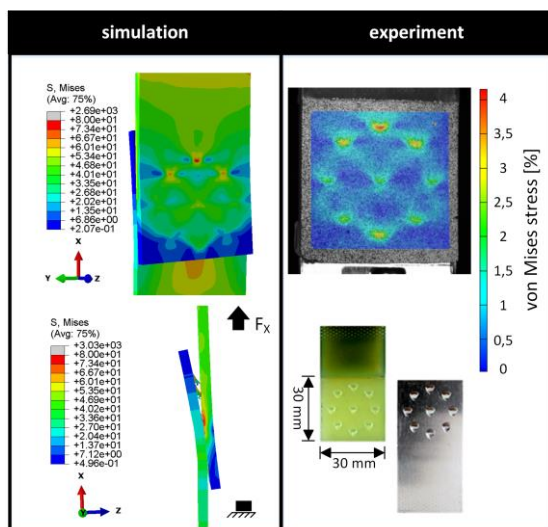


Fig. 12 Circle pattern

In both methods of analysis, different types of failure were identified dependent on the respective structure pattern. In case of the U shape pattern, the FRP failed at the weakest cross-section line. In case of the circular pattern, the FRP fails only locally within the structured area. Here, the failure starts at the front row structure where the stress is largest due to the smallest projected area. After failure of the front row structure, failure was observed to continue in the remaining structures until complete joint failure of the specimen.

The results of ultimate loads measured in U shape and circular patterns, respectively, indicate a superior performance of the circular pattern in terms of transmittable tensile loads. This could be detected in the simulation and the experiment (figure 13).

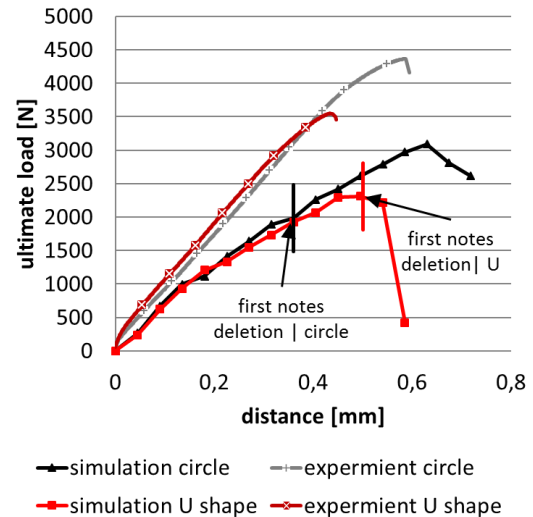


Fig. 13 Comparison between U shape and circle pattern

However, further analysis of the simulation results showed that the first structure failure is caused significantly earlier compared to U shape patterns. This is due to the unequal distribution of stress across the structure pattern. In Figure 13, the distance at the simulated graphs is marked where the first notes were deleted in the FEM model. This is the moment at which the stresses are so high that the FRP begins to break. Although the circular structure pattern provided a significantly higher ultimate tensile load to the hybrid joint, the thermoplastic FRP material was observed to fail earlier than in U shape patterns.

6 CONCLUSIONS

This Paper presents a method to generate a mechanical interlocking effect between metal and FRP (PA6GF30) by means of an individual metal structuring process. It was shown that the transmittable loads depend on the structure size, the number of structures and the specific structure pattern. In terms of size and number of structures, a linear correlation of structure size and ultimate joint strength was found. Furthermore, the stress distribution of different structure patterns was analyzed through FEM calculations and experimental studies. Therein, a circular pattern was found capable of transmitting significantly higher tensile loads than a U shape pattern. However, initial failure occurred earlier in circuit pattern than in U shape patterns. However, the structure pattern design is

strictly dependent on the properties of the respective polymer. Thus, a new structure pattern will have to be designed if other polymer qualities are employed.

7 ACKNOWLEDGEMENT

This research is conducted in collaboration with the Institute of Polymer Materials and Plastics Engineering, Technische Universität Clausthal. The authors would like to thank the Federal Ministry of Economics and Technology (BMWi) for the financial funding via the Europäische Forschungsgesellschaft für Blechverarbeitung (EFB) and the Arbeitsgemeinschaft industrieller Forschungsvereinigungen (AiF), Project No. 18112N.

REFERENCES

- [1] T. Wibbeke, M. Horstmann, R. Timmermann, Optimierte Blindnietverklebungen in Leichtbauanwendungen, Adhäsion Kleben & Dichten, 49 (2005) 42-44
- [2] T. Draht, Einseitig Verbinden ohne Vorlöchen, Lightweight Design, 1 (2008) 20-23
- [3] S.M. Goushegir, J.F. dos Santos, S.T. Amancio-Filho, Friction Spot Joining of aluminum AA2024/carbon-fiber reinforced poly (phenylene sulfide) composite single lap joints: Microstructure and mechanical performance, J. Mat. & Des. 54 (2014) 196-206, DOI: 10.1016/j.matdes.2013.08.034
- [4] R. Szlosarek, T. Karall, N. Enzinger, C. Hahne, N. Meyer, Mechanical Testing of Flow Drill Screw Joints Between Fibre-Reinforced Plastics and Metals. J Mat. Test, 55 (2013) 737-742. DOI: 10.3139/120.110495
- [5] U. Endemann, S. Glaser, M. Völker: Kunststoff und Metall im festen Verbund. In Kunststoffe. Carl Hanser Verlag, München, 2002
- [6] C.M. Chimani: Leichtmetallentwicklungen für hybride Leichtbaulösungen. AIT Austrian Institut of Technologie. LKR Leichtmetallkompetenzzentrum Ranshofen GmbH. FillAcademy, Gurten, 2012
- [7] C. Hopmann, A. Böttcher, K.Fischer, Investigations of bonding approaches and initial bond strength for the intrinsic manufacturing of laminary bonded hybrids made of thermoplastic composite and metal. J. Plast. Tech. 9 (2013) 253-274
- [8] G. Thomas, R. Vincent, G. Matthews, B. Dance, P.S Grant: Interface topography and residual stress distributions in W coatings for fusion armour applications. J. Mat. Sci. Eng. 477 (2008) 35-42
- [9] Patentschrift DE 600 19 560 T2: Rückenplatte für einen Bremsbelag sowie Verfahren und Apparat für dessen Herstellung, 2006-02-23, Arbesman R., Toronto - Ontario, CA.
- [10] S. Müller, M. Brand, K. Dröder, D. Meiners, Increasing the Structural Integrity of Hybrid Plastics-Metal Parts by an Innovative Mechanical Interlocking Effect, In: 20th Symposium on Composites, Wien, Trans Tech Publications, Switzerland, 2015, Seite 416, ISBN 978-3-03835-515-1
- [11] K. Dröder, M. Brand, A. Gerdes, T. Große, K. Dilger, F. Fischer, K. Lippky, H. Grefe, An innovative approach for joining of hybrid CFRP-Metal parts by mechanical undercuts Auf: EURO HYBRID - Materials and Structures 2014, Stade, Deutschland, 2014
- [12] E. Corona; E. G. Orient, An Evaluation of the Johnson-Cook Model to Simulate Puncture of 7075 Aluminum Plates, Sandia Report, SAND2014-1550, 2014

EFFECTS OF MELTING LAYERS ON NANOBONDING USING REACTIVE MULTILAYER NANOFOILS

S. Sen^{1,2*}, G. Langels¹, M. Lake¹, P. Schaaf²

¹ Niederrhein University of Applied Sciences, Krefeld, Germany

² Technical University of Ilmenau, Ilmenau, Germany

ABSTRACT: The advanced joining technique of nanobonding using reactive multilayer nanofoils has attracted a great deal of attention as localized heat source. In this study, the Ni/Al nanofoils were used to join stainless steel components for different melting layers. The melting layers of Sn and Ni-Sn have been coated on the steel components by electrodeposition process. The overall bonding was performed at room temperature by applying electrical ignition on the Ni/Al nanofoil. After ignition, the exothermic reaction between nanoscale Ni and Al layer produces a quantified reaction heat. This heat concentrates and melts the component within millisecond during nanobonding. Here the microstructural analysis of the joints has been performed by Scanning Electron Microscope (SEM) and Energy Dispersive X-ray Spectroscopy (EDX). The bonding properties were investigated by the tensile shear test and nanoindentation. The results show the high nominal bond strength for the joints with Ni coated Sn melting layers. The micromechanical properties in the joint interface also show the higher indentation hardness for the Ni-Sn melting layers compare to Sn melting layers. In addition, this nanobonding opens up a wide range of potentials with the important aspect of concentrated heat input and very fast joining process.

KEYWORDS: Nanofoil, nanobonding, melting layer, bond strength, nanoindentation.

1 INTRODUCTION

The reactive multilayer nanofoils are one of the most promising materials as they produce local heat in the modern joining technology. These foils consist of several hundred to a few thousand of alternating nanoscale layers of at least two elements with the large negative heats of mixing [1, 2]. For certain designs, these reactive multilayer films exhibit fast exothermic reaction that could be initiated by an external energy source such as an electric spark, thermal excitation, laser or a mechanical load [2 - 4]. The Ni/Al NanoFoil[®] and the NanoBond[®] process have been tailored by Indium Corporation [3]. For this nanobonding process, the nanofoil is placed between joined components under pressure along with melting layers (solder or brazed layers). The heat from exothermic self-propagating reaction of the nanofoil melts the bonding components. A large amount of localized energy is created from the nanofoils within very short time. Therefore, this nanobonding is performed without exposing components to high temperature flow. Compare to the common joining

process, this nanobonding opens up a wide range of applications, particularly the joining of temperature sensitive materials. The potential advantages of the nanofoils demonstrate the rapid heating and cooling within a very short period of millisecond. This type of bonding can be easily performed in air at room temperature without the facility of a furnace. The recent study shows the uses of Ni/Al nanofoils in various structural joining applications of microelectronic components [4], titanium alloys [5, 6], ceramics [7], metallic glasses [8] and steels [9, 10].

In this work, we studied the nanobonding of stainless steels using Ni/Al nanofoils. The stainless steel components have been electroplated with only Sn and Ni coated Sn melting layers and then joined. Here the microstructural and chemical characterizations have been analysed. The mechanical properties of the bonding were investigated by the tensile shear test and nanoindentation. In addition, the failure mode has been analysed. The overall bonding quality of the hybrid structure was evaluated based on two different types of melting layers.

* Corresponding author: Gustav-Kirchhoff-Str. 5, 98693 Ilmenau, Reinartzstraße 49, 47805 Krefeld, Phone: +4902151 822-5086, seema.sen@tu-ilmenau.de

2 EXPERIMENTAL

2.1 CONCEPTS OF NANOBONDING

Here the nanobonding uses the commercially available Ni/Al nanofoils developed by Indium Corporation [3]. The Ni/Al nanofoils possess the properties of the reaction velocity in the range of 6.5 – 8 m/s and the maximum reaction temperature of 1350 – 1500 °C with the reaction heat of 1050 - 1250 J/g [3]. The nanofoil consists of alternating layers of Aluminium and Nickel with the bilayer thickness of 50 nm, which is shown in the figure 1 (a). The atomic ratio of the Al to the Ni layer was 1:1. After activation, the chemical stored energy of the nanofoil released as the thermal energy. This thermal energy has been utilized to join the components. The figure 1 (b) shows the exothermic reaction front propagation of Ni/Al nanofoils within millisecond, which has captured by Keyence high speed camera.

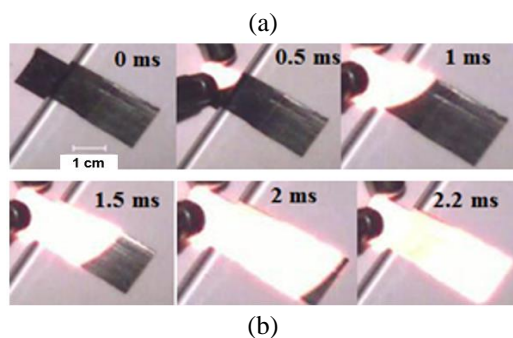
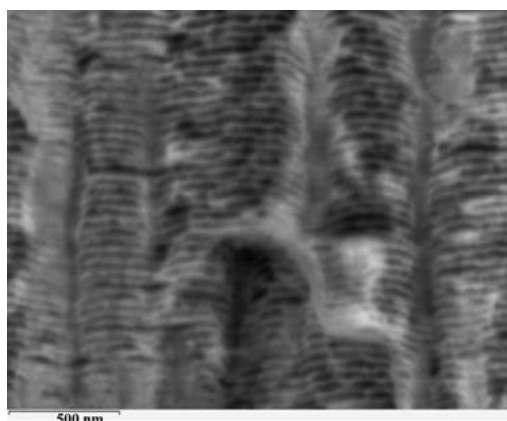


Fig. 1 Cross-sectional SEM image of the commercial Ni/Al nanofoil (a). High speed photographic images of reaction front propagation of the Ni/Al nanofoil at 9 V ignition (b).

Two different types of melting layers were used to fabricate the joints. In the first case, the bond has only Sn melting layer between components and nanofoil. The Sn layer with the thickness of 18 µm was electrodeposited on the stainless steels. In the

second case, the 6 µm thick Ni layer was electrodeposited and then 10 µm thick Sn layer was deposited at the top on it. Before electrodeposition, the stainless steels have been cleaned. The overall dimension of the sample was 5 cm × 2 cm × 0.5 cm. Then they have been coated with the dimension of 1 cm × 2 cm, which indicated the joint area. The nanofoils slightly larger than the size of bonded area have been sandwiched between the components. The schematic representation of nanobonding process has shown in the figure 2. The overall nanobonding process can be divided into following steps;

- (1) Introducing nanofoils between joined components coated or arranged with melting layers.
- (2) Applying uniaxial compressive load to the joint assembly in order to build uniform contact. The choice of the pressure depends on the types of the components to be joined.
- (3) Ignition of the nanofoils for starting the self-propagating reaction.
- (4) Joining and cooling within milliseconds and then elimination of the pressure.
- (5) Removal of the joint assembly and inspection.

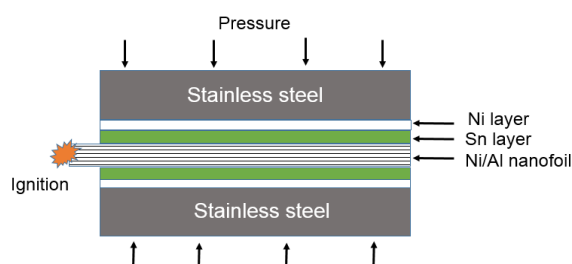


Fig. 2 Schematic representation of the nanobonding process with a transverse cross-sectional view.

In this work, nanobonding has performed by stacking 80 µm thick Ni/Al nanofoil between the stainless steel components coated with two different types of melting layers. The compressive pressure has been applied according to the work of Wang et al. [10]. An electrical ignition of 15 V has been used to activate the nanofoil. Heat released from the exothermic reaction of the nanofoil caused the melting layers to melt, wet each other and then they solidify within millisecond. The overall joining has performed at room temperature in air.

2.2 EXPERIMENTAL INVESTIGATION

After nanobonding, the joints were characterized using optical and scanning electron microscope. The microstructural and elemental analyses of the

cross-sections were performed by using SEM (Zeiss DSM 982) with EDX.

In order to evaluate the bonding quality, the tensile shear tests were performed using Zwick Roell Z050 tensile testing machine. The nominal bond strength is estimated taking the peak load from the test and divided it by the bond area. The tensile testing facility with sample alignment has been shown in the figure 3. The bonding components were tested by a static tensile shear loading with a speed of 2 mm/min until the joints break. Then the fracture surfaces were examined by SEM and EDX.

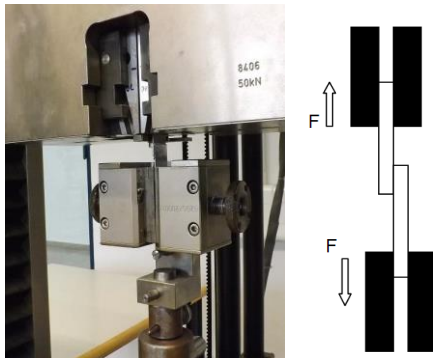


Fig. 3 Zwick Roell Z050 tensile testing machine with the sample alignment.

The nanoindentation test was performed to determine the micromechanical behaviour of the joint interface. The CSM Instruments Nanoindentation Tester (NHT) equipped with Berkovich diamond indenter has been used. The maximum force of 20 mN has been taken with the loading and unloading rate of 40 mN/min. The indentation hardness and elastic modulus have been evaluated for the hybrid structures at the joint interface.

3 RESULTS AND DISCUSSIONS

3.1 CHARACTERIZATION

The cross sections of the nanobonding are shown in the figure 4 for the Ni coated Sn melting layer. The nanofoils react and release heat for the joining. Then they contract from the high temperature due to quick cooling. As a result, cracks formed on the reacted nanofoils. The figure 4 (a - b) shows the important features of crack formation by the nanofoils. During bonding the melting layers flow and fill the crack gap and provide the sound joints.

The EDX mapping in the figure 4 shows the homogeneous distribution of Ni, Sn and Al elements in the joint interface. It also indicates the occurrence of crack filling characteristics of Sn between

reacted nanofoils. The EDX line scan at the Ni - Sn interface has been illustrated in the figure 5. In that interface, it is expected to be formed the intermetallic phases. The alternating layers of the nanofoil have been changed after exothermic reaction. The EDX analysis of the reacted Ni/Al nanofoil shows the composition of 51.5 at. % Ni and 48.5 at. % Al. It confirms the formation of intermetallic phase of NiAl from the alternating layers of Ni and Al.

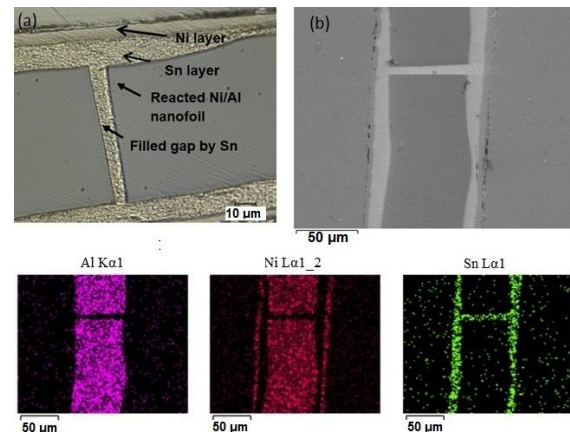


Fig. 4 Cross-sectional image of the joint interface captured by light optical microscope (a) and SEM (b). EDX mapping at the joint interface of the corresponding SEM image.

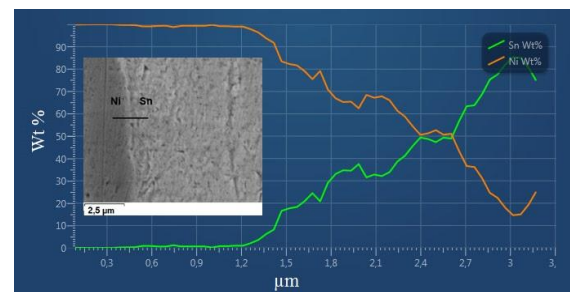


Fig. 5 EDX line scan at the Ni - Sn interface.

3.2 TENSILE SHEAR PROPERTIES OF NANOBONDING

The tensile shear strength results are listed in the table 1. It shows the sound bond formation for Ni coated Sn melting layer with bonding strength of 9.2 ± 1.3 MPa. For the Sn melting layer, the nominal bond strength is about 4.4 ± 1.2 MPa. The additional Ni layer influences on the adhesion and the crack filling of Sn layer. Therefore the nominal bond strength for Ni - Sn combination is higher than the only Sn layer. Compare to the recent studies, the nominal bond strength of this work shows the consistency with the reactive joining of steels for SnAg and AuSn solders mentioned in Refs [9-10].

Table 1: Nominal bond strength of the nanobonding of stainless steels for different melting layers.

Joints	Layer Type	Layer Thickness [μm]	Nanofoil [80 μm]	Bond Strength [MPa]
Steel/ steel	Sn	18±2	Ni/Al	4.4±1.2
Steel/ steel	Ni Sn	6±0.7 10±2	Ni/Al	9.2±1.3

However, the bond strength can be enhanced by the crack filling and wetting characteristics. Therefore, we also investigate the failure mode of the tensile shear test samples. The fracture surfaces of the joints were examined by using optical and scanning electron microscopy. The elemental analysis was performed by EDX. The fracture surfaces of the two variables are shown in the figure 6 (a, b). A rugged fracture surface is identified after breaking of the joints. Moreover, the globular microstructure of the fracture surface also indicates the wetting characteristics with the joined components.

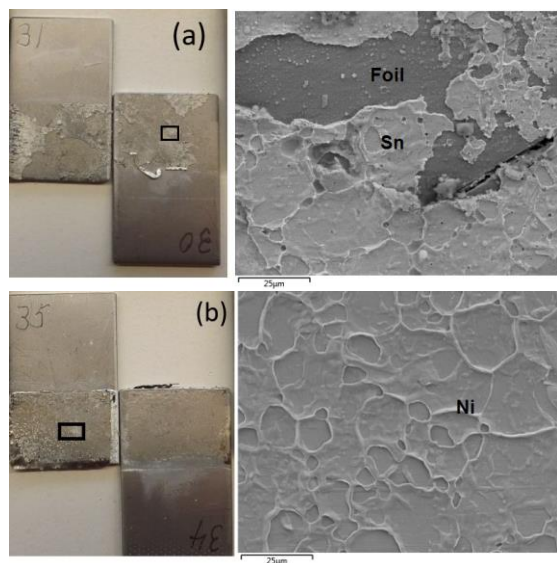


Fig. 6 Fracture surface of the nanobonding after tensile shear tests for Sn (a) and Ni coated Sn melting layer (b).

For the joints coated with only Sn melting layer, the fracture occurred almost exclusively along the component melting layer and foil interface, which is shown in the figure 6 (a). It illustrates the poor crack filling and also partial wetting to the joined components. It indicates a cohesive failure at the bond interface.

The fracture surface of the joint with Ni coated Sn layer is presented in the figure 6 (b). EDX analysis shows the presence of Ni at the joined component. It shows nearly an adhesive failure mode at the bond interface. Moreover, the presence of Ni enhances the crack filling and the wetting of the melting layer. Therefore, the nanobonding with Ni coated Sn melting layer shows relatively sound joints. However, the bonding strength can be further increased by providing good surface treatments, selecting proper melting layers and controlling process parameters.

3.3 INDENTATION HARDNESS AND ELASTIC MODULUS

The nanoindentation tests were conducted using a CSM instruments nanoindenter. A maximum load of 20 mN was taken for the tests to investigate the micromechanical behaviour at the joint interfaces. A typical load versus indentation depth curves of the reacted Ni/Al nanofoil, stainless steel, Ni - Sn interface and Sn layer have been shown in the figure 7. The measured curves consist of three segments - loading at a constant rate of 40 mN/min to the maximum load, the creep for 10 s and the unloading at the same loading rate. Then the hardness and elastic modulus could be extracted using the approach proposed by Oliver and Pharr [11].

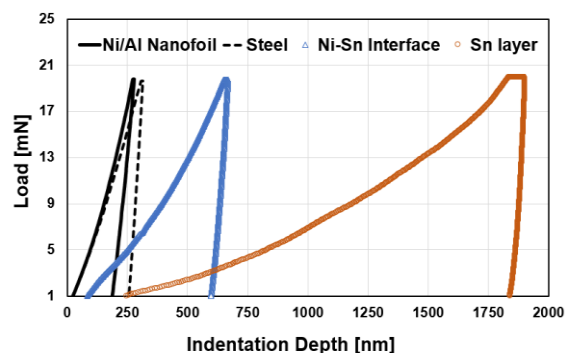


Fig. 7 Load vs indentation depth plots at the joint interface by nanoindentation test.

The micromechanical properties in terms of indentation hardness and elastic modulus are listed in table 2. The reacted Ni/Al nanofoil has higher indentation hardness of 10.6 GPa. The indentation hardness and elastic modulus of Ni - Sn interface are much higher than only Sn layer. Therefore, the Ni coated Sn layer enhances the bonding strength.

Table 2: Indentation hardness and elastic modulus at the joint interface.

Joint Interface	Indentation Hardness HIT [GPa]	Indentation Elastic Modulus EIT [GPa]
Stainless steel	6.8±2.0	203±36
Reacted Ni/Al	10.6±1.8	160±20
Ni - Sn	2.3±1.0	156±37
Sn	0.25±0.1	67±35

4 CONCLUSIONS

The nanobonding using Ni/Al nanofilm has been demonstrated for the stainless steels for two types of melting layers. The bonding process has performed within millisecond. The joints with Ni-coated Sn melting layers offer higher bonding strength compare to only Sn melting layers. However, the uses of Ni layer with Sn melting layers not only enhance the crack filling and wetting behaviour but also improve the indentation hardness, which influence positively on the bonding quality. Further investigations will be concentrated in order to achieve even higher bonding strength. In addition, this nanobonding shows enormous potentials in the industrial joining applications as a quick bonding process.

5 ACKNOWLEDGEMENT

The authors would like to thank Dipl.-Ing. R. Erdkamp for the support with tensile shear tests. The authors also gratefully acknowledge Professor J. Wilden and Mr. G. Hemken for the helpful discussions.

REFERENCES

- [1] Rogachev A. S.: *Waves of exothermal reactions in multilayer nanofilms*. Usp. Khimii, 77, No.1, 22-38, 2008.
- [2] Barbee T. W., Weihs T.: *Ignitable heterogeneous stratified structure for the propagating of an internal exothermic chemical reaction along an expanding wavefront and method of making same*. US Pat. 5538795, 1996.
- [3] Indium Cooperation, *Nanofilm Product datasheet*, 2015 (www.indium.com/nanofilm).
- [4] Wiemer M., Bräuer J., Wünsch D., Gessner T.: *Reactive Bonding and Low Temperature Bonding of Heterogeneous Materials*. ECS Transactions, 33 (4) 307-318, 2010.
- [5] Duckam A., Spey S. J., Wang J., Reiss M. E., Weihs T. P., Besnoin E. and Knio O. M.: *Reactive nanostructured foil used as a heat source for joining titanium*, Journal of Applied Physics, 96, 2336, 2004.
- [6] Cao J., Song X. G., Wu L. Z., Qi J. L., Feng J. C.: *Characterization of Al/Ni Multilayers and their application in diffusion bonding of TiAl to TiC Cermet*. Thin Solid films, 520, 3528-353, 2012.
- [7] Grieseler R., Welker T., Müller J., Schaaf P.: *Bonding of low temperature co-fired ceramics to copper and to ceramic blocks by reactive aluminum/nickel multilayers*. Phys. Status Solidi A, Vol. 209, No. 3, pp.512-518, 2012.
- [8] Swiston A. J., et al.: *Thermal and microstructural effects of welding metallic glasses by self-propagating reactions in multilayer foils*. Acta materialia 53.13: 3713-3719, 2005.
- [9] Sun X.: *Joining lightweight materials using reactive nanofilms*. Woodhead Publishing Limited, 2010.
- [10] Wang, J., Besnoin, E., Duckham, A., Spey, S. J., Reiss, M. E., Knio, O. M., & Weihs, T. P.: *Joining of stainless-steel specimens with nanostructured Al/Ni foils*. Journal of applied physics, 95(1), 248-256, 2004.
- [11] Oliver W. C., and Georges M. P.: *Measurement of hardness and elastic modulus by instrumented indentation: Advances in understanding and refinements to methodology*. Journal of materials research, 19.01: 3-20, 2004.

BONDING BY MICROBRACING: A DIE CONCEPT FOR THE QUANTIFICATION OF INFLUENCING VARIABLES USING MULTI-COMPONENT HIGH PRESSURE DIE CASTING (M-HPDC)

P. Messer^{1*}, A. Bührig-Polaczek¹, U. Vroomen¹

¹Foundry-Institute, RWTH Aachen University

ABSTRACT: Highly innovative lightweight design concepts demand for materials with specifications that cannot be reached by just one material. Besides fiber reinforced plastics (FRP), plastic-aluminum-hybrids contain a high potential for weight reduction. An innovative manufacturing process for those hybrids is the Multi-Component High Pressure Die Casting process (M-HPDC), which is an extension of the conventional high pressure die casting by an injection molding (IM) process. The aspired bond is realized by microbracing without any macroscopic undercuts, wherefore a lot of process knowledge needs to be acquired in order to achieve a loadable bond. In order to gain this knowledge die inserts are being conceived, which enable a precise regulation and monitoring of the die temperature. Especially the surface temperature of the aluminum component appears to have a major impact on the bond strength. These new die inserts will be used to make quantifiable propositions regarding the temperature influence. The high precision regarding the temperature control system will be achieved by using heat cartridges which are arranged contour adapted. Combined with thermocouples placed close to the overlap area, the temperatures will be monitored during the process.

KEYWORDS: hybrid, bond characterization, die concept, temperature management, joining method

1 INTRODUCTION

A lot of branches request highly innovative concepts for lightweight design. Since the demanded specifications are often not compliable by just one material, hybrids are needed which allow combining the advantages of two or more materials.

Besides fiber reinforced plastics (FRP), plastic-metal-hybrids contain a high potential for weight reduction. Due to the fact, that the production of FRP still requires a high manual effort, plastic-metal-hybrids can be produced using the well automatable processes High Pressure Die Casting (HPDC) and Injection Molding (IM). These circumstances allow the economic production of complex plastic-metal-hybrids even in high wage countries.

The good mechanical properties of aluminum combined with the high design flexibility and low density of plastics represent a predestined combination for complex lightweight applications.

By now several applications regarding plastic-metal-hybrids already exist and can be categorized in Post-Mold-Assembly (PMA) and In-Mold-Assembly (IMA) processes. Using the PMA-process, both joining members are produced sepa-

rately by independent processes and are finally put together by an additional step, such as gluing, riveting or welding. The IMA-process combines the primary forming of the second component and the joining process of the two components within one step, with the result of a shorter process chain. In both cases, the bond is mostly realized by a macroscopic tight fit, wherefore an adequate preparation of the semi-finished products becomes necessary. This additional effort results in long process chains and the necessity of extensive manufacturing equipment.

In the context of the Cluster of Excellence “Integrative Production Technology for High-Wage Countries” a combined HPDC- and IM-process is being developed. The major achievement of this development is a distinctly shortened process chain combining the primary shaping of both components and the actual joining process within one machine. Both joining members are produced on a die casting machine, which is expanded by an IM-unit. Thus the joining members are being primary shaped and joined even within the same die. The bond is realized by microbracing whereby sophisticated undercuts in the joining area become obso-

* Corresponding author: Foundry-Institute of RWTH Aachen University, Intzestr. 5, 52072 Aachen, phone: +49/241/80-98243, fax: +49/241/80-92276, p.messer@gi.rwth-aachen.de

lete. The shorter process results in lower investments for machinery and less required space. Using the developed M-HPDC-process, the thermal balance within the joining area has a major impact on the bond strength. Besides the melt temperature of the plastic component during injection, especially the surface temperature of the already solidified aluminum is of importance. Right now, die inserts are being developed with the view to making quantifiable points regarding the influence of thermal variables on the bond strength. The die inserts are equipped with extensive sensor technology close to the joining area as well as several possibilities of temperature control, so that the thermal conditions in the joining area will be precisely adjustable in small ranges.

2 CLASSIFICATION OF THE M-HPDC-PROCESS

M-HPDC is an advancement of the conventional HPDC-process which in turn belongs to the permanent mold casting processes. For classification and a better comprehension a brief overview of the area of application regarding the permanent mold casting in general and especially the HPDC will be given.

Compared to lost mold processes like sand casting, permanent molds can be used for more than one casting cycle and are not being destroyed during or after the casting. Permanent molds will usually be applicable for greater piece numbers due to high investment costs associated with the mold fabrication and depending on the process for fabrication plants.

2.1 HPDC-PROCESS

The most important process for thin-walled components or structural parts is the HPDC-process. The HPDC-process is mostly used for processing aluminum, magnesium and zinc. For example aluminum-HPDC is the most important casting process and accounted for more than 50% of the entire aluminum castings production in 2010. The HPDC-dies often need to last for more than 100.000 cycles [1].

The HPDC process begins with dosing a precise amount of the molten aluminum in the shot chamber by using a dispense robot. Subsequent to the dosing of the melt a piston pushes the material into the die with very high speed and high pressure. The actual filling process of the die just takes around 50-100 ms. During the solidification pressure period, which takes place right after the filling, there is still pressure on the piston in order to compensate the shrinkage resulting from the solidification of the aluminum underneath solidus temperature. As soon as a sufficient solidification is reached, the die opens and the part is ejected.

2.2 M-HPDC: HIGH PRESSURE DIE CASTING EXTENDED BY AN IM-PROCESS

Regarding the M-HPDC-process, the processing of the plastic component is added before ejecting the aluminum component. The M-HPDC-process is shown in Fig. 1.

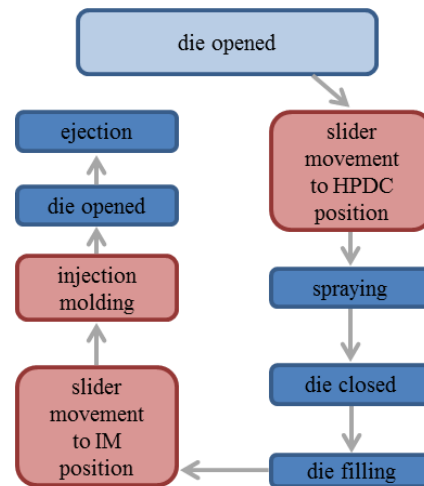


Fig. 1 Process cycle of the M-HPDC-process

Therefore a second cavity inside the die is opened by a slider. Parallel to the die casting of the aluminum, granulated plastic is already being dosed inside the injection molding unit by rotation of the screw. During the rotation, the granulated material is heated up predominantly by friction and transported to the front of the screw due to the rotation, so that the screw moves back during the dosing process. For the actual injection molding step, the screw is locked in the direction of rotation with the result that the screw can be used as a piston to inject the molten plastic by a translational movement. To ensure the plastic doesn't solidify between the injection molding unit and the actual plastic cavity, a hot runner system is used to keep plastic on the designated temperature. Similar to the HPDC-process, a solidification pressure phase follows immediately after injecting the plastic, which is kept until the gate is solidified. Finally the hybrid part gets ejected due to movements of the ejector pins.

3 INITIAL SITUATION

The Hybrid-I die, which has been used for the development of the M-HPDC-process in the first place, is shown in Fig. 2. The geometry of the part is an overlap shear tensile sample. Three temperature control channels are integrated in the movable die half for the temperature control of the metal-, plastic and overlap-zone and can be controlled independently.

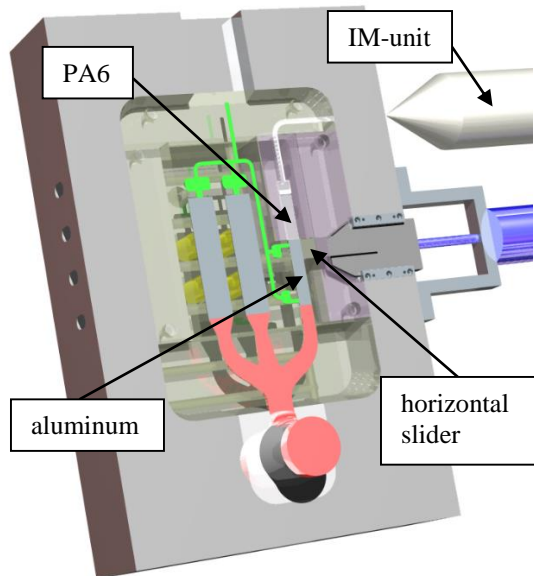


Fig. 2 Movable die half of the Hybrid-I die used for the development of the M-HPDC-process

3.1 TEMPERATURE INFLUENCE ON BOND STRENGTH

The research proceeded with the Hybrid-I die already showed, that the temperature has the major impact on the bond strength. The results presented in [2] show, that the temperature of the aluminum component needs to be kept on a high level until the plastic is completely injected in order to achieve a good bond strength. Besides high temperatures in the temperature control channel underneath the joining area, the plastic cavity also needs to be kept on a high level, since the molten plastic is passing the entire plastic cavity before the plastic reaches the joining area. Due to this fact, quite a significant amount of energy already dissipates before reaching the joining area so that the best results were achieved with inlet temperatures of the tempering oil above 180°C. The cycle time increases enormously, since the heat dissipation is a lot slower due to a smaller difference in temperature.

3.2 RESTRICTIONS REGARDING TEST EXECUTION

The Hybrid-I die has been constructed in order to be used on an HPDC-machine type Bühler H630SC, combined with an IM-unit provided by Maicopresse. The machine control that has been used only allows closing and opening the die once during each cycle, so that the slider movements need to be possible while the die is closed. Besides that, a suitable control program combining the functionalities of the HPDC-machine and IM-unit didn't exist. A detailed view of the joining area and the slider is shown in Fig. 3.

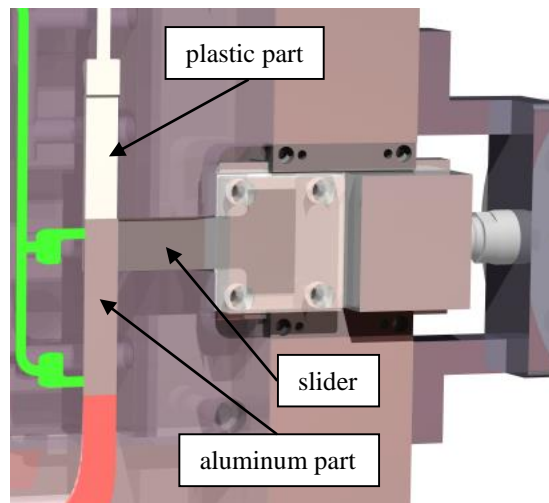


Fig. 3 Hybrid-I die: Detailed view on joining-area and slider

Although the tolerances of the slider are chosen as tight as possible, the low viscosity of liquid aluminum leads to flash insurance as well as problems regarding the movement of the slider. Besides that, the Hybrid-I die doesn't provide the possibility of integrating thermocouples, especially not close to the joining area. In this way the in- and outlet temperatures of the tempering oil are the only information that can be used for estimations regarding the actual temperature in the joining area. Since this information is quite vague it can only be used for qualitative estimations and not for quantitative propositions, which are necessary for the process comprehension.

Besides the Hybrid-I die, another die called "Hybrid-II" is used for manufacturing a more complex geometry with the shape of the "Erlangen-Beam".

4 CONCEPT OF NEW DIE INSERTS

Based on the gained knowledge and experiences with the dies mentioned above, the new die inserts are being developed.

In this chapter the requirements towards the die inserts are presented as well as underlying circumstances regarding existing machinery etc. Based on these conditions, the functionality of the slider and the concept of temperature management will be explained.

4.1 REQUIREMENTS TOWARDS THE DIE INSERTS AND UNDERLYING CIRCUMSTANCES

As shown in Chapter 3, the temperature is the most important factor concerning the bond strength. Therefore possibilities of monitoring temperatures close to the joining area are necessary, e.g. by using thermocouples. Since temperature control systems based on fluids are sluggish and thermal energy can hardly be brought in just locally, an

additional possibility for local heat input is demanded. The heat dissipation of the plastic melt which is reaching the joining area, needs to be counteracted by a reasonable placement of the gate. Besides the aspects addressing the temperature control of the die, the comparability with specimens joined by different joining methods also is of importance. The geometry is to be kept as close as possible to the DIN EN 1465 standard “Adhesives - Determination of tensile lap-shear strength of bonded assemblies” [3], since adhesive bonding is the most competing joining method.

For the setup of Hybrid-III, the existing die frame of Hybrid-II will be used, which results in limitations regarding e.g. outer dimensions and slider positions.

Table 1: Outer dimensions of the die inserts

	fixed die half	movable die half
Width [mm]	360	360
Height [mm]	500	500
Depth [mm]	80	110

4.2 SET UP OF DIE INSERTS

Fig. 4 shows the movable- and fixed-die-half of the conceptualized die inserts, which in the following will be called Hybrid-III. A more detailed view of the Hybrid-III-die-inserts is shown in Fig. 5.

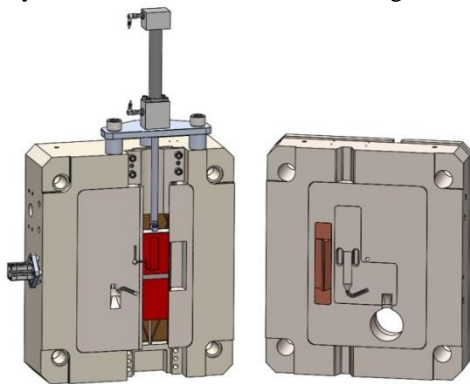


Fig. 4 Hybrid-III-die: Movable- (left) and fixed-die-half (right). Slider in IM-Position.

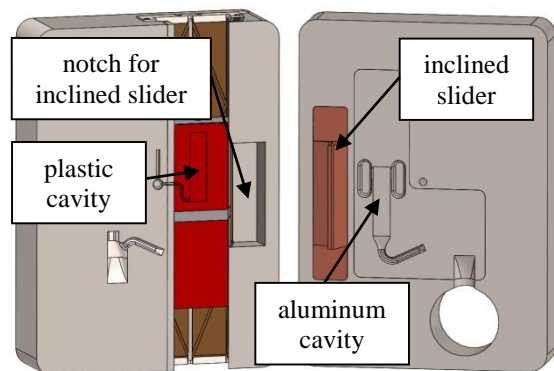


Fig. 5 Die inserts of movable- (left) and fixed-die-half (right). Slider in IM-Position.

The cavity of the aluminum component is placed in the fixed die half and the plastic cavity in the slider which in turn is located in the movable die half. Most of the runner as well as an additional cavity is placed in the movable die half to ensure the part will stick on this half when the die opens. The additional geometry is necessary due to the fact that the filling degree of the shot chamber should be between 50% and 70% [4]. Since the design of this additional cavity is not important for the functionality of this concept, it is not shown in the figures.

Depending on the sliders guiding system, the runner cannot be integrated totally in the movable die half. An extensive effort of sealing would be necessary due to the low melt viscosity of aluminum at processing temperature. The last sections of the runner (Fig. 6) are transferred to the fixed die half in which the aluminum cavity is located. On the challenge of sealing the slider towards the movable die half against aluminum melt will be gone into in Chapter 4.3.

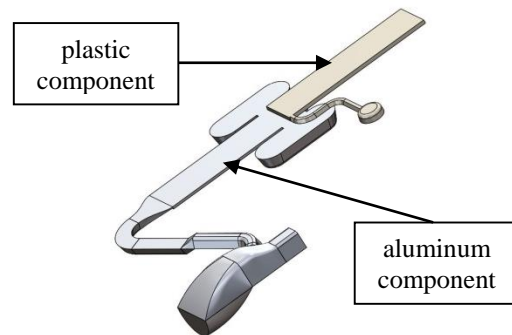


Fig. 6 Hybrid part consisting of actual specimen, gating system with runner and overflow

Based on the standard [3] the dimensions of each component are shown in Table 2. The part shown in Fig. 6 consists besides the actual specimen of the gating system with runner and overflow.

Table 2: Dimensions of the specimen (each component without runner etc.)

Width [mm]	25
Height [mm]	100
Depth [mm]	2,3
Overlap length [mm]	12,5

The chosen overflow length is 12,5 mm according to the standard. Nevertheless the construction is kept flexible in order to vary from that length by using different end stops for the slider. This way, the influence of the overlapping length towards the bond strength can be investigated.

The plastic cavity is arranged in the upper half of the slider (Fig. 5) since there is less sealing effort due to the higher viscosity of the plastic melt. The plastic melt is directed from the hot runner system, located in the fixed die half, towards the movable

die half. At this point the melt stream will be split up, partly filling the actual specimen cavity and partly filling an additional cavity which is necessary due to the size of the used injection molding unit.

4.3 SLIDER MOVEMENT AND FUNCTIONALITY OF THE LOCKING MECHANISM

The M-HPDC-process requires a possibility to disconnect the plastic cavity from the aluminum cavity during the HPDC-process. Due to the difficulties regarding the denseness of the horizontal slider used in the Hybrid-I die, a construction has been chosen that doesn't lead to the same difficulties. Instead of using the slider for disconnecting the aluminum cavity from the plastic cavity, the plastic cavity of the specimen is completely placed in it. The following paragraph will explain the slider movements and the functionality of the locking mechanism.

While the die is open, the slider moves to the HPDC-position and the spraying process starts. The die closes whereby the inclined slider (Fig. 7), which is part of the fixed die half, gets pressed in the notch of the movable die half (Fig. 5). Hereby, the slider is pressed to the left using the locking force (Fig. 7) with the result that a possibly existing gap at the sealing edge gets closed. Additionally the slider gets locked towards vertical movement by the locking pin shown in Fig. 7. In this position the HPDC-process follows. After the solidification pressure phase, the die opens, the slider unlocks and moves down towards an end stop, which ensures reproducibility regarding the overlap length.

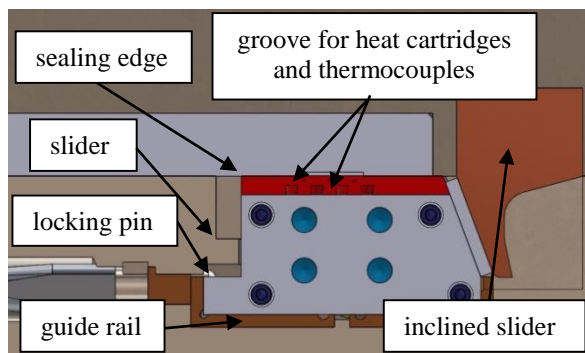


Fig. 7 Cross-sectional view of locking mechanism

4.4 TEMPERATURE MANAGEMENT

As already mentioned, the temperature management has a substantial influence on the bond strength. Since the aim of these investigations is not merely the achievement of loadable bonds but rather gaining knowledge of the parameters influencing the bond strength, thermocouples are essential and to be placed as close as possible to the joining area. The slider (Fig. 8) is designed modularly, so that the 7,5 mm cavity-plates on the slider

can be changed or replaced just by small effort. The initial set up provides grooves for heat cartridges 3,5 mm under the cavity surface to keep the later joining surface on a designated temperature. Small holes are provided for the integration of thermocouples 2 mm underneath the cavity-surface on the aluminum side of the slider, enabling a temperature control close to the surface. An insulating board will be used for thermal separation of both cavities, so that the temperature management of one half hardly affects the other.

Different from the positioning in the Hybrid-I die, the gate of the plastic cavity in the Hybrid-III die is placed right at the joining area. This way, the melt stream of the plastic moves release agent residues away from the joining area. Even more important is the fact that the melt is not cooling down so much before reaching the joining area. Additionally the solidification pressure applies longer on the melt in the joining area, whereby the amount of thermally indicated stresses will be reduced. This way a better and more reproducible bond is to be expected.

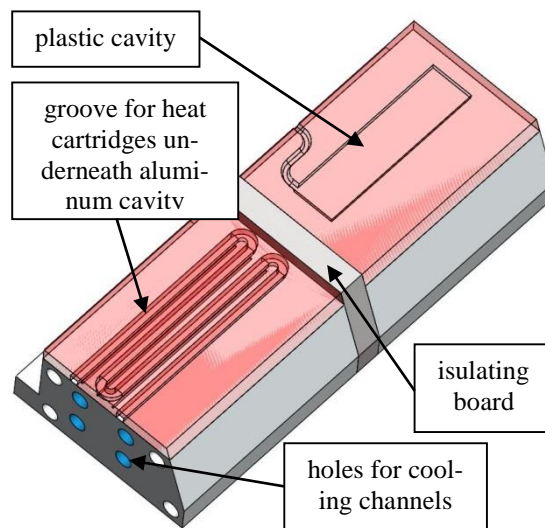


Fig. 8 Positioning of heat cartridges and thermocouples inside the slider

Furthermore the possibility of using alternating temperature technology enables additional options of temperature control. By this reason, the size of the slider is kept as small as possible, in order to reduce mass, affected by the alternating temperature technology.

5 CONCLUSION AND OUTLOOK

The temperature management has a major impact on the bond strength of hybrids, manufactured using the M-HPDC-process. Therefore quantifiable information regarding the actual temperature in the joining area are essential for enabling a well-founded die construction of more complex dies. The presented die concept provides the necessary requirements for the investigations addressing the

thermal influence on the bond strength. The new slider design minimizes the risk of gaining leakages due to the interlock mechanism which uses the locking force of the HPDC-machine. Furthermore the design of the specimen is chosen according to a standard, to allow a better comparability towards other joining methods.

Based on the current status, simulative investigations will follow, in order to place the temperature control channels and to determine the exact positions of the contour adapted heating cartridges and thermocouples.

6 ACKNOWLEDGEMENT

The authors would like to thank the German Research Foundation DFG for the kind support within the Cluster of Excellence „Integrative Production Technology for High-Wage Countries”.

REFERENCES

- [1] Bührig-Polaczek, A., W. Michaeli, and G. Spur, *Handbuch Urformen*. 2014: Carl Hanser Verlag GmbH & Co. KG
- [2] Brecher, C., *Integrative Produktionstechnik für Hochlohnländer*. VDI. 2011, Heidelberg [u.a.]: Springer. XXIII, 1177 S. : Ill., graph. Darst.
- [3] *DIN EN 1465, Klebstoffe –Bestimmung der Zugscherfestigkeit von Überlappungsklebungen; Deutsche Fassung EN 1465:2009*.
- [4] Nogowizin, B., *Theorie und Praxis des Druckgusses*. 2011: Schiele & Schön Berlin.

INDEX OF AUTHORS

A

Aldinger, S. 178
Arik, C. 157

B

Backe, S. 44
Baeten, A. 97, 105
Balle, F. 44
Bartelt, P. 75
Bernarding, S. 201
Bergmann, J.P. 36, 236
Bertram, B. 50
Beuscher, J. 188
Beyer, E. 125
Bielenin, M. 236
Brand, M. 184, 251
Brandt, R. 241
Braun, S. 225
Bräutigam, K. 36
Breidenstein, B. 211
Breuer, U. P. 44
Büttemeyer, H. 194
Bührig-Polaczek, A. 262
Busch, A. B. 241
Busse, M. 30, 146

C

Caba, S. 170
Carrado, A. 69
Caspari, T. 81
Clausen, J. 30

D

Decker, R. 118
Denkena, B. 211
Dietrich, F. 188
Dietrich, G. 225
Dilger, K. 188
Dlugosch, M. 63
Drechsler, K. 97, 105, 129, 247
Dröder, K. 184, 188, 251

E

Ehard, S. 129
Ellouz, M. 75
Emmelmann, C. 81, 194
Eyßell, C. 8, 12

F

Fang, X. F. 92
Fauster, E. 142
Fette, M. 164
Fiebig, C. 170
Frick, A. 178
Fritsch, J. 63
Fürst, A. 125, 146

G

Gall, M. 8, 12
Gebken, T. 146
Geweth, C. A. 135
Gödde, S. 157
Graf, A. 118
Grote, M. 92

H

Haack, M. 81
Hannemann, B. 44
Harhash, M. 69
Hauptmann, J. 125
Helbig, F. 151
Henning, F. 157
Hentschel, M. 164
Hergan, P. 142
Herrmann, A. S. 164, 194
Herrmann, H.-G. 201, 207, 216
Hiermaier, S. 63
Hinterhötzl, R. 247
Hipp, D. 125
Hühne, C. 22
Hülsbusch, D. 81
Hümbert, M. 230

I

Ihle, J. 63
Ireka, I. E. 151

J

Jelinek, M. 97, 105

K

Klaerner, M.	135
Klotzbach, A.	125, 225
Knabl, W.	86
Koch, M.	170
Kordisch, T.	75
Kräusel, V.	118
Kregl, L.	8, 12
Kreling, S.	188
Kroll, L.	112, 118, 135, 151
Krüger, L.	17
Kühn, M.	146, 188, 251
Kunze, A.	30

L

Lake, M.	257
Ladstätter, E.	129
Landgrebe, D.	118, 135
Langels, G.	257
Lang, H.	97
Lang, R. W.	8, 12
Leson, A.	225
Lippky, K.	188
Lukaszewicz, D.	63

M

Mader, A.	129
Mandel, M.	17
Marburg, S.	135
Meiners, D.	184
Messer, P.	262
Mitschang, P.	230
Mrotzek, T.	86
Müller, A.	188, 251
Müller, R.	135
Müller, S.	184

N

Nestler, D.	112
Neudel, C.	236
Neuhaus, S.	216
Niedziela, D.	151

O

Oblinger, C.	97, 105
-------------------	---------

P

Palkowski, H.	69
Pautzsch, R.	225
Pflug, E.	225
Pinter, P.	50
Prasanthan, V.	211
Prussak, R.	22

Q

Quirin, S.	216
-----------------	-----

R

Reinhart, G.	97, 105
Reuter, C.	75
Riemer, M.	135

S

Schaaf, P.	257
Schäfer, K.	15
Schledjewski, R.	142
Schmeer, S.	44
Schnurr, R.	188
Schricker, K. M.	36
Schwarz, M.	201, 207
Seiß, M.	86
Sen, S.	257
Sinapius, M.	22
Solbach, A.	81, 194
Spadaro, M.	178
Stambke, M.	36
Stefaniak, D.	22
Steffen, M. E.	170
Steiner, K.	151
Steinberg, J.	146
Steuernagel, L.	184
Stoess, N.	164
Stoll, M.	38
Strauß, B.	8, 12
Summa, J.	201, 207
Szallies, K.	236

T

Trauth, A.	57
Trautmann, M.	112
Tröltzsch, J.	151
Tröster, T.	75

V

van der Auwera, R.	30, 146
von Hehl, A.	30
Vroomen, U.	262

W

Wagner, G.	112
Wallner, G. M.	8, 12
Walther, F.	81
Weidenmann, K. A.	38, 50, 57, 157
Wetzig, A.	125
Wöstmann, F.-J.	146
Wührl, M.	135
Wulfsberg, J.	164

Y

Yüksel, F.	247
-----------------	-----

Z

Zoch, H.-W.	30
Zopp, C.	112

IMPRINT - IMPRESSUM

EURO HYBRID - MATERIALS AND STRUCTURES 2016 - PROCEEDINGS

Editors

Joachim M. Hausmann, Marc Siebert

Compilation

Fraunhofer-Institut für Intelligente Analyse- und Informationssysteme IAIS

© Deutsche Gesellschaft für Materialkunde e.V.

Hahnstraße 70, D-60528 Frankfurt

E-Mail: dgm@dgm.de

ISBN 978-3-88355-414-3

Das Werk einschließlich seiner Teile ist urheberrechtlich geschützt. Jede Verwertung außerhalb der engen Grenzen des Urheberrechtsgesetzes ist ohne Zustimmung der DGM und der Herausgeber unzulässig und strafbar. Das gilt insbesondere für Vervielfältigungen, Übersetzungen, Mikroverfilmungen und die Einspeicherung und Verarbeitung in elektronischen Systemen.

This work including all its parts is protected by copyright. Any use outside the strict constraints of the German Copyright Law without the permission of the DGM and the editors is prohibited and liable to prosecution. This applies particularly for reproduction, translation, adaption on microfilm, and storage or processing in electronic systems.